IFM-GEOMAR
Leibniz-Institut für Meereswissenschaften
an der Universität Kiel

# THE INFLUENCE OF SUBDUCTION ZONE DEFORMATION AND GEOMETRY ON THE GENESIS OF MEGATHRUST EARTHQUAKES AND TSUNAMIS

**Habilitationsschrift vorgelegt von**

**Heidrun Kopp**

am

Institut für Geowissenschaften
Christian-Albrechts-Universität zu Kiel

im November 2010

**Zusammenfassung / Abstract**

**1. Motivation and Aims**

**2. Introduction**
**2.1 Subduction Zone Kinematics**
**2.2 Megathrust Seismogenesis**

**3. Original Research**
**3.1 Framework Concept on Margin Structure and Geometry of Accreting and Eroding Systems**
3.1.1 Distinct domains: Across-strike margin segmentation
3.1.1.1 From one big accretionary wedge to three individual domains
3.1.1.2 Erosive margin segmentation: differences and similarities to accretive systems
3.1.1.3 Continent-island arc collision: choking subduction
3.1.2 Mechanisms of mass transfer: Along-strike margin segmentation
3.1.2.1 From accretion to erosion: varying mass transfer offshore Java
3.1.2.2 A closer look: lower slope morphology in response to modes of mass transfer
3.1.2.3 Lower plate impact: forearc segmentation related to lower plate structural diversity
3.1.3 The décollement zone
3.1.3.1 The subduction channel: spatial variations of the plate interface
3.1.3.2 Subduction erosion: dismembering the margin from below
3.1.4 Evolving methodology
3.1.4.1 More than imaging: combining tomographic inversion and forward modeling
3.1.4.2 Using statistics: divergence analysis of seismic data

**3.2 Subducting basement relief: subduction zone deformation and upper plate response**
3.2.1 Ridge subduction: Deep structure of the Lesser Antilles Island Arc
3.2.2 Plateau subduction I: Forearc deformation at the northern Hikurangi Margin
3.2.3 Plateau subduction II: Roo Rise subduction and the 1994 Java tsunami earthquake

**3.3 Seismic rupture and tsunami hazard in relation to plate interface geometry**

**4. Synopsis**

**5. Future Prospects**

**Acknowledgements**

**References**

**Appendix**

## Zusammenfassung

Die hier vorgelegte kumulative Habilitation umfasst die Resultate eines fast zehnjährigen Vorhabens mit dem Ziel, das 'Innenleben' konvergenter Plattengrenzen abzubilden. Diese Subduktionszonen werden durch das Aufeinandertreffen zweier Lithosphärenplatten gebildet, bei dem sich üblicherweise die ozeanische Lithosphärenplatte unter die Oberplatte schiebt und entlang der Subduktionsverwerfung mit einer Geschwindigkeit von einigen Zentimetern pro Jahr in den Erdmantel zurückgeführt wird. Der dabei erfolgende Spannungsaufbau kann sich während eines Erdbebens schlagartig lösen. Starkbeben, wie sie in Subduktionszonen beobachtet werden, treten in der seismogenen Zone auf, die sich entlang der Plattengrenze typischerweise in Tiefen zwischen 5-40 km findet. Diese Interplattenbeben sind die stärksten Erdbeben auf unserem Planeten. Als Folge der submarinen Lokation vieler Subduktionszonen sind Tsunamis ein häufiges Phänomen in Verbindung mit Subduktionsbeben. Aufgrund der Tatsache, dass 60% der Weltbevölkerung in einer Entfernung von weniger als 50 km von der Küste leben, gehören die Auswirkungen von Subduktionsbeben und damit verbundener Sekundärprozesse zu den schlimmsten durch Naturgefahren verursachten Schäden mit den höchsten Opferzahlen. Das Sumatra-Beben vom Dezember 2004 und der dadurch ausgelöste Tsunami haben eindringlich verdeutlicht, dass diese Prozesse nicht nur die Bevölkerung vor Ort treffen, sondern globale gesellschaftliche Auswirkungen zeigen können. Vor diesem Hintergrund wurden die hier vorgestellten Studien initiiert, um zu einem verbesserten Verständnis der geologischen Rahmenbedingungen der unterschiedlichen Klassen von Subduktionszonen, sowie des Einflusses und der Kontrolle der Geometrie der Verwerfungszone auf das seismische Verhalten und die Entstehung von Tsunamis zu gelangen. Im Rahmen von insgesamt sieben Forschungsfahrten im Indischen Ozean, im Atlantik sowie Pazifik wurden geophysikalische Daten gewonnen, deren Informationsgehalt im Zuge der hier vorgestellten Untersuchungen ausgewertet wird. Die Ergebnisse dieser Studien sind in einer Reihe inhaltlich zusammenhängender Publikationen eingeflossen, die im Anhang vorgestellt werden und im folgenden in **Fettschrift** referenziert sind. Die nachstehenden Kapitel bilden das Dachpapier dieser Untersuchungen:

Kapitel 1 stellt die Motivation und die in den Studien verfolgten Ziele vor. Ausgehend von der Beobachtung, dass manche Segmente oder Teilbereiche von Subduktionszonen Starkbeben mit Magnituden > 8.5 erzeugen, während in benachbarten Segmenten lediglich Beben mit wesentlich geringerer Magnitude auftreten, wird vermutet, dass die Struktur und Geometrie einzelner Subduktionszonen hochvariabel ausgebildet sein müssen, um diese Magnitudenverteilung auslösen zu können. Eines der Ziele dieser Arbeit ist daher, die strukturelle Variabilität zwischen Teilbereichen einer Subduktionszone zu erfassen. Dies geschieht exemplarisch anhand mariner Daten der Sunda-Subduktionszone vor Indonesien. In Kapitel 2 wird der Stand der Forschung in Bezug auf die Kinematik konvergenter Plattenränder zusammengefasst. Dabei kommt der Rolle des Subduktionskanals, also des Bereiches zwischen den beiden Platten, in dem Material aus dem Tiefseegraben in größere Tiefen geführt wird, bei der Erdbebenentstehung besondere Bedeutung zu. Auch wird die mögliche Funktion subduzierter Morphologie als Nukleations- bzw. Terminierungslokation seismischer Ruptur beleuchtet. Diese Konzepte werden in Kapitel 3 vertieft, in dem die im Appendix gesammelten Originalarbeiten in Bezug zueinander gesetzt werden. Kapitel 3.1 befasst sich mit dem strukturellen Rahmenkonzept konvergenter Plattenränder, das aus den Untersuchungen entwickelt wurde, die in den insgesamt zehn Publikationen der Unterkapitel 3.1.1.1-3.1.4.2 vorgestellt werden. Durch die Abbildung multipler kinematischer Grenzflächen innerhalb des Subduktionskomplexes, die Ausdruck der Segmentierung des Akkretionskeils sind, wurde darin die ursprünglich vorherrschende Vorstellung einer kontinuierlichen Akkretion widerlegt. Der Vergleich mit erosiven Systemen hat gezeigt, dass sich eine ganze Anzahl struktureller Elemente sowohl in akkretionären als auch in erosiven Systemen ausbildet. Zudem führen Variationen im Materialtransfer zwischen Unterplatte und Oberplatte zu einer Segmentierung der Plattengrenze in Streichrichtung. Abschließend werden in diesem Kapitel neue methodische Ansätze diskutiert, die im Rahmen der

Datenanalyse entwickelt wurden. In Kapitel 3.2 wird die Subduktion ozeanischer Rücken- und Plateaustrukturen anhand dreier Lokationen im Atlantik, Pazifik sowie im Indischen Ozean untersucht. Der letzte Abschnitt in Kapitel 3 fasst die vorhergehenden Ergebnisse zusammen und analysiert den Einfluss subduzierter morphologischer Strukturen auf die Seismizität vor Java. Die strukturelle Variabilität der Subduktionszone kontrolliert maßgeblich die Entstehung von Erdbeben entlang des Sunda-Bogens. Kapitel 4 umfasst eine Übersicht aller hier vorgestellten Arbeiten sowie einer Anzahl von Dissertationen, die aus den Untersuchungen hervorgegangen sind. Das Schlusskapitel stellt eine Reihe innovativer Forschungsstrategien und neue Forschungsfelder vor, mit deren Hilfe offene Fragestellungen in Zukunft beantworten werden können.

## Abstract

The results presented in this cumulative 'Habilitation' document a nearly decade-long effort to image the interior regime of convergent margins. Subduction zones are formed by the underthrusting of a lithospheric plate (commonly of oceanic nature) underneath the overriding plate along the subduction thrust fault or 'megathrust'. The subducting plate moves into the earth's mantle at rates typically measured in centimeters per year. Stress accumulation in this high-friction setting may be released through seismic slip during an earthquake. The interplate environment hosts the seismogenic zone (typically at depths ranging from 5-40 km) where megathrust earthquakes are generated. These interplate earthquakes are the largest occurring on the planet. Due to the marine setting of subduction zones, tsunami waves are a common phenomenon in relation with megathrust events. As 60% of the global population lives within 50 km of the coast, damage and casualties related to subduction zone earthquakes or earthquake-triggered events rank highest among all geohazard-associated losses. The 2004 Sumatra earthquake and associated secondary processes served as a reminder that these hazards are major threats to society not only in regions from which they originate, but also on a global scale. Against this backdrop, the studies summarized here were initiated to improve our knowledge on the geological framework of the different types of subduction zones and on the control of the geometry of the subduction zone on seismic rupture and tsunami hazard. Data acquisition during seven research cruises in the Indian Ocean, Caribbean, and Pacific yielded a wealth of information that was analyzed in the course of these investigations. The results have been published in a series of inter-related scientific papers presented in the Appendix and referenced in **bold** font in the main text. The umbrella for these investigations is provided in the following chapters:

Chapter 1 sets the stage by introducing the motivation and aims of the studies. Based on the observation that some segments of subduction zones produce large megathrust events of moment magnitudes > 8.5, whereas other portions of the same margin experience only moderate size earthquakes, the implication is drawn that individual subduction zones must show a high variability in their structure and geometry to induce such diverse seismicity. Elucidating the structural diversity between different margin segments using exemplary field data from Indonesia's Sunda Margin is therefore one of the goals of this work. Chapter 2 summarizes the current knowledge on convergent margin kinematics. The notion that the subduction channel, which hosts the material sandwiched between upper and lower plate, influences megathrust seismogenesis is introduced here in relation to the role of subducted basement relief serving as earthquake nucleation or termination patches. These concepts are expanded and discussed in Chapter 3, which presents the original research documented in the contributions comprising the Appendix and puts them in context. Chapter 3.1 reviews the framework concept on margin structure and geometry, which was developed based on the investigations published in the ten papers discussed in Chapter 3.1.1.1-3.1.4.2. The traditional perception of 'steady-state' accretion is disproved by the recognition of multiple kinematic boundaries in a single subduction complex, resulting in across-strike forearc segmentation. Comparison with erosive systems shows that

many elements present in accretionary settings are also recognized in erosive margins. Furthermore, variations in lower to upper plate mass transfer result in along-strike margin segmentation. This chapter also inspects new analysis schemes developed during the course of the studies. Chapter 3.2 then lays the bridge between kinematics and dynamics and links three papers, which examine oceanic plateau and ridge subduction at locations in the Atlantic, Pacific, and Indian Ocean. The last section of Chapter 3 extracts the essence of the previous investigations and reviews the notion that subducting oceanic relief may act as 'asperities' or 'barriers' to seismic rupture and relates this to the observed absence of magnitude > 8 subduction earthquakes along the Java Trench.

A synopsis is provided in Chapter 4, which also inspects the results of a number of PhD-theses that emerged from the studies. The final Chapter 5 discusses unresolved issues and problems in subduction zone research and provides an outlook on future research strategies to tackle these open questions.

# 1. Motivation and Aims

The recurrence of catastrophic earthquakes and tsunamis at convergent plate boundaries provides the lasting motivation and impetus to investigate the influence of subduction zone deformation and habitats on the hazardous behavior of continental margins. The fundamental concept of plate tectonics has been established decades ago, along with the observation that the largest earthquakes on the planet occur along the megathrust fault of subduction zones. In that timespan, however, our understanding of what governs the magnitude, source region and recurrence interval of megathrust events has not advanced sufficiently to provide robust answers (Chapter 2) to open problems. This must be attributed to the fact that large parts of the seismogenic zone and forearc are commonly submerged in deep water and difficult to access at the majority of margins. Marine geophysical techniques, which are able to image the complex structures in these settings with sufficient coherency and depth penetration, have only evolved in recent years. And while satellite altimetry provides images of the seafloor and its large-scale structures on a global scale (Smith & Sandwell 1997), local tectonic features may only be identified in ship-based high-resolution bathymetric maps. It is thus crucial for the advancement of our scientific knowledge to expand the marine observational basis of subduction zones – an effort that is certainly not completed.

To elucidate the controls on megathrust rupture events requires an improved understanding of their nucleation. A key question here is why some subduction zones host Mw > 8.5 earthquakes, whereas others are limited to magnitudes < 8. While it is observed that Mw > 8.5 earthquakes commonly nucleate in margins fronted by sediment-flooded trenches (e.g. 1960 S. Chile, 1964 Alaska, 1965 Rat Islands, 1986 Aleutians, 2004 / 2005 Sumatra), these events also occur at erosional margins (e.g. 1877 N. Chile, 1952 Kamchatka, 1963 Kuril Islands). Though a number of correlations between the nature and behavior of the seismogenic zone and geological parameters have been brought forward (e.g. sediment input (Ruff 1984), thermal evolution (Hyndman *et al.* 1997), upper and lower plate inhomogeneities (e.g. Collot *et al.* 2004; Bilek 2007)), the robustness of these connections may only be evaluated as assumptions are replaced by data. Obviously, it will take the effort of the entire scientific community to establish the influence of the diverse geological, physical and geochemical parameters on the evolution and behavior of subduction zones. A decisive factor in that context is provided by geophysical methods, which open the opportunity for a re-assessment of convergent margin structural models (Chapter 3.1) in order to 1) study the tectonic habitat of earthquake slip and tsunami source regions and 2) understand the related processes and mechanisms, i.e. what processes govern the heterogeneous slip distribution observed at many margins and what mechanisms trigger tsunamis (Chapters 3.2 & 3.3) such as the 2004 Sumatra event.

The catastrophic earthquake and tsunami of December 26, 2004 offshore northern Sumatra sparked many of the questions addressed in this work: why, along a single convergent margin, do some segments produce large megathrust events whereas other portions of the very same margin only nucleate earthquakes of moderate magnitude? How and why are devastating tsunamis generated in both segments? These observations implicate the notion that individual subduction zones or segments thereof differ in their structure and geometry to induce such diverse behavior, but the structural details remained elusive. One of the aims of the studies presented here is to unravel the structural diversity of convergent margins and between individual subduction zone segments. Field data from Indonesia's Sunda Margin have provided an important stepping-stone in resolving these issues, by delivering images of the seafloor and subsurface in unprecedented resolution, which show segmentation to be far more complex than previously inferred. The Sunda accretionary wedge was a type-example of 'steady-state' accretion forming a uniform body of imbricate thrusts (Hamilton, 1988). However, the newly observed segmentation of structure *across-strike* (3.1.1) correlates to mechanics that vary during an earthquake cycle (Wang & Hu

2006). Furthermore, the recognition of splay faults (3.1.3) and their potential role in tsunami excitation (Moore *et al.* 2007) represents an important advance for hazard mitigation efforts. In addition, the impact of lower plate structural diversity on *along-strike* segmentation is further unraveled (3.1.2). Beside these aspects, which apply to the lower plate as well as to the upper plate, the nature of the plate interface must be elucidated (3.1.3) to decipher mechanisms of mass transfer as well as the geometry of the décollement zone. A positive spin-off product of these studies is the development of novel techniques and tools, which provide different avenues for the analysis of seismic data (3.1.4).

One aspect, which is still not well understood, is the impact of underthrusting lower plate relief on the deep deformation of a subduction zone and on the spatial and temporal variation in slip behavior. While the surface effects of subducting seamounts have been documented in high-resolution bathymetry data (e.g. von Huene *et al.* 2000), their influence on fault zone structure at depth remains elusive (Bangs *et al.* 2006). Lower plate heterogeneities occur at subduction zones worldwide (Chapter 3.2) and thus pose a common phenomenon, whose role as asperities or barriers to seismic rupture (Chapter 3.3) constitute a central control on subduction zone seismicity.

# 2. Introduction

## 2.1 Subduction Zone Kinematics

The division of convergent margins into two basic types based on their dominating mode of mass flux (accretionary or erosive) (e.g. Clift & Vannucchi 2004) represents a simplification for many margins globally, where an along-strike segmentation results in accretionary segments contiguous to erosive segments along a single margin. Accretion and erosion may occur coevally (e.g. Bangs *et al.* 2006) and, more importantly, must be viewed as transient processes dependent on sediment supply and lower plate structure. Any subduction zone classification must thus include a time reference to account for the structural evolution of the margin.

The seismic images and multibeam bathymetry presented in Chapter 3 offer a detailed view into the shallow and deeper portions of subduction zones. Common to both, accretionary and erosive settings, is a frontal prism up to 30 km wide (von Huene *et al.* 2009), but usually of smaller dimensions, adjacent to the trench. The frontal prism is composed of trench sediments or upper plate material, which was transported into the trench by mass wasting processes and which is subsequently recycled into the upper plate. Topographic perturbations of the frontal prism are commonly observed where lower plate basement relief ploughs through the frontal prism and causes erosional scars and entrant structures. Large embayments mark areas where the frontal prism has been partially or completely eroded (e.g. von Huene 2008). These features are transient, and the prism will heal and retain its original pre-collisional configuration after the basement topography is subducted to greater depth. Mechanically, the frontal prism is significant as it increases the load on the subduction channel, thereby increasing pore fluid pressures and reducing interplate friction (von Huene *et al.* 2009).

Towards the arc, the frontal prism merges into the outer wedge (Wang & Hu 2006), which may represent an accretionary prism in accretionary settings or may be composed of disaggregated arc material where erosion dominates. Seismic velocities are similar in both settings and thus the composition is difficult to distinguish from seismic records alone. A clear increase in seismic velocities from the frontal prism to the outer wedge is generally observed in refraction seismic data (e.g. Kopp *et al.* 2002) and indicates increasing rigidity and material strength. Seismic velocities may thus be used as a reference to define the trenchward extent of the outer wedge,

which is commonly several tens of kilometers wide. In accretionary settings, the prism grows seaward by incorporation of trench sediment transferred from the frontal prism and thickens by imbricate thrusting (a process that is also observed in the frontal prism). In the erosional case, the outer wedge forms the seaward part of the arc framework rock characterized by fracturing and disintegration of the material, which results in reduced seismic velocities.

The outer wedge fronts the inner wedge, which may be composed of igneous or metamorphic basement or of metamorphosed and lithified fossil accretionary prisms (von Huene *et al.* 2009). Structurally, this margin core forms the strongest and most uniform segment. In accretionary settings, the inner wedge is often termed 'backstop' (Byrne *et al.* 1993), in analogy to a rigid 'bulldozer blade'. At the Sunda Margin, the transition from the inner wedge to the outer wedge is not gradational, but marked by a splay fault system (Kopp *et al.* 2001; 2002). Splay faults connect to the subduction zone main thrust at depth and intercept the seafloor at high angles. An extensive splay fault system has also been recognized at the Nankai Margin (Bangs *et al.* 2007) where its role in tsunami generation is discussed (Moore *et al.* 2007).

The key control on mass flux in accretionary and erosive settings is the sediment supply in the trench in relation to the capacity of the subduction channel, which is the conduit for the subducted sediment between the upper plate and lower plate. The subduction channel is commonly a low velocity zone (e.g. Calahorrano *et al.* 2008), which is fed with trench sediment and / or erosional debris. While thickness variations of the subduction channel can be attributed to structural variations of the incoming plate (e.g. Sage *et al.* 2006), controls on absolute capacity remain elusive. Trench sediment abundance of ~1 km seems to be a benchmark threshold globally (Clift & Vannucchi 2004), as frontal accretion starts when this value is exceeded, whereas the entire sediment column is subducted for values up to 1 km thickness. Recent studies indicate that physical properties vary spatially along the subduction channel (Calahorrano *et al.* 2008; Vannucchi *et al.* 2008) and rigidity, compaction and friction increase with depth until overburden load is high enough to allow elastic deformation in the seismogenic zone (Calahorrano *et al.* 2008). Updip of the seismogenic portion of the subduction thrust, the absence of seismicity in the frontal prism segment is related to the material weakness of both the frontal prism and the subduction channel. The interplate fault, which separates both regimes, is therefore weak as well.

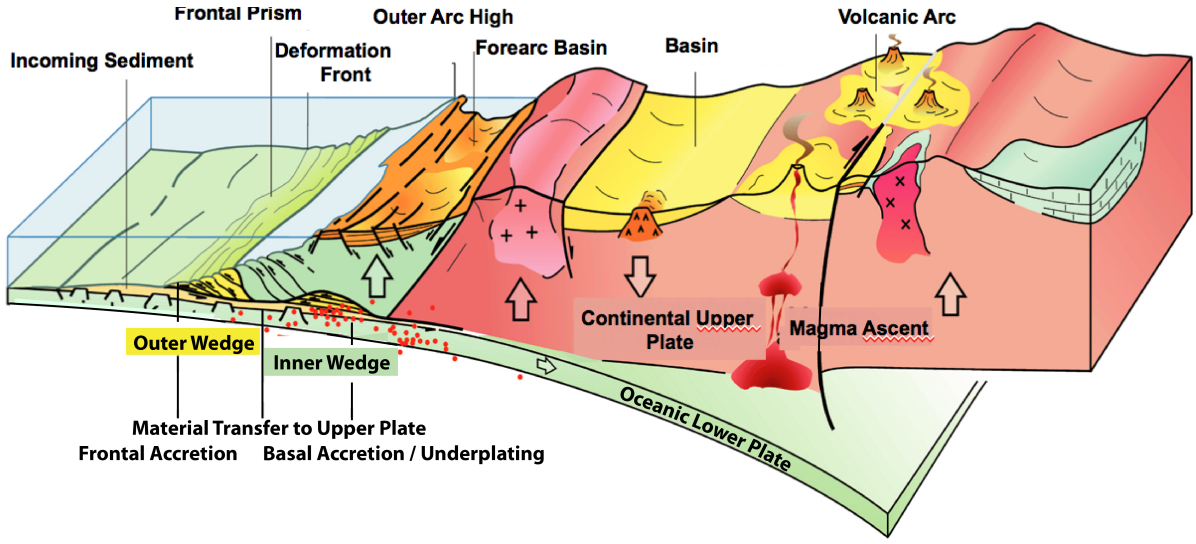


*Sketch through an accretionary subduction zone: The oceanic lithosphere subducts beneath the upper plate. Material transfer occurs in the marine forearc, where incoming sediment is frontally accreted and incorporated into the frontal prism or underplated beneath the outer forearc high. Basal erosion would dominate in erosive settings (not shown). The updip limit of the seismogenic zone correlates with the transition from outer wedge to inner wedge. = Seismogenic Zone. Modified from GFZ Potsdam.*

### 2.2 Megathrust Seismogenesis

In addition to the societal relevance related to geohazards, subduction zone processes are crucial for understanding fundamental scientific questions, such as the evolution of continental crust and the fate of subducted material or the role of subduction as a driving force for plate tectonics. A prerequisite for the resolution of these issues is obviously a detailed knowledge of the anatomy of subduction systems, because any unifying concept must be based on this framework. The observations on margin structure and geometry of different systems provided in Chapter 3.1 contribute towards this goal. While obviously fundamental differences regarding mass flux exist in accretionary and erosive margins, structural similarities such as the existence of a subduction channel or across-strike segmentation defined by transient mechanical behavior may help to explain the observed seismic slip distribution. Slip motion on a fault depends on the tectonic environment of the source region (Bilek 2007). Two concepts are considered in Chapter 3.3: (1) the role of the subduction channel or décollement zone and (2) the role of underthrusting oceanic basement relief forming heterogeneities along the megathrust fault of subduction zones.

(1) The original notion that trench sediments influence megathrust seismogenesis (Ruff 1989) is expanded in Chapter 3.3 to the concept of the subduction channel. This may potentially explain the occurrence of large Mw > 8.5 earthquakes in accretionary as well as erosional margins (Scholl 2010). The magnitude of an earthquake is associated with the size of its rupture zone. Where rupture propagation is facilitated along margin segments characterized by a subduction channel filled by trench sediment and/or upper plate erosional debris, larger magnitudes may be expected. This hypothesis implies that the geometry and thickness of the subduction channel exerts a greater influence on rupture propagation than the nature of material in it (trench sediments and/or upper plate erosional debris) (Tanioka *et al.* 1997; Bilek & Lay 1999). Continuation of rupture would thus be expected to efficiently occur in margin segments where material is underthrust to the depth of the seismogenic zone and where little perturbation by subducted basement relief occurs. This may provide an explanation for the observed large megathrust events in accretionary as well as erosive segments of e.g. the Chile subduction zone (1877 Northern Chile: Mw = 8.8; 1960 Southern Chile Mw = 9.6; 2010 Central Chile Mw = 8.8).

(2) The second aspect applies to margins where the subduction channel is breached by underthrusting basement relief, which is then in direct contact with the upper plate. The question of whether subducting topography acts as an asperity or barrier to seismic rupture is still not solved (Bilek & Lay 2002). Underthrusting basement highs (seamounts, aseismic ridges, oceanic plateaus etc.) will lead to variations in mechanical coupling, but to what consequence remains unclear. The control of seamounts on the frictional environment is discussed in Chapter 3.3 and related to the tectonic setting along the Java convergent margin, where seismicity is documented in moderate magnitude earthquakes.

## 3. Original Research

### 3.1 Framework concept on margin structure and geometry of accreting and eroding systems

'Steady-state' accretion of sedimentary wedges crossing the entire forearc has formed the basis for many early concepts on subduction zone evolution. In particular, the Sunda Margin south of the Indonesian archipelago has been cited as type example of a 'classical accretionary subduction zone' (e.g. Hamilton 1988). The concepts presented in this chapter document that the structural

evolution of convergent margins is far more complex, resulting in distinct domains of *across-strike* segmentation (3.1.1). Many similarities in the structural elements are identified in accretionary as well as erosive margins. Furthermore, despite its popular simplicity, the end-member classification (accretionary vs. erosive) generally does not apply to margins as a whole, as rapid transition from accretionary to erosive regimes (3.1.2) results in *along-strike* segmentation. The subduction channel or décollement zone is common to both settings and its characteristics control sediment flux and govern whether accretion or erosion dominates (3.1.3). The concepts outlined here have developed from observations identified in high-quality data (seismic wide-angle refraction and multichannel reflection data, high-resolution bathymetry), which have been analyzed using state-of-the art processing modules in combination with novel methods (3.1.4).

### 3.1.1 Distinct domains: Across-strike margin segmentation

The recognition of discrete margin segmentation into a frontal prism, outer and inner wedge has resolved many assumptions on structural differences between accretionary and erosive settings (e.g. von Huene *et al.* 2009). Though mass flux differs significantly in both regimes, the corresponding structural segments behave similar during a seismic cycle (Wang & Hu 2006). The frontal prism, which is either composed of trench sediments in the accretionary mode or of slope debris in the erosive mode, is too weak to effectively store elastic strain from plate convergence and thus deforms permanently. Elastic strain is stored in the outer wedge during the interseismic phase and is released during the co-seismic period, causing deformation and increased pore-fluid pressures in the frontal prism.

#### 3.1.1.1 From one big accretionary wedge to three individual domains

The recognition of multiple kinematic boundaries in a single subduction complex across the Sunda Margin (**Kopp & Kukowski 2003**) disproved the notion of 'steady-state' accretion lasting millions of years. For the first time, segmentation into three discrete domains was identified from a combined analysis of pre-stack depth migrated seismic data and deep-penetrating refraction data and replaced the previous assumption of a uniform wedge. Landward of the deformation front, the unstable frontal prism is characterized by numerous slides in the high-resolution bathymetry data. Its variable seismic character is associated with constant deformation as trench sediment is frontally accreted. Structural investigations of conjugate faults indicate a weak basal detachment in the décollement zone. A stable seafloor is imaged across the outer wedge. A lateral increase in seismic velocities indicates increasing material strength. The outer wedge is composed of accreted sediment transferred from the frontal prism and is built against the arc framework basement rock of the inner wedge, which acts as backstop to the outer wedge. While shallow backstops at less than 10 km depth have been identified e.g. off Peru (von Huene *et al.* 1988), off Alaska (Fruehn *et al.* 1999) or in the Ryukyu forearc (Font *et al.* 2001), **Kopp & Kukowski (2003)** for the first time successfully image the backstop underneath the forearc basin at >10 km depth in reflection and refraction data. Its significance for subduction zone evolution results from the distinct strength contrast between the outer wedge and the inner wedge, controlling forearc geometry (Dahlen 1990). In addition, the across strike segmentation defined here was observed along margin segments characterized by frontal as well as by oblique subduction.

#### 3.1.1.2 Erosive margin segmentation: differences and similarities to accretive systems

Many elements of the across-strike segmentation of three distinct domains established for accretionary settings (**Kopp & Kukowski 2003**) are also recognized in erosive regimes. **Zhu et al. (2010)** investigate the Central American Margin offshore Costa Rica. This erosion-dominated trench system is characterized by a highly tectonized frontal prism extending ~15 km landward from the deformation front. Similar to the accretionary setting, the frontal prism transitions into the outer wedge, which here, however, consists of disaggregating basement rock compared to the lithified trench sediment in the accretionary setting described by **Kopp & Kukowski (2003)**. Amplitude analysis of wide-angle seismic data by **Zhu et al. (2010)** documents landward

decreasing seismic attenuation from the frontal prism to the outer wedge. This is consistent with a change in lithology from the sedimentary composition of the frontal prism to the igneous rocks of the outer wedge. Generally low Qp values are indicative of highly fractured basement rocks in the outer wedge, which is experiencing basal erosion and disintegration of rock units by hydrofracturing.

#### 3.1.1.3 Continent-island arc collision: choking subduction

The systems described in 3.1.1.1 and 3.1.1.2 represent the accretionary and erosive end-members of oceanic subduction. Continent-island arc collision forms the counterpart to these systems and is discussed in **Shulgin et al. (2009).** In **Shulgin et al. (2009)** we investigate the margin geometry at the transition from oceanic subduction to continent-island arc collision by studying the incipient collision of the Australian margin with the Banda Island Arc. This system may be regarded as a precursor of a fold-and-thrust belt, which may develop in the forearc as collision progresses. A number of tectonic structures observed across the system are similar to elements documented in the accretion-dominated margin segments to the west described in **Kopp & Kukowski (2003)**, including a subduction channel imaged beneath the broad frontal prism and the accretionary prism forming the outer wedge. Dynamics are controlled by the deep geometry of the system: the collision of the 10-12 km thick Australian crust causes wide-spread backthrusting of the accretionary prism over the up to 24 km thick Sumba Ridge in the north. The structural diversity along the transect could be characteristic of systems at the transition from oceanic subduction to island arc collision. The study of **Shulgin et al. (2009)** hence documents the structural framework and deep geometry of nascent collisional systems as they are observed e.g. around Taiwan (Huang *et al.* 2006).

### 3.1.2 Mechanisms of mass transfer: Along-strike margin segmentation

Despite its elegant simplicity, the commonly employed division of subduction zones into three types (accretionary, intermediate, erosive) (e.g. Clift & Vannucchi 2004) falls short of accurately describing variations in mass flux along individual margins. Sediment input, subduction channel capacity and plate convergence rate exert first-order controls on the mode of mass transfer (accretion vs. erosion). While sediment may be abundant for millions of years, a change to conditions impeding sediment supply may occur over very short distances (e.g. offshore Chile, where the crest of the underthrusting Juan Fernandez Ridge causes uplift of the trench and forearc, blocking axial sediment transport in the trench (Kopp *et al.* 2004) and causing a change in mass flux from south to north along the Chilean continental margin). Accretion and erosion as a function of sediment supply, convergence rate and subduction channel capacity controlled by subducting basement relief (compare 3.1.3) are consequently transient processes in space and time. Spatial variations are often caused by a variation in lower plate structure, i.e. incipient subduction of seamounts, aseismic ridges or oceanic plateaus. 'Far-field' changes e.g. related to variation in climate, orogenies, sea-level changes etc. will affect sediment abundance over time, but changes are not as abrupt.

#### 3.1.2.1 From accretion to erosion: varying mass transfer offshore Java

The interplay of basement relief subduction, negligible sediment supply and a high convergence rate tremendously affects the morphology of the forearc as well as mass flux. **Kopp et al. (2006)** investigate the forearc structure offshore Java, Indonesia and extend the studies by **Kopp & Kukowski (2003)** to the east. The Java Margin has traditionally been categorized as an accretionary subduction zone (Hamilton 1979). This classification is disproved by **Kopp et al. (2006)** who show that frontal erosion related to the subduction of the oceanic Roo Rise on the Indo-Australian plate has removed the entire frontal prism causing a steepening of the slope angle in the morphology offshore central Java. This results in an along-strike segmentation of the Java Margin, with accretion dominating in the west and erosion prevailing in the east. The transition between these two regimes occurs over a very short distance of less than 100 km and is

associated with the incipient subduction of the Roo Rise. Masson *et al.* (1990) have mapped numerous local seamount re-entrant scars along the margin and **Kopp et al. (2006)** quantified an area affected by erosion of 25,000 $km^2$, corresponding to an estimated total volume of 75,000 $km^3$ or 160 $km^3$ per trench km.

**3.1.2.2 A closer look: lower slope morphology in response to modes of mass transfer**
The frontal prism of a subduction zone is the area, which responds most rapidly to changes in boundary conditions (e.g. von Huene *et al.* 2009). Frontal prism response hence sheds light on current subduction processes. **Kopp et al. (2008)** investigate the lower slope morphology of the accretionary Sumatra Trench system to establish correlations between the morphotectonic expression of the frontal prism and the mode of sediment accretion. Lower plate fabric extensively modulates upper plate topography, leading to frontal erosion and mass-wasting processes. Diverse accretion mechanics, however, pose a second-order factor in shaping upper plate morphology at the deformation front, in response to alternating phases of frontal accretion and sediment underthrusting. Cyclical accretion of frontal and basal sediment transfer (Gutscher *et al.* 1998) explains the morphotectonic segmentation of the forearc, which is punctuated by local accelerated frontal erosion resulting from subduction of pronounced oceanic basement relief. **Kopp et al. (2008)** document a change in accretionary mechanics from frontal erosion off southern Sumatra as studied in Kopp *et al.* 2001 and **Kopp & Kukowski (2003)** to sediment underthrusting and basal accretion as the dominating process offshore northern Sumatra.

**3.1.2.3 Lower plate impact: forearc segmentation related to lower plate structural diversity**
The Sunda Margin offers an exceptional setting by including segments of accretion **(Kopp & Kukowski 2003; Kopp et al. 2008)** and erosion **(Kopp et al. 2006)** as well as a transition from oceanic subduction to continent-island arc collision **(Shulgin et al. 2009)**. **Planert et al. (2010)** study the impact of a dramatically changing lower plate structure on the deformation and segmentation of the upper plate along the Sunda-Banda arc transition. Their combined analysis of seismic wide-angle reflection and refraction data, multichannel streamer data and shipboard gravity data in combination with high-resolution bathymetry reveals the velocity and density distribution at depth and the morphotectonic structure of the seafloor. The unique data set described by **Planert et al. (2010)** unravels fundamental differences between individual margin segments characterized by the subduction of thickened and altered oceanic crust, 'normal' oceanic crust of conventional thickness and thinned continental crust, respectively. Unique to the oceanic segments is a shallow upper plate Moho present underneath the forearc basin, which controls the depth extent of the seismogenic zone along the margin (compare 3.3). A shallow serpentinized mantle wedge may control the seismological stick-slip behavior of the megathrust and in particular reduce the width of the coupling zone. An extensive splay fault system, as imaged in the accompanying data set of Lueschen *et al. (*2010), however, demonstrates that co-seismic motion may be transmitted to the seafloor and constitutes a severe tsunami hazard.

**3.1.3 The décollement zone**
When the original subduction channel model was introduced (Shreve & Cloos 1986; Cloos & Shreve 1988) few seismic images resolving the décollement zone existed and structural details remained elusive until documented in modern transects (e.g. Moore *et al.* 1990; Shipley *et al.* 1994; Bangs *et al.* 2009). Recent investigations on the physical properties of the subduction channel (Calahorrano *et al.* 2008; Vannucchi *et al.* 2008) have resolved a segmentation of the subduction channel, which roughly corresponds to upper plate segmentation (von Huene *et al.* 2009). Subduction channels have been documented in accretionary and erosive margins where they are on average ~1 ± 0.5 km thick. Consequently, accretion occurs for sediment abundance exceeding channel thickness, while erosion prevails when material input is less. While the simplicity of these concepts is intriguing, deep penetrating seismic data reveal a complex variation of the décollement zone associated with the subduction of seamounts (e.g. Macintosh *et al.* 2007), the

occurrence of thickened sedimentary patches (Sage *et al.* 2006) or the dissection of the overlying margin wedge by fluid expulsion (Ranero *et al.* 2008). Imaging of the décollement zone in an accretionary (3.1.3.1) and an erosive (3.1.3.2) setting reveals that these structural variations may occur in either regime.

### 3.1.3.1 The subduction channel: spatial variations of the plate interface

The central Sunda Margin segment spanning from southern Sumatra to western Java is an example of an accretion dominated subduction complex **(Kopp & Kukowski 2003; Kopp et al. 2008)**, where ~1/3 of the trench sediment fill is underthrust beneath the frontal prism in a subduction channel, while the remainder is incorporated into the frontal prism by imbricate thrusting. The plate interface imaged by **Kopp et al. (2009)** shows a complex configuration marked by distinct morphological structures resulting from underthrust basement relief alternating with thickened sedimentary patches. These findings differ significantly from other accretionary margins such as Nankai (e.g. Moore *et al.* 1990) or Barbados (e.g. Westbrook *et al.* 1988) where a uniform, continuous décollement reflector has been imaged. **Kopp et al. (2009)** used the effective combination of refraction / deep-penetrating reflection seismic data and multibeam bathymetry to investigate the deep geometry of the margin. The combination of seismic data and high-resolution seafloor images has proven extremely powerful in deciphering processes at depth, because the different seismic acquisition schemes yield depth images at different resolution (crustal scale to fault-scale) while the bathymetry resolves structures not seen in the seismic data and at the same time expands the seismic transects into a third dimension. Pre-stack depth migrated seismic images of the western Java forearc document a non-uniform décollement zone of irregular thickness, modulated by subducting seamounts of <1 km height. Lower plate fabric, however, is not as pronounced as along the eastern margin segments investigated by **Kopp et al. 2006** and **Planert et al. 2010**. Based on the spatially variable, nonlinear pattern of the subduction channel, **Kopp et al. (2009)** infer that differential friction along the décollement may influence earthquake seismogenesis. The study is conducted approximately 100 km west of the source area of the 2006 Java tsunami earthquake, leading to the hypothesis that the alternating pattern of enhanced frictional contact zones associated with lower plate fabric and weak material patches of subducted sediment influences seismic coupling and possibly contributed to the heterogeneous slip distribution observed for the 2006 event (compare 3.3). Importantly, **Kopp et al. (2009)** image a steeply dipping splay fault, which originates at the décollement and terminates at the sea floor. The corresponding fault system can be traced for more than 600 km in the high-resolution bathymetry data and potentially contributes to tsunami generation during the co-seismic phase; a scenario also discussed for the eastern Java Margin **(Planert et al. 2010)**.

### 3.1.3.2 Subduction erosion: dismembering the margin from below

In comparison to the accretion dominated western Java case, **Zhu et al. (2009)** studied the décollement zone across the erosive central Costa Rica Margin using coincident seismic reflection data and a densely spaced grid of ocean bottom seismometer recordings, yielding unprecedented details on the velocity-depth distribution of the subduction complex. The transects investigated by **Zhu et al. (2009)** image a bifurcation of the plate boundary, termed 'megalens' structure in earlier studies (e.g. Ranero & von Huene 2000) for which velocity information was not available previously, thus leaving the possibility that this structure is a solid block of upper plate basement rock. The investigations by **Kopp et al. (2009)** and **Zhu et al. (2009)** both image a low velocity zone beneath the décollement of comparable velocities (with a variation of ±0.5 km/s underneath the frontal prism, resulting from material differences and travel time discrepancies) in an accretionary and erosive setting, respectively. The higher resolution due to denser instrument spacing on the sea floor offshore Costa Rica additionally images lateral variations in seismic velocities, indicating changing physical properties in the subduction channel. The discontinuous amplitude distribution of the décollement reflection is likely caused by localized pore pressure

anomalies and migrating fluids (**Zhu et al. 2009**). In the absence of direct sampling, the 'megalens' structure is interpreted as a mixture product, consisting of a buried sedimentary mélange including rocks sheared from the lower plate and highly fractured material eroded from the upper plate. Basement material is also inferred from the increased seismic velocities (> 4km/s) here compared to the trench sediment-filled subduction channel analyzed offshore Java (**Kopp et al. 2009**).

### 3.1.4 Evolving methodology

The extensive interdisciplinary analysis of diverse data sets spanning from vertical-incidence to wide-angle data (e.g. **Kopp et al. 2009, Zhu et al. 2009**) to potential field data (e.g. **Shulgin et al. 2009, Planert et al. 2010**) to high-resolution bathymetry (**Kopp et al. 2006, 2008**) certainly constitutes a unique characteristic of these studies and opens the opportunity to develop new methodological approaches in geophysical data analysis. Seismic tomography has evolved as a standard, state-of-the-art technique rendering images of the subsurface based on the inversion of travel-time information and in the ideal case largely independent of *a priori* information or the – possibly- unobjective input of the researcher. The results yield a continuous velocity-depth distribution, which is intriguing to interpret geologically especially in tectonically highly complex settings such as subduction zones. This has led **Koulakov et al. (2010)** to develop an iterative forward modeling and tomographic inversion scheme (3.1.4.1), which combines both approaches to draw on the strengths of each method. **Weinzierl & Kopp (2010)** introduce a resolution analysis based on probability distributions using a statistical approach (3.1.4.2).

#### 3.1.4.1 More than imaging: combining tomographic inversion and forward modeling

Tomographic images commonly display continuous velocity-depth fields and do not include first-order velocity discontinuities, which are associated with major changes in e.g. lithology (e.g. Hole 1992, Zelt & Barton 1998, Korenaga *et al.* 2000, Hobro *et al.* 2003). A pitfall in interpreting these images is to use velocity isolines as indicators for geological boundaries (e.g. 8.0 km/s isoline representing the crust-mantle boundary). Forward kinematic modeling consists of computing travel times in a layered velocity model, which is adjusted manually and may include *a priori* information (e.g. Luetgert 1992; Zelt & Smith 1992). The final model then commonly reflects a structural tectonic model of the transect. The dramatically increasing data density along seismic profiles, however, progressively requires automatic modeling tools. **Koulakov et al. (2010)** present a new code, which combines both methods to take advantage of automatic modeling tools in combination with additional information based on the researcher's experience. At first, a synthetic model is constructed, which already includes *a priori* information (e.g. a subducting plate). Based on this model, synthetic travel times are calculated using identical parameters as for the inversion of the observed data. A comparison of the synthetic model and the tomogram will yield discrepancies, which lead the modeler to adjust the synthetic model. Through an iterative process, **Koulakov et al. (2010)** achieve similar images by updating the synthetic model, which renders a structural model incorporating the observed velocity-depth distribution. Future adjustments of the code will in addition allow accounting for reflections and secondary arrivals.

#### 3.1.4.2 Using statistics: divergence analysis of seismic data

Because the solution to a non-linear inversion is non-unique, assessing the quality of the solution is fundamental in seismic modeling. In the Bayesian formulation, the most general solution of any inverse problem is a probability distribution of the model space. Analytic techniques solving this problem only apply in the simplest case, i.e. exactly one global minimum and no local minima exist. As these criteria are commonly not met, the model space must be explored extensively. **Weinzierl & Kopp (2010)** present a statistical separation strategy using an automated fitting routine to analyze the velocity-depth model space derived from inversion of seismic refraction data (e.g. **Kopp et al. 2009, Shulgin et al. 2009, Planert et al. 2010, Zhu et al. 2010**). A subsequent resolution analysis of the structural heterogeneity includes a divergence analysis that

can dissect long wide-angle profiles. The complete information of any parameterized physical system is contained in the *a posteriori* distribution. Velocity variations are mapped in their extent and structure by measuring the total as well as relative divergence of the velocity structure (i.e. global and singular misfits of velocities) in the a posteriori space. By comparing velocity distributions with the result of a tomographic inversion along the profile, **Weinzierl & Kopp (2010)** resolve the spatial distribution of subsurface structures. In particular, they resolve the shallow backstop location in an accretionary setting (comparable to the one imaged by **Kopp & Kukowski 2003, Kopp et al. 2009** and **Planert et al. 2010** offshore Indonesia) and provide a resolution analysis to assess the minimal structure of the backstop.

### 3.2 Subducting basement relief: subduction zone deformation and upper plate response

Intuitively, seafloor topography will cause deformation of the upper plate's weak frontal prism when passing the deformation front. The dramatic effects of subducting oceanic basement topography, which commonly reaches relative heights of several kilometers (Hillier & Watts 2007) is best observed in high-resolution bathymetry data (e.g. von Huene *et al.* 2000). Examples have been reported for margins worldwide (e.g. von Huene & Lallemand 1990, Font & Lallemand 2007, Bell *et al.* 2010, **Kopp et al. 2008**, Bangs *et al.* 2008, **Planert et al. 2010**) and have successfully been simulated in analog models (Dominguez *et al.* 1998, 2000) and numerical experiments (e.g. Baba *et al.* 2001). The physical expressions of geomorphological fabric are highly diverse: ranging from volcanic features emplaced on pre-existing seafloor (e.g. seamounts, LIPs, aseismic ridges) to crustal structures (e.g. fracture zones, faults, ridges, troughs, oceanic plateaus). There exists mounting evidence that bathymetric highs, in particular seamounts, remain intact after subduction. While seamount obduction has also been documented (Macpherson 1981), the reported number of seamounts being underthrusted is far greater (e.g. Kodaira *et al.* 2000, Bangs *et al.* 2006). Subduction of oceanic basement relief will affect the subduction complex in a number of ways: deep furrows mark the re-entrant scars where seamounts have eroded the frontal prism. Local seafloor uplift commonly marks the location of subducted relief at depth (von Huene 2008) where they disrupt the planar surface of the megathrust. Where topographic height exceeds the thickness of the subduction channel, it is in direct contact with the upper plate. **Kopp et al. (2010)** image the deeply submerged topography of two contiguous ridge structures on the Lesser Antilles megathrust surface (3.2.1). The ridges serve as backstop to the voluminous accretionary wedge, comparable to the setting on the Sunda Margin (**Kopp & Kukowski 2003, Kopp et al. 2009**). At the Hikurangi Margin north of New Zealand, subduction of the Hikurangi Plateau fundamentally influences forearc deformation as reported by **Scherwath et al. (2010)** in 3.2.2. **Shulgin et al. (2010)** relate similar basement topography as described in **Kopp et al. (2010)** to accretion of fragments of a buoyant aseismic oceanic plateau (3.2.3).

#### 3.2.1 Ridge subduction: Deep structure of the Lesser Antilles Island Arc

A complex interplay of oceanic basement block subduction and deformation of the upper plate basement occurs on the central Lesser Antilles Margin in the segment defined by the subduction of the Tiburon and Barracuda ridges near 16°N. Along-strike forearc segmentation here is governed by lower plate fabric as suggested by **Planert et al. (2010)** for the eastern Sunda Margin. A significant accretionary prism termed the Barbados Ridge Accretionary Complex, which forms by subduction accretion initiated in the Eocene, dominates the Lesser Antilles forearc. In the central margin segment around 16°N, approximately 1/3 of the sediment input is frontally accreted, while the remaining ~500-700 m of sediment are underthrust beneath the accretionary prism adjacent to the deformation front (Westbrook *et al.* 1988). The prism has a width of ~125 km here and fronts a backstop characterized by considerable relief as documented by two ridges rising 1-6 km above the adjacent basement (Christenson *et al.* 2003). Fragments

thereof are possibly sourced from an accreted aseismic ridge (Bangs *et al.* 2003). **Kopp et al. (2010)** investigate the subducted relief, which now forms part of the complex backstop using the method proposed by **Weinzierl & Kopp (2010)**. A composition sourced from different units (i.e. competent upper plate material and former lower plate relief accreted to the upper plate) is supported by the segmentation of the arc basement underneath the ridges, where a steeply landward dipping fault separates two basement blocks. The original backstop fronting the volcanic arc was uplifted to form the arcward ridge when a second unit arrived, which was subsequently deformed as the seaward ridge evolved. Deformation of a backstop has also been documented for the Nankai Margin, where a landward indentation of the crustal block of old accreted sediments has been attributed to the subduction of oceanic basement relief (Nakanishi *et al.* 2002). Intense deformation of the forearc crust is also observed on the Ryukyu Margin (Font & Lallemand 2009). Strong trench-perpendicular compression of the forearc basement concurs with the uplift of a broken piece of Ryukyu arc basement caused by the subduction of basement topography. Accretion of crustal blocks deforming the backstop is also suggested by **Shulgin et al. (2010)** for the Java Margin.

### 3.2.2 Plateau subduction I: Forearc deformation at the northern Hikurangi Margin

The Hikurangi Plateau currently subducted along the Hikurangi Trench east of New Zealand's North Island is the largest subducting bathymetric feature investigated in the scope of the studies presented here **(Scherwath et al. 2010)**. It is a Cretaceous Large Igneous Province of the Pacific Plate of 10-15 km thickness (Davy & Wood 1994), which upon subduction causes uplift of Raukumara Peninsula on North Island (Litchfield *et al.* 2007) and of the marine forearc between East Cape Ridge and the trench **(Scherwath et al. 2010)** similar to the setting in central Java **(Kopp et al. 2006)**. Crustal underplating is occurring in a 100 km wide region, which is experiencing active uplift that causes oversteepening of the lower slope. Material collapses and enters the subduction channel from which it is underplated and uplifted again. This close to zero net balance subduction zone material transfer is also suggested for the eastern Sunda Margin (Lueschen *et al.* 2010; **Planert et al. 2010**). At the Hikurangi Margin, subsidence occurs underneath the forearc basin, leading to the evolution of one of the deepest known forearc basins at an active margin (**Scherwath et al. 2010**). It is commonly assumed that margins with evidence for subsidence and collapse of the trench slope, as reported for the Hikurangi Margin, are regions of trench retreat and long-term recycling of forearc crust into the mantle (e.g. Clift & Vannucchi 2004), but **Scherwath et al. (2010)** argue that the significance of underplating at the base of the crust may not have been fully recognized. This would imply an overestimation of continental mass flux into the mantle at subduction zones.

### 3.2.3 Plateau subduction II: Roo Rise subduction and the 1994 Java tsunami earthquake

The trench system offshore eastern Java experiences the early phase of oceanic plateau subduction. The underthrusting of the oceanic Roo Rise triggers qualitatively different processes in the subduction complex, including active frontal erosion at the trench, oversteepening of the lower slope, heterogeneous uplift and deformation as reported by **Shulgin et al. (2010)**. The complex geometry of the backstop imaged by **Shulgin et al. (2010)** suggests two possible models for the structural formation within this segment of the margin: either accumulation of the Roo Rise crustal fragments above the backstop or alternatively uplift of the backstop caused by basal accumulation of crustal fragments, also discussed in **Kopp et al. (2010)** for the Lesser Antilles Margin. The forearc high offshore Eastern Java is characterized by isolated discrete peaks and shows an average elevation of 800-1200 m, contrasting with the deeper forearc high ridges to the west **(Kopp et al. 2006)** and to the east offshore Lombok **(Planert et al. 2010)**. The location of the forearc high peaks correlates with the proposed locations of completely subducted seamounts; however, the estimated subducted volume is smaller than the observed uplift of the forearc (Masson *et al.* 1990). Subducting bathymetric elevations will also affect seismic behavior (Yamazaki & Okamura 1989, Scholz & Small 1997). The underthrusting oceanic plateau affects

the stress field within the accretionary complex and the backstop edge, thereby favoring the initiation of large, potentially tsunamogenic earthquakes such as the 1994 Mw=7.8 tsunamogenic event (Abercrombie *et al.* 2001) (compare 3.3).

### 3.3 Seismic rupture and tsunami hazard in relation to plate interface geometry

The hypothesis that topography on the subducting oceanic plate may influence earthquake rupture was developed in the 1970's when Kelleher & McCann (1976) proposed a control of subducting bathymetric relief on earthquake location. Two notions are nested under this theme: subducting lower plate features may act as *asperities* or as *barriers* to seismic rupture (or possibly both, as discussed below). In seismology, asperities are defined as areas of high slip (equivalent to high stress drop), while barriers are regions with little or no slip (e.g. Das & Watts 2009). Along a single plate boundary, the barrier of one event may consequently act as asperity of a future earthquake. It has long been recognized that $M_w$~8 earthquakes along the Nankai Margin rupture distinct segments (Ando 1975), which are inferred to represent high-strength regions associated with high co-seismic slip. Slip terminates at a segment boundary, which is a zone of low or no slip and thus a barrier. However, this relation is not linear as rupture along the Nankai Margin commonly extends over several segments, propagating across the barrier. The definition of asperities as high strength contact zones is based on early rock physics experiments (Byerlee 1967). Their physical causes may be diverse and are associated with physical properties of the fault zone material as well as with the geometry of the fault (Bilek 2007). A detailed understanding of the interplay of these features is still lacking, but the progressing observational data basis provides increasing evidence for a correlation between earthquake rupture patterns and fault structure and properties at depth. Heterogeneity in earthquake rupture is evident from seismic segmentation as e.g. observed in Nankai, but also from earthquake source time functions (Kikuchi & Kanamori 1986). Rupture of smooth and strongly coupled plate contacts with a homogeneous asperity distribution will often result in long (> 500 km) rupture lengths (Bilek 2007) and will produce a trapezoidal source time function (e.g. Chile 1960, Alaska 1964). Increasing complexity in the source time functions indicate variations in the rupture process with earthquakes breaking a single segment or rupturing adjacent margin sections (Lay 1982) as documented e.g. for Nankai. Shorter rupture lengths must be attributed to heterogeneous asperity size distribution, inhibiting continuous rupture propagation and resulting in complex source time functions (Bilek 2007). These observations lead to the question of which physical conditions are required to produce high slip sections (asperities) or low slip patches (barriers), respectively. Seamounts and oceanic basement relief are obvious candidates to cause high strength contact zones (Cloos 1992, Scholz & Small 1997) and observations exist where subducting seamounts act as asperities (e.g. Das & Kostrov 1990, Abercrombie *et al.* 2001). However, evidence also exists for subducting relief acting as barriers to seismic rupture (e.g. Tanioka *et al.* 1997, Kodaira *et al.* 2000). Bilek *et al.* (2003) discuss the scenario that subducting topography may act as either asperity or barrier in the Central American Margin. Collot *et al.* (2004) document how upper plate segmentation influences rupture propagation offshore Ecuador, where crustal scale faults have segmented seismic rupture.

Offshore Java, a number of tsunamogenic earthquakes has been recorded in areas of seamount subduction, which brings these locations into special focus in terms of geohazards **(Kopp 2010)**. In 1994 and 2006, magnitude 7.8 earthquakes stroke offshore Java causing more than 1000 deaths due to the associated tsunamis (Bilek & Engdahl 2007). Abercrombie *et al.* (2001) showed that the highest slip was collocated with the proposed location of a subducted seamount. More recently, Bilek & Engdahl (2007) and **Kopp et al. (2009)** enhanced the idea of the correlation of structural forearc highs and associated subducted structures with the maximum slip of tsunami-generating earthquakes. **Kopp (2010)** uses tomographic models of refraction seismic profiles and

reflection seismic lines in combination with high-resolution multibeam bathymetric data to reveal the variability in the deep structure and deformation along strike of the Java forearc. Sediment supply as well as the nature and fabric of the oceanic lithosphere govern shallow subduction processes in the trench **(Kopp & Kukowski 2003, Kopp et al. 2006, 2008, 2009, Shulgin et al. 2009)**. Deeper into the subduction system, a shallow upper plate crust-mantle transition is observed along the entire Java Margin section (**Planert et al. 2010, Shulgin et al. 2010**, Kopp *et al.* 2002). The serpentinized forearc mantle wedge occupies the depth extent of the seismogenic zone (Grevemeyer & Tiwari 2006), which is narrower compared to its Sumatran analog. The Java Margin is characterized by a notable absence of Mw>8 earthquakes compared to its Sumatran counterpart, leading to the question of what controls seismic rupture and consequently the potential size of earthquakes offshore Java. As the magnitude of an earthquake is associated with the size of its rupture zone, slip motion on a fault will depend on the tectonic environment of the source region (Bilek, 2007). Two aspects are related to slip motion: (1) the role of the décollement zone and (2) the role of seafloor relief acting as asperities or barriers to rupture as indicated above. The notion that trench sediments affect seismogenesis was brought forward by Larry Ruff (Ruff, 1989) and is discussed in **Kopp (2010)** based on the concept of the subduction channel in general. On a global scale, giant megathrust earthquakes (Mw ≥ 8.5) are observed in systems characterized by sediment-flooded trenches (e.g. Sumatra (1883, 2004, 2005), Southern Chile (1960, 2010), Alaska/Aleutians (1964, 1965, 1986)) as well as at erosional margins (Kamchatka (1952), Kuril Islands (1963), Northern Chile (1868, 1877)), which show a subduction channel of several hundred meters in thickness. The existence and geometry (thickness) of a subduction channel as described e.g. in **Kopp et al. (2009)** and **Zhu et al. (2009)** (3.1.3) thus influences rupture propagation to a greater degree than the nature of the material in it (trench sediment vs. upper plate erosional debris) (Tanioka *et al.* 1997; Bilek & Lay 1999).

The second aspect regards sea floor roughness and the question of whether basement relief acts as an asperity or barrier to seismic rupture (Bilek & Lay 2002) as introduced above. Certainly this will not play a role where basement highs are deeply buried in the subduction channel. Here, subduction channel material smoothens sea floor relief and cushions upper plate contact. Where this is not the case, underthrusting seamounts or ridges may pose a limit to lateral rupture propagation. Bathymetric relief on the underthrusting plate will lead to variations in mechanical coupling and high friction models as well as low friction models have been proposed (Cloos 1992; Mochizuki *et al.* 2008). Large seamounts (≥ 3 km height) may increase the normal stress between the plates and increase interplate coupling (Scholz & Small 1997). On the contrary, reduction of normal stress has been proposed to result from elevated pore pressure of entrained fluid-rich sediment during erosion (von Huene *et al.* 2004). Weak interplate coupling may be related to the damage caused by erosion that inhibits the accumulation of elastic strain energy (Mochizuki *et al.* 2008). Recurring Mw ~7 earthquakes are related to seamount subduction in the Japan Trench (Mochizuki *et al.* 2008) where weak coupling has been linked to fluid-rich sediment and migration of fluids at the base of the seamount.

Along the Java subduction zone, different tectonic features exert a first-order control on the seismogenesis of the margin and govern the lack of Mw > 8 megathrust earthquakes as stated in **Kopp (2010)**:

1) The tomographic images reveal a shallow upper plate Moho with low mantle velocities indicative of hydrated minerals (3.1.2.3). Hydration is caused by fluids, which are released from the subducting slab and entrenched sediments, leading to serpentinization of the mantle wedge (Hyndman & Peacock 2003). The limited downdip extent of the seismogenic zone is also supported by gravity data and thermal modeling (Grevemeyer & Tiwari 2006) as well as by the forearc morphology (Krabbenhoeft *et al.* 2010).

2) In the central Java segment, seismic rupture would additionally be limited along-strike by subducted basement relief acting as barriers that will resist co-seismic slip. Erosional damage related to seamount/Roo Rise plateau subduction may hinder the accumulation of elastic strain (Mochizuki *et al.* 2008). Local elevation in pore pressure of sediment entrained during underthrusting of a seamount may also be expected. The uneven slip distribution recorded during the co-seismic phases of the recurring tsunami earthquakes on this margin sector (Ammon *et al.* 2006; Bilek & Engdahl 2007) document the highly heterogeneous plate coupling of the forearc resulting from the structural diversity of the underthrusting plate in conjunction with fluid-related processes. Though earthquakes along the Java Margin are of moderate magnitude, they frequently cause significant tsunamis. High-resolution bathymetry offshore Java did not reveal landslides that may have caused these events (Brune *et al.* 2010, **Kopp et al. 2006, Kopp 2010**). An alternative process for tsunami generation is the potential activation of splay faults during the co-seismic phase (Moore *et al.* 2007). Splay faults connect to the megathrust at depth and dip steeply to the surface, as imaged offshore western Java (**Kopp et al. 2009**) and off the Lesser Sunda islands (Lueschen *et al.* 2010, **Planert et al. 2010**). Thus the low-angle slip of the megathrust will potentially be transferred to a higher angle, which may greatly enhance seafloor displacement (Tanioka & Satake 1996). Due to the lack of deeply penetrating multichannel seismic data, the role of potential splay faults in the generation of the 1994 and 2006 Java tsunamis remains unresolved.

In summary, **Kopp (2010)** concludes that the complex megathrust interface geometry is the main factor for the observed absence of large (> 8) magnitude earthquakes offshore Java (Newcomb & McCann 1987), while smaller magnitude earthquakes frequently occur. The interplay between the tectonic habitat of the source region and the seismogenesis of large megathrust earthquakes is only crudely understood to date. The topic invites further research in the future to better understand the seismogenic segmentation and the specific geohazard potential of convergent plate boundaries.

## 4. Synopsis

The deep imaging of margin structures in both accretionary and erosive settings as presented in the examples in 3.1 and 3.2 is of pivotal importance to advance our understanding of subduction zone processes and to assess and constrain the numerous analogue and numerical simulations of convergent margin processes (e.g. Davis *et al.* 1983, Gutscher *et al.* 1998, Upton *et al.* 2003, Litchfield *et al.* 2007). The availability of a broad range of complementary data types has proven crucial to this task. Sophisticated data analysis may be applied to extract information dedicated to the scientific issue at hand, e.g. amplitude information contained in refraction data in addition to the seismic velocity field (J. Zhu, PhD-Thesis, 2010). The combined analysis of deep-penetrating seismic data and seafloor morphology images along the Sunda Margin has resolved the interconnectedness of surface processes and deeper dynamics. One of the more surprising findings of these studies is a cluster of earthquakes located in the mantle wedge offshore central Java (D. Wagner, PhD-Thesis, 2007). A possible explanation for this observation may be that these 'supraslab' events represent the seismological expression of underplating related to the detachment of seamounts (A. Wittwer, PhD-Thesis, 2010) as proposed by Uchida *et al.* (2010) for the Japan Margin. Due to the lack of local earthquake data this issue cannot unambiguously be resolved at this point. Passive seismic data recorded on a local network is also a pre-requisite to firmly establish under what conditions subducted basement relief offshore Java acts as asperities or barriers to seismic rupture. The processes associated with the subduction of pronounced lower plate fabric are causally related to the co-seismic behavior of the subduction thrust and faults within both the footwall and hanging wall. Furthermore, the geometry of the subduction complex is significant for understanding seismic and tsunami hazards. A number of subducted

features have been identified in the seismic data (Chapter 3), however, without locally recorded seismicity, their influence on earthquake rupture patterns cannot be defined in detail (A. Shulgin, PhD-Thesis, in preparation).

Megathrust events in subduction zones are the tectonic expression of potentially striking and hazardous geo-processes. They are the consequence of the accumulation and distribution of elastic deformation in space and time and thus define the seismic hazard potential and its variations. Even though the economic consequences of large earthquakes are of significant societal relevance, their mechanisms at depth and their relation to surface deformation are still little understood. The identification of margin segmentation has proven an important milestone in the analysis of plate boundary deformation and seismic risk. The dynamic Coulomb theory (Wang & Hu 2006) is based on the recognition of an actively deforming outer wedge overlying the velocity-strengthening portion of the megathrust and a less deformed inner wedge covering the velocity-weakening part as described for the results presented in Chapter 3. The concepts unifying these phenomena have led to the recognition of margin segments prone to failure, e.g. the Mentawai segment offshore Sumatra (K. Sieh, pers. communication) or the Iquique segment of northern Chile monitored by the Integrated Plate Boundary Observatory network (IPOC). In the Antilles, the segment defined by the subducting Tiburon and Barracuda Ridges may potentially generate a $M_w$ 7.6 earthquake if rupture of the seismogenic zone covers the entire extent between the two ridges between 16°N and 17°N (W. Weinzierl, PhD-Thesis, 2010). The identification of a splay-fault system on the Sunda subduction zone (**Kopp & Kukowski 2003, Kopp et al. 2009**, Lueschen *et al.* 2010) documents the high tsunami potential of the margin and merits further investigation to fully comprehend the role of this system in tsunamigenesis. Splay faults represent one controlling factor in the generation of tsunamis along many margin segments worldwide (Moore *et al.* 2007), but either are absent or have not been identified at other segments. The identification and seismic imaging of splay fault systems is therefore pivotal for margins prone to tsunamigenesis. Where splay faults are not developed, other structures affect the triggering of tsunamis. Along the Chile Margin, the updip limit of the aseismic/seismic transition zone controlled the size of the tsunamis associated with the 1960 Valdivia earthquake ($M_w$=9.5) and the 2010 Maule rupture ($M_w$=8.8) (Contreras-Reyes *et al.* 2010). The magnitude of both earthquakes was sufficient to cause devastating tsunamis, however, the 2010 regional tsunami was much smaller than the 1960 trans-oceanic tsunami. This is likely associated with the size of the frontal prism along the corresponding margin segments: the frontal prism in the Maule segment is of larger dimension (~30 km) compared to its Chiloé analogue (≤10 km). The seismogenic zone in the presence of a small frontal prism will extend further seaward and reach greater water depth and consequently the height of the water column overlying the seismogenic zone will be larger (Contreras-Reyes *et al.* 2010). If the updip limit of the seismogenic zone were controlled by the location of the backstop and the size of the frontal prism, then a small frontal prism would favor trans-oceanic tsunamis compared to a larger frontal prism and deeper updip limit.

## 5. Future Prospects

One of the most probing issues in future margin research regards the evolution of plate boundary deformation over an entire seismic cycle to arrive at an improved comprehension of earthquake-related processes at convergent margins and their variations at different stages of the seismic cycle. Our limited knowledge of these processes and their variation in time and space is mainly due to the fact that their source location (i.e. plate margins and zones of contact deformation) is difficult to probe by deep drilling. An additional impediment that we need to overcome results from the marine setting of subduction zones.

A common aspect of recent margin studies is a surprising complexity of deformation patterns as well as hazard distribution on plate boundaries. Previous conceptions regarded deformation on plate margins as a continuous, stationary process occasionally interrupted by earthquakes. Newer findings however imply that a broad spectrum of deformation processes occurs simultaneously along a plate margin, ranging from fast, seismic shock to slow, stationary creep (Shelly *et al.* 2007, Kanamori 2008). In addition it has become increasingly clear that fault zones and their related earthquake activity form communicating systems. This may pose an explanation for the clustering of seismicity in time (Peltzer *et al.* 2001). Furthermore, it may be possible that not only seismic activity may be related through complex interaction, but also that the entire non-linear spectrum of deformation may depend on numerous, coupled mechanisms. Our perception of the evolution of elastic deformation and the associated seismic hazard on the time scale of a human lifetime (ranging from an individual earthquake to several seismic cycles) will have to evolve and requires state-of-the-art observations as well as a progression of existing models and conceptions. Until today, however, the database to investigate these processes, which are transient in space and time, is too sparse and is insufficient to provide information on fundamental mechanics and control mechanisms. This information is, however, essential to identify coupling mechanisms and to derive systematic deformation patterns and hazard models. The efforts of the NanTroSEIZE expeditions (www.iodp.org/NanTroSEIZE/) will provide important stepping-stones to fill this gap by logging the subduction zone input (i.e. incoming sediments and oceanic crust) as well as by drilling the outer and inner wedges offshore Kii Peninsula in Japan. Sampling the seismogenic zone and splay fault system of the Nankai Trough will deliver data on the physical properties (e.g. coefficients of friction, permeability pore-fluid pressure, state of stress) characterizing the fault zones and will eventually be complemented by corresponding data from the erosive Costa Rica Margin (www.iodp.org/expeditions). While drilling provides direct sampling of fault zone material, it may only yield information limited to the borehole locations, in addition to being extremely cost-intensive and time-consuming and thus currently in progress at only two subduction zones. The wide variety of deformation patterns and seismic behavior observed at margins globally, however, requires the study of different systems. Geophysical methods are capable of sensing an entire volume of the margin wedge through 3D acquisition schemes (Moore *et al.* 2007). Even though direct sampling is not provided, these data cubes may be analyzed to gain information on physical properties and the hydrogeology of subduction megathrusts to advance our understanding of the mechanics and dynamics of faulting processes as well as the along-strike segmentation of convergent margins. A combination of different seismic methods complemented by additional measurements (e.g. marine electromagnetic methods (Worzewski *et al.* 2010) or potential field data) will be crucial to this task. The collocated acquisition of wide-angle and reflection seismic data as described in Chapter 3 is still not established as a standard routine. Furthermore, we need to move forward to acquire three-dimensional data sets to access the interior regime of subduction zones and trench systems to image *in situ* processes. This will provide the quantitative observational foundation from which to assess the spatial and temporal variation of interplate seismicity. Introducing a fourth dimension through real-time observation and monitoring allows detection of time-dependent, transient processes (e.g. time evolution of $v_p/v_s$ ratio associated with post-seismic fluid flow (Husen & Kissling 2001). Monitoring of stress redistribution during the progressing seismic cycle for example will relate the associated transient deformation to seismicity at depth. Stress increase in the oceanic crust is manifested in the intensified compressional component of intraplate focal mechanisms (Dmowska & Lovison 1988) and may be gauged through the extraction of horizontal/vertical components of ocean bottom seismometers.

A couple of margin segments proposed to enter the end of the seismic cycle have been identified in Chapter 4 and could serve as candidates to investigate transient processes at the termination of the interseismic phase. One obstacle is the technologically induced frequent separation of geophysical studies into an offshore domain and an onshore sector. We need to literally

'overcome the shoreline' in data analysis, qualitative interpretation and modeling by fostering amphibious investigations to capture the dynamics controlling plate boundary deformation as well as the submarine-subaerial transport paths that control material accumulation and dispersal. Another missing link and stepping stone required to fully capture forearc deformation at subduction zones is the offshore recording of seafloor displacement and strain. Above the shoreline, this information is supplied by satellite observations. This technology fails in the marine environment. The development of novel approaches in the emerging field of marine geodesy combined with geophysical methods may in the future provide a comprehensive conception of subduction zone deformation through the seismic cycle through *in situ* monitoring of strain, tilt, pressure, and seismicity. The advancement of techniques to explore the interseismic variations of these critical parameters will open new directions in the field of solid earth dynamics.

## Acknowledgements

The work presented here would not have been possible without the enthusiastic input of many colleagues. The concepts presented here have evolved from the many discussions with my group at IFM-GEOMAR (D. Hindle, L. Planert, M. Scherwath, A. Shulgin, W. Weinzierl, A. Wittwer, J. Zhu and M. Zillmer).

The interdisciplinary environment and stimulating scientific exchange at IFM-GEOMAR during the recent years have provided constant impetus. Fruitful discussions and support by J. Behrmann, C. Berndt, J. Bialas, C. Devey, E. Flueh, K. Hoernle, M. Jegen, D. Klaeschen, A. Krabbenhoeft, S. Krastel, C. Papenberg, M. Stipp and W. Weinrebe have contributed to the excellent working environment.

I thank R. von Huene, O. Oncken and D. Scholl for sparking my interest in convergent margin processes many years ago and D. Klaeschen and C. Kopp for sharing the magic of seismic data processing even longer ago.

The Geodynamics Department is warmly acknowledged for providing acquisition systems and J. Bialas, E. Flueh, A. Krabbenhoeft, C. Papenberg, J. Petersen and K.-P. Steffen are warmly thanked for providing their expertise in marine data acquisition.

The results documented here are based on the continuous support of the German Research Vessel fleet through the German Federal Ministry for Science and Technology BMBF and the German Science Foundation DFG. I am indebted to the captains and crews of RV SONNE and RV Maria S. MERIAN for the excellent support and performance at sea and to all colleagues for participating in the cruises. Cruises SO137, SO138, SO176, SO179 and SO190 were supported by grants 03G0137A (GINCO I), 03G0138A (GINCO II), 03GO176A (MERAMEX), 03G03G0190A and 03G0190B (SINDBAD project)). Additional support was supplied by the DFG through the SUNDA project (grant KO2961/1-2) and TRAIL cruise (MSM 04/2) and by the GEOTECHNOLOGIEN program of BMBF and DFG for the SUNDAARC project (grant 03G0579B).

Special thanks go out to my colleague and friend Prof. E. R. Flueh for his invaluable support while my children were young.

I thank Chrischan for the best years of my life and I look forward to many more to come. And of course, I thank Yara and Lennart for sharing their lives with us and filling our days with laughter, joy, tears, enthusiasm, anger, exhaustion and sunshine – in short: for making us whole.

## References

Abercrombie, R., Antolik, M., Felzer, K., Ekström, G., 2001. The 1994 Java tsunami earthquake: slip over a subducting seamount. J. Geophys. Res., 106, 6595–6607.

Ando, M., 1975. Source mechanisms and tectonic significance of historical earthquakes along the Nankai trough. Tectonophysics, 27, 119-140.

Baba, T., Hori, T., Hirano, S., Cummins, P. R., Park, J., Kameyama, M., Kaneda, Y., 2001. Deformation of a seamount subducting beneath an accretionary prism: Constraints from numerical simulation. Geophys. Res. Lett., 28(9), 1827–1830, doi:10.1029/2000GL012266.

Bangs, N. L., Christeson, G. L., Shipley, T. H., 2003. Structure of the Lesser Antilles subduction zone backstop and its role in a large accretionary system. J. Geophys. Res., 108, 2358, doi:10.1029/2002JB002040.

Bangs, N. L. B., Gulick, S. P. S., Shipley, T. H., 2006. Seamount subduction erosion in the Nankai Trough and its potential impact on the seismogenic zone. Geology, 34, doi:10.1130/G22451.1.

Bangs, N. L. B., Moore, G. F., Gulick, S. P. S., Pangborn, E. M., Tobin, H. J., Kuramoto, S., Taira, A., 2009. Broad, weak regions of the Nankai Megathrust and implications for shallow coseismic slip. Earth Planet. Sci. Lett., 284, 44-49, doi:10.1016/j.epsl.2009.04.26.

Barker, D. H. N., Sutherland, R., Henrys, S., Bannister, S., 2009. Geometry of the Hikurangi subduction thrust and upper plate, North Island, New Zealand. Geochem. Geophys. Geosyst., 10, Q02007, doi:10.1029/2008GC002153.

Bell, R., Sutherland, R., Barker, D.H.N., Henrys, S., Bannister, S., Wallace, L., Beavan, J., 2010. Seismic reflection character of the Hikurangi subduction interface, New Zealand, in the region of repeated Gisborne slow slip events. Geophys. J. Int., 180, 34-48, doi: 10.1111/j.1365-246X.2009.04401.x.

Bilek, S. & Lay, T., 1999. Rigidity variations with depth along interplate megathrust faults in subduction zones. Nature, 400, 443-446.

Bilek, S. & Lay, T., 2002. Tsunami earthquakes possibly widespread manifestations of frictional conditional stability. Geophys. Res. Lett., 29, 14, doi: 10.1029/2002GL015215.

Bilek, S., 2007. Influence of subducting topography on earthquake rupture. In: Dixon, T. & Moore, J.C. (eds) The seismogenic zone of subduction thrust faults. Columbia University Press.

Bilek, S. & Engdahl, E.R., 2007. Rupture characterization and aftershock relocations for the 1994 and 2006 tsunami earthquakes in the Java subduction zone. Geophys. Res. Lett., 34, L20311.

Brune, S., Ladage, S., Babeyko, A.Y., Müller, C., Kopp, H., Sobolev, S.V., 2010. Submarine landslides at the eastern Sunda margin: observations and tsunami impact assessment. Natural Hazards, doi:10.1007/s11069-009-9487-8.

Byrne, D. E., Wang, W.-H., Davis, D. M., 1993. Mechanical role of backstops in the growth of forearcs. Tectonics, 12, 1, 123-144.

Calahorrano, A. B., Sallares, V., Collot, J.-Y., Sage, F., Ranero, C., 2008. Nonlinear variations of the physical properties along the southern Ecuador subduction channel: Results from depth-migrated seismic data. Earth Planet. Sci. Lett., 267, 453-467, doi:10.1016/j.epsl.2007.11.061.

Christeson, G. L., Bangs, N. L., Shipley, T. H., 2003. Deep structure of an island arc backstop, Lesser Antilles subduction zone. J. Geophys. Res., 108, 2327, doi:10.1029/2002JB002243.

Clift, P.D. & Vannucchi, P., 2004. Controls on tectonic accretion versus erosion in subduction zones: Implications for the origin and recycling of the continental crust. Rev. Geophys., 42, doi:10.1029/2003RG000127.

Cloos, M. & Shreve, R. L., 1988. Subduction-channel model of prism accretion, melange formation, sediment subduction, and subduction erosion at convergent plate margins: 1. Background and description. Pure Appl. Geophys., 128, 455-500.

Cloos, M., 1992. Thrust-type subduction zone earthquakes and seamount asperities: A physical model for earthquake rupture. Geology, 20, 601–604.

Collot, J.-Y., Marcaillou, B., Sage, F., Michaud, F., Agudelo, W., Charvis, P., Graindorge, D., Gutscher, M.-A., Spence, G., 2004. Are rupture zone limits of great subduction earthquakes controlled by upper plate structures? Evidence from multichannel seismic reflection data acquired across the northern Ecuador-southwest Colombia margin. J. Geophys. Res., 109, doi:10.1029/2004JB003060.

Contreras-Reyes, E., Flueh, E. R., Grevemeyer, I., 2010. Tectonic control on sediment accretion and subduction off south-central Chile: Implications for coseismic rupture processes of the 1960 and 2010 megathrust earthquakes. Tectonics, in press.

Cummins, P.R. & Kaneda, Y., 2000. Possible splay fault slip during the 1946 Nankai earthquake. Geophys. Res. Lett., 27, 2725–2728.

Dahlen, F. A., 1990. Critical taper model of fold-and-thrust belts and accretionary wedges. Annu. Rev. Earth Planet. Sci., 18, 55-99.

Das, S. & Kostrov, B.V., 1990. Inversion of seismic slip rate and distribution with stabilising constraints: Application to the 1986 Andreanof Islands earthquake. J. Geophys. Res., 95, 6899-6913.

Das, S. & Watts, A.B., 2009. Effect of subducting seafloor topography on the rupture characteristics of great subduction zone earthquakes. In: Lallemand, S. & Funiciello, F. (eds) Subduction Zone Geodynamics, doi:10.1007/978-3-540-87974-9.

Davis, D. M., Suppe, J., Dahlen, F. A., 1983. Mechanics of fold and thrust belts and accretionary wedges. J. Geophys. Res., 88, 1153–1172, doi:10.1029/JB088iB02p01153.

Davy, B. & Wood, R., 1994. Gravity and magnetic modeling of the Hikurangi Plateau. Mar. Geol., 118(1–2), 139–151, doi:10.1016/0025- 3227(94)90117-1.

Dmowska, R. & Lovison, L. C., 1988. Intermediate-term seismic precursors for some coupled subduction zones, Pure and Appl. Geophys., doi: 10.1007/BF00879013, 126, 2-4 , 643 – 664.

Dominguez, S., Lallemand, S.E., Malavieille, J., von Huene, R., 1998. Upper plate deformation associated with seamount subduction. Tectonophysics, 293, 207–224.

Dominguez, S., Malavieille, J., Lallemand, S.E., 2000. Deformation of accretionary wedges in response to seamount subduction: Insights from sandbox experiments. Tectonics, 19, 182–196.

Font, Y., Liu, C.-S., Schnuerle, P., Lallemand, S., 2001. Constraints on backstop geometry of the southwest Ryukyu subduction based on reflectin seismic data. Tectonophysics, 333, 135-158.

Font, Y. & Lallemand, S., 2009. Subducting oceanic high causes compressional faulting in southernmost Ryukyu forearc as revealed by hypocentral determinations of earthquakes and reflection/refraction seismic data. Tectonophysics, 466, doi:10.1016/j.tecto.2007.11.018.

Fruehn, J., Huene, R. von, Fisher, M. A., 1999. Accretion in the wake of terrane collision: The Neogene accretionary wedge off Kenai peninsula, Alaska. Tectonics, 18, 263–277.

Grevemeyer, I. & Tiwari, T.M., 2006. Overriding plate controls spatial distribution of megathrust earthquakes in the Sunda-Andaman subduction zone. Earth Planet. Sci. Lett., 251, 199-208.

Gutscher, M.-A., Kukowski, N., Malavieille, J., Lallemand, S., 1998. Episodic imbricate thrusting and underthrusting: Analog experiments and mechanical analysis applied to the Alaskan accretionary wedge. J. Geophys. Res., 103, 10161-10176.

Hamilton, W., 1979. Tectonics of the Indonesian region. U.S. Geological Survey Professional Paper, 1078.

Hamilton, W., 1988. Plate tectonics and island arcs, Geol. Soc. Am. Bull., 100, 1503-1527.

Hillier, J.K. & Watts, A.B., 2007. Global distribution of seamounts from ship-track bathymetry data. Geophys. Res. Lett., 34, doi:10.1029/2007GL029874.

Hobro, J. W. D., Singh, S. C., Minshull, T. A., 2003. Three-dimensional tomographic inversion of combined reflection and refraction seismic travel- time data. Geophys. J. Int., 152, 1, 79–93.

Hole, J. A., 1992. Nonlinear high-resolution three-dimensional seismic travel time tomography. J. Geophys. Res., 97, B5, 6553– 6562.

Huang, C-Y., Yuan, P.B., Tsao, S-J., 2006. Temporal and spatial records of active arc-continent collision in Taiwan: a synthesis. Geol. Soc. Am. Bull., 118, 274-288.

Husen, S. & Kissling, E., 2001. Postseismic fluid flow after the large subduction earthquake of Antofagasta, Chile. Geology, 29, 847-850, doi:10.1130/0091-7613(2001)029<0847:PFFATL>2.0.CO;2

Hyndman, R.D., Yamano M., Oleskevich, D.A., 1997. The seismogenic zone of subduction thrust faults. Island Arc, 6, 3, doi: 10.1111/j.1440-1738.1997.tb00175.x.

Kanamori, H., 2008. Earthquake physics and real-time seismology. Nature, 451, 271–273, doi:10.1038/nature06585.

Kelleher, J. & McCann, W., 1976. Buoyant zones, great earthquakes, and unstable boundaries of subduction. J. Geophys. Res., 81, 4885-4896.

Kikuchi, M. & Kanamori, H., 1986. Inversion of complex body waves-II. Phys. Earth Planet. Int., 43, 205-222.

Kodaira, S., Takahashi, N., Nakanishi, A., Miura, A., Kaneda, Y., 2000. Subducted seamount imaged in the rupture zone of the 1946 Nankaido earthquake. Science, 289, 104-106.

Kopp, H., Flueh, E. R., Klaeschen, D., Bialas, J., Reichert, C., 2001. Crustal structure of the central Sunda margin at the onset of oblique subduction. Geophys. J. Int., 147, 449-474.

Kopp, H., Klaeschen, D., Flueh, E. R., Bialas, J., Reichert, C., 2002. Crustal structure of the Java margin from seismic wide-angle and multichannel reflection data. J. Geophys. Res., 107. doi:10.1029/2000JB000095.

**Kopp, H. & Kukowski, N., 2003. Backstop geometry and accretionary mechanics of the Sunda margin. Tectonics, 6, doi:10.1029/2002TC001420.**

**Kopp, H., Flueh, E. R., Petersen, C. J., Weinrebe, W., Wittwer, A., Meramex Scientists, 2006. The Java margin revisited: Evidence for subduction erosion off Java. Earth Planet. Sci. Lett., 242, 130-142.**

**Kopp, H., Weinrebe, W., Ladage, S., Barckhausen, U., Klaeschen, D., Flueh, E. R., Gaedicke, C., Djajadihardja, Y., Grevemeyer, I., Krabbenhoeft, A., Papenberg, C., Zillmer, M., 2008. Lower slope morphology of the Sumatra trench system. Basin Research, doi: 10.1111/j.1365-2117.2008.00381.x.**

**Kopp, H., Hindle, D., Klaeschen, D., Oncken, O., Scholl, D., 2009. Anatomy of the western Java plate interface from depth-migrated seismic images. Earth Planet. Sci. Lett., doi:10.1016/j.epsl.2009.09.043.**

**Kopp, H., Weinzierl, W., Becel, A., Charvis, P., Evain, M., Flueh, E. R., Gailler, A., Galve, A., Hirn, A., Kandilarov, A., Klaeschen, D., Laigle, M., Papenberg, C., Planert, L., Roux, E., Trail and Thales teams, 2010. Deep structure of the central Lesser Antilles Island Arc: relevance for the formation of continental crust. Earth Planet. Sci. Lett., submitted.**

**Kopp, H., 2010. The Java Convergent Margin: Structure, Deformation and Subduction Processes. In: Hall, R. (edt) The SE Asian gateway: history and tectonics of Australia-Asia collision. Geol. Soc. London Spec. Publ., in press.**

Korenaga, J., Holbrook, S., Kent, G., Kelemen, P, Detrick, R. S., Larsen, H.-C., Hopper, J. R., Dahl-Jensen, T., 2000. Crustal structure of the southeast Greenland margin from joint refraction and reflection seismic tomography. J. Geophys. Res., 105, doi:10.1029/2000JB900188.

**Koulakov, I., Stupina, T., Kopp, H., 2010. Creating realistic models based on combined forward modeling and tomographic inversion of seismic profiling data. Geophysics, 75, doi:10.1190/1.3427637.**

Lay, T., Kanamori, H., Ruff, L., 1982. The asperity model and the nature of large subduction zone earthquakes. Earthquake Predict. Res., 1, 3-71.

Litchfield, N., Ellis, S., Berryman, K., Nicol, A., 2007. Insights into subduction related uplift along the Hikurangi margin, New Zealand, using numerical modeling. J. Geophys. Res., 112, F02021, doi:10.1029/ 2006JF000535.

Lueschen, E., Mueller, C., Kopp, H., Engels, M., Lutz, R., Planert, L., Shulgin, A., Djajadihardja, Y., 2010. Structure, evolution and tectonic activity of the eastern Sunda forearc, Indonesia, from marine seismic investigations. Tectonophysics, doi:10.1016/j.tecto.2010.06.008.

McIntosh, K. D., Silver, E. A., Ahmed, I., Berhorst, A., Ranero, C. R., Kelly, R. K., Flueh, E. R., 2007. The Nicaragua convergent margin: seismic reflection imaging of the source of a tsunami earthquake, in: Dixon, T. J., Moore, J. C. (eds.) The seismogenic zone of subduction thrust faults. Columbia University Press, New York, pp. 476-511.

Macpherson, G.J., 1981. The Snow Mountain volcanic complex: an on-land seamount in the Franciscan terrain. California J. Geol., 91, 73–92.

Masson, D.G., Parson, L.M., Milsom, J., Nichols, G., Sikumbang, N., Dwiyanto, B., Kallagher, H., 1990. Subduction of seamounts at the Java Trench: a view with long-range sidescan sonar. Tectonophysics, 18551– 18565.

Mochizuki, K., Yamada, T., Shinohara, M., Yamanaka, Y., Kanazawa, T., 2008. Weak interplate coupling by seamounts and repeating M ~ 7 earthquakes. Science, 321, 5893, 1194-1197, doi:10.1126/science.1160250.

Moore, G. F., Shipley, T. H., Stoffa, P. L., Karig, D. E., Taira, A., Kuramoto, S., Tokuyama, H., Suyehiro, K., 1990. Structure of the Nankai Trough accretionary zone from multichannel seismic reflection data. J. Geophys. Res., 95, 8753-8765.

Moore, G.F., Bangs, N.L., Taira, A., Kuramoto, S., Pangborn, E., Tobin, H.J., 2007. Three- dimensional splay fault geometry and implications for tsunami generation. Science, 318, 1128–1131.

Nakanishi, A., Kodaira, S., Park, J.-O., Kaneda, Y., 2002. Deformable backstop as seaward end of coseismic slip in the Nankai Trough seismogenic zone. Earth Planet. Sci Lett., 203, 255-263.

Newcomb, K.R. & McCann, W.R., 1987. Seismic history and seismotectonics of the Sunda Arc. J. Geophys. Res., 92, (B1), 421–439.

Peltzer, G., Crampe, F., Hensley, S., Rosen, P., 2001. Transient strain accumulation and fault interaction in the Eastern California Shear Zone. Geology, 29, 975–978.

**Planert, L., Kopp, H., Lueschen, E., Mueller, C., Flueh, E.R., Shulgin, A., Djajadihardja, Y., Krabbenhoeft, A., 2010. Lower plate structure and upper plate deformational segmentation at the Sunda-Banda arc transition, Indonesia. J. Geophys. Res., 115, doi:10.1029/2009JB006713.**

Ranero, C.R., & von Huene, R., 2000. Subduction erosion along the Middle America convergent margin. Nature, 404, 748–752.

Ranero, C. R., Grevemeyer, I., Sahling, H., Barckhausen, U., Hensen, C., Wallmann, K., Weinrebe, W., Vannucchi, P., von Huene, R., McIntosh, K., 2008. Hydrogeological system of erosional convergent margins and its influence on tectonics and interplate seismogenesis. Geochem. Geophys. Geosyst., 9, Q03S04, doi:10.1029/2007GC001679.

Ruff, L., 1989. Do Trench Sediments Affect Great Earthquake Occurrence in Subduction Zones? Pageoph, 129, 1-2, 262-282.

Sage, F., Collot, J.-Y., Ranero, C. R., 2006. Interplate patchiness and subduction-erosion mechanisms: Evidence from depth-migrated seismic images at the central Ecuador convergent margin. Geology, 34, doi:10.1130/G22790A.1.

Sandwell, D.T. & Smith, W. H. F., 1997. Marine gravity anomaly from Geosat and ERS1 satellite altimetry. J. Geophys. Res., 102, B5, 10039-10054.

**Scherwath, M., Kopp, H., Flueh, E. R., Henrys, S., Sutherland, R., Stagpoole, V. M., Barker, D.H.N., Reyners, M.E., Basset, D.G., Planert, L., Dannowski, A., 2010. Fore-arc deformation and underplating at the northern Hikurangi margin, New Zealand. J. Geophys. Res., 115, doi:10.1029/2009JB006645.**

Scholl, D., Keranen, K., von Huene, R., Wells, R., Ryan, H., Kirby, S., 2010. Megathrust earthquakes and sediment input to the subduction channel. Geophys. Res. Abstr., 12, EGU2010-7226-1.

Scholz, C. & Small, C., 1997. The effect of seamount subduction on seismic coupling. Geology, 25, 487-490.

Shelly, D., Beroza, G., Ide, S., 2007. Non-volcanic tremor and low-frequency earthquake swarms. Nature, 446, doi: 10.1038/nature05666.

Shipley, T. H., Moore, G. F., Bangs, N. L., Moore, J. C., Stoffa, P. L., 1994. Seismically inferred dilatancy distribution, northern Barbados Ridge decollement: Implications for fluid migration and fault strength. Geology, 22, 411-414.

Shreve, R. L. & Cloos, M., 1986. Dynamics of sediment subduction, melange formation, and prism accretion, J. Geophys. Res., 91, 10.229-10.245.

Shulgin, A., Forearc deformation across three transects along the Sunda margin, Indonesia, PhD-Thesis, University of Kiel, in preparation.

**Shulgin, A., Kopp, H., Mueller, C., Lueschen, E., Planert, L., Engels, M., Flueh, E.R., Krabbenhoeft, A., Djajadihardja, Y., 2009. Sunda-Banda arc transition: Incipient continent-island arc collision (northwest Australia). Geophys. Res. Lett., 36, L10304, doi:10.1029/2009GL037533.**

**Shulgin, A., Kopp, H., Mueller, C., Planert, L., Lueschen, E., Flueh, E.R., Djajadihardja, Y., 2010. Structural architecture of oceanic plateau subduction offshore Eastern Java and the potential implications for geohazards. Geophys. J. Int., doi:10.1111/j.1365-246X.2010.04834.x.**

Tanioka, Y. & Satake, K., 1996. Tsunami generation by horizontal displacement of ocean bottom. Geophys. Res. Lett., 23(8), 861–864.

Tanioka, Y., Ruff, L., Satake, K., 1997. What controls the lateral variation of large earthquake occurrence along the Japan Trench? Island Arc, 6, 3, 261-266, 10.1111/j.1440-1738.1997.tb00176.x.

Upton, P., Koons, P. O., Eberhart-Phillips, D., 2003. Extension and partitioning in an oblique subduction zone, New Zealand: Constraints from three dimensional numerical modeling. Tectonics, 22(6), 1068, doi:10.1029/2002TC001431.

Vannucchi, P., Remitti, F., Bettelli, G., 2008. Geologic record of fluid flow and seismogenesis along an erosive subducting plate boundary. Nature, 451, 699-703, doi:10.1038/nature06486.

von Huene, R. & Lallemand, S. E., 1990. Tectonic erosion along the Japan and Peru convergent margins. GSA Bull., 102, 704–720.

von Huene, R., Ranero, C., Scholl, D., 2009. Convergent margin structure in high-quality geophysical images and current kinematic and dynamic models. In: Lallemand, S. & Funiciello, F. (eds) Subduction Zone Geodynamics, doi:10.1007/978-3-540-87974-9.

von Huene, R. 2008. When Seamounts subduct. Science, 10.1126/science.1162868.

von Huene, R., Suess, E. and Leg 112 Shipboard Scientists, 1988. Ocean drilling program Leg 112, Peru continental margin: Part I, tectonic history. Geology, 16, 934 – 938.

von Huene, R., Ranero, C.R., Weinrebe, W., 2000. Quaternary convergent margin tectonics of Costa Rica, segmentation of the Cocos plate, and Central American volcanism. Tectonics, 19, 314–334.

von Huene, R., Ranero, C., Vannucchi, P. 2004. Generic model of subduction erosion. Geology, 32, 913-916, doi: 10.1130/G20563.1.

Wang, K. & Hu, Y., 2006. Accretionary prisms in subduction earthquake cycles: The theory of dynamic Coulomb wedge. J. Geophys. Res., 111, B06410, doi:10.1029/2005JB004094.

**Weinzierl, W. & Kopp, H., 2010. Statistical separation strategy to analyze velocity structure obtained by seismic tomography. Geophysics, 75, doi:10.1190/1.3432406.**

Weinzierl, W., 2010. Crustual structure of the Central Lesser Antilles Island Arc: seismic near-vertical and wide-angle profiling, PhD-Thesis, University of Kiel, Germany, 79 pp.

Westbrook, G., Ladd, J. W., Buhl, P., Bangs, N., Tiley, G. J., 1988. Cross section of an accretionary wedge: Barbados Ridge complex. Geology, 16, 631-635.

Wittwer, A., 2010. Investigating the crustal and upper mantle structure of the central Java subduction zone with marine wide-angle seismic and gravity data. PhD-Thesis, University of Kiel, Germany, 143 pp.

Worzewski, T., Jegen, M., Kopp, H., Brasse, H., Taylor, W., 2010. Magnetotelluric image of the fluid cycle in the Costa Rican subduction zone. Nature Geoscience, in press.

Yamazaki, T. & Okamura, Y., 1989. Subducting seamounts and deformation of overriding forearc wedges around Japan. Tectonophysics, 160, 207-229.

Zelt, C. A. & Smith, R. B., 1992. Seismic traveltime inversion for 2-D crustal velocity structure. Geophys. J. Int., 108, doi: 10.1111/j.1365-246X.1992.tb00836.x.

Zelt, C. A. & Barton, P. J., 1998. Three-dimensional seismic refraction tomography: A comparison of two methods applied to data from the Faeroe basin. J. Geophys. Res, 103, 7189–7210.

Zhu, J., 2010. Crustal structure and subduction erosion in the central Costa Rica subduction zone, PhD-Thesis, University of Kiel, Germany, 129 pp.

**Zhu, J., Kopp, H., Papenberg, C., Klaeschen, D., Flueh, E. R., Planert, L., 2010. Seismic attentuation across the central Costa Rica margin wedge. Marine Geology, 276, 30-41, doi:10.1016/j.margeo.2010.07.004.**

**Zhu, J., Kopp, H., Flueh, E. R., Klaeschen, D., Papenberg C., 2009. Crustal structure of the central Costa Rica subduction zone and basal erosion of the upper margin wedge from seismic wide-angle data. Geophys. J. Int., 178, 1112-1131, doi: 10.1111/j.1365-246X.2009.04208.x.**

# APPENDIX

## Catalogue of publications

1) Kopp & Kukowski 2003

This paper provided evidence for across-strike margin segmentation along the Sunda margin, resulting from non-steady state accretion. H. Kopp was responsible for data analysis and writing the manuscript. N. Kukowski assisted in data interpretation.

2) Zhu et al. 2010

This study investigated across-strike segmentation in an erosive setting, unraveling a number of similarities to the accretionary case described in Kopp & Kukowski 2003. J. Zhu processed and analyzed the data and wrote the manuscript. H. Kopp was head of the seismic group on FS SONNE responsible for data acquisition and supervised J. Zhu's PhD thesis. She reviewed the manuscript and provided input for data interpretation.

3) Shulgin et al. 2009

A. Shulgin was responsible for data analysis and interpretation of a wide-angle profile covering the incipient collision of the Australian margin with the Banda island arc east of Sumba island. H. Kopp was PI on the SINDBAD project, wrote the proposal and supervised the research. E. R. Flueh served as chief scientist on cruise SO190.

4) Kopp et al. 2006

This paper established frontal erosion as the main mechanism of mass transfer offshore Central Java. H. Kopp was PI on the MERAMEX project, analyzed the data and wrote the paper. E. R. Flueh was chief scientist on cruise SO179.

5) Kopp et al. 2008

This contribution investigates the lower slope morphology offshore Sumatra using high-resolution seismic data. H. Kopp was PI on the SEACAUSE project, interpreted the data and wrote the manuscript. W. Weinrebe provided important input during data analysis and S. Ladage assisted in data compilation and merging of various data sets.

6) Planert et al. 2010

L. Planert analyzed and interpreted two regional wide-angle dip lines and strike-lines along the eastern Sunda margin. This work provided the first deep-penetrating seismic images of this margin segment. H. Kopp was PI on the SINDBAD project, assisted in data interpretation and reviewed the paper. E. R. Flueh was chief scientist on cruise SO190.

7) Kopp et al. 2009

This paper investigates the deep structure of the Java subduction zone and images the plate boundary in unprecedented detail. D. Hindle and D. Klaeschen processed the data. H. Kopp was PI on the SUNDA project and interpreted the multiscale data set consisting of seismic multichannel and refraction data and high-resolution bathymetry data. O. Oncken and D. Scholl provided important comments during data interpretation.

8) Zhu et al. 2009

This study was a precursor of the Zhu et al. 2010 publication. The central Costa Rica margin is investigated using densely spaced refraction data along two parallel strike and two parallel dip lines. J. Zhu conducted the data processing and forward modeling/inversion. H. Kopp interpreted the data and jointly with J. Zhu wrote the paper.

9) Koulakov et al. 2010

This contribution introduces a new inversion approach by combining seismic tomography and forward modeling. I. Koulakov and T. Stupina programmed the code and H. Kopp provided insight regarding inversion and modeling of refraction seismic data as well as writing the data analysis and conclusions chapters of the manuscript.

10) Weinzierl & Kopp 2010

W. Weinzierl used refraction data from the Antilles margin to develop a novel data analysis scheme based on statistics. H. Kopp wrote the TRAIL cruise proposal, supervised the PhD thesis of W. Weinzierl including this study and reviewed the manuscript.

11) Kopp et al. 2010

The data presented in this paper were acquired in the scope of one of the largest European amphibious initiatives ever conducted. A regional wide-angle profile crossing the Lesser Antilles island arc was processed and analyzed by W. Weinzierl together with multichannel seismic data that were depth-migrated by D. Klaeschen. H. Kopp interpreted the data with substantial input from E. Flueh, M. Laigle and A. Hirn and wrote the paper. E. Flueh was chief scientist of cruise MSM04/2.

12) Scherwath et al. 2010

This paper presents the analysis of wide-angle and reflection seismic data in combination with magnetic data across the Hikurangi subduction zone. M. Scherwath was responsible for modeling the data and drafting the manuscript. Data interpretation was a joint effort of M. Scherwath, H. Kopp, S. Henrys, R. Sutherland and E. Flueh. H. Kopp was PI on the MANGO project and provided comments during the manuscript review process. E. Flueh was chief scientist of cruise SO192.

13) Shulgin et al. 2010

This study investigates the deep structure of the eastern Java margin and the source region of the 1994 Java tsunami earthquake. A. Shulgin conducted the data processing and analysis and wrote the manuscript. A. Shulgin, H. Kopp and E. Flueh jointly interpreted the data set. H. Kopp served as PI on the SINDBAD project and supervised the PhD thesis of A. Shulgin and revised the manuscript. E. Flueh was chief scientist on cruise SO190.

14) Kopp 2010

This paper presents a synopsis of the work conducted along the Java sector of the Sunda margin. It is an invited contribution to a Geological Society of London Special publication (Southeast Asian Gateways volume). H. Kopp compiled the data and was responsible for data interpretation. The manuscript reviews the structure, deformation and seismicity offshore Java.

# 1

Kopp, H. & Kukowski, N., 2003.

**Backstop geometry and accretionary mechanics of the Sunda margin.**

Tectonics, 6, doi:10.1029/2002TC001420.

# Backstop geometry and accretionary mechanics of the Sunda margin

Heidrun Kopp

GEOMAR Research Center for Marine Geosciences, Kiel, Germany

Nina Kukowski

GFZ GeoForschungsZentrum, Potsdam, Germany

Received 29 May 2002; revised 14 March 2003; accepted 18 July 2003; published 11 December 2003.

[1] The convergent Sunda margin off Indonesia displays all geological features characteristic of an accretion-dominated subduction zone. A combined interpretation of prestack depth-migrated seismic reflection data and velocity information gained from refraction studies is supplemented by high-resolution bathymetric data and for the first time allows the exact mapping of backstop regimes. Initially, the outer high evolved as material was pushed against a static rigid arc framework backstop underlying a forearc basin. Increasing material strength of the outer high due to lithification formed a dynamic backstop, which controls accretion today. An out-of-sequence thrust marks the transition from the recent active frontal accretionary prism to the outer high and may be traced in the seismic and bathymetric data over the whole extent of the study area. The existence of a static as well as a dynamic backstop controls the forearc geometry and is associated with the segmentation of the forearc, which is observed in regimes of frontal as well as of oblique subduction. Mass balance calculations, which account for porosity changes and metamorphism, indicate a subduction history dominated by accretionary processes since the late Eocene. Accretion is associated with the low values of basal friction inferred for the Sunda margin. Structural investigations of conjugate fault planes indicate a very weak basal detachment. Effective stress analyses reveal that intrinsically weak material causes the high strength ratio of the detachment to the overlying sediments, whereas overpressuring within the frontal accretionary prism is negligible. *INDEX TERMS:* 8020 Structural Geology: Mechanics; 8045 Structural Geology: Role of fluids; 8010 Structural Geology: Fractures and faults; 8015 Structural Geology: Local crustal structure; 9340 Information Related to Geographic Region: Indian Ocean; *KEYWORDS:* morphotectonics, mass balance, effective stress analysis, backstop geometry, prestack depth migration, wide-angle seismics. **Citation:** Kopp, H., and N. Kukowski, Backstop geometry and accretionary mechanics of the Sunda margin, *Tectonics*, *22*(6), 1072, doi:10.1029/2002TC001420, 2003.


0278-7407/03/2002TC001420$12.00

## 1. Introduction

[2] A wide variety of tectonic styles at subduction zones, including erosional and accretionary regimes, has been documented by seismic data. Most subduction zone histories are nonuniform and are characterized by alternate phases of subduction erosion and subduction accretion. The fundamental role of a mechanical boundary or "backstop" on the evolution of forearc geometries, especially on the evolution of a structural outer high as is characteristic for many accretionary type margins, has been recognized by *Dahlen* [1990]. The term backstop defines a region within a forearc that is characterized by an increased yield strength compared to the region trenchward of it and thus its ability to support larger deviatoric stresses. The seaward material then deforms at a greater rate and thus presents a contrast in strain rate to the landward section [*Davis*, 1996], resulting in a segmentation of an accretionary complex, as described for the Sunda margin by *Schlüter et al.* [2002]. Zones of distinct strength contrast may result from changes in lithology and thus naturally coincide with contrasts in material properties such as density and seismic velocity. A variety of materials may act as backstop, ranging from arc framework (continental or oceanic) to features like an allochthonous terrane or well-lithified paleoaccreted material displaying a higher degree of consolidation and densification than the more recently accreted sediment seaward of it. The kinematic discontinuities which form a backstop may be "static", as would be the case for continental arc basement, or "dynamic" and thus still deforming, though at a slow rate, as may be expected for compacted accreted material resulting from an earlier phase of accretion. Though numerous backstop geometries have been modeled for different subduction settings, their identification in nature, especially for deeper lying backstops, is often difficult due to the limited penetration of seismic reflection data. Shallow backstops at less than 10 km depth have successfully been imaged, e.g., off Peru [*von Huene et al.*, 1988], off Alaska [*Fruehn et al.*, 1999], and in the Ryukyu forearc [*Font et al.*, 2001]. In this study, the existence of multiple kinematic boundaries in a single subduction complex is inferred from the combined interpretation of seismic reflection profiles and deeply

penetrating seismic refraction data as well as high-resolution bathymetry from the Sunda margin off Indonesia. The seaward dipping arc basement acts as a strong static backstop, whereas a weaker and younger backstop composes the fossil part of the accretionary wedge. It will be shown in this paper that the existence of the main forearc structures (i.e., forearc basin and outer high) is fundamentally linked to the presence of the static arc framework backstop. The younger minor backstop is a dynamic, still deforming zone of low strain rate along a kinematic boundary in the segmented forearc. The presence of a strong static backstop as well as a weaker dynamic backstop plays the crucial role in the development of tectonic features along this margin, whereas the oblique component of subduction results in transpressional expressions of the plate collision.

[3] An additional aspect of this study investigates the influence of the varying mechanical properties on the segmentation of the forearc and the corresponding morphological attributes. Implications on accretionary mechanics are drawn from structural relations of conjugate failure planes. Conjugate forethrusts and back thrusts are imaged in a depth section near the Sunda deformation front and are employed in an effective stress analysis.

## 2. Tectonic Setting of the Sunda Convergent Margin

[4] The Sunda Arc convergent margin curves along the islands of Sumatra and Java in Indonesia and marks the collision zone between the Indo-Australian plate and Eurasia. This sector of the subduction system has been active since middle Tertiary time, as inferred from dating of the Sunda system volcanism [*Hamilton*, 1988]. The northern and central part of the margin, from northern Sumatra to western Java, has been the site of geophysical and geological research, mainly attracted by the unique setting of an increasing subduction obliqueness to the north [*Fitch*, 1972; *Hamilton*, 1979; *Huchon and Le Pichon*, 1984; *McCaffrey*, 1992; *Diament et al.*, 1992; *Malod and Kemal*, 1996]. While the nature of the outer high, which is present all along the subduction zone and emerges subaerially as a chain of islands off Sumatra, has long been debated, recent studies support an accretionary origin of the outer high and a subduction history dominated by accretion over erosion. At present times, the central Sunda margin may be described as accretionary and thus, in view of the large fraction of modern subduction zones that have been found to be erosional [*von Huene and Scholl*, 1991; *Ranero and von Huene*, 2000], represents one end-member of convergent margins. It displays a deep trench, an actively accreting frontal prism and a massive fossil outer high adjacent to a well-developed forearc basin, which carries several kilometers of sediment fill [*Moore et al.*, 1980]. Numerous geological parameters change along the arc, including the age of the oceanic plate and the convergence rate, both of which increase toward Java and Bali, while the thickness of the incoming ocean basin deposits and trench fill decrease in the same direction [*Hamilton*, 1979]. The curvature of the trench results in regimes of frontal subduction off Java to oblique subduction off Sumatra [*Fitch*, 1972; *Moore et al.*, 1980; *McCaffrey*, 1996; *McCaffrey et al.*, 2000]. The central part of the Sunda margin marks the onset of oblique subduction south of the Sunda Strait [*Malod et al.*, 1995]. Though the oblique collision results in the development of the lithospheric-scale Sumatra Fault [*Sieh and Natawidjaja*, 2000] and possibly the offshore Mentawai Fault zone [*Diament et al.*, 1992], structural effects from the change in orientation of the trench on the adjacent subduction complex are limited and not yet clearly evidenced. The existence of the highly deformed outer high and the seemingly paradoxical presence of mainly undeformed sedimentary units in the adjacent forearc basin result from the influence of a static backstop as shown here which is formed by the arc framework of the upper plate's leading edge. Refraction seismic studies have shown that the arc basement is continental in nature along southern Sumatra, changing to an oceanic character off western Java [*Kopp et al.*, 2001, 2002]. The outer high, which represents the fossil part of the accretionary wedge, is of Eocene-Oligocene age [*Pubellier et al.*, 1992; *Samuel and Harbury*, 1996] and most likely composed of accreted material, as suggested by field mapping [*Moore and Karig*, 1980], refraction and gravity data [*Kieckhefer et al.*, 1981; *Kopp et al.*, 2001, 2002], though deep drilling information is not available. Seismic investigations in the forearc basin off northern Sumatra have been correlated to drilling information and suggest an Oligocene age for the oldest sediments trapped here [*Beaudry and Moore*, 1981, 1985; *Izart et al.*, 1994; *Schlüter et al.*, 2002]. An Oligocene origin has also been attributed to the oldest sediments in the Sunda Strait [*Diament et al.*, 1990; *Lelgemann et al.*, 2000].

## 3. Data

### 3.1. Bathymetry

[5] A grid of bathymetric data, mostly along single ship tracks, was acquired along the central portion of the Sunda margin (Figure 1) in late 1998 and early 1999. Full coverage was gained in an area off southern Sumatra between 102°E to 103°E and 6°25′S to 7°10′S as well as off western Java at about 9.3°S. The swath mapping was achieved using R/V Sonne's onboard Hydrosweep multibeam system [*Grant and Schreiber*, 1990] with a 90° beam angle. Subsequent processing of each sweep was conducted using mbsystem [*Caress and Chayes*, 1996] and GMT [*Wessel and Smith*, 1991]. Sonic velocity was measured employing a CTD instrument. To guarantee preservation of morphological detail, no data smoothing or filtering was performed. Track noise of overlapping parts of adjacent tracks in perspective views (Figures 2 and 3) then allows an optical assessment of peak noise level.

### 3.2. Seismic Data and Processing

[6] Seismic wide-angle data were acquired along the black tracks shown in Figure 1 using a total of 40 ocean bottom hydrophone and seismometer stations [*Flueh and Bialas*, 1996; *Flueh and Shipboard Science Party*, 1999]. Seismic reflection data were collected on coincident lines

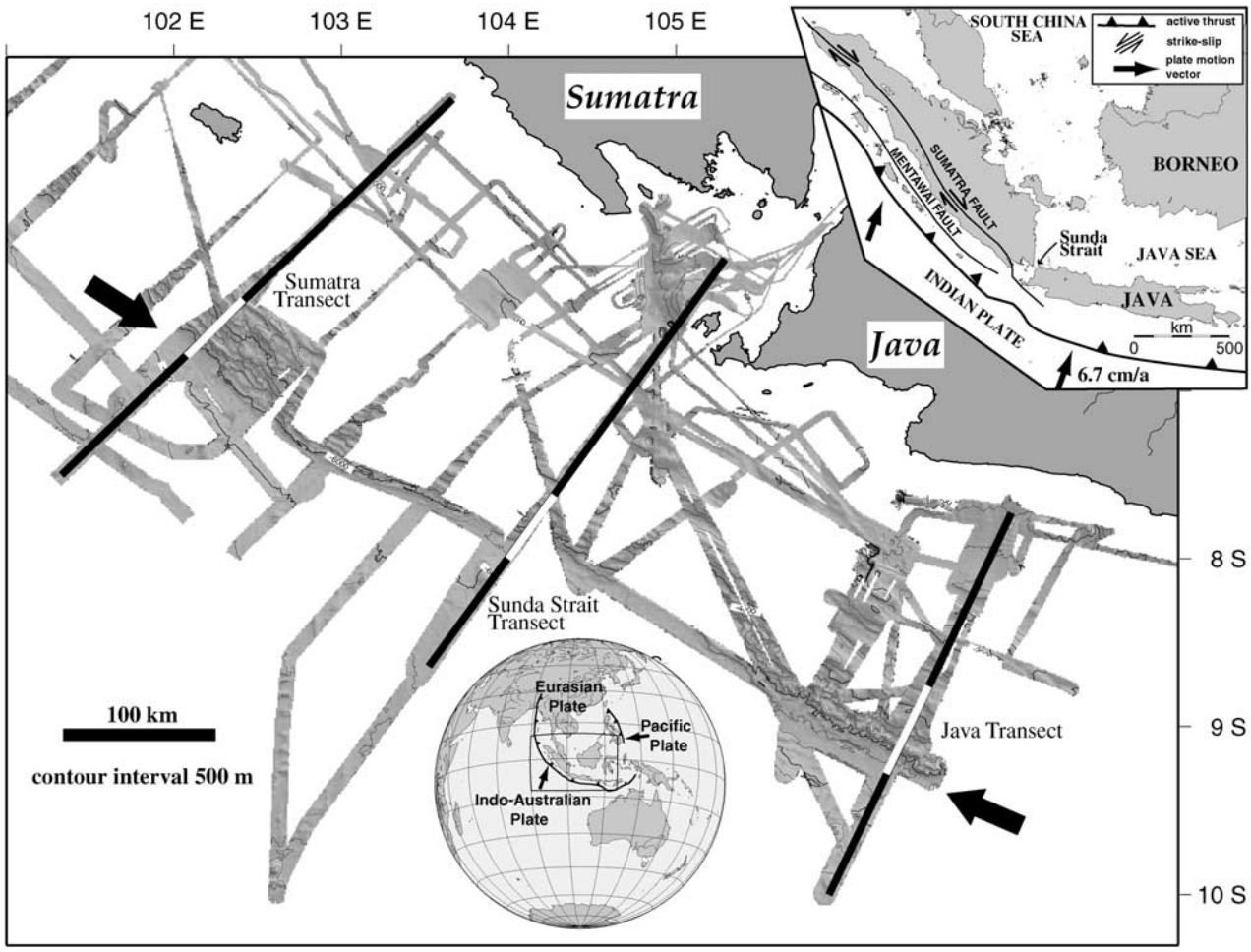


**Figure 1.** Bathymetric survey conducted along the central Sunda margin. Thick black lines depict the location of the seismic refraction profiles, and white sections along these lines represent the extent of the depth-migrated multichannel data. The Sunda Strait Transect is presented in Figure 4, and the Sumatra and Java Transects are shown in Figure 5. Arrows indicate the view direction for the 3-D bathymetric images presented in Figures 2 and 3.

by the BGR, Hannover, Germany [*Reichert et al.*, 1999].The entire data set and processing are described in detail by *Kopp et al.* [2001, 2002]. For this study, the white portions along the seismic tracks in Figure 1 were prestack depth migrated. The migrated reflection data are shown in Figures 4 and 5. An iterative migration procedure was applied which uses seismic velocities constrained by focusing analyses and common reflection point gathers [*Mackay and Abma*, 1993] as well as velocity information gained from the wide-angle data. Seismic velocities used during the migration process are interval velocities. The energy of a reflection point in the subsurface is focused using a range of velocities until an optimal image is achieved, which provides the highest energy at zero offset. Using an ideal velocity, the reflection position will be corrected. This in turn will yield better constraints on velocities during the next iteration and ray paths are determined more accurately. Prestack depth migration thus images complex dipping structures even in the presence of a strong lateral velocity gradient far better than conventional poststack migration procedures.

### 3.3. Seismic Sections: Tectonic Interpretation

[7] The seismic sections derived from prestack depth migration offer the precise image of the active frontal accretionary prism allowing the recognition of several common tectonic features characteristic for this margin. Three adjacent segments are recognized on all seismic sections (Figures 4 and 5) and will be described based on the interpretive section of the Sunda Strait profile presented in Figure 4. Segment I includes the sediment flooded trench. Vague seaward and landward vergent faults, originating several tens to hundreds of meters below the seafloor, cut the trench sediment sequences down to near the top of the igneous crust and mark the onset of deformation in the protothrust zone. The devel-

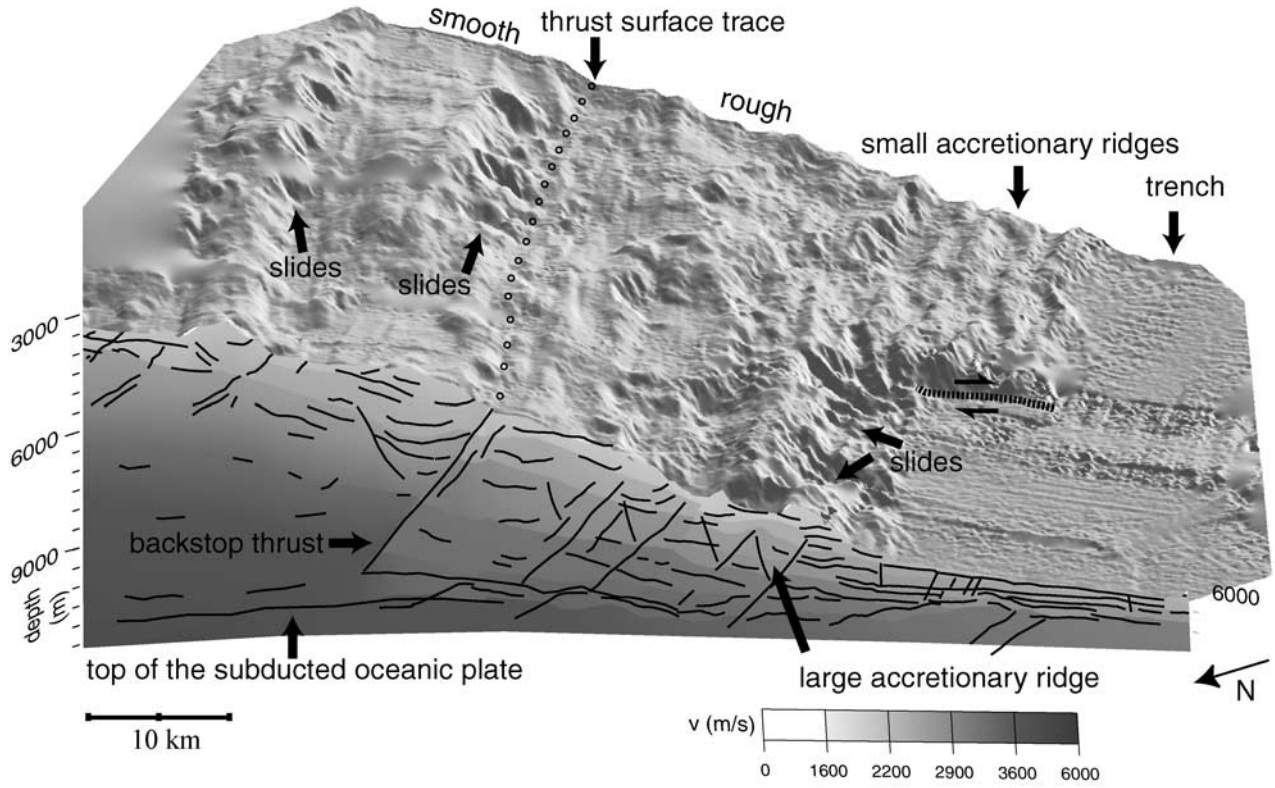


**Figure 2.** Three-dimensional bathymetric image of the deformation front and frontal accretionary prism off southern Sumatra viewed from the northwest. A line drawing of the depth-migrated profile and the corresponding velocity field are displayed in the cross section in the foreground. An increase in seismic velocities across an out-of-sequence thrust indicates a positive arcward gradient in material strength. The corresponding surface expression of this backstop thrust may be traced along the whole extent of the bathymetry survey as indicated by the circles. The striking retreat of the deformation front of about 8 km marks a transfer fault connecting supercritical portions of the slope characterized by slumps and slides in the NW to regularly spaced accretionary ridges in the SE.

opment of a pair of conjugate forethrust and back thrust manifests the inception of faulting at the deformation front. The occurrence of steep sets of conjugate reverse faults represents an extremely unusual geometry for a frontal zone of shallow thrusts above a décollement. The Sunda Strait line shows the finest example of a conjugate thrust pair near the deformation front (Figure 4). As addition of new material progresses, the shallower dipping forethrust becomes the dominant fault. Segment II forms the active accretionary domain and is characterized by tilted, regularly spaced thrust slices. These are separated by thrust faults (at times accompanied by secondary branch thrusts), which may cause minor offsets of the seafloor and cut the complete accreted wedge down to a detachment surface. These high-amplitude reflections are characteristic for a classical imbricate accretionary prism [*Davis and Hyndman*, 1989; *Moore et al.*, 1990; *von Huene and Klaeschen*, 1999] and indicate shear zones, which actively retain a constant surface slope along this segment. The increasing thrust length indicates the laterally increasing material strength due to dewatering which is highly effective along faults acting as conduits [*von Huene and Klaeschen*, 1999].

[8] Along all lines, an out-of-sequence thrust separates segments II and III, which correspond to the active accretionary domain and the fossil outer high, respectively (Figures 4 and 5). The difference in surface slope from segment II to segment III as well as out-of-sequence thrusting implies arcward variations in material properties [*Gutscher*, 1996]. A shallowing of the surface slope in segment III marks a gradual transition to material of greater strength, for which the taper must be adjusted. Little coherent imaging is resolved in the different structural style of segment III. Formerly generated, additional out-of-sequence thrusts are present in segment III, these are rotated and most of the time nonactive, as the outer high forms the fossil part of the accretionary prism [*Schlüter et al.*, 2002]. The possible intermittent reactivation of these faults helps adjust the taper [*Lohrmann et al.*, 2002], thus deformation results in vertical uplifting of the outer high rather than horizontal shortening, which is predominant in segment II of the frontal active accretionary domain. Overall, active

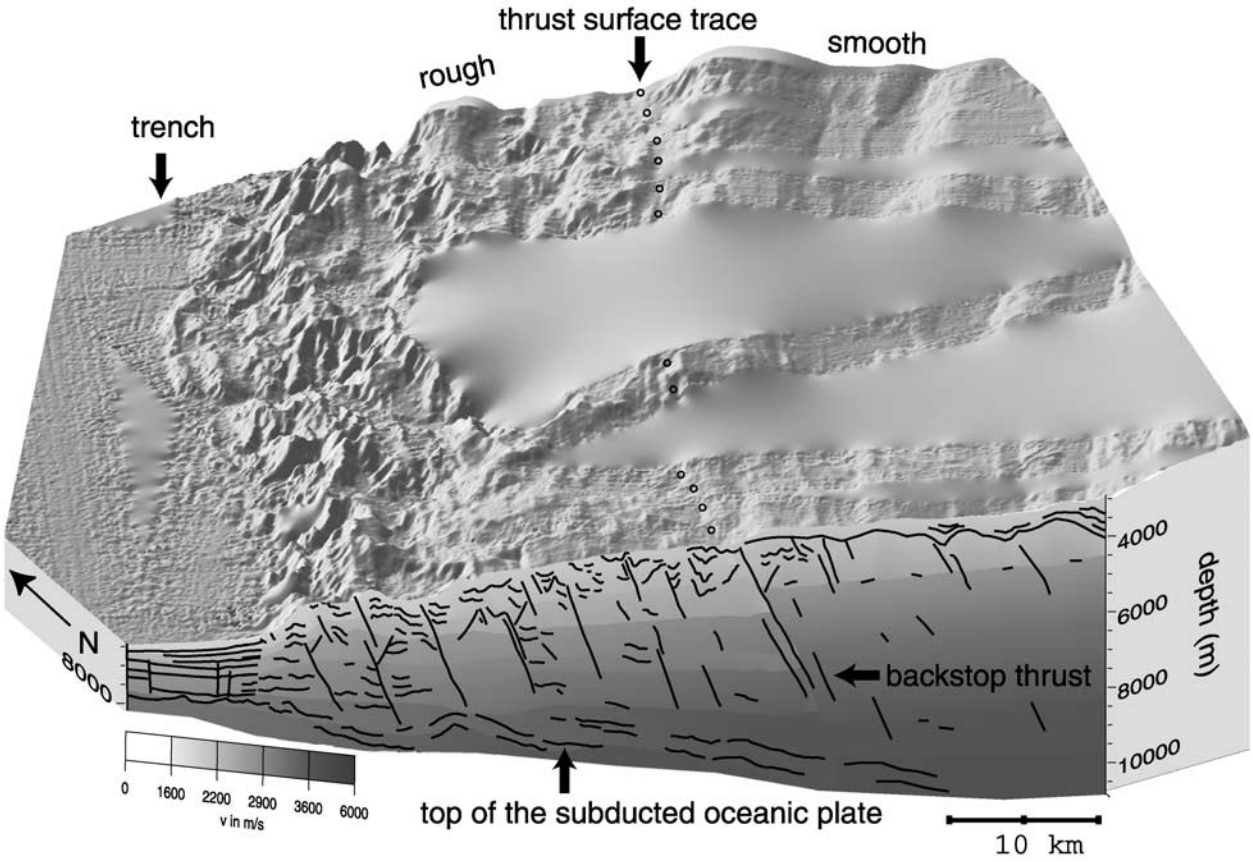


**Figure 3.** Bathymetric view of the deformation front and lower slope off Java viewed from the southeast. Please refer to Figure 2 for display information. An out-of-sequence thrust marking the seaward limit of the dynamic backstop corresponds to an increase in seismic velocities and is also recognized in the surface morphology. The rough topography in between the trench and the surface trace of the out-of-sequence thrust changes to a smooth seafloor arcward of the backstop thrust, where the intense fault activity is reduced.

faulting along the outer high is much reduced compared to segment II as the carbonate sedimentary cover [*Reichert et al.*, 1999] of the outer high is commonly not affected by the identified thrusts which cut the solidified portion of the outer high. Seismic velocities derived from prestack depth migration indicate a significant lateral velocity increase over the transition from segment II to segment III (Figures 2 and 3), which manifests the elevated material strength of the highly compacted accreted mass that comprises the outer high. Thus segment III acts as a transient backstop to the newly accreted material of segment II, as discussed further below.

[9] A detachment surface is most coherently imaged along the Sunda Strait segment, however, along all three profiles approximately 11–14% of the input sediment sequence is underthrust in a subduction window defined through the distance to the detachment surface and the top of the igneous crust beneath segment II and segment III (Figures 4 and 5). This low percentage of subducted material is to be expected for margins with large accretionary prisms, as observed along the Sunda margin [*von Huene and Scholl*, 1991]. Possible underplating of this material underneath the outer high is not resolved in our data.

## 4. Static and Dynamic Backstops: Control on Forearc Geometry

[10] The extensive folding and faulting of the incoming trench sediments in the vicinity of the deformation front is documented in the highly variable morphology here (Figures 2 and 3), which smoothes further landward in segment III, where active faulting of the accreted strata is reduced or ceases (Figures 4 and 5). Recent accretionary ridges are only recognized along the southeastern portion of the Sumatran transect (Figure 2). Velocities increase with depth, as may be expected from the larger overburden, but show little lateral variation up to the location of the out-of-sequence thrust. The thrust surface trace is clearly visible in the seafloor topography and may be followed along the whole extent of the bathymetry survey (black circles in Figures 2 and 3). It marks the seaward limit of the dynamic

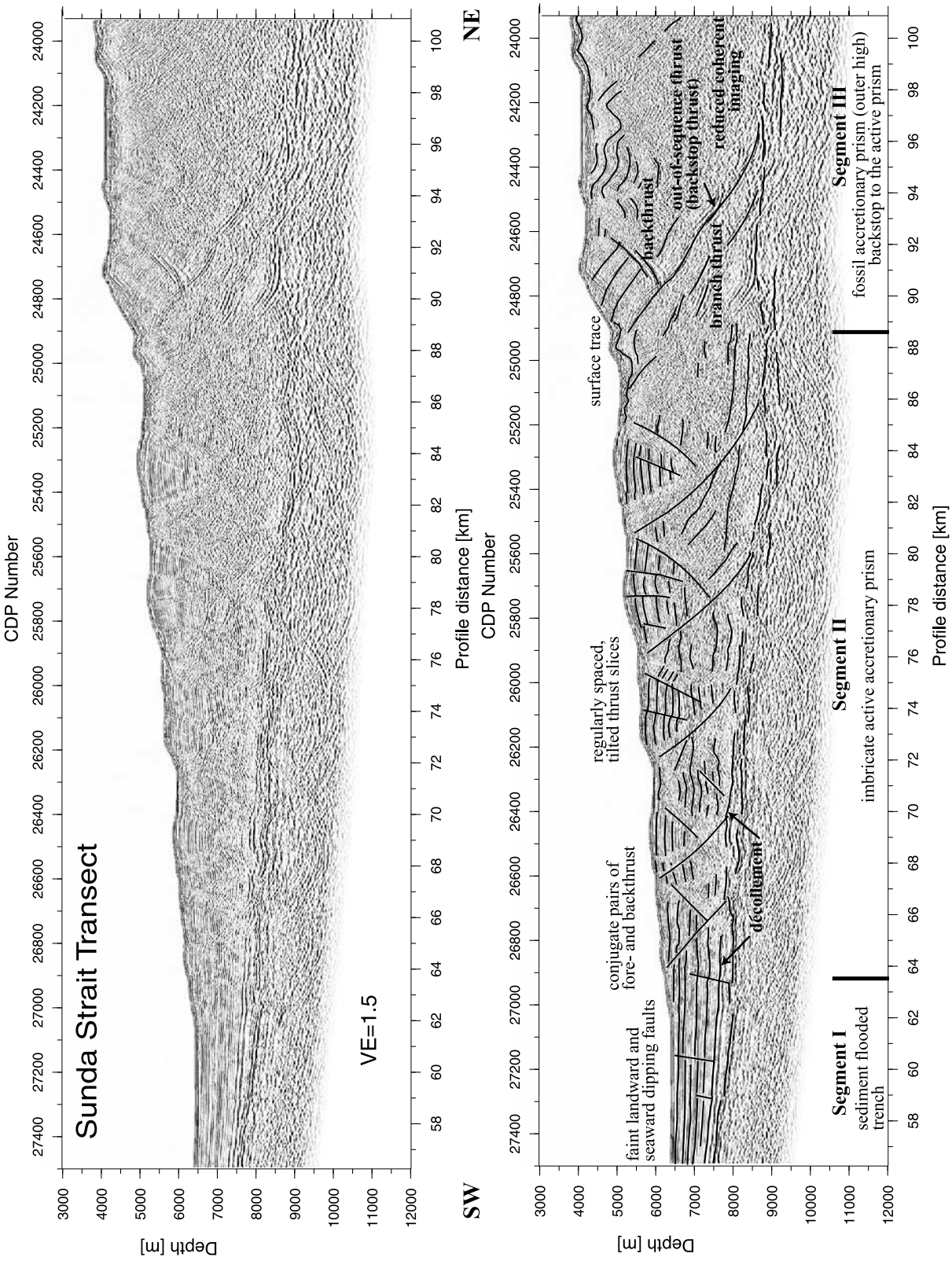
Sunda Strait Transect
VE=1.5
CDP Number
Profile distance [km]
Depth [m]
SW
NE
surface trace
backthrust
out-of-sequence thrust (backstop thrust)
branch thrust
reduced coherent imaging
regularly spaced, tilted thrust slices
conjugate pairs of fore- and backthrust
faint landward and seaward dipping faults
décollement
Segment I
sediment flooded trench
Segment II
imbricate active accretionary prism
Segment III
fossil accretionary prism (outer high) backstop to the active prism

backstop (segment III) (Figures 4 and 5). The sharp lateral velocity contrast across the out-of-sequence thrust is also recognized in the wide-angle sections covering these lines (Figure 6). The dynamic backstop is composed of fossil accreted material, which shows a positive landward gradient in the rate of lithification. Any nonuniform phase of accretion will cause a discontinuity in lithification and thus a contrast in strength sufficient to classify the landward portion as backstop to the unconsolidated ocean basin deposits and turbidites accreted at the deformation front. Deformation of the dynamic backstop is still occurring through intermittent reactivation of older thrusts in segment III. However, the rate of deformation is much lower than within the frontal accretionary prism. The frontal prism will have stress conditions consistent with predominantly arcward thrust dips [*Byrne et al.*, 1993], as established by the seismic images shown in Figures 4 and 5. This preferred dip will generally not extend past the dynamic backstop and is manifested in the area of intense faulting across the active accretionary domain of segment II. The outer high, which is the fossil portion of the accretionary wedge (i.e., the dynamic backstop), then experiences less arcward dipping faulting, as is also evident from the morphology in places where the seafloor roughness of the sediments overlying the dynamic backstop landward of the out-of-sequence thrust is reduced compared to the seaward portion (Figures 2 and 3).

[11] The downward limit of the dynamic backstop is provided by the subducting oceanic plate; the landward termination is marked by the leading edge of the upper plate arc framework underlying the forearc basin (Figure 6). This boundary between the outer high, which composes the dynamic backstop, and the arc framework, which acts as a static backstop, corresponds to a second kinematic boundary within this margin. The change in composition of this static backstop from continental arc framework off Sumatra to oceanic arc basement off western Java, as induced from refraction and gravity data [*Kopp et al.*, 2001, 2002] is subordinate for the development of the subduction zone complex, as a backstop is not linked to a specific composition but is characterized by a strength contrast, given here between the lithified paleoaccreted mass of the outer high and the stronger arc framework. The initial development of the outer high results from the gradual increase in both strength and bulk density as the material is compacted with depth and distance from the deformation front [*Byrne et al.*, 1993]. When this gradual increase in rock strength is replaced by a sharp transition at the static backstop, which can support larger loads, the increased net horizontal load is accommodated without further buildup of topography. As a result, the outer high develops above the seaward end of the static backstop. The backstop geometry found along the central Sunda margin (Figure 6) puts the toe of the static backstop near the top of the subducted oceanic plate (at profile km 130 for the Sumatra and Sunda Strait transects and at 105 km for the Java transect, compare Figure 6), so that little sediment is thrust beneath the backstop (trenchward dipping type I geometry of *Byrne et al.* [1993]). The static backstop casts a stress shadow over the area above itself, allowing the presence of a forearc basin which will experience no or little deformation as sediments are deposited within it [*Malavieille*, 1984; *Byrne et al.*, 1993]. The backstop then supports most of the regional horizontal compressive plate boundary stresses. The models presented in Figure 6 show an almost perfect alignment of the crest of the outer high to the toe of the static backstop, as has been predicted from numerical and sandbox modeling [*Byrne et al.*, 1993]. As the outer high is uplifted, the seaward part of the forearc basin experiences some uplift and deformation, resulting in landward tilting and pinching out of the older strata near the outer high as seen on line SO137-03 in *Kopp et al.* [2002].

## 5. Quantitative Estimates From Volume Balance Calculations

[12] Geological sampling on Nias Island, which forms part of the Outer High off northern Sumatra, suggest an Eocene-Oligocene age for this fossil part of the accretionary prism, i.e., recent dynamic backstop [*Moore and Karig*, 1980; *Moore et al.*, 1982; *Pubellier et al.*, 1992; *Samuel and Harbury*, 1996], which corresponds to a proposed Eocene onset or reinitiation of the current subduction phase [*Hamilton*, 1988; *Schlüter et al.*, 2002]. The forearc basin infill is younger as an Oligocene origin for the oldest sediment has been inferred [*Beaudry and Moore*, 1981, 1985; *Diament et al.*, 1990; *Lelgemann et al.*, 2000].

[13] The exact mapping of the tectonic regime along the central Sunda margin allows observations on the period of accretion on this convergence zone. The pure dimensions of the fossil accretionary wedge or outer high with a thickness of more than 15 km (compare Figure 6) suggest a long period of convergent processes dominated by accretion, which would be necessary to accumulate the amount of material observed here today. Mass balance calculations will give a rough estimate on the percentage of sediment subducted beneath the backstop and material accreted to form today's accretionary complex. Little information is available on the variation of geological parameters with time, foremost the convergence rate and the amount of

**Figure 4.** (opposite) Prestack depth-migrated section of the multichannel profile off the Sunda Strait. An arcward increase in material strength results in a segmentation of the margin. Faint seaward and landward dipping faults cut the trench fill in the protothrust zone of segment I, indicating the first stages of faulting. The deformation front marks the onset of faulting in conjugate pairs of forethrusts and back thrusts. The frontal active accretionary prism (segment II) is composed of tilted thrust slices separated by regularly spaced thrust faults. The transition to the fossil accretionary prism of the outer high is marked by a prominent out-of-sequence thrust. Segment III forms the backstop to the frontally accreted material and displays much reduced tectonic activity mainly manifested in the occasional reactivation of previous thrusts which helps adjust the taper.

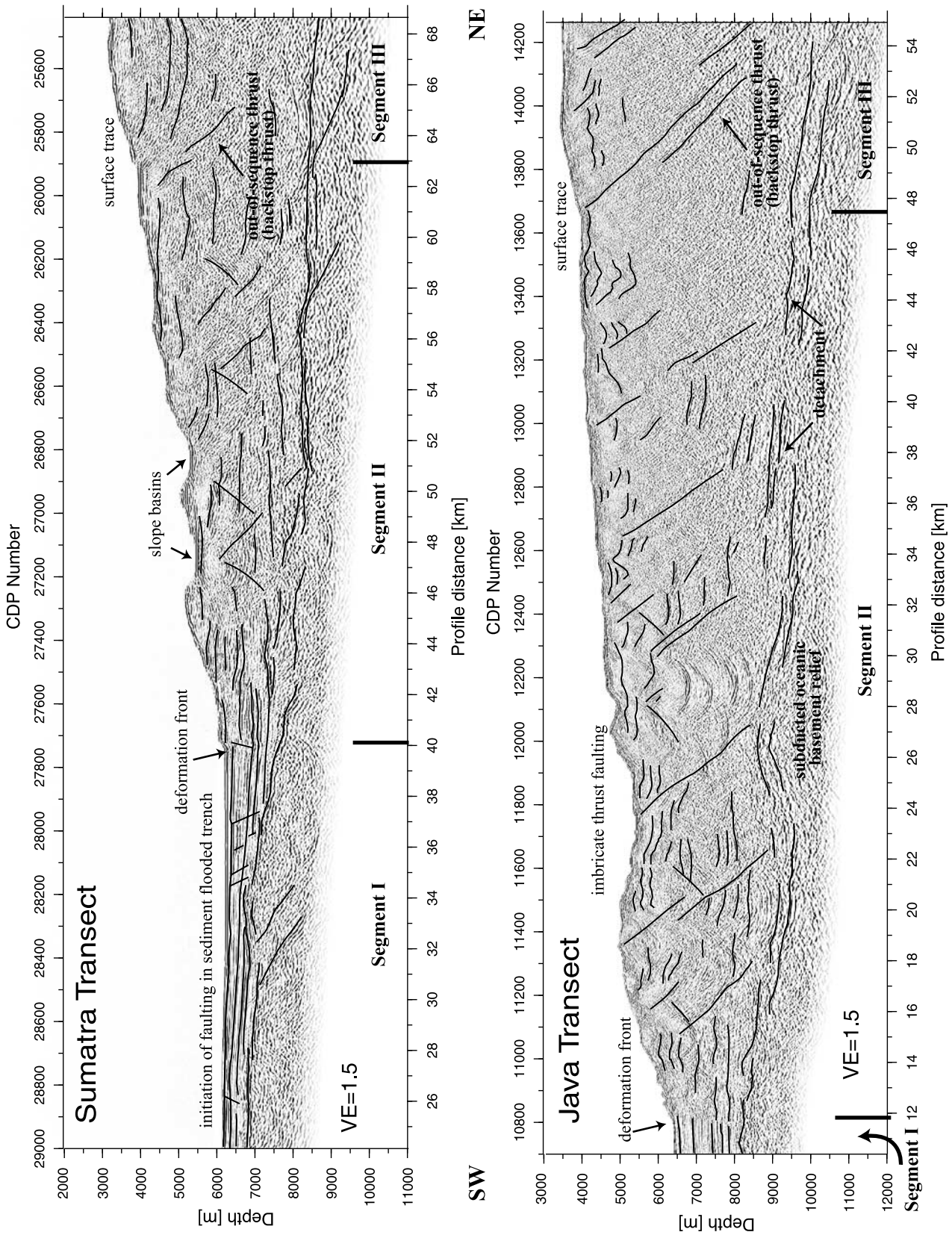
Sumatra Transect
surface trace
slope basins
deformation front
initiation of faulting in sediment flooded trench
out-of-sequence thrust (backstop thrust)
Segment I
Segment II
Segment III
VE=1.5
CDP Number
Profile distance [km]
Depth [m]
SW
NE
Java Transect
surface trace
imbricate thrust faulting
deformation front
subducted oceanic basement relief
detachment
out-of-sequence thrust (backstop thrust)
Segment I
Segment II
Segment III
VE=1.5
CDP Number
Profile distance [km]
Depth [m]

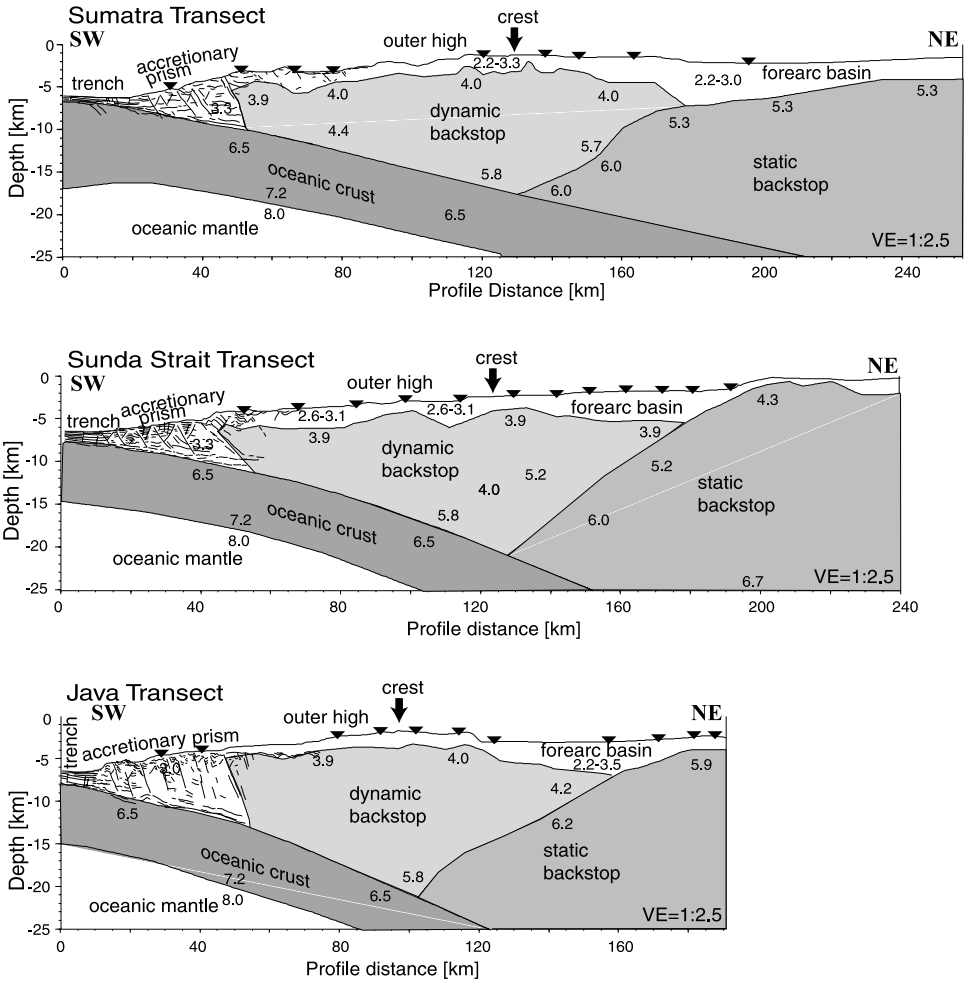


**Figure 6.** Structural models for the Sumatra, Sunda Strait, and Java sector, respectively. The line drawing of the depth-migrated multichannel data is incorporated near the seaward portion of the subduction zone. The extent of the dynamic and static backstops has been inferred from refraction seismic data and gravity modeling. Velocity labels are given in km $s^{-1}$. Inverted triangles depict OBH positions. The consecutive shallowing of the surface slope from the deformation front to the forearc basin is a response to changing material properties within the wedge and along the base. The coarse structural features observed along the margin include the active frontal accretionary prism, the fossil outer high, which is of accretionary origin, and the deep forearc basin. The development of the morphological outer high results from the presence of the static backstop of arc framework, which sheds a stress shadow to the overlying area, where a forearc basin carrying undeformed sedimentary strata develops. The dynamic backstop evolves from the well-lithified fossil accretionary wedge.

sediment input into the trench. Today's conditions are well known from numerous geophysical and geological studies and are thus applied to the volume estimations. However, severe limitations on any mass balance calculations result from the long period considered, as any tectonic framework will not have remained uniform. Today, the convergence rate increases from 6.3 cm/yr off southern Sumatra to 6.7 cm/yr off western Java [*Prawirodirdjo et al.*, 2000; *Tregoning et al.*, 1994]. The trench fill along the central Sunda margin decreases toward the east, as the sediment

**Figure 5.** (opposite) Prestack depth-migrated sections of the MCS profiles off southern Sumatra (upper image) and off Java (lower image). Similar structural features as along the Sunda Strait line are recognized. The frontal active accretionary prism (segment II) is separated from the stronger material of the backstop (segment III) by an out-of-sequence thrust. The increased material strength may support a narrower wedge along segment III, resulting in a decreased surface slope. Imbrication of segment II along regularly spaced thrust faults affects the whole accreted section down to the décollement, indicating near constant material properties for the entire wedge.

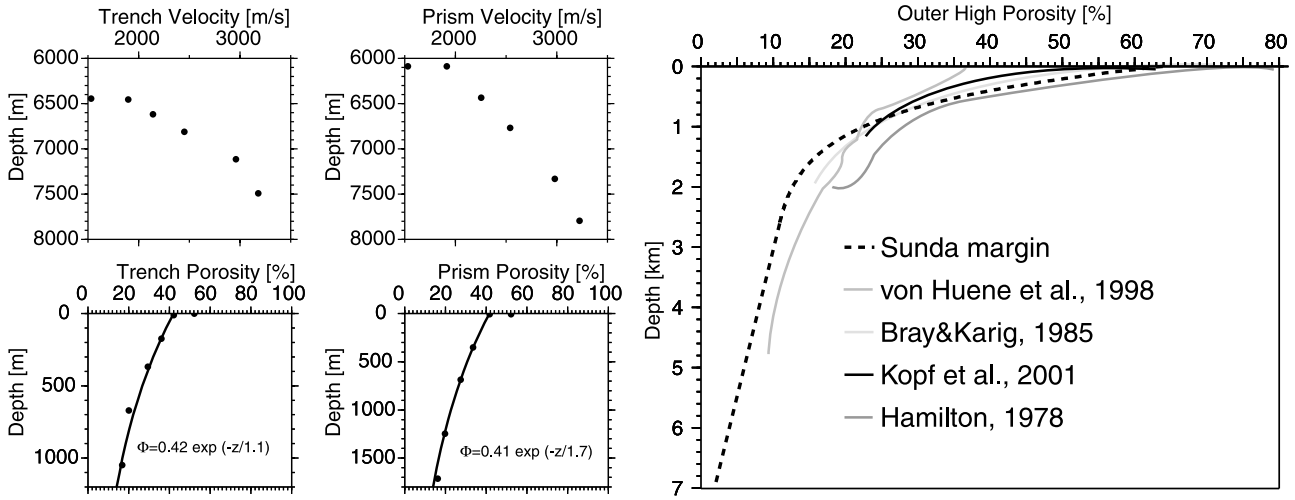


**Figure 7.** Porosity-depth relations for segments I to III of the margin. In the trench and lower accretionary prism, porosities are inferred from seismic interval velocities gained during prestack depth migration, which are transformed into porosities using a standard velocity-density relationship. Porosities Φ follow an exponential decay curve according to Athy's law. Along the outer high, exponential porosity decay in the upper 2.5 km is assumed, followed by a linear decay to 7 km depth (dashed curve). Below 7 km, porosities are negligible. Porosity-depth relations from other margins are displayed for comparison.

input from the Ganges-Bahmaputra system is reduced. A decreasing average trench fill from 1.3 km off Sumatra to 1.1 km off Java is used for the following discussion. These average values must be assumed, as the trench fill observed along the seismic lines shown here represent only a "snapshot" in time. Earlier investigations have shown that the ocean basin deposits input into the trench show a highly variable thickness on the oceanic plate seaward of the trench, ranging from 0 m to 900 m [*Kopp et al.*, 2001], thus the momentary trench fill does not reflect the overall decreasing sediment availability to the east. An areal balancing of the outer high (i.e., the dynamic backstop) is based on the combined reflection-refraction models presented in Figure 6 for which the estimated area was calculated from the pixel information contained in the graphical display of the model. This area estimated from the 2D display is then normalized to trench units to yield mass volume per trench kilometer. The observed volume of the outer high must be balanced against the trench input to derive the approximate period of accretion necessary to accumulate the observed accreted mass volume. To account for the varying pore space due to dehydration in the trench sediment and the outer high, the observed volumes are corrected to 0% porosity volume and thus converted to a solid mass equivalent for which the values derived for the trench and the outer high may be balanced directly. Today's volumes are derived from the pixel information contained in Figure 6, where a 10 × 10 km reference box contains 2352 pixels. As is obvious from Figure 6, the volume of the outer high decreases to the southeast, which corresponds to the pixel-derived mass volume values of 1372 $km^3$ per trench kilometer off southern Sumatra, 1210 $km^3$ off Sunda Strait and 967 $km^3$ off western Java. This also corresponds to the decreasing lateral extent of the dynamic backstop from 130 km off Sumatra to 94 km off Sunda Strait and 67 km off western Java. Reduction of the observed volumes to their solid mass equivalents is based on an empirical porosity-depth relationship (Figure 7) that was defined based on general information on sediment porosity in accretionary wedges and on laboratory measurements of porosity from Nias Island samples [*Bray and Karig*, 1985]. The porosity-depth curve is divided into four depth domains (a–d) for which different decay functions apply (Table 1): exponential porosity loss resulting from lithification is expected in a depth range down to 2.5 km below the surface (domain a); from 2.5 to 7 km depth (domain b), a linear decrease is assumed (Figure 7). At greater depth between 7 and 14 km (domain c), pore space is neglectable. Below 14 km depth (domain d), an increase in volume averaging approximately

**Table 1.** Porosity Decay Functions[a]

| | Exponential Decay Function | Linear Decay Function | Assumed Constant Porosity |
|---|---|---|---|
| Outer high | | | |
| Domain a, 0–2.5 km | $\Phi = 0.6 \exp(-1.437z - 0.1) + 0.16$ | | |
| Domain b, 2.5–7 km | | $\Phi = (z - 8)/50$ | |
| Domain c, 7–14 km | | | $\Phi = 2\%$ |
| Domain d, >14 km[b] | | | |
| Trench | $\Phi = 0.42 \exp(-z/1.1)$ | | |
| Frontal prism | $\Phi = 0.41 \exp(-z/1.7)$ | | |

[a]Here Φ is porosity, and $z$ is depth.
[b]Metamorphic processes leading to an assumed 1% volume increase.

**Table 2.** Mass Volumes

| Area | Observed Volume, km$^3$ | Solid Mass Equivalent, km$^3$ |
|---|---|---|
| Sumatra | 1372 | 1207 |
| Sunda Strait | 1210 | 1083 |
| Java | 967 | 871 |

1% resulting from metamorphic processes is included in the volume balancing. A solid mass volume for the dynamic backstop or outer high then is derived from the observed volume (corresponding to the four depth domains) and converted to a solid mass equivalent (Table 2) of 0% porosity by applying the porosity decay relationships applicable to the different depth domains.

[14] The derived solid mass volume comprises the fossil accretionary ridge which today forms the dynamic backstop and must thus be balanced against the input sequence (1.3 km off Sumatra, 1.25 km off Sunda Strait, 1.1 km off Java), which is converted to its solid mass equivalent using an exponential porosity-depth decay based on Athy's law (Figure 7, trench porosity) [*von Huene et al.*, 1998]. Seismic velocities derived from the focusing analyses performed during prestack depth migration were converted to porosities based on a standard velocity-density relationship [*Hamilton*, 1978; *Fruehn et al.*, 1997] using a pore water density of 1050 kg m$^{-3}$ and an average grain density of 2760 kg m$^{-3}$ for sediment. Global glacial conditions resulted in an increased sedimentation during glaciation during the last 2.5 Ma [*von Huene and Scholl*, 1991]. The Sunda margin however is located at low latitudes and receives almost all sediment input from the Ganges-Bahmaputra fan deposits, which arrived along the Sunda margin approximately 5 Ma [*Hamilton*, 1979]. Prior to this period, a reduced trench fill of 45% of the entire sequence is considered [*Hamilton*, 1979]. In addition, a seaward propagation of the deformation front of 2.75 km/Ma is assumed which corresponds to an Eocene onset or intensification of accretion.

[15] Analog to the trench, the solid mass equivalent of the frontal active accretionary prism in between the deformation front and the backstop (segment II in Figures 4 and 5) was gained by applying the porosity-depth relation shown in Figure 7 (prism porosity), which was also derived from the interval velocity field.

[16] From the seismic data presented here it cannot be judged unambiguously if the sediment sequence underthrusting the dynamic backstop within the subduction window is removed from the system by bypassing the static backstop or if it is underplated underneath the outer high. The mass balance calculations yield a solid mass equivalent of 1207 km$^3$ for the outer high off southern Sumatra (1083 km$^3$ off Sunda Strait and 871 km$^3$ off western Java). The period necessary to accrete this mass must comply with the mid- to late Eocene age of the outer high (45–37 Ma) assuming today's conditions on subduction and accretion, which are taken as a basis for the calculations. On the basis of today's conditions (e.g., convergence rate, deformation front propagation, trench input), a possible average fraction of minimum 13% (yielding an accretion period of 37 Ma) to maximum 26% (yielding 45 Ma) sediment may have been subducted along the margin to still accrete the observed mass volume in the given time range, e.g., removing 14% of the trench sequence from the system will yield an average period of accretion of 38 Ma to account for the solid fraction of the outer high (39.9 Ma off Sumatra, 38.5 Ma off Sunda Strait, 35.3 Ma off Java, corresponding to the decreasing volume of the outer high). Presuming all incoming sediment would remain in the system (0% subducted sediment), the mean period necessary to accumulate the outer high mass would be reduced by about 6.5 Ma. Mass balance calculations for the frontal accretionary prism (segment II) yield a Late Pliocene age for the material of this domain, averaging 2.6 Ma for 14% subducted trench fill.

[17] All these possible values are based on the tectonic conditions observed along the margin today. It is unlikely that the geological framework remained constant over such long periods, so the values indicated here only supply a mean average. The error bars are inversely proportional to the input error, i.e., assuming only half the convergence rate or trench fill of today's conditions will result in a time period that is doubled to what today's conditions would require. Distinct phases of the subduction history will have been characterized by varying sediment supply and convergence rate and by possible alternating phases of accretion and erosion. Assuming 30% subducted trench fill will yield an average period of 50 Ma to account for the outer high mass and a thus an initiation of subduction in the Middle to Early Eocene. Increasing this value to 50% would require a subduction period since the late Cretaceous and 80% would move this date to the Early Jurassic. Thus overall, accretion must have been the dominating process to account for the Eocene age of the outer high, which was emplaced before sedimentation filled the evolving forearc basin, where the oldest deposited strata are of Oligocene age.

## 6. Accretionary Mechanics

### 6.1. Implications From Structural Relations of Conjugate Faults

[18] The mechanics of submarine compressive accretionary prisms may be described by theoretical mechanical models, in which deforming material slides along a weak basal detachment and grows self-similar (analog to Dahlen's bulldozer wedge). The critical Coulomb wedge model [*Davis et al.*, 1983; *Dahlen*, 1990] predicts that the material within the wedge will deform under horizontal compression until a critical taper is reached and subsequently maintained. The general Coulomb criterion for shear stress $\tau$ of a cohesionless wedge at failure is of the form

$$\tau - \mu\sigma_n^*$$

where $\mu$ is the coefficient of internal friction [*Davis et al.*, 1983]. $\sigma_n^*$ is the effective stress and equals $\sigma_n = p_f$ with $\sigma_n$ denoting the vertical compressive stress and $p_f$ denoting the fluid pressure. The shear stress at the detachment is of equivalent form employing the analogue basal values. A weak detachment is thus a consequence of either intrinsically weak material at the base showing a low coefficient of

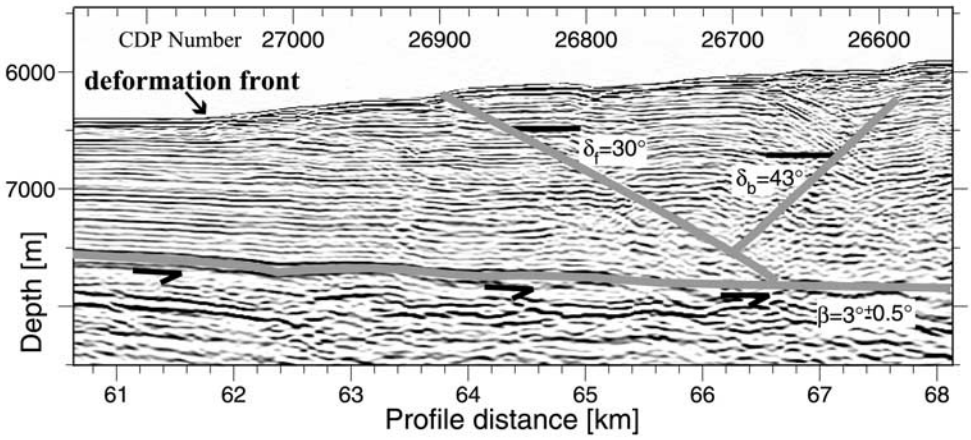


**Figure 8.** Detailed view of the deformation front and lower slope along the Sunda Strait transect. The structural analysis of the Sunda accretionary wedge is based on the geometry of the conjugate pair of forethrust and back thrust imaged in the depth-migrated profile. The relative dip angles of the thrusts to the décollement are gained from the relation $\delta_{\mathrm{Frel}} = \delta_f - \beta$ and $\delta_{\mathrm{Brel}} = \delta_b + \beta$.

basal friction $\mu_b$ or of a high degree of overpressuring at the base, or, as is most common, a combination of both. Analysis of structures within an accretionary prism, which is assumed to be a Coulomb wedge under horizontal compression (i.e., brittle fracture and frictional sliding occur), allows estimates on the angle $\phi$ and coefficient $\mu$ of internal friction and the basal stress orientation $\Psi_b$. Structural resolution of the Sunda Strait transect after prestack depth migration is sufficient to determine angular relations among a pair of conjugate thrust faults and the décollement (Figure 8). A prominent forethrust cuts the sedimentary sequence from the seafloor down to the décollement. Its conjugate back thrust is not as clearly imaged, but may be identified from truncated horizontal reflections. It offsets the seafloor near CDP 26600 and merges with the forethrust at CDP 26700. This pristine conjugate pair has not been rotated yet and the next pair of conjugate thrusts toward the deformation front has not fully developed and may only faintly be anticipated. Earlier error analyses [*Gutscher*, 1996] have shown that employing a pristine fault set is crucial for this method as a wrong estimate of $\Psi_b$ (e.g., due to slight rotation) will yield a 2.7 times larger error of $\mu$.

[19] From the dip angles of the thrusts ($\delta_f$ and $\delta_b$ in Figure 8) a basal stress orientation of $\Psi_b = 9.5°$ is derived [*Davis and von Huene*, 1987]. This direction of maximum compressive stress with the décollement follows from

$$\Psi_b = (\delta_{\mathrm{Brel}} - \delta_{\mathrm{Frel}})/2$$

The angle of internal friction $\phi$ may be derived from the relation

$$\phi = 90° - \delta_{\mathrm{Brel}} - \delta_{\mathrm{Frel}}$$

and is determined to be 17°. The coefficient of internal friction $\mu = \tan\phi$ then equals 0.31. Sediments of the frontal part of the accretionary wedge show only low cohesion, as the thrusts disclose neglectable bending (Figure 8) near the deformation front. For low cohesion, the direction of maximum compressive stress $\Psi_b$ is related to the coefficients of friction of the wedge ($\mu$) and the detachment zone ($\mu_b$) by

$$\Psi_b = \frac{1}{2}\arcsin(\sin\phi_{\mathrm{beff}}/\sin\phi) - \frac{1}{2}\phi_{\mathrm{beff}}$$

where $\phi_{\mathrm{beff}}$ is the angle of basal friction, from which the effective basal friction $\mu_{\mathrm{beff}} = \tan\phi_{\mathrm{beff}}$ may be derived after rearranging [*Kukowski et al.*, 2001]:

$$\mu_{\mathrm{beff}} = \sin(2\Psi_b)/(1/\sin\phi - \cos(2\Psi_b)) = 0.1316$$

The effective basal friction $\mu_{\mathrm{beff}}$ accounts for variations in fluid pressure in the prism ($\lambda$) and along the detachment ($\lambda_b$):

$$\mu_{\mathrm{beff}} = \mu_b(1-\lambda_b)/(1-\lambda)$$

where $\lambda$ is the ratio of fluid pressure to overburden pressure of Hubbert and Rubey [*Davis et al.*, 1983]. The ratio $\mu/\mu_{\mathrm{beff}}$ then expresses the strength ratio between the detachment zone and the sediment wedge above, as discussed, e.g., by *Davis and von Huene* [1987] and *Kukowski et al.* [2001]. As a result, the accreted sedimentary sequences along the Sunda Strait transect should be 2.3 times stronger than the detachment zone, either resulting from intrinsically weak material or from overpressuring near the base.

### 6.2. Effective Stress Analyses

[20] Investigations on the effective stress along the detachment will yield information on the fluid pressure ratio $\lambda$. Seismic velocities determined by focusing analyses during the prestack depth migration are converted to porosities using a standard velocity-density relationship as described above for the decompaction of the trench sediments (Figure 7). The porosity-depth relationship follows an

exponential decay corresponding to Athy's law [*Fruehn et al.*, 1997] of the form

$$\Phi = \Phi_0 \exp\{-z/c\}$$

where $\Phi$ is the porosity and $\Phi_0$ is the porosity at the seafloor, z is depth and c = 1.65 km is the compaction length. Using the definition of the effective stress $\sigma_n^*$ in terms of $\lambda$ yields

$$\sigma_n^* = (1-\lambda)\rho g z$$

where g is acceleration due to gravity. By eliminating z, porosities may be expressed as a function of $\lambda$:

$$\Phi = \Phi_0 \exp\{-((1-\lambda)\rho d/(\rho_w - \rho)c)\}$$

where $\rho$ is density, $\rho_w$ is water density, and d is depth below seafloor [*Allen and Allen*, 1990]. Determining $\lambda$ from this relationship yields slight overpressuring within the frontal prism ($\lambda$ = 0.46) and only marginal higher values at the basal detachment ($\lambda_b$ = 0.47). Pressure conditions throughout the prism thus remain nearly constant ($\lambda_b \approx \lambda$) and the coefficient of basal friction is only slightly larger than its effective value ($\mu_{beff}$ = 0.1316 and $\mu_b$ = 0.1346), accounting for the strength contrast of the overlying sediments to the weak décollement ($\mu_b < \mu$).

[21] The shear stress at the base, which describes the frictional sliding resistance, is given by:

$$\tau_b = (\rho - \rho_w) g d \alpha + (1-\lambda) K \rho g d (\alpha + \beta)$$

In the case of the prescribed physical properties $\mu$, $\mu_b$, and $\lambda_b \approx \lambda$, the dimensionless coefficient K may be derived directly from the angles of internal and basal friction $\phi$ and $\phi_b$, respectively [*Davis et al.*, 1983]. The low values of internal and basal friction encountered at the Sunda margin correspond to a value of K = 0.8. The frictional sliding resistance $\tau_b$ is thus counteracted by two effects: the first term is due to gravity acting on the slope of the accretionary prism ("glacier term"), while the second term results from the horizontal compression ("bulldozer term") [*Davis et al.*, 1983]. For the Sunda margin, the second term is about 20% larger than the glacier term, so that compressive stresses are an important, though not a sole dominating contribution to the basal shear stress.

## 7. Discussion

[22] The lateral variations in material strength along the Sunda margin play a crucial role in the evolution of the structural characteristics of this subduction zone. Fluctuations in internal as well as basal friction are directly linked to surface expressions along the forearc. An increase in internal material strength from the frontal accretionary prism (segment II) to the outer high (segment III) may be inferred from the increase in seismic velocities here. The stronger material supports a narrower wedge while still undergoing stable sliding at its base. This results in a decrease in surface slope landward of the out-of-sequence thrust. This effect is also witnessed at other accretionary subduction zones (e.g., Barbados accretionary wedge [*Bangs et al.*, 1990] or Alaska margin [*Ryan and Scholl*, 1989; *Fruehn et al.*, 1999]). Variations in the surface slope may alternatively evolve from fluctuations in basal friction, possibly resulting from a change in stratigraphy of the décollement material, or for areas where Coulomb behavior is no longer valid. Reduced basal resistance is expected beneath the outer high, as it occurs below the brittle-plastic transition below 12–16 km depth [*Davis et al.*, 1983]. It is here that the surface slope is shallowest (Figure 6) as a response to the plastic sliding along the detachment at greater depth. The surface slopes of individual thrust slices or accretionary ridges may be significantly steeper, though, as they are governed by the friction along the adjacent thrusts cutting through the stronger upper section of the accretionary prism. As the material composing the individual ridges is dehydrated and becomes stronger, thus showing a positive gradient in the coefficient of internal friction, the ridges may become supercritical. This is observed in the bathymetry, e.g., off southern Sumatra, where slumps and slides manifest an unstable regime.

[23] Overpressuring along the Sunda margin is insignificant, as most pore fluids have already been expelled near the deformation front where the numerous fractures act as conduits [*Faber et al.*, 2001; *Kopp*, 2002]. Dewatering is highly effective across stratigraphically controlled boundaries in the presence of fluid migration paths [*von Huene and Klaeschen*, 1999], prohibiting high pore pressures in the detachment zone. Thus dewatering likely contributes to the laterally increasing material strength, which leads to a segmentation of the frontal part of the margin and is also linked to the loss in brightness of the reflections in segment III. The composition, grain size, or conditions during sedimentation may also influence the low overpressuring. Comparably low values of basal friction and overpressuring have also been reported from the Makran accretionary wedge bordering the northern Indian Ocean [*Fruehn et al.*, 1997; *Kukowski et al.*, 2001], while high pore fluid pressures have been inferred for most other accretionary complexes (e.g., Alaska, Barbados, Nankai, Cascadia) [*Davis et al.*, 1983; *Lallemand et al.*, 1994]. Another similarity between Makran and Sunda is the intrinsic strength contrast between the décollement and the overlying sediments [*Kukowski et al.*, 2001].

[24] The mechanical properties of the wedge are essential for the material transfer. On the basis of the mass balance calculations, a possible scenario to account for the Eocene age of the outer high would imply that on average less than 30% of the sediment input is subducted and passes the static backstop. Frontal accretion is the dominant mode of transfer along the Sunda margin, and only a low percentage of sediment is underplated or subducted, similar to the situation along the Cascadia margin [*Davis and Hyndman*, 1989]. However, when new basal material transported into the subduction zone has properties such that $(1-\lambda_b)\mu_b > (1-\lambda)\mu$, it cannot form a décollement and a new décollement

must form higher in the wedge, leading to tectonic erosion. For an earlier phase of higher basal friction, a prism may partially be supercritical. Local variations of the surface slope along the Nankai accretionary wedge have been attributed to fluctuations in basal friction [*Moore et al.*, 1990]. Along the central Sunda margin, the dip of the décollement remains constant at ≈3°, whereas the surface slope decreases from ≈5.5° off Sumatra to 3° off Java. This slight decrease in surface slope may be caused by minor changes in material and basal properties. On a smaller scale, fluctuations in basal friction may also be linked to the local retreat of the deformation front off southern Sumatra, as recognized in the bathymetry image displayed in Figure 2. However, a detailed evaluation lies beyond the scope of the data.

[25] The structural effects resulting from a Sunda-type backstop geometry have been reproduced in analogue and numerical modeling [e.g., *Malavieille et al.*, 1993; *Byrne et al.*, 1993; *Buck and Sokoutis*, 1994; *Kukowski et al.*, 1994; *Wang and Davis*, 1996]. In the experiments, an outer high always developed in the presence of a strong trenchward dipping backstop, accompanied by the evolution of a depression between the morphological high and the arc, which becomes a forearc basin upon sedimentation [*Larroque et al.*, 1995]. Subcrustal erosion may enhance forearc basin evolution. It has been shown that the morphological effects are most pronounced for a seaward dipping backstop (type I geometry of Byrne). The growth of an outer high is diminished for a landward dipping backstop (type II geometry of Byrne) or intermediate geometry (i.e., toe of static backstop occurs at shallower depth within forearc), as have been mapped along the Cascadia and Peru margins, respectively [*Davis and Hyndman*, 1989; *von Huene et al.*, 1988]. Even though several types of backstops may exist simultaneously within a single margin, similar structural features resulting from backstop mechanics are predicted by modeling, even in the presence of a complex or multiple backstop [*Byrne et al.*, 1993] and are observed in nature along the Sunda margin. The existence of multiple backstops has also been proposed for the accretionary Barbados wedge [*Byrne et al.*, 1993] and is also inferred for the erosional Peru margin (A. Krabbenhoeft, personal communication, 2000) as well.

## 8. Conclusions

[26] Employing different data acquisition methods for the first time enables the exact mapping of the backstop system geometry along the Sunda subduction zone. An additional important aspect of this study is the observation that the structural elements characteristic for this subduction zone are present in regimes of frontal convergence in the east as well as in regimes of oblique convergence to the northwest. Oblique convergence was addressed by analogue modeling [*Calassou et al.*, 1993], which found that the main structural features perpendicular to the backstop would always develop, even for highly oblique convergence like off northern Sumatra. *Fitch* [1972] discussed the evolution of strike-slip faults along oblique convergence zones to compensate the lateral component of motion. Strike-slip faulting was reproduced in analogue experiments, where flower structures would develop near the static backstop [*Calassou et al.*, 1993]. Along the Sunda margin, the Mentawai fault zone has been proposed to take up the majority of displacement along strike [*Diament et al.*, 1992], though a stretching of the forearc sliver has also been inferred from geodetic data and slip vectors [*Fitch*, 1972; *Moore et al.*, 1980; *McCaffrey*, 1992; *McCaffrey et al.*, 2000].

[27] The Sunda plate boundary along its northern and central part represents a classic accretionary margin and in view of the low percentage of subducted trench material poses an end-member for this class of subduction zones. The geological framework of a subduction zone, namely the material input, the oceanic plate roughness, and the convergence rate, control whether accretion or erosion will dominate. The formation of the décollement is fundamentally linked to the mechanical properties of the progressing frontal prism and is essential for the size of the subduction window. The stress reduction observed along the Sunda décollement results from the intrinsically weak material observed here. Excess fluid pressures, which have been found to play a dominant role in a number of subduction zones, are inhibited along the Sunda margin by the intense degree of faulting and fracturing which is initiated in the trench and intensified along the frontal active accretionary prism. The evolution of morphological features, foremost of the outer high and forearc basin, however, are ruled by backstop dynamics above the static backstop. As accretion has remained stable along this margin, the outer high evolved as a consolidated and tectonically quiescent dynamic backstop, which controls recent accretionary processes.

[28] **Acknowledgments.** We are indebted to the BGR, Hannover, Germany, for providing the MCS and Bathymetry data collected during cruises SO137 and SO139 of R/V Sonne. Many thanks to the participants of the GINCO cruises for their help with data acquisition and preprocessing. Capt. Papenhagen and his crew ably assisted us at sea. We kindly acknowledge the help of W. Weinrebe with the processing of the Hydrosweep data and thank D. Klaeschen for support during prestack depth migration. We thank J. Lohrmann for discussions concerning wedge mechanics. Discussions with C. Kopp and A. Kopf helped clarify aspects on mass balancing. We thank E. R. Flueh for comments on the manuscript. Careful reviews by G. Moore, Associate Editor D. Cowan and Editor B. Wernicke helped tighten the manuscript considerably.

## References

Allen, P. A., and J. R. Allen, *Basin Analysis: Principles and Applications*, Blackwell Sci., 451 pp., Malden, Mass., 1990.

Bangs, N. L. B., G. K. Westbrook, J. W. Ladd, and P. Buhl, Seismic velocities from the Barbados Ridge Complex: Indicators of high pore fluid pressures in an accretionary complex, *J. Geophys. Res.*, *95*, 8767–8782, 1990.

Beaudry, D., and G. Moore, Seismic-stratigraphic framework of the forearc basin off central Sumatra, Sunda Arc, *Earth Planet. Sci. Lett.*, *54*, 17–28, 1981.

Beaudry, D., and G. Moore, Seismic stratigraphy and Cenozoic evolution of west Sumatra forearc basin, *AAPG Bull.*, *69*, 742–759, 1985.

Bray, C. J., and D. E. Karig, Porosity of sediments in accretionary prisms and some implications for dewatering processes, *J. Geophys. Res.*, *90*(B1), 768–778, 1985.

Buck, W. R., and D. Sokoutis, Analogoue model of gravitational collapse and surface extension during continental convergence, *Nature*, *369*, 737–740, 1994.

Byrne, D. E., W.-H. Wang, and D. M. Davis, Mechanical role of backstops in the growth of forearcs, *Tectonics*, *12*, 123–144, 1993.

Calassou, S., C. Larroque, and J. Malavieille, Transfer zones of deformation in thrust wedges: An experimental study, *Tectonophysics*, *221*, 325–344, 1993.

Caress, D. W., and D. N. Chayes, Improved processing of Hydrosweep DS multibeam data on the R/V *Maurice Ewing*, *Mar. Geophys. Res.*, *18*, 631–650, 1996.

Dahlen, F. A., Critical taper model of fold-and-thrust belts and accretionary wedges, *Annu. Rev. Earth Planet. Sci.*, *18*, 55–99, 1990.

Davis, D. M., Accretionary mechanics with properties that vary in space and time, in *Subduction: Top to Bottom*, *Geophys. Monogr. Ser.*, vol. 96, pp. 39–48, edited by G. E. Bebout et al., AGU, Washington, D. C., 1996.

Davis, E. E., and R. Hyndman, Accretion and recent deformation of sediments along the northern Cascadia subduction zone, *Geol. Soc. Am. Bull.*, *101*, 1465–1480, 1989.

Davis, D. M., and R. von Huene, Inferences on sediment strength and fault friction from structures at the Aleutian Trench, *Geology*, *15*, 517–522, 1987.

Davis, D. M., J. Suppe, and F. A. Dahlen, Mechanics of fold-and-thrust belts and accretionary wedges, *J. Geophys. Res.*, *88*, 1153–1172, 1983.

Diament, M., C. Deplus, H. Harjono, M. Larue, O. Lassal, J. Dubois, and V. Renard, Extension in the Sunda Strait (Indonesia): A review of the Krakatau programme, *Oceanol. Acta, Spec.* Vol., 10, 31–42, 1990.

Diament, M., H. Harjono, K. Karta, C. Deplus, D. Dahrin, M. T. Zan Jr., M. Gerard, O. Lassal, A. Martin, and J. Malod, Mentawai fault zone off Sumatra: A new key to the geodynamics of western Indonesia, *Geology*, *20*, 259–262, 1992.

Faber, E., J. Poggenburg, and W. Stahl, Methane in water and sediments, in *Summary and Synthesis of RV Sonne Cruises SO137-139 and Final Report Cruise SO139*, edited by H. Beiersdorf, *BGR Rep. 10815/01*, vol. *IV*, pp. 1–25, 2001.

Fitch, T. J., Plate convergence, transcurrent faults and internal deformation adjacent to Southeast Asia and the western Pacific, *J. Geophys. Res.*, *77*, 4432–4460, 1972.

Flueh, E. R., and J. Bialas, A digital, high data capacity ocean bottom recorder for seismic investigations, *Int. Underwater Syst. Design*, *18*(3), 18–20, 1996.

Flueh, E. R., and Shipboard Science Party, GINCO2 (*Sonne* Cruise SO-138): Geo-scientific investigations along the active convergence zone between the eastern Eurasian and Indo-Australian Plates off Indonesia, cruise report, Geomar, Kiel, Germany, 1999.

Font, Y., C.-S. Liu, P. Schnuerle, and S. Lallemand, Constraints on backstop geometry of the southwest Ryukyu subduction based on reflection seismic data, *Tectonophysics*, *333*, 135–158, 2001.

Fruehn, J., R. S. White, and T. A. Minshull, Internal deformation and compaction of the Makran accretionary wedge, *Terra Nova*, *9*, 101–104, 1997.

Fruehn, J., R. von Huene, and M. A. Fisher, Accretion in the wake of terrane collision: The Neogene accretionary wedge off Kenai peninsula, *Alaska, Tectonics*, *18*, 263–277, 1999.

Grant, J. A., and R. Schreiber, Modern swath sounding and subbottom profiling technology for research applications: The Atlas Hydrosweep and Parasound systems, *Mar. Geophys. Res.*, *12*, 9–19, 1990.

Gutscher, M.-A., Growth, erosion and material transfer in accretionary wedges: A quantitative analysis based on analog modeling and the implications for the evolution of convergent margins, Ph.D. thesis, Univ. Kiel, Kiel, Germany, 1996.

Hamilton, E. L., Sound velocity-density relations in sea-floor sediments and rocks, *J. Acoust. Soc. Am.*, *63*, 366–377, 1978.

Hamilton, W., Tectonics of the Indonesian region, *U.S. Geol. Surv. Prof. Pap.*, *1078*, 1979.

Hamilton, W., Plate tectonics and island arcs, *Geol. Soc. Am. Bull.*, *100*, 1503–1527, 1988.

Huchon, P., and X. Le Pichon, Sunda Strait and central Sumatra fault, *Geology*, *12*, 668–672, 1984.

Izart, A., B. Mustafa Kemal, and J. A. Malod, Seismic stratigraphy and subsidence evolution of the northwest Sumatra fore-arc basin, *Mar. Geol.*, *122*, 109–124, 1994.

Kieckhefer, R. M., G. F. Moore, and F. J. Emmel, Crustal structure of the Sunda forearc region west of central Sumatra from gravity data, *J. Geophys. Res.*, *86*, 7003–7012, 1981.

Kopf, A., D. Klaeschen, and J. Mascle, Extreme efficiency of mud volcanism in dewatering accretionary prisms, *Earth Planet. Sci. Lett.*, *189*, 295–313, 2001.

Kopp, H., BSR occurrence along the Sunda margin: Evidence from seismic data, *Earth Planet. Sci. Lett.*, *197*, 225–235, 2002.

Kopp, H., E. R. Flueh, D. Klaeschen, J. Bialas, and C. Reichert, Crustal structure of the central Sunda margin at the onset of oblique subduction, *Geophys. J. Int.*, *147*, 449–474, 2001.

Kopp, H., D. Klaeschen, E. R. Flueh, J. Bialas, and C. Reichert, Crustal structure of the Java margin from seismic wide-angle and multichannel reflection data, *J. Geophys. Res.*, *107*(B2), 2034, doi:10.1029/2000JB000095, 2002.

Kukowski, N., R. von Huene, J. Malavieille, and S. E. Lallemand, Sediment accretion against a buttress beneath the Peruvian continental margin as simulated with sandbox modeling, *Geol. Rundsch.*, *83*, 822–831, 1994.

Kukowski, N., T. Schillhorn, K. Huhn, U. von Rad, S. Husen, and E. R. Flueh, Morphotectonics and mechanics of the central Makran accretionary wedge off Pakistan, *Mar. Geol.*, *173*, 1–19, 2001.

Lallemand, S. E., P. Schnuerle, and J. Malavieille, Coulomb theory applied to accretionary and nonaccretionary wedges: Possible causes for tectonic erosion and/or frontal accretion, *J. Geophys. Res.*, *99*, 12,033–12,055, 1994.

Larroque, C., S. Calassou, J. Malavieille, and F. Chanier, Experimental modelling of forearc basin development during accretionary wedge growth, *Basin Res.*, *7*, 255–268, 1995.

Lelgemann, H., M.-A. Gutscher, J. Bialas, E. R. Flueh, W. Weinrebe, and C. Reichert, Transtensional basins in the western Sunda Strait, *Geophys. Res. Lett.*, *27*, 3545–3548, 2000.

Lohrmann, J., N. Kukowski, J. Adam, and O. Oncken, The impact of analogue material properties on the geometry, kinematics, and dynamics of convergent sand wedges, *J. Struct. Geol.*, *27*(21), 3545–3548, 2002.

Mackay, S., and R. Abma, Depth focusing analysis using wavefront-curvature criterion, *Geophysics*, *58*, 1148–1156, 1993.

Malavieille, J., Modelization exprimentale des chevauchements imbriqus: Application aux chaines de mountagnes, *Bull. Soc. Geol. Fr.*, *7*, 129–138, 1984.

Malavieille, J., C. Larroque, and S. Calassou, Modelization experimentale des relations tectonique-sedimentation entre bassin avant-arc et prisme d'accretion, *C. R. Acad. Sci., Ser. II*, *316*, 1131–1137, 1993.

Malod, J. A., and B. M. Kemal, The Sumatra margin: Oblique subduction and lateral displacement of the accretionary prism, in *Tectonic Evolution of Southeast Asia*, edited by R. Hall and D. Blundell, *Geol. Soc. Spec. Publ.*, *106*, 19–28, 1996.

Malod, J. A., K. Karta, M. O. Beslier, and M. T. Zen Jr., From normal to oblique subduction: Tectonic relationships between Java and Sumatra, *J. SE Asian Earth Sci.*, *12*, 85–93, 1995.

McCaffrey, R., Oblique plate convergence, slip vectors, and forearc deformation, *J. Geophys. Res.*, *97*, 8905–8915, 1992.

McCaffrey, R., Slip partitioning at convergent plate boundaries of SE Asia, in *Tectonic Evolution of Southeast Asia*, edited by R. Hall and D. Blundell, *Geol. Soc. Spec. Publ.*, *106*, 3–18, 1996.

McCaffrey, R., P. C. Zwick, Y. Bock, L. Prawirodirdjo, J. F. Genrich, C. W. Stevens, S. S. O. Puntodewo, and C. Subarya, Strain partitioning during oblique plate convergence in northern Sumatra: Geodetic and seismologic constraints and numerical modeling, *J. Geophys. Res.*, *105*, 28,363–28,376, 2000.

Moore, G. F., and D. E. Karig, Structural geology of Nias Island, Indonesia: Implications for subduction zone tectonics, *Am. J. Sci.*, *280*, 193–223, 1980.

Moore, G. F., J. R. Curray, D. G. Moore, and D. E. Karig, Variations in geologic structure along the Sunda fore arc, northeastern Indian Ocean, in *The Tectonic and Geologic Evolution of Southeast Asian Seas and Islands*, *Geophys. Monogr. Ser.*, vol. 23, edited by D. Hayes, pp. 145–160, AGU, Washington, D. C., 1980.

Moore, G. F., J. R. Curray, and F. J. Emmel, Sedimentation in the Sunda trench and forearc region, in *Trench-Forearc Geology*, edited by J. K. Leggett, *Geol. Soc. Spec. Publ.*, *10*, 245–258, 1982.

Moore, G. F., T. H. Shipley, P. L. Stoffa, D. E. Karig, A. Taira, S. Kuramoto, H. Tokuyama, and K. Suyehiro, Structure of the Nankai Trough Accretionary Zone from multichannel seismic reflection data, *J. Geophys. Res.*, *95*, 8753–8765, 1990.

Prawirodirdjo, L., Y. Bock, J. F. Genrich, S. S. O. Puntodewo, J. Rais, C. Subarya, and S. Sutisna, One century of tectonic deformation along the Sumatran fault from triangulation and Global Positioning System surveys, *J. Geophys. Res.*, *105*, 28,343–28,361, 2000.

Pubellier, M., C. Rangin, J.-P. Cadet, I. Tjashuri, J. Butterlin, and C. Mueller, L'ile de Nias, un edifice polyphase sur la bordure interne de la fosse de la Sonde (Archipel de Mentawai, Indonesie), *C. R. Acad. Sci., Ser. II*, *8*, 1019–1026, 1992.

Ranero, C. R., and R. von Huene, Subduction erosion along the Middle America convergent margin, *Nature*, *404*, 748–752, 2000.

Reichert, C., and Shipboard Science Party, GINCO1 (*Sonne* Cruise SO-137): Geo-scientific investigations along the active convergence zone between the eastern Eurasian and Indo-Australian Plates off Indonesia, cruise report, BGR, Hannover, Germany, 1999.

Ryan, H. F., and D. W. Scholl, The evolution of forearc structures along an oblique convergent margin, central Aleutian arc, *Tectonics*, *8*, 497–516, 1989.

Samuel, M. A., and N. A. Harbury, The Mentawai fault zone and deformation of the Sumatran forearc in the Nias area, in *Tectonic Evolution of Southeast Asia*, edited by R. Hall and D. Blundell, *Geol. Soc. Spec. Publ.*, *106*, 337–351, 1996.

Schlüter, H. U., C. Gaedicke, H. A. Roeser, B. Schreckenberger, H. Meyer, C. Reichert, Y. Djajadihardja, and A. Prexl, Tectonic features of the southern Sumatra-western Java forearc of Indonesia, *Tectonics*, *21*(5), 1047, doi:10.1029/2001TC901048, 2002.

Sieh, K., and D. Natawidjaja, Neotectonics of the Sumatran fault, Indonesia, *J. Geophys. Res.*, *105*, 28,295–28,326, 2000.

Tregoning, P., F. K. Brunner, Y. Bock, S. S. O. Puntodewo, R. McCaffrey, J. F. Genrich, E. Calais, J. Rais, and C. Subarya, First geodetic measurement of

convergence across the Java Trench, *Geophys. Res. Lett.*, *21*, 2135–2138, 1994.

von Huene, R., and D. Klaeschen, Opposing gradients of permanent strain in the aseismic zone and elastic strain across the seismogenic zone of the Kodiak shelf and slope, Alaska, *Tectonics*, *18*, 248–262, 1999.

von Huene, R., and D. W. Scholl, Observations at convergent margins concerning sediment subduction, subduction erosion and the growth of continental crust, *Rev. Geophys.*, *29*, 279–316, 1991.

von Huene, R., E. Suess, and Leg 112 Shipboard Scientists, Ocean drilling program Leg 112, Peru continental margin: Part I, tectonic history, *Geology*, *16*, 934–938, 1988.

von Huene, R., D. Klaeschen, M. Gutscher, and J. Fruehn, Mass and fluid flux during accretion at the Alaskan margin, *Geol. Soc. Am. Bull.*, *110*, 468–482, 1998.

Wang, W.-H., and D. M. Davis, Sandbox model simulation of forearc evolution and noncritical wedges, *J. Geophys. Res.*, *101*, 11,329–11,339, 1996.

Wessel, P., and W. H. F. Smith, Free software helps map and display data, *Eos Trans. AGU*, *72*, 441, 445–446, 1991.

H. Kopp, GEOMAR Research Center for Marine Geosciences, Wischhofstr. 1-3, D-24148 Kiel, Germany. (hkopp@geomar.de)

N. Kukowski, GFZ GeoForschungszentrumPotsdam, Telegrafenberg, D-14473 Potsdam, Germany. (nina@gfz-potsdam.de)

# 2

Zhu, J., Kopp, H., Papenberg, C., Klaeschen, D., Flueh, E. R., Planert, L., 2010.

**Seismic attentuation across the central Costa Rica margin wedge.**

Marine Geology, 276, 30-41, doi:10.1016/j.margeo.2010.07.004.

Marine Geology 276 (2010) 30–41

Contents lists available at ScienceDirect

Marine Geology

journal homepage: www.elsevier.com/locate/margeo

# Margin architecture and seismic attenuation in the central Costa Rican forearc

J. Zhu *, H. Kopp, C. Papenberg, D. Klaeschen, E.R. Flueh, L. Planert

*Leibniz-Institute of Marine Sciences (IFM-GEOMAR) and SFB574, Wischhofstrasse 1-3, 24148 Kiel, Germany*

ARTICLE INFO

*Article history:*
Received 23 January 2010
Received in revised form 3 July 2010
Accepted 12 July 2010
Available online 17 July 2010

Communicated by D.J.W. Piper

*Keywords:*
Seismic attenuation
Amplitude modeling
Décollement
Seismic tomography
Middle America Trench

ABSTRACT

Seismic attenuation across the central Costa Rican margin wedge is determined from amplitude analysis of wide-angle seismic data. Travel time and amplitude modeling are applied to ocean bottom hydrophones along two trench-parallel profiles, located 30 km (P21) and 35 km (P18) landward of the deformation front northeast of Quepos Plateau. Tomographic inversion images a progressively thinning margin wedge from the coast to the lower slope at the trench. A 1–1.5 km thick décollement zone with seismic velocities of 3.5–4.5 km/s is sandwiched between the margin wedge and the subducting Cocos plate. For strike line P21, amplitude modeling indicates a Qp value of 50–150 for the upper margin wedge with seismic velocities ranging from 3.9 km/s to 4.9 km/s. Along strike line P18, Qp values of 50–150 are determined with velocities of 4.3–5.0 km/s in the upper margin wedge, increasing to 5.1–5.4 km/s in the lower margin wedge. Quantitative amplitude decay curves support the observed upper plate Qp values. In conjunction with earlier results from offshore Nicoya Peninsula, our study documents landward decreasing attenuation across the margin wedge, consistent with a change in lithology from the sediment-dominated frontal prism to the igneous composition of the forearc middle prism.


## 1. Introduction

Seismic attenuation is an inherent property of wave propagation and a measure of the total energy loss when a seismic wave propagates through the earth. The amplitude and waveform characteristics of seismograms may be modeled using the reflectivity method (Fuchs and Mueller, 1971; Braile and Smith, 1975), adapted to the calculation of pressure or displacement waveforms and thus suitable for either hydrophone or seismometer refraction recordings (Kennett, 1977). We employ the seismic attenuation factor for the calculation of synthetic seismograms to investigate the effect of inelastic attenuation in the Costa Rican margin wedge northeast of the Quepos Plateau (Fig. 1).

The Pacific margin of Costa Rica is characterized by the subduction of the oceanic Cocos plate underneath the Caribbean plate and has been imaged along several refraction profiles deployed since 1996 (Ye et al., 1996; Stavenhagen et al., 1998; Christeson et al., 1999; Walther, 2003; Zhu et al., 2009). The age, thickness and seismic velocities of the downgoing plate vary from the Nicoya Peninsula in the northwest to the Osa Peninsula in the southeast (Fig. 1, inset). Whereas the thickness of the oceanic crust increases from 5–6 km in the northwest to up to 14 km in the southeast, the age decreases from 22–24 Ma to 15–18 Ma from NW to SE as inferred from the seafloor spreading anomalies (Barckhausen et al., 2001). Along most profiles, an upper mantle velocity of 8.0–8.1 km/s is revealed. An exception to this is the area underneath the Quepos plateau where upper mantle velocities of 7.6–7.8 km/s prevail. Comparably low mantle velocities are also imaged underneath the outer flank of the Cocos Ridge, where it has been attributed to remnants of mafic material in the upper mantle or a plume signature (Walther, 2003). The core of the forearc margin wedge incorporates a fragment of the Caribbean oceanic plateau (Nicoya complex) (Hauff et al., 1997; Sinton et al., 1997). This igneous rock unit forms the forearc basement and is covered by a sediment apron (Ye et al., 1996). Fronting this unit is the frontal prism, which consists of accreted upper plate sediment (von Huene et al., 2000).

To the southeast, from the tip of Nicoya Peninsula to the northern limit of Osa Peninsula, numerous bathymetric features dot the incoming plate and upon entry in the trench modulate forearc deformation and morphology (e.g. Dominguez et al., 1998; Ranero and von Huene, 2000; von Huene et al., 2000). In addition to tectonic erosion caused by the impinging bathymetric features (von Huene et al., 1995), outer forearc kinematics are characterized by widespread subsidence resulting from subduction erosion (Lallemand et al., 1992; Vannucchi et al., 2003), i.e. material removal from the base of the upper plate.

One of the major objectives of examining the lateral variations of Qp values is to evaluate lateral seismic velocity and physical state variations of the margin wedge. The seismic velocity structure of the Costa Rican margin wedge has been obtained by a number of

* Corresponding author. Now at: Key Laboratory of Marginal Sea Geology, South China Sea Institute of Oceanology, Chinese Academy of Sciences, Guangzhou 510301, China. Tel.: +86 20 89023155; fax: +86 20 89023135.
*E-mail addresses:* jzhu@ifm-geomar.de (J. Zhu), hkopp@ifm-geomar.de (H. Kopp), cpapenberg@ifm-geomar.de (C. Papenberg), dklaeschen@ifm-geomar.de (D. Klaeschen), eflueh@ifm-geomar.de (E.R. Flueh), lplanert@ifm-geomar.de (L. Planert).

0025-3227/$ – see front matter. 
doi:10.1016/j.margeo.2010.07.004

refraction experiments (e.g. Ye et al., 1996; Stavenhagen et al., 1998; Christeson et al., 1999; Walther, 2003; Zhu et al., 2009) and reflects the tectonic segmentation into a frontal prism, middle prism and inner prism as introduced by von Huene et al. (2009). We expect Qp variations to define these tectonic segments. The high signal-to-noise ratio of the first arrivals of the seismic data presented here facilitates amplitude modeling, as peak amplitudes are clearly identifiable. In this study, we firstly use seismic tomography to verify the velocity structure along two dip lines P15 and P24 and two strike lines P18 and P21 located offshore central Costa Rica (Fig. 1). We then employ the reflectivity method to constrain attenuation and velocity gradients in the margin wedge along the two strike lines. We compare our results to previous investigations of seismic attenuation conducted offshore Nicoya Peninsula, approximately 210 km to the northwest of our lines (Christeson et al., 2000) (Fig. 1). The generally low Qp values of the margin wedge indicate a highly tectonized frontal and middle prism, characterized by a high degree of fracturing. The seismic attenuation variations from the frontal prism to the middle prism document the lateral variations in lithology and physical state of the rock units.

## 2. Wide-angle seismic data

In 2002, a total of 42 IFM-GEOMAR ocean bottom hydrophones (OBH) (Flueh and Bialas, 1996) and 22 ocean bottom seismometers (OBS) (Bialas and Flueh, 1999) were deployed along four seismic profiles located about 25 km northeast of the Quepos Plateau (Zhu et al., 2009) (Fig. 1). Instruments were deployed along two dip lines P15 and P24 and two strike lines P21 and P18 (Fig. 1). The two dip lines P15/P24 were shot with a G-gun cluster (total volume 1800 in.$^3$) whereas the data along the two strike lines P18/P21 were acquired using a 32 l Boltgun (1952 in.$^3$). Both source types generated a seismic signal with frequencies from 4 to 40 Hz. A trigger interval of 30 s at a speed of 3.5 knots resulted in an average shotpoint distance of 54 m. Instrument positions on the seafloor were determined by analysis of the water wave arrivals. A time- and offset-dependent frequency filter in addition to a predictive deconvolution was applied to improve data resolution. A total of 32,058 first arrival picks and 7789 secondary arrival picks from 61 stations were used as input to a tomographic inversion. Comparing the reciprocity of the travel times for all possible source–receiver pairs validated phase coherency. Picking of seismic phases was conducted manually, and picking errors were assigned on the basis of the dominant period of the phase as well as data quality. We assigned 50 ms picking uncertainties at near offsets and 70 ms at far offsets for the first arrivals, and 80 ms for secondary arrivals.

The refractions through the upper margin wedge (Pumw) and the lower margin wedge (Plmw) are clearly observed on the record sections (e.g. Figs. 2–4). Station OBH 53 records refracted arrivals through the oceanic crust (Poc) and the upper mantle (Pn) (Fig. 2). The reflections from the top (PtP) and the bottom (PbP) of the décollement zone are recorded on several stations (e.g. Figs. 2 and 4) as are the intracrustal reflections PiP and crust–mantle boundary reflections (PmP) (Figs. 3 and 4). All of these arrivals are incorporated in the tomographic inversion.

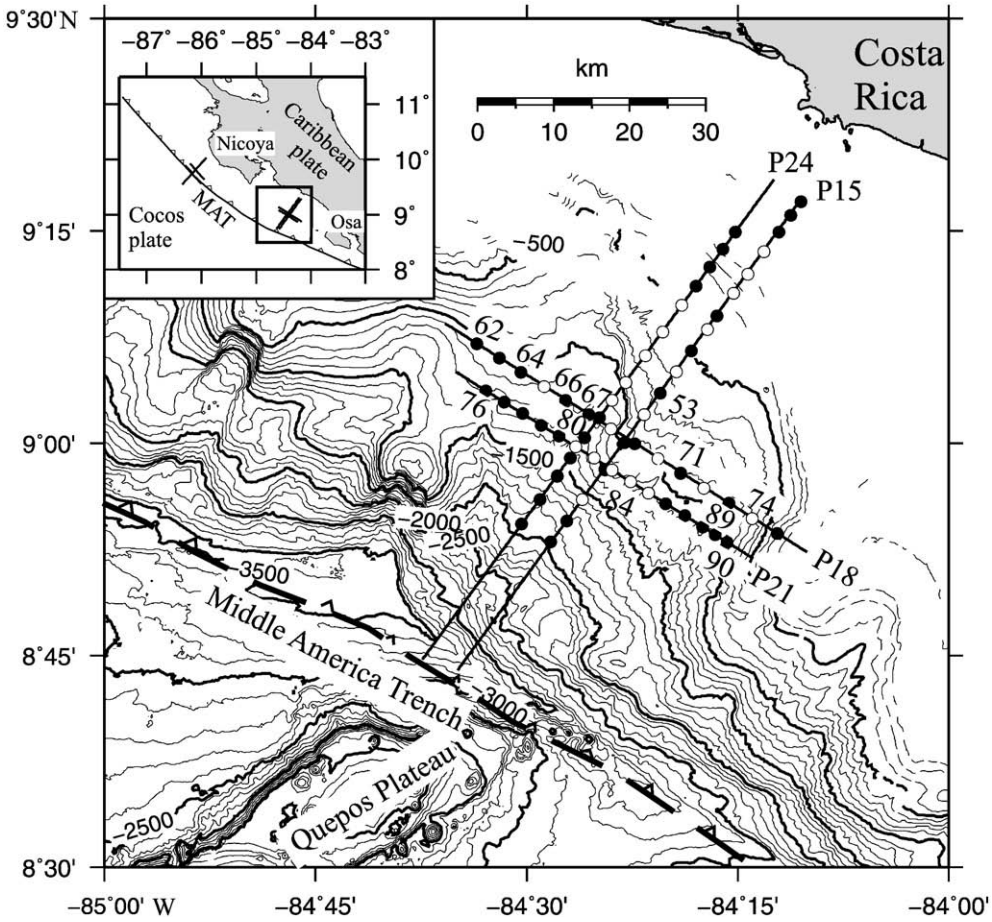


**Fig. 1.** Location map of seismic refraction profiles discussed in this study. Circles indicate positions of 40 ocean bottom hydrophones (OBH) (black) and 21 ocean bottom seismometers (OBS) (white) along the two strike and two dip lines. Stations used during amplitude modeling are marked by numbers. Seafloor topography is contoured at 100 m intervals. The inset map shows locations of the previous wide-angle seismic experiment by Christeson et al. (2000) offshore Nicoya Peninsula as well as this study. MAT: Middle America Trench.

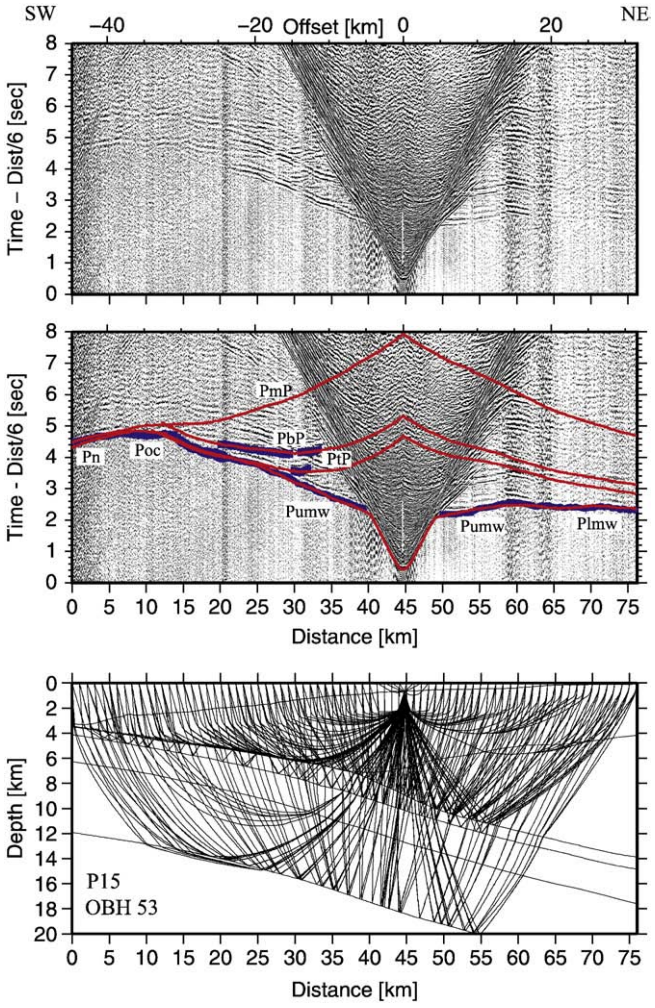


**Fig. 2.** Record section and ray paths for OBH 53 deployed on profile P15. Observed data are shown in the upper panel. Picked (blue line with picking error bars) and calculated travel times (red lines) are displayed in the center panel. Ray paths and phase abbreviations are shown in the lower panel. Refracted phase Pumw travels through the upper margin wedge and Plmw travels through the lower margin wedge. Poc is refracted through the oceanic crust. Reflection phase PtP tracks the top of the décollement zone and PbP tracks the bottom of this zone. PmP and Pn phases result from the oceanic crust–mantle boundary.

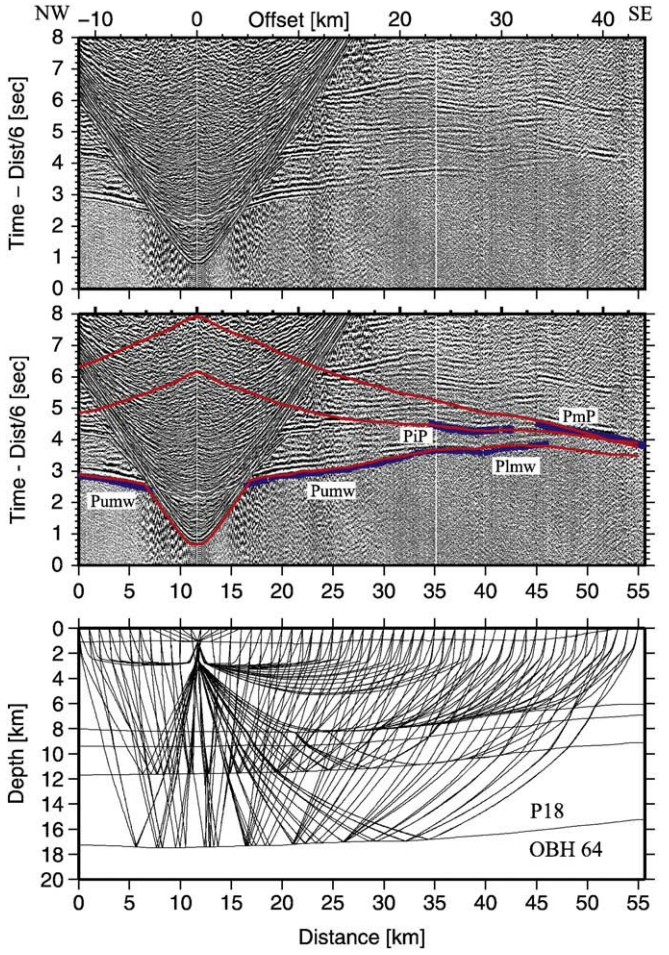


**Fig. 3.** Record section and ray paths for OBH 64 deployed on strike line P18. Reflection phase PiP originates at the boundary between oceanic layer 2 and layer 3. Please refer to Fig. 2 for display information and phase nomenclature.

## 3. Seismic travel time tomography

### 3.1. Method

The velocity–depth distribution of the seismic profiles is determined using the joint refraction and reflection travel time inversion method of Korenaga et al. (2000). The sedimentary section of the two dip lines (P15 and P24) has been modeled by forward ray tracing incorporating multichannel seismic reflection data (Zhu et al., 2009) and it is integrated in a starting model as a priori information. The fine mesh we apply in the tomographic inversion is better suited to resolve lateral variations in the short-wavelength structure compared to forward modeling. Lateral velocity variations, as observed e.g. in the upper margin wedge of our profile, are difficult to resolve using a layered model in the forward approach (Zhu et al., 2009). In Fig. 5a (profile distance 45–51 km), the high velocity variation within the upper margin wedge imaged by the tomographic inversion is resolved as a robust feature as validated by resolution tests. For all profiles, first arrivals and reflection travel times from floating reflectors were inverted to retrieve the 2-D velocity field. The forward travel time calculation uses a hybrid approach based on the graph method and the ray-bending method (Moser et al., 1992). For the inversion, the velocity field is parameterized as a mesh of nodes hanging below the seafloor with laterally and vertically varying node spacing. Horizontal grid size is 0.25 km, whereas vertical grid size varies from 0.05 km at the top of the model to 0.2 km at the bottom. We used horizontal correlation lengths ranging from 2 km at the top to 8 km at the bottom and vertical correlation lengths varying from 0.5 km at the top to 2 km at the bottom. A floating reflector is represented as an array of linear segments, whose nodal spacing is independent of that used in the velocity grid. The horizontal coordinates of reflector nodes are fixed so that each node has only one degree of freedom in the vertical direction (Korenaga et al., 2000). To incorporate multiple reflectors in the inversion procedure, we used the top–bottom modeling strategy to update the velocity model, i.e. the final velocity model with the first reflector fixed by damping serves as the initial model for the second reflector and so on. In this study, we chose to invert four reflectors corresponding to (1) the décollement, (2) the oceanic basement, (3) the upper–lower oceanic crust boundary and (4) the crust–mantle boundary (Moho discontinuity).

### 3.2. Results of tomographic inversion and interpretation

#### 3.2.1. Seismic structure

The marine forearc is dominated by the upper margin wedge with a high velocity gradient of 0.4/s, which decreases in the lower margin

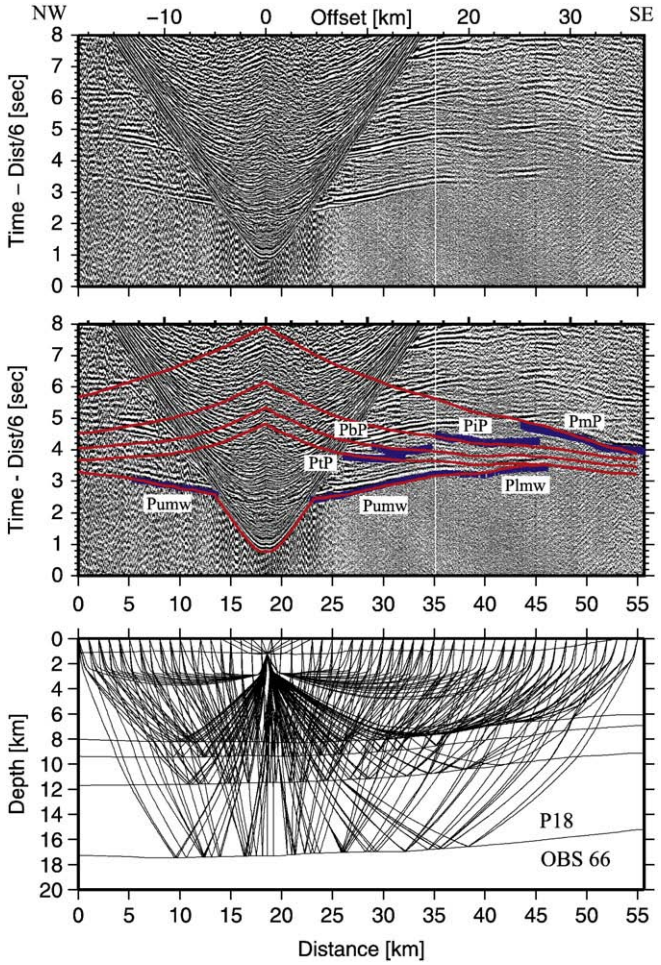


**Fig. 4.** Record section and ray paths for OBS 66 deployed on strike line P18. Please refer to Fig. 2 for display information and phase nomenclature.

wedge (Fig. 5). The tomographic images display laterally increasing seismic velocities within the margin wedge. Near the tip (Fig. 5, profile distance km 10–18), seismic velocities increase from 3 km/s to 4.5 km/s over the margin's thickness of ~2 km. From the middle slope to the upper slope, seismic velocities range from 4 km/s to 5.5 km/s and increase from 5.5 km/s to 6.5 km/s in the lower margin wedge. The subducting Caribbean oceanic plate is divided into two layers with distinct vertical velocity gradients: The upper layer is characterized by a large vertical velocity gradient, with velocities ranging from 5.0 km/s to 6.0 km/s and is identified as oceanic layer 2. The lower layer is traced by the 6 km/s isocontour at the top and the Moho interface with velocities of 7.2 km/s at the base and is considered to represent oceanic layer 3. A uniform thickness of 2 km and 5.5 km is observed for layers 2 and 3, respectively. Along all profiles, the décollement zone between the subducting Cocos plate and overriding Caribbean plate is characterized by a velocity inversion with a mean velocity of 4.0 km/s. The thickness of the décollement zone varies from ~1.0 km to ~1.5 km and is continuous up to our model boundaries.

The dense instrument spacing of 2.5 km to 3 km along the strike lines resolves fine structural variations of the margin wedge. Along strike line P18, 30 km from the deformation front, *P*-wave velocities of 4 km/s to 5.2 km/s are identified in the upper margin wedge where thickness variations do not exceed 1.5 km (Fig. 6a). The thin lower margin wedge shows velocities of 5.2 km/s to 5.5 km/s. The seismic structure of the margin wedge as imaged along P18 correlates to strike line P21, located 35 km from the deformation front (Fig. 6a). P21 displays an even more homogeneous structure, with layer thickness variations not exceeding 500 m and no considerable velocity variations (Fig. 6b). The structure of the lower plate is clearly two-dimensional, and velocities increase with depth and distance from the trench.

### 3.2.2. Model uncertainty and resolution tests

Using the inversion scheme described in Section 3.1, we have to consider two interrelated issues:

(1) The trade-off between depth and velocity parameters is linked to the reflected phase travel time inversion and depends on the source–receiver geometry. A conventional method to estimate the velocity–depth ambiguity is to perform sensitivity tests, such as checkerboard tests and Gaussian anomaly tests. In this procedure, different synthetic anomalies of various sizes are placed at specific positions in the models to assess at what point these anomalies are well resolved by the travel time inversion.

(2) Another issue is the uncertainty estimation in the velocity model, i.e. how well-resolved are the different parts of the model. This may be evaluated by estimating the influence of the initial model upon the obtained solution, as well as by estimating uncertainties applying a Monte Carlo analysis. The method involves a number of inversions with a variety of initial models using travel time picks with random errors applied. If all the Monte Carlo realizations have the same probability and if the initial models cover the full region of non-null probability within the space of parameters, the standard deviation of the obtained solutions can be interpreted as a measure of the final model parameter uncertainty.

To address the first issue, we conducted a resolution test by calculating synthetic data for a perturbed velocity model with a source–receiver geometry identical to the experiment setup. The synthetic data are then inverted with the initial unperturbed model to analyze how well the given perturbations are recovered. The perturbed velocity model is constructed using the final average velocity model with ±5% Gaussian anomalies placed at different positions in the model (Fig. 7). After 6 iterations, the position, shape and amplitude of the velocity anomalies are well recovered within the margin wedge and adequately recovered along the model periphery (Fig. 7). The relative high velocities found at profile distances of 45–52 km at around 4 km depth on profile 15 (Fig. 5a) in the margin wedge are a robust feature of the inversion solution.

Additionally, a nonlinear Monte Carlo uncertainty analysis (Tarantola and Valette, 1982) was conducted to estimate the model uncertainty and dependence of the obtained solutions on the initial model as addressed by the second issue mentioned above. The nonlinear Monte Carlo uncertainty was estimated as an a posteriori model covariance matrix (Tarantola, 1987), which can also be approximately expressed by the standard deviation of a number of Monte Carlo realizations (Korenaga et al., 2000). We constructed 100 Monte Carlo ensembles by inverting data with random errors with random initial velocity models (see Appendix). The 100 2-D initial velocity models were built by adding velocity values (randomly chosen between certain predefined limits) on a reference model beneath the basement. In addition, 100 noisy travel time data sets were constructed by adding random phase errors (±50 ms) and common-receiver errors (±50 ms) on the original data set (Zhang and Toksöz, 1998; Korenaga et al., 2000). Finally, each velocity model and corresponding reflector were inverted together with a noisy data set to estimate the influence of the starting model and the effect of realistic travel time errors. We used a top–bottom strategy to run the inversion step for each reflector, as described above. We added random velocities on the 2-D forward model of profile P24 including

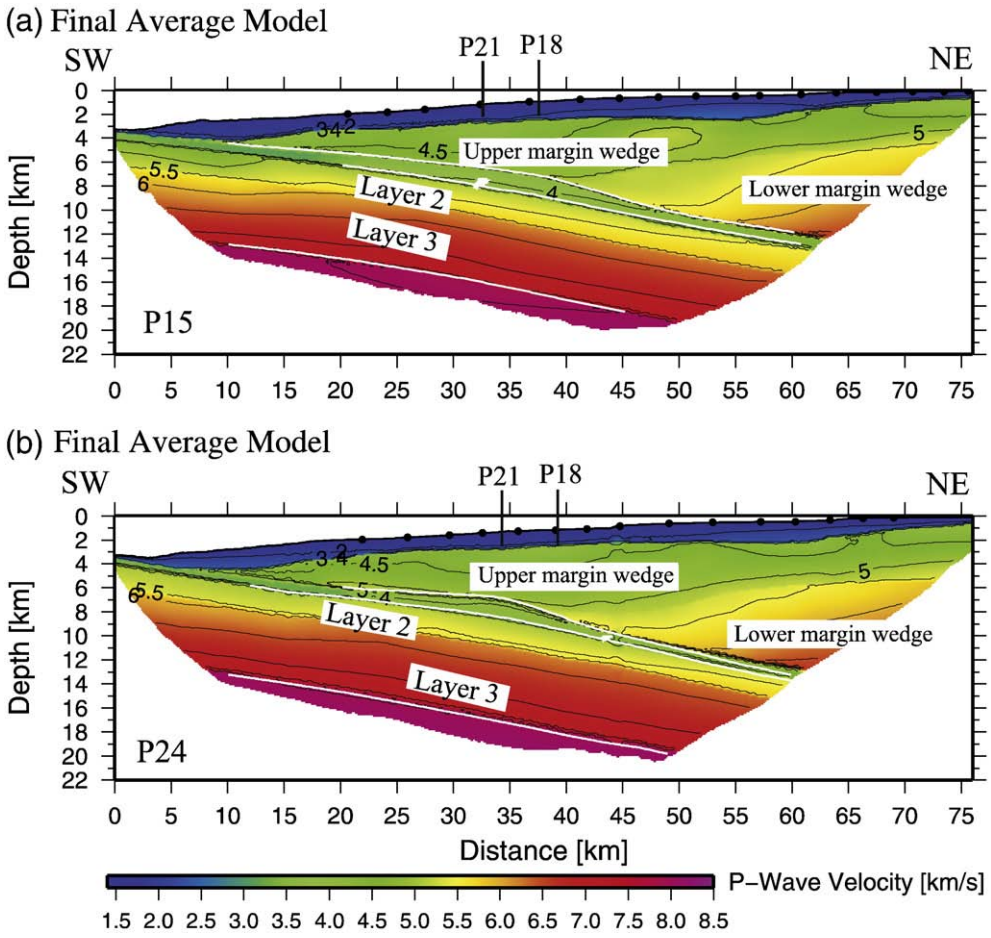


**Fig 5.** (a) Velocity–Depth distributions for profiles P15 (a) and P24 (b). The velocity models for P15 and P24 were derived by averaging 100 Monte Carlo ensembles for each line. The corresponding standard deviation of velocity and depth nodes for profile P24 is shown in Fig. 8. White lines mark reflectors. Contours are drawn at 0.5 km/s intervals.

two floating reflectors (top and base of the décollement zone, random variations within ±1 km) at the plate interface and one reflector (Moho, random variations within ±2 km) in the lower plate. One hundred input models were tested for each reflector during 10 iterations each, thus reducing the travel time root-mean-square misfits from several hundred milliseconds to about 70–90 ms. The average values and uncertainty of model parameters are obtained by averaging all Monte Carlo solutions and computing the corresponding standard deviation. The resulting deviation for profile P24 is shown in Fig. 8. Velocity uncertainties of the upper plate are usually lower than 0.15 km/s within the margin wedge (Fig. 8a, b). The largest velocity uncertainties occur within the low velocity décollement zone and reach 0.18 km/s here (Fig 8c). The depth uncertainties of the first and the second reflector reach about 500 m within the range of ray coverage. The velocity uncertainties within the subducting oceanic crust are comparable (0.06–0.15 km/s) (Fig. 8e, f). Uncertainties in Moho depth show values around ±1.5 km.

## 4. Reflectivity method

In this study, the amplitude modeling was performed using the 1D reflectivity code of Sandmeier and Wenzel (1986). The one-dimensional waveform modeling was exclusively applied to strike profiles P18 and P21 because the structural heterogeneity of the two dip lines prohibits one-dimensional modeling based on the reflectivity method along these transects. The 1-D initial velocity–depth model was provided by the tomography results of strike lines P18 and P21. The modeling procedure is a trial-and-error process in which we propose a model consisting of many plane homogeneous layers, each showing a distinct *P*-wave velocity (Vp), *S*-wave velocity (Vs), density ($\rho$), and *P* and *S* attenuation quality factors (Qp and Qs). Velocity gradients are approximated by a stack of layers with corresponding velocity contrasts. Calculated synthetic seismograms are compared with the observed seismograms, until an optimal fit is realized. For our amplitude modeling, we used a constant Poisson ratio of 0.28 and set Qp = 2Qs (as used by Spudich and Orcutt, 1980; Christeson et al., 2000). A Qp value of 300–500 for the crustal and sub-crustal environment is in agreement with earlier observations (Bowman, 1988). Densities were set to 1.5 g/cm$^3$ for the slope sediments and 1.8 g/cm$^3$ within the margin wedge (Kimura et al., 1997; Christeson et al., 2000). Densities for the oceanic crust were calculated using the relationship $\rho = 1.85 + 0.165$Vp (Christensen and Shaw, 1970; Christeson et al., 2000).

As the airgun source signature was unknown, we used a Fuchs-Mueller signal as input source wavelet. The source wavelet is defined by the equation given by Fuchs and Mueller (1971):

$$s(t) = \begin{cases} \sin \delta t - \frac{1}{m} \sin m\delta t, & 0 \le t \le T \\ 0 & t < 0, t > T \end{cases}$$

Where

$$\delta = \frac{N\pi}{T}, \quad m = \frac{N+2}{N}$$

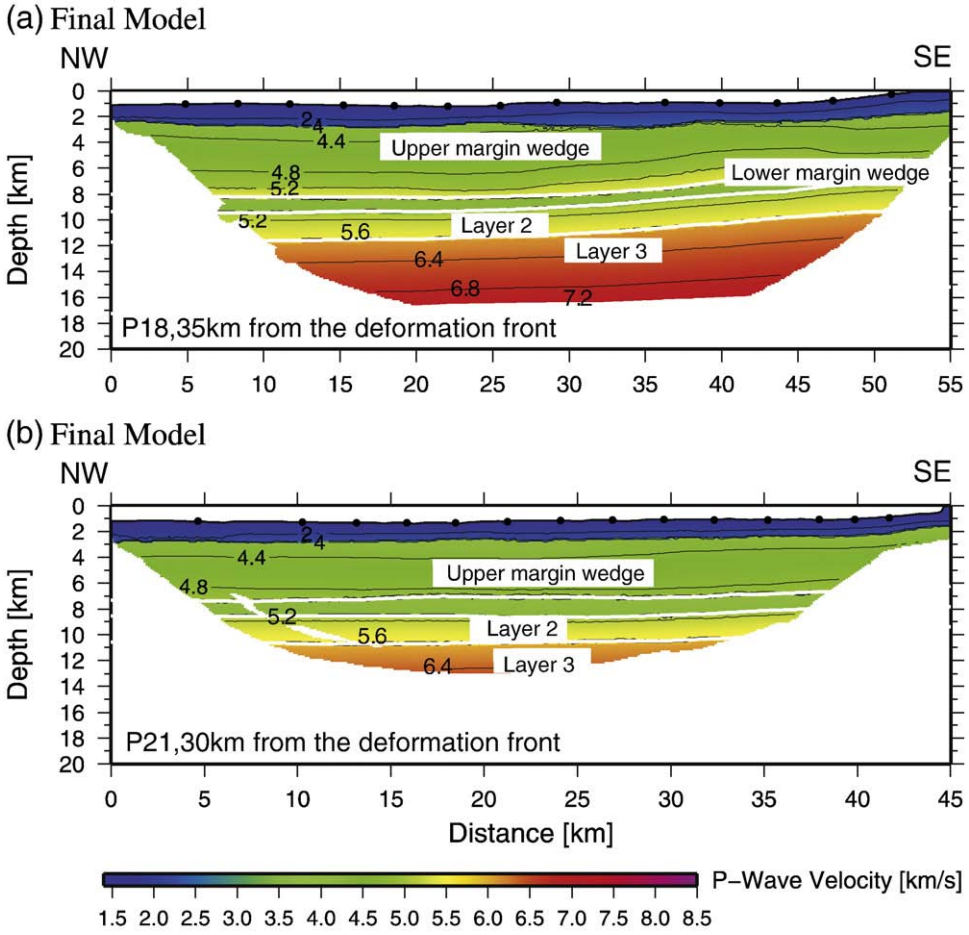


**Fig 6.** Velocity–Depth distributions for profiles P18 (a) and P21 (b) derived by tomographic inversion. White lines show reflectors. Contours are drawn at 0.4 km/s intervals.

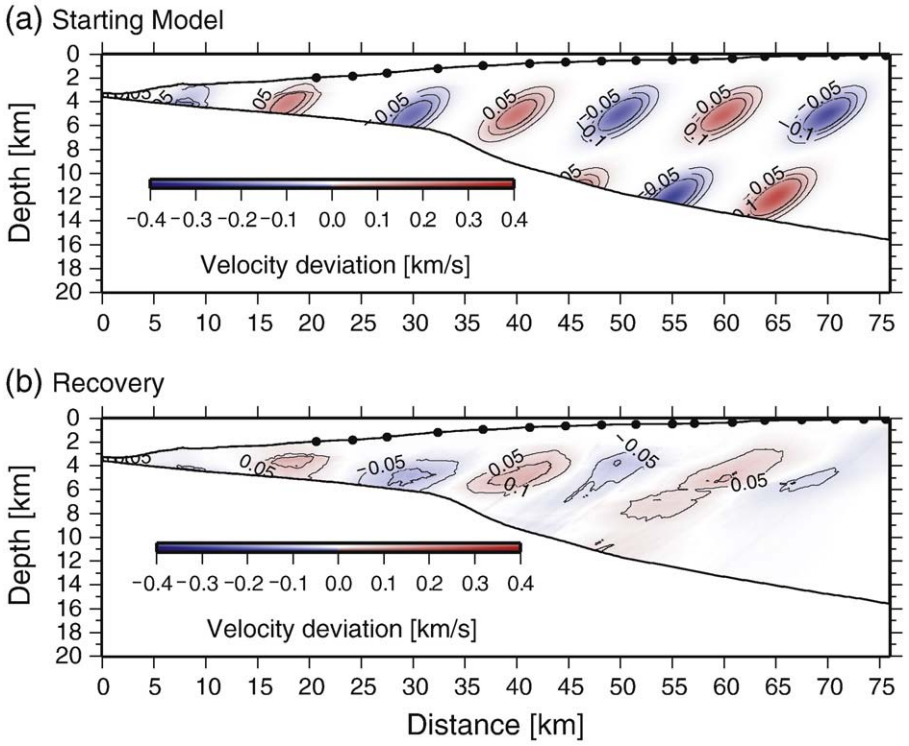


**Fig 7.** Upper plate resolution test for profile P15. (a) Velocity anomalies of ±5% in the synthetic model are given with respect to the initial velocity model. Velocity anomalies are applied to Gaussian anomalies rotated by 30 degrees. The source and receiver geometry used for synthetic travel time calculation is identical to the experiment layout. (b) Recovery obtained after 6 iterations.

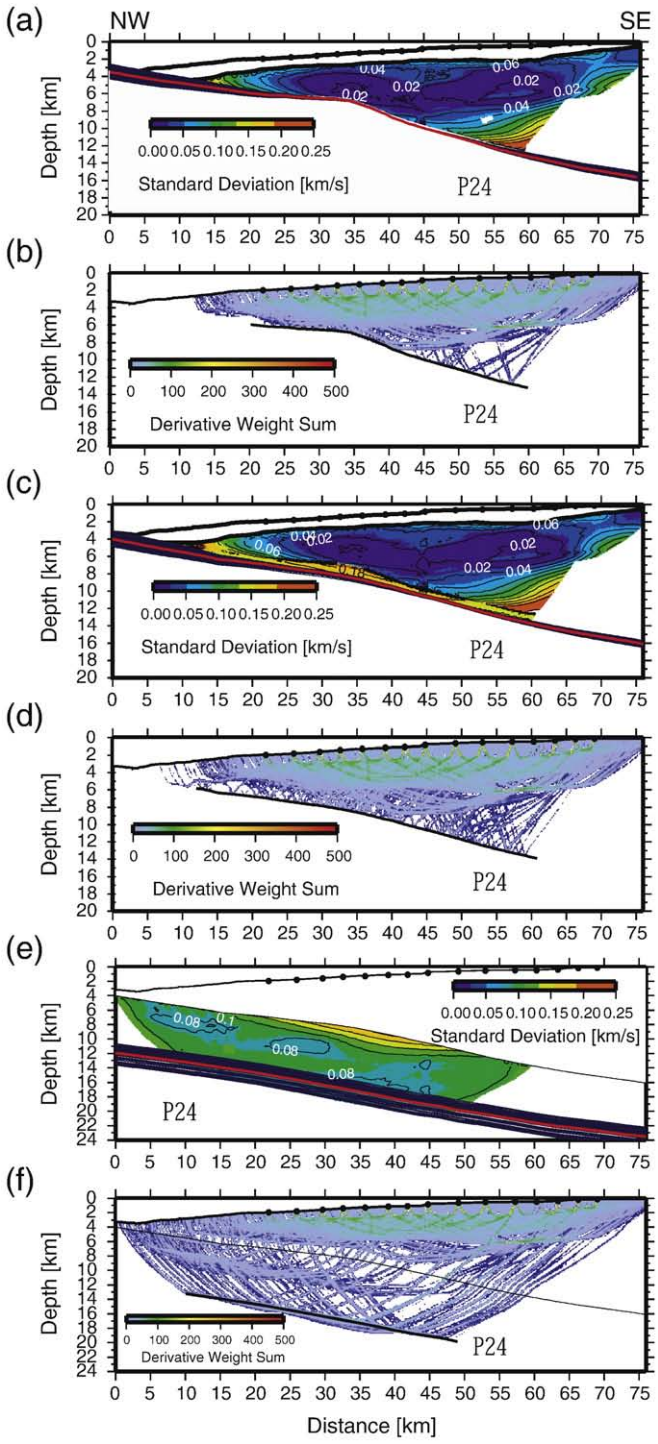


**Fig 8.** Standard deviations for velocity and reflector depth nodes of profile P24 derived from 100 Monte Carlo ensembles (a, c, e) and corresponding derivative weight sum from the average 100 realizations (b, d, f). Red lines show the average depth of reflectors and contours are drawn at 0.02 km/s intervals (a, c, e).

$N$ is an integer defining the number of extrema and $T$ is the duration of the wavelet in seconds. For our synthetic seismogram, $N=4$ and $T=0.4$ s were used. The frequency content of the Fuchs-Mueller signal used here has corner frequencies of 1/3–18/24 Hz, to simulate the dominant frequencies of the airgun signal recorded in the seismic section. Peak amplitudes of the refracted phases through the margin wedge are picked in the seismic record sections and synthetic seismograms along the two strike lines. The direct wave is used as reference to calibrate the amplitude data while considering the geometry spreading factors.

### 4.1. Strike lines P18 and P21

In our data, frequencies of the refracted waves in the margin wedge mainly focus between 5 Hz and 15 Hz, e.g. for OBS 68 in Fig. 9 (traces 200 to 330). Thus it is reasonable to use 12 Hz as the dominant frequency for the source signal during the amplitude modeling.

It is well known that the velocity gradient influences the amplitude of refracted phases (Banda et al., 1982). To verify the sensitivity of our analysis, we compare the amplitude behavior for varying velocity gradients for different Qp values (Fig. 10). We systematically vary the velocity gradient in the upper plate (margin wedge) according to the uncertainties obtained in Section 3.2.2 and then use the reflectivity method to calculate the synthetic seismograms and obtain the corresponding amplitude–distance curves (Fig. 10). The detailed model parameters are presented in Table 1. The resulting amplitude–distance curves show some variations in the near offset domain (offset<10 km), but at larger offsets, no significant variation conditional to different velocity gradients is observed (Fig. 10, models m1Q50, m2Q50 and m3Q50). The variations at near offsets are likely mainly related to interference from reflection phases here. The velocity model m1 corresponds to the velocity distribution retrieved by the tomographic inversion as was thus chosen to test the effect of increasing Qp values (Qp of 50, 75, 100, 150, and 200) on the amplitudes (Fig. 10, Table 1). The resulting curves in Fig. 10 show a relative sensitivity to the analyzed Qp range. Consequently, we assume that the velocity gradient has a relatively minor influence on our investigation (especially at offset>10 km), which is expressed within the general uncertainty (Fig. 10).

Two record sections along the strike lines P18 and P21 are shown in Fig. 11. The locations of OBS 84 and OBH 67 are indicated in Fig. 1. The primary travel time characteristic of the record section is interpreted as refracted arrivals through the margin wedge. First arrivals document both the velocities and Qp within the margin wedge and are clearly reproduced in the synthetic seismograms (Fig. 11a–b). We calculated synthetic seismograms using different attenuation (1/Qp) values and various vertical velocity gradients to test their effect on the seismic wave field. For OBS 84 displayed in Fig. 11a, the velocity–depth function of P21 (Fig. 11a, in panel vi) represents the margin wedge velocity, which is modestly slower (0.2–0.3 km/s) than the corresponding function determined by ray tracing (Fig. 6b) without including the effect of attenuation. Fig. 11b displays the original record section and synthetic seismograms calculated for OBH 67 of strike line P18. The primary arrivals through the upper margin wedge are focused between offsets 5 and 25 km (Fig. 11b). Again, synthetic seismograms are displayed for the different Qp values. For both profiles, it is difficult to define the proper Qp values from the synthetic seismograms, but a Qp of 300 yields unrealistically high amplitudes in the margin wedge compared to the real data (panels v in Fig. 11a, b). A quantitative estimation of Qp values is required as introduced below.

### 4.2. Quantitative estimations of Qp values

In order to estimate the Qp values of the upper plate in a quantitative manner, we analyze amplitude variations of first arrivals from the margin wedge. The amplitude–offset decay curve is used as a criterion to assess the validity of different Qp models by comparing the amplitude characteristics of the observed data and synthetic models. The peak amplitude values of the refracted phase from the margin wedge are picked manually using the Hampson-Russell software. This method is applied to the record sections indicated in Fig. 1. A prerequisite of this approach is the calibration of amplitudes,

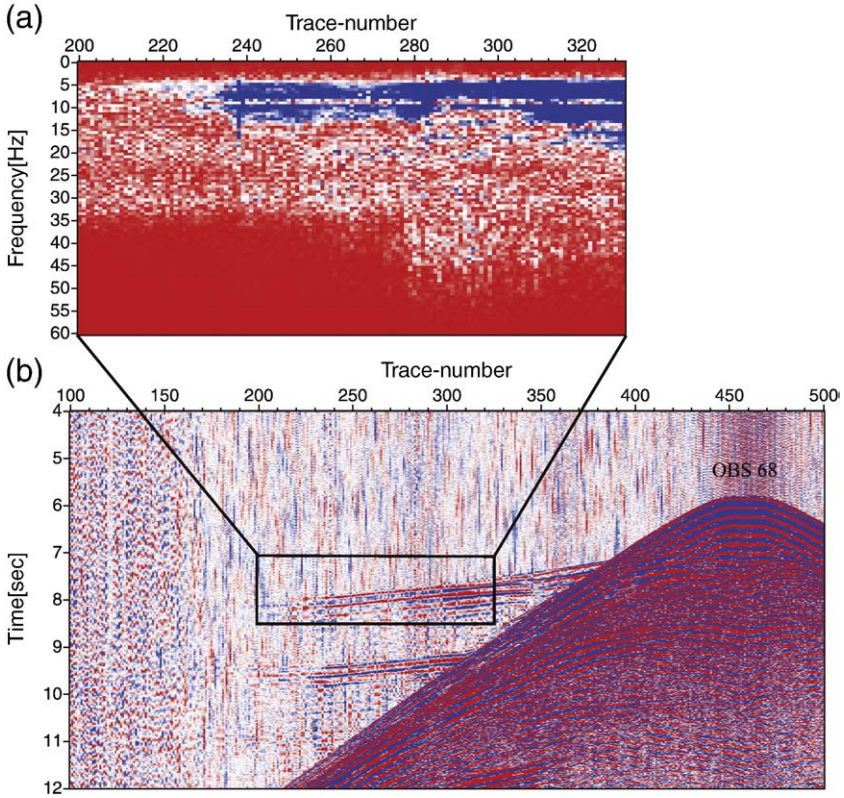


**Fig. 9.** Frequency spectrum of OBS 68. (a) Trace numbers from 200 to 330, (b) time domain data of OBS 68. The square area shows the time window from 7 s to 8.5 s used for the frequency spectrum.

usually with reference to the direct/water wave. The peak amplitudes of the direct wave from the synthetic seismograms and real data are matched firstly by applying geometric spreading corrections, and are then applied to the refracted phase. The relative amplitude curves are presented in Fig. 12. The amplitudes of the synthetic data decrease fairly smoothly with distance, whereas the recorded data show a rougher variation mainly caused by the complexity of the subsurface generating signal interference compared to the smooth phase of the synthetic model. The lower signal-to-noise ratio of the recorded data will enhance this scattering. In addition, although the tomographic images for lines P18 and P21 suggest a fairly smooth structure, the recorded data obviously are not one-dimensional and thus will to some degree violate the most important prerequisite for amplitude modeling. For this reason we conducted the modeling for two profiles at a distance of only approximately 5 km from each other to circumnavigate possible 3-D effects and minimize the effect statistically. For OBS 84, OBH 89, and OBH 90 of strike line P21, a Qp value of 50–150 generates comparable amplitudes between the observed and synthetic data (Fig. 12a–c). On average and for offsets greater than 10 km, the amplitude–distance curves of these record sections trend along the Qp = 75 synthetic curve. For OBS 68, OBH 71, and OBS 74 of strike line P18, a Qp value of 50–150 best produces similar amplitude characteristics between the observed and synthetic data (Fig. 12d–f).

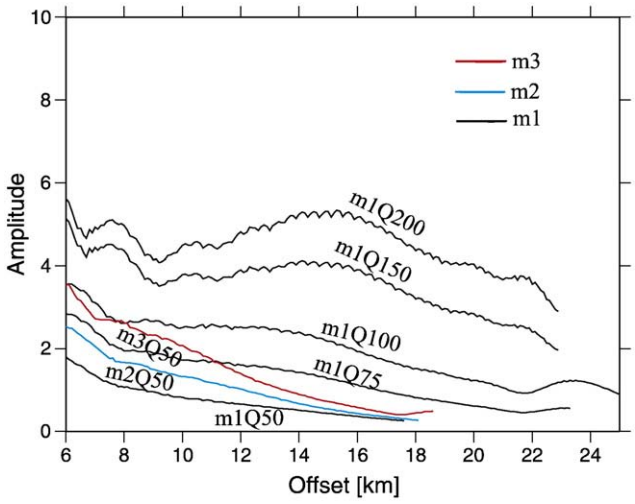


**Fig. 10.** Amplitude–Distance curves for models m1, m2, and m3 (different positive velocity gradients, see Table 1 for model parameters). Amplitude–Distance curves of m1 model with different Qp values are displayed.

### 4.3. Uncertainty estimations of the seismic attenuation

The forward amplitude modeling conducted for the two strike lines returns modest Qp values of 50–150, which correlate with the observed wavefield and amplitude–distance curves along profiles P18 and P21. Higher Qp values (> 200) in the margin wedge will

**Table 1**
Model parameters.

| Model | Thickness of margin wedge (km) | Vp (km/s) | Velocity gradients of layers (km/s/km) |
|---|---|---|---|
| m1 | 4.46 | 4.0–4.8 | 0.18 |
| m2 | 4.46 | 3.8–4.8 | 0.224 |
| m3 | 4.46 | 3.9–5.2 | 0.269 |

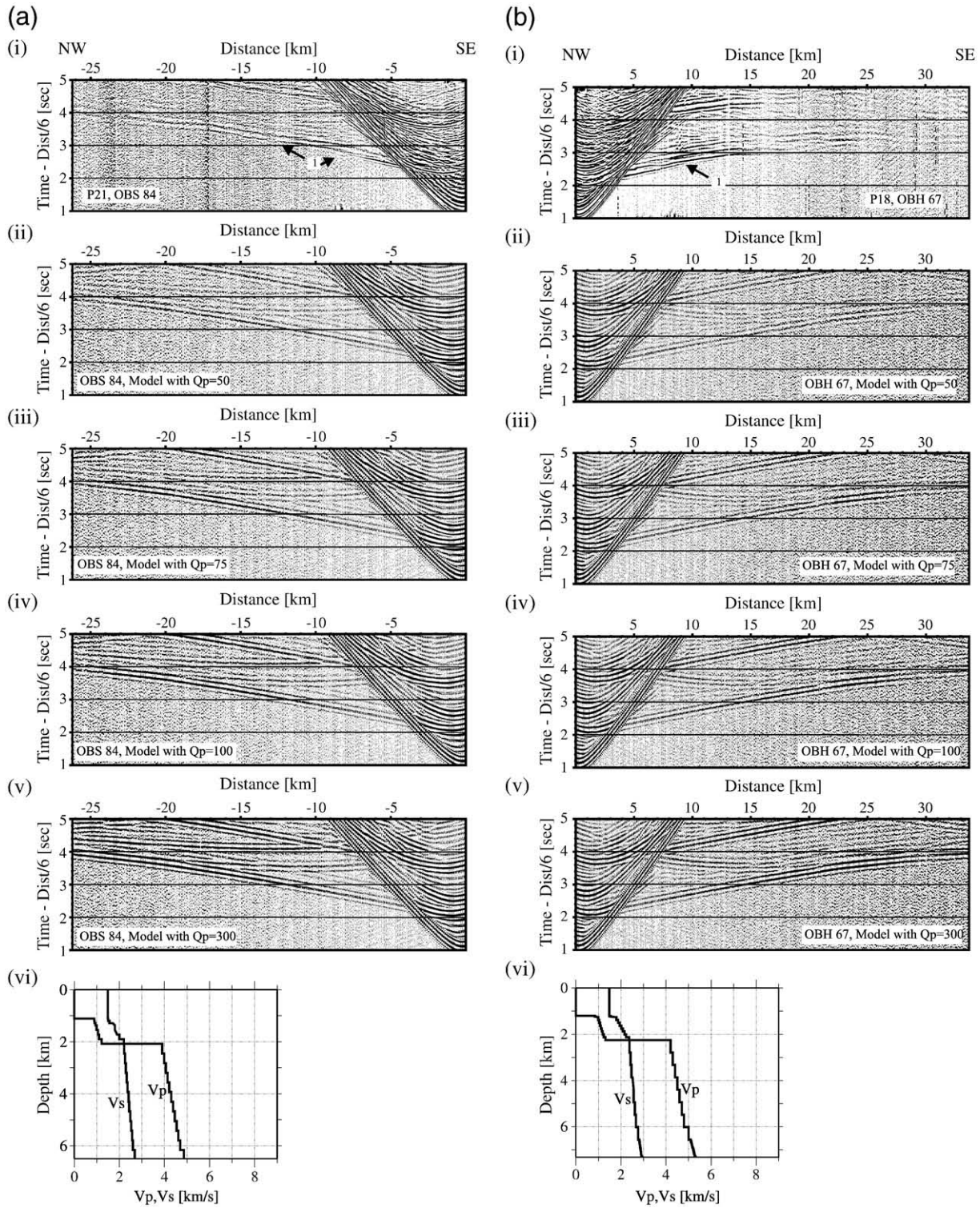


**Fig. 11.** Record section and synthetic seismograms of strike line P18 and P21. Ambient noise has been added to the synthetic record sections. Increasing Qp values of 50, 75, 100, and 300 within the margin wedge are shown in panels ii–v. The velocity–depth function is shown in panel vi. (a) OBS 84, (b) OBH 67.

generate high peak amplitude values at the related offset (Fig. 12) and will not reproduce a comparable amplitude behavior between the observed and synthetic data. A similar pattern is observed for all stations modeled on the two strike lines, where overestimated Qp values generate artificially high amplitude arrivals. The less homogeneous velocity distribution and structure of line P18 as discussed in Section 3.2.1 leads to a higher degree of scattering in the amplitude–distance curves of OBS 68, OBH 71, and OBS 74 (Fig. 12), however, the general trend of all curves on average will not exceed Qp values of 200.

In addition to the upper plate Qp values, other factors affecting the modeled amplitude pattern include the vertical velocity gradient of

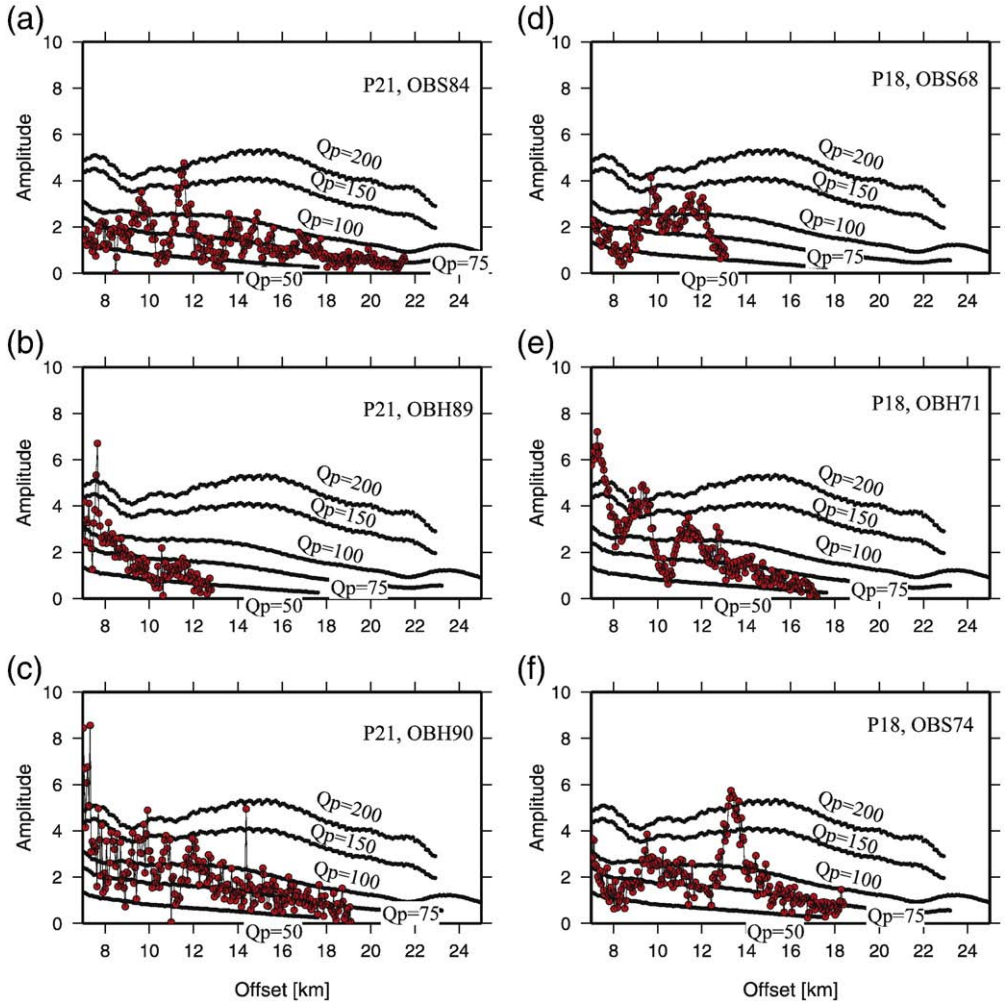


**Fig. 12.** Amplitude versus offset variations for refracted phases through the margin wedge of stations OBS 84, OBH 89, and OBH 90 along strike line P21, and OBS 68, OBH 71 and OBS 74 along the strike line P18. Red dotted lines show the amplitude decay curves of the record sections. Black lines show a constant Qp of 50, 75, 100, 150, and 200 in the margin wedge.

the margin wedge as discussed in Section 4.1. A high velocity gradient in the margin wedge (e.g. m3 model, velocity gradient of 0.269/s, Table 1) generates relative high amplitudes at corresponding offsets with an identical Qp of 50. Therefore, high vertical velocity gradients will lead to an underestimation of Qp values. The amplitude of the refracted phase can be decreased by either a decrease in the vertical velocity gradient or a decrease in the margin wedge Qp values. In order not to overestimate upper plate Qp values, we chose a vertical velocity gradient of 0.18/s (m1 model, Table 1) for the margin wedge consistent with the result of the tomographic inversion, yielding a minimum Qp value here (Fig. 12).

For station OBS 84 and OBH 90 of profile P21 (Fig. 12a, c), the amplitude–distance curves at offsets greater than 14 km closely correlate with the Qp = 75 curve. Scattering is higher at the near offsets, which are more affected by the larger variation of physical properties in the sedimentary cover as well as by interference of sediment reflections. This effect is also observed for station OBH 89 of the same line (Fig. 12b), however amplitudes could only be picked up to an offset of 13 km, impeding the analysis. Even more difficult to analyze due to the lack of far offset amplitude values are the data of OBS 68 of profile P18 (Fig. 12d). As for OBH 89, the low signal-to-noise ratio of this station inhibited exact amplitude picking at offset>13 km. Both stations, however, seem to follow the general trend not to exceed Qp values of 200. For OBH 71 (Fig. 12e), the slope of the amplitude–distance curve does not match the synthetic values. This is associated with the velocity gradient and comparison with curve m3Q50 of Fig. 10 implies that the velocity gradient is not matched underneath this station. As discussed in Section 4.1, the gradient will influence the slope of the curve but is less sensitive to the relative amplitude values. Data of OBS 74 (Fig. 12f) mainly trend around Qp = 75 and show a decisive maximum at 12–14 km offset. We interpret this peak to be caused by a low signal-to-noise ratio in the original data and thus to be artificial.

## 5. Discussion

The results of the tomographic inversion reveal more details of the seismic structure in the model space compared to the forward modeling results (Zhu et al., 2009). The fine shear mesh of velocity nodes of the velocity field indicates the *P*-wave velocity variation from 4.0–4.5 km/s at the tip of the margin to 4.1–6.5 km/s near the coast (Fig. 5). The thickness of the margin wedge increases at the trench axis from several hundred meters to about of 15 km at the coast (Fig. 5). Similar structural units as observed here (upper and lower margin wedge) are also resolved along the north Ecuador–south Colombia margin (Agudelo et al., 2009), where a significant accretionary wedge is missing.

The décollement zone is imaged as a 1–1.5 km thick low velocity zone sandwiched between the margin wedge basement and the subducting Cocos plate. The velocity model of dip lines P15 reveals a zonation of the décollement zone with velocities rapidly increasing from 3.0 km/s to 3.5 km/s from the deformation front over a distance of 15 km (P15). Velocities then remain constant (~3.5–3.6 km/s between 20 and 35 km offset) until they increase again underneath the lower margin wedge (~4.2 km/s at 50 km offset) (this velocity increase is not unambiguously resolved for P24). A similar velocity pattern of the underthrust material has also been reported for the erosional south Ecuadorian margin (Calahorrano et al., 2008), where a clear segmentation of the décollement zone could be inferred from pre-stack depth migrated multichannel seismic data. The progressively increasing seismic velocities concur with a reduction in porosity resulting from sediment compaction associated with fluid drainage.

The amplitude of a refracted seismic wave is controlled by the velocity of the medium through which it propagates as well as by the anelastic attenuation characteristics of the medium. The degree of cracking and water or gas in fractures will directly influence seismic attenuation by reducing Qp values (Bourbiè et al., 1987). This is consistent with the observation that Qp values generally increase with depth in the oceanic crust, which is attributed to the decrease in fracturing and structural heterogeneity (Wilcock et al., 1995).

In Costa Rica, previous studies have reported high attenuation (Qp = 25–50) approximately 10 km landward of the deformation front offshore Nicoya Peninsula (about 210 km northwest of our study area) (Christeson et al., 2000). These values are consistent with the low Qp values from marine sediment (Qp = 25–30) (Hamilton, 1972) and reflect the sedimentary composition of the highly tectonized frontal prism. This frontal prism is present along the entire ~500 km Costa Rican margin (von Huene et al., 2009) and is self-limiting in size, which is a function of material supply, convergence rate and taper. The width of the frontal prism off Costa Rica does not exceed 15 km landward of the deformation front. Approximately 20 km from the deformation front, Christeson et al. (2000) observed Qp values of 50–75, which is only slightly lower than our results from strike lines P21 and P18, located 30 km and 35 km from the trench, respectively (Fig. 1). The lower attenuation of our lines (Qp = 50–150) compared to the values (Qp = 25–50) recorded on the frontal prism (Christeson et al., 2000, Table 2) reflects the tectonically more stable domain of the middle prism and a change in lithology. The values are consistent with a Nicoya complex composition of the central Costa Rican margin wedge. The Nicoya complex is exposed on Nicoya Peninsula as ophiolitic rocks, composed of massive flows, pillows, dikes, basaltic breccias, gabbros, plagiogranites and radiolarian chert (Kuijpers, 1980). This unit has been interpreted as the seaward extent (Ye et al., 1996; Christeson et al., 1999) of the Caribbean Cretaceous oceanic plateau (Bowland and Rosencrantz, 1988; Sinton et al., 1997). Though attenuation across the middle prism decreases relative to the frontal prism, Qp values remain comparatively low. This may be associated to the fracturing of the middle prism, which has been documented in numerous studies. Faults penetrate deep into the slope sediment and into the basement rock (McIntosh et al., 1993; Hinz et al., 1996; Ranero and von Huene, 2000). Seismic attenuation is influenced by the material composition, which is reflected in the Qp structure of the margin wedge. The increase in Qp values from the frontal prism, to the middle and inner prism allows assessment of the changes in lithology. The overall relative low Qp may be related to the fluid budget of the margin as expressed in fluid expulsion through mud volcanoes distributed along the margin wedge. The fault pattern is intrinsically related to the hydrogeological system of the margin where the majority of focused fluid seepage occurs on the middle slope (Ranero et al., 2008). Fluid flow constitutes one cause of attenuation, however, only at frequencies below the frequency range of our study (Toksöz et al., 1987).

**Table 2**
Margin wedge velocities and Qp values from wide-angle strike lines.

| Region | Costa Rica, Nicoya Peninsula | | Central Costa Rica | |
|---|---|---|---|---|
| Distances from trench | 10 km | 20 km | 30 km | 35 km |
| Velocity ranges (km/s) | 4–4.4 | 4.4–4.8 | 3.9–4.9 | 4.2–5.0 (upper margin wedge)<br>5.1–5.4 (lower margin wedge) |
| Thickness of the margin wedge (km) | 1.5 | 3.0 | 4–4.5 | 3.5–5 (upper margin wedge)<br>1–1.5 (lower margin wedge) |
| Qp | 25–50 | 50–75 | 50–150 | 50–150 |

Reference Christeson et al., 2000 this study.

## 6. Conclusions

We apply the reflectivity method and incorporate the Q parameter to obtain a 1D model for Qp on the Costa Rican margin wedge (Table 2). By comparison with previous studies (Christeson et al., 2000) we document a lateral decrease of attenuation across the margin wedge with distance from the trench, implying physical and lithologic variations along the lower slope of the marine forearc. This is related to material strength variations associated with a change in lithology from the sediment-dominated frontal prism to the igneous composition of the middle prism of the forearc. Seismic velocities and Qp values of the margin wedge are consistent with a high degree of fracturing as suggested by previous studies (Ranero et al., 2008), which facilitates mass wasting and subduction erosion processes.

## Acknowledgments

We are grateful to all colleagues and participants of Cruise SO163 for their help with data acquisition and processing, particularly to the skillful crew of the RV Sonne. We used the GMT software (Wessel and Smith, 1991) and Seismic Unix software package (Stockwell, 1999) to plot several figures. We also wish to thank Editor David J. W. Piper for providing a very useful pre-review of the manuscript and two anonymous reviewers whose suggestions contributed to improving the original manuscript. J.Z. gratefully acknowledges a scholarship granted by the German Academic Exchange Service (DAAD) and the financial support from the National Natural Science Foundation of China (40674051) and the Knowledge Innovation Program of the Chinese Academy of Sciences (SQ200910).

## Appendix

### 1. Monte Carlo analysis

A practical way to estimate the model uncertainty for tomographic inversion is the Monte Carlo method (Tarantola and Valette, 1982; Tarantola, 1987; Korenaga et al., 2000). The nonlinear Monte Carlo uncertainty was estimated as an a posteriori model covariance matrix (Tarantola, 1987), which can also be approximately expressed by the standard deviation of a number of Monte Carlo realizations assuming that all realizations have the same probability (Korenaga et al., 2000). Commonly, 100 random initial velocity models are generated by adding the predefined random numbers to velocity values and depth ranges of a reflector on a 1-D reference model. In this study we modify a 2D forward modeling velocity field by adding the constant random values at the same layer and also modify the depths of the different

reflectors to construct 100 2D random velocity models. See main text for further information. The following chart presents the detailed process:

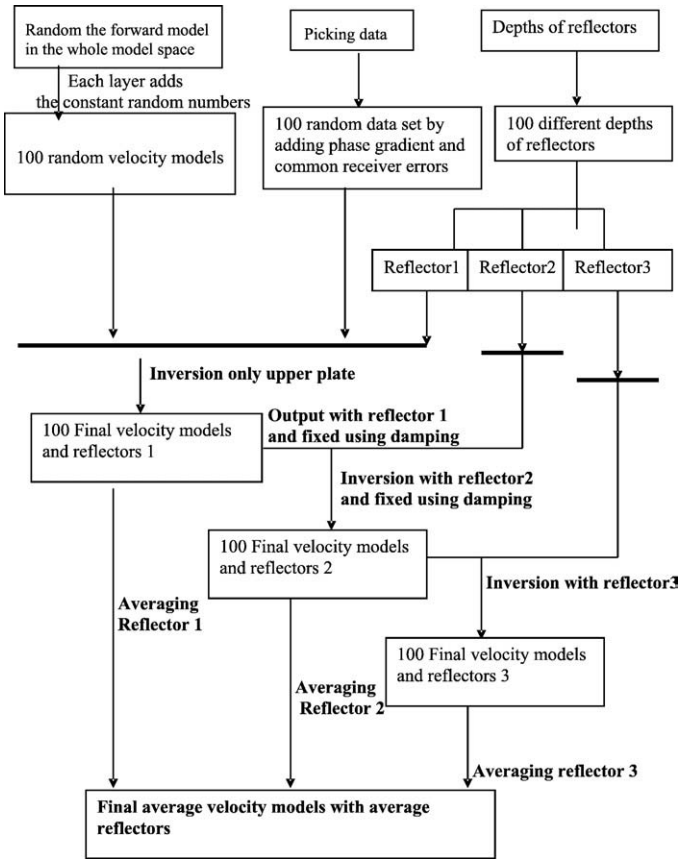


## References


Agudelo, W., Ribodetti, A., Collot, J.-Y., Operto, S., 2009. Joint inversion of multichannel seismic reflection and wide-angle seismic data: Improved imaging and refined velocity model of the crustal structure of the north Ecuador–south Colombia convergent margin. Journal of Geophysical Research 114, B02306 doi:10.1029/2008JB005690.

Banda, E., Deichmann, N., Braile, L.W., Ansorge, J., 1982. Amplitude study of the Pg phase. Journal of Geophysics 51, 153–164.

Barckhausen, U., Ranero, C.R., von Huene, R., Cande, S.C., Roeser, H., 2001. Revised tectonic boundaries in the Cocos Plate off Costa Rica: implication for the segmentation of the convergent margin and for plate tectonic models. Journal of Geophysical Research 106, 19207–19220.

Bialas, J., Flueh, E.R., 1999. Ocean bottom seismometers. Sea Technology 40 (4), 41–46.

Bourbiè, T., Coussy, O., Zinszner, B., 1987. Acoustics of Porous Media. Gulf Publishing Company, Houston, Tex.

Bowland, C.L., Rosencrantz, E., 1988. Upper crustal structure of the western Colombian basin. Caribbean Sea, Geological Society America Bulletin 100, 534–546.

Bowman, J.R., 1988. Body wave attenuation in the Tonga subduction zone. Journal of Geophysical Research 93 (B3), 2125–2139.

Braile, L.W., Smith, R.B., 1975. Guide to the interpretation of crustal refraction profiles. Geophysical Journal of the Royal Astronomical Society 40, 145–176.

Calahorrano, B.A., Salleres, V., Collot, J.-Y., Sage, F., Ranero, C.R., 2008. Nonlinear variation of the physical properties along the southern Ecuador subduction channel: results from depth-migrated seismic data. Earth and Planetary Science Letters 267, 453–467.

Christensen, N.I., Shaw, G.H., 1970. Elasticity of mafic rocks from the Mid-Atlantic Ridge. Geophysical Journal of the Royal Astronomical Society 20, 271–284.

Christeson, G.L., McIntosh, K.D., Shipley, T.H., 2000. Seismic attenuation in the Costa Rica margin wedge: amplitude modeling of ocean bottom hydrophone data. Earth and Planetary Science Letters 179, 391–405.

Christeson, G.L., McIntosh, K.D., Shipley, T.H., Flueh, E.R., Goedde, H., 1999. Structure of the Costa Rica convergent margin, offshore Nicoya Peninsula. Journal of Geophysical Research 104, 25443–25468.

Dominguez, S., Lallemand, S.E., Malavieille, J., von Huene, R., 1998. Upper plate deformation associated with seamount subduction. Tectonophysics 293, 207–224.

Flueh, E.R., Bialas, J., 1996. A digital, high data capacity ocean bottom recorder for seismic investigations. International Underwater System Design 18 (3), 18–20.

Fuchs, K., Mueller, G., 1971. Computation of synthetic seismograms with the reflectivity method and comparison with observation. Geophysical Journal of the Royal Astronomical Society 23, 417–433.

Hamilton, E.L., 1972. Compressional-wave attenuation in marine sediments. Geophysics 37, 620–646.

Hauff, F., Hoernle, K., Schmincke, H.-U., Werner, R., 1997. A mid Cretaceous origin for the Galápagos hotspot: volcanological, petrological and geochemical evidence from Costa Rican oceanic crustal segments. Geologische Rundschau 86, 141–155.

Hinz, K., von Huene, R., Ranero, C.R., PACOMAR Group, 1996. Tectonic structure of the convergent Pacific margin offshore Costa Rica from multichannel seismic reflection data. Tectonics 15, 54–66.

Kennett, B.L.N., 1977. Towards a more detailed seismic picture of the oceanic crust and mantle. Marine Geophysical Researches 3, 7–42.

Kimura, G., Sliver, E., Blum, P., et al., 1997. Proceedings of the Ocean Drilling Program, Initial Report, vol. 170. Ocean Drilling Program, College Station, Texas. (458 p.).

Korenaga, J., Holbrook, W.S., Kent, G.M., Kelemen, P.B., Detrick, R.S., Larsen, H.-C., Hopper, J.R., Dahl-Jensen, T., 2000. Crustal structure of the southeast Greenland margin from joint refraction and reflection seismic tomography. Journal of Geophysical Research 105 (B9), 21591–21614.

Kuijpers, E.P., 1980. The geologic history of the Nicoya Ophiolitite Complex Costa Rica, and its geotectonic significance. Tectonophysics 68, 233–255.

Lallemand, S.E., Schnurle, P., Manoussis, S., 1992. Reconstruction of subduction zone paleogeometries and quantification of upper plate material losses caused by tectonic erosion. Journal of Geophysical Research 97, 217–239.

McIntosh, K., Silver, E., Shipley, T., 1993. Evidence and mechanisms for forearc extension at the accretionary Costa Rica convergent margin. Tectonics 12, 1380–1392.

Moser, T.J., Nolet, G., Snieder, R., 1992. Ray bending revisited. Bulletin. Seismological Society of America 82, 259–288.

Ranero, C.R., von Huene, R., 2000. Subduction erosion along the Middle America convergent margin. Nature 404, 748–752.

Ranero, C.R., Grevemeyer, I., Sahling, H., Barckhausen, U., Hesen, C., Wallmann, K., Weinrebe, W., Vannucchi, P., von Huene, R., McIntosh, K., 2008. Hydrogeological system of erosional convergent margins and its influence on tectonics and interplate seismogenesis. Geochemistry, Geophysics, Geosystems 9 (Q03S04) doi:10.1029/2007GC001679.

Sandmeier, K.J., Wenzel, F., 1986. Synthetic seismograms for a complex crustal model. Geophysical Research Letters 13, 22–25.

Sinton, C.W., Duncan, R.A., Denyer, P., 1997. Nicoya Peninsula, Costa Rica: a single suite of Caribbean oceanic plateau magmas. Journal of Geophysical Research 102 (B7), 15,507–15,520.

Spudich, P., Orcutt, J., 1980. Petrology and porosity of an ocean crustal site: results from wave form modeling of seismic refraction data. Journal of Geophysical Research 85 (B3), 1409–1433.

Stavenhagen, A.U., Flueh, E.R., Ranero, C.R., McIntosh, K.D., Shipley, T., Leandro, G., Schulze, A., Dañobeitia, J.J., 1998. Seismic wide-angle investigations in Costa Rica—a crustal velocity model from the Pacific to the Caribbean coast. Zentralblatt für Geological und Paläontologie, Teil I 3–6, 393–408.

Stockwell, J.W., 1999. The CWP/SU: Seismic Un*x package. Computers and Geosciences 25 (4), 415–419.

Toksöz, M.N., Wu, R.S., Schmitt, D.P., 1987. Physical mechanisms contributing to seismic attenuation in the crust. In: Erdik, M.O., Toksöz, M.N. (Eds.), Strong Ground Motion Seismology. D. Reidel Publishing Company, Dordrecht, pp. 225–247.

Tarantola, A., 1987. Inverse Problem Theory: Methods for Data Fitting and Model Parameter Estimation. Elsevier, New York (613 pp.).

Tarantola, A., Valette, B., 1982. Inverse problems = quest for information. Journal of Geophysics 50, 159–170.

Vannucchi, P., Ranero, C.R., Galeotti, S., Straub, S.M., Scholl, D.W., McDougall-Reid, K., 2003. Fast rates of subduction erosion along the Costa Rica Pacific margin: implications for nonsteady rates of crustal recycling at subduction zones. Journal of Geophysical Research 108 (B11), 2511 doi:10.1029/2002JB002207.

von Huene, R., Bialas, J., Flueh, E., Cropp, B., Csernok, T., Fabel, E., Hoffmann, J., Emeis, K., Holler, P., Jeschke, G., Leandro, M.C., Perez Fernandes, I., Chavarria, S.J., Florez, H.A., Escobado, Z.D., Leon, R., Barrios, L.O., 1995. Morphotectonics of the Pacific convergent margin of Costa Rica. In: Mann, P. (Ed.), Geologic and Tectonic Development of the Caribbean Plate Boundary in Southern Central America: Geological Society of America, Special Paper, vol. 295, pp. 291–307.

von Huene, R., Ranero, C.R., Weinrebe, W., 2000. Quaternary convergent margin tectonics of Costa Rica, segmentation of the Cocos Plate, and Central American volcanism. Tectonics 19, 314–334.

von Huene, R., Ranero, C.R., Scholl, D.W., 2009. Convergent margin structure in high quality geophysical images and current kinematic and dynamic models. In: Lallemand, S., Funiciello, F. (Eds.), Subduction Zones Geodynamics. : Frontiers in Earth Sciences, vol. 2, XXII. Springer, Berlin, Heidelberg, pp. 137–157.

Walther, C.H.E., 2003. The crustal structure of the Cocos ridge off Costa Rica. Journal of Geophysical Research 108 (B3), 2136 doi:10.1029/2001JB000888.

Wessel, P., Smith, W.H.F., 1991. Free software helps map and display data. EOS. Transactions of the American Geophysical Union 72, 445–446.

Wilcock, W.S.D., Solomon, S.C., Purdy, G.M., Toomey, D.R., 1995. Seismic attenuation structure of the East Pacific Rise near 9°30′N. Journal of Geophysical Research 100 (B12), 24147–24165.

Ye, S., Bialas, J., Flueh, E.R., Stavenhagen, A., von Huene, R., Leandro, G., Hinz, K., 1996. Crustal structure of the Middle American trench off Costa Rica from wide-angle seismic data. Tectonics 15, 1006–1021.

Zhang, J., Toksöz, M.N., 1998. Nonlinear refraction traveltime tomography. Geophysics 63, 1726–1773.

Zhu, J., Kopp, H., Flueh, E.R., Klaeschen, D., Papenberg, C., Planert, L., 2009. Crustal structure of the central Costa Rica subduction zone: implications for basal erosion from seismic wide-angle data. Geophysical Journal International 178, 1112–1131.

# 3

Shulgin, A., Kopp, H., Mueller, C., Lueschen, E., Planert, L., Engels, M., Flueh, E.R., Krabbenhoeft, A., Djajadihardja, Y., 2009.

**Sunda-Banda arc transition: Incipient continent-island arc collision (northwest Australia).**

Geophys. Res. Lett., 36, L10304, doi:10.1029/2009GL037533.

GEOPHYSICAL RESEARCH LETTERS, VOL. 36, L10304, doi:10.1029/2009GL037533, 2009



# Sunda-Banda arc transition: Incipient continent-island arc collision (northwest Australia)

A. Shulgin,[1] H. Kopp,[1] C. Mueller,[2] E. Lueschen,[2] L. Planert,[1] M. Engels,[2] E. R. Flueh,[1] A. Krabbenhoeft,[1] and Y. Djajadihardja[3]

Received 29 January 2009; revised 15 April 2009; accepted 17 April 2009; published 27 May 2009.

[1] The eastern Sunda arc represents one of the few regions globally where the early stages of continent-arc collision can be studied. We studied along the western limit of the collision zone at the Sunda-Banda arc transition, where the Australian margin collides with the Banda island arc, causing widespread back arc thrusting. We present integrated results of a refraction/wide-angle reflection tomography, gravity modeling, and multichannel reflection seismic imaging using data acquired in 2006 southeast of Sumba Island. The composite structural model reveals the previously unresolved deep geometry of the collision zone. Changes in crustal structure encompass the 10–12 km thick Australian basement in the south and the 22–24 km thick Sumba ridge in the north, where backthrusting of the 130 km wide accretionary prism is documented. The structural diversity along this transect could be characteristic of young collisional systems at the transition from oceanic subduction to continent-arc collision. **Citation:** Shulgin, A., H. Kopp, C. Mueller, E. Lueschen, L. Planert, M. Engels, E. R. Flueh, A. Krabbenhoeft, and Y. Djajadihardja (2009), Sunda-Banda arc transition: Incipient continent-island arc collision (northwest Australia), *Geophys. Res. Lett.*, *36*, L10304, doi:10.1029/2009GL037533.

## 1. Introduction

[2] The convergence of the Indo-Australian plates and Eurasia and resulted in the formation of the Sunda and Banda island arcs. The transitional zone between the arcs is located south of Flores Island and is characterized by the change in the tectonic regime along the boundary. This segment of the plate boundary was only little investigated previously. In the scope of this study we address the problem of constraining the entire crustal scale structure and current geodynamic regime at the transitional zone using seismic reflection and wide-angle investigations and gravity modeling.

## 2. Tectonic Setting

[3] The plate boundary south of Sumba Island, Indonesia, is marked by a change in the tectonic regime (Figure 1) from subduction of the Indo-Australian oceanic lithosphere along the Sunda margin in the west that began ~45 m.y. ago [*Hall*, 2002] to continent - island arc collision along the Banda arc in the east [*Audley-Charles*, 1975; *Katili*, 1989; *Milsom*, 2001; *Audley-Charles*, 2004]. This margin experiences the early stages of continent-island arc collision as a result of the interaction between the Australian margin and the Banda island arc in the Pliocene [*Hall and Smyth*, 2008].

[4] Our goal is to constrain the deep crustal structure and tectonic evolution of the forearc using geophysical data collected during the RV Sonne SO-190 cruise in 2006. Our profile starts at ca. 12.5°S at the transition from the Late Jurassic oceanic lithosphere of the Argo Abyssal plain to the rifted Triassic continental crust of the Scott plateau [*van der Werff*, 1995] that is marked by the eastern termination of the Java trench at the transition to the Timor trough (Figure 1). Northwards, the oblique collision of the rifted continental crust of the Scott plateau with the forearc commenced 3–5 Ma ago [*Harris*, 1991] at a rate of ~7 cm/yr [*Curray*, 1989]. The current convergence rate at the Timor trough is ~15 mm/yr [*Bock et al.*, 2003] and it is manifested in back arc thrusting [*Silver and Reed*, 1988]. The Sumba Block, farther north, is believed to be an isolated tectonic block trapped between the trench and the volcanic arc (see *Rutherford et al.* [2001] and *Hall and Smyth* [2008] for discussion). Ridge structures of the Sumba Ridge include the submarine basement high, extending from Sumba Island to Savu Island and then merging with outer high crest towards Timor Island (Figure 1) [*Silver et al.*, 1983]. The basement of the ridge is dated from >80 to ~18 Ma, as inferred from the outcrops of intrusives and volcanic rocks together with sediments on Sumba and Savu Islands [*Karig et al.*, 1987], which might have been a part of the Paleogene Sumba-Banda forearc [*Hall and Smyth*, 2008].

[5] The origin of the abnormal width of the forearc south of Flores Island is enigmatic (Figure 1). Seismicity deeper than 30 km is absent between the islands of Sumba and Timor, while further north common earthquakes deeper than 100 km [*Engdahl and Villaseñor*, 2002] suggest the presence of the subducting slab below the Banda island arc, further confirmed by geochemical data from Flores Island [*Elburg et al.*, 2004]. However, most volcanic rocks of the Banda islands consist of primitive basalts typical of a volcanic arc built on oceanic lithosphere [*Hamilton*, 1988]. The complex basement thus reflects different periods of extension, subduction, and collision in Eastern Indonesia [*Hall and Smyth*, 2008].

## 3. Data Acquisition and Modeling

[6] Here we present a Vp seismic tomography model along the Sunda - Banda arc transition, further constrained by gravity modeling. Marine seismic investigations (Figure 1) were carried out by multichannel seismic reflection profiling (MCS), accompanied by gravity measurements, and seismic refraction profiling with ocean-bottom seismometers (OBS)

[1]Leibniz Institute of Marine Sciences, IFM-GEOMAR, Kiel, Germany.
[2]Federal Institute for Geosciences and Natural Resources, Hannover, Germany.
[3]Agency for the Assessment and Application of Technology, Jakarta, Indonesia.


0094-8276/09/2009GL037533$05.00

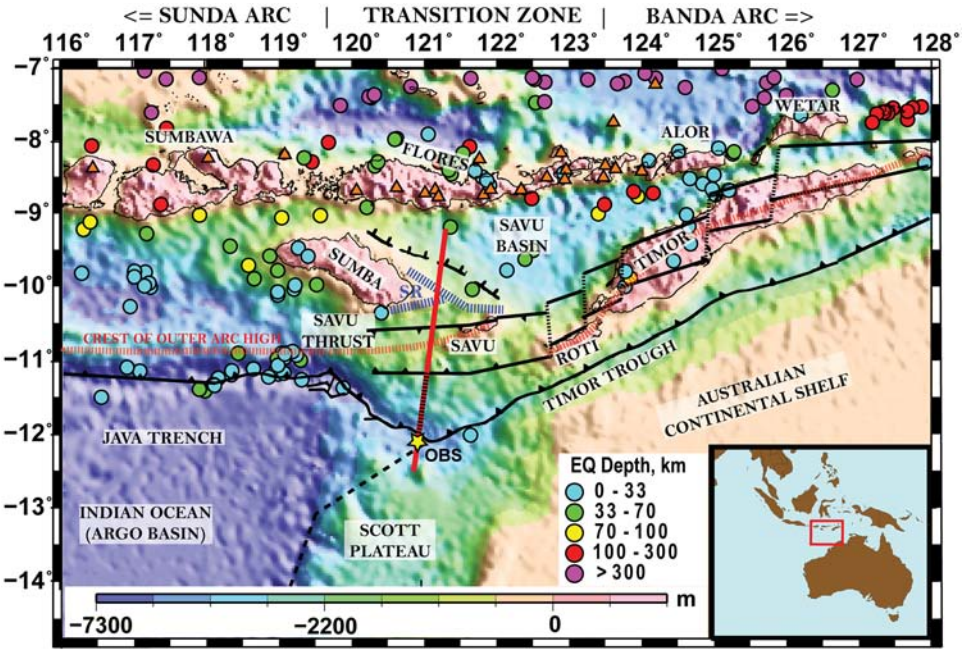


**Figure 1.** Simplified tectonic and bathymetric map of the Sunda-Banda Arc transition. Red line - seismic profile discussed in this study. Dashed red-black line - the MCS section shown in Figure 2. Yellow star - OBS location shown in Figure 2. Red triangles - active and Neogene volcanoes. Dashed blue line - a submarine Sumba Ridge (SR). Dashed red line - the crest of the outer forearc high. Black lines - faults [after *Rutherford et al.*, 2001; *Audley-Charles*, 2004]. Relocated earthquakes in the region are shown by filled circles, color-coded with depth [after *Engdahl and Villaseñor*, 2002].

and hydrophones (OBH) [*Mueller et al.*, 2008] (Text S1 of the auxiliary material).[1]

[7] The seismic velocity model was constrained by joint refraction/reflection 2D tomographic inversion [*Korenaga et al.*, 2000]. Data from a total of 36 stations were used as input to the tomographic modeling. First, ~16,000 first arrival phases with offsets of up to 120 km were picked; subsequently, ~4,000 reflected phases were added to the dataset. We applied a "top to bottom" approach with a simple layered starting model, initially constraining the model only for the near offsets and then increasing the depth extent of the ray coverage to constrain the entire model space. The structure of the sediments and the upper crust was controlled by the MCS data (Figure 2), thus constraining the upper section of the profile in great detail. Calculated uncertainty of traveltimes for ~85% of the all picked phases lies within the picking error range of 50 ms.

[8] The resulting Vp seismic tomography model was extended 100 km to the north and south and to a depth of 75 km to be used in forward gravity modeling. Velocities were converted to densities [*Christensen and Mooney*, 1995; *Carlson and Herrick*, 1990] and the subducting slab extended to 75 km depth underneath the island arc, where the deep seismicity commences. A constant density of 3.35 g/cm$^3$ was assumed for the mantle (Figure 3c).

## 4. Results (South to North Along 121°E)

### 4.1. Scott Plateau: Australian Crust

[9] The 2 km thick sedimentary cover of the Java trench has average Vp seismic velocities of 2–3 km/s in the trench section. A facies transition from deep marine fine grained carbonates to Upper Cretaceous shallow marine clastic deposits [*Stagg and Exon*, 1979] recognized in the MCS data forms the décollement at ~5 km depth (Figure 2a). A mud diapir observed at CDP 12900 (Figure 2) may be related to high pore pressures in the lower unit, also a series of linear mud diapirs nearby have been reported by *Breen et al.* [1986]. At depths between 6 km and 10 km Vp below the reflection gradually change from 3.5 km/s to 5 km/s (Figure 3a). Upper crustal velocities are ~6.0 km/s and increase to 6.7–7.0 km/s in the lower crust (Figure 3a), as revealed by the Puc and Plc phases (Figure 2c). The transition from the upper to the lower crust is marked by a strong reflection well documented by Pic phases. The Moho is recovered by the PmP phases at a depth of 20 km and is apparently dipping northwards at an angle of ~1°. Thus, the thickness of the crystalline crust reaches 10 to 12 km only. Although a continental crust with an Australian affinity was proposed to exist further east [*Kaneko et al.*, 2007], these values are in contrast to the typical thickness of the continental crust in NW Australia [*Collins et al.*, 2003] and at other continental shelves [e.g., *Ritzmann and Faleide*, 2007].

### 4.2. Frontal Prism and the Neogene Accretionary Wedge

[10] Imbricate thrusting (Figure 2a) and relatively low seismic velocities of 2.5–3.5 km/s down to 6–7 km depth indicate the presence of a large, ~20 km wide, frontal prism arcward of the deformation front (51 km distance). The ~60 km wide Neogene accretionary prism, imaged in the MCS data and confirmed by Vp values <4.0 km/s, is located between 85–130 km profile distance and forms the middle prism, app. bounded by the 3 km/s isoline. It is characterized by a laterally inhomogeneous velocity field and thrust fault-

[1] Auxiliary materials are available in the HTML. doi:10.1029/2009GL037533.

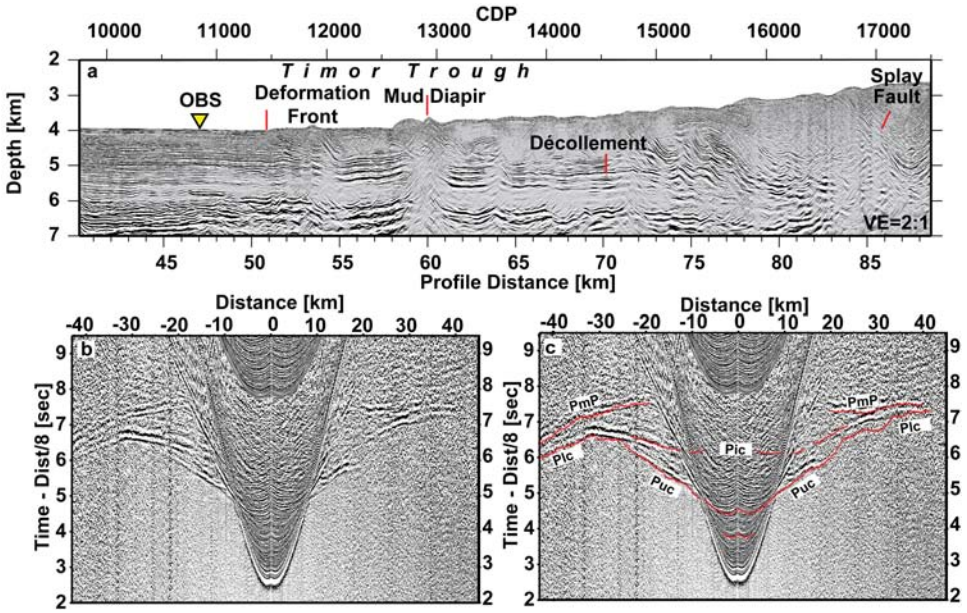


**Figure 2.** (a) MCS depth migrated section for the areas around Timor Trough (location shown in Figure 1). (b and c) example of the OBS data used in this study. Yellow triangle - the OBS position, shown in Figure 2b and 2c. Red dots show the computed travel-times of the seismic rays shot through the tomography model.

ing, observed in the MCS data. A system of splay faults that originate at the décollement and trend upwards at the angle of ~20° marks the transition to the middle prism (Figure 2a). The trench fill is composed of Mesozoic and Cenozoic sediments, eroded from the Australian continental shelf, with the lower part composed of clastic and volcano-clastic rocks, and the upper part composed of deep-water carbonates [*Breen et al.*, 1986]. The upper half of the sediments in the Timor trough is incorporated into the frontal prism. The lower 1000–1200 m of the clastic unit are currently bypassing the frontal prism (Figures 2a and 3a) and most likely underplate below the accretionary prism. The décollement is traced as a high-amplitude reflector for 30 km landward of the deformation front and extends to a depth of 6 km.

### 4.3. Paleo-accretionary Wedge

[11] The central section of the profile (140–210 km) suffers from limited energy penetration due to anomalous high attenuation and/or significant scattering. The opaque seismic character of the forearc high as observed both in the wide-angle and MCS data together with moderate Vp in the sedimentary cover (ranging from 2 km/s below the sea floor to 5 km/s at a depth of 10 km) (Figure 3a) suggests that the forearc high is composed of pre-Neogene accreted material that forms the paleo-accretionary complex. This material is probably derived from the stratigraphic units currently present on the Scott Plateau, which are composed of Jurassic sandstones overlain by Cretaceous marine shales [*Breen et al.*, 1986] and could have accumulated during the initial subduction of the passive Australian margin [*van der Werff et al.*, 1994] or during the subduction of Jurassic oceanic lithosphere of the Banda embayment (as shown by *Hall and Smyth* [2008]). Geologically the prism may be linked to the southern part of Timor, underlain by the outcropping Kolbano Complex, including Jurassic-Pliocene folded sediments of Australian origin, representing a segment of the accretionary complex [*Karig et al.*, 1987]. As suggested by numerical modeling of collisional margin settings [*Selzer et al.*, 2008], the opaque seismic character of the deeper portion may be caused by basally stacked packages of highly scattering rock fabric thus inhibiting deep energy penetration.

### 4.4. Sumba Ridge

[12] The crest of the Sumba ridge [*Silver et al.*, 1983] is located at 250 km profile distance; the basement top (app. corresponding to the 4 km/s isoline) is at a depth of 3 km below sea level at the crest and slopes down to 9 km depth in the south and to 6 km depth in the north (Figure 3a). A sharp velocity change in the upper crust at ~200 km distance marks the southern limit of the Sumba ridge. A vertical displacement of the basement occurs at 260 km underneath a small sedimentary basin and again at the northern edge of the ridge (at 310 km). The ridge is covered by sediments (presumably eroded from the Sumba, Savu and Timor islands) with a thickness of 0.5 km increasing to more than 2 km in thickness at its flanks. A crustal reflection observed below the entire northern portion of the profile at depths of 15–17 km probably corresponds to the transition between the upper and the lower crust (Figure 3a). Vp velocities vary from 5.5 km/s to 6.4–6.5 km/s in the upper crust, and from 6.7–6.8 km/s to 7.1 km/s in the lower crust and are typical of a mature arc massif or possibly of a fragment of a continental crust, which can be linked to the existence of a volcanic arc in the eastern Indonesia during the Paleogene, traces of which may be found in the highest nappes of Timor and other Banda islands [*Hall and Smyth*, 2008]. The PmP phases indicate the slightly southwards dipping Moho at a depth of ~26 km below the Sumba ridge. Available Pn phases indicate Vp ~ 8.0 km/s in the forearc mantle.

### 4.5. Savu Basin

[13] The transition from the Sumba ridge to the Savu basin (at 310 km) is marked by sea floor deepening and an increase in sedimentary thickness. The sedimentary fill eroded from

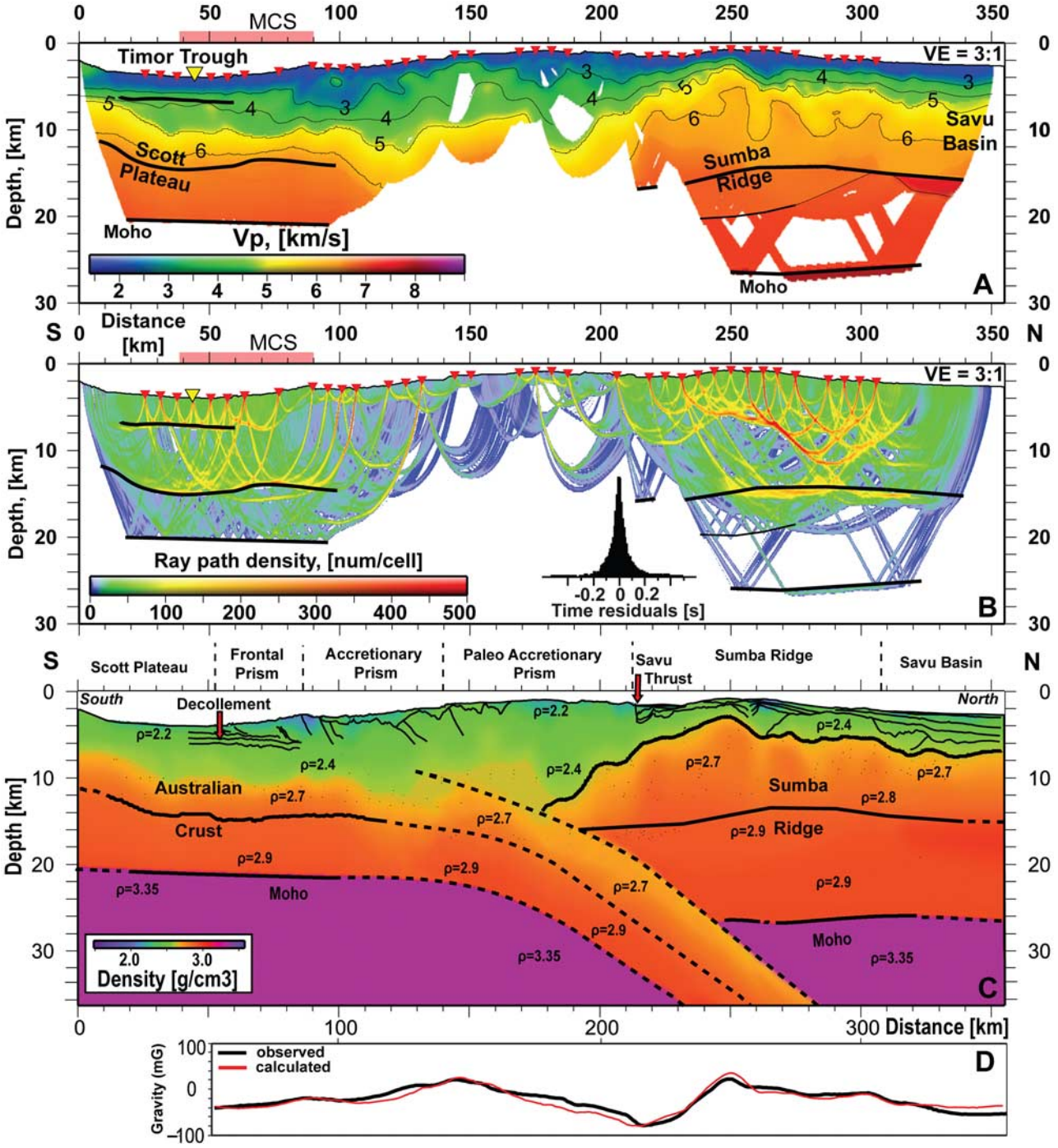


**Figure 3.** (a) Results of seismic tomography and gravity modeling a) Recovered tomography model, black lines - seismic reflectors. Red triangles - the OBS/OBH locations. Yellow triangle - OBS location (Figure 2). Pink line along the distance axis - MCS data shown in Figure 2. (b) Ray path coverage obtained during the tomographic inversion. Insert shows the time residuals distribution. (c) Combined model. Background color and numbers - density based the tomography and gravity results. Thin solid black lines - reflection horizons from the MCS data. Thick black lines - interfaces used in the gravity modeling. Interfaces not seismically resolved - dashed lines. (d) results of gravity modeling. Red line - observed data; black line - calculated gravity field.

the island arc [*Audley-Charles*, 2004] reaches a total thickness of 3 km with Vp velocities ranging from <2 km/s to 4 km/s (Figure 3a). The basement topography and sedimentary layering are consistent with earlier seismic reflection profiles in the Savu basin [*Karig et al.*, 1987; *Breen et al.*, 1986; *van der Werff et al.*, 1994]. Our wide-angle data for the first time document the Moho at a depth of 26 km.

### 4.6. Crustal Structure From Seismic Inversion and Gravity Modeling

[14] Figure 3c shows the tectonic model based on the results of the reflection seismic imaging, the wide-angle tomography, and gravity modeling. In the south, the crust of Australian affinity is dipping arcward at an angle of ~10–11°. The 10–12 km thick crystalline crust of the Scott plateau as a promontory of the Australian continent (described above) underthrusts the Banda forearcs.

[15] Between the Sumba ridge and the trough, the accretionary complex shows thrusting and represents a nascent orogeny, forced by post-Pliocene convergence and buoyant uplift associated with the transition from active oceanic subduction to continent-island arc collision. The complex is composed of a frontal prism, where active frontal accretion is documented, juxtaposed against a 130 km wide accretionary prism. The central section of the profile (140–210 km distance) consists of the paleo-accretionary prism bounded northwards by the Sumba ridge, which acted as backstop to the paleo-prism during the time of accretion. Most likely the paleo-prism was added to the Sumba ridge, during the SSW tectonic escape of Sumba Island, caused by the initial contact of Australia and the Banda arc [*Rutherford et al.*, 2001]. The Savu thrust marks the tectonic transition from the accretionary wedge to the tectonic units of the Sumba ridge. Vertical growth of the prism facilitated backthrusting over the Sumba ridge along the Savu thrust [*Silver and Reed*, 1988], however, motion along the Savu thrust must primarily be driven by high basal friction due to the low relief difference between the prism and the ridge. The crustal thickness of the Sumba ridge is ~23 km with crustal densities ranging from 2.65 g/cm$^3$ to 2.90 g/cm$^3$. Towards the island arc, the thickness of the crystalline crust is ~20 km below the Savu basin with the upper plate Moho at a depth of ~26–27 km, as also supported by gravity modeling. The crustal thickness is increased compared to the Lombok basin west of Sumba Island, which is underlain by 7 km thick crust (E. Lueschen et al., Structure, evolution and tectonic activity at the Eastern Sunda forearc, Indonesia, from marine seismic investigations, submitted to *Tectonophysics*, 2009).

## 5. Discussion

[16] Newly acquired seismic reflection/refraction and gravity data east and south of Sumba Island resolve the deep crustal structure at the Sunda-Banda arc transition (Figure 3c). The current system can be regarded as a precursor of a fold-and-thrust belt, which may develop in the forearc as the collision progresses. The wide-angle seismic data resolve the full crustal structure of the Sumba ridge and the Savu basin and for the first time provide the geophysical background for geodynamic models of nascent collisional systems. The observed variations in crustal structure along the profile may be typical for tectonic settings with continental margins approaching island arcs. The observed variations in the crustal structure along the profile are similar to the present structure around Taiwan, formed by the transition from subduction to collision of Eurasia and the Philippine Sea plate [*Huang et al.*, 2006; *Sibuet and Hsu*, 2004].

[17] **Acknowledgments.** We would like to thank Captain Meyer and the crew of R/V Sonne and the SINDBAD Working group for their enormous help in collecting and processing of the data. Authors express great gratitude to Jun Korenaga for the discussion on seismic tomography and Tomo2D code. We would like to thank the GRL editor Fabio Florindo and reviewers for their help in improving the manuscript. The SINDBAD project is funded by the German Federal Ministry of Education and Research (BMBF) (grants 03G0190A and 03G0190B).

## References

Audley-Charles, M. G. (1975), The Sumba fracture: A major discontinuity between eastern and western Indonesia, *Tectonophysics*, *26*, 213–228.

Audley-Charles, M. G. (2004), Ocean trench blocked and obliterated by Banda forearc collision with Australian proximal continental slope, *Tectonophysics*, *389*, 65–79.

Breen, N. A., E. A. Silver, and D. M. Hussong (1986), Structural styles of an accretionary wedge south of the island of Sumba, Indonesia, revealed by SeaMARC II side scan sonar, *Geol. Soc. Am. Bull.*, *97*, 1250–1261.

Bock, Y., L. Prawirodirdjo, J. F. Genrich, C. W. Stevens, R. McCaffrey, C. Subarya, S. S. O. Puntodewo, and E. Calais (2003), Crustal motion in Indonesia from Global Positioning System measurements, *J. Geophys. Res.*, *108*(B8), 2367, doi:10.1029/2001JB000324.

Carlson, R. L., and C. N. Herrick (1990), Densities and porosities in the oceanic crust and their variations with depth and age, *J. Geophys. Res.*, *95*, 9153–9170.

Christensen, N. I., and W. D. Mooney (1995), Seismic velocity structure and composition of the continental crust: A global view, *J. Geophys. Res.*, *100*, 9761–9788.

Collins, C. D. N., B. J. Drummond, and M. G. Nicoll (2003), Crustal thickness patterns in the Australian continent, *Geol. Soc. Am. Spec. Pap.*, *372*, 121–128.

Curray, J. R. (1989), The Sunda arc: A model for oblique plate convergence, *Neth. J. Sea Res.*, *24*, 131–140.

Elburg, M. A., M. J. van Bergen, and J. D. Foden (2004), Subducted upper and lower continental crust contributes to magmatism in the collision sector of the Sunda-Banda arc, Indonesia, *Geology*, *32*, 41–44.

Engdahl, E. R., and A. Villaseñor (2002), Global seismicity: 1900–1999, in *International Handbook of Earthquake and Engineering Seismology*, pp. 665–690, Academic, San Diego, Calif.

Hall, R. (2002), Cenozoic geological and plate tectonic evolution of SE Asia and the SW Pacific: Computer-based reconstructions, model and animations, *J. Asian Earth Sci.*, *20*, 353–434.

Hall, R., and H. R. Smyth (2008), Cenozoic arc processes in Indonesia: Identification of the key influences on the stratigraphic record in active volcanic arcs, *Geol. Soc. Am. Spec. Pap.*, *436*, 27–54.

Hamilton, W. B. (1988), Plate tectonics and island arcs, *Geol. Soc. Am. Bull.*, *100*, 1503–1527.

Harris, R. A. (1991), Temporal distribution of strain in the active Banda orogen: A reconciliation of rival hypotheses, *J. Southeast Asian Earth Sci.*, *6*, 373–386.

Huang, C.-Y., P. B. Yuan, and S.-J. Tsao (2006), Temporal and spatial records of active arc-continent collision in Taiwan: A syntasis, *Geol. Soc. Am. Bull.*, *118*, 274–288.

Kaneko, Y., S. Maruyama, A. Kadarusman, T. Ota, M. Ishikawa, T. Tsujimori, A. Ishikawa, and K. Okamoto (2007), On-going orogeny in the outer-arc of the Timor-Tanimbar region, eastern Indonesia, *Gondwana Res.*, *11*, 218–233.

Karig, D., A. Barder, T. Charlton, S. Klemperer, and D. Hussong (1987), Nature and distribution of deformation across the Banda Arc: Australia collision zone at Timor, *Geol. Soc. Am. Bull.*, *98*, 18–32.

Katili, J. A. (1989), Review of past and present geotectonic concepts of eastern Indonesia, *Neth. J. Sea Res.*, *24*, 103–129.

Korenaga, J., et al. (2000), Crustal structure of the southeast Greenland margin from joint refraction and reflection seismic tomography, *J. Geophys. Res.*, *105*, 21,591–21,614.

Milsom, J. (2001), Subduction in eastern Indonesia: How many slabs?, *Tectonophysics*, *338*, 167–178.

Mueller, C., et al. (2008), From subduction to collision: The Sumba-Banda Arc transition, *Eos Trans. AGU*, *89*, 49–50.

Ritzmann, O., and J. I. Faleide (2007), Caledonian basement of the western Barents Sea, *Tectonics*, *26*, TC5014, doi:10.1029/2006TC002059.

Rutherford, E., K. Burke, and J. Lytwyn (2001), Tectonic history of Sumba Island, Indonesia, since the Late Cretaceous and its rapid escape into forearc in the Miocene, *J. Asian Earth Sci.*, *19*, 453–479.

Selzer, C., S. J. H. Buiter, and O. A. Pfiffner (2008), Numerical modeling of frontal and basal accretion at collisional margins, *Tectonics*, *27*, TC3001, doi:10.1029/2007TC002169.

Sibuet, J.-C., and S.-K. Hsu (2004), How was Taiwan created?, *Tectonophysics*, *379*, 159–181.

Silver, E. A., and D. L. Reed (1988), Backthrusting in accretionary wedges, *J. Geophys. Res.*, *93*, 3116–3126.

Silver, E. A., D. L. Reed, and R. McCaffrey (1983), Back arc thrusting in the eastern Sunda arc, Indonesia: A consequence of arc-continent collision, *J. Geophys. Res.*, *88*, 7429–7448.

Stagg, H. M. J., and N. F. Exon (1979), Western margin of Australia: Evolution of a rifted arch system—Discussion, *Geol. Soc. Am. Bull.*, *90*, 795–797.

van der Werff, W. (1995), The evolution of the Savu Forearc Basin, Indonesia (Forearc response to arc/continent collision), *J. Mar. Petrol. Geol.*, *12*, 247–262.

van der Werff, W., D. Kusnida, and H. Prasetyo (1994), On the origin of the Sumba forearc basement, *J. Mar. Petrol. Geol.*, *11*, 363–374.

Y. Djajadihardja, Agency for the Assessment and Application of Technology, Jl.M.H. Thamrin No. 8, Jakarta 10340, Indonesia.

M. Engels, E. Lueschen, and C. Mueller, Federal Institute for Geosciences and Natural Resources, Stilleweg 2, D-30655 Hannover, Germany.

E. R. Flueh, H. Kopp, A. Krabbenhoeft, L. Planert, and A. Shulgin, Leibniz Institute of Marine Sciences, IFM-GEOMAR, Wischhofstr. 1-3, D-24148 Kiel, Germany. (ashulgin@ifm-geomar.de)

# 4

Kopp, H., Flueh, E. R., Petersen, C. J., Weinrebe, W., Wittwer, A., Meramex Scientists, 2006.

**The Java margin revisited: Evidence for subduction erosion off Java.**

Earth Planet. Sci. Lett., 242, 130-142.

Available online at www.sciencedirect.com
SCIENCE DIRECT®
Earth and Planetary Science Letters 242 (2006) 130–142
EPSL
www.elsevier.com/locate/epsl

# The Java margin revisited: Evidence for subduction erosion off Java

H. Kopp *, E.R. Flueh, C.J. Petersen, W. Weinrebe, A. Wittwer, Meramex Scientists

*IFM-GEOMAR Research Center for Marine Sciences, Kiel, Germany*

Received 21 June 2005; received in revised form 22 November 2005; accepted 27 November 2005
Available online 10 January 2006
Editor: R.D. van der Hilst

**Abstract**

The eastern Sunda margin off Indonesia (from central Java to Sumba Island) remains a little investigated subduction zone, contrary to its well-studied northwestern segment. Whereas large portions of the Sunda margin are considered a classical accretionary zone, subduction characteristics along the central Java sector indicate erosive processes as the dominant mode of mass transfer. The tectonic framework of the central Java margin, with a convergence rate of 6.7 cm/yr, insignificant sediment input and a pronounced seafloor roughness where the oceanic Roo Rise is subducting underneath Java, facilitates subduction erosion. Evidence for erosion comes from newly acquired geophysical data off central Java: local erosive processes in the wake of seamount subduction are documented by a high-resolution bathymetric survey and result in an irregular trend of the deformation front sculpted by seamount collision scars. Subduction of oceanic basement relief leads to large-scale uplift of the forearc, as recorded on a reflection seismic profile, and to a dismemberment of the previous outer forearc high, giving way to isolated topographic elevations. The broad retreat of the Java Trench and deformation front above the leading edge of the Roo Rise has exposed an area of approximately 25,000 km$^2$ of deeper seafloor formerly covered by the previous frontal prism. Frontal erosion coincides with a steepening of the lower slope angle in the central Java sector compared to the neighbouring segments. In global compilations, the key geological parameters of the central Java margin lie in the erosive regime, reflecting the interplay of basement relief subduction, negligible sediment supply and a high convergence rate on the evolution of the margin.


*Keywords:* Java margin; subduction erosion; morphotectonics; high-resolution bathymetry; seamount subduction; taper analysis

## 1. Introduction

Modes of mass transfer at subduction zones vary greatly and include both accretionary and erosive styles. Most margins are non-uniform either in alternating phases of accretion and erosion, or in supporting accretive and erosive regimes simultaneously. While accretionary systems are comparatively easy to identify due to the material accumulation in a compressive setting, the 'loss' of material in erosive systems is a more obscure target. The last two decades, however, have brought a tremendous advancement in the understanding of erosive systems (e.g. [1–9]). A limited number of geological and tectonic factors appear to control tectonic erosion over subduction accretion or intermediate non-accretive styles. These include convergence rates exceeding 6 cm/yr, thin (<1 km) sediment cover in the trench, and seafloor roughness, all of which prevail along the central Java margin, implying an erosive regime here. Tectonic erosion may either occur along the front of the margin or along the base of the forearc wedge causing dismemberment of upper plate material

* Corresponding author. Tel.: +49 431 600 2334; fax: +49 431 600 2923.
*E-mail address:* hkopp@ifm-geomar.de (H. Kopp).

0012-821X/$ - see front matter © 2005 Elsevier B.V. All rights reserved.
doi:10.1016/j.epsl.2005.11.036

along the shallow part of the plate interface updip of the seismogenic zone and transfer of material to the downgoing oceanic plate [10]. From their global compilation of subduction zones, Clift and Vannucchi [9] recognized that effective erosion is foremost controlled by the collision of bathymetric elevations with the margin. Even though collision of large topographic units is episodic and short-lived along most margins, its influence on the evolution of that margin is profound as it governs the rates of material transfer (e.g. collision of Louisville Ridge with the Kermadec margin [11]). This paper investigates new geophysical data collected offshore central Java, where the oceanic Roo Rise is currently being subducted. Based on a combined analysis with the regional bathymetry, we propose subduction erosion as the dominant tectonic process off central Java. Geological indicators for tectonic erosion at the Java margin include landward retreat of the trench and deformation front, dismemberment of the previous outer forearc high by underthrusting of oceanic basement relief and steepening of the trench slope. In global compilations of accretionary and erosive systems, the central Java margin clearly maps in the erosive regime, contrary to the classical accretionary concept previously applied to this margin segment.

## 2. Tectonic framework of the Sunda margin

The Sunda margin, including the Sumatra and Java sectors, extends from the Bay of Bengal and the Andaman Sea in the northwest to Sumba Island in the southeast and has been the site of ongoing geophysical and geological surveys since the early years of the last century (e.g. [12,13]). It is regarded as a classical example for an accretionary type margin and was used to promote models of sediment accretion and on the evolution of forearc tectonic structures (e.g. [14–25]). The present subduction system evolved after the Eocene collision of India with Eurasia and has been active since the middle Tertiary, as inferred from dating of the Sunda-system volcanism [26]. The subduction zone is mainly characterized by the variation of two parameters: subduction obliqueness and sediment supply to the trench. The high degree of slip partitioning arising from the oblique plate convergence along the Sumatran sector of the margin gives rise to the lithospheric-scale Sumatra strike-slip fault [27] and additional marine transpressional features [28] to compensate for the lateral component of motion.

Frontal accretion is the dominant mode of mass transfer along the central Sunda margin, where a massive accretionary prism has formed as a result of the high ratio of accreted to subducted sediment [21,22]. Adjacent to the active frontal accretionary prism off southern Sumatra and western Java along the central sector of the margin, the now fossil portion of the accretionary wedge shapes a well-developed outer forearc high of Eocene–Oligocene age [29,30]. The accretionary origin of the outer forearc high is supported by field mapping [25], refraction and gravity data [29,30]. Landward of the outer forearc high, a series of mature forearc basins has developed [31]. Along the central Sunda margin, these basins form between the landward arc-massif backstop and the large accretionary wedge on the seaward side and are of the ‘constructed type’ identified by Dickinson and Seely [32]. Stratigraphic investigations and drilling information on the forearc basins suggest an Oligocene age for the oldest sediments trapped here [33–35,21]. Mass balance calculations conducted along the central sector of the margin from southern Sumatra to western Java have shown that the age of the outer forearc high and the forearc basin sediment fill correlate with an accretionary convergence history that must have remained fairly constant since Eocene times [22], even though a number of geologic and tectonic parameters, such as plate age, sediment load and subduction angle, show a high variability along strike of the margin. Frontal accretion is the dominant mode of mass transfer along the northern and western segments of the margin off Sumatra and western Java [17,21], and only a low percentage of sediment is underplated or subducted, similar to the current situation along the Cascadia margin [36]. Thus, in view of the large fraction of modern margins that have been found to be erosive, the northern and central Sunda subduction zone has been classified as an end-member of convergent margins. However, geophysical and geological investigations along the eastern portion of the Sunda margin, from central Java to Sumba Island, are scarce. This margin sector includes the ocean–continent transition between the Indo-Australian plate and the Australian continent across the North Wilson Fault Zone, which separates the two plates (approximate location shown in Fig. 1) [37].

Along this segment, convergence at a rate of $6.7 \pm 0.7$ cm/yr in a direction N11°E is approximately orthogonal to the trench, as determined by GPS measurements between Christmas Island and West Java [38]. At present, 135 Ma oceanic crust subducts off eastern Java and crustal ages decrease to 96 Ma off western Java and southern Sumatra [17,39]. In correlation with an increasing distance from the Ganges-Brahmaputra Delta, trench sediment thickness decreases along strike of the margin. Sediment input from Suma-

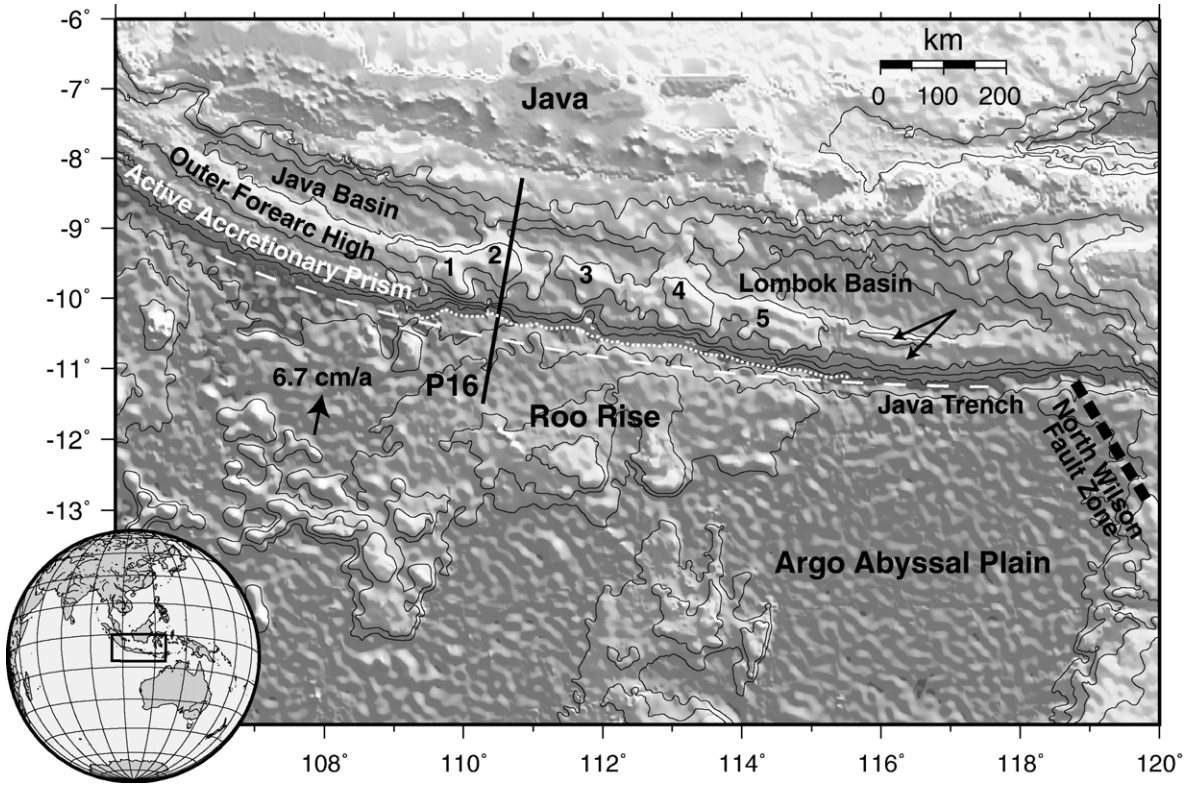


Fig. 1. Bathymetric map of the Java margin displaying main morphological features (taken from the Topex data set of Sandwell and Smith [62]). Subduction of oceanic basement relief such as the Roo Rise causes active erosion of the margin wedge as manifested in the retreat of the Java Trench between 109°E and 115°E. The deformation front has progressed up to 60 km northward from its normal curvature trend. Between the former trend of the deformation front (stippled line) and its current track (dotted line), an area of approximately 25,000 km$^2$ formerly covered by the frontal prism has been eroded. Black arrows depict trench-parallel elongated highs running along the outer forearc south of the Lombok Basin.

tra and Java is trapped in the forearc basins here and does not reach the trench. In association with the declining sediment supply to the southeast, the size and volume of the accretionary wedge observed off Sumatra and western Java shrinks steadily to the east, where the trench along extensive segments is devoid of any sediment fill.

## 3. Observations on tectonic style off Java

The western Java margin currently receives approximately 1.3 km of sediment trench input, a large fraction of which is accreted and incorporated into the active frontal accretionary prism (Fig. 1). At present, less than 15% of the trench material is subducted and passes the accretionary prism in a subduction window [22]. Off western Java, a continuous and homogeneously developed frontal accretionary prism and outer forearc high have evolved in conjunction with a mature forearc basin (Fig. 1). More than 4 km of mainly terrigenous sediment with minor volcanic ashes have accumulated in the basin [30]. The horizontal-layered strata lie roughly parallel to the seafloor and are generally undeformed, apart from several anticlinal structures, the largest of which most likely represents the offshore prolongation of the Sumatra strike-slip fault system. The lateral extent of the frontal accretionary prism, the outer forearc high and the forearc basin are abruptly disrupted around 109°E. No distinct frontal prism or prolonged outer forearc high are recognizable along the central Java sector (109°E–115°E) and a continuous forearc basin is not present (Fig. 1). Here, the outer forearc high is characterized by isolated bathymetric highs (labelled 1 through 5 in Fig. 1) contrasting with a continuous ridge, as it exists in the western (105°E–109°E) and eastern Java sectors (115°E–119°E). These isolated highs reach water depths of less than 1000 m, compared to the approximately 2000 m water depth attained by the continuous ridge-like outer forearc high in the neighbouring segment. An active frontal accretionary prism bordering the outer forearc high, as recognized off western Java and Sumatra, is not present off central Java. The subducting oceanic crust of the Argo Abyssal Plain (Fig. 1)

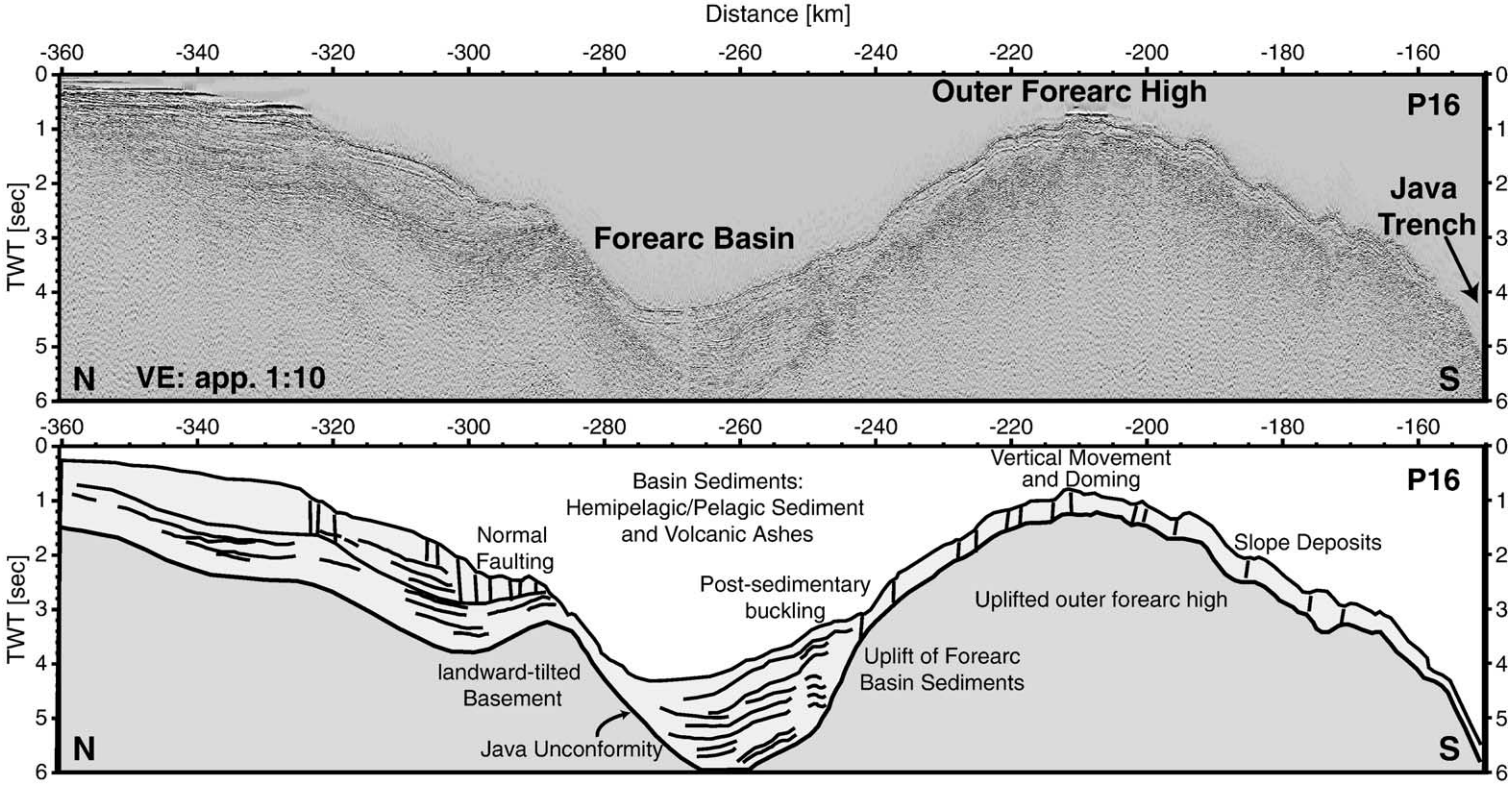


Fig. 2. Four-channel streamer section across the Java margin (location shown in Fig. 1). Uplift caused by the underthrusting of oceanic basement relief affects the outer forearc high, which reaches approximately 1000 m shallower water depth than in adjacent areas. The forearc basin strata onlap the outer forearc high and are tilted landward, indicating syndepositional and postdepositional vertical movement of the seaward portion of the basin and the forearc high. Recent deformation is also indicated by the landward-tilted basement north of the forearc basin.

carries only a thin coverage of Mesozoic and Tertiary pelagic sediments reaching a few hundred meters thickness (Fig. 2) [40]. Whereas the deep-sea trench off western Java displays a flat morphology resulting from >1 km infill, along the central Java segment, the trench forms a V-shaped structure and is generally

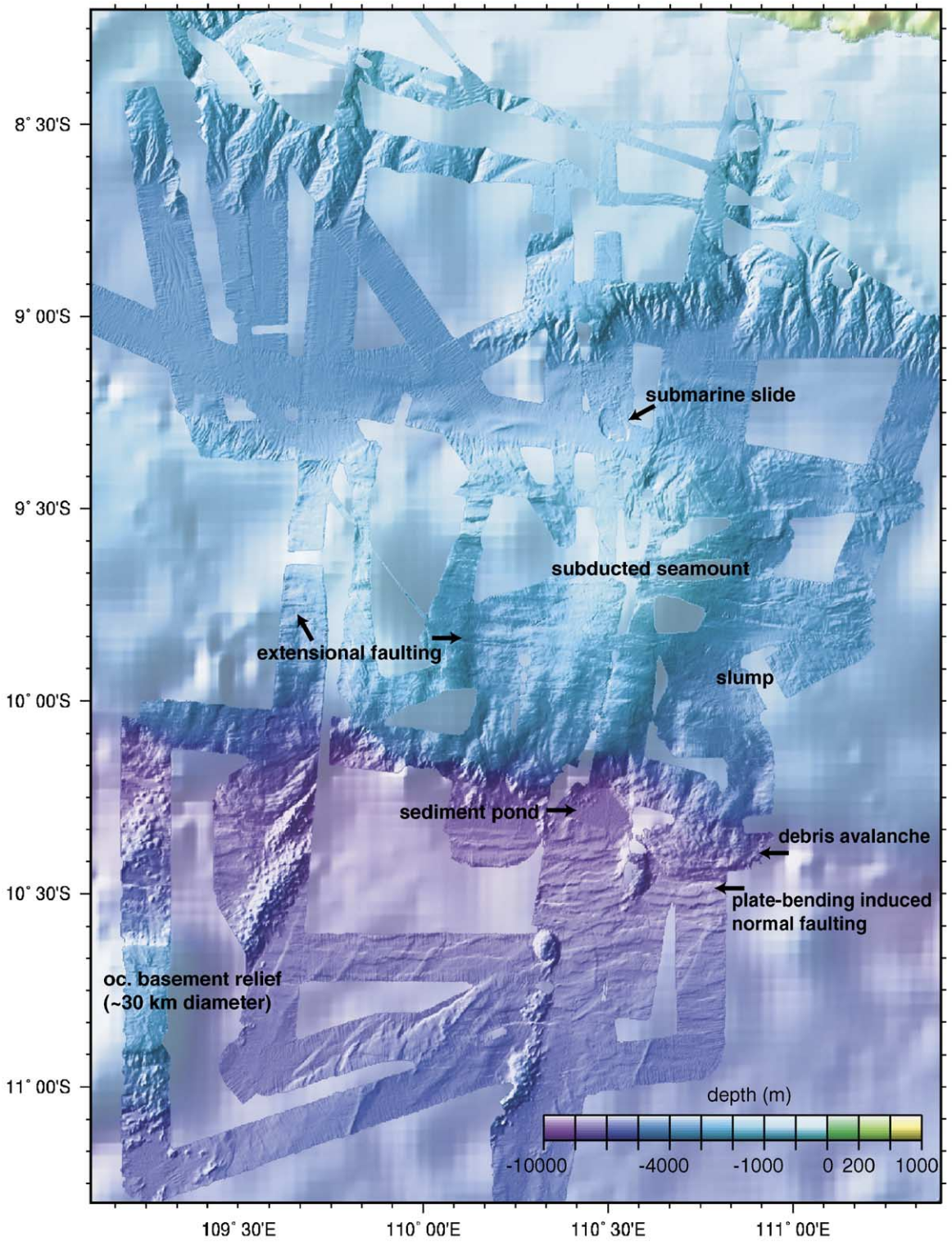

devoid of sediment. Along this section of the margin, the trench and deformation front show an irregular shape (Fig. 1). The trench is less deep here, reaching depths of 5600–6000 m, while it is more than 7000 m deep off western Java and seaward of the Lombok Basin [41].

## 4. Subduction of oceanic basement relief

### 4.1. Subduction of the oceanic Roo Rise

Subduction processes off central Java are dominated by the collision of the oceanic Roo Rise with the forearc between 109°E and 115°E (Fig. 1). The Roo Rise represents a little investigated oceanic topographic feature, which forms an irregularly shaped broad swell dotted with isolated morphological summits (Fig. 1). It reaches heights of about 2.0–2.5 km above the general level of the surrounding ocean floor. Early refraction profiles indicate thickened oceanic crust underneath the Roo Rise [42] with an average thickness of 11.5 km. The lack of a pronounced free-air gravity response to the relief of the Roo Rise implies that this plateau may be compensated by a low-density root [43], as is common for volcanic features formed at or near spreading centers (e.g. Cocos Ridge [44] or Malpelo Ridge [45]). The Roo Rise continues into the trench and is interacting with the margin, causing large-scale uplift of the entire forearc (Fig. 1). Fig. 2 shows a reflection seismic line (P16) across the Java margin extending from 110°17′E/11°28′S to 110°51′E/8°15′S (location shown in Fig. 1), which was acquired during cruise SO179 of the German RV SONNE in 2004 [40]. This profile was recorded using a four-channel streamer and runs roughly parallel to the western flank of the Roo Rise and its projection underneath the forearc [46]. Underthrusting of oceanic basement relief results in uplift and doming of the outer forearc high, which here reaches approximately 1000 m shallower water depths than observed for those adjacent areas not affected by Roo Rise subduction. Uplift also affects the forearc basin sediments (Fig. 2) and causes a narrowing of the basin compared to the western Java or Lombok Basins (Fig. 1). Seismic reflections within the basin are continuous and of variable amplitude and are interpreted as facies of terrigenous origin alternating with volcanic ashes. The forearc basin strata onlap the outer forearc high and are tilted landward, indicating syn-and post-depositional vertical movements of the seaward portion of the basin and the forearc high. Uplift has also been documented by Newcomb and McCann [43] on two seismic profiles crossing the margin at 113°E and 114°E (profiles away from the projection of the Roo Rise at 109°E across the West Java forearc basin and at 115.2°E across the Lombok Basin recorded undisturbed strata). Recent deformation is indicated by the elevated and landward-tilted basement north of the forearc basin. Normal faulting of the landward slope of the forearc basin (Fig. 2) may be an indication of extension due to basal erosion; however, the lack of data penetration in this streamer section prevents any further investigation. Large-scale subsidence, which is recognized as an indicator of basal tectonic erosion of forearc crust elsewhere, is not documented for the central Java margin and would be overcast by the vertical tectonics caused by the subduction of the Roo Rise. Where the leading edge of the Roo Rise enters, the deep-sea trench is uplifted and is anomalously shallow, as discussed in the previous section. The collision of the Roo Rise with the margin causes a displacement of the trench and deformation front to the north (Fig. 1). This general retreat of the trench between 109°E and 115°E is superimposed over small-scale anomalies in the curvature of the deformation front. These smaller-scale displacements result from the collision of seamounts with the deformation front.

### 4.2. Seamount subduction

Numerous seamounts more than 10 km in diameter and at different stages of subduction (e.g. at approximately 108.5°E, 111.1°E, 111.5°E, 113°E and 114.8°E) have been mapped using side-scan sonar [39,41] and high-resolution bathymetry (Fig. 3). The seamount population tremendously increases the roughness of the seafloor entering the trench off central and eastern Java. Bathymetric seafloor investigations further west off southern Sumatra, Sunda Strait and West Java did not detect comparable seamount fields [47]. The indentations of the deformation front caused by the incipient

Fig. 3. High-resolution bathymetric survey of the central Java margin. The swath data are underlain by predicted bathymetry from satellite altimetry data (Sandwell and Smith [62]). Recent subduction of a seamount results in uplift of the outer forearc high and in extensional structures cutting the middle slope. In the wake of seamount subduction, a retreat of the deformation front coincides with mass-wasting processes, which form a local sediment pond in the otherwise sediment-starved trench. A slump at the flank of the subducted seamount caused a debris avalanche into the trench. The oceanic crust is characterized by extensive normal faulting parallel to the trench and is dotted by numerous seamounts and bathymetric elevations up to several tenths of kilometres in diameter. The continental slope in the north is cut by numerous canyons, which act as pathways for terrigenous material fed to the forearc basin.

subduction of seamounts are commonly a few kilometres broad, but reach widths of 50 km where the deformation front has retreated in excess of 10 km [41]. The swath data shown in Fig. 3 reveal a recently subducted seamount ~50 km in diameter at 110°30′E, which causes a northward deflection of the deformation front by ~15 km. Masson et al. [41] noted a correlation between the re-entrant scars along the deformation front and the isolated topographic highs (1–5 in Fig. 1) composing the outer forearc high off central Java (e.g. at 109°E, between 109°45′E and 110°45′E, at 111°40′E, and possibly between 112°45′E and 113°45′E). They proposed that the topographic highs represent completely subducted seamounts, as these are predicted to cause continued uplift of the forearc after subduction [48]. A continuous forearc ridge is again present between 115°E and 118°E, comparable to the fossil accretionary wedge off western Java, however, of much smaller dimensions. The morphology of this forearc ridge south of the Lombok Basin is characterized by two trench-parallel elongated highs (Fig. 1), which run along the entire extent of the forearc ridge and are also developed across the easternmost high discussed by Masson et al. [41] between 114°E and 115°E (5 in Fig. 1). This high does not show a seaward scar, but judging from the continuous morphology to the east, we believe that this high is a prolongation of the outer forearc ridge south of the Lombok Basin and does not represent an underthrust seamount causing a re-entrant scar. In the opposite sense, Masson et al. (1991) also note that the indentation of the deformation front at 118°E does not have a correlative high further landward. This site however is the locus of the transition from oceanic subduction to continent–island arc collision [49]. The northward displacement of the trench here may possibly be associated with the North Wilson Fault Zone (Fig. 1) [37], which marks the boundary between the plates here.

### 4.3. Re-entrant morphology

The collision scars mapped along the deformation front furthermore commonly correlate with sediment accumulations of up to several hundred meters in thickness [17] in the otherwise sediment-devoid trench. These isolated sediment ponds are derived from local erosive processes associated with seamount collision [50,51,6,46]: as any given seamount is completely underthrust under the margin wedge, it is uplifted and shortened, the lower slope experiences oversteepening above the trailing flank of the seamount, inducing gravitational failure and mass-wasting of the margin toe (Fig. 3). In the example shown in Fig. 3, a submarine landslide has disassociated into a debris avalanche, which has slumped into the trench at 110°45′E/10°15′S. The sediment accumulation mapped in Fig. 3 occurs in a local deep within the trench that results from the exposure of deeper levels of the downthrusting plate in the wake of seamount subduction. Masson et al. [41] recorded areas of high backscatter within the collision scars, which are interpreted to be caused by outcropping strata arising from frontal erosion of the margin wedge due to seamount collision. The margin segment mapped during our recent survey (Fig. 3) displays a truncated lower slope, which is indented by the seamount re-entrant. It is sculpted by slumps and normal fault scarps similar to those shown by von Huene et al. [52] in Costa Rica, which developed after the seamount passed the deformation front. Re-entrant scars have been modelled by analogue experiments, which suggest that subducting seamounts of considerable relief will shift the interplate décollement to an elevated level tangential to the crest of the seamount into the trailing wedge of the upper plate [51]. Upper plate and trench material is transferred to the subducted plate behind the underthrusting seamount, which casts a low-stress shadow, allowing passive subduction of debris and sediment [6]. This process accelerates basal erosion in the vicinity of the trench and leads to extensional faulting along the lower and middle slope of the outer forearc high as seen in Fig. 3.

### 4.4. Lower plate tectonism

The outer rise region of the subducting plate south of the central and eastern Java Trench is fractured by abundant normal faults on the oceanic plate as mapped during the bathymetric survey (Fig. 3). Outer rise normal faulting has been mapped along a variety of subduction zones [39,53,54] and commonly arises from plate-bending induced tectonic stresses. This stress pattern is also reflected in the local seismicity: The outer rise is characterized by intense normal faulting earthquake activity [55]. The distance between the fault zones is only about 2–10 km; the faults display lengths of 5–20 km. However, fault lengths of up to 60 km are also frequently recognized [39,41]. The vertical throw along these faults in the vicinity of the trench reaches 100–500 m [56,57,17,14]. Profile P16 acquired during RV SONNE cruise SO179 records vertical offsets at the seafloor reaching more than 350 m south of the trench. This intense pattern of trench-parallel normal faulting increases oceanic plate seafloor roughness south of the Java Trench in addition to the morphological effects caused by the Roo Rise

and seamount population. Charging of the upper oceanic crust with water is facilitated by the intense fracturing and normal faulting of the oceanic plate. Subduction of water may enhance basal erosion by hydrofracturing in the deeper parts of the forearc: Overpressured water may be expelled into fractures along the base of the upper plate and disintegrate basal rock [7,10]. Outer rise normal faulting varies along strike of the margin. Whereas the lower plate south of the central and eastern Java Trench is characterized by abundant faulting, previous surveys along the central sector of the margin from western Java to southern Sumatra did not reveal comparable plate-bending induced tectonism [21,22,29,30,47] and thus these accretionary parts of the margin are not affected by an intense lower plate topography. In addition, the thicker sediment cover on the oceanic plate to the northwest will mask oceanic relief, whereas the oceanic crust south of central Java lacks any significant sedimentary coverage. Deep-penetrating reflection seismic data would be required to unravel whether erosion along the central Java margin results mainly from hydrofracturing (which would require a clastic interplate layer) or from the lack of trench sediment.

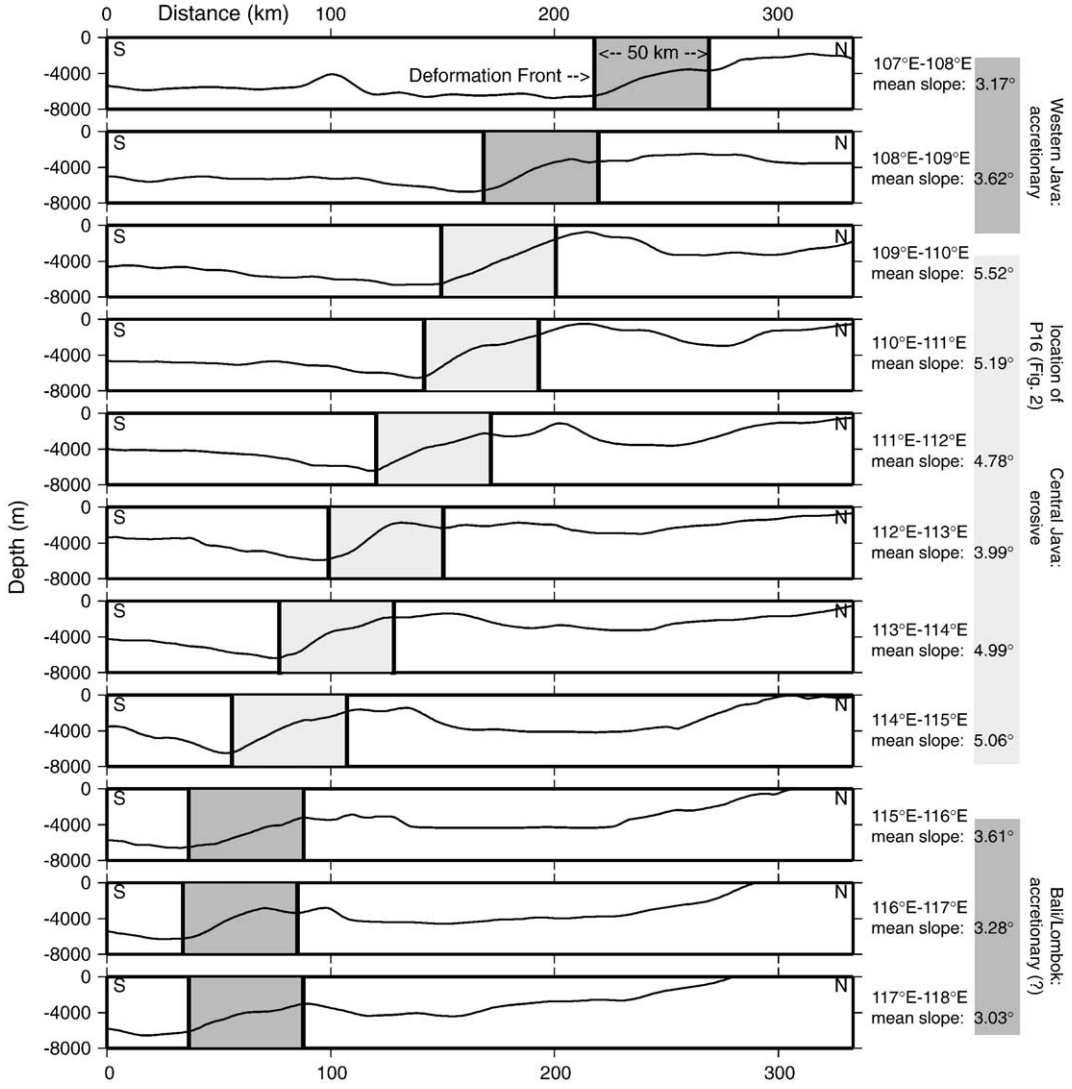


Fig. 4. Bathymetric tracks across the Java margin between 107°E and 118°E. The mean frontal slope presented here was calculated over a distance of 50 km from tracks taken every minute longitude and sampled at 0.01°. The tracks displayed run in a N–S direction and are representative for the geographical region indicated to the right of the track. The frontal slope between roughly 109°E and 115°E, where the Roo Rise is currently subducted underneath Java, is increased compared to the neighbouring regions, which is interpreted as an indication for subduction erosion.

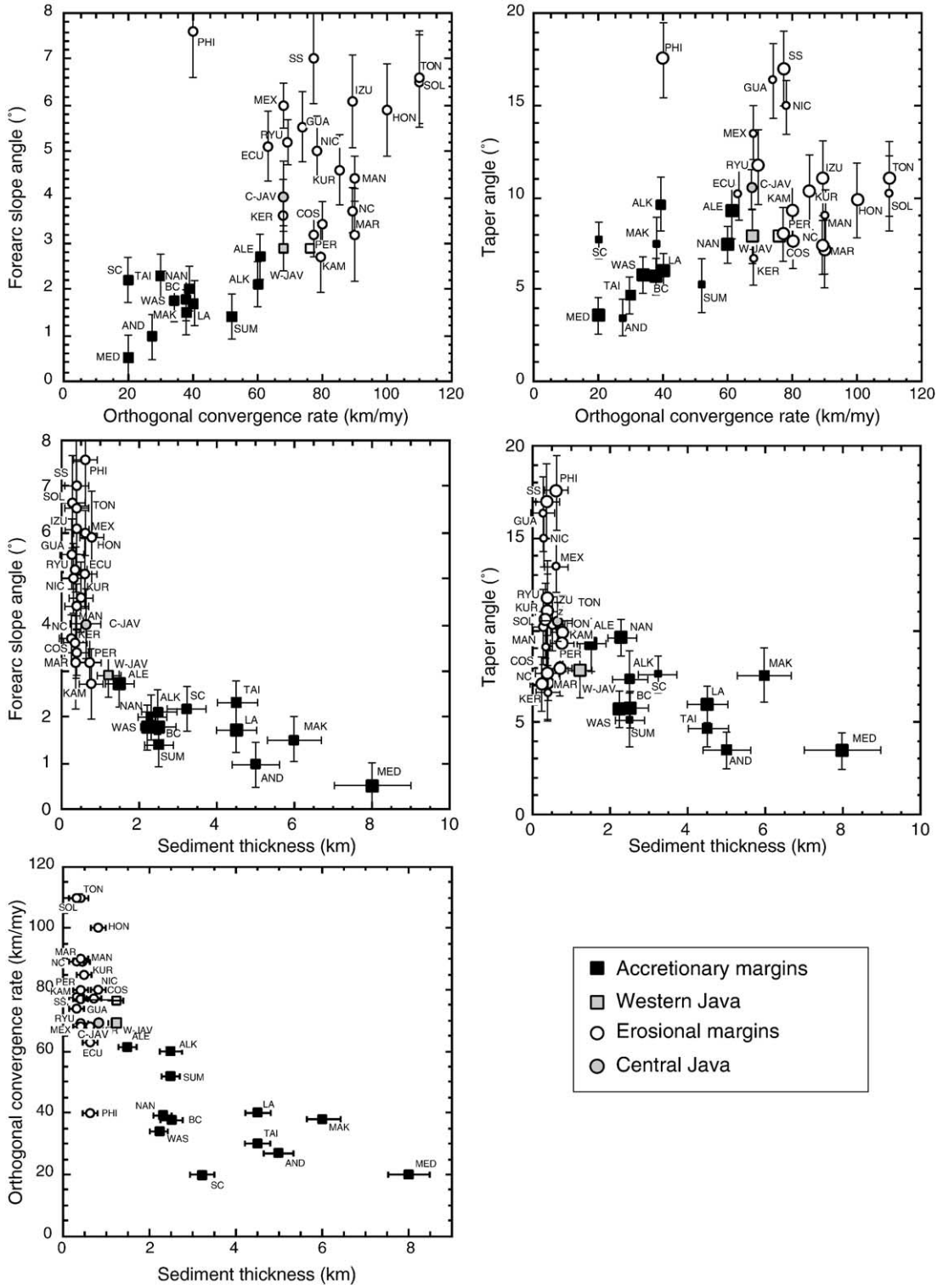


Fig. 5. Global compilation of convergent margins modified from Clift and Vannucchi [9]. Erosive and accretive systems map in two different regimes when plotted against geological key parameters. The central Java margin clearly maps in the erosive regime, whereas western Java experiences accretion.

## 5. Key indicators for subduction erosion off central and eastern Java

### 5.1. Bathymetric slope and taper analysis

Tectonic erosion has been found to have the potential to steepen trench slopes (e.g. [58,59,9]). Steepening of the lower slope angle is also recognized along the Java margin (Fig. 4). The mean frontal bathymetric slope between 109°E and 115°E is gained from 60 bathymetry tracks trending orthogonal to the trench at an incremental distance of 0.1° longitude and sampled at 0.01°. We follow the approach of Clift and Vannucchi [9] and calculate the average slope angle over a distance of 50 km to eliminate small-scale anomalous trends. Some variation in slope angle occurs along the trench, such as the anomalously large angle of >13° at 110°E, reflecting the domal uplift of the forearc high by seamount subduction as displayed in Fig. 3, that causes slope failure on the leading flank of the seamount as manifested in a submarine landslide here. The mean forearc slope angle of 4.0°, however, reflects the overall trend of the inner trench slope. To the east and west of the central area affected by the Roo Rise subduction between 109°E and 115°E, forearc slopes decrease again (Fig. 4). The accretionary plate margins compiled by Clift and Vannucchi [9] exclusively display forearc slope angles smaller than 3° (Fig. 5). Their analysis of the Java margin is mainly based on data from the western Java segment and thus maps in the accretionary regime. Due to lack of seismic data in the area considered here, the exact dip of the oceanic plate underneath the forearc is unknown. The nearest modern seismic refraction profile crossing the forearc is found off western Java at 107°E [30] (Fig. 6). The oceanic plate is underthrust at an average dip of more than 6.5° underneath the accretionary complex here. Tomographic investigations indicate a general increase in plate dip from Sumatra to Java [60,61] and do not reveal any large-scale anomaly in plate dip due to the increased buoyancy of the Roo Rise, so we consider it reasonable to extrapolate this value to central Java. This then yields a forearc taper of 10.5°, which again is larger than for any of the accretionary margins documented by Clift and Vannucchi [9], but lies well within the range of values gained for erosive plate boundaries (Fig. 5).

### 5.2. Estimation of eroded volume

The geological framework of a subduction zone, namely the thickness and the properties of the subducting sediments, the convergence rate and the oceanic plate roughness, control whether accretion or subduction erosion will dominate, since these features guide the amount of material necessary for accretion and subsequent growth of a wedge or prism. Off central Java, these three factors clearly favour tectonic erosion over sediment accretion. While the minimal sediment supply (0<trench fill<1 km) and convergence rate (6.7 cm/yr) would also be sufficient for intermediate type processes, i.e. non-accretive subduction, the subduction of the severe oceanic basement relief causes active tectonic erosion of the forearc. This is best documented by the broad retreat of the Java Trench and deformation front in the projection of the Roo Rise (stippled white line in Fig. 1). Between 109°E and 115°E, over a distance of more than 600 km, the trench is deflected northward by 40 km on average from its normal curvature trend. Frontal erosion has exposed an area of approximately 25,000 km$^2$ of deeper seafloor where the trench has retreated northward. This area (between the white stippled line and the current trend of the deformation front tracked by the white dotted line in Fig. 1) correlates with the expanse of the active frontal accretionary prism as observed off western Java, implying that the entire frontal prism has been eroded by the

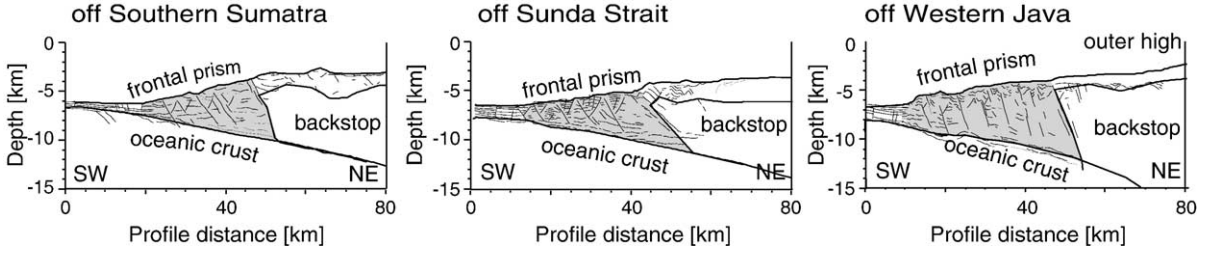


Fig. 6. Structural models of the frontal accretionary prism off southern Sumatra (102°E/7°S), Sunda Strait (104°E/8°S) and western Java (107°E/9°S) developed from refraction seismic surveys and pre-stack depth migrated MCS-data (black line-drawing) along coincident profiles (modified from Kopp and Kukowski [22]). The frontal accretionary prism, underlain in grey, extends from the deformation front neighbouring the Sunda Trench to the active backstop composing the outer forearc high. Off central Java, the frontal prism has been eroded and the deformation front shifted northward by 40 km on average.

subduction of oceanic basement relief and the seamount population. From existing refraction and reflection seismic profiles [29,30] off southern Sumatra, off the Sunda Strait and off western Java (Fig. 6), the size of the frontal prism here, which extends about 40 km from the deformation front across strike of the margin, has been mapped. From the pixel information contained in the graphic display of these seismic lines, we calculate an average volume of eroded forearc per trench km of 160 $km^3$. To account for the decreasing sediment availability along the central to eastern Java margin segment, this value is adjusted and reduced by 25%. This yields a total estimated volume of 75,000 $km^3$ of eroded material (with an error of $\pm 30\%$) above the now exposed area of 25,000 $km^2$. Judging from the large-scale topographic features visible in the bathymetry map, seamount and oceanic basement relief subduction has completely eroded the frontal prism and has furthermore largely destroyed the previous outer forearc high as its ridge-like framework gave way to isolated topographic units arising from subducted basement relief. As the onset of the Roo Rise subduction is unknown, it is impossible to provide rates of margin erosion; however, it may be expected that erosive processes due to ridge subduction are extremely effective as suggested by Clift and Vannucchi [9]. Without better seismic coverage of the region, it remains unclear what volume of the eroded material has been displaced landward, as suggested by Masson et al. [41], and to what extent the material has been transported beyond the forearc to the magmatic roots of the arc or back into the upper mantle. Subduction erosion is typically documented along convergent plate boundaries with negligible trench sediment input, such as the central to eastern Java margin. The impact of underthrusting oceanic basement relief, such as ridges and seamounts, will accelerate forearc truncation along these margins. With its large forearc slope and taper, the high convergence rate and low trench sediment fill, the central Java margin clearly maps in the erosive regime of global diagram compilations, reflecting the destructive influence of the Roo Rise on the margin.

## Acknowledgements

This is publication no. GEOTECH-132 of the programme GEOTECHNOLOGIEN of BMBF and DFG, Grant 03G0579B.

The offshore data were acquired from the RV SONNE, a facility supported by the BMBF (German Federal Ministry for Education and Research). We are grateful to Cpts. Papenhagen and Mallon and their crews for their professional assistance at sea. We thank our Indonesian partners and all participants of the MERAMEX cruises (SO176 and SO179) for their help with data acquisition. Discussions with D. Klaeschen and C. Kopp on subduction mechanics are warmly acknowledged. Comments by two anonymous reviewers significantly improved an earlier version of the manuscript.

## References

[1] R. von Huene, S. Lallemand, Tectonic erosion along the Japan and Peru convergent margins, Geol. Soc. Amer. Bull. 102 (1990) 704–720.

[2] R. von Huene, D.W. Scholl, Observations at convergent margins concerning sediment subduction, subduction erosion, and the growth of continental crust, Rev. Geophys. 29 (1991) 279–316.

[3] S. Lallemand, P. Schnuerle, J. Malavieille, Coulomb theory applied to accretionary and nonaccretionary wedges: possible causes for tectonic erosion and/or frontal accretion, J. Geophys. Res. 99 (1994) 12033–12055.

[4] P. Clift, C.J. MacLeod, Slow rates of tectonic erosion estimated from the subsidence and tilting of the Tonga forearc basin, Geology 27 (1999) 411–414.

[5] J. Adam, C.-D. Reuther, Crustal dynamics and active fault mechanics during subduction erosion. Application of frictional wedge analysis on to the North Chilean Forearc, Tectonophysics 321 (2000) 297–325.

[6] J. Laursen, D.W. Scholl, R. von Huene, Neotectonic deformation of the central Chile margin: deepwater forearc basin formation in response to hot spot ridge and seamount subduction, Tectonics 21 (5) (2002) 1038, doi:10.1029/2001TC901023.

[7] R. von Huene, C.R. Ranero, Subduction erosion and basal friction along the sediment starved convergent margin off Antofagasta, Chile, J. Geophys. Res. 108 (B2) (2003) 2079, doi:10.1029/2001JB001569.

[8] P. Vannucchi, C.R. Ranero, S. Galeoti, S.M. Straub, D.W. Scholl, K. McDougall-Ried, Fast rates of subduction erosion along the Costa Rica Pacific margin: implications for nonsteady rates of crustal recycling at subduction zones, J. Geophys. Res. 108 (B11) (2003) 2511, doi:10.1029/2002JB002207.

[9] P. Clift, P. Vannucchi, Controls on tectonic accretion versus erosion in subduction zones: implications for the origin and recycling of the continental crust, Rev. Geophys. 42 (2004) RG2001, doi:10.1029/2003RG000127.

[10] R. von Huene, C.R. Ranero, P. Vannucchi, Generic model of subduction erosion, Geology 32 (10) (2004) 913–916.

[11] P.F. Balance, D.W. Scholl, T.L. Vallier, A.J. Stevenson, H.F. Ryan, R.H. Herzer, Subduction of a Late Cretaceous seamount of the Louisville Ridge at the Tonga Trench: a model of normal and accelerated tectonic erosion, Tectonics 8 (5) (1989) 953–962.

[12] H.A. Brouwer, The Geology of the Netherlands East Indies, Macmillan, New York, 1925, pp. 1–160.

[13] F.A. Vening Meinesz, The earth's crust deformation in the East Indies, Proc. K. Ned. Akad. Wet. 43 (1940) 2778–2793.

[14] W. Hamilton, Tectonics of the Indonesian region, U. S. Geol. Surv. Prof. Pap. (1979) 1078.

[15] D.E. Karig, S. Suparka, G.F. Moore, P.E. Hehunassa, Structure and Cenozoic evolution of the Sunda Arc in the central Sumatra region, Am. Assoc. Pet. Geol. Bull. 29 (1979) 223–237.

[16] D.E. Karig, G.F. Moore, J.R. Curray, M.B. Lawrence, Lawrence, morphology and shallow structure of the lower trench slope off Nias Island, Sunda Arc, in: D.E. Hays (Ed.), The Tectonic and Geologic Evolution of Southeast Asian Seas and Islands, Geoph. Mon., vol. 23, 1980, pp. 179–208.
[17] G.F. Moore, J.R. Curray, D.G. Moore, D.E. Karig, Variations in geologic structure along the Sunda Fore Arc, northeastern Indian Ocean, in: D.E. Hays (Ed.), The Tectonic and Geologic Evolution of Southeast Asian Seas and Islands, Geoph. Mon., vol. 23, 1980, pp. 145–160.
[18] J.R. Curray, The Sunda Arc: a model for oblique plate convergence, Proc. Snellius-II Symp., Neth. Jl. Sea Res., vol. 24, 1989, pp. 131–140.
[19] P. Huchon, X. LePichon, Sunda Strait and central Sumatra fault, Geology 12 (1984) 668–672.
[20] M.A. Samuel, The structural and stratigraphic evolution of islands of the active margin of the Sumatra forearc, Indonesia. PhD-Thesis University of London, 1994 p. 345.
[21] H.-U. Schlueter, Ch. Gaedicke, H.A. Roeser, B. Schreckenberger, H. Meyer, Ch. Reichert, Y. Djajadihardja, A. Prexl, Tectonic features of the Sumatra-Java forearc of Indonesia, Tectonics, 21, 5, (2002) 1047, 11–1 to 11–15.
[22] H. Kopp, N. Kukowski, Backstop geometry and accretionary mechanics of the Sunda margin, Tectonics 6 (2003) 22, doi:10.1029/2002TC001420.
[23] M. Pubellier, C. Rangin, J.-P. Cadet, I. Tjashuri, J. Butterlin, C. Mueller, L'isle de Nias, un édifice polyphasé sur la bordure interne de la fosse de la Sonde (Archipel de Mentawai, Indonésie), C. R. Acad. Sci. Paris 315 (1992) 1019–1026.
[24] M.A. Samuel, N.A. Harbury, The Mentawai fault zone and deformation of the Sumatran Forearc in the Nias area, in: R. Hall, D. Blundell (Eds.), Tectonic Evolution of Southeast Asia, Geol. Soc. Spec. Publ., vol. 106, 1996, pp. 337–351.
[25] G.F. Moore, D.E. Karig, Structural geology of Nias Island, Indonesia: implications for subduction zone tectonics, Am. J. Sci. 280 (1980) 193–223.
[26] W. Hamilton, Plate tectonics and island arcs, Geol. Soc. Amer. Bull. 100 (1988) 1503–1527.
[27] K. Sieh, D. Natawidjaja, Neotectonics of the Sumatran fault, Indonesia, J. Geophys. Res. 105 (12) (2000) 28295–28326.
[28] M. Diament, H. Harjono, K. Karta, C. Deplus, D. Dahrin, M.T. Zen Jr., M. Gerard, O. Lassal, A. Martin, J. Jamold, Mentawai fault zone off Sumatra: a new key to the geodynamics of western Indonesia, Geology 20 (1992) 259–262.
[29] H. Kopp, E.R. Flueh, D. Klaeschen, J. Bialas, C. Reichert, Crustal structure of the central Sunda margin at the onset of oblique subduction, Geophys. J. Int. 147 (2001) 449–474.
[30] H. Kopp, D. Klaeschen, E.R. Flueh, J. Bialas, C. Reichert, Crustal structure of the Java margin from seismic wide-angle and multichannel reflection data, J. Geophys. Res. 107 (B2) (2002), doi:10.1029/2000JB000095.
[31] R.M. Kieckhefer, G.G. Shor Jr., J.R. Curray, Seismic refraction studies of the Sunda Trench and forearc basin, J. Geophys. Res. 85 (B2) (1980) 863–889.
[32] W.R. Dickinson, D.R. Seely, Structure and stratigraphy of forearc regions, Am. Assoc. Pet. Geol. Bull. 63 (1979) 2–31.
[33] D. Beaudry, G.F. Moore, Seismic-stratigraphic frame work off central Sumatra, Sunda Arc, Earth Planet. Sci. Lett. 54 (1981) 17–28.
[34] D. Beaudry, G.F. Moore, Seismic stratigraphy and Cenozoic evolution of the west Sumatra forearc basin, Am. Assoc. Pet. Geol. Bull. 69 (5) (1985) 742–759.
[35] A. Izart, B. Mustafa Kemal, J.A. Malod, Seismic stratigraphy and subsidence evolution of the northwest Sumatra fore-arc basin, Mar. Geol. 122 (1994) 109–124.
[36] E.E. Davis, R. Hyndman, Accretion and recent deformation of sediments along the northern Cascadia subduction zone, Geol. Soc. Amer. Bull. 101 (1989) 1465–1480.
[37] K. Hinz, H. Beiersdorf, N.F. Exon, H.A. Roeser, H.M.F. Stagg, U. Von Stackelberg, Geoscientific Investigations from the Scott Plateau off north-western Australia to the Java Trench, using R.V. Valdivia, J. Austr. Geol. Geophys. 3 (1978) 319–340.
[38] P. Tregoning, F.K. Brunner, Y. Bock, S.S.O. Puntodewo, R. McCaffrey, J.F. Genrich, E. Calais, J. Rais, C. Subarya, First geodetic measurement of convergence across the Java Trench, Geophys. Res. Lett. 21 (19) (1994) 2135–2138.
[39] D.G. Masson, Fault patterns at outer trench walls, Mar. Geophys. Res. 13 (1991) 209–225.
[40] H. Kopp, E.R. Flueh (Eds.), Cruise Report SO176 and 179, MERAMEX, IFM-Geomar Rep. 1, Kiel, 2004, 206 pp.
[41] D.G. Masson, L.M. Parson, J. Milsom, G. Nichols, N. Sikumbang, B. Dwiyanto, H. Kallagher, Subduction of seamounts at the Java Trench: a view with long-range sidescan sonar, Tectonophysics 185 (1990) 51–65.
[42] J.R. Curray, G.G. Shor, R.W. Rait, W. Henry, Seismic refraction and reflection studies of crustal structure of the eastern Sunda and western Banda Arcs, J. Geophys. Res. 82 (1977) 2479–2493.
[43] K.R. Newcomb, W.R. McCann, Seismic history and seismotectonics of the Sunda Arc, J. Geophys. Res. 92 (B1) (1987) 421–439.
[44] C.H.E. Walther, The crustal structure of the Cocos Ridge off Costa Rica, J. Geophys. Res. 108 (B3) (2003) 2136, doi:10.1029/2001JB000888.
[45] V. Sallarès, P. Charvis, E.R. Flueh, C.H. Walther, J. Bialas, Seismic structure of Cocos and Malpelo volcanic ridges and implications for hotspot–ridge interaction, J. Geophys. Res. B12 (2003), doi:10.1029/2003JB002431.
[46] H. Kopp, A. Wittwer, E.R. Flueh, Geophysical investigations of the Java margin, Indonesia, in: Intermargins Newsletter, vol. 5, 2004, pp. 7–9.
[47] E.R. Flueh, B. Schreckenberger (Eds.), Cruise Report SO138, GINCO2, Geomar, Kiel, 1999, 333 pp.
[48] S. Lallemand, R. Culotta, R. von Huene, Subduction of the Daiichi Kashima Seamount in the Japan Trench, Tectonophysics 160 (1989) 231–247.
[49] W. Van Der Werff, Forearc development and early orogenesis along the eastern Sunda/western Banda Arc (Indonesia), PhD-Thesis, Vrije Universiteit Amsterdam, 1995, pp. 311.
[50] S. Dominguez, S. Lallemand, J. Malavieille, R. von Huene, Upper plate deformation associated with seamount subduction, Tectonophysics 293 (1998) 207–224.
[51] S. Dominguez, J. Malavieille, S. Lallemand, Deformation of accretionary wedges in response to seamount subduction: insights from sandbox experiments, Tectonics 19 (2000) 182–196.
[52] R. von Huene, C.R. Ranero, W. Weinrebe, Quaternary convergent margin tectonics of Costa Rica, segmentation of the Cocos plate, and Central American volcanism, Tectonics 19 (2000) 314–334.
[53] K. Kobayashi, M. Nakanishi, K. Tamaki, Y. Ogawa, Outer slope faulting associated with the western Kuril and Japan Trenches, Geophys. J. Int. 134 (1998) 356–372.
[54] C.R. Ranero, J. Phipps Morgan, K. McIntosh, C. Reichert, Bending-related faulting and mantle serpentinization at the Middle America Trench, Nature 425 (2003) 367–373.

[55] R. Abercrombie, M. Antolik, K. Felzer, G. Ekström, The 1994 Java tsunami earthquake: slip over a subducting seamount, J. Geophys. Res. 106 (2001) 6595–6607.
[56] R.H. Beck, P. Lehner, Oceans, new frontier in exploration, Am. Assoc. Pet. Geol. Bull. 58 (1974) 376–395.
[57] B.M. Ganie, Syaifuddin, A. Superman, E. Honza, Geomorphological features in the eastern Sunda Trench, CCOP Techn. Bull. 19 (1987) 7–12.
[58] S. Lallemand, X. Le Pichon, Coulomb wedge model applied to subduction of seamounts in the Japan Trench, Geology 15 (1987) 1065–1069.
[59] J. Dupont, R.H. Herzer, Effect of subduction of the Louisville Ridge on the structure and morphology of the Tonga Arc in: D.W. Scholl, T.L. Vallier (Eds.), Geology and Offshore Resources of Pacific Island Arcs-Tonga Region, Earth Sci. Ser., vol. 2, Circum-Pac. Counc. For Energy and Miner. Resou, Houston, Tex., 1985, pp. 323–332.
[60] R. Ghose, K. Oike, Characteristics of seismicity distribution along the Sunda Arc: some new observations, Bull. Disas. Rev. Res. Inst., Kyoto Univ. 38, 2, 332 (1988) 29-48.
[61] R. Ghose, S. Yoshioka, K. Oike, Three-dimensional numerical simulation of the subduction dynamics in the Sunda Arc region, Southeast Asia, Tectonophysics 181 (1990) 223–255.
[62] D. Sandwell, W.H.F. Smith, Global marine gravity from Geosat and ERS-1 satellite altimetry, J. Geophys. Res. 102 (1997) 10,039–10,054.

# 5

Kopp, H., Weinrebe, W., Ladage, S., Barckhausen, U., Klaeschen, D., Flueh, E. R., Gaedicke, C., Djajadihardja, Y., Grevemeyer, I., Krabbenhoeft, A., Papenberg, C., Zillmer, M., 2008.

**Lower slope morphology of the Sumatra trench system.**

Basin Research, doi: 10.1111/j.1365-2117.2008.00381.x.

*Basin Research* (2008) **20**, 519–529, doi: 10.1111/j.1365-2117.2008.00381.x

# Lower slope morphology of the Sumatra trench system

H. Kopp,* W. Weinrebe,* S. Ladage,† U. Barckhausen,† D. Klaeschen,* E. R. Flueh,* C. Gaedicke,† Y. Djajadihardja,‡ I. Grevemeyer,* A. Krabbenhoeft,* C. Papenberg* and M. Zillmer*[1]

**IFM-GEOMAR Leibniz-Institute of Marine Sciences, Kiel, Germany*
†*BGR, Federal Institute for Geosciences and Natural Resources, Hannover, Germany*
‡*BPPT, Agency for the Assessment and Application of Technology, Jakarta, Indonesia*

## ABSTRACT

At convergent margins, the structure of the subducting oceanic plate is one of the key factors controlling the morphology of the upper plate. We use high-resolution seafloor mapping and multichannel seismic reflection data along the accretionary Sumatra trench system to investigate the morphotectonic response of the upper plate to the subduction of lower plate fabric. Upper plate segmentation is reflected in varying modes of mass transfer. The deformation front in the southern Enggano segment is characterized by neotectonic formation of a broad and shallow fold-and-thrust belt consistent with the resumption of frontal sediment accretion in the wake of oceanic relief subduction. Conversely, surface erosion increasingly shapes the morphology of the lower slope and accretionary prism towards the north where significant oceanic relief is subducted. Subduction of the Investigator Fracture Zone and the fossil Wharton spreading centre in the Siberut segment exemplifies this. Such features also correlate with an irregularly trending deformation front suggesting active frontal erosion of the upper plate. Lower plate fabric extensively modulates upper plate morphology and the large-scale morphotectonic segmentation of the Sumatra trench system is linked to the subduction of reactivated fracture zones and aseismic ridges of the Wharton Basin. In general, increasing intensity of mass-wasting processes, from south to north, correlates with the extent of oversteepening of the lower slope (lower slope angle of 3.8° in the south compared with 7.6° in the north), probably in response to alternating phases of frontal accretion and sediment underthrusting. Accretionary mechanics thus pose a second-order factor in shaping upper plate morphology near the trench.

## INTRODUCTION

The eastern Indian Ocean is dominated by the Wharton Basin, which is limited to the west by the Ninetyeast Ridge, to the north and east by the Sunda trench along Sumatra and Java and by the Broken Ridge at ~30°S (Fig. 1, inset panel). Seafloor of the Wharton Basin was generated between 85 and 45 Ma at the Wharton Ridge that consists of east–west-trending segments of a fossil spreading axis (Liu *et al.*, 1983; Royer & Sandwell, 1989) (Fig. 1, inset panel). Bathymetric features are prominent in the Wharton Basin (Stein *et al.*, 1989) and trend in a N–S direction (black lines in Fig. 1) following fossil transform faults that are currently being reactivated as left-lateral strike–slip faults (Deplus *et al.*, 1998; Abercrombie *et al.*, 2003). Four N5°E-trending faults occur in the western Wharton Basin between the Ninetyeast Ridge and the Investigator Fracture Zone and enter the Sunda Trench at ~93, 94, 96 and 97°E (Sandwell & Smith, 1997; Hébert, 1998) (Fig. 1). The morphologic expression of the 93 and 94°E fault zones is covered by Nicobar Fan sediment deposits in the northern extension of the Wharton Basin NW of Simeulue Island. The 96°E Fracture Zone shows considerable basement relief as evidenced in seismic data (Franke *et al.*, 2008). An additional fracture zone is visible in the bathymetry, crossing the Wharton Ridge and entering the trench at 97°E (Barckhausen & SeaCause Scientific Party, 2006) (Fig. 1). To the SE, the Investigator Fracture Zone at 98.25°E outcrops at the seafloor and comprises four individual ridges of parallel trend of up to 1900 m relief and ~120 km total width.

Fracture zone geometry has been documented from seismic and magnetic data. (Barckhausen & SeaCause Scientific Party, 2006; Franke *et al.*, 2008). Magnetic spreading anomalies, which trend E–W in the Wharton Basin, are offset left-laterally by the fracture zones (Cande *et al.*, 1989). Seafloor age contrast is greatest across the

Correspondence: Heidrun Kopp, IFM-GEOMAR Leibniz-Institute of Marine Sciences, Kiel, Germany. E-mail: hkopp@ifm-geomar.de
[1] Present address: Institut de Physique du Globe, Strasbourg, France.

 

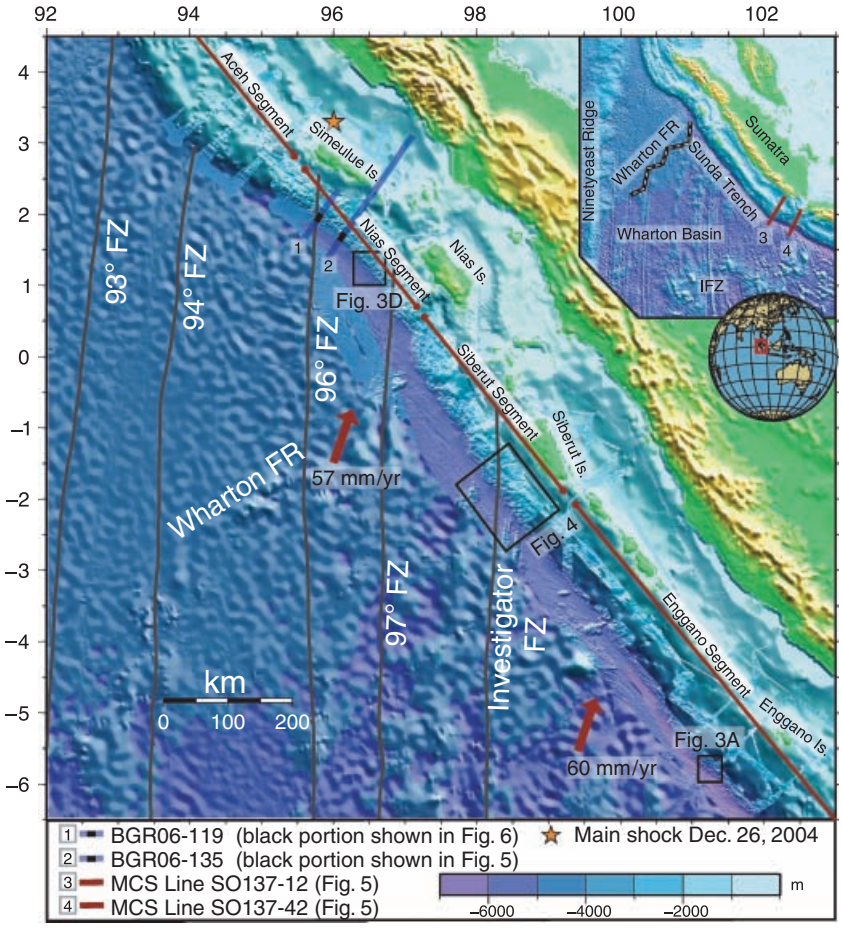


**Fig. 1.** Composite bathymetric map of the Sumatra trench system: The global satellite altimetry (Sandwell & Smith, 1997) is overlain by high-resolution swath mapping data. The bathymetry data were acquired using RV Sonne's 12 kHz Simrad EM120 echosounder system. The extent of the Enggano, Nias and Siberut segments discussed in the text is shown by red bars. Location of multichannel seismic lines presented in Figs 5 and 6 is indicated. Black boxes show location of data presented in Figs 3 and 4. Fracture zones are from Cande *et al.* (1989). IFZ, Investigator Fracture Zone; FR, fossil ridge; FZ, fracture zone.

Investigator Fracture Zone, where the magnetic data to the east of the fracture zone correlates to anomalies of Chrons 31–29 (68–64 Ma) from south to north. To the west, anomalies 21–23 (47–52 Ma) are identified, resulting in age differences across the Investigator Fracture Zone of up to 15 m.y. (Gaedicke, 2006).

The scientific objective of this study is to investigate the effect of the incoming basement structure on the evolution of the upper plate. The lower slope, forming the outermost part of the upper plate, linearly responds to the subducting plate impact and thus poses the focus of our investigations. The lower slope of convergent margins defines a morphological province and covers the area of the upper plate immediately landward of the trench. In an accretionary setting such as the Sumatra margin, the lower slope oftentimes comprises imbricate thrust slices formed by frontally accreted sediment and thus displays a more rugged topography compared with the landward portion of the prism (Kopp *et al.*, 2001). Oceanic plate fabric exerts a first-order control on the morphology of the lower slope of the accretionary prism.

The seafloor mapping described in Kopp & Flueh (2006) provides the bathymetric data used in this study. Seafloor mapping concentrated on the surface contact zone between upper and lower plates (i.e. the deformation front) south–west of the Sumatran forearc islands of Simeulue, Nias, Siberut and Enggano (Fig. 2) to geographically complement bathymetric mapping to the NW conducted by HMS Scott along the southern part of the rupture zone of the 26 December 2004 Banda Aceh earthquake (Henstock *et al.*, 2006). The high-resolution bathymetric mapping reveals a morphological segmentation of

**Fig. 2.** Swath survey covering the Sumatra trench and deformation front (top panel). Black boxes indicate location of data examples shown in panels (i)–(iii). A segmentation of the upper plate's lower slope is observed based on morphotectonic variations along the margin: in the southern Enggano Segment, nascent fold-and-thrust belts are the geomorphic expression of frontal sediment accretion (e.g. yellow arrow) (panel i). Conversely, the Siberut segment experiences re-working of the lower slope due to subduction of bathymetric features. Frontal erosion results in an irregular trend of the deformation front where landward offsets correspond to the entry of pronounced lower plate fabric into the trench (e.g. green arrow) (panel ii). In the northern Nias segment, extensive surface erosion of the steep and narrow active accretionary prism is manifested in slumps and ramified gully systems (panel iii). Upper plate material and debris is displaced to several kilometres onto the trench. White boxes indicate location of data shown in Fig. 3 (a, d). Short red lines show position of across slope tracks of Fig. 3 (c, f). Large red square displays location of data shown in Fig. 4. Blue arrow indicates entry point of a seamount in the Enggano segment. Red arrows indicate convergence.

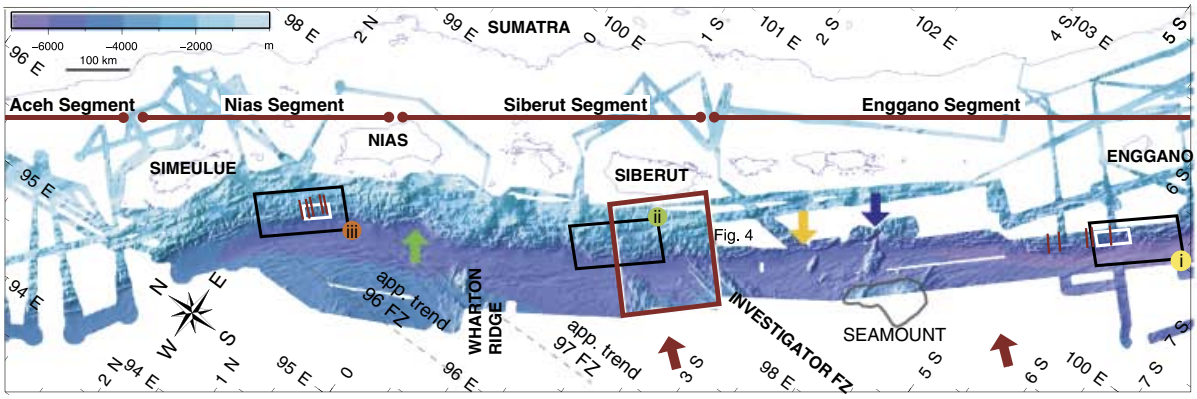


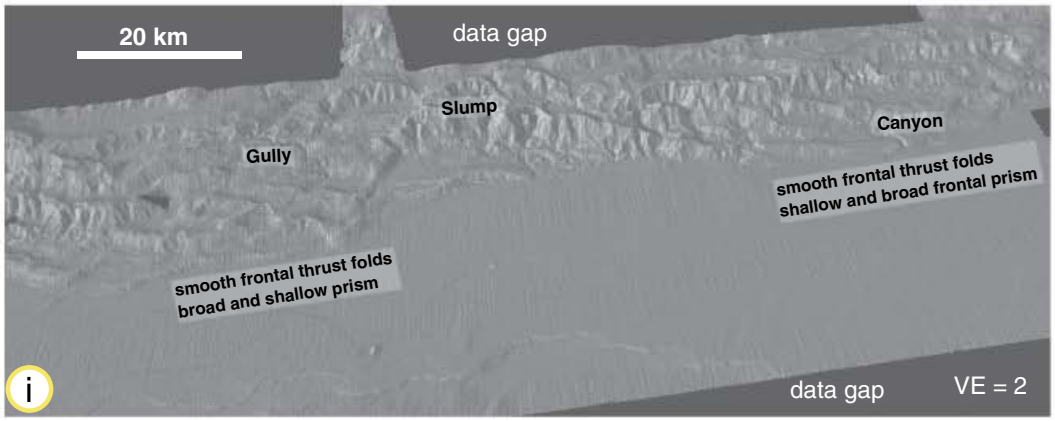


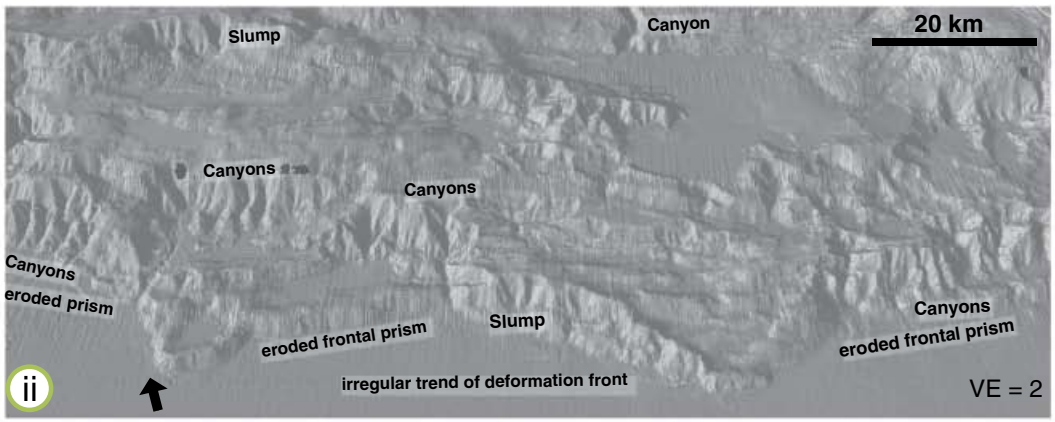


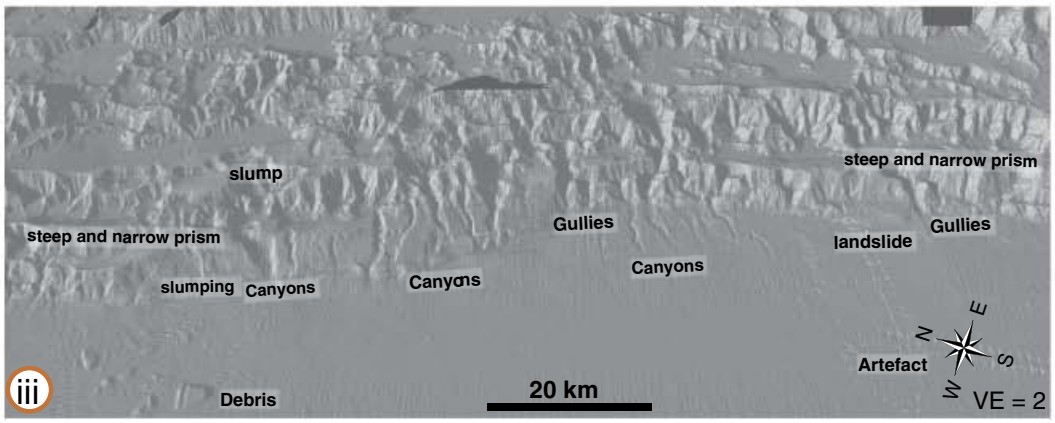


 

the upper plate that correlates with incoming plate structure (Fig. 2). In addition, we show multi-channel seismic reflection data to unravel the internal structure of the lower slope. We discuss how material transfer by cyclical frontal and basal accretion and mass-wasting processes shape the lower slope morphology.

## DATA

### Bathymetric mapping

The bathymetry data were acquired from October 2005 to March 2006 using RV Sonne's Simrad echosounder system (Ladage *et al.*, 2006). The EM120 system is a multibeam echosounder providing accurate bathymetric mapping of areas at depths down to 11 000 m. This system is composed of two transducer arrays fixed to the ship's hull. It sends successive frequency-coded acoustic signals. Data acquisition is based on successive emission–reception cycles of this signal. The nominal sonar frequency is 12 kHz with an angular coverage sector of up to 150° and 191 beams per ping. The emission beam is 150° wide across track, and 2° along track direction. The reception is obtained from 191 beams, with widths of 2° across track and 20° along track. Thus the actual footprint of a single beam has a dimension of $2 \times 2°$. Achievable swath width on a flat bottom will normally be up to six times the water depth dependent on the character of the seafloor. The angular coverage sector and beam pointing angles may be set to vary automatically with depth according to achievable coverage. This maximizes the number of usable beams. The beam spacing is normally equidistant with equiangle available.

For depth measurements, 191 isolated depth values are obtained perpendicular to the track for each ping. Using the two-way-travel-time and the beam angle known for each beam, and taking into account the ray bending due to refraction in the water column by sound speed variations, depth is calculated for each beam. A combination of amplitude (for the central beams) and phase (slant beams) is used to provide a measurement accuracy practically independent of the beam pointing angle.

### Multibeam bathymetry data processing

Generally, processing of multibeam data requires two sequences of processing steps: a profile-oriented sequence followed by an area-based processing. The profile-oriented processing of the EM-120 data comprises the merging with navigation data to compute the geographic position, interpolating missing navigation values, the calculation of the water depth and position of the footprints of the beams by raytracing through the water-column taking into account the sound velocity profile, and removing artefacts and erroneous data points. Area-based processing comprises the calculation of a digital terrain model (DTM) and the visualization of the data in various different presentations. For these purposes several software packages were used [SIMRAD applications, the academic software packages MB-System (Caress & Chayes, 1996) and GMT (Wessel & Smith, 1995)].

### Seismic multichannel data

Multichannel seismic reflection data were collected during RV SONNE cruise SO-137 (lines SO137-12 and SO137-42) (Kopp *et al.*, 2001) and SO186 (line BGR06-135) (Franke *et al.*, 2008). Profile SO137-12 is located ~75 km SE of the island of Enggano offshore southern Sumatra (Profile 2 in inset panel of Fig. 1). Profile SO137-42 was shot further SE offshore the Sunda Strait (Profile 3 in inset panel of Fig. 1), trending in a SW–NE direction. Both lines were acquired on 120 channels using a 3500-m-long source-receiver offset. Seismic signals were generated by a tuned set of 20 airguns grouped in two identical linear sub-arrays. The total volume of the array is 51.2 L (3.124 cu. in.). A shot interval of 50 m and a hydrophone spacing of 25 m were chosen, resulting in a common depth point (CDP) distance of 12.5 m and a maximum fold of 30. Pre-processing included frequency filtering after an amplitude balancing and trace editing of the shot gathers. An enhanced signal resolution was achieved by a two-gated predictive deconvolution. An iterative migration procedure was applied, which uses seismic velocities constrained by focusing analyses and common reflection point gathers (Mackay & Abma, 1993) as well as velocity information gained from corresponding wide-angle data. The energy of a reflection point in the subsurface is focused using a range of velocities until an optimal image is achieved, which provides the highest energy at zero-offset. Using an ideal velocity, the reflection position will be corrected. This in turn will yield better constraints on velocities during the next iteration and ray paths are determined more accurately. Pre-stack depth migration thus images complex dipping structures even in the presence of a strong lateral velocity gradient far better than conventional post-stack migration

Line BGR06-135 was acquired offshore northern Sumatra (Profile 1 in Fig. 1) SE of Simeulue Island. Data were recorded on 240 channels spaced 12.5 m apart at a shot-point interval of 50 m. The resulting CDP distance is 6.25 m with a nominal coverage of 30. A G-Gun airgun array of 16 airguns subdivided into two sub-array consisting of four two-gun clusters was used as seismic source [total volume of 50.8 L (3.100 cu. in.)]. Pre-processing as described above included a post-stack time migration for line BGR06-135.

## LOWER SLOPE MORPHOLOGY AND SUBDUCTION OF OCEANIC PLATE RELIEF

The various bathymetric data sets acquired by RV Sonne yield a continuous seafloor swath map of the trench and deformation front from Simeulue Island off northern Sumatra to southern Sumatra at around 7°S, covering an

extent of more than 1300 km (Fig. 2). These new data reveal a highly segmented regional morphology of the lower slope. The morphology of the lower slope and how this interacts with oceanic relief being subducted is described in three segments (Enggano segment, Siberut segment and Nias segment in Fig. 2). We follow the nomenclature of Ladage *et al*. (2006) for the segment names, which are termed after nearby islands (Fig. 1). Taking the segments in turn from SE to NW a qualitative description is given and quantitative parameters are derived.

## Enggano segment

*Segment definition and limits*

The Enggano segment off southern Sumatra extends for ~600 km from the Sunda Strait (7°S) to where the Investigator Fracture Zone is currently being subducted ( ~2.5°S). A broad and shallow frontal accretionary prism defines this segment (Fig. 2i), which displays a moderate surface gradient (Fig. 3b). It is characterized by the growth of a smooth fold-and-thrust-belt through active frontal accretion as evidenced in seismic data (Kopp *et al*., 2001; Schlüter *et al*., 2002). Evidence for large-scale frontal erosion or surface erosion, as discussed below for the Siberut and Nias segments, is scarce along the Enggano segment, where frontal accretion is the dominating process shaping the geomorphology of the upper plate.

*Qualitative description of morphology*

The active frontal accretionary prism shows a lateral extent of ~20 km as identified from depth-migrated multichannel data in conjunction with velocity information obtained from refraction data (Kopp & Kukowski, 2003). Slope morphology is distinguished by the presence of young and relatively smooth frontal thrust folds (Figs 2 and 3a). Evidence for landslides or material transport paths such as canyon systems dissecting the lower slope are infrequent along this margin segment and key slope failure features such as slumps, rockslides and topples are scarce or absent (Fig. 2). Indications for major current erosional processes are only found where an isolated, irregularly shaped seamount of 25 km in diameter impinges on the margin at 99.6°E/3.8°S (blue arrow in Fig. 2, upper panel). It causes frontal erosion of the lower slope, locally scarring the margin toe. Away from the seamount collision zone though, trench material is frontally accreted and subparallel nascent thrust folds develop at the slope base with a singular fold length of 20–70 km (e.g. yellow arrows in Fig. 2, upper panel).

*Quantitative morphology*

The Enggano segment displays an overall smooth and coherent appearance with a mean surface slope $\alpha$ of 3.8° of the lower slope (Fig. 3c). This value is obtained by averaging the gradient perpendicular to the trench axis along five tracks over a distance of 15 km from the deformation front (red bars in Fig. 2, upper panel). We re-sampled the bathymetry grid in steps of 0.004° and subsequently averaged the data along the five tracks. As our morphological investigations focus on the deformation front and lower slope, it would not be feasible to use a longer distance as this would result in an underestimate of surface slope $\alpha$ and an overestimate of plate dip $\beta$ (Wang & Hu, 2006). This results from the fact that the plate dip $\beta$ is not defined by a straight line, but shows a curved trend as the oceanic plate is thrust underneath the upper plate. Simultaneously, the surface slope will shallow due to compaction and lithification of the prism. Thus, the taper angle changes from the lower slope to the shallower portion of the forearc. For investigations limited to the lower slope portion of the prism, taking an average value across the entire forearc would bias both the surface slope angle $\alpha$ as well as the plate dip $\beta$.

## Siberut segment

*Segment definition and limits*

Lower slope morphology changes abruptly where the ridges composing the Investigator Fracture Zone dissect the trench sediments at 98.25°E/2°S (Fig. 2, upper panel). This marks the southern limit of the Siberut segment, which is defined by frontal erosion of the lower slope due to subduction of oceanic plate relief. The geomorphology of the upper plate is profoundly modulated by the subducted bathymetric elevations (Fig. 4). The segment extends northward to the location of the Wharton fossil ridge re-entrant at 97°E/0.2°N. The smooth fold-and-thrust belt of the Enggano segment has been frontally eroded along the Siberut segment by the northward migration of the Investigator Fracture Zone as well as the Wharton Ridge, resulting in an irregular trend of the deformation front (Figs 2 and 4).

*Qualitative description*

The Investigator Fracture Zone affects the structure and morphology of the oceanic lithosphere in a zone of ~120 km width. In the trench and on the outer rise, the Investigator Fracture Zone outcrops along four individual parallel ridges (IFZ Ridge 1–4 in Fig. 4), ranging from ~1100 to 1900 m height above the trench. The four ridges show lateral widths of ~40 km (IFZ Ridge 1), 5 km (IFZ Ridge 2), 15 km (IFZ Ridge 3) and 10 km (IFZ Ridge 4) (Fig. 4) in the surveyed trench area and reach water depth of 4313, 4461, 3850 and 3777 m, respectively. Isolated seamounts are observed on top of the ridges and on their flanks (black arrows in Fig. 4) as well as in the more diffuse area of altered crust, which displays remnants of the original spreading fabric (white arrows in Fig. 4).

The lower slope has extensively been re-worked and the frontal accretionary prism partially eroded as the Wharton Ridge and the Investigator Fracture Zone migrated along the trench (Figs 2 and 4), resulting in kinks in the trend of the deformation front (stippled line in Fig. 4). Most

 

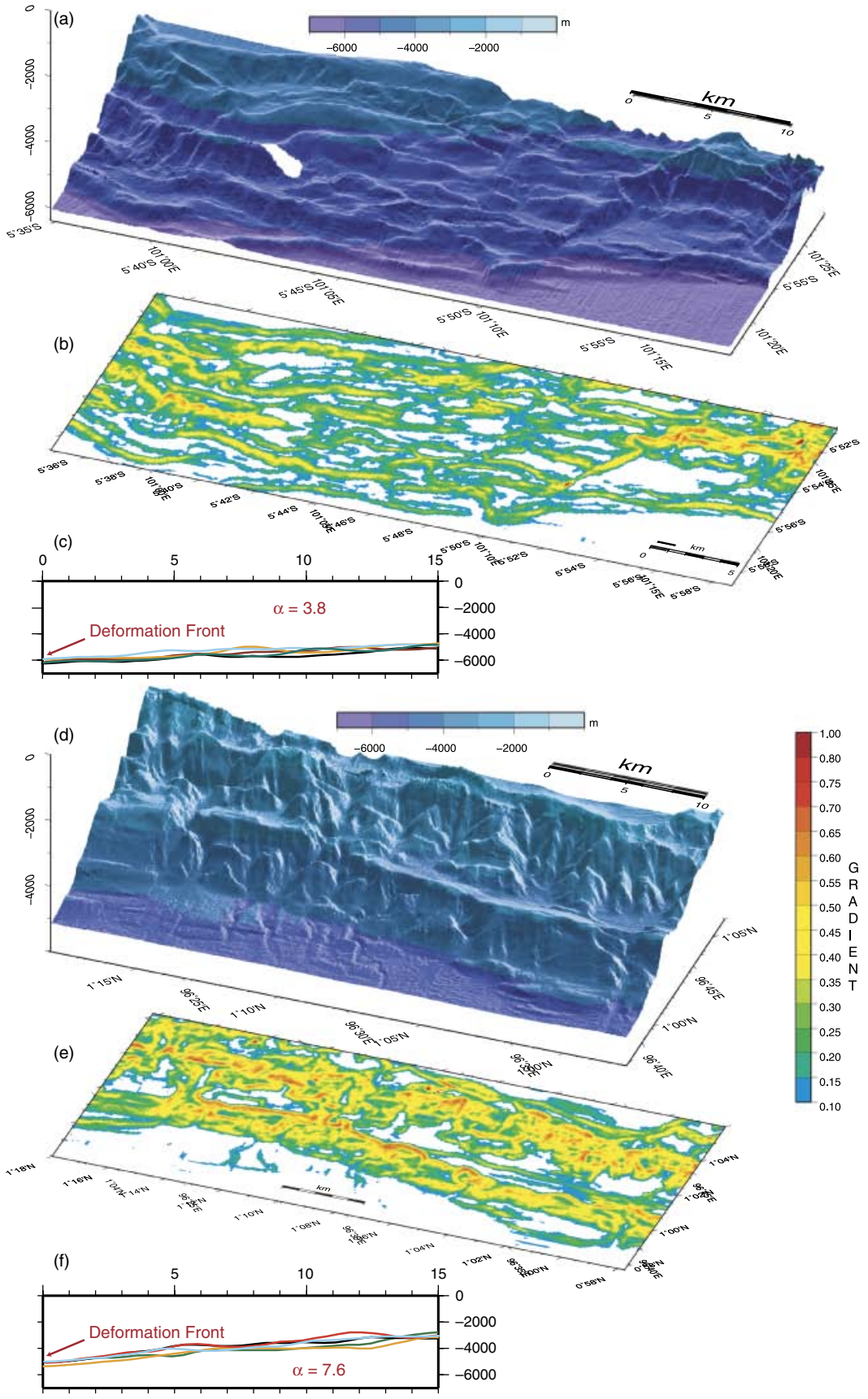


**Fig. 3.** High-resolution bathymetry in the Enggano (a) and Nias (d) segments (compare black boxes in Fig. 1 or white boxes in Fig. 2 for location) and corresponding projected gradients (b and e). The surface slope angle α is obtained by averaging the slope angle across five tracks perpendicular to the trench axis over a distance of 15 km from the deformation front (c and f, location shown by red lines in Fig. 2). The increased slope angle in the northern Nias segment (e) corresponds to an increase in surface slope gradient (f).

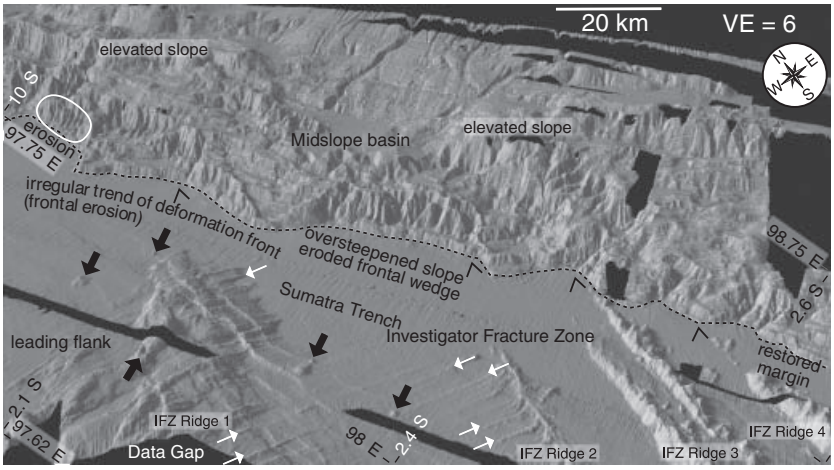


**Fig. 4.** Perspective view of the entry point of the Investigator Fracture Zone (IFZ) into the Sumatra trench. The IFZ consists of four individual ridges (IFZ Ridge 1–4) and migrates northwards along the Sumatra trench. The geomorphology of the upper plate is profoundly modulated by the subducted bathymetric elevations. To the south, margin healing after the passage of the IFZ is manifested in juvenile frontal thrust folds as frontal sediment accretion recommences. The margin segment currently affected by the subduction of the IFZ shows ubiquitous evidence of erosion. The frontal accretionary wedge has in parts completely been eroded, resulting in an irregular trend of the deformation front (stippled line) and local oversteepening of the lower slope (white ellipse). Alternating zones of uplift (local highs on an elevated slope) and subsidence are generated as the IFZ migrates along the margin. Thick black arrows show isolated volcanoes. White arrows indicate original spreading fabric. Open arrows point to kinks in the deformation front associated with the subduction of the individual ridges.

striking is the step-wise retreat of the deformation front in response to frontal erosion along this segment (black arrow in Fig. 2ii). Offsets of the deformation front and thus volumes of eroded material are closely associated with the entry of the individual ridges composing the Investigator Fracture Zone (open arrows in Fig. 4). The magnitude of the offsets primarily correlates to the geographical width of the ocean floor topography. The northernmost 40-km-wide ridge (IFZ Ridge 1) causes a 5 km retreat of the lower slope normal to the deformation front, whereas the 10-km-wide ridge (IFZ Ridge 4) results in a deformation front offset of only 2 km. The wider ridges cause a more pronounced landward retreat of the deformation front, irrespective of their height. A broad (~100 km width scale) landward retreat of the deformation front and forearc high, upon which the smaller-scale offsets or kinks related to the subduction of discrete ridges might be superimposed, is not observed. Trench sediment supply is thus sufficient to restore the lower slope and margin wedge after cessation of erosive processes after a ridge propagates northward, rebuilding the frontal fold-and-thrust belt as described above for the Enggano segment and as observed immediately south of IFZ Ridge 4 in Fig. 4.

*Quantitative description*

Kinematic considerations yield a current migration velocity for the Investigator Fracture Zone of 4.0–4.5 cm year$^{-1}$ along the margin. Owing to the variable angle of the segmented Wharton Ridge with the trench (Fig. 1, inset), the lateral migration velocity of the northward-migrating abandoned spreading centre is highly erratic. Segments perpendicular to the convergence vector migrate at a fast rate (exceeding the convergence rate), whereas the offset segments which trend nearly parallel to the convergence vector have an almost stationary entry point to the trench (as observed in the bathymetry data) (compare also Hampel, 2002).

The current entry of the Wharton Ridge into the trench is marked by a 13-km-deep embayment where the lower slope has been eroded (green arrow in Fig. 2, upper panel). Several mid-slope basins are neighbouring local elevations along the slope (Fig. 4) and by analogy represent remnant tectonic imprints of oceanic relief subduction as observed along other margins and in sandbox modelling (Collot & Fisher, 1989; Dominguez *et al.*, 1998, Laursen *et al.*, 2002). Uplift of the margin wedge occurs over the leading flank of the subducting Wharton Ridge, whereas a mid-slope basin south of Nias at 0.5°N/97.5°E (landward of the embayment shown by the green arrow in Fig. 2, upper panel) originates from subsidence over the trailing flank (Hampel *et al.*, 2004). Equivalent structures are also witnessed offshore Siberut where the Investigator Fracture Zone impinges on the margin (Fig. 4). Only detailed analysis of seismic data would allow to evaluate if these basins are solely related to depocentres forming on top of the moving thrust sheets as observed e.g. along the Enggano segment (Fig. 5b) or if they are additionally enhanced by basal erosion.

Where incipient subduction of pronounced lower plate fabric has eroded the frontal wedge, the lower slope shows inclination angles in excess of 10° (e.g. white ellipse in Fig. 4). It is not feasible to average lower slope angles or gradients along this margin segment, as the lower slope has been intensely re-worked and extremely steep portions of the lower slope lie adjacent to shallower

 

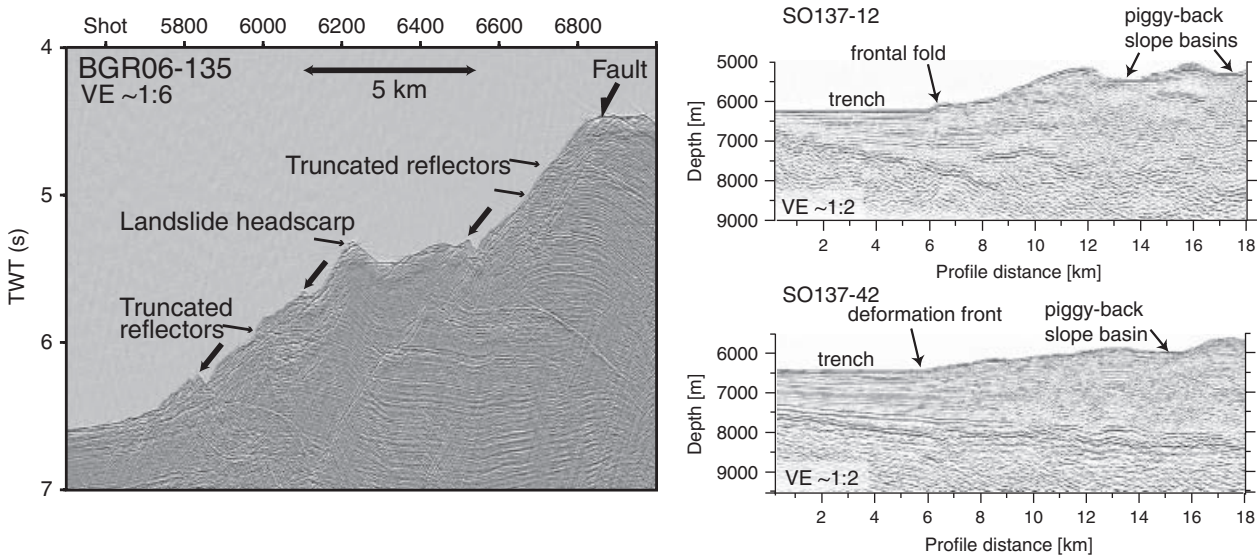


**Fig. 5.** Truncated reflectors in the time-migrated section of the lower slope on MCS Line BGR06-135 in the northern Nias segment (see Fig. 1 for location) indicate surface erosion and mass wasting processes resulting in slumps (thick black arrows). Jumbled and chaotic reflectors characterize the slump masses on top of the active folds, which are linked to landslide headscarps. Reflection profiles SO137-12 and SO137-42 (modified from Kopp & Kukowski, 2003) (see Fig. 1 inset for location) are located in the Enggano Segment offshore southern Sumatra and off the Sunda Strait, respectively, and are characterized by the evolution of relatively smooth frontal folds and a shallower lower slope compared with the Nias segment. Evidence for prominent surface erosion of the frontal folds is not recognized on these seismic lines. MCS data were acquired by the BGR, Hannover, Germany during SONNE cruises SO137 and SO186.

sections, resulting in erratic variations of the lower slope geometry (Fig. 4).

## Nias segment

*Segment definition and limits*

Slope morphology changes again to the NW of the Wharton Ridge in the Nias segment (Figs 2 and 3). The Nias segment is defined by a narrow and steep frontal prism compared with the shallow and broad prism of the Enggano segment (Fig. 2i and iii). The deformation front shows a uniform trend, without the kinks and offsets resulting from frontal erosion as observed in the Siberut segment. The lower slope consists of steep thrust folds, which show extensive geomorphic evidence of surface erosion, corresponding to Morphology B of Henstock *et al*. (2006), which is characterized by widespread and complex erosion.

*Qualitative description*

Although the frontal accretionary prism along the Nias segment is still intact (Fig. 2), the morphology along this margin segment has a generally much rougher appearance than along the Enggano segment and shows a higher gradient of the lower slope compared with the southern area (Fig. 3c and f). Collapse structures such as slumps are ubiquitous along the lower slope. Ladage *et al*. (2006) conclude that the frontal folds along the Nias segment may be older or may not have been tectonically reactivated compared with the nascent frontal thrust folds in the Enggano segment. This is based on the observation of short tributaries to the trench, cross-cutting the frontal folds in the Nias segment (Fig. 2iii). This pattern may only have developed during or after the folding events (Ladage *et al*., 2006) and is not observed in the southern Enggano segment. The prism is narrower and steeper along the Nias segment compared with the adjacent segments (Ladage *et al*., 2006). An extensive transverse pattern of downslope gullies and rills dissects the prism into the trench and supplies material to the trench by transverse mass wasting (Fig. 2iii). Transport of material in the canyons occurs over a distance of more than 10 km towards the ocean basin (Fig. 2iii). The seaward faces of frontal folds show slope failure in the form of slumping as described by Henstock *et al*. (2006) for the lower slope located north of Simeulue. Debris flows deposit material on the trench fill, including blocks of 100 m height, which are displaced to more than 15 km seaward of the deformation front (Fig. 2iii). Sediment transport paths are mainly short and restricted to the fold limbs and tributaries do not generally cross-cut the entire accretionary prism. Evidence for erosion also comes from seismic data. MCS profiles acquired in the Nias segment (Fig. 5a), the Enggano segment (Fig. 5b) and off the Sunda Strait (Fig. 5c) show striking dissimilarities, reflecting the distinct morphotectonic regimes. The time-migrated seismic reflection line of the Nias segment is characterized by truncated reflectors indicative of downslope mass wasting (Fig. 5a) as evidenced in slump masses, which have accumulated downslope from landslide headscarps.

*Quantitative description*

The lower slope shows an increased surface gradient along this segment compared with the southern Enggano

segment. The slope angle takes the value of $\alpha = 7.6^{\circ}$ (Fig. 3f) averaged over a distance of 15 km along five tracks perpendicular to the deformation front (red bars in Fig. 2, upper panel). This corresponds to slope values inferred from seismic data acquired off Nias (Line 7 of Moore & Curray, 1980). In the Nias segment, water depth decreases from 4950 m in the trench to 3375 m at 8 km from the deformation front along Line BGR06-135. Conversely, off southern Sumatra, MCS lines SO137-12 and SO137-42 (Kopp & Kukowski, 2003) show little evidence of downslope material transport across the well-developed fold-and-thrust belt. The seafloor ascends by 1000 m over a distance of 8 km from the frontal fold along profile SO137-12 and by only 700 m over the same distance on line SO137-42.

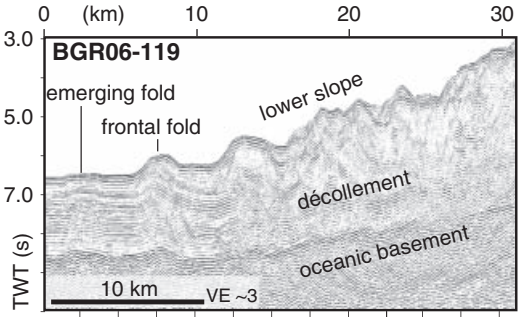


**Fig. 6.** MCS line BGR06-119 (modified from Franke *et al.*, 2008) shows a subduction channel sandwiched between the décollement and the oceanic basement. Approximately one-third of the trench sediment fill is currently underthrust beneath the lower slope and frontal prism. Cyclical phases of imbricate thrusting and sediment underthrusting strongly affect the lower slope surface gradient. Line BGR06-119 was processed at BGR, Hannover, Germany.

## DISCUSSION

Surface erosion offshore Simeulue and Nias (Fig. 2) correlates with the increase in frontal slope angle (Fig. 3) from the Enggano segment to the Nias segment. The steeper morphology of the Nias segment is reflected in the increased gradient (Fig. 3b and e) of the seafloor. On a regional scale, the seafloor gradient of the southern Enggano segment is only half of that in the northern Nias segment.

Changes in the surface slope angle at a convergent margin may be attributed to modifications in material strength caused by variations in physical properties such as porosity or fluid pressure (Lallemand *et al.*, 1994). Compression and dewatering are most prevalent in the frontal prism, where the trench material is initially deformed and fluid expulsion occurs along fluid pathways. (von Huene *et al.*, 1998). These processes may be invoked to explain commonly observed arcward changes in surface slope (Kopp & Kukowski, 2003; Fisher *et al.*, 2007) in the context of critical wedge mechanics (Davis *et al.*, 1983). However, lateral variations along trench strike as observed between the Enggano, Siberut and Nias segments are more difficult to explain by systematic changes in physical properties in a single margin.

Episodic wedge growth by frontal and basal accretion poses an alternative explanation for surface slope adjustments along trench strike. Cyclical accretion with alternating phases of frontal accretion and sediment underplating has been simulated in analogue experiments (Gutscher *et al.*, 1998). Episodic underthrusting of sediment sheets or duplexes underneath the frontal accretionary prism will cause a steepening of the frontal slope and thus facilitate surface erosion. During this phase, growth of the prism by sediment accretion occurs in the vertical dimension (i.e. uplift). Conversely, imbricate thrusting during frontal accretion will advance the frontal accretionary prism trenchwards, lowering the surface slope and reducing the overburden. Both mechanisms, frontal accretion and basal accretion, may occur at a single margin (e.g. Alaska) and result in a high variation of the surface slope angle of the lower slope. Whereas frontal accretion and the formation of imbricate thrust slices is the dominant process off southern Sumatra as documented in MCS Lines SO137-12 and SO137-42 (Fig. 5), about one-third of the trench fill is currently subducted underneath the lower slope along MCS Line BGR06-119 (Franke *et al.*, 2008) (Fig. 6). A layered sheet of sediment sandwiched between the detachment and the oceanic basement is traced for at least 20 km beyond the frontal fold. This material is currently trapped in the subduction channel and transported beyond the deformation front. Underthrusting of sediment concurs with an increase in surface slope and a retreat of the deformation front as shown from sandbox modelling (Gutscher *et al.*, 1998). This process continues until the overburden of the steep frontal prism reaches a critical value, hindering further underthrusting. In addition, the coefficient of basal friction plays a crucial role with high basal friction resulting in steeper angles. Increased basal friction has been proposed by Fisher *et al.* (2007) to occur in the frontal prism offshore Banda Aceh (northern Sumatra). Thus underthrusting of sediment sheets in a high friction setting may explain the increased surface slope in the Nias segment compared with the Enggano segment, where the formation of imbricate thrust slices by frontal accretion and the observed low basal friction (Kopp & Kukowski, 2003) decrease the surface slope. The opening of the frontal taper leads to an oversteepening of the lower slope in the Nias and Siberut segments and thus facilitates surface erosion as witnessed in the bathymetric data. The variation in deformation mode and surface slope between the Enggano and Nias segments thus suggest a change in the accretionary mechanics from frontal accretion in the south (Kopp *et al.*, 2001) to underthrusting as the dominating process in the north. An important observation in this context is the along-strike change in sediment supply to the trench offshore Sumatra. The trench off Simeulue Island is found at a water depth of $<4900$ m, whereas it reaches water depths of more than 6200 m to the SE in the Enggano segment. Axial material transport in the trench is manifested in channel systems of up to 280 km length, as

 

for example observed originating south of the Investigator Fracture Zone entry point. The Investigator Fracture Zone poses an effective barrier to the axial material transport in the trench, where the trench fill is declining from ~2500 m in the NW (Line BGR06-135 in Fig. 1) to 1300 m to the SE of Enggano Island (Kopp *et al*., 2001; Kopp & Kukowski 2003). As the sediment supply exceeds the subduction channel capacity along the entire length of the Sumatra trench, it remains unresolved if and to what degree the variation in sediment supply influences the mechanical mode of accretion.

Accelerated frontal erosion in the central Siberut segment results from the subduction of the pronounced oceanic basement relief of the Wharton Ridge and Investigator Fracture Zone, This segment encompasses the most deformed and in parts largely eroded frontal prism along the Sumatra margin and local slope angles are approaching or are in excess of the angle of repose. Restoration of the margin toe in the southern Enggano segment after the passage of the Investigator Fracture Zone occurs by frontal sediment accretion. Imbricate thrusting at the deformation front lowers the oversteepened surface slope and favours the seaward growth of a fold-and-thrust-belt as imaged in the bathymetric and seismic data.

## ACKNOWLEDGEMENTS

We would like to thank our Indonesian partners, namely the BPPT (Agency for the Assessment and Application of Technology), Jakarta for their continuous assistance. The SeaCause and GITEWS projects, on which this study is based, are supported by the German Ministry of Education and Science BMBF, grants 03G0186 and 03TSU01. The offshore data were acquired by the RV SONNE. The support of the vessel's captains and their crews is warmly acknowledged. We would furthermore like to thank all participants of the related cruises for their professional help at sea. MCS data were acquired by the BGR, Hannover, Germany. Line BGR06-119 was processed at BGR, Hannover, Germany. We wish to thank editors J. K. Hillier and F. Tilmann and reviewer L. McNeill for their constructive and critical reviews, which have greatly improved an earlier version of the manuscript.

## REFERENCES

Abercrombie, R.E., Antolik, M. & Ekström, G. (2003) The June 2000 Mw 7.9 earthquakes south of Sumatra: deformation in the India-Australia plate. *J. Geophys. Res.*, **108**(B1), 2018, doi: 10.1029/2001JB000674.

Barckhausen, U. & SeaCause Scientific Party (2006) The segmentation of the subduction zone offshore Sumatra: relations between upper and lower plate, *EOS Trans*. AGU, 87(52), Fall Meet. Suppl., Abstract U53A-0029.

Cande, S.C., LaBrecque, J.L., Larson, R.L., Pitman, W.C., Golovchenko, X. & Haxby, W.F. (1989) Magnetic lineations of World's Ocean Basins. *Amer. Ass. Petrol. Geol.*, Tulsa.

Caress, D.W. & Chayes, D.N. (1996) Improved processing of Hydrosweep DS multibeam data on the R/V Maurice Ewing. *Mar. Geophys. Res.*, **18**, 631–650.

Collot, J.-Y. & Fisher, M.A. (1989) Formation of forearc basins by collision between seamounts and accretionary wedges: an example from the New Hebrides subduction zone. *Geology*, **17**, 930–933.

Davis, D., Suppe, J. & Dahlen, F.A. (1983) Mechanics of fold-and-thrust belts and accretionary wedges: cohesive coulomb theory. *J. Geophys. Res.*, **88**, 1153–1172.

Deplus, C., Diament, M., Hébert, H., Bertrand, G., Dominguez, S., Dubois, J., Malod, J., Patriat, P., Pontoise, B. & Sibilla, J.-J. (1998) Direct evidence of active deformation in the eastern Indian oceanic plate. *Geology*, **26**, 131–134.

Dominguez, S., Lallemand, S., Malavielle, J. & Schnuerle, P. (1998) Oblique subduction of the Gagua Ridge beneath the Ryukyu accretionary wedge system: insights from marine observations and sandbox experiments. *Mar. Geophys. Res.*, **20**, 383–402.

Fisher, D., Mosher, D., Austin, J.A., Gulick, S., Masterlark, T. & Moran, K. (2007) Active deformation across the Sumatran forearc over the December 2004 Mw 9.2 rupture. *Geology*, **35**(2), 99–102, doi: 10.1130/G22993A.1.

Franke, D., Schnabel, M., Ladage, S., Tappin, D.R., Neben, S., Djajadihardja, Y., Mueller, C., Kopp, H. & Gaedicke, C. (2008) The great Sumatra–Andaman earthquakes-imaging the boundary between the ruptures of the great 2004 and 2005 earthquakes. *Earth Planet. Sci. Lett.*, **269**, 1–2, doi: 10.1016/j.epsl.2008.01.047.

Gaedicke, C. (Ed). (2006) Cruise Report SO186 Leg 2 Seacause II, *BGR Report*, 0125999, 144pp.

Gutscher, M.-A., Kukowski, N., Malavielle, J. & Lallemand, S. (1998) Episodic imbricate thrusting and underthrusting: analog experiments and mechanical analysis applied to the Alaskan Accretionary Wedge. *J. Geophys. Res.*, **103**, 10161–10176.

Hampel, A. (2002) The migration history of the Nazca Ridge along the Peruvian active margin: a re-evaluation. *Earth Planet. Sci. Lett.*, **203**, 665–679.

Hampel, A., Adam, J. & Kukowski, N. (2004) Response of the tectonically erosive south Peruvian forearc to subduction of the Nazca Ridge, Analysis of three-dimensional analogue experiments. *Tectonics*, **23**, TC5003, doi: 10.1029/2003TC001585.

Hébert, H. (1998) Etudes géophysiques d'une dorsale naissante (dorsale d'Aden à l'Ouest de 46°E) et d'une dorsale fossile (dorsale de Wharton): implications sur les processus de l'accrétion océanique, et la deformation intraplaque de l'Océan Indien, PhD Thesis, University of Paris, 372pp.

Henstock, T.J., McNeill, L.C. & Tappin, D.R. (2006) Seafloor morphology of the Sumatran subduction zone: surface rupture during megathrust earthquakes? *Geology*, **34**, 485–488.

Kopp, H. & Flueh, E.R. (Eds). (2006) Cruise Report SO186 Leg 3 Seacause II, *IFM-GEOMAR Rep*., 6, 205pp.

Kopp, H., Flueh, E.R., Klaeschen, D., Bialas, J. & Reichert, C. (2001) Crustal structure of the central Sunda margin at the onset of oblique subduction. *Geophys. J. Int.*, **147**, 449–474.

Kopp, H. & Kukowski, N. (2003) Backstop geometry and accretionary mechanics of the Sunda margin. *Tectonics*, **22**(6), 1072, doi: 10.1029/2002TC001420.

Ladage, S., Weinrebe, W., Gaedicke, C., Barckhausen, U., Flueh, E.R., Heyde, I., Krabbenhoeft, A., Kopp, H., Fajar, S. & Djajadihardja, Y. (2006) Bathymetric survey images structure off Sumatra. *EOS*, **87**(17), 165–172.

Lallemand, S., Schnürle, P. & Mallavielle, J. (1994) Coulomb theory applied to accretionary and nonaccretionary wedges: possible causes for tectonic erosion and/or frontal accretion. *J. Geophys. Res.*, **99**, 12033–12055.

Laursen, J., Scholl, D.W. & von Huene, R. (2002) Neotectonic deformation of the central Chile margin: deepwater forearc basin formation in response to hot spot and seamount subduction. *Tectonics*, **21**(5), 1038, doi: 10.1029/2001TC901023.

Liu, C., Curray, J.R. & McDonald, J.M. (1983) New constraints on the tectonic evolution of the eastern Indian Ocean. *Earth Planet. Sci. Lett.*, **65**, 331–342.

Mackay, S. & Abma, R. (1993) Depth focusing analysis using wavefront-cruvature criterion. *Geophysics*, **58**, 1148–1156.

Moore, G.F. & Curray, J. (1980) Structure of the Sunda trench lower slope off Sumatra from multichannel seismic reflection data. *Mar. Geophys. Res.*, **4**, 319–340.

Royer, J.Y. & Sandwell, D.T. (1989) Evolution of the eastern Indian ocean since late cretaceous: constraints from Geosat altimetry. *J. Geophys. Res.*, **94**, 13755–13782.

Sandwell, D.T. & Smith, W.H.F. (1997) Marine gravity anomaly from Geosat and ERS-1 altimetry. *J. Geophys. Res.*, **102**(B1), 10039–10054.

Schlüter, H.U., Gaedicke, C., Roeser, H.A., Schreckenberger, B., Meyer, H., Reichert, C., Djajadihardja, Y. & Prexl, A. (2002) Tectonic features of the southern Sumatra-western Java forearc of Indonesia. *Tectonics*, **21**(5), 1047, doi: 10.1029/2001TC901048.

Stein, C.A., Cloethingh, S. & Wortel, R. (1989) Seasat-derived gravity constraints on stress and deformation in the northeastern Indian Ocean. *Geophys. Res. Lett.*, **16**, 823–826.

Von Huene, R., Klaeschen, D., Gutscher, M.-A. & Fruehn, J. (1998) Mass and fluid flux during accretion at the Alaska margin. *Geol. Soc. Am. Bull*, **110**(4), 468–482.

Wang, K. & Hu, Y. (2006) Accretionary prisms in subduction earthquake cycles: the theory of dynamic Coulomb wedge. *J. Geophys. Res.*, **111**, B06410, doi: 10.1029/2005JB004094.

Wessel, P. & Smith, W.H.F. (1995) New Version of the Generic Mapping Tools Released, EOS Trans. AGU, 76, 329.

*Manuscript received 29 January 2008; Manuscript accepted 25 July 2008*

 

# 6

Planert, L., Kopp, H., Lueschen, E., Mueller, C., Flueh, E.R., Shulgin, A., Djajadihardja, Y., Krabbenhoeft, A., 2010.

**Lower plate structure and upper plate deformational segmentation at the Sunda-Banda arc transition, Indonesia.**

J. Geophys. Res., 115, doi:10.1029/2009JB006713.

# Lower plate structure and upper plate deformational segmentation at the Sunda-Banda arc transition, Indonesia

L. Planert,[1] H. Kopp,[1] E. Lueschen,[2] C. Mueller,[2] E. R. Flueh,[1] A. Shulgin,[1] Y. Djajadihardja,[3] and A. Krabbenhoeft[1]

Received 22 June 2009; revised 23 April 2010; accepted 29 April 2010; published 27 August 2010.

[1] The Sunda-Banda arc transition at the eastern termination of the Sunda margin (Indonesia) represents a unique natural laboratory to study the effects of lower plate variability on upper plate deformational segmentation. Neighboring margin segments display a high degree of structural diversity of the incoming plate (transition from an oceanic to a continental lower plate, presence/absence of an oceanic plateau, variability of subducting seafloor morphology) as well as a wide range of corresponding fore-arc structures, including a large sedimentary basin and an accretionary prism/outer arc high of variable size and shape. Here, we present results of a combined analysis of seismic wide-angle refraction, multichannel streamer and gravity data recorded in two trench normal corridors located offshore the islands of Lombok (116°E) and Sumba (119°E). On the incoming plate, the results reveal a 8.6–9.0 km thick oceanic crust, which is progressively faulted and altered when approaching the trench, where upper mantle velocities are reduced to ~7.5 km/s. The outer arc high, located between the trench and the fore-arc basin, is characterized by sedimentary-type velocities (Vp < 5.5 km/s) down to the top of the subducting slab (~13 km depth). The oceanic slab can be traced over 70–100 km distance beneath the fore arc. A shallow serpentinized mantle wedge at ~16 km depth offshore Lombok is absent offshore Sumba, where our models reveal the transition to the collisional regime farther to the east and to the Sumba block in the north. Our results allow a detailed view into the complex structure of both the deeper and shallower portions of the eastern Sunda margin.

**Citation:** Planert, L., H. Kopp, E. Lueschen, C. Mueller, E. R. Flueh, A. Shulgin, Y. Djajadihardja, and A. Krabbenhoeft (2010), Lower plate structure and upper plate deformational segmentation at the Sunda-Banda arc transition, Indonesia, *J. Geophys. Res.*, *115*, B08107, doi:10.1029/2009JB006713.

## 1. Introduction

[2] The Sunda-Banda arc transition comprises the portions of the Indonesian island arc where the tectonic regime changes from oceanic-island arc subduction along the eastern Sunda arc to continent-island arc collision along the Banda arc (Figure 1). Such a setting offers a broad spectrum of tectonic/geologic variation regarding the lower plate as well as the upper plate, which makes this plate boundary an ideal target to study detailed aspects of subduction zone processes.

[3] Scientific investigations at subduction zones conducted during recent years have increasingly put their focus on the physical interaction between the lower plate and the fore arc and related aspects of material transfer and balancing. The physical and chemical properties of the lower plate, including its crustal and mantle structure/composition, fluid content, sedimentary cover, and thermal character (plate age), as well as the convergence rate are essential to processes of accretion, erosion and arc magmatism of the upper plate (see *Clift and Vannucchi* [2004] for a review). However, modern seismic and acoustic data are still rare for the eastern Sunda arc and the transition to the Banda arc and hence, this study aims at providing a clearer picture of the area's tectonic setting.

[4] Subduction zones may grow by frontal or basal accretion and may be classified as a compressive regime. Extension and large-scale subsidence on the contrary originate from erosive processes, which are often favored by a rough seafloor topography and a sediment-starved deep sea trench. Thus a change from an accretionary to a non-accretionary/erosive regime may be expected, concurrent with a change in the tectonic evolution of fore-arc structure. The eastern Sunda arc comprises a well-developed outer arc high and a major fore-arc basin (Lombok Basin). The deeper

[1]IFM-GEOMAR, Leibniz Institute of Marine Sciences at the University of Kiel, Kiel, Germany.
[2]BGR, Federal Institute for Geosciences and Natural Resources, Hannover, Germany.
[3]BPPT, Agency for the Assessment and Application of Technology, Jakarta, Indonesia.


0148-0227/10/2009JB006713

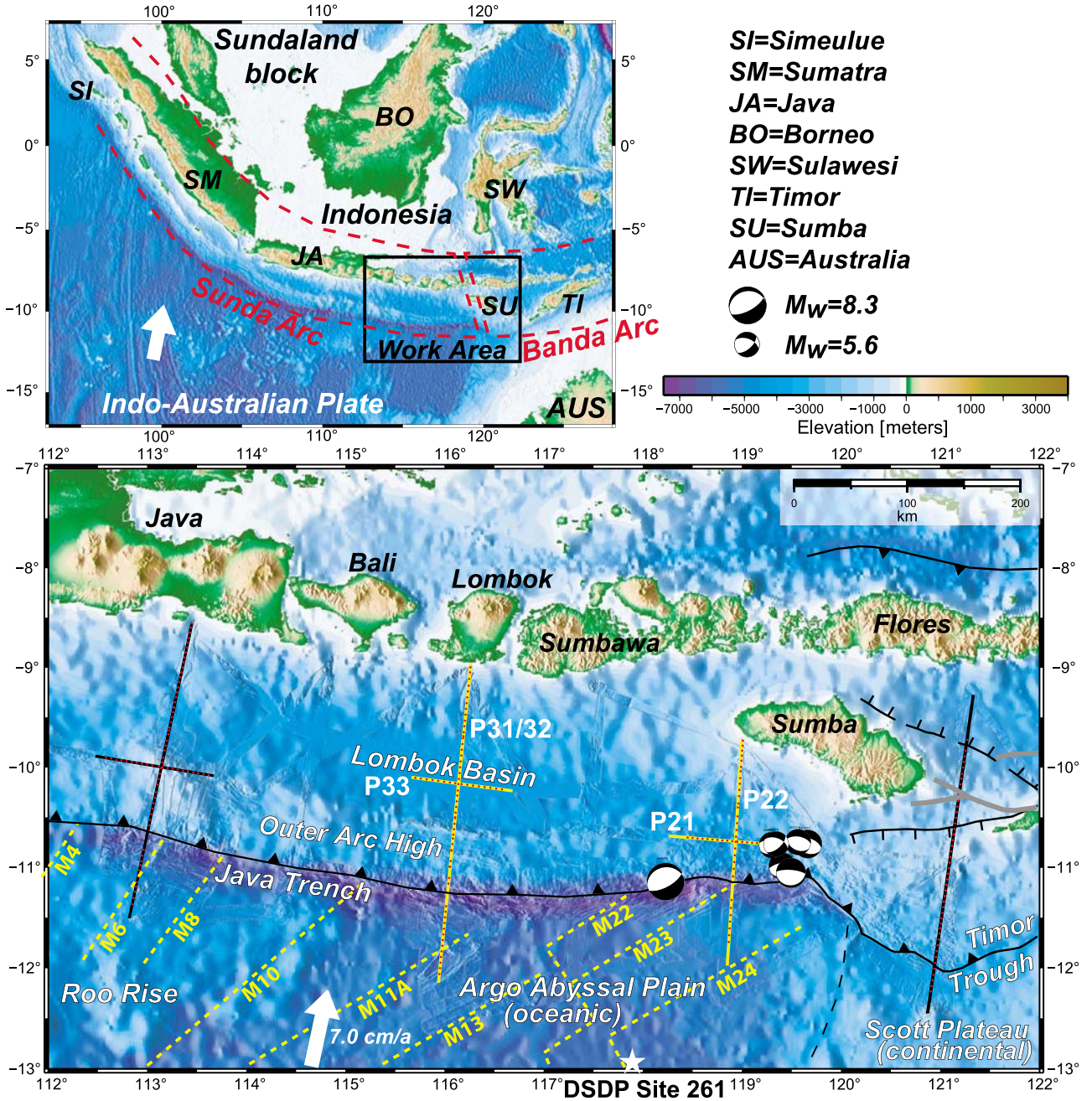


**Figure 1.** Regional map with features discussed in the text and close-up of work area with profile distribution of the SINDBAD seismic refraction experiment. Red points mark the locations of ocean bottom seismic recorders. In this study we present results for the corridors at 116°E and 119°E (yellow profiles) characterized by the subduction of oceanic crust of the Argo Abyssal Plain. The westernmost (113°E) as well as easternmost (121°E) corridors (black profiles) represent distinct tectonic regimes dominated by the subduction of thickened crust of the Roo Rise and Scott Plateau, respectively. The 121°E corridor is discussed in the work of *Shulgin et al.* [2009] and Shulgin et al (submitted manuscript, 2010). Focal mechanisms correspond to Mw = 8.3 main shock and 4 days aftershock series of the 1977 Sumba earthquake (http://www.globalcmt.org). Yellow dashed lines display magnetic anomalies from *Müller et al.* [2008]. Plate convergence is (white arrow) from *Simons et al.* [2007].

structure of these features is, however, not yet resolved and their origin is still not fully understood.

[5] Near the trench, the formation and reactivation of faults is related to the bending of the oceanic plate and often results in the hydratization of the oceanic crust and mantle [e.g., *Ranero et al.*, 2003]. The 1977 Sumba earthquake, one of the largest normal-faulting earthquakes (Mw = 8.3) near an oceanic trench, occurred at the extreme eastern limb of the Java trench in our study area (Figure 1). Hence, it provides an opportunity to examine the amount and depth

extent of lower plate alteration as response to large bending stresses. Possible dewatering processes in the lower plate during subduction may also control the long-term tectonics of the fore arc, because these processes are pertinent to the functioning of seismogenic zones [e.g., *Peacock*, 2001; *Bostock et al.*, 2002; *Ranero et al.*, 2008]. At the eastern Sunda arc, there is a historical absence of large interface thrust earthquakes in a strip of 50–150 km between the along-trench seismicity and the onset of the Wadati-Benioff zone, which still requires further explanation [e.g., *Špičák et al.*, 2007].

[6] The seismic and acoustic measurements, combined with gravimetric studies, conducted during R/V *Sonne* cruise SO190 allow a quantification of the "raw materials" (seafloor sediments, oceanic crust and mantle lithosphere), which are carried into the system at the deep sea trench, but also investigate the complex structure of the adjacent fore arc up to close to the volcanic arc. The results of this study may offer insights into the role of the lower plate, as the point of origin in the "subduction factory", as well as into the reactions and consequences for the tectonic evolution of the overriding plate.

## 2. Tectonic Setting

[7] Convergence between the Indo-Australian Plate in the south and the Eurasian Plate in the north is active since the late Oligocene [*Hamilton*, 1988; *Hall and Smyth*, 2008] and currently occurs at a rate of ~70 mm/yr in N13°E direction offshore Bali [*Simons et al.*, 2007]. Eastward from about 121°E, however, the relative motion at the Timor Trough has slowed down to ~15 mm/yr, and the development of back-arc thrusts appears to account for sustained northward motion of Australian lithosphere [*Bock et al.*, 2003] (Figure 1). The seismic profile offshore Flores from *Shulgin et al.* [2009] shows a 12–15 km thick crust comprising the promontory of the Australian continental shelf, which currently underthrusts beneath the Banda fore arc, resulting into thickening and uplift of the outer arc ridge. Hence, conventional subduction cannot be occurring here.

[8] The transition from the Scott Plateau, which is marked by shallower seafloor depths and increased sedimentary coverage on the Australian continental shelf, to the oceanic lithosphere comprising the Argo Abyssal Plain occurs at ~120°E (Figure 1). The 1977 Sunda earthquake series [e.g., *Spence*, 1986] occurred at this transition region in the oceanic plate. Relocation of hypocenters and focal mechanisms are consistent with normal faulting throughout the upper 28 km of oceanic lithosphere (Figure 1). The earthquake produced a 10 m tsunami wave height on the island of Sumbawa, which suggests substantial deformation of the ocean bottom and associated fault displacement at very shallow depths. The aftershock area implies at least 200 km of fault rupture, with a concentration of aftershocks ~100 km northeast of the main shock close to the termination of the Java trench, where the underthrust Scott Plateau could have acted as a rupture barrier [*Spence*, 1986; *Lynnes and Lay*, 1988]. *Spence* [1986] attributes the origin of the large tensional stresses which caused the Sumba earthquake series to large bending stresses of slab-pull origin, facilitated by increased resistance to subduction of the adjacent Scott Plateau. Yet the resulting consequences of the inferred large bending stresses on the structure of the subducting oceanic lithosphere in this area are unresolved.

[9] Seafloor age of the oceanic lithosphere increases toward the east from Early Cretaceous at 110°E to Late Jurassic close to 120°E [*Heine et al.*, 2004; *Müller et al.*, 2008]. The trend of magnetic seafloor anomalies is ~45–60° and thus oblique to the relative plate motion, which is almost perpendicular to the trench (Figure 1). The westernmost portions of our study area comprise the branches of an oceanic plateau, the Roo Rise, which is characterized by seafloor up to 1500 m shallower compared to the adjacent seafloor of the Argo Abyssal Plain.

[10] Fore-arc structures along this margin include a well-developed outer arc high (OAH) which is visible as a continuous bathymetric feature along the entire Indonesian fore arc, starting with Simeulue island offshore northern Sumatra as its subaerial expression and continuing as a submarine bathymetric elevation from offshore western Java to offshore the island of Sumba (Figure 1). The observed decrease in dimension and height of the OAH toward the east is related to the younger age of the eastern Sunda margin [e.g., *Van der Werff*, 1995] and to changes in trench sediment contribution and subducting seafloor morphology of the incoming Indo-Australian Plate. The related subduction processes at the plate boundary result in an accretionary regime offshore Sumatra and western Java [*Schlüter et al.*, 2002; *Kopp and Kukowski*, 2003], whereas erosive processes dominate off central and eastern Java, where the subduction of the Roo Rise results in a northward retreat of the trench and the OAH [*Kopp et al.*, 2006]. Farther east offshore Lombok and Sumbawa, however, the sediment input to the trench as well as the internal structure of the oceanic crust are largely unknown and as a consequence the processes governing the origin and evolution of the OAH are still unclear. A good indication of sediment origin and thickness farther south in the Argo Abyssal Plain can be gained from the results of DSDP site 261 (Figure 1), which drilled into a rugged oceanic basement of late Jurassic age at ~530 m below seafloor covered by Cretaceous claystones, Upper Miocene and Pliocene nannofossil oozes and Quaternary radiolarian clays [*Heirtzler et al.*, 1974].

[11] The overriding plate is of continental nature off Sumatra [*Kopp et al.*, 2001] and changes to an island arc type off Java/Lombok and farther east, although the internal structure of the islands and the adjacent fore arc is still largely unknown due to the lack of deep seismic data. The Lombok Basin forms a major fore-arc basin and is located between the OAH and the volcanic arc in the north (Figure 1). Its termination in the west is controlled by the subduction of the Roo Rise and related uplift of the adjacent fore arc [*Kopp et al.*, 2006] and in the east by the collision of the Australian continental shelf with the crystalline basement comprising the island of Sumba [*Shulgin et al.*, 2009]. The origin of Sumba is still enigmatic; it is not part of the modern Banda volcanic arc but according to a number of investigators [e.g., *Rutherford et al.*, 2001; *Hall*, 2002] originated at a relict northern hemispheric arc system, situated south of West Sulawesi. The island migrated to its current position in the middle to late Miocene, as response to incipient collision with Australia, and now forms an integral part of the fore arc.

[12] In 2006, R/V *Sonne* cruise SO190 investigated the Sunda-Banda arc transition during two consecutive legs within the scope of the Seismic and Geoacoustic Investigations Along the Sunda-Banda Arc Transition (SINDBAD) project. During leg 1, almost 5000 km of multichannel streamer (MCS) seismic data and coincident shipboard gravity data were acquired between 112°E and 122°E. The MCS data are discussed in the work of *Lüschen et al.* [2010]. Leg 2 included the acquisition of more than 1700 km of wide-angle reflection and refraction seismic profiles in four different corridors of the margin (Figure 1), at 113°E (offshore eastern Java), 116°E (offshore Lombok), 119°E (offshore Sumba) and 121°E (offshore Flores). Additionally, seafloor swath mapping on both legs resulted in an almost complete coverage of the trench and the lower slope between 113°E and 121°E. The westernmost (113°E) as well as easternmost (121°E) corridors represent distinct tectonic regimes dominated by the subduction of thickened crust of the Roo Rise and Scott Plateau, respectively. The 121°E area is discussed in the work of *Shulgin et al.* [2009] and A. Shulgin et al. (Structural architecture of oceanic plateau subduction offshore Eastern Java and the potential implications for geohazards, submitted to *Geophysical Journal International*, 2010). In this study we present results from the analysis of deep penetrating seismic and shipboard gravity data to resolve the internal structure of the incoming and the overriding plates for the corridors at 116°E and 119°E.

## 3. Bathymetric Features

[13] At 116°E offshore Lombok, seafloor depths on the incoming oceanic plate are in the range of 5.0–5.5 km and reach up to 6.8 km in the trench. In the Argo Abyssal Plain, basement structures can be traced on the seafloor, aligned at angles of 45–60° and subparallel to the magnetic anomalies (Figure 1). Hence, these structures most likely correspond to original seafloor fabric imprinted during seafloor spreading. For distances less than ~40 km seaward of the trench, however, the prevailing strike of basement structures changes to a more trench parallel tectonic fabric (compare white-dashed lines in Figure 2), which may reflect recent activity and the onset of plate-bending related normal faulting in the oceanic plate.

[14] Where our seismic profile crosses the trench, the deformation front reveals a local indentation, indicating the erosion of the lowermost inner trench slope. Farther east, however, equivalent portions of the inner trench wall (>5 km depths) appear to be rather undisturbed. Here, more than three arrays of trench-parallel ridges and troughs suggest the presence of a frontal imbricate fan (Figure 2).

[15] Landward of the trench, the OAH seafloor rises up to water depths of 2.4 km (slope angle ~5°). Corresponding seafloor portions are characterized by a trench-parallel tectonic fabric including two pronounced ridges spaced ~25 km apart (Figure 2). On a MCS seismic profile located at ~114°E, *Müller et al.* [2008] identified recent vertical displacements of the seafloor and associated deformation at shallow depths as manifested in the uplift and tilting of small piggyback basins between the two tectonic ridges atop of the OAH. These structures are associated with landward dipping splay faults, which penetrate the entire crust and connect to the plate interface. The importance of such faults for tsunami generation during great subduction zone earthquakes was recently demonstrated for Sumatra [*Sibuet et al.*, 2007], North Ecuador [*Collot et al.*, 2008] and Nankai [*Moore et al.*, 2007]. North of the OAH, the Lombok Basin exhibits a very smooth and virtually flat seafloor with water depths of 4.4 km.

[16] At 119°E offshore Sumba, water depths are slightly shallower for the oceanic plate and the trench (4.8–5.0 km and 6.5 km) and the corresponding seafloor is smoothed by a sediment blanket for distances >30 km seaward of the trench (Figure 2). Farther north, seafloor morphology changes abruptly, where a series of northward dipping normal faults induces intense fracturing and stepwise downflexure of the oceanic crust at the outer trench wall. In the trench, however, two faults, dipping to the south and striking at low angles relative to the trench, subduct beneath the inner trench wall, which results in pronounced indentations of the deformation front and the adjacent slope (Figure 2). The strike of these features is ~65°, i.e., subparallel to the magnetic anomalies. The 1977 Sumba earthquake epicenter [*Engdahl and Villaseñor*, 2002] is located roughly where the western fault subducts beneath the inner trench wall. The focal mechanism of the main shock (strike angle 61°; dip angle 67°; slip angle −98°; Global CMT Catalog, http://www.globalcmt.org) and the location of aftershocks with respect to the main shock (Figure 1) are consistent with a rupture zone striking at low angles relative to the trench. Hence, theses data suggest a possible link between plate-bending related normal faulting, extending to perhaps 30–50 km depth [*Spence*, 1986; *Lynnes and Lay*, 1988], and the reactivation of inherited fault structures in the oceanic crust, as indicated by the observed trend oblique to the trench and subparallel to the magnetic anomalies. Fan-shaped slide deposits with a lateral dimension of ~25 km are visible ~30 km east of where our profile crosses the trench (Figure 2). We speculate that this slide was caused by slope failure due to the subduction of equivalent seafloor fabric.

[17] Offshore Sumba, the lateral and vertical dimensions of the outer arc high are smaller (~55 km compared to ~80 km offshore Lombok) and the transition in seafloor topography from the elevated segments toward the adjacent fore-arc portions in the north is much more subdued (Figure 2).

## 4. Seismic Data

[18] Offshore Lombok, profile 31/32 consists of two overlapping profiles and runs perpendicular to the trench reaching a full length of 354 km (Figure 2). A total of 46 IFM-GEOMAR ocean bottom hydrophones/seismometers (OBH/S) [*Bialas and Flueh*, 1999] were deployed on this line at ~6 km average instrument spacing. The profile extends from 100 km seaward of the trench to close to the island of Lombok, crossing the Lombok Basin and profile 33 at ~222 km profile distance. Profile 33 runs in a trench-parallel direction and covers a 113 km long portion of the Lombok Basin. On this line, 16 OBH/S were deployed at ~6 km instrument spacing.

[19] The 119°E corridor offshore Sumba comprises two additional seismic profiles: the 250 km long trench-perpendicular profile 22 and the 145 km long crossing profile 21, covered with 27 and 18 OBH/S at ~6 km

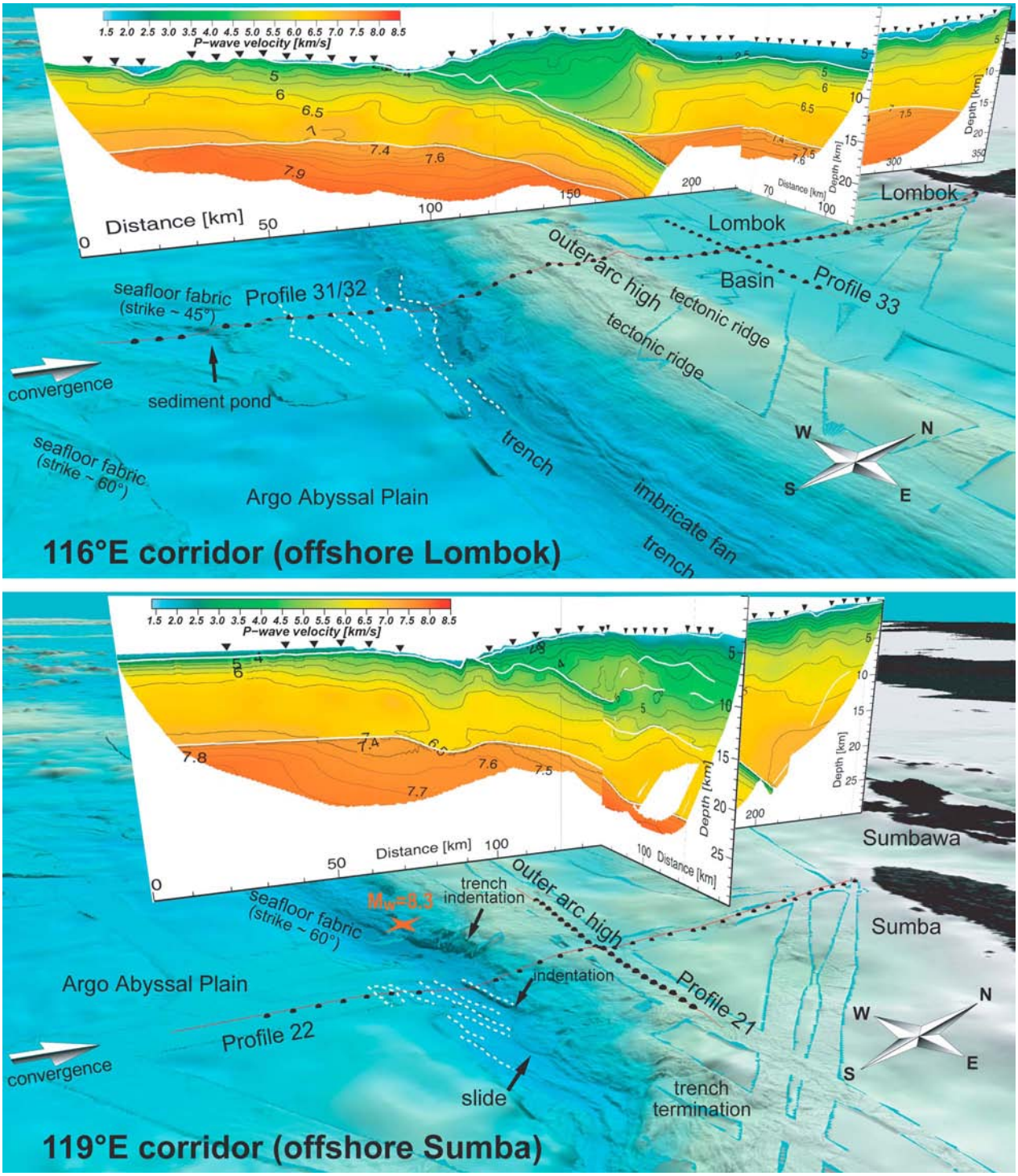


**Figure 2.** Perspective views of the (top) 116°E and (bottom) 119°E corridors including acquired seafloor bathymetry and seismic velocity profiles. The red lines are seafloor projections of the seismic shots; black spheres mark the instrument locations. Seafloor fabric locally crops out as basement structures on the oceanic plate. Offshore Lombok, inherited seafloor fabric strikes at angles of 45°–60°; plate-bending related normal faults trend more parallel to the trench (white dashed lines). The trench is largely devoid of sediment. A well-developed outer arc high comprises pronounced ridge structures. The Lombok Basin is characterized by a virtually flat seafloor. Offshore Sumba, inherited seafloor fabric strikes at angles of 60°–70° and seems to be reactivated as response to plate bending (red star marks epicenter of 1977 Sumba main shock). The subduction of basement structures locally results in the erosion of the lower slope and subsequent slope failure (note the coincidence of the eastern indentation and the slide). Annotated features are discussed in the text.

instrument spacing, respectively (Figure 2). Line 21 covers the OAH at its highest elevation.

[20] The seismic source used for wide-angle profiling was an eight element 64 l G-gun cluster fired at 3000 psi in constant time intervals, resulting in a nominal shot spacing of 130 m. Data processing included the localization of the ocean bottom instruments using the arrival time of the direct wave and the exact shot point geometry. In a second step, a time-gated deconvolution was applied to remove predictable bubble reverberations to produce a signal free of the disturbing interference of multiple and primary phases [*Wiener*, 1949]. Finally, a time and offset-variant Butterworth filter was applied in which the passband moves toward lower frequencies as record time and offset increases to account for frequency changes caused by signal attenuation.

[21] For the seismic velocity analysis we chose the tomographic method of *Korenaga et al.* [2000] (TOMO2D), which determines the 2-D velocity structure together with a floating reflector from the simultaneous inversion of refracted and reflected phases. The method employs a hybrid ray-tracing scheme combining the graph method with further refinements utilizing ray bending with the conjugate gradients method. Smoothing and damping constraints regularize the iterative inversion. The velocity model is defined as an irregular grid hung from below the seafloor. We used a horizontal node spacing of 250 m and a vertical node spacing, which linearly increases from 100 m at the seafloor to 250 m at 30 km depth below seafloor. Model regularization is accomplished by the use of correlation lengths, which control the size of those model areas affected by a velocity update of a grid cell [*Korenaga et al.*, 2000]. We used a horizontal correlation length, which linearly increases from 1.5 km at the seafloor to 6 km at the model bottom, and a vertical correlation length with corresponding values of 0.2 km and 1.5 km, respectively. For reflector nodes, the appropriate regularization length scales are taken from the horizontal 2-D velocity correlation lengths at the corresponding depths.

[22] From the coincident MCS seismic profiles we incorporated the well resolved sedimentary portions as a priori structure into our starting models and fixed these areas during the iterations using spatially variable velocity damping. To make use of secondary arrivals and different reflections we utilized a "layer stripping" approach and subsequently built the velocity model from top to bottom. This approach further involves the use of spatially variable velocity damping for the upper layers, e.g., when restricting the picks to the lower layers, and the incorporation of velocity jumps into the input models at primary features such as the basement, plate boundary and the crust-mantle boundary (Moho). In practice, we used a 1-D velocity starting model and inverted first for the upper units (fore arc, outer arc high) down to the next major structural interface (fore-arc Moho, plate boundary). We then again used a 1-D velocity starting model for the inversion of the next deeper unit (fore-arc mantle, oceanic crust, oceanic mantle). RMS travel time misfits for the final velocity models shown here are in the range of 60 ms for a total of 9.000 (profile 21) to 26.000 (profile 31/32) arrivals, which were manually picked and assigned with individual pick uncertainties in the processed seismic sections (see Figures 3 and 4 for data examples of profile 31/32).

### 4.1. Profile 31/32

[23] Figure 5 shows the final tomographic solution of profile 31/32, the corresponding derivative weight sum (DWS), which is a measure of ray density in the neighborhood of a model node [*Toomey and Foulger*, 1989], and the coincident prestack depth-migrated (PSDM) MCS profile from *Lüschen et al.* [2010]. The incoming oceanic crust is on average 8.6 km thick and largely devoid of sediment, except for an isolated sediment pond at ~20 km profile distance (Figure 5a). This sediment accumulation occurs in a structural trap related to the original seafloor fabric imprinted during seafloor spreading (compare Figure 2). About 40–50 km seaward of the trench velocities start to decrease in the crust and in the underlying mantle, resulting in anomalously low mantle velocities of ~7.5 km/s directly beneath the Moho (Figure 5a; see Figure 3 for data examples). The area of reduced velocities coincides with the onset of plate-bending related normal faulting in the MCS seismic data (Figure 5c; compare white-dashed lines in Figure 2).

[24] The OAH reveals relatively low velocities of 2.5–5.5 km/s above the plate boundary. The plate boundary is constrained by reflections in both the wide-angle and MCS seismic data over a distance of at least 70 km beneath the OAH down to ~15 km depth (dip: 5–8°) (Figure 6). The plate interface is of irregular shape, suggesting in places several hundreds of meters vertical displacement.

[25] The Lombok Basin is characterized by up to 2.8 km of sediment infill comprising velocities of 1.6–2.8 km/s (Figures 5 and 6). The underlying crust is 9–10 km thick and reveals a pronounced model portion with velocities of 6–6.8 km/s (see Figure 4 for data example). The transition from the low velocity portions beneath the OAH to velocities >5.5 km/s beneath the Lombok Basin occurs abruptly over a distance of 10–30 km around profile km 180 (Figure 6). Velocities in the upper fore-arc mantle are in the range of 7.4–7.8 km/s and thus significantly lower compared to those expected for unaltered mantle peridotite [*Carlson and Miller*, 2003].

[26] In order to demonstrate the resolving power of the data in different parts of the model, a synthetic test was performed where a known model has to be resolved using the same profile geometry and data coverage as in the real experiment. A set of Gaussian velocity anomalies of ±3% velocity perturbation and dimensions of 25 km × 5 km was imposed in a checkerboard pattern on the final velocity solution of profile 31/32 (Figure 7). Synthetic traveltimes were computed through this model and Gaussian noise with a standard deviation equal to a quarter of the individual pick uncertainty was added to the synthetic traveltimes. The inversion was initialized using the underlying velocity model as a starting model. The aim of this approach is to test the algorithm's capability of resolving small perturbations within the original tomographic output and whether anomalies are transferred into different areas during this process. Lower and upper plates were investigated separately, in order to incorporate reflections from the major interfaces and according to the tomographic approach chosen for these profiles. As displayed in the recovery panels of Figure 7, the incoming oceanic crust is well resolved, as is the oceanic uppermost mantle. Resolution of the upper plate

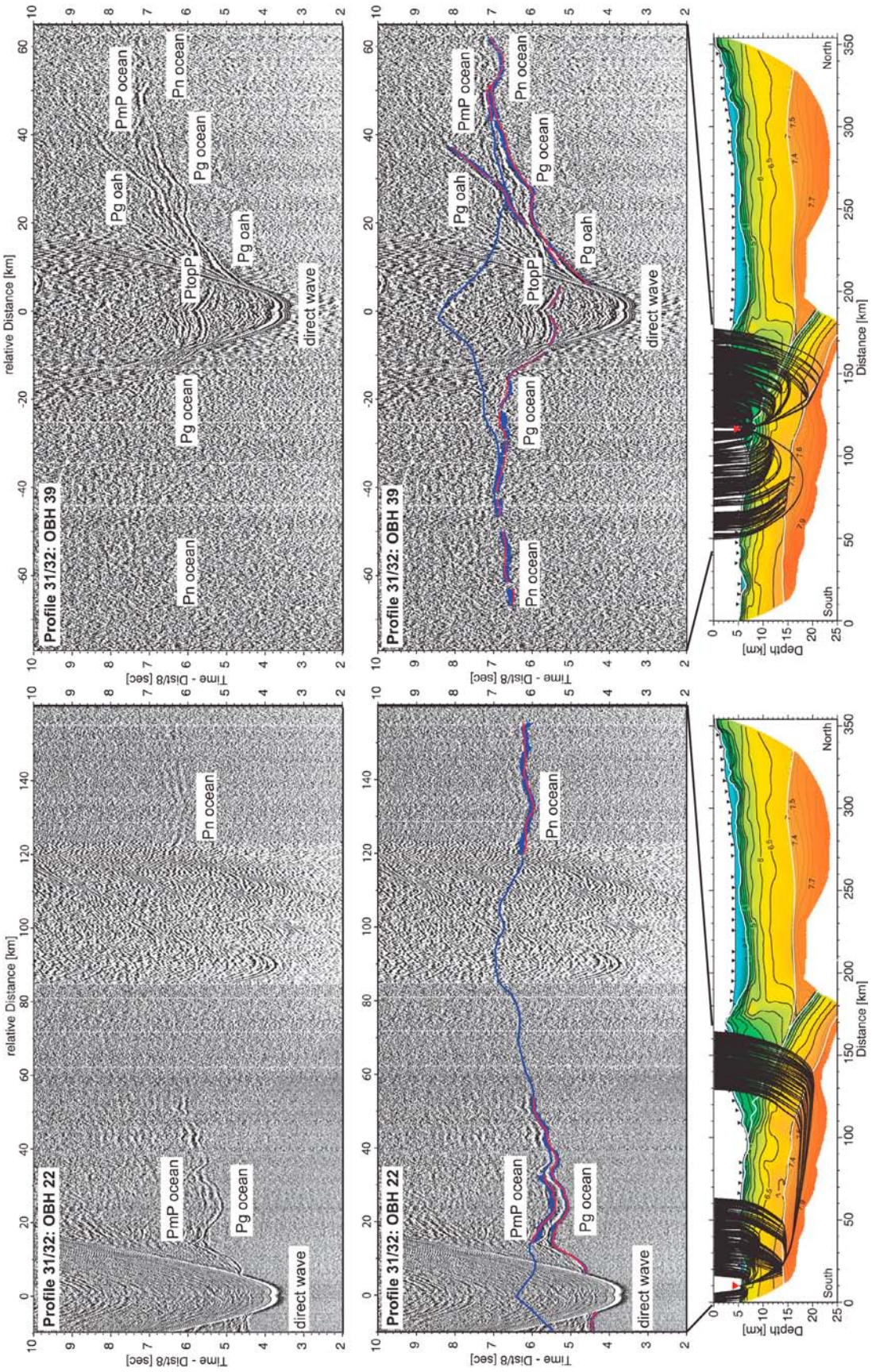


**Figure 3.** Seismic record sections (reduced to 8 km/s) of OBH 22 and OBH 39 on profile 31/32. (top) Interpreted seismic arrivals are labeled: Pg oah (turning rays within the outer arc high), Pg ocean (turning rays within the oceanic crust), Pn ocean (turning rays in the upper oceanic mantle), PtopP (reflected rays at the plate boundary), and PmP ocean (reflected rays at the oceanic Moho). (middle) Picks are shown as blue bars according to their pick uncertainty; computed traveltimes are shown as red dots. Blue lines represent traveltimes for offsets not constrained by picks. (bottom) Corresponding raypaths of the picked traveltimes through the final tomographic solution of profile 31/32.

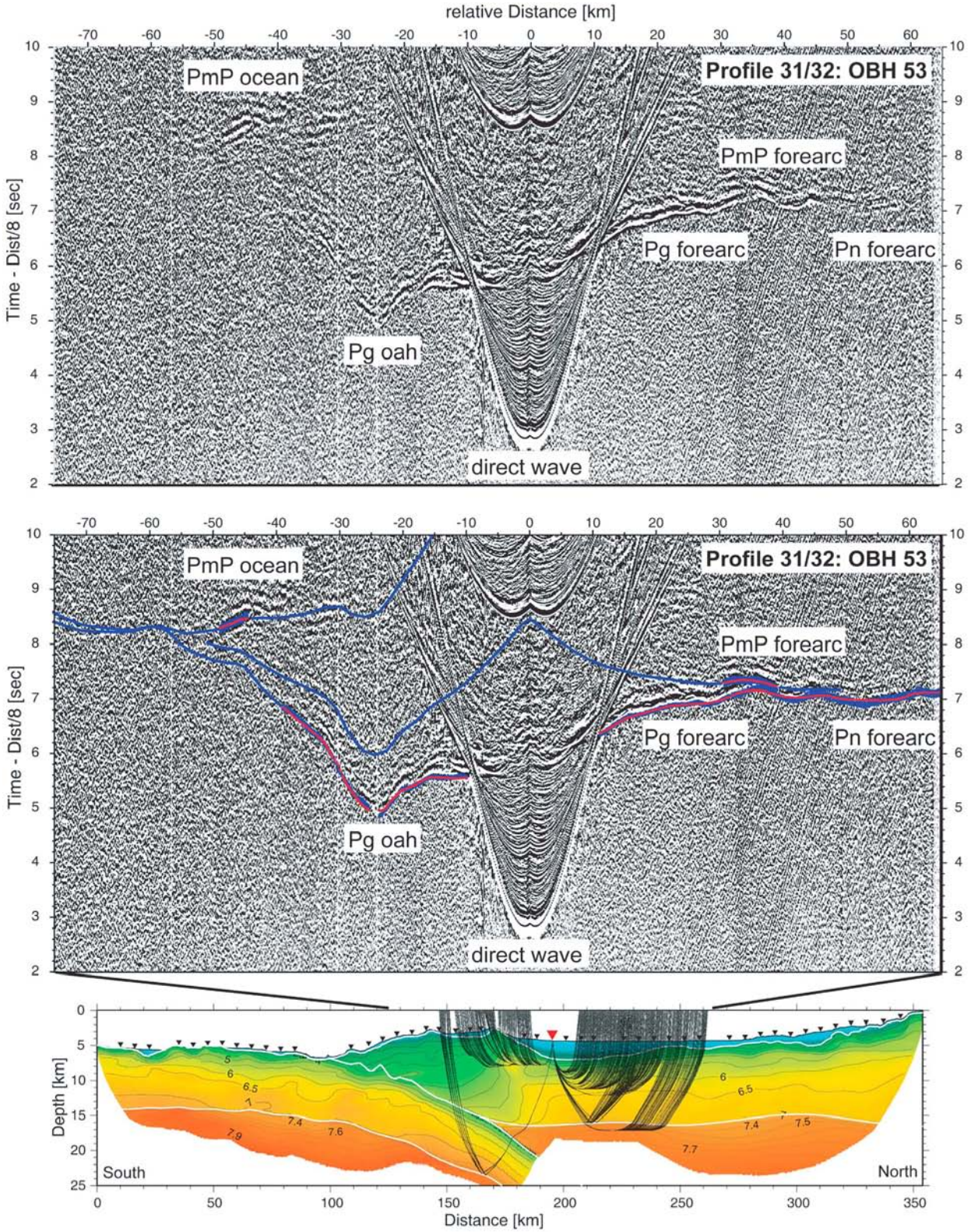


**Figure 4.** Seismic record section (reduced to 8 km/s) of OBH 53 on profile 31/32. (top) Interpreted seismic arrivals are labeled: Pg oah (turning rays within the outer arc high), Pg fore arc (turning rays within the fore-arc crust), Pn fore arc (turning rays in the upper fore-arc mantle), PmP fore arc (reflected rays at the fore-arc Moho), and PmP ocean (reflected rays at the oceanic Moho). (middle) Picks are shown as blue bars according to their pick uncertainty; computed traveltimes are shown as red dots. Blue lines represent traveltimes for offsets not constrained by picks. (bottom) Corresponding raypaths of the picked traveltimes through the final tomographic solution of profile 31/32.

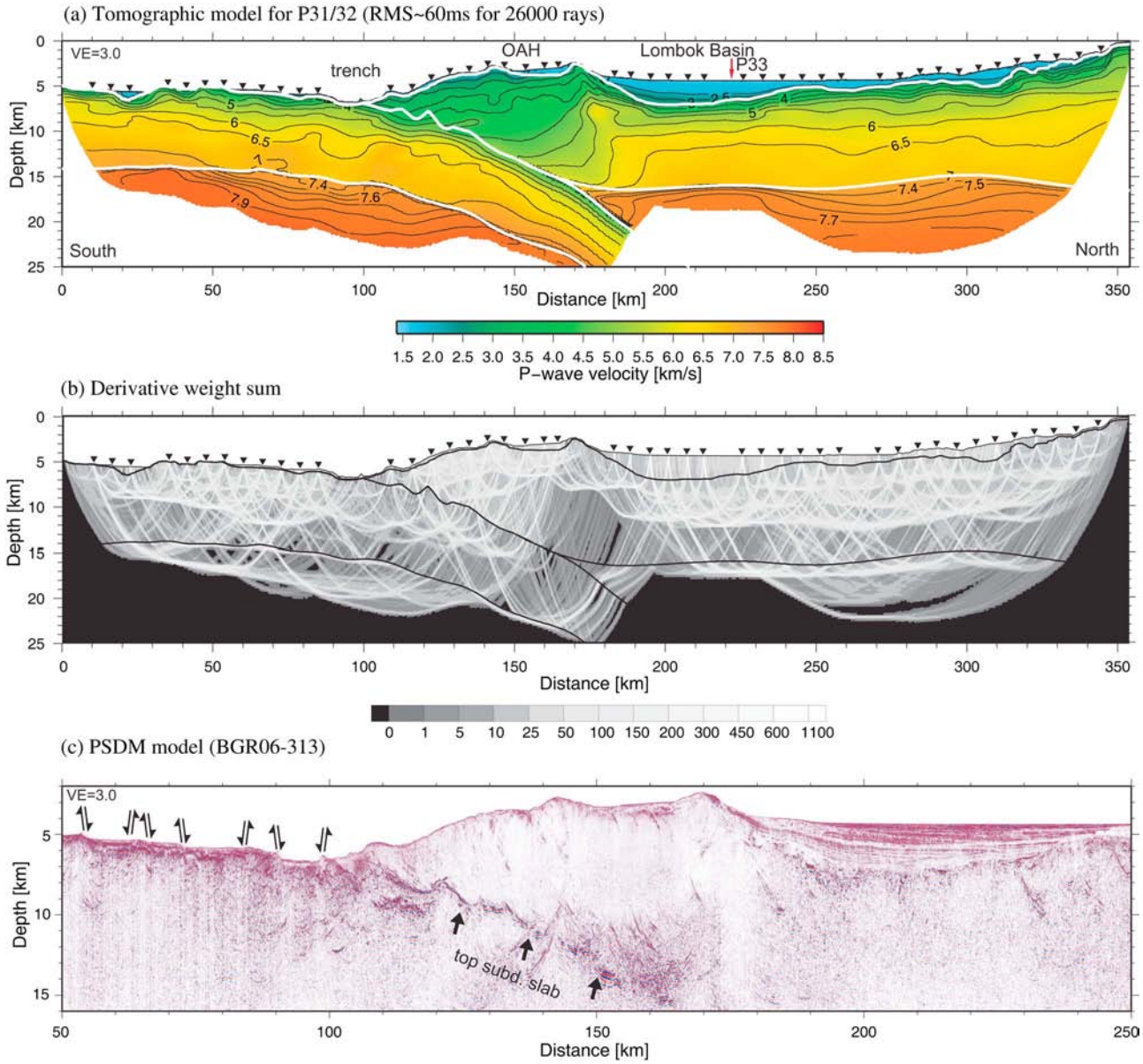


**Figure 5.** (a) Final tomographic velocity model of profile 31/32. Triangles indicate locations of ocean bottom seismographs. Red arrow displays line intersection with profile 33. White lines mark structural interfaces: sedimentary portions are derived from the analysis of high-resolution MCS seismic data; plate boundary, oceanic Moho and fore-arc Moho are obtained from the joint refraction and wide-angle reflection tomography. (b) Derivative weight sum for the final tomographic velocity model. (c) Prestack depth-migrated MCS line BGR06-313 from *Lüschen et al.* [2010]. All models are plotted at 3 × vertical exaggeration. OAH, outer arc high.

diminishes at a depth of 18 km, but the entire crust and upper mantle wedge are resolved (please refer to Figures S1 and S2 of the auxiliary material for additional resolution tests with synthetic anomalies confined to the oceanic mantle underneath the trench and an evaluation of the impact of different mantle starting models on the tomographic solution of profile 31/32).[1]

### 4.2. Profile 33

[27] On this line, the basement of the Lombok Basin is found in depths of 2.0 km to 3.7 km beneath the seafloor and resolved sediment velocities reach 2.8 km/s (Figure 8). Since no MCS seismic data are available for profile 33 also the sedimentary portions were modeled using refracted and wide-angle reflected seismic phases (see Figure 9 for data examples). The underlying crust shows some thickness variations around average values of 10 km and it includes a ~6 km thick portion of velocities of 6–6.8 km/s and relatively low velocity gradients. The velocities in the upper-

[1]Auxiliary materials are available in the HTML. doi:10.1029/2009JB006713.

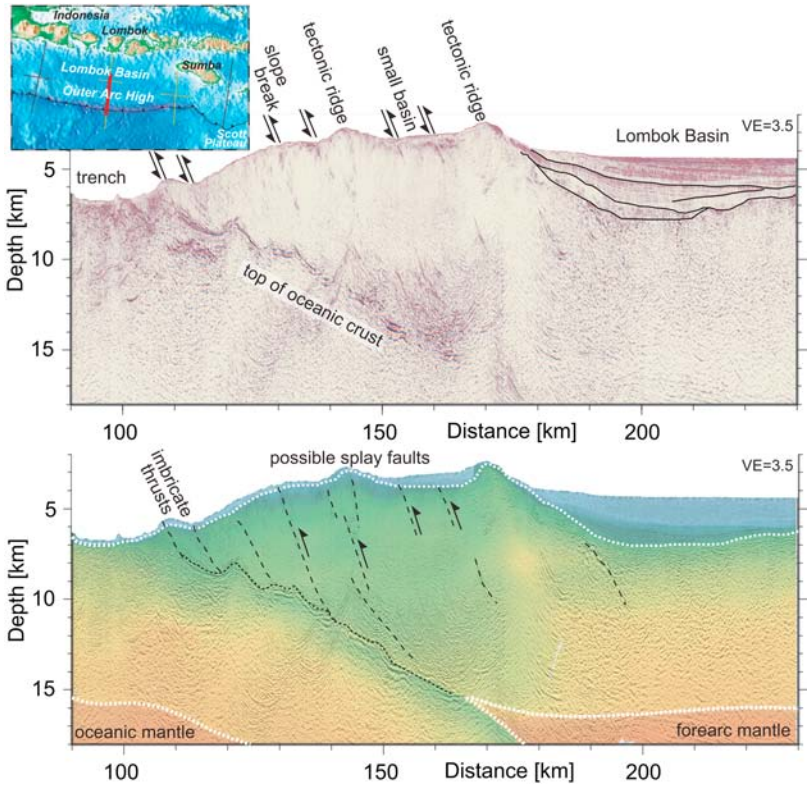


**Figure 6.** (top) Close-up of prestack depth-migrated MCS line BGR06-313 (modified from *Lüschen et al.* [2010]). The plate interface reveals a pronounced vertical relief. The outer arc high is characterized by landward dipping faults. (bottom) Final tomographic velocity model and line drawing overlain over PSDM image. Possible splay faults connect to the seafloor, where they are associated with changes in slope angle and tectonic ridges. Arrows indicate movement along faults. See text for discussion. Models are plotted at 3.5× vertical exaggeration.

most mantle are in the range of 7.4 km/s, reaching 7.7 km/s in 21 km depth and thus are slightly lower compared to profile 31/32 at the line intersection.

### 4.3. Profile 22

[28] In the southernmost model portions the incoming oceanic plate reveals an up to 600 m thick and largely undisturbed sedimentary cover; approaching the trench, however, the sediments are entirely crosscut by plate-bending faults (Figure 10). The onset of basement structures at the seafloor ~30 km seaward of the trench coincides with a vigorous decrease of crustal and upper mantle velocities. Compared to those velocity portions located 60 km south of the trench, corresponding velocities at the trench are up to 1.2 km/s lower in the mid crust and 0.6 km/s in the lower crust directly above the Moho. The oceanic crustal thickness is 9.0 km on average and hence slightly thicker than on profile 31/32. The resolved upper mantle portions reveal velocities of 7.4–7.8 km/s (see Figure 11 for data examples), which is perhaps slightly lower than corresponding velocities on profile 31/32.

[29] The plate interface is constrained by wide-angle reflections up to distances of 100 km landward of the trench down to ~22 km depth (dip: 5–8°) (Figure 10a). The boundary is of irregular shape, at least in its shallower portions, with pronounced indentations suggesting vertical displacements locally exceeding 1 km (Figure 10d). The pronounced asperity close to 105 km profile distance (Figure 10d) appears to lie in the trace of equivalent structure subducted at the western indentation of the lowermost inner-trench slope (compare Figure 2). Hence, the relief on the oceanic plate beneath the lower OAH slope may in places be associated with the subduction of inherited seafloor fabric, which is likely reactivated as response to plate bending.

[30] On this line, velocities beneath the OAH are <5.5 km/s down to ~11 km depth and thus only slightly lower than corresponding velocity portions farther north (Figure 10a). Different to the fore-arc setting observed offshore Lombok, there is only a thin sedimentary cover (no mature sedimentary basin) and crustal type velocities are observed down to ~25 km depth. Beneath the northern model edge, some steep seaward dipping reflections are observed in the wide-angle seismic data set (Figure 10b; see Figure 12 for data example). From the velocity information gained from the few rays penetrating those areas, however, it seems unlikely that this reflector is associated with a major velocity discontinuity such as the crust-mantle boundary.

### 4.4. Profile 21

[31] Compared to the previous lines data quality on profile 21 is only moderate, which is most likely related to the

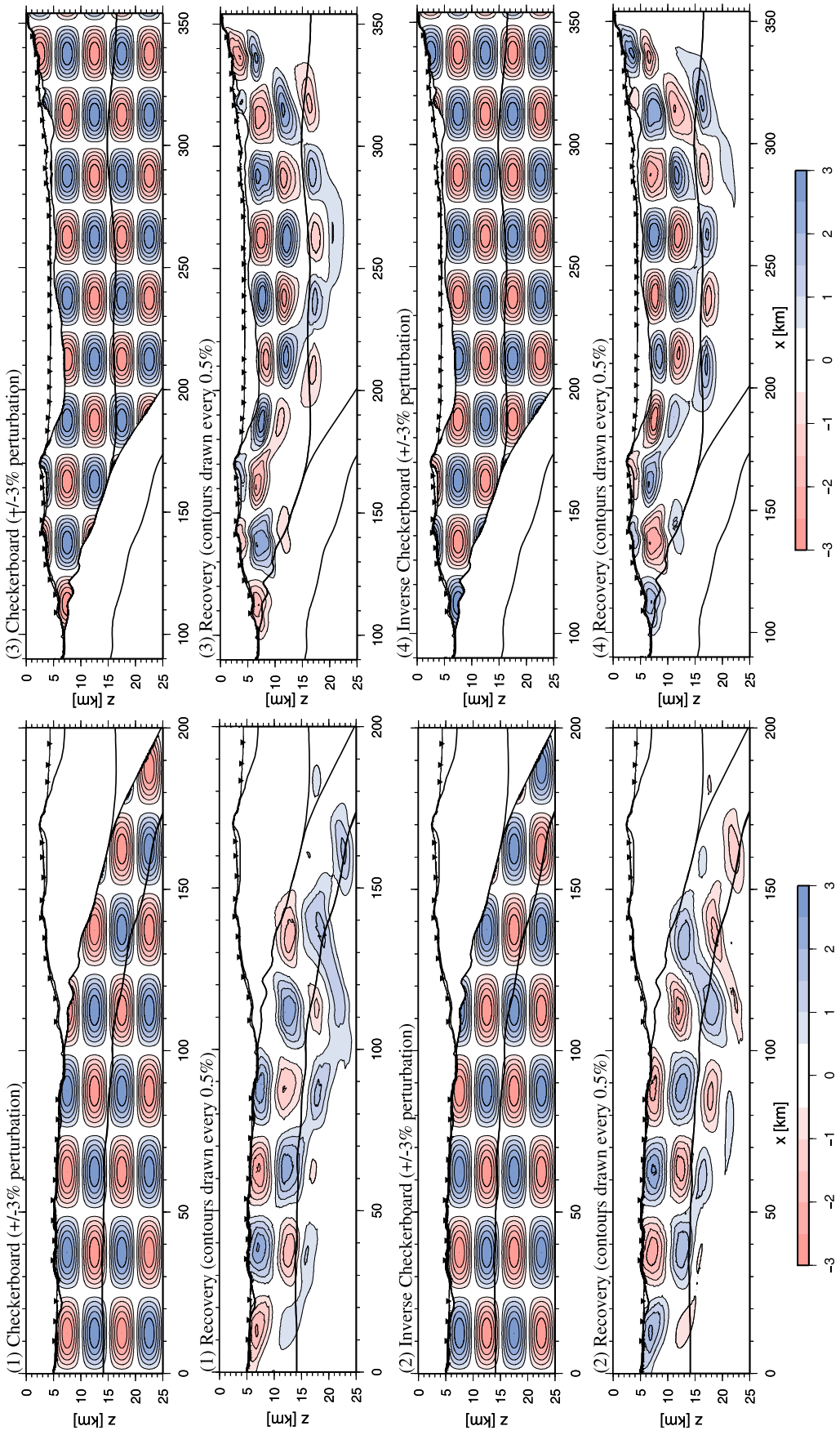


**Figure 7.** Resolution tests using a ±3%, 25 km × 5 km checkerboard pattern of synthetic velocity anomalies (left) within the oceanic model portions and (right) within the fore-arc model portions of profile 31/32. Tests show normal and inverse checkerboard patterns, original perturbation model and recovery after three iterations, respectively. The background model for the anomalies is the tomographic velocity model of Figure 5a. See text for discussion.

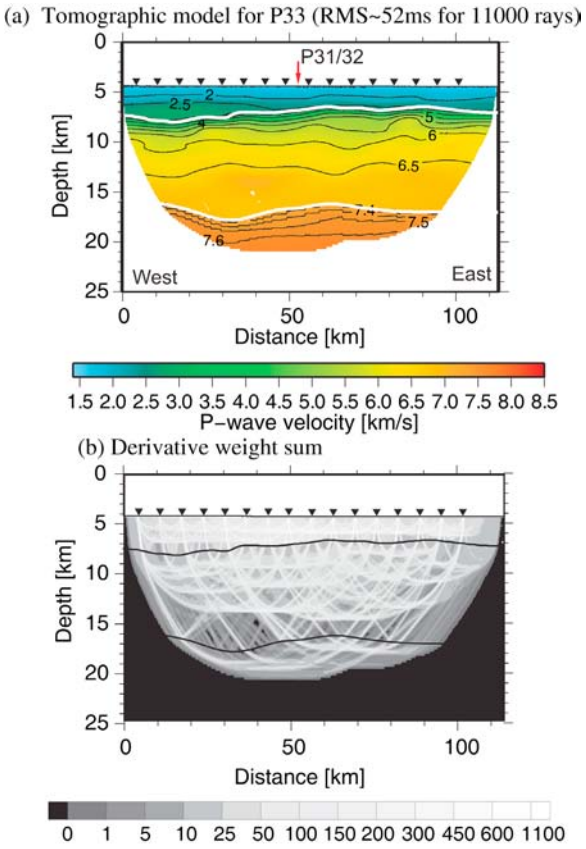


**Figure 8.** (a) Final tomographic velocity model of profile 33 (Lombok Basin). Triangles indicate locations of ocean bottom seismographs. Red arrow displays line intersection with profile 31/32. White lines mark structural interfaces: basement and fore-arc Moho are obtained from the joint refraction and wide-angle reflection tomography. (b) Derivative weight sum for the final tomographic velocity model.

rather complex morphology and internal structure of the OAH close to the transition to the collisional regime (see Figure 13 for data examples). The velocity model suggests significant structural changes between the western and the eastern model portions and a transition zone between ~60 km and ~100 km profile distance where the depth of the oceanic Moho increases from 19 km to 23 km (Figure 14). In the western model portions velocities reach 5.3 km/s above the plate boundary which can be traced as a continuous reflector in 11–12 km depth up to ~80 km profile distance (Figure 14b). Along the entire profile, the oceanic slab is characterized by an intracrustal reflector, which is associated with the 5.5–6.0 km/s iso-velocity line. In the eastern model portions, there is evidence for two shallower reflectors, although their continuation is sometimes unclear due to the lack of reflection coverage. If the lower reflector represents the eastern continuation of the plate boundary, this would imply a ~13 km thick subducting oceanic slab in the eastern model portions versus a 8–9 km thick slab in the western model portions (Figure 14). Accordingly, we interpret the observed change toward greater thickness of the lower plate as the transition to the collisional setting comprising the promontory of the Australian continental shelf. Resolved mantle velocities are in the range of 7.7–8.0 km/s and thus, ~0.3 km/s higher compared to corresponding velocities on profile 22 at the line intersection.

## 5. Gravity Data

[32] Gravity data were acquired every second using the KSS31M sea gravimeter system built by Bodenseewerk Geosystem GmbH. Using the navigation information from the ship, the measured data were corrected for the Eötvös effect and for the instrumental drift by tying it to calibrated land stations after completion of the cruise. The Free-Air Anomaly (FAA) was then obtained by subtracting the WGS67 normal gravity.

[33] We used the TOMO2D code [*Korenaga et al.*, 2001], which adopts the method of *Parker* [1973] modified by topographic correction terms, to calculate the 2-D FAA gravity response to a velocity-derived density model. For sediment, as resolved from MCS seismic data, we used the empirical velocity-density relationship $\rho = 1 + 1.18(\mathrm{Vp} - 1.5)^{0.22}$ [e.g., *Korenaga et al.*, 2000]. *Carlson and Herrick*'s [1990] conversion formula for igneous crust, $\rho = 3.81 - 6.0/\mathrm{Vp}$, was adopted for the upper oceanic crust ($\mathrm{Vp} < 6.0$ km/s) and we used a constant density of 2.90 g/cm$^3$ for the lower oceanic crust. Beyond the depth of seismic penetration the thickness and velocity structure of the subducting slab were held constant and its geometry was inferred from the distribution of Wadati-Benioff hypocenters [*Engdahl and Villaseñor*, 2002]. For the upper oceanic mantle we used the Vp versus $\rho$ relationship of *Carlson and Miller* [2003], which accounts for the dependence of Vp with the degree of serpentinization and we limited the density to maximal 3.23 g/cm$^3$ for the deeper mantle portions.

[34] According to thermal simulations, serpentine breaks down via dehydration reactions in the subducting oceanic mantle at depths greater ~50 km (>600°C) and for old/cold slabs likely at much greater depths [*Peacock*, 2001; *Rüpke et al.*, 2004]. Hence, we expect that hydrated oceanic mantle will not recover its density by metamorphic deserpentinization reactions within the depth range of our models. We thus held constant the reduced mantle densities within the shallowmost oceanic mantle portions landward of the trench, even though Vp partly increases in our models by possible fracturing recover.

[35] For the subsequent gravity modeling we tested several models, keeping unchanged the density distribution in the oceanic crust and mantle, and changing only the densities in the overriding plates. The major aim of the applied approach is to test whether our seismically derived fore-arc geometries (mantle wedge offshore Lombok, crustal wedge offshore Sumba) can explain the gravity data reasonably well by using widely accepted velocity to density conversions.

### 5.1. Gravity Modeling of Profile 31/32

[36] For the overriding plate we used *Hamilton*'s [1978] relation for shale, $\rho = 0.917 + 0.747\mathrm{Vp} - 0.08\mathrm{Vp}^2$, for

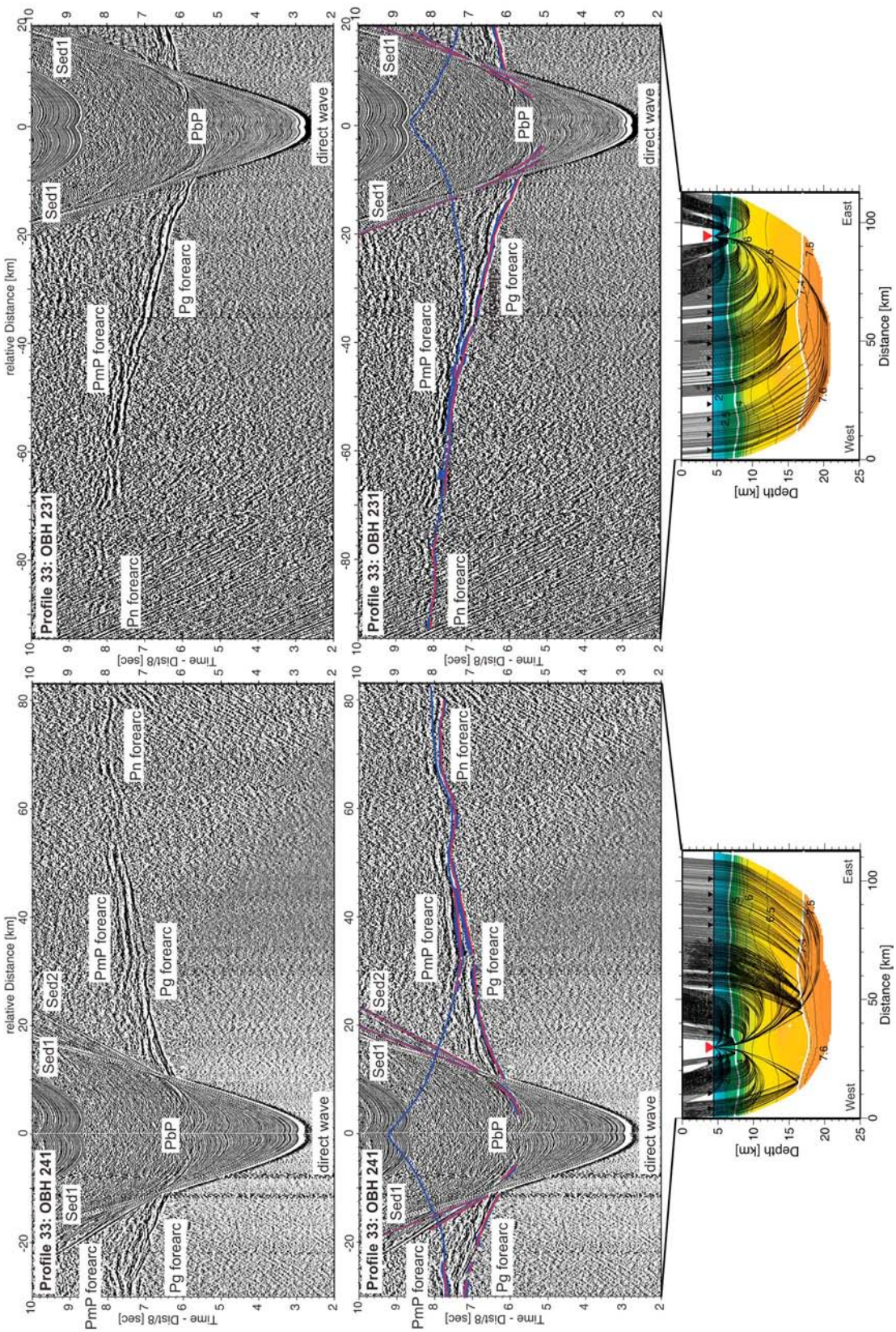


**Figure 9.** Seismic record sections (reduced to 8 km/s) of OBH 231 and OBH 241 on profile 33. (top) Interpreted seismic arrivals are labeled: Sed1, Sed2 (sedimentary phases), Pg fore arc (turning rays within the fore-arc crust), Pn fore arc (turning rays in the upper fore-arc mantle), PbP (reflected rays at the basement), and PmP fore arc (reflected rays at the fore-arc Moho). (middle) Picks are shown as blue bars according to their pick uncertainty, computed traveltimes are shown as red dots. Blue lines represent traveltimes for offsets not constrained by picks. (bottom) Corresponding raypaths of the picked traveltimes through the final tomographic solution of profile 33.

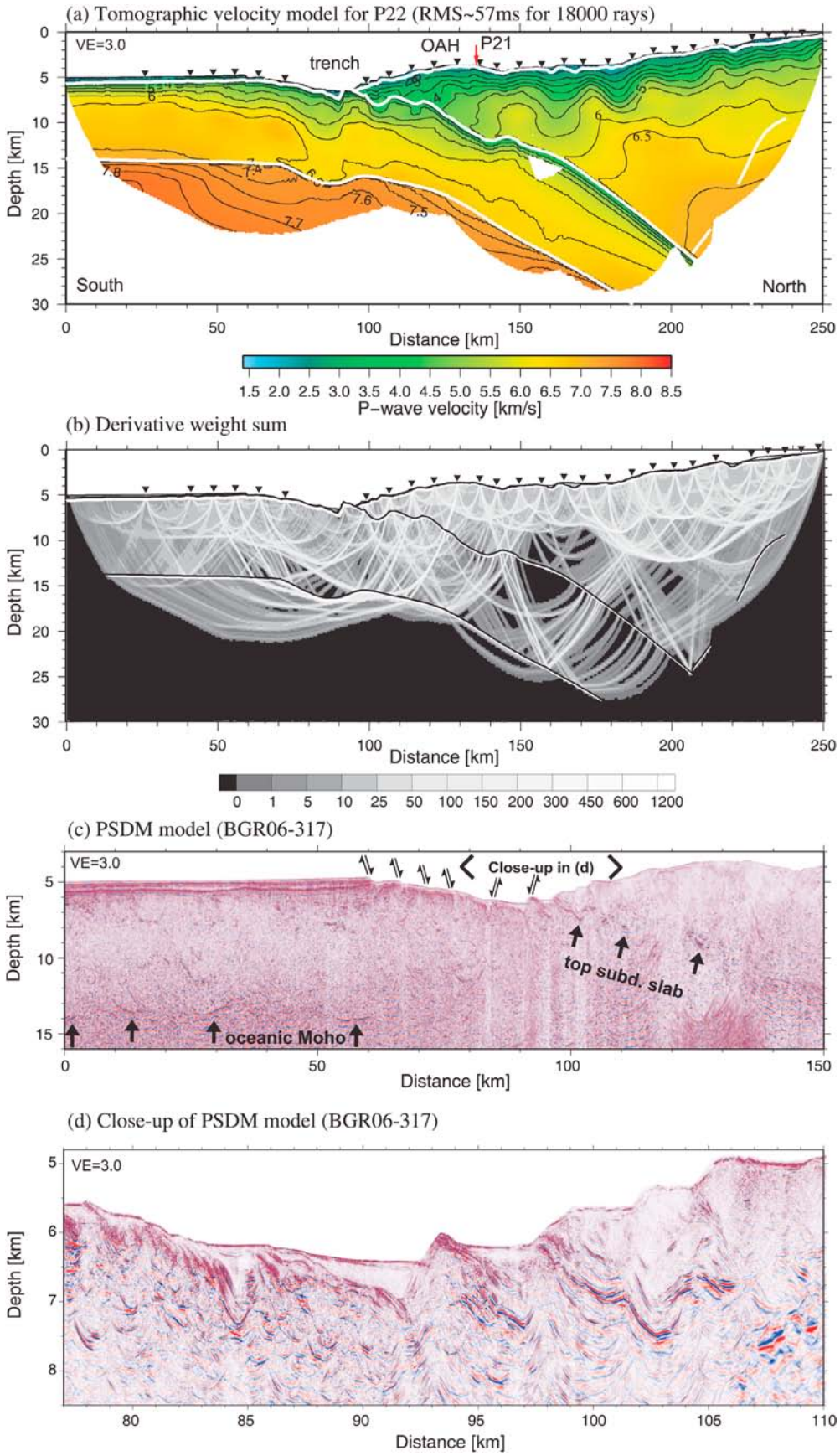
(a) Tomographic velocity model for P22 (RMS~57ms for 18000 rays)
VE=3.0
trench
OAH
P21
South
North
Depth [km]
Distance [km]
1.5 2.0 2.5 3.0 3.5 4.0 4.5 5.0 5.5 6.0 6.5 7.0 7.5 8.0 8.5
P−wave velocity [km/s]
(b) Derivative weight sum
Depth [km]
Distance [km]
0 1 5 10 25 50 100 150 200 300 450 600 1200
(c) PSDM model (BGR06-317)
VE=3.0
Close-up in (d)
top subd. slab
oceanic Moho
Depth [km]
Distance [km]
(d) Close-up of PSDM model (BGR06-317)
VE=3.0
Depth [km]
Distance [km]

**Figure 10**

crustal portions characterized by Vp < 5.7 km/s. We then tested three different laws for the deeper crustal portions and the fore-arc mantle (Figure 15): (1) *Carlson and Herrick*'s [1990] relation (igneous crust) and a constant mantle density of 3.20 g/cm$^3$, (2) *Christensen and Mooney*'s [1995] nonlinear regression for continental crustal rocks, $\rho$ = 5.055 − 14.094/Vp, and a constant mantle density of 3.21 g/cm$^3$, and (3) a constant density of 2.80 g/cm$^3$ for the crust and the same Vp versus $\rho$ relationship used for oceanic mantle.

[37] For the overriding plate, the relationships of *Carlson and Herrick* [1990] (igneous crust) and *Christensen and Mooney* [1995] (continental crust) yield a comparable fit by adjusting the fore-arc mantle density from 3.20 g/cm$^3$ to 3.21 g/cm$^3$ (Figure 15b). The fit is slightly improved for a model comprising a constant crustal density of 2.80 g/cm$^3$ and a fore-arc mantle comprising the same Vp versus $\rho$ relationship used for oceanic mantle (Figure 15c). Thus, the gravity data is consistent with mantle alteration and a shallow fore-arc mantle, as inferred from the analysis of seismic refraction data.

### 5.2. Gravity Modeling of Profile 22

[38] Similar to the above described scheme we tested four different scenarios for those fore-arc portions characterized by Vp > 5.7 km/s (Figure 16): (1) a constant density of 2.75 g/cm$^3$ and *Birch*'s [1961] conversion law for lower crustal rocks, $\rho$ = (Vp + 1.0)/2.67, for model portions between the intracrustal reflector and the top of the subducting slab, (2) *Carlson and Herrick*'s [1990] relationship (igneous crust) for the entire crust, (3) *Christensen and Mooney*'s [1995] relationship (continental crust) for the entire crust, and (4) a constant density of 2.80 g/cm$^3$ and a constant density of 2.95 g/cm$^3$ for model portions between the intracrustal reflector and the top of the subducting slab.

[39] The results show that a model comprising a locally lightened mantle density yields a good match to the observed gravity anomaly, again implying that the oceanic mantle beneath the trench has been altered. For the overriding plate, the relationship of *Carlson and Herrick* [1990] yields a rather poor match to the observed gravity anomaly, at least up to ~200 km profile distance (Figure 16b). Applying *Christensen and Mooney*'s [1995] conversion law (continental crust) provides a much better match to the observed data for these model portions but underpredicts the FAA anomaly for greater profile distances. Accounting for the dichotomy of the crust (upper fore arc and lower fore arc), either by using constant densities of 2.80 g/cm$^3$ and 2.95 g/cm$^3$ or by using 2.75 g/cm$^3$ and *Birch*'s [1961] conversion law, respectively, yield an altogether better RMS fit. However, assuming the presence of crustal-type densities beneath the steeply seaward-dipping reflector yields a good fit of the gravity data. Hence, these results are in accordance with our seismically derived model, which lacks a shallow mantle wedge offshore Sumba.

## 6. Discussion

### 6.1. Oceanic Plate and Trench

[40] A thickened oceanic crust is observed on both trench-perpendicular profiles. In case of profile 31/32, average values of 8.6 km are interpreted as the transition to the easternmost extensions of the Roo Rise and another bathymetric high near the trench close to 114.5°E (Figure 1), which locally reveal crustal thicknesses >15 km [*Curray et al.*, 1977; Shulgin et al. (submitted manuscript, 2010)]. The refraction profile offshore Lombok Strait from *Curray et al.* [1977] runs ~50 km west of profile 31/32 and reveals velocities of 8.1 km/s at 23 km depth at the trench (compared to velocities of ~7.9 km/s at ~22 km depth at the trench on profile 31/32). Owing to the large shot spacing and related difficulties in following secondary arrivals from one record to another, their evaluation of layer thickness is mainly based on the recordings of refracted arrivals, which makes their interpretation of Moho depths from these early shot records ambiguous. Hence, their depth for the 8.1 km/s velocity layer may not mark the top of the mantle, which here is constrained at ~17 km depth, but may indicate the lower limit of the observed mantle alteration.

[41] On profile 22 the crustal thickness of 9.0 km is likely related to the transition to the Scott Plateau representing the promontory of the Australian continental shelf [*Shulgin et al.*, 2009]. This is confirmed by the trench-parallel profile 21 off Sumba which suggests structural changes of the subducting crust manifested in a thickness increase of ~5 km over a distance of 40 km to the east (Figure 14). Most of the observed crustal thickening is related to the thickening of the upper crustal layer. The profile of *Shulgin et al.* [2009] at 121°E (Figure 1) reveals a 15 km thick crust beneath the Scott Plateau which seems to thin out northward when subducting beneath the Sumba Ridge. The crust shows a pronounced intracrustal reflector at roughly mid-crustal depths and is interpreted to be of continental nature. Accordingly, we interpret the easternmost portions of profile 21 as the ocean-continent transition in the subducting plate (Figure 14).

[42] Both trench-perpendicular profiles show a reduction of crustal and upper mantle velocities at distances <30–50 km seaward of the trench (Figures 5a and 10a). Obtained uppermost mantle velocities (down to ~2 km beneath the Moho) in the trench are well resolved and independent of the mantle starting model; they represent a robust feature of the tomographic inversion (please refer to Figures S1 and S2 in the auxiliary material for additional resolution tests with

**Figure 10.** (a) Final tomographic velocity model of profile 22. Triangles indicate locations of ocean bottom seismographs. Red arrow displays line intersection with profile 21. White lines mark structural interfaces: sedimentary portions are derived from the analysis of high-resolution MCS seismic data; plate boundary, oceanic Moho and seaward dipping intra-fore-arc reflector are obtained from the joint refraction and wide-angle reflection tomography. (b) Derivative weight sum for the final tomographic velocity model. (c) Prestack depth-migrated MCS line BGR06-317 from *Lüschen et al.* [2010]. (d) Close-up of BGR06-317. Subduction of basement asperities, located near 95 km and 105 km profile distance, results in local indentations of the deformation front (compare Figure 2). All models are plotted at 3 × vertical exaggeration. OAH, outer arc high.

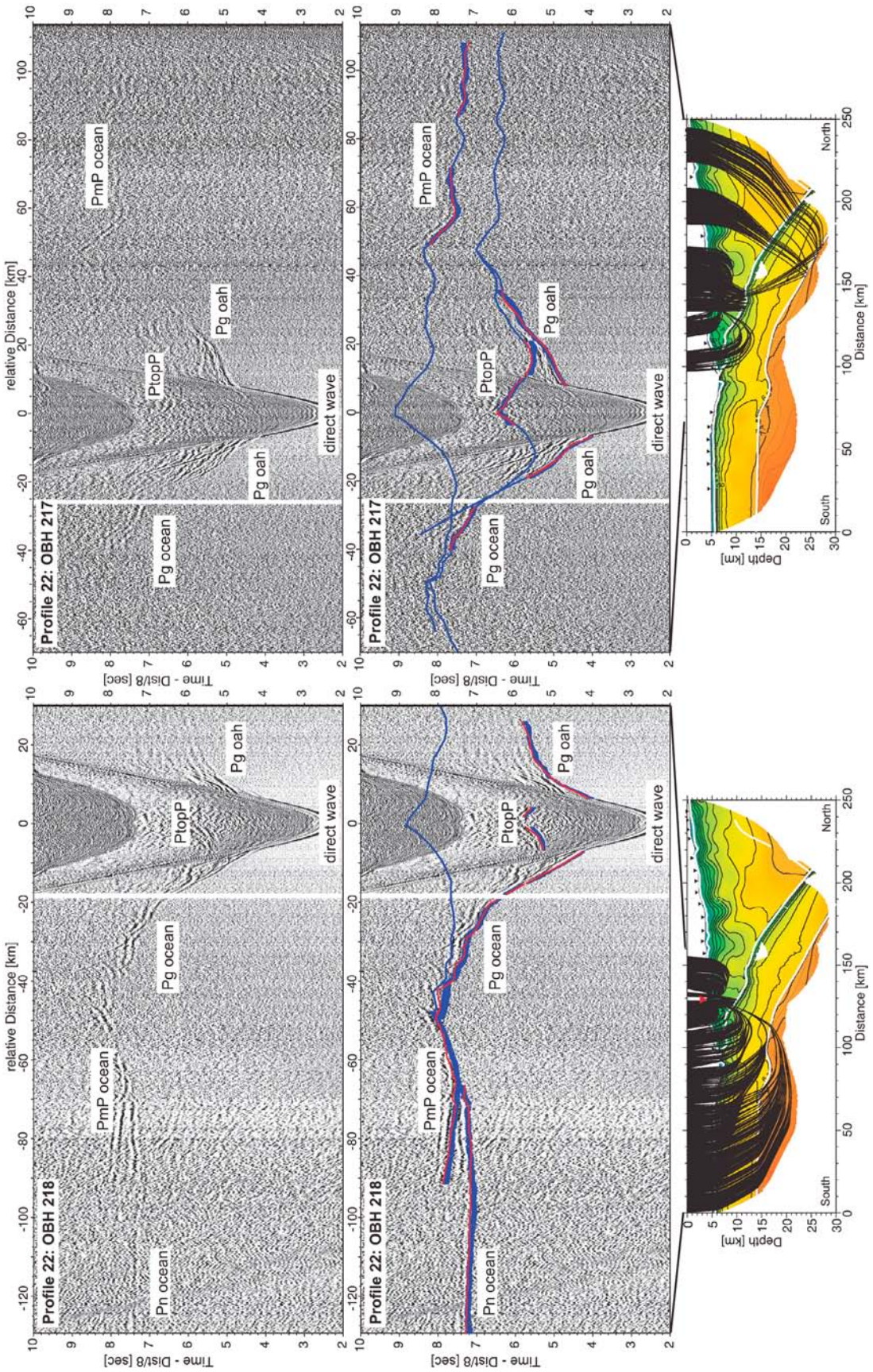


**Figure 11.** Seismic record sections (reduced to 8 km/s) of OBH 217 and OBH 218 on profile 22. (top) Interpreted seismic arrivals are labeled: Pg oah (turning rays within the outer arc high), Pg ocean (turning rays within oceanic crust), Pn ocean (turning rays in the upper oceanic mantle), PtopP (reflected rays at the plate interface), and PmP ocean (reflected rays at the oceanic Moho). (middle) Picks are shown as blue bars according to their pick uncertainty, computed traveltimes are shown as red dots. Blue lines represent traveltimes for offsets not constrained by picks. (bottom) Corresponding raypaths of the picked traveltimes through the final tomographic solution of profile 22.

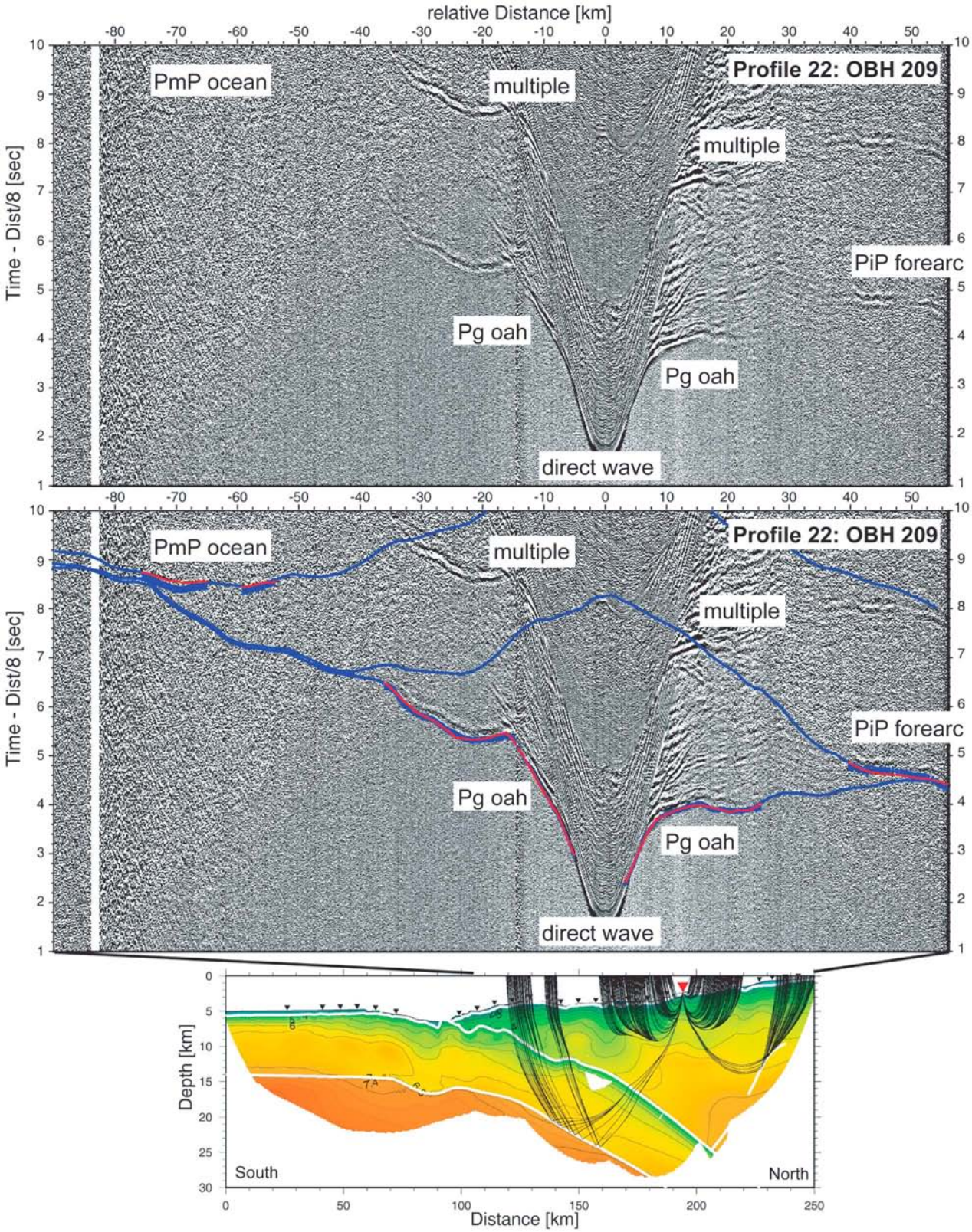


**Figure 12.** Seismic record section (reduced to 8 km/s) of OBH 209 on profile 22. (top) Interpreted seismic arrivals are labeled: Pg oah (turning rays within the outer arc high/fore arc), PiP fore arc (reflected rays at the intracrustal fore-arc reflector), and PmP ocean (reflected rays at the oceanic Moho). (middle) Picks are shown as blue bars according to their pick uncertainty, computed traveltimes are shown as red dots. Blue lines represent traveltimes for offsets not constrained by picks. (bottom) Corresponding raypaths of the picked traveltimes through the final tomographic solution of profile 22.

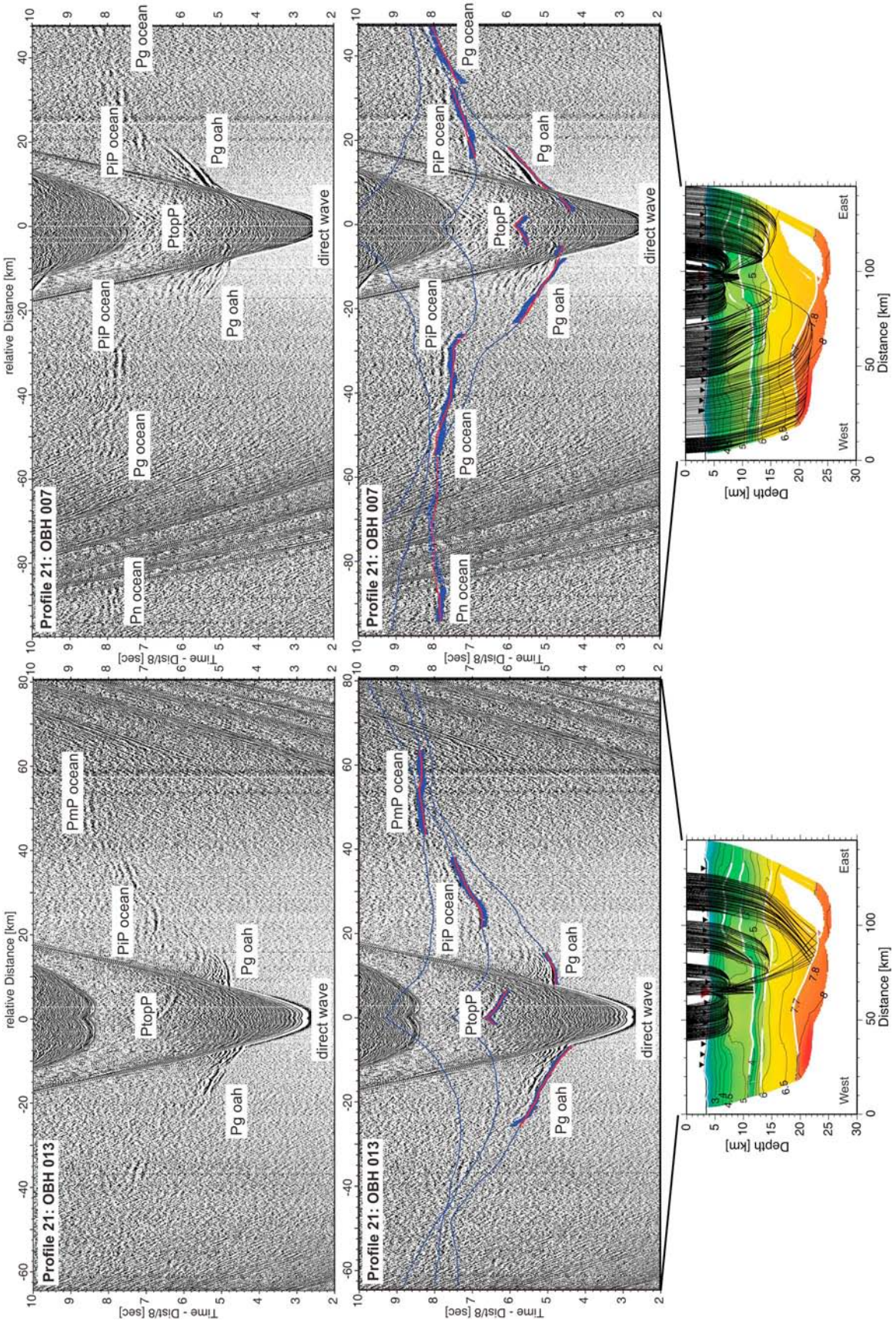
Profile 21: OBH 013
Profile 21: OBH 007
relative Distance [km]
Time - Dist/8 [sec]
PmP ocean
PiP ocean
PtopP
Pg oah
direct wave
Pn ocean
Pg ocean
Depth [km]
Distance [km]
West
East

Figure 13

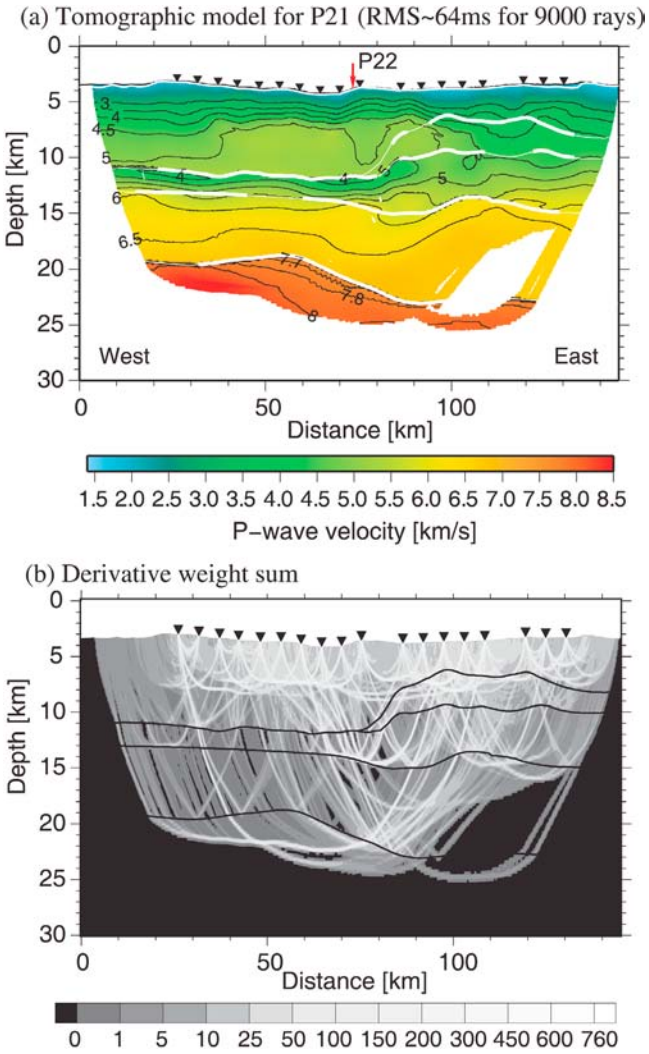


**Figure 14.** (a) Final tomographic velocity model of profile 21 (outer arc high). Triangles indicate locations of ocean bottom seismographs. Red arrow displays line intersection with profile 22. White lines mark structural interfaces obtained from the joint refraction and wide-angle reflection tomography (see text for details). (b) Derivative weight sum for the final tomographic velocity model.

synthetic anomalies confined to the oceanic mantle underneath the trench and an evaluation of the impact of different mantle starting models on the tomographic solution of profile 31/32). The apparent coincidence of the velocity decrease with the onset of faulting can be interpreted as the result of fracturing and subsequent alteration of the oceanic crust and serpentinization of the underlying upper mantle. Reduced upper mantle velocities within a similar range close to the trench and associated with the bending of the oceanic plate prior to subduction are found, e.g., at the Middle America trench [*Grevemeyer et al.*, 2007; *Ivandic et al.*, 2008] and offshore Chile [*Contreras-Reyes et al.*, 2007].

[43] Assuming that the velocity reduction in the upper mantle is exclusively caused by serpentinization, velocities of 7.9–7.4 km/s would imply a 0.6–2.4% increase in water content resulting in 5–19% serpentinization of mantle peridotite as a maximum estimate [*Carlson and Miller*, 2003]. However, the velocity model of profile 31/32 shows that upper mantle velocities recover to some extent from ~7.5 km/s at the trench to ~7.7 km/s beneath the lower slope of the OAH (Figure 5a; please also refer to Figure S2 of the auxiliary material). The partial recovery of mantle velocities at depths of ~20 km may indicate compressive sealing of cracks by slab-refolding and fracture-filling precipitation, because metamorphic de-serpentinization reactions occur at much greater depth during subduction of old (cold) oceanic lithosphere [*Peacock*, 2001; *Rüpke et al.*, 2004; *Faccenda et al.*, 2009]. Hence, the presence of mantle-penetrating cracks and faults likely controls the extent of the low velocity anomaly at the trench and reduces the possible degree of mantle serpentinization to probably less than 15%.

[44] On profile 22, the amplitude and intensity of the crustal low-velocity anomaly is larger and occurs more tightly confined to the trench, respectively. This is likely related to the stronger fragmentation of the oceanic crust as indicated by the greater basement relief with vertical throws of sometimes >1 km (Figure 10d). Moreover, upper mantle velocities in the uppermost 2–3 km depth beneath the Moho do not recover within the resolved model portions downdip of the trench. These observations may indicate increased tensional tectonic forces in the subducting plate.

[45] *Spence* [1986] inferred from the absence of large interface thrust earthquakes in the Sumba region, that gravitational pull of the old (dense) sinking oceanic lithosphere might have partially decoupled the subducted plate from the overriding plate. The juxtaposition of old (Late Jurassic) oceanic crust and continental crust close to ~120°E provides one of the most dramatic lateral gradients in interplate seismic coupling in the world. The combination of slab-pull on an uncoupled slab in the Java trench and the strong resistive force of the buoyant crust of the Scott Plateau to the east appears to store a tremendous amount of elastic tensile strain energy in the lithosphere at the junction of the two zones [*Spence*, 1986]. The inferred stress in the oceanic slab is transferred updip to the bending-region at the trench, leading to the 1977 Sumba earthquake, and to intense fracturing and alteration of the subducting oceanic crust and the underlying upper mantle.

### 6.2. Fore-Arc Offshore Lombok

[46] The most striking feature of the OAH offshore Lombok is the portion of low seismic velocities (Vp < 5.5 km/s)

**Figure 13.** Seismic record sections (reduced to 8 km/s) of OBH 007 and OBH 013 on profile 21. (top) Interpreted seismic arrivals are labeled: Pg oah (turning rays within the outer arc high), Pg ocean (turning rays within oceanic crust), Pn ocean (turning rays in the upper oceanic mantle), PtopP (reflected rays at the plate interface), PiP ocean (reflected rays at an intracrustal oceanic reflector), and PmP ocean (reflected rays at the oceanic Moho). (middle) Picks are shown as blue bars according to their pick uncertainty; computed traveltimes are shown as red dots. Blue lines represent traveltimes for offsets not constrained by picks. (bottom) Corresponding raypaths of the picked traveltimes through the final tomographic solution of profile 21.

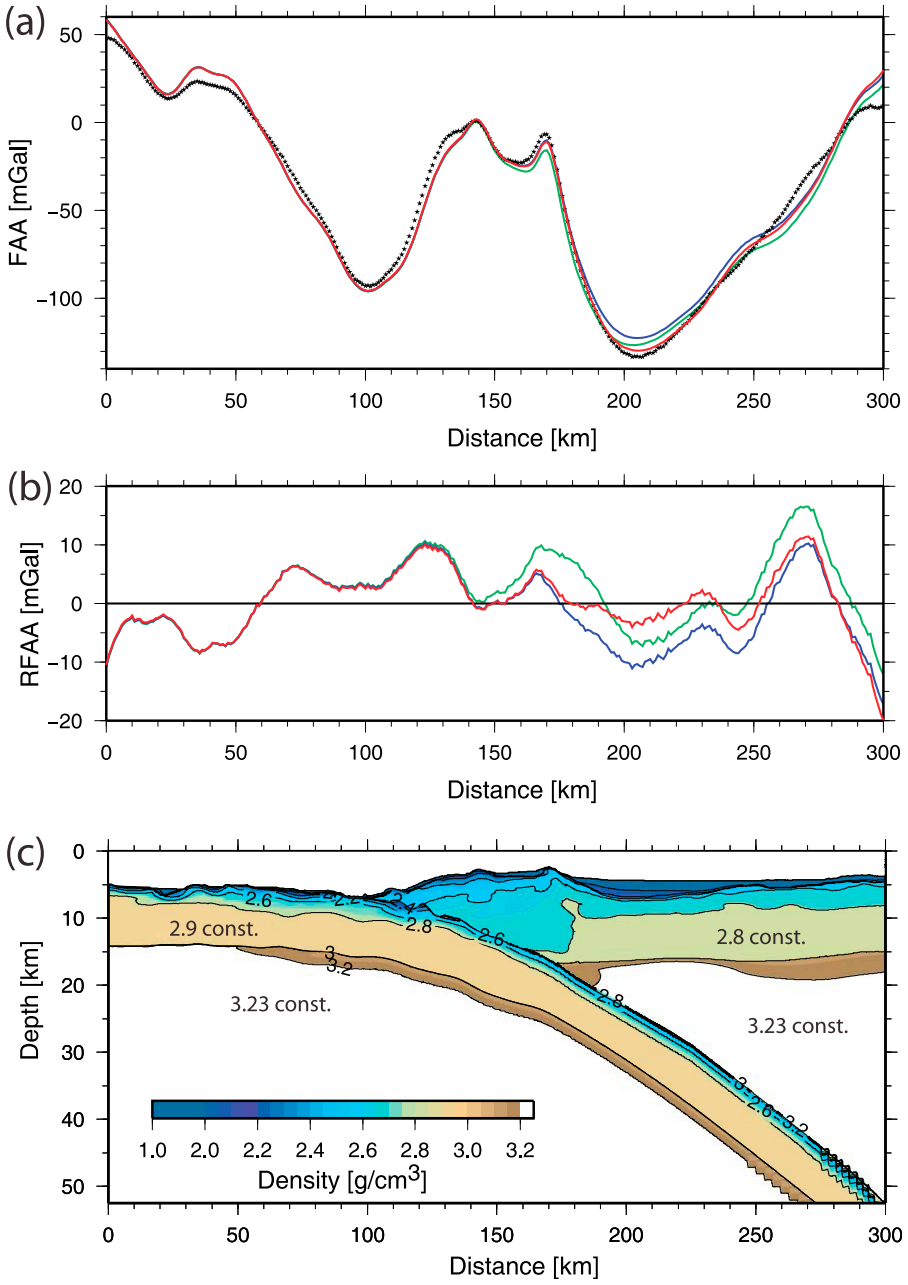


**Figure 15.** Gravity modeling of profile 31/32. (a) Observed free-air gravity anomaly (black points). Solid lines are from models obtained by changing overriding plate densities and keeping the same structure for oceanic crust and mantle (see text). For all calculations, *Hamilton*'s [1978] conversion law for shale is used for fore-arc portions characterized by Vp < 5.7 km/s. Blue line is for using *Carlson and Herrick*'s [1990] conversion law (igneous crust) for fore-arc crust (Vp > 5.7 km/s) and a constant fore-arc mantle density of 3.20 g/cm$^3$. Green line is for using *Christensen and Mooney*'s [1995] conversion law (continental crust) for fore-arc crust (Vp > 5.7 km/s) and a constant fore-arc mantle density of 3.21 g/cm$^3$. Red line is preferred model shown in Figure 15c. (b) Residual free-air gravity anomaly (RFAA) obtained by subtracting calculated from observed anomaly. Model with *Carlson and Herrick*'s [1990] conversion law has RMS of 6.5 mGal (blue line). Model with *Christensen and Mooney*'s [1995] conversion law has RMS of 6.2 mGal (green line). Preferred model has RMS of 5.7 mGal (red line). (c) Preferred density model using a constant density of 2.8 g/cm$^3$ for fore-arc crust (Vp > 5.7 km/s) and *Carlson and Miller*'s [2003] conversion law for both the oceanic and fore-arc mantle (restricted to maximal 3.23 g/cm$^3$).

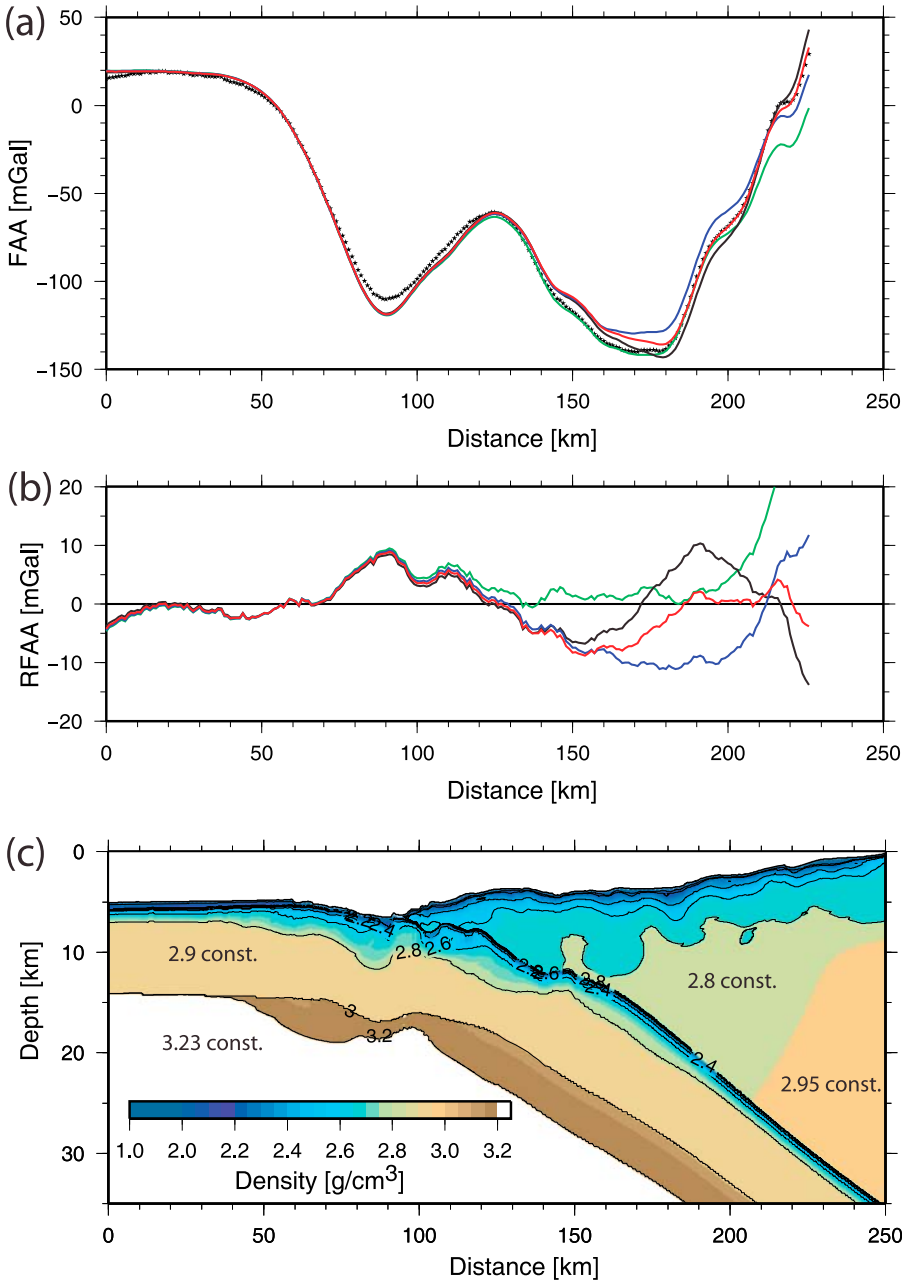


**Figure 16.** Gravity modeling of profile 22. (a) Observed free-air gravity anomaly (black points). Solid lines are from models obtained by changing overriding plate densities and keeping the same structure for oceanic crust and mantle (see text). For all calculations, *Hamilton*'s [1978] conversion law for shale is used for fore-arc portions characterized by Vp < 5.7 km/s. Black line is for using a constant density of 2.75 g/cm$^3$ for the upper fore arc (Vp > 5.7 km/s) and *Birch*'s [1961] conversion law (lower crust) for the lower fore arc between intracrustal reflector and top of subducting slab. Blue line is for using *Carlson and Herrick*'s [1990] conversion law (oceanic crust), restricted to maximal 2.9 g/cm$^3$, for the entire fore arc (Vp > 5.7 km/s). Green line is for using *Christensen and Mooney*'s [1995] conversion law (continental crust), restricted to maximal 2.9 g/cm$^3$, for the entire fore arc (Vp > 5.7 km/s). Red line is preferred model shown in Figure 16c. (b) Residual free-air gravity anomaly (RFAA) obtained by subtracting calculated from observed anomaly. Model with *Carlson and Herrick*'s [1990] conversion law has RMS of 6.4 mGal (blue line). Model with *Christensen and Mooney*'s [1995] conversion law has RMS of 5.8 mGal (green line). Model with *Birch*'s [1961] conversion law for the lower fore arc has RMS of 4.5 mGal (black line). Preferred model has RMS of 4.0 mGal (red line). (c) Preferred density model using a constant density of 2.8 g/cm$^3$ for the upper fore arc (Vp > 5.7 km/s) and 2.95 g/cm$^3$ for the lower fore arc between intracrustal reflector and top of subducting slab.

down to the plate interface (down to ~13 km depth), which points toward a sedimentary rock origin of this feature (Figure 5). On the lowermost inner trench slope (>5 km depth) profile 31/32 suggests the presence of a frontal prism, which displays low seismic velocities (Vp~3 km/s) and originates from frontal accretion of trench sediments. The MCS profile draws only one imbricate thrust sheet (Figure 6), probably due to local indentations of the trench, but more than three arrays of thrust ridges appear at the seafloor farther to the east (Figure 2).

[47] Currently, only moderate sedimentary portions are involved in the formation of the OAH, comprising mainly the thin (<600 m) predominantly pelagic sedimentary cover visible atop the oceanic plate and some turbidites and slump deposits from the inner trench slope [*Lüschen et al.*, 2010]. A possible sediment supply from the fore arc is blocked due to the higher elevation of the OAH representing an effective barrier from the depocenters of the Lombok Basin. However, taking into account the ~25 Ma long period of subduction at the eastern Sunda Arc [e.g., *Hall and Smyth*, 2008], continuous accretion of sediment could have formed major portions of the OAH although involved sedimentary volumes are moderate [*Van der Werff*, 1995].

[48] Sediment supply may have been more abundant before the approach of the Roo Rise to the trench. Off eastern Java, the onset of subduction of the Roo Rise resulted in an uplift of the trench and subsequent truncation of sediment supply from the Bengal Fan. At present, however, only ~1.5 km sediment thickness are trapped west of this barrier in the trench off western Java [*Kopp et al.*, 2002], which suggests little effects on trench sediment contribution off Lombok and farther east.

[49] Beneath the higher elevated OAH portions the MCS seismic profile of *Lüschen et al.* [2010] displays a number of landward dipping faults associated with a prominent slope break and with the system of tectonic ridges and the small basin in between (Figure 6). This morphological array of ridges and piggyback basins in between correlates with similar structures farther west, where these features are associated with landward dipping splay faults [*Müller et al.*, 2008; *Lüschen et al.*, 2010]. Offshore Lombok, at least two faults seem to penetrate the entire OAH and connect to the plate interface (Figure 6). The higher-elevated OAH portions display only minimal reflectivity. Hence, from the available data it is difficult to judge whether these faults are "out of sequence" splay faults or reactivated imbricate thrust faults which are shortened and steepened due to compression.

[50] Profile 31/32 reveals a sharp lateral increase of crustal velocities beneath the landward slope break of the OAH suggesting distinct lithological changes associated with the transition from the northern ridge to those fore-arc portions capped by the sedimentary strata comprising the Lombok Basin (Figure 5). Crustal velocities beneath the basin rapidly increase to 5.5–6.0 km/s and then rise somewhat more gentle to ~6.8 km/s above the upper plate Moho. A similar lateral velocity change from 4.0 km/s to 5.5 km/s is observed offshore Chile at the transition from the outer rise to the Valparaiso Basin and is interpreted as a lithological transition from accreted sediment to continental margin framework [*Flueh et al.*, 1998]. On profile 31/32, there is a portion of high velocities, located at 7–10 km depth and ~180 km profile distance, which are bounded by landward dipping reflections (Figure 6). The observed structure could be interpreted as the tip of the basement of the Lombok Basin, which was tilted and lifted up by underthrusting along with the thickening of sediments during OAH generation. Such architectures are common in ancient accretionary terranes exposed on land [*Dickinson and Seely*, 1979]. The uplift and northward tilt of the basement beneath the northern ridge and the seismic facies of the Lombok Basin crust distinct from the OAH may be suggestive for an arcward dipping backstop located beneath the landward slope break of the OAH. On a magnetic profile crossing the OAH this transition is marked by a sharp negative anomaly (~40 km wide, −300 nT amplitude), which might result from a package of steeply inclined tectonically accreted volcanic sills [*Mueller and Neben*, 2006]. Results from the analysis of MCS data show an irregular topography of the Lombok fore-arc basement reminiscent of horst and graben structures at rifted continental margins or stacked ophiolite sheets and nappes, which could be formed by underthrusting of younger oceanic blocks and subsequent steepening due to continuous compression [*Lüschen et al.*, 2010].

[51] The thickness of the fore-arc crust on profile 31/32 ranges from 9 km beneath the portions of highest sedimentary infill to 11 km at ~250 km profile distance (Figure 5). There is no distinct lateral change in crustal velocities in the northernmost model portions, but crustal thickness likely increases to >14 km here. A high velocity lower crust (6.8–7.2 km/s), which represents about 30% of the total crust of the subducting oceanic plate, is lacking in the fore-arc crust, resulting in an average crustal velocity (considering crustal velocity portions characterized by Vp > 6.0 km/s) of 6.51 ± 0.07 km/s compared to 6.71 ± 0.09 km/s for the subducting plate. From the distribution of zircon ages in sedimentary and igneous rocks from southeast Java, *Smyth et al.* [2007] infer the presence of a Gondwana continental fragment from northwest Australia, which was accreted offshore East Java in the Late Cretaceous; the eastern extent of this fragment is unknown but the oceanic type velocity structure beneath the Lombok Basin rather precludes a possible continuation into this area.

[52] The fore-arc crust in our models could be interpreted as an altered, heavily fractured piece of an older oceanic terrane, perhaps formed during the opening of the Indian Ocean during Cretaceous to middle Eocene times, which was hindered from subduction due to its increased buoyancy; a similar scenario was previously invoked to explain the origin of the fore arc offshore Lombok Strait [*Curray et al.*, 1977] and western Java [*Kopp et al.*, 2002]. The relatively constant crustal velocity of the fore-arc basement may imply a distinct change in lithological composition toward the volcanic arc, unless the arc massif is composed mainly of oceanic crust or ophiolite as the fore-arc basement. The base of the fore-arc basement marks the crust mantle boundary, as the seismic and gravity data strongly support the presence of shallow mantle material here.

[53] The uppermost mantle offshore Lombok exhibits rather low velocities (7.4–7.8 km/s). Similar velocity structures are observed beneath the Izu-Bonin intraoceanic arc and are interpreted as "Moho transition zone" comprising mafic restite and cumulatives resulting from processes of anatexis and magmatic differentiation of the mafic and ultramafic crustal components [*Tatsumi et al.*, 2008; *Kodaira et al.*, 2008]. In order to invoke analogous processes beneath the

fore arc offshore Lombok, this scenario would imply the presence of a paleoarc ~100 km south of the present volcanic front near 250–300 km profile distance on line 31/32, where the velocity reduction in the upper mantle appears to be enhanced. In East Java a paleoarc, which was active from Eocene to early Miocene times, is located ~50 km south of the current volcanic front [*Smyth et al.*, 2008; *Hall and Smyth*, 2008]. The coincident magnetic profile of line 31/32 shows a generally smooth magnetic field across the Lombok Basin, but beginning with ~265 km profile distance displays magnetic anomalies of ±100 nT [*Mueller and Neben*, 2006], which would correspond to the location of enhanced velocity reduction in the upper mantle and thus to the inferred origin of this structure from a possible paleovolcanic arc.

[54] However, the strong Moho reflection associated with the top of the 7.4–7.8 km/s layer beneath the Lombok Basin (see Figures 4 and 9) argues for a distinct lithological boundary rather than a "chemically transparent" Moho located within the mafic restite/cumulate layer. In this alternative scenario, sub-fore-arc water release from subducted sediment and crust facilitates a significant degree of mantle serpentinization (up to 19% according to the Vp relationship of *Carlson and Miller* [2003]) [*Bostock et al.*, 2002; *Hyndman and Peacock*, 2003; *Rüpke et al.*, 2004].

[55] The presence of a shallow mantle wedge off Java was already proposed by *Kopp et al.* [2002, 2009] based on seismic wide-angle and refraction data, and a possible continuation farther east of this feature was suggested by *Grevemeyer and Tiwari* [2006] on the basis of gravity modeling. The profile of *Curray et al.* [1977] conducted ~50 km west of profile 31/32 shows a fore-arc Moho at ~18 km depth and upper mantle velocities of 7.8–8.4 km/s in the fore arc off the Lombok Strait. Hence, their Moho depths are ~2 km deeper and observed mantle velocities are 0.4–0.6 km/s higher than the results of this study (compare discussion of the results of *Curray et al.* [1977] in section 6.1).

[56] *Oleskevich et al.* [1999] suggest that the downdip limit and thus the width of the seismogenic coupling zone, which controls the potential magnitude of large megathrust earthquakes, is governed by the depth of the intersection of the thrust with the fore-arc mantle and the presence of weak hydrous minerals in the mantle wedge, which do not support seismogenic stick-slip behavior. Offshore Java a shallow serpentinized mantle wedge underlying the fore-arc basin would limit the width of the coupling zone to only 30–40 km, compared to >120 km offshore Sumatra [*Grevemeyer and Tiwari*, 2006]. Thermal modeling shows that the updip limit of the seismogenic zone (~100°C isotherm [*Hyndman and Wang*, 1993]) offshore Java is located ~80 km landward from the trench [*Grevemeyer and Tiwari*, 2006]. Offshore Lombok, the similar trench-normal convergence rate and dip but the older age of the subducting plate suggest a thermally defined updip limit that reaches farther landward from the trench and thus, the width of the seismogenic coupling zone is likely to be even narrower here. The distribution of earthquake hypocenters off Lombok and Sumbawa shows a band of extensional mechanisms closely confined to the trench and some events revealing compressional mechanisms beneath the fore-arc basin and the volcanic arc [*Špičák et al.*, 2007]. The OAH belongs to a >100 km wide zone in between characterized by virtually no teleseismically recorded earthquakes related to the plate boundary (down to a regional threshold magnitude of ~5.5) [e.g., *Engdahl and Villaseñor*, 2002]. These observations strongly contrast with the adjacent Sumatra-Andaman margin segment where the recent and historic earthquake record suggests a much larger potential for destructive subduction zone megathrust earthquakes than for Java and Lombok [*Lay et al.*, 2005; *Newcomb and McCann*, 1987]. Thus, the shallow serpentinized mantle wedge, which is absent offshore Sumatra [*Kieckhefer et al.*, 1980; *Kopp et al.*, 2002], might be the major factor limiting the magnitude of rupture offshore Java and Lombok. The system of possible splay faults in the outer arc high, however, demonstrates that potential movements can be transmitted to shallow seafloor portions and thus, this margin is nevertheless prone to a serious tsunami hazard [*Müller et al.*, 2008; *Kopp et al.*, 2009; *Lüschen et al.*, 2010] (Figure 6).

### 6.3. Fore-Arc Offshore Sumba

[57] The strong relief of the plate boundary imaged in both the wide-angle and MCS seismic data suggests significant vertical steps between dissected oceanic blocks, probably further increased due to plate bending during subduction (Figure 10d). Where these asperities subduct beneath the trench they entrain lower slope material and cause slope failure in their wake (see slide in Figure 2) and thus, may unbalance the mass budget along this margin segment toward local erosion of the frontal prism.

[58] Contrary to the geometry offshore Lombok, the similar velocity structure of the OAH and the adjacent fore-arc portions farther north may imply similar constituents (Figure 10). Velocities in the northern fore-arc portions suggest a greater heterogeneity and related vertical velocity gradients are lower (velocities do not reach 6 km/s within the uppermost 6–10 km beneath the basement, compared to ~5 km on profile 31/32). In our models the base of this unit is marked by the steep seaward dipping reflector identified in the wide-angle seismic data. The seismic refraction data, however, do not support the presence of mantle velocities directly below this reflector and the gravity data go conform with the presence of crustal-type densities between the reflector and the plate interface (Figure 16). We interpret this deeper unit as the westward extension of the crystalline basement beneath the Sumba Ridge in the seismic profile of *Shulgin et al.* [2009] at 121°E and eventually as the onset of the "Sumba block" [e.g., *Rutherford et al.*, 2001]. In the structural interpretation of *Shulgin et al.* [2009], the seaward dipping interface separates the paleoaccretionary prism from the Sumba Ridge crust, which extends down to the crust-mantle boundary at 26–28 km depth. Hence, these models do not support the presence of a shallow mantle wedge south and east of the island of Sumba.

## 7. Conclusions

[59] The combined analysis of seismic wide-angle reflection and refraction data, multichannel streamer data and shipboard gravity data, reveals the velocity and density structure of the incoming oceanic plate and the overriding plate offshore Lombok and offshore Sumba at the transition to the collisional regime farther east.

[60] 1. Offshore Lombok, the incoming oceanic crust is on average 8.6 km thick and largely devoid of sediment.

Seismic velocities in the crust and in the uppermost mantle are reduced within 40 km seaward of the trench, which coincides with the onset of normal faulting in the bathymetry and MCS seismic data. Velocities of 7.4–7.9 km/s in the uppermost ~2 km beneath the Moho suggest the presence of mantle-penetrating cracks and faults as well as significant degrees of mantle serpentinization.

[61] 2. Velocities in the outer arc high rarely exceed 5.5 km/s down to the top of the subducting slab, which is traced over at least 70 km beneath the fore arc down to ~15 km depth. These bulk velocities are characteristic of an accretionary origin, with highly compacted sediments (possibly partially metamorphosed) at depth. The complex shape of the plate boundary in our models indicates a highly fractured oceanic crust.

[62] 3. In the Lombok Basin up to 3.7 km of sedimentary strata overlies a 9–11 km thick crust which is characterized by an oceanic type velocity structure. Velocities of 7.4–7.8 km/s beneath a distinct Moho reflector suggest a hydrated mantle wedge at ~16 km depth beneath the Lombok Basin, which is also supported by the gravity modeling for this corridor. Because serpentinites are expected at shallow depths in the mantle wedge, they may control, at least partially, the seismological stick-slip behavior of the megathrust; in particular, they may reduce the width of the seismic coupling zone and thus limit the potential magnitude of large subduction megathrust earthquakes offshore Lombok. The system of possible splay faults in the outer arc high, however, demonstrates that potential movements can be transmitted to shallow seafloor portions and thus poses a serious tsunami threat for this margin.

[63] 4. Offshore Sumba, the oceanic crust is on average 9.0 km thick and at greater distance from the trench comprises a thin (<600 m) largely undisturbed sedimentary cover. Within 30 km seawards of the trench, intense fracturing of the crust coincides with a vigorous decrease of crustal velocities. Here, upper mantle velocities reach 7.4–7.8 km/s. If the adjacent Scott Plateau resists to be subducted, pervasive rupture of the oceanic crust and subsequent serpentinization of the underlying mantle may be the effect of increased tensional tectonic forces due to sustained slab-pull.

[64] 5. Slope indentations and the presence of fan-shaped slide deposits in the trench suggest that subduction of pronounced seafloor asperities, including reactivated seafloor fabric and plate-bending faults, locally contribute to the frontal erosion of the lower slope.

[65] 6. From west to east the subducting slab thickens from ~9 km to ~13 km beneath the outer arc high, which we interpret as the transition from the oceanic crust of the Argo Abyssal Plain to the promontory of the Australian continental shelf comprising the Scott Plateau.

[66] 7. Our seismic and gravity models do not support the presence of a shallow mantle wedge beneath the fore arc. A steep seaward dipping reflector in the northernmost model portions of profile 22 may be related to the transition to the "Sumba block" farther north.

[67] **Acknowledgments.** This paper benefited from the constructive reviews by H. Ueda and an anonymous reviewer. The SINDBAD project was funded by the German Federal Ministry of Education and Research (BMBF) under grants 03G0190A and 03G0190B. We would like to thank the master and crew of R/V *Sonne* for their professional assistance during cruise SO190 and the SINDBAD scientific party for their enormous help during data acquisition.

## References

Bialas, J., and E. R. Flueh (1999), Ocean bottom seismometers, *Sea Technol.*, *40*(4), 41–46.

Birch, F. (1961), The velocity of compressional waves in rocks to 10 kilobars, *J. Geophys. Res.*, *66*, 2199–2224, doi:10.1029/JZ066i007p02199.

Bock, Y., L. Prawirodirdjo, J. F. Genrich, C. W. Stevens, R. McCaffrey, C. Subarya, S. S. O. Puntodewo, and E. Calais (2003), Crustal motion in Indonesia from Global Positioning System measurements, *J. Geophys. Res.*, *108*(B8), 2367, doi:10.1029/2001JB000324.

Bostock, M. G., R. D. Hyndman, S. Rondenay, and S. M. Peacock (2002), An inverted continental Moho and the serpentinization of the forearc mantle, *Nature*, *417*, 536–538, doi:10.1038/417536a.

Carlson, R. L., and C. N. Herrick (1990), Densities and porosities in the oceanic crust and their variations with depth and age, *J. Geophys. Res.*, *95*(B6), 9153–9170, doi:10.1029/JB095iB06p09153.

Carlson, R. L., and D. J. Miller (2003), Mantle wedge water contents estimated from seismic velocities in partially serpentinized peridotites, *Geophys. Res. Lett.*, *30*(5), 1250, doi:10.1029/2002GL016600.

Christensen, N. I., and W. D. Mooney (1995), Seismic velocity structure and composition of the continental crust: A global view, *J. Geophys. Res.*, *100*(B6), 9761–9788, doi:10.1029/95JB00259.

Clift, P., and P. Vannucchi (2004), Controls on tectonic accretion versus erosion in subduction zones: Implications for the origin and recycling of the continental crust, *Rev. Geophys.*, *42*, RG2001, doi:10.1029/2003RG000127.

Curray, J. R., G. S. Shor, R. W. Raitt, and M. Henry (1977), Seismic refraction and reflection studies of crustal structure of the eastern Sunda and western Banda arcs, *J. Geophys. Res.*, *82*, 2479–2489, doi:10.1029/JB082i017p02479.

Collot, J.-Y., W. Agudelo, A. Ribodetti, and B. Marcaillou (2008), Origin of a crustal splay fault and its relation to the seismogenic zone and underplating at the erosional north Ecuador–south Colombia oceanic margin, *J. Geophys. Res.*, *113*, B12102, doi:10.1029/2008JB005691.

Contreras-Reyes, E., I. Grevemeyer, E. R. Flueh, M. Scherwath, and M. Heesemann (2007), Alteration of the subducting oceanic lithosphere at the southern central Chile trench–outer rise, *Geochem. Geophys. Geosyst.*, *8*, Q07003, doi:10.1029/2007GC001632.

Dickinson, W. R., and D. R. Seeley (1979), Structure and stratigraphy of forearc regions, *AAPG Bull.*, *63*, 2–31.

Engdahl, E. R., and A. Villaseñor (2002), Global seismicity: 1900–1999, in *International Handbook of Earthquake and Engineering Seismology*, edited by W. H. K. Lee et al., pp. 665–690, doi:10.1016/S0074-6142(02)80244-3, Academic, Amsterdam.

Faccenda, M., T. V. Taras, and L. Burlini (2009), Deep slab hydration induced by bending-related variations in tectonic pressure, *Nat. Geosci.*, *2*, 790–793, doi:10.1038/ngeo656.

Flueh, E. R., N. Vidal, C. R. Ranero, A. Hoijka, R. von Huene, J. Bialas, K. Hinz, D. Cordoba, J. J. Danobeitia, and C. Zelt (1998), Seismic investigations of the continental margin off- and onshore Valparaiso, Chile, *Tectonophysics*, *288*, 251–263, doi:10.1016/S0040-1951(97)00299-0.

Grevemeyer, I., and V. M. Tiwari (2006), Overriding plate controls spatial distribution of megathrust earthquakes in the Sunda–Andaman subduction zone, *Earth Planet. Sci. Lett.*, *251*(3–4), 199–208, doi:10.1016/j.epsl.2006.08.021.

Grevemeyer, I., C. R. Ranero, E. R. Flueh, D. Klaeschen, and J. Bialas (2007), Passive and active seismological study of bending-related faulting and mantle serpentinization at the Middle America trench, *Earth Planet. Sci. Lett.*, *258*, 528–542, doi:10.1016/j.epsl.2007.04.013.

Hall, R. (2002), Cenozoic geological and plate tectonic evolution of SE Asia and the SW Pacific: Computer-based reconstructions, model and animations, *J. Asian Earth Sci.*, *20*, 353–431, doi:10.1016/S1367-9120(01)00069-4.

Hall, R., and H. R. Smyth (2008), Cenozoic arc processes in Indonesia: Identification of the key influences on the stratigraphic record in active volcanic arcs, in *Formation and Applications of the Sedimentary Record in Arc Collision Zones*, edited by A. E. Draut, P. D. Clift, and D. W. Scholl, *Spec. Pap. Geol. Soc. Am.*, 436, 27–54, doi:10.1130/2008.2436(03).

Hamilton, E. L. (1978), Sound velocity–density relations in sea-floor sediment and rocks, *J. Acoust. Soc. Am.*, *63*(2), 366–377, doi:10.1121/1.381747.

Hamilton, W. B. (1988), Plate tectonics and island arcs, *Geol. Soc. Am. Bull.*, *100*, 1503–1527, doi:10.1130/0016-7606(1988)100<1503:PTAIA>2.3.CO;2.

Heine, C., R. D. Mueller, and C. Gaina (2004), Reconstructing the lost Tethys Ocean basin: Convergence history of the SE Asian margin and marine gateways, in *Continent-Ocean Interactions Within East Asian Marginal Seas*, *Geophys. Monogr. Ser.*, vol. 149, edited by P. Clift et al., pp. 37–54, AGU, Washington, D. C.

Heirtzler, J. R., et al. (1974), Site 261, *Initial Rep. Deep Sea Drill. Proj.*, *27*, 129–192.

Hyndman, R. D., and S. M. Peacock (2003), Serpentinization of the forearc mantle, *Earth Planet. Sci. Lett.*, *212*, 417–432, doi:10.1016/S0012-821X(03)00263-2.

Hyndman, R. D., and K. Wang (1993), Thermal constraints on the zone of major thrust earthquake failure: The Cascadia subduction zone, *J. Geophys. Res.*, *98*, 2039–2060, doi:10.1029/92JB02279.

Ivandic, M., I. Grevemeyer, A. Berhorst, E. R. Flueh, and K. McIntosh (2008), Impact of bending related faulting on the seismic properties of the incoming oceanic plate offshore of Nicaragua, *J. Geophys. Res.*, *113*, B05410, doi:10.1029/2007JB005291.

Kieckhefer, R. M., G. G. Shor Jr., J. R. Curray, W. Sugiarta, and F. Hehuwat (1980), Seismic refraction studies of the Sunda Trench and forearc basin, *J. Geophys. Res.*, *85*, 863–889, doi:10.1029/JB085iB02p00863.

Kodaira, S., T. Sato, N. Takahashi, M. Yamashita, T. No, and Y. Kaneda (2008), Seismic imaging of a possible paleoarc in the Izu-Bonin intraoceanic arc and its implications for arc evolution processes, *Geochem. Geophys. Geosyst.*, *9*, Q10X01, doi:10.1029/2008GC002073.

Kopp, H., and N. Kukowski (2003), Backstop geometry and accretionary mechanics of the Sunda margin, *Tectonics*, *22*(6), 1072, doi:10.1029/2002TC001420.

Kopp, H., E. R. Flueh, D. Klaeschen, J. Bialas, and C. Reichert (2001), Crustal structure of the central Sunda margin at the onset of oblique subduction, *Geophys. J. Int.*, *147*, 449–474, doi:10.1046/j.0956-540x.2001.01547.x.

Kopp, H., D. Klaeschen, E. R. Flueh, J. Bialas, and C. Reichert (2002), Crustal structure of the Java margin from seismic wide-angle and multichannel reflection data, *J. Geophys. Res.*, *107*(B2), 2034, doi:10.1029/2000JB000095.

Kopp, H., E. R. Flueh, C. J. Petersen, W. Weinrebe, A. Wittwer, and Meramex Scientists (2006), The Java margin revisited: Evidence for subduction erosion off Java, *Earth Planet. Sci. Lett.*, *242*, 130–142, doi:10.1016/j.epsl.2005.11.036.

Kopp, H., D. Hindle, D. Klaeschen, O. Oncken, C. Reichert, and D. Scholl (2009), Anatomy of the western Java plate interface from depth-migrated seismic images, *Earth Planet. Sci. Lett.*, *288*, 399–407, doi:10.1016/j.epsl.2009.09.043.

Korenaga, J., W. Holbrook, G. Kent, P. Kelemen, R. Detrick, H.-C. Larsen, J. Hopper, and T. Dahl-Jensen (2000), Crustal structure of the southeast Greenland margin from joint refraction and reflection seismic tomography, *J. Geophys. Res.*, *105*(B9), 21,591–21,614, doi:10.1029/2000JB900188.

Korenaga, J., W. S. Holbrook, R. S. Detrick, and P. B. Kelemen (2001), Gravity anomalies and crustal structure across the southeast Greenland margin, *J. Geophys. Res.*, *106*, 8853–8870, doi:10.1029/2000JB900416.

Lay, T., et al. (2005), The Great Sumatra-Andaman earthquake of 26 December 2004, *Science*, *308*(5725), 1127–1133, doi:10.1126/science.1112250.

Lüschen, E., C. Mueller, H. Kopp, M. Engels, R. Lutz, L. Planert, A. Shulgin, and Y. Djajadihardja (2010), Structure, evolution and tectonic activity at the eastern Sunda forearc, Indonesia, from marine seismic investigations, *Tectonophysics*, doi:10.1016/j.tecto.2010.06.008, in press.

Lynnes, C. S., and T. Lay (1988), Source process of the great 1977 Sumba earthquake, *J. Geophys. Res.*, *93*(B11), 13,407–13,420, doi:10.1029/JB093iB11p13407.

Moore, G. F., N. L. Bangs, A. Taira, S. Kuramoto, E. Pangborn, and H. J. Tobin (2007), Three-dimensional splay fault geometry and implications for tsunami generation, *Science*, *318*, 1128–1131, doi:10.1126/science.1147195.

Mueller, C., and S. Neben (Eds.) (2006), *Cruise report: SO190 Leg 1: Seismic and geoacoustic investigations along the Sunda-Banda Arc transition*, 142 pp., Bundesanstalt für Geowiss. und Rohstoffe, Hannover, Germany.

Müller, C., et al. (2008), From subduction to collision: The Sunda-Banda arc transition, *Eos Trans. AGU*, *89*(6), 49–60, doi:10.1029/2008EO060001.

Newcomb, K. R., and W. R. McCann (1987), Seismic history and seismotectonics of the Sunda arc, *J. Geophys. Res.*, *92*, 421–439, doi:10.1029/JB092iB01p00421.

Oleskevich, D. A., R. D. Hyndman, and K. Wang (1999), The updip and downdip limits to great subduction earthquakes: Thermal and structural models of Cascadia, south Alaska, SW Japan, and Chile, *J. Geophys. Res.*, *104*(B7), 14,965–14,991, doi:10.1029/1999JB900060.

Parker, R. L. (1973), The rapid calculation of potential anomalies, *Geophys. J. R. Astron. Soc.*, *31*, 447–455, doi:10.1111/j.1365-246X.1973.tb06513.x.

Peacock, S. M. (2001), Are the lower planes of double seismic zones caused by serpentine dehydration in subducting oceanic mantle, *Geology*, *29*(4), 299–302, doi:10.1130/0091-7613(2001)029<0299:ATLPOD>2.0.CO;2.

Ranero, C. R., J. Phipps-Morgan, K. McIntosh, and C. Reichert (2003), Bending-related faulting and serpentinzation at the Middle America trench, *Nature*, *425*, 367–373, doi:10.1038/nature01961.

Ranero, C. R., I. Grevemeyer, H. Sahling, U. Barckhausen, C. Hensen, K. Wallmann, W. Weinrebe, P. Vannucchi, R. von Huene, and K. McIntosh (2008), Hydrogeological system of erosional convergent margins and its influence on tectonics and interplate seismogenesis, *Geochem. Geophys. Geosyst.*, *9*, Q03S04, doi:10.1029/2007GC001679.

Rutherford, E., K. Burke, and J. Lytwyn (2001), Tectonic history of Sumba Island, Indonesia, since the Late Cretaceous and its rapid escape into forearc in the Miocene, *J. Asian Earth Sci.*, *19*, 453–479, doi:10.1016/S1367-9120(00)00032-8.

Rüpke, L. H., J. P. Morgan, M. Hort, and J. A. D. Conolly (2004), Serpentine and the subduction zone water cycle, *Earth Planet. Sci. Lett.*, *223*, 17–34, doi:10.1016/j.epsl.2004.04.018.

Schlüter, H. U., C. Gaedicke, H. A. Roeser, B. Schreckenberger, H. Meyer, C. Reichert, Y. Djajadihardja, and A. Prexl (2002), Tectonic features of the southern Sumatra-western Java forearc of Indonesia, *Tectonics*, *21*(5), 1047, doi:10.1029/2001TC901048.

Shulgin, A., H. Kopp, C. Mueller, E. Lüschen, L. Planert, M. Engels, E. R. Flueh, A. Krabbenhoeft, and Y. Djajadihardja (2009), Sunda-Banda arc transition: Incipient continent-island arc collision (northwest Australia), *Geophys. Res. Lett.*, *36*, L10304, doi:10.1029/2009GL037533.

Sibuet, J.-C., et al. (2007), 26th December 2004 great Sumatra–Andaman earthquake: Co-seismic and postseismic motions in northern Sumatra, *Earth Planet. Sci. Lett.*, *263*, 88–103, doi:10.1016/j.epsl.2007.09.005.

Simons, W. J. F., et al. (2007), A decade of GPS in Southeast Asia: Resolving Sundaland motion and boundaries, *J. Geophys. Res.*, *112*, B06420, doi:10.1029/2005JB003868.

Smyth, H. R., P. J. Hamilton, R. Hall, and P. D. Kinny (2007), The deep crust beneath island arcs: Inherited zircons reveal a Gondwana continental fragment beneath East Java, Indonesia, *Earth Planet. Sci. Lett.*, *258*, 269–282, doi:10.1016/j.epsl.2007.03.044.

Smyth, H. R., R. Hall, and G. J. Nichols (2008), Cenozoic volcanic arc history of East Java, Indonesia: The stratigraphic record of eruptions on an active continental margin, in *Lessons From the Stratigraphic Record in Arc Collision Zones*, edited by A. E. Draut, P. D. Clift, and D. W. Scholl, *Spec. Pap. Geol. Soc. Am.*, 436, 27–54, doi:10.1130/2008.2436(10).

Spence, W. (1986), The 1977 Sumba earthquake series: Evidence for slab pull force acting at a subduction zone, *J. Geophys. Res.*, *91*(B7), 7225–7239, doi:10.1029/JB091iB07p07225.

Špičák, A., V. Hanuš, and J. Vaněk (2007), Earthquake occurrence along the Java trench in front of the onset of the Wadati-Benioff zone: Beginning of a new subduction cycle?, *Tectonics*, *26*, TC1005, doi:10.1029/2005TC001867.

Tatsumi, Y., H. Shukuno, K. Tani, N. Takahashi, S. Kodaira, and T. Kogiso (2008), Structure and growth of the Izu-Bonin-Mariana arc crust: 2. Role of crust-mantle transformation and the transparent Moho in arc crust evolution, *J. Geophys. Res.*, *113*, B02203, doi:10.1029/2007JB005121.

Toomey, D. R., and G. R. Foulger (1989), Tomographic inversion of local earthquake data from the Hengill-Grensdalur central volcano complex, Iceland, *J. Geophys. Res.*, *94*, 17,497–17,510, doi:10.1029/JB094iB12p17497.

Van der Werff, W. (1995), Structure and morphotectonics of the accretionary prism along the eastern Sunda–western Banda Arc, *J. Southeast Asian Earth Sci.*, *11*, 309–322, doi:10.1016/0743-9547(94)00038-G.

Wiener, N. (1949), *Extrapolation, Interpolation, and Smoothing of Stationary Time Series*, John Wiley, New York.

E. R. Flueh, H. Kopp, A. Krabbenhoeft, L. Planert, and A. Shulgin, IFM-GEOMAR, Leibniz Institute of Marine Sciences at the University of Kiel, Wischhofstr. 1-3, D-24148, Germany. (lplanert@ifm-geomar.de)

E. Lueschen and C. Mueller, BGR, Federal Institute for Geosciences and Natural Resources, Stilleweg 2, D-30655 Hannover, Germany.

Y. Djajadihardja, BPPT, Agency for the Assessment and Application of Technology, Jl. M.H. Thamrin No. 8, Jakarta 10340, Indonesia.

# 7

Kopp, H., Hindle, D., Klaeschen, D., Oncken, O., Scholl, D., 2009.

**Anatomy of the western Java plate interface from depth-migrated seismic images.**

Earth Planet. Sci. Lett., doi:10.1016/j.epsl.2009.09.043.

Earth and Planetary Science Letters 288 (2009) 399–407

Contents lists available at ScienceDirect

Earth and Planetary Science Letters

journal homepage: www.elsevier.com/locate/epsl

# Anatomy of the western Java plate interface from depth-migrated seismic images

H. Kopp [a,*], D. Hindle [a], D. Klaeschen [a], O. Oncken [b], C. Reichert [c], D. Scholl [d]

[a] IFM-GEOMAR, Leibniz Institute of Marine Sciences, Wischhofstr. 1-3, 24148 Kiel, Germany
[b] GeoForschungsZentrum Potsdam, Potsdam, Germany
[c] BGR Federal Institute of Geosciences and Natural Resources, Hannover, Germany
[d] U.S. Geological Survey, Menlo Park, CA, USA

ARTICLE INFO

*Article history:*
Received 25 July 2009
Received in revised form 28 September 2009
Accepted 28 September 2009
Available online 27 October 2009

Editor: R.D. van der Hilst

*Keywords:*
décollement
splay fault
prestack depth migration
subduction zone
tsunami earthquake
Indonesia

ABSTRACT

Newly pre-stack depth-migrated seismic images resolve the structural details of the western Java forearc and plate interface. The structural segmentation of the forearc into discrete mechanical domains correlates with distinct deformation styles. Approximately 2/3 of the trench sediment fill is detached and incorporated into frontal prism imbricates, while the floor sequence is underthrust beneath the décollement. Western Java, however, differs markedly from margins such as Nankai or Barbados, where a uniform, continuous décollement reflector has been imaged. In our study area, the plate interface reveals a spatially irregular, nonlinear pattern characterized by the morphological relief of subducted seamounts and thicker than average patches of underthrust sediment. The underthrust sediment is associated with a low velocity zone as determined from wide-angle data. Active underplating is not resolved, but likely contributes to the uplift of the large bivergent wedge that constitutes the forearc high. Our profile is located 100 km west of the 2006 Java tsunami earthquake. The heterogeneous décollement zone regulates the friction behavior of the shallow subduction environment where the earthquake occurred. The alternating pattern of enhanced frictional contact zones associated with oceanic basement relief and weak material patches of underthrust sediment influences seismic coupling and possibly contributed to the heterogeneous slip distribution. Our seismic images resolve a steeply dipping splay fault, which originates at the décollement and terminates at the sea floor and which potentially contributes to tsunami generation during co-seismic activity.



## 1. Introduction

Active convergent margins displaying sediment accretion as the predominant mode of mass transfer have been identified as an end-member type of subduction zones (von Huene and Scholl, 1991; Clift and Vannucchi, 2004). In these systems, sediment may be added to the toe of the margin wedge forming a frontal prism (frontal accretion) or at depth to the base of the upper plate causing uplift (underplating or basal accretion) or both (Moore and Silver, 1987). Basal accretion requires sediment underthrusting beyond the frontal accretionary prism along the décollement zone. Décollements at accretionary margins form detachments between the upper deforming accretionary prism and the underthrusting sequence (Chapple, 1978; Davis et al., 1983) and at some margins continuous, high-amplitude horizons have been imaged for tens of kilometers landward of the deformation front (e.g. Barbados (Westbrook et al., 1988; Shipley et al., 1994), and Nankai (Moore et al., 1990; Bangs et al., 2009)).

Décollement reflection characteristics have been analyzed at the Nankai and Barbados margins to reveal spatial variations of fault properties (e.g. Shipley et al., 1994; Bangs et al., 1996, 1999, 2004; Park et al., 2002a; Tsuji et al., 2005). Underneath the northern Barbados accretionary prism, the décollement zone encompasses a heterogeneously consolidating sedimentary sequence (Moore et al., 1998). Pore fluid pressures in excess of hydrostatic within the underthrust sequence have been predicted by e.g. Saffer (2003) and Tsuji et al. (2008) off Muroto (Nankai) and by e.g. Bekins et al. (1995) for Barbados. Elevated pore pressures beneath the décollement are linked to a decrease in effective stress along the plate boundary (e.g. Skarbek and Saffer, 2009) and are related to the onset of the seismogenic zone (e.g. Moore and Saffer, 2001). Calahorrano et al. (2008) recently quantified physical and mechanical property variations of the underthrusting sedimentary sequence using seismic velocities along the southern Ecuador margin. A common aspect of all these studies is that they reveal a complicated, non-uniform pattern of physical properties along the décollement zone.

Here we present the detailed structure of the accretionary convergent margin off western Java. Frontal accretion has previously been imaged along this central segment of the Sunda margin off southern Sumatra to western Java from refraction/reflection seismics and bathymetric data (Kopp et al., 2001; Schlueter et al., 2002; Kopp et al., 2002, 2008). Mass balance calculations indicate a subduction history dominated by accretion since the Late Eocene (Kopp and Kukowski, 2003). In this study, based on pre-stack depth-migrated

* Corresponding author. Now at: Freiburg University, Freiburg, Germany. Tel.: +49 431 6002334.
*E-mail address:* hkopp@ifm-geomar.de (H. Kopp).

0012-821X/$ – see front matter © 2009 Elsevier B.V. All rights reserved.
doi:10.1016/j.epsl.2009.09.043

seismic reflection data, we resolve the anatomy of the plate boundary fault. The 190 km long multichannel seismic (MCS) line SO137-03 is located across the western Java forearc (Fig. 1), covering the trench, frontal prism, active and fossil accretionary prisms (forearc high) and forearc basin (Fig. 2). Acquired in 1998 and using a 3500 m long source–receiver offset, these data comprise the highest quality MCS profile available in the area and are complemented by velocity information gained from coincident refraction data (ocean-bottom hydrophone (OBH) line SO138-05, Fig. 1) (Kopp et al., 2001). Wide-angle velocity information was incorporated into the pre-stack depth migration (Fig. 3). We applied an iterative migration procedure, which uses seismic velocities constrained by focusing analyses and common reflection point gathers (Mackay and Abma, 1993). Seismic velocities used during the migration process are interval velocities. The energy of a reflection point in the subsurface is focused using a range of velocities until an optimal image is achieved, which provides the highest energy at zero offset. Using an ideal velocity, the reflection position will be corrected. This in turn will yield better constraints on velocities during the next iteration and ray paths are determined more accurately. Pre-stack depth migration thus images complex, dipping structures even in the presence of a strong lateral velocity gradient far better than conventional time migration procedures (Guo and Fagin, 2002).

## 2. Margin architecture

### 2.1. Structural segmentation of the forearc

The central Sunda margin off western Java to southern Sumatra marks the transition from orthogonal convergence in the east to oblique subduction to the northwest (Fig. 1) (e.g. Hamilton, 1979; Lelgemann et al., 2000). The broad-scale margin architecture (Fig. 2), which is predominantly characterized by the evolution of an asymmetrical bivergent wedge (Willet et al., 1993; Hoth et al., 2007), arises from a compressive regime related to the active subduction of the Indo-Australian plate underneath Eurasia since the Eocene (Hall and Smyth, 2008). Initial formation of the wedge occurred against the original arc rock framework, which is of continental origin off Sumatra and its character changes to an oceanic-type basement rock off western Java, as inferred from seismic and gravity data (Kieckhefer et al., 1980; Grevemeyer and Tiwari, 2006). The seaward tapering terminus of this original margin wedge is located under the forearc basin and during the early phases of subduction served as backstop to the juvenile accretionary wedge. This deep-lying boundary previously remained unresolved in conventional processing (Kopp et al., 2001), but is now imaged in the pre-stack depth-migrated section as a highly reflective transition zone (Fig. 4). It coincides with a decisive increase in seismic velocities as revealed by refraction models (Kopp and Kukowski, 2003).

The now quiescent, >80 km wide accretionary wedge (Schlueter et al., 2002), termed the inner wedge' (Fig. 1) fronts the forearc basin and forms the forearc high with vertical dimensions exceeding 15 km between the seafloor and the subducting plate (Kopp and Kukowski, 2003). Accretion rates are sufficiently high for a landward slope to develop at the transition from the inner wedge to the forearc basin (Fig. 4), similar to corresponding structures offshore Sumatra (Moore et al., 1980; Karig et al., 1980a) or offshore Bali/Lombok (Planert et al., in review). Continued wedge growth results in thrusting at the rear (km 125–140), causing progressive deformation of the lower forearc

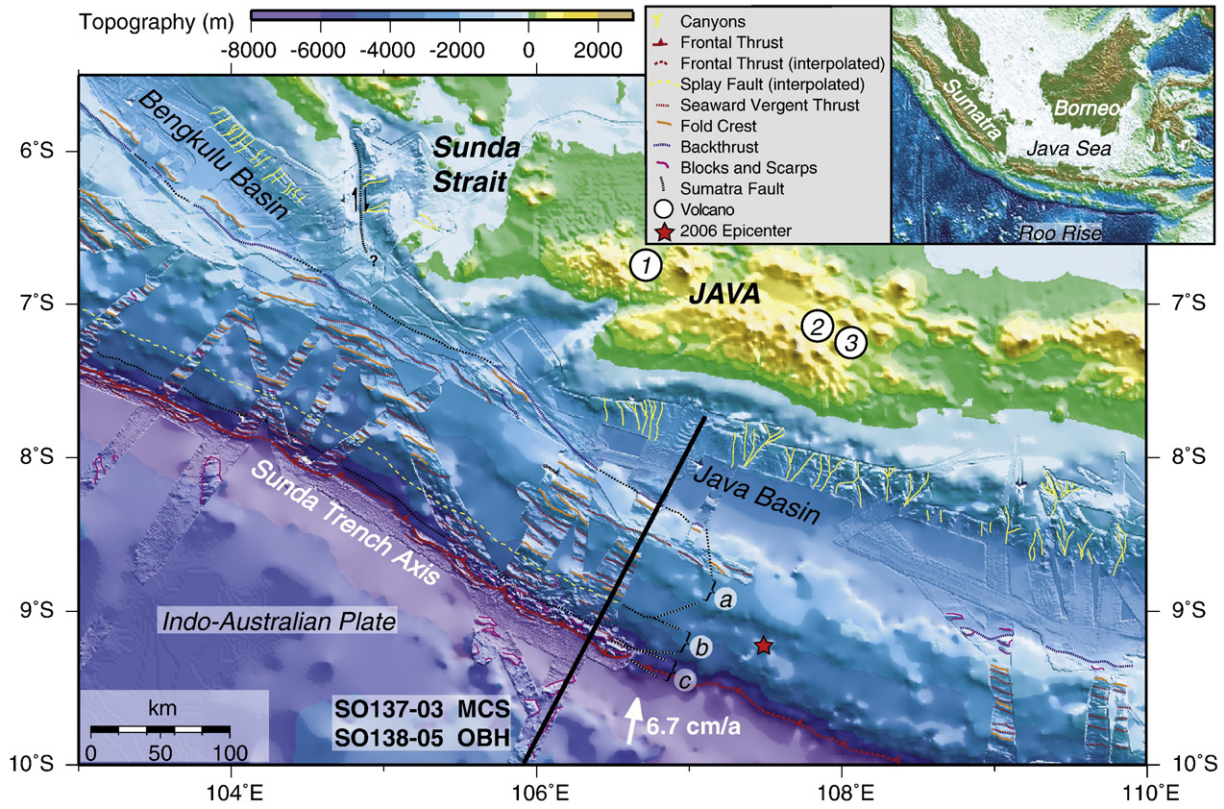


**Fig. 1.** Shaded bathymetry map of the Sunda trench offshore western Java. Global relief (Amante and Eakins, 2008) is overlain by high-resolution ship track data acquired by RV SONNE (cruises SO137, SO138, SO139, SO176, SO179). Morphotectonic interpretation is based on high-resolution swath data as well as existing seismic data (Schlueter et al., 2002; Kopp and Kukowski, 2003). Thick black line: coincident seismic reflection and refraction profile SO137-03/SO138-05. Forearc segmentation correlates with structural domains: a = Inner Wedge, b = Outer Wedge, c = Frontal Prism. Yellow stippled line tracks surface trace of splay fault system. Star shows epicenter of 2006 Java tsunami earthquake. White circles show western Java volcanoes for which magma geochemical data exist: 1 = Mt. Salak, 2 = Mt. Guntur, 3 = Mt. Gallunggung. Inset shows study area on the Sunda margin.

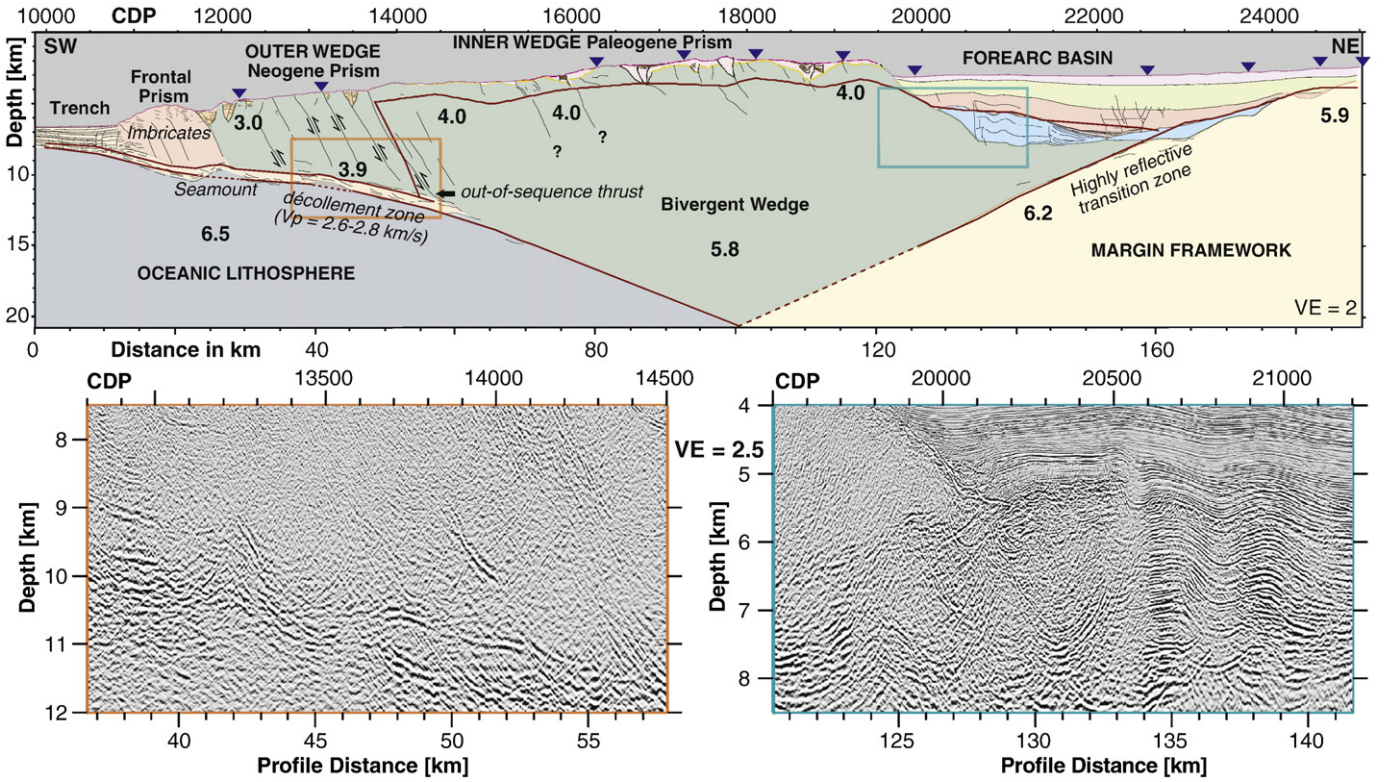


**Fig. 2.** Structural interpretation (upper panel) and depth-migrated seismic images of the décollement zone (lower left) and seaward limit of the forearc basin (lower right). Colored boxes in the upper panel indicate location of seismic data examples displayed below. The margin macrostructure consists of a >6000 m deep trench adjacent to a frontal prism characterized by imbricate thrusting. The large bivergent wedge is composed of an outer wedge (Neogene accretionary prism) and an inner wedge (Paleogene accretionary prism) (compare Fig. 1).

basin sediment infill as imaged along the seaward margin of the basin in the MCS data (Fig. 2 inset). The upper strata onlap the inner wedge and are only moderately warped.

The internal seismic structure of the inner wedge exhibits limited coherency (Fig. 4), probably due to late stage deformation dismembering former accreted sediment slices, as also seen in the Nankai margin (Moore et al., 1990). Internal deformation of the inner wedge is, at least episodically, persistent, as documented by active out-of-sequence thrusting, which offsets the seafloor (Fig. 2, e.g. around profile km 70–80 and 100). The internal deformation documented by inner wedge thrusting compensates geometry re-arrangements to adjust to boundary conditions and wedge strength (Davis, 1996). Due to limited resolution, the depth extent of these thrust faults remains undetermined.

Fronting the inner, fossil wedge is the outer, Neogene wedge, which is characterized by landward-dipping, thrust-bound sheets each approximately 4–6 km wide (Fig. 3). The imbricate thrusting results in an arcward thickening from 5.5 km at the seaward limit to over 7 km at the transition to the inner wedge (i. e., over a distance of less than 25 km). Tectonic thickening by imbrication is a commonly observed process in accretionary subduction zones where the wedge becomes progressively more consolidated and cemented towards the arc (e.g. von Huene et al., 2009). The outer wedge represents a compressive zone with discrete localization of deformation along the thrust faults. The transition from the outer wedge to the inner wedge is marked by a splay fault system, whose surface trace is recognized in multibeam bathymetry for at least 600 km along strike of the margin (Fig. 1) (Kopp and Kukowski, 2003). A megasplay fault system forming a comparable structural segment boundary and mechanical discontinuity has recently been imaged along the Nankai subduction zone in 2-D and 3-D seismic data (Park et al., 2000, 2002b; Moore et al., 2007; Bangs et al., 2009), along the Ecuador–Colombia margin (Collot et al., 2008) and offshore Bali–Lombok (Lueschen et al., in review).

The internal structure of the inner and outer wedges reflects their evolution history: the lateral growth of the inner wedge is mainly attained by tectonic addition of material from the outer wedge (von Huene et al., 2009). Both wedges are uniformly developed from Sumatra to western Java (compare Fig. 1). They form a characteristic feature along those margin segments dominated by accretionary processes. Off central Java (110°E), however, where underthrusting of an oceanic plateau is occurring, inner and outer wedges cannot be uniquely distinguished and a frontal prism, which is present trenchward of the outer wedge off western Java (Fig. 1), is missing entirely owing to recent and ongoing erosion (Kopp et al., 2006). A structural segmentation similar to our seismic line, however, is also observed along the erosion-dominated Ecuador–Colombia margin, as described by Collot et al. (2008), implying that this general segmentation is not a direct function of material flux (i.e. accretion or erosion).

### 2.2. Décollement zone and plate boundary structures

Approximately 1.9 km of sediment is found at the deformation front in the sector of the Java trench (Fig. 3) covered by our seismic line. Normal faulting of the lower trench sediment sequence precedes the compressional deformation in the ~13 km wide frontal prism. Normal faulting in the incoming hemipelagic sediments has also been observed in the Nankai subduction zone (Heffernan et al., 2004), where polygonal fault patterns are attributed to differential compaction above irregular oceanic basement.

Seaward growth of the frontal prism occurs by tectonic addition of detached lower plate sediment (Kopp et al., 2001, 2002). Trench sediment uplift is initiated by displacement along a frontal thrust, abruptly truncating the upper portion of the stratified trench sequences at the deformation front and marking the onset of horizontal shortening and contractive deformation of the frontal prism (Fig. 3). Imbricate thrusting is the dominant structural style of the frontal prism, similar to

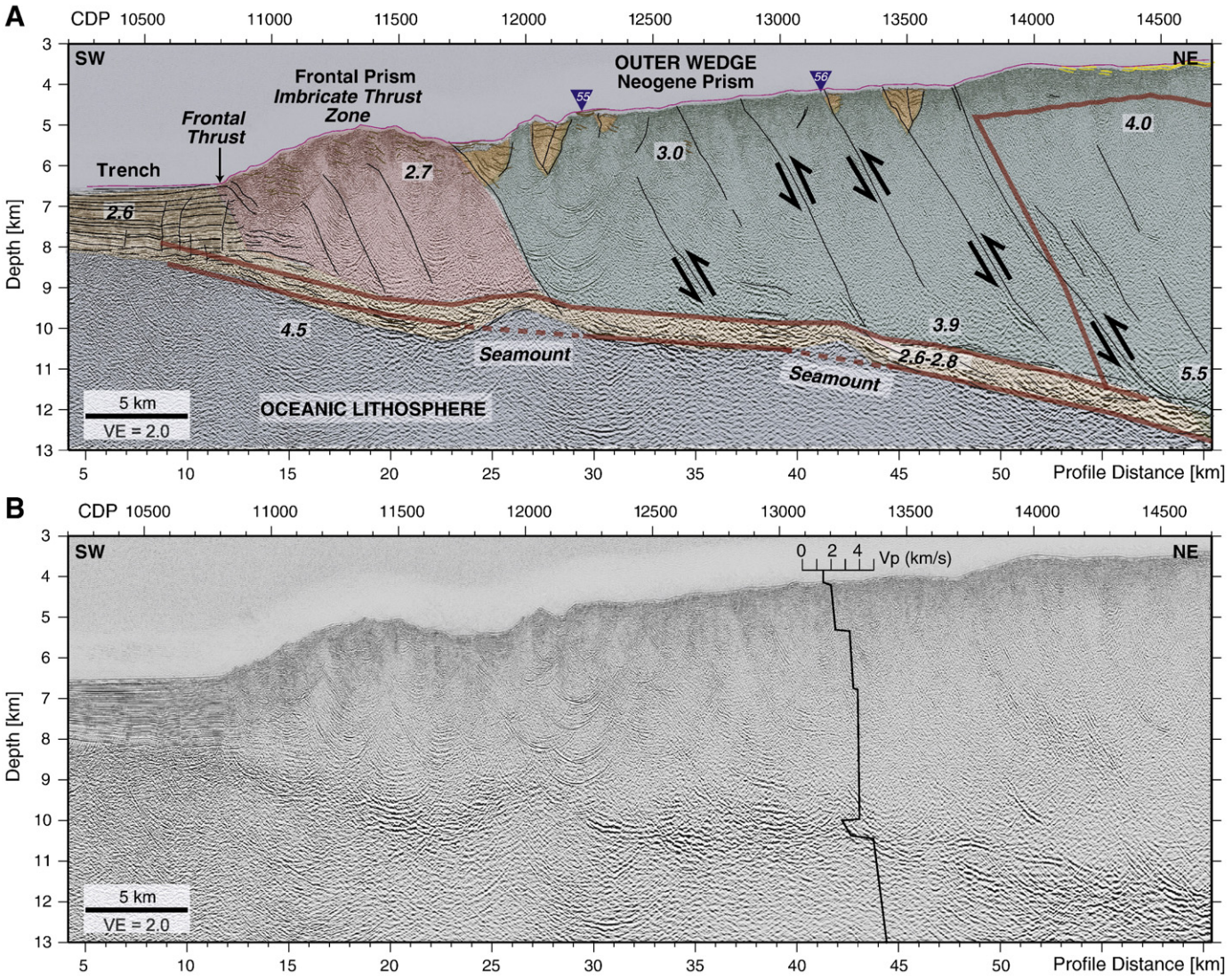


**Fig. 3.** Pre-stack depth-migrated seismic images of MCS profile SO137-03 (location shown in Fig. 1). A: seismic image of the trench, frontal prism and outer wedge overlain by the interpretive linedrawing of Fig. 2. Thick red lines trace velocity-based boundaries of the corresponding wide-angle model. Numbers are seismic velocities in km/s. Blue triangles denote ocean-bottom hydrophone positions. B: corresponding seismic image. Shortening is accommodated by imbricate thrusting of the frontally accreted sediment in the frontal prism. Approximately 1/3 of the trench material is underthrust beneath the frontal prism in a 500–900 m thick décollement zone, characterized by discontinuous high amplitudes. An upward bulging of the reflective band indicates the location of two subducted oceanic basement highs between 25–29 km and 41–44 km offset, likely small seamounts of approximately 1.4 km and 0.8 km height, respectively. The v–z function of OBH 56 is displayed, showing the seismic velocity inversion in the décollement zone.

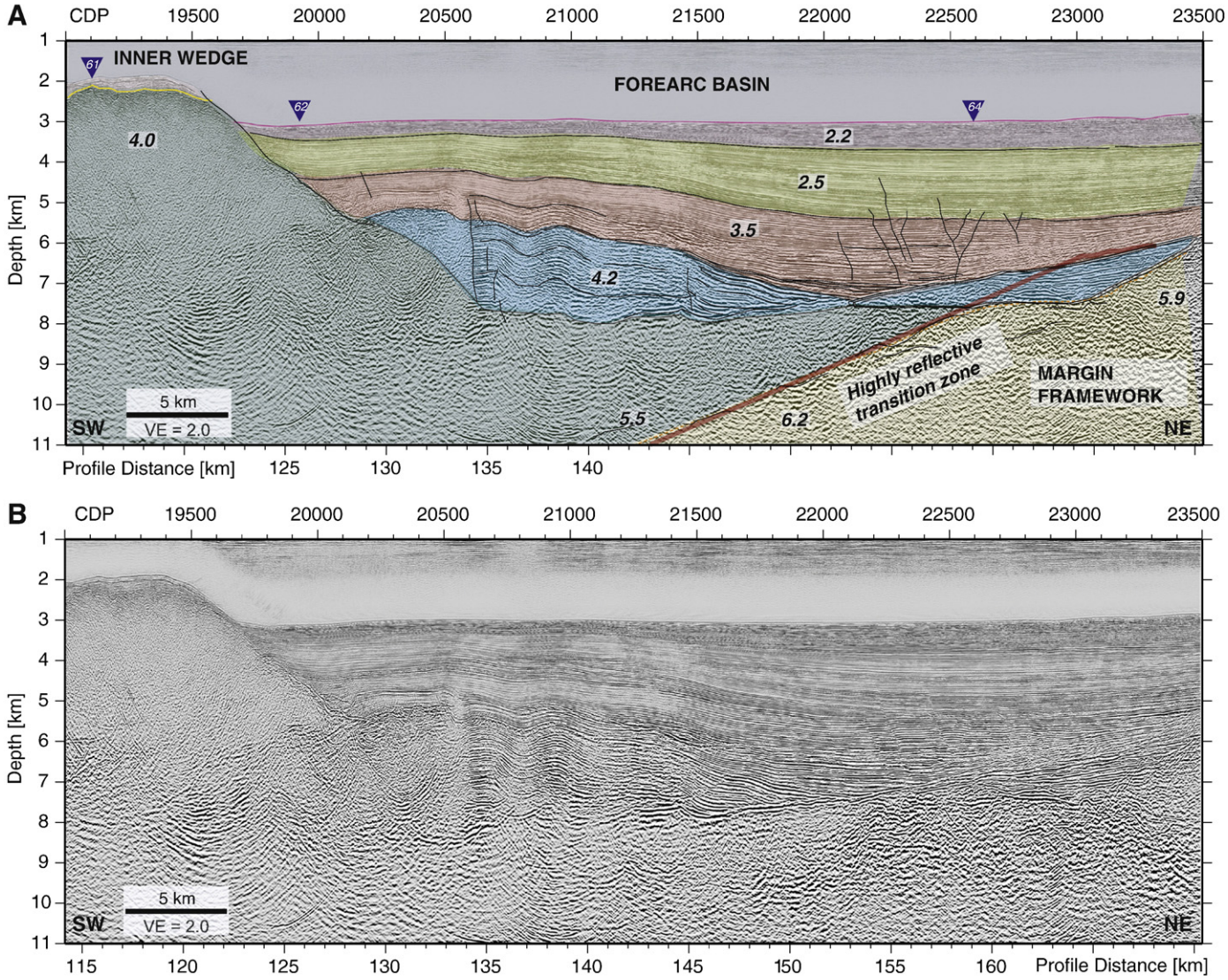


**Fig. 4.** A: seismic image of the landward portion of the inner wedge and the forearc basin. (Display information as in Fig. 3) B: corresponding seismic image. Thrusting causes deformation of the lower sedimentary units of the seaward portion of the forearc basin (around km 125–140). The highly reflective zone below the basin at ~150 km offset corresponds to a first-order velocity boundary observed in the refraction data. This transition from the inner wedge to the original margin framework plays an important role in the margin kinematics and the formation of a bivergent wedge, but is commonly not observed in reflection data because of limited energy penetration.

the folding and thrusting observed off Nias Island offshore Sumatra (Moore and Curray, 1980; Karig et al., 1980b; Franke et al., 2008). The intense deformation observed here is common for prisms experiencing mass transfer by sediment accretion (e.g. Cascadia (MacKay et al., 1992; Cochrane et al., 1994) or South Chile (Polonia et al., 2007)), though the deformation pattern off Java is more complex than e.g. the classical fold-and-thrust belt with hanging wall anticlines observed in Nankai (Taira et al., 1991; Moore et al., 2001). However, the increase in thickness and length of the imbricate sequences from the frontal prism to the outer wedge as seen off Java has also been observed in the Muroto transect of the Nankai subduction zone (Bangs et al., 2004).

The floor sediment sequence in the proto-thrust zone of the trench is bound on top by a proto-décollement located approximately 700 m above the oceanic basement (Fig. 3). It is in the proto-thrust zone that slip along the décollement is initiated (Tsuji et al., 2005). The stratigraphic level of the décollement is typically governed by changes in physical properties (e.g. Le Pichon et al., 1993; Moore et al., 1998; Bangs et al., 2004) or may be controlled by lithology (MacKay, 1995). Whereas in Nankai (e.g. Moore et al., 1990; Bangs et al., 2006; Moore et al., 2007), Barbados (e. g. Bangs and Westbrook, 1991; Shipley et al., 1994), Ecuador (Calahorrano et al., 2008), and Costa Rica (e.g. Saffer, 2003) a distinct, sharp décollement reflector forms above a minimally deformed subducted section that still retains a stratified structure, a band of semi-continuous, high-amplitude, low-frequency landward-dipping reflections delineates the interplate boundary off Java (Fig. 3) and coincides with the plate interface observed in the corresponding wide-angle data. A moderate strength contrast between overlying, accreting sediment and the underthrusting sequence landward of the deformation front may explain why a sharp décollement reflection similar to Nankai or Barbados is not observed off Java (Tsuji et al., 2008).

The ~500–900 m thick, high-amplitude reflective zone overlying the oceanic basement is resolved to a depth of 15 km underneath the frontal prism and the outer wedge (Fig. 3), but loses its distinct seismic character underneath the inner, fossil accretionary wedge. The interpretation as a décollement zone is supported by the velocity information gained from the wide-angle data, which reveal a low velocity zone associated with the underthrust sediment (Fig. 3). A similar velocity inversion has been identified from pre-stack depth-migrated data e.g. at Nankai (Costa Pisani et al., 2005) and Ecuador (Sage et al., 2006; Calahorrano et al., 2008), where comparable velocity values (2.6 km/s – 2.8 km/s) have been determined. Subducting oceanic basement relief modulates the thickness of the décollement zone, which thins above two subducting seamounts identified between profile km 25–29 and km 41–44, while adjacent lows (at km 19–22, km 37–40 and km 47–53) carry thicker than average sediment. An analogous pattern has also been observed along the Ecuadorian margin (Sage et al., 2006). In addition, differential subduction rates and sediment supply to the trench will result in a variable thickness of the décollement zone, as observed off Java (Fig. 3).

Similar reflective zones have been attributed to subduction erosion involving underthrust sediment and upper plate material fragments disintegrated by hydrofracturing and fluid-induced erosive processes, causing enhanced reflectivity (Sage et al., 2006; Ranero et al., 2008). However, instead of subsidence of the forearc as commonly associated with subduction erosion (von Huene et al., 2004), the Java forearc is experiencing uplift (Schlueter et al., 2002). We thus speculate that basal accretion of trench sediment underthrust beyond the frontal prism and the outer wedge contributes to the vertical growth of the forearc high. Active underplating has previously been observed in pre-stack depth-migrated data e.g. underneath the Nankai accretionary wedge (Park et al., 2002a), where a down stepping of the décollement at ~25 km and at ~45 km landward of the deformation front is resolved in 3-D data (Bangs et al., 2004) and is associated with material transfer to the base of the upper plate, resulting in complete underplating of the entire underthrust sequence. Offshore Alaska, underplating of long, undeformed sheets is observed (Gutscher et al., 1998).

Underthrust sediment that is not underplated but transported to mantle depths of magma generation (~100 km) is often recognized by its imprint on arc magma chemistry (Plank and Langmuir, 1993; Stern, 2002). Underplating is not clearly resolved in our depth section, partially due to multiple interference. Minimal sediment recycling to mantle depth, however, is supported by geochemical data from western Java volcanoes Mt. Guntur and Mt. Gallunggung (Fig. 1), which indicate a low Th/La ratio (Plank, 2005). Other volcanic centers in western Java, however, show more complex differentiation and contamination processes. Mt. Salak is the best-studied volcano today in western Java (Fig. 1) (Handley et al., 2008). Geochemical evidence from Mt. Salak indicates the incorporation of subducted sediment with Nd–Hf isotopic data suggesting a high terrigenous component (Handley et al., 2008). However, the young sediments in the trench and underneath the frontal prism today do not interact with the source of present-day Sunda arc magmas (Gasparon and Varne, 1998) due the potential recycling period of 4 Ma (based on a convergence rate of 6.7 cm/a and a magma-generating depth of 100 km). The geochemical variability and isotopic heterogeneity observed along the Sunda margin (Handley, 2006) reflect the variability of near-trench subduction processes. Reflection seismic data acquired along the Sunda margin (Moore and Curray, 1980; Karig et al., 1980b; Moore et al., 1980, 1982; Schlueter et al., 2002; Franke et al., 2008; Mueller et al., 2008; Singh et al., 2008; Lueschen et al., in review) in combination with refraction data (Kopp and Kukowski, 2003, Kopp et al., 2006; Shulgin et al., 2009; Planert et al., in review) show a remarkable variation in the amount of sediment accreted to the frontal prism or underthrust in the décollement zone. The existence of a large bivergent accretionary wedge implies, however, that only a small fraction of the underthrust sediment is subducted to mantle depth. The marked differences in the deformational framework along strike of the Sunda margin have also been documented for other subduction zones, e.g. at Nankai (Moore et al., 2001) or southern Chile (Polonia et al., 2007) and have been attributed to variations in lithology, physiography of the incoming plate and physical property variations of the prism and décollement zone.

## 3. Seismogenic processes

Our seismic profile is located approximately 100 km west of the 2006 Java tsunami earthquake epicenter (Fig. 1). Co-seismic strain release of this event involved the shallow portion of the megathrust and triggered a tsunami, which caused more than 630 casualties (Ammon et al., 2006). In the shallow subduction environment, the anatomy of the décollement zone regulates the friction behavior of the megathrust fault, which is influenced by the thickness and physical properties of the underthrust sediment as well as by lower plate basement relief (Bilek, 2007). Based on the model by Bilek and Lay (2002), several authors have speculated that the 2006 Java earthquake involved rupture of regions of unstable friction embedded in areas of conditionally stable material, resulting in the observed slip heterogeneity (Ammon et al., 2006; Bilek and Engdahl, 2007). Subducted high-relief features, including seamounts, ridges or fracture zones, may account for locally enhanced frictional contacts (e.g. Bilek, 2007; Lay and Bilek, 2007) along the Java margin, which otherwise shows low seismic coupling (Newcomb and McCann, 1987; Pacheco et al., 1993). Direct evidence for features causing strong coupling patches for the 2006 event is missing so far due to lack of seismic data. The 1994 Java tsunami earthquake off eastern Java is associated with a subducted seamount, which can be identified in the bathymetric data (Abercrombie et al., 2001). Our seismic line shows two moderate sized seamounts subducted beneath the outer wedge whose passage has left no surface trace. Though our seismic line lies east of the slip region, the tectonic setting of the 2006 rupture area is comparable and we speculate that similar subducted lower plate relief will influence seismogenesis there. The heterogeneous plate interface off western Java is characterized by marked morphological structure,

which potentially serves as an asperity and nucleus to an earthquake. Energy would subsequently be transferred into weaker material patches, as imaged along our profile, thus slowing energy propagation (Bilek and Engdahl, 2007). A retreat of the deformation front seaward of the epicenter location as well as the local morphological structure in the vicinity of the epicenter are indicative of subducted seafloor relief deforming the upper plate (Fig. 1).

The 1992 Nicaragua tsunami earthquake was a comparable event (Ammon et al., 2006; Lay and Bilek, 2007). At least three moderately-sized subducted seamounts (1–2 km high) have been identified from seismic data in the zones of enhanced moment release (McIntosh et al., 2007). The Java and Nicaragua margins, however, show fundamental differences: igneous oceanic crust extents close to the trench off Nicaragua, while an accretionary prism characterizes the upper plate off Java. This may be the cause why subducted seamounts, which are present in both margins, modify upper plate seafloor morphology off Nicaragua, whereas off Java, though comparable in size along our profile, they cannot be unambiguously identified from seafloor deformation.

Another difference regards the splay fault system, which separates the outer and inner wedges off western Java. The splay fault is an out-of-sequence thrust (Kopp and Kukowski, 2003) associated with strain localization and the onset of seismic behavior (Moore et al., 2007). Splay faulting is not observed off Nicaragua (McIntosh et al., 2007), but has been associated with tsunamigenic earthquakes along the Nankai margin (Moore et al., 2007; Bangs et al., 2009). Splay faults are ubiquitous along the northern and central Sunda margin (Kopp and Kukowski, 2003; Sibuet et al., 2007) as well as offshore Bali and Lombok (Lueschen et al., in review). According to the 'dynamic Coulomb model' of Wang and Hu (2006) co-seismic velocity strengthening of the shallow décollement during enhanced compressive deformation of the outer wedge will stimulate upward slip diverged along the splay fault. The splay fault system imaged in our seismic line thus is an attractive candidate for slip to the seafloor, causing tsunamigenesis.

## 4. Conclusions

The re-processed and newly pre-stack depth-migrated profile across the western Java margin images the structural segmentation of the forearc and provides an account of the kinematic evolution of the subduction complex. The complex plate interface is characterized by local morphologic structure and underthrust sediment patches, which likely influence the frictional properties of the shallow megathrust zone. Compared to other décollement zones in large accretionary systems (e.g. Barbados (Westbrook et al., 1988), Cascadia (Adam et al., 2004) or Nankai (Bangs et al., 2004)), the Java case shows a non-uniform character of irregular thickness (Figs. 2 and 3). Unlike for the well-studied Barbados or Nankai margins, for which a remarkable imaging quality has been documented (e.g. Bangs et al., 1999, 2009), the western Java data are not sufficient to quantify physical property changes along the décollement. The seismic images of the spatially variable, nonlinear pattern of the décollement zone, however, support the inference that differential friction along this margin segment may influence earthquake seismogenesis. The splay fault system, which serves as a mechanical boundary between the inner and outer wedges, potentially transfers slip to the seafloor (Kame et al., 2003). This thrust fault connects to the décollement at a depth of approximately 12 km, rising to the seafloor where it reaches its steepest slope, thus potentially causing significant vertical displacement of the seafloor as often associated with tsunami generation. The 2006 tsunami earthquake occurred 100 km east of our line and underscores the persistent seismic and tsunamigenic hazard of this margin (e.g. Abercrombie et al., 2001; Bilek and Engdahl, 2007; Brune et al., in review).

## Acknowledgements

MCS line SO137-03 was acquired during cruise SO137 of RV SONNE by the Federal Institute of Geosciences and Natural Resources, BGR, Hannover, Germany. The SHAPE project is supported by the Deutsche Forschungsgemeinschaft DFG (grant KO2961/1-2). We thank H. Smyth, H. Handley and T. Plank for discussion on arc magma signatures of the Sunda margin and J. Behrmann for discussion on slope basin formation. Reviews by G. Moore helped greatly in improving an earlier version. We thank A. Krabbenhoeft for editing Fig. 1.

## References

Abercrombie, R., Antolik, M., Felzer, K., Ekström, G., 2001. The 1994 Java tsunami earthquake: slip over a subducting seamount. J. Geophys. Res. 106, 6595–6607.
Ammon, C., Kanamori, H., Lay, T., Velasco, A., 2006. The 17 July 2006 Java tsunami earthquake. Geophys. Res. Lett. 33. doi:10.1029/2006GL028005.
Adam, J., Klaeschen, D., Kukowski, N., Flueh, E.R., 2004. Upward delamination of Cascadia Basin sediment infill with landward frontal accretion thrusting caused by rapid glacial age material flux. Tectonics 23. doi:10.1029/2002TC001475.
Amante, C., Eakins, B.W., 2008. ETOPO1 1 Arc-Minute Global Relief Model: Procedures, Data Sources and Analysis. National Geophysical Data Center, NESDIS, NOAA. U.S. Department of Commerce, Boulder, CO.
Bangs, N.L.B., Westbrook, G., 1991. Seismic modeling of the décollement zone at the base of the Barbados Ridge accretionary complex. J. Geophys. Res. 96, 3853–3866.
Bangs, N.L.B., Shipley, T.H., Moore, G.F., 1996. Elevated fluid pressure and fault zone dilation inferred from seismic models of the northern Barbados Ridge decollement. J. Geophys. Res. 101, 627–642.
Bangs, N.L.B., Shipley, T.H., Moore, J.C., Moore, G.F., 1999. Fluid accumulation and channeling along the northern Barbados Ridge decollement thrust. J. Geophys. Res 104, 20.399–20.414.
Bangs, N.L.B., Shipley, T.H., Moore, G.F., Gulick, S.P.S., Nakamura, Y., 2004. Evolution of the Nankai trough decollement from the trench into the seismogenic zone: inferences from three-dimensional seismic reflection imaging. Geology 32, 273–276.
Bangs, N.L.B., Gulick, S.P.S., Shipley, T.H., 2006. Seamount subduction erosion in the Nankai Trough and its potential impact on the seismogenic zone. Geology 34. doi:10.1130/G22451.1.
Bangs, N.L.B., Moore, G.F., Gulick, S.P.S., Pangborn, E.M., Tobin, H.J., Kuramoto, S., Taira, A., 2009. Broad, weak regions of the Nankai Megathrust and implications for shallow coseismic slip. Earth Planet. Sci. Lett. 284, 44–49. doi:10.1016/j.epsl.2009.04.26.
Bekins, B.A., McCaffery, A.M., Dreiss, S.J., 1995. Episodic and constant flow models for the origin of the low-chloride waters in a modern accretionary complex. Water Res. Res. 31, 3205–3215.
Bilek, S., Lay, T., 2002. Tsunami earthquakes possibly widespread manifestations of frictional conditional stability. Geophys. Res. Lett. 29, 14. doi:10/1029/2002GL015215.
Bilek, S., Engdahl, E.R., 2007. Rupture charaterization and aftershock relocations for the 1994 and 2006 tsunami earthquakes in the Java subduction zone. Geophys. Res. Lett. 34. doi:10.1029/2007GL031357.
Bilek, S., 2007. Influence of subducting topography on earthquake rupture. In: Dixon, T.J., Moore, J.C. (Eds.), The Seismogenic Zone of Subduction Thrust Faults. Columbia University Press, New York, pp. 123–146.
Brune, S., Ladage, S., Babeyko, A. Y., Mueller, C., Kopp, H., Sobolev, S. V., in review. Submarine landslides at the eastern Sunda margin: observations and tsunami impact assessment. Natural Hazards.
Calahorrano, A.B., Sallares, V., Collot, J.-Y., Sage, F., Ranero, C., 2008. Nonlinear variations of the physical properties along the southern Ecuador subduction channel: results from depth-migrated seismic data. Earth Planet. Sci. Lett. 267, 453–467. doi:10.1016/j.epsl.2007.11.061.
Chapple, W.M., 1978. Mechanics of thin-skinned fold-and-thrust belts. Geol. Soc. Am. Bull. 89, 1189–1198.
Clift, P.D., Vannucchi, P., 2004. Controls on tectonic accretion versus erosion in subduction zones: implications for the origin and recycling of the continental crust. Rev. Geophys. 42. doi:10.1029/2003RG000127.
Cochrane, G.R., Moore, J.C., MacKay, M.E., Moore, G.F., 1994. Velocity and inferred porosity model of the Oregon accretionary prism from multichannel seismic reflection data: implications on sediment dewatering and overpressure. J. Geophys. Res. 99, 7033–7043.
Collot, J.-Y., Agudelo, W., Ribodetti, A., Marcaillou, B., 2008. Origin of a crustal splay fault and its relation to the seismogenic zone and underplating at the erosional north Ecuador–south Colombia oceanic margin. J. Geophys. Res. 113. doi:10.1029/2008JB005691.
Costa Pisani, P., Reshef, M., Moore, G.F., 2005. Targeted 3-D prestack depth imaging at Legs 190–196 ODP drill sites (Nankai Trough, Japan). Geophys. Res. Lett. 32. doi:10.1029/2005GL024191.
Davis, D.M., Suppe, J., Dahlen, F.A., 1983. Mechanics of fold-and-thrust belts and accretionary wedges. J. Geophys. Res. 88, 1153–1172.
Davis, D.M., 1996. Accretionary mechanics with properties that vary in space and time. In: Bebout, G.E., Scholl, D.W., Kirby, S.H., Platt, J.P. (Eds.), Subduction Top To Bottom. Geophys. Geophys. Monograph, 96. American Geophysical Union, pp. 39–48.
Franke, D., Schnabel, M., Ladage, S., Tappin, D.R., Neben, S., Djajadihardja, Y.S., Mueller, C., Kopp, H., Gaedicke, C., 2008. The great Sumatra–Andaman earthquakes —

imaging the boundary between the ruptures of the great 2004 and 2005 earthquakes. Earth Planet. Sci. Lett. 269. doi:10.1016/j.epsl.2008.01.047.
Gasparon, M., Varne, R., 1998. Crustal assimilation versus subducted sediment input in west Sunda arc volcanics: an evaluation. Mineral. Petrol. 64, 89–117.
Grevemeyer, I., Tiwari, V.M., 2006. Overriding plate controls spatial distribution of megathrust earthquakes in the Sunda–Andaman subduction zone. Earth Planet. Sci. Lett. 251. doi:10.1016/j.epsl.2006.08.021.
Guo, N., Fagin, S., 2002. Becoming effective velocity model builders and depth imagers, part 1— basics of prestack depth migration. Leading Edge 21, 1205–1209.
Gutscher, M.-A., Kukowski, N., Malavielle, J., Lallemand, S., 1998. Episodic imbricate thrusting and underthrusting: analog experiments and mechanical analysis applied to the Alaskan Accretionary Wedge. J. Geophys. Res. 103, 10161–10176.
Hall, R., Smyth, H.R., 2008. Cenozoic arc processes in Indonesia: identification of the key influences on the stratigraphic record in active volcanic arcs. In: Draut, A.E., Clift, P.D., Scholl, D.W. (Eds.), Formation and Application of the Sedimentary Record in Arc Collision Zones: Geological Society of America Special paper, 436, pp. 27–54. doi:10.1130/2008.2436(03).
Hamilton, W., 1979. Tectonics of the Indonesian region. U.S. Geol. Surv. Prof. Paper, p. 1078.
Handley, H.K., 2006. Geochemical and Sr–Nd–Hf–O isotopic constraints on volcanic petrogenesis at the Sunda arc, Indonesia, PhD Thesis, Durham University, UK.
Handley, H.K., Davidson, J.P., Macpherson, C.G., Stimac, J.A., 2008. Untangling differentiation in arc lavas: constraints from unusual minor and trace element variations at Salak Volcano, Indonesia. Chem. Geol. doi:10.1016/j.chemgeo.2008.07.007.
Heffernan, A.S., Moore, J.C., Bangs, N.L., Moore, G.F., Shipley, T.H., 2004. Initial deformation in a subduction thrust system: polygonal normal faulting in the incoming sedimentary sequence of the Nankai subduction zone, Southwestern Japan. Geol. Soc. London Mem. 29. doi:10.1144/GSL.MEM.2004.029.01.14, 143–148.
Hoth, S., Hoffmann-Rothe, A., Kukowski, N., 2007. Frontal accretion: an internal clock for bivergent wedge deformation and surface uplift. J. Geophys. Res. 112. doi:10.1029/2006JB004357.
Kame, N., Rice, J.R., Dmowska, R., 2003. Effects of prestress state and rupture velocity on dynamic fault branching. J. Geophys. Res. 108. doi:10.1029/2002JB002189.
Karig, D.E., Lawrence, M.B., Moore, G.F., Curray, J.R., 1980a. Structural frame work of the fore-arc basin, NW Sumatra. J. Geol. Soc. 137. doi:10.1144/gsjgs.137.1.0077.
Karig, D.E., Moore, G.F., Curray, J.R., Lawrence, M.B., 1980b. Morphology and shallow structure of the trench slope off Nias Island, Sunda Arc. In: Hayes, D.E. (Ed.), The tectonic and geologic evolution of Southeast Asian seas and islands: Geophys. Monogr, 23, pp. 179–208. Washington.
Kieckhefer, R.M., Shor Jr., G.G., Curray, J.R., 1980. Seismic refraction studies of the Sunda trench and forearc basin. J. Geophys. Res. 85 (B2), 863–889.
Kopp, H., Flueh, E.R., Klaeschen, D., Bialas, J., Reichert, C., 2001. Crustal structure of the central Sunda margin at the onset of oblique subduction. Geophys. J. Int. 147, 449–474.
Kopp, H., Klaeschen, D., Flueh, E.R., Bialas, J., Reichert, C., 2002. Crustal structure of the Java margin from seismic wide-angle and multichannel reflection data. J. Geophys. Res. 107. doi:10.1029/2000JB000095.
Kopp, H., Kukowski, N., 2003. Backstop geometry and accretionary mechanics of the Sunda margin. Tectonics 6. doi:10.1029/2002TC001420.
Kopp, H., Flueh, E.R., Petersen, C.J., Weinrebe, W., Wittwer, A., Scientists, Meramex, 2006. The Java margin revisited: evidence for subduction erosion off Java. Earth Planet. Sci. Lett. 242, 130–142.
Kopp, H., Weinrebe, W., Ladage, S., Barckhausen, U., Klaeschen, D., Flueh, E.R., Gaedicke, C., Djajadihardja, Y., Grevemeyer, I., Krabbenhoeft, A., Papenberg, C., Zillmer, M., 2008. Lower slope morphology of the Sumatra trench system. Basin Res. doi:10.1111/j.1365-2117.2008.00381.x.
Lay, T., Bilek, S., 2007. Anomalous earthquake ruptures at shallow depth on subduction zone megathrusts. In: Dixon, T.J., Moore, J.C. (Eds.), The Seismogenic Zone of Subduction Thrust Faults. Columbia University Press, New York, pp. 476–511.
Lelgemann, H., Gutscher, M.-A., Bialas, J., Flueh, E.R., Weinrebe, W., Reichert, C., 2000. Transtensional basins in the western Sunda Strait. Geophys. Res. Lett. 27 (21), 3545–3548.
Le Pichon, X., Henry, P., Lallemand, S., 1993. Accretion and erosion in subduction zones: the role of fluids. Annu. Rev. Earth Planet. Sci. 21, 307–331.
Lueschen, E., Mueller, C., Kopp, H., Engels, M., Lutz, R., Planert, L., Shulgin, A., Djajadihardja, Y., in review. Structure, Evolution and Tectonic Activity of the Eastern Sunda Forearc, Indonesia, from Marine Seismic Investigations. Tectonophys.
MacKay, M., Moore, G.F., Cochrane, G.R., Moore, J.C., Kulm, L.D., 1992. Landward vergence and oblique structural trends in the Oregon margin accretionary prism: implications and effect on fluid flow. Earth Planet. Sci. Lett. 109, 477–491.
MacKay, S., Abma, R., 1993. Depth focusing analysis using wavefront-curvature criterion. Geophysics 58, 1148–1156.
MacKay, M., 1995. Structural variation and landward vergence at the toe of the Oregon accretionary prism. Tectonics 14, 1309–1320.
McIntosh, K.D., Silver, E.A., Ahmed, I., Berhosrt, A., Ranero, C.R., Kelly, R.K., Flueh, E.R., 2007. The Nicaragua convergent margin: seismic reflection imaging of the source of a tsunami earthquake. In: Dixon, T.J., Moore, J.C. (Eds.), The Seismogenic Zone of Subduction Thrust Faults. Columbia University Press, New York, pp. 476–511.
Moore, G.F., Curray, J.R., 1980. Structure of the Sunda trench lower slope off Sumatra from multichannel seismic reflection data. Marine Geophys. Res. 4, 319–340.
Moore, G.F., Curray, J.R., Moore, D.G., Karig, D.E., 1980. Variations in geologic structure along the Sunda fore arc, Northeastern Indian Ocean. In: Hayes, D.E. (Ed.), The tectonic and geologic evolution of Southeast Asian seas and islands: Geophys. Monogr, 23, pp. 145–160. Washington.
Moore, G.F., Curray, J.R., Emmel, F.J., 1982. Sedimentation in the Sunda trench and forearc region. In: Leggett, J.K. (Ed.), Trench Forearc Geology: Geol. Soc. London Spec. Publ., 10.
Moore, G.F., Shipley, T.H., Stoffa, P.L., Karig, D.E., Taira, A., Kuramoto, S., Tokuyama, H., Suyehiro, K., 1990. Structure of the Nankai Trough accretionary zone from multichannel seismic reflection data. J. Geophys. Res. 95, 8753–8765.
Moore, G.F., Taira, A., Klaus, A., Becker, L., Boeckel, B., Cragg, B.A., Dean, A., Fergusson, C.L., Henry, P., Hirano, S., Hisamitsu, T., Hunze, S., Kastner, M., Maltman, A.J., Morgan, J.K., Murakami, Y., Saffer, D.M., Sánchez-Gómez, M., Screaton, E.J., Smith, D.C., Spivack, A.J., Steurer, J., Tobin, H.J., Ujiie, K., Underwood, M.B., Wilson, M., 2001. New insights into deformation and fluid flow processes in the Nankai Trough accretionary prism: results from Ocean Drilling Program Leg 190. Geochem. Geophys. Geosyst. 2. doi:10.1029/2001GC000166.
Moore, G.F., Bangs, N.L., Taira, A., Kuramoto, S., Pangborn, E., Tobin, H.J., 2007. Three-dimensional splay fault geometry and implications for tsunami generation. Science 318. doi:10.1126/science.1147195.
Moore, J.C., Silver, E.A., 1987. Continental margin tectonics: submarine accretionary prisms. Rev. Geophys. 25, 1305–1312.
Moore, J.C., Klaus, A., Bangs, N.L., Bekins, B., Bücker, C.J., Brückmann, W., Erickson, S.N., Hansen, O., Horton, T., Ireland, P., Major, C.O., Moore, G.F., Peacock, S., Saito, S., Screaton, E.J., Shimeld, J.W., Stauffer, P.H., Taymaz, T., Teas, P.A., Tokunaga, T., 1998. Consolidation patterns during initiation and evolution of a plate-boundary decollement zone: Northern Barbados accretionary prism. Geology 26 (9), 811–814.
Moore, J.C., Saffer, D.M., 2001. Updip limit of the seismogenic zone beneath the accretionary prism of southwest Japan: an effect of diagenetic to low-grade metamorphic processes and increasing effective stress. Geology 29, 183–186.
Mueller, C., Kopp, H., Djajadihardja, Y.S., Barckhausen, U., Ehrhardt, A., Engels, M., Flueh, E.R., Gaedicke, C., Keppler, H., Lutz, R., Lueschen, E., Neben, S., Seeber, L., Dzulkarnaen, D.P.S., 2008. From subduction to collision: The Sunda-Banda arc transition. EOS Transact. 89, 49–50.
Newcomb, K.R., McCann, W.R., 1987. Seismic history and seismotectonics of the Sunda arc region. J. Geophys. Res. 92, 421–439.
Pacheco, J.F., Sykes, L.R., Scholz, C.H., 1993. Nature of seismic coupling along simple plate boundaries of the subduction type. J. Geophys. Res. 98, 14.133–14.159.
Park, J.-O., Tsuru, T., Kodaira, S., Nakanishi, A., Miura, S., Kaneda, Y., Kono, Y., 2000. Out-of-sequence thrust faults developed in the coseismic slip zone of the 1946 Nankai earthquake (Mw = 8.2) off Shikoku, southwest Japan. Geophys. Res. Lett. 27 (7), 1033–1036.
Park, J.-O., Tsuru, T., Takahashi, N., Hori, T., Kodaira, S., Nakanishi, A., Miura, S., Kaneda, Y., 2002a. A deep strong reflector in the Nankai accretionary wedge from multichannel seismic data: implications for underplating and interseismic shear stress release. J. Geophys. Res. 107, 3.1–3.19.
Park, J.-O., Tsuru, T., Kodaira, S., Cummins, P.R., Kaneda, Y., 2002b. Splay fault branching along the Nankai subduction zone. Science 297. doi:10.1126/science.1074111.
Planert, L., Kopp, H., Lueschen, E., Mueller, C., Flueh, E. R., Shulgin, A., Djajadihardja, Y., Krabbenhoeft, A., in review. Lower plate structure and upper plate deformational segmentation at the Sunda–Banda arc transition, Indonesia, resolved from the analysis of seismic and gravity data. J. Geophys. Res.
Plank, T., Langmuir, C.H., 1993. Tracing trace elements from sediment input to volcanic output at subduction zones. Nature 362, 739–743.
Plank, T., 2005. Constraints from Th/La sediment recycling at subduction zones and the evolution of the continents. J. Petrol. 46. doi:10.1093/petrology/egi005.
Polonia, A., Torelli, L., Brancolini, G., Loreto, M.-F., 2007. Tectonic accretion versus erosion along the southern Chile trench: oblique subduction and margin segmentation. Tectonics 26. doi:10.1029/2006TC001983.
Ranero, C.R., Grevemeyer, I., Sahling, H., Barckhausen, U., Hensen, C., Wallmann, K., Weinrebe, W., Vannucchi, P., von Huene, R., McIntosh, K., 2008. Hydrogeological system of erosional convergent margins and its influence on tectonics and interplate seismogenesis. Geochem. Geophys. Geosyst. 9. doi:10.1029/2007GC001679.
Saffer, D.M., 2003. Pore pressure development and progressive dewatering in underthrust sediments at the Costa Rican subduction margin: Comparison with Northern Barbados and Nankai. J. Geophys. Res. 108 (B5), 2261. doi:10.1029/2002JB001787.
Sage, F., Collot, J.-Y., Ranero, C.R., 2006. Interplate patchiness and subduction–erosion mechanisms: evidence from depth-migrated seismic images at the central Ecuador convergent margin. Geology 34. doi:10.1130/G22790A.1.
Schlueter, H.-U., Gaedicke, C., Roeser, H.A., Schreckenberger, B., Meyer, H., Reichert, C., Djajadihardja, Y.S., Prexl, A., 2002. Tectonic features of the Sumatra–Java forearc of Indonesia. Tectonics 21. doi:10.1029/2001TC901048.
Shipley, T.H., Moore, G.F., Bangs, N.L., Moore, J.C., Stoffa, P.L., 1994. Seismically inferred dilatancy distribution, northern Barbados Ridge decollement: implications for fluid migration and fault strength. Geology 22, 411–414.
Shulgin, A., Kopp, H., Mueller, C., Lueschen, E., Planert, L., Engels, M., Flueh, E.R., Krabbenhöft, A., Djajadihardja, Y., 2009. Sunda–Banda Arc transition: incipient continent-island arc collision (northwest Australia). Geophys. Res. Lett. 36, L10304. doi:10.1029/2009GL037533.
Sibuet, J.-C., Rangin, C., Le Pichon, X., Singh, S., Cattaneo, A., Graindorge, D., Klingelhoefer, F., Lin, J.-Y., Malod, J., Maury, T., Schneider, J.-L., Sultan, N., Umber, M., Yamaguchi, H., Team, Sumatra Aftershocks, 2007. 26th December 2004 Great Sumatra–Andaman Earthquake: co-seismic and post-seismic motions in northern Sumatra. Earth Planet. Sci. Lett. 263. doi:10.1016/j.epsl2007.09.005.
Singh, S.C., Carton, H., Tapponier, P., Hananto, N.D., Chauhan, A.P.S., Hartoyo, D., Bayly, M., Moeljopranoto, S., Bunting, T., Christie, P., et al., 2008. Seismic evidence for broken oceanic crust in the 2004 Sumatra earthquake epicentral region. Nature Geoscience 1. doi:10.1038/ngeo336.
Skarbek, R.M., Saffer, D.M., 2009. Pore pressure development beneath the décollement at the Nankai subduction zone: implications for plate boundary fault strength and sediment dewatering. J. Geophys. Res. 114. doi:10.1029/2008JB006205.

Stern, R.J., 2002. Subduction zones. Rev. Geophys. 40 (4), 1012. doi:10.1029/2001RG000.
Taira, A., Hill, I., Firth, J.V., Scientific Party, 1991. Proceedings of Ocean Drilling Program, Initial Reports: Ocean Drill. Program, College Station, Tex., 131.
Tsuji, T., Matsuoka, T., Yamada, Y., Nakamura, Y., Ashi, J., Tokuyama, H., Kuramoto, S., Bangs, N.L., 2005. Initiation of plate boundary slip in the Nankai Trough off the Muroto peninsula, southwest Japan. Geophys. Res. Lett. 32. doi:10.1029/2004GL021861.
Tsuji, T., Tokuyama, H., Costa Pisani, P., Moore, G.F., 2008. Effective stress and pore pressure in the Nankai accretionary prism off the Muroto peninsula, southwestern Japan. J. Geophys. Res. 113. doi:10.1029/2007JB005002.
von Huene, R., Scholl, D.W., 1991. Observations at convergent margins concerning sediment subduction, subduction erosion, and growth of continental crust. Rev. Geophys. 29, 279–316.
von Huene, R., Ranero, C.R., Vannucchi, P., 2004. Generic model of subduction erosion. Geology 32. doi:10.1130/G20563.1.
von Huene, R., Ranero, C.R., Scholl, D., 2009. Convergent margin structure in high-quality geophysical images and current kinematic and dynamic models. In: Lallemand, S., Funiciello, F. (Eds.), Subduction Zone Geodynamics. Springer-Verlag, Heidelberg, pp. 137–157.
Wang, K., Hu, Y., 2006. Accretionary prisms in subduction earthquake cycles: the theory of dynamic Coulomb wedge. J. Geophys. Res. 111. doi:10.1029/2005JB004094.
Westbrook, G., Ladd, J.W., Buhl, P., Bangs, N., Tiley, G.J., 1988. Cross section of an accretionary wedge: Barbados Ridge complex. Geology 16, 631–635.
Willet, S., Beaumont, C., Fullsack, P., 1993. Mechanical model for the tectonics of doubly vergent compressional orogens. Geology 21, 371–374.

# 8

Zhu, J., Kopp, H., Flueh, E. R., Klaeschen, D., Papenberg C., 2009.

**Crustal structure of the central Costa Rica subduction zone and basal erosion of the upper margin wedge from seismic wide-angle data.**

Geophys. J. Int., 178, 1112-1131, doi: 10.1111/j.1365-246X.2009.04208.x.

*Geophys. J. Int.* (2009) **178,** 1112–1131 doi: 10.1111/j.1365-246X.2009.04208.x

# Crustal structure of the central Costa Rica subduction zone: implications for basal erosion from seismic wide-angle data

Junjiang Zhu, Heidrun Kopp, Ernst R. Flueh, Dirk Klaeschen, Cord Papenberg and Lars Planert

*Leibniz-Institute of Marine Sciences* (IFM-GEOMAR) *and* SFB574*, Wischhofstrasse* 1-3*,* 24148 *Kiel, Germany. E-mail: jzhu@ifm-geomar.de*

Accepted 2009 April 14. Received 2009 February 4; in original form 2008 May 29

## SUMMARY

On the Pacific margin off central Costa Rica, an anomalous lens-shaped zone is located between the overriding plate and the subducting oceanic lithosphere approximately 25 km landward of the deformation front. This feature was previously recognized in reflection seismic data when it was termed 'megalens'. Its origin and seismic velocity structure, however, could not unambiguously be derived from earlier studies. Therefore during RV SONNE cruise SO163, seismic wide-angle data were acquired in 2002 using closely spaced ocean bottom hydrophones and seismometers along two parallel strike and two parallel dip lines above the 'megalens', intersecting on the middle slope. The *P*-wave velocities and structure of the subducting oceanic Cocos Plate and overriding Caribbean Plate were determined by modelling the wide-angle seismic data in combination with the analysis of coincident reflection seismic data and the use of synthetic seismograms. The margin wedge is defined by high seismic velocities (4.3–6.1 km $s^{-1}$) identified within a wedge-shaped body covered by a slope sediment drape. It is divided into two layers with different velocity gradients. The lower margin wedge is clearly constrained by decreasing velocities trenchward and terminates beneath the middle slope at the location of the 'megalens'. Seismic velocities of the 'megalens' are lower (3.8–4.3 km $s^{-1}$) relative to the margin wedge. We propose that the 'megalens' represents hybrid material composed of subducted sediment and eroded fragments from the base of the upper plate. Upward-migrating overpressured fluids weaken the base of the margin wedge through hydrofracturing, thus causing material transfer from the upper plate to the lower plate. Results from amplitude modelling support that the 'megalens' observed off central Costa Rica is bound by a low-velocity zone documenting fluid drainage from the plate boundary to the upper plate.

**Key words:** Subduction zone processes; Continental margins: convergent; Oceanic transform and fracture zone processes; Crustal structure.



## 1 INTRODUCTION

Convergent margins are dynamic plate boundaries characterized geomorphically by deep ocean trenches, seismically by landward dipping zones of earthquakes, tectonically by regional-scale crustal faulting and terrane movements, and magmatically by arcuate and linear belts of eruptive centres—the volcanic arc (von Huene & Scholl 1991). Convergent margins appear to fall into one of two classes, accretionary and non-accretionary/erosive (Clift & Vannucchi 2004). Subduction erosion at present dominates the Middle America convergent margin (Meschede *et al.* 1999a,b; Ranero & von Huene 2000; Vannucchi *et al.* 2001, 2003) where the frontal prism or outer wedge structure (Wang & Hu 2006) is limited to approximately 15 km adjacent to the trench axis (von Huene & Flueh 1994; Hinz *et al.* 1996). The process of subduction erosion is defined as the mass removal and transport of upper plate material toward subcrustal and mantle depth resulting in extension and subsidence of the forearc (Vannucchi *et al.* 2001, 2003). The recovery of shallow water sediment at Site 1042 (Fig. 1) documents margin-wide subsidence off Costa Rica during the past 16–17 Myr (Vannucchi *et al.* 2001). The short-term rate of removal of rock from the forearc in Central America was calculated to be about 107–123 $km^3$ $(Myr\ km)^{-1}$ (Vannucchi *et al.* 2003). Subduction of positive morphological features like seamounts, ridges, and rises have been reported to facilitate subduction erosion at convergent plate margins (von Huene 1986; von Huene *et al.* 2000; Miura *et al.* 2004; Kopp *et al.* 2006). In addition, hydrofracturing was proposed as a possible mechanism to explain the material removal from the base of the upper plate (Behrmann 1991; Le Pichon *et al.* 1993; von Huene & Ranero 2003). Separated upper plate fragments are subsequently dragged along the plate interface to subcrustal depth (von Huene *et al.* 2004).

In a previous study, multichannel seismic data (MCS) with 48 channels at a 4-ms sampling rate were acquired off central Costa

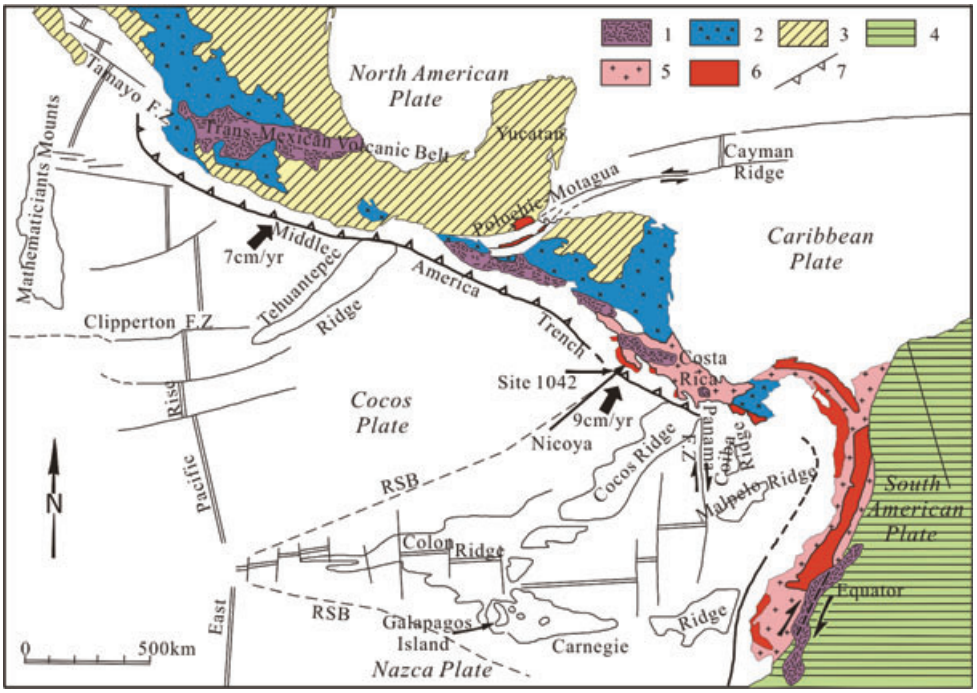


**Figure 1.** Tectonic setting of the Central America convergent margin (after Azéma *et al.* (1985)): (1) Pliocene and Pleistocene volcanism; (2) Oligocene and Miocene volcanism; (3) North America plate; (4) South America plate; (5) Cenozoic formations of ophiolitic Andes and southern Central America; (6) Mesozoic and Cenozoic ophiolitic complex; (7) Subduction zone. RSB: rough–smooth boundary.

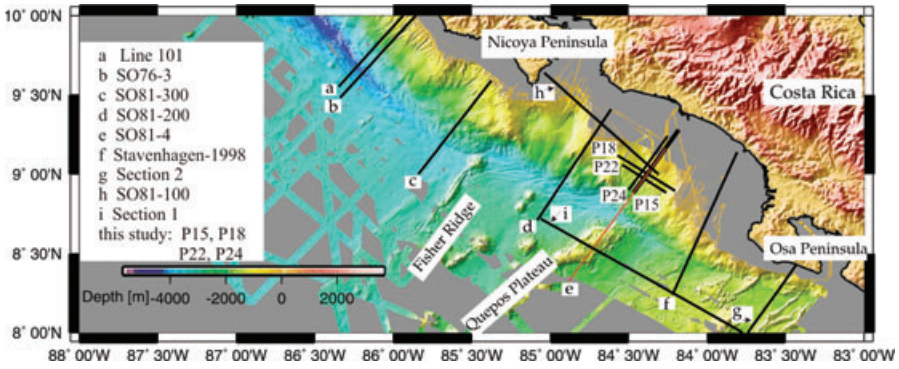


**Figure 2.** Location map of seismic wide-angle profiles offshore of Costa Rica with seafloor bathymetry illuminated from the NE. The positions of wide-angle profiles SO76-3, SO81-100, SO81-200 and SO81-300 are from Ye *et al.* (1996). Section 1 and section 2 are after Walther (2003). Line 101 is after Christeson *et al.* (1999). Stavenhagen-1998 line is after Stavenhagen *et al.* (1998). P15, P18, P22 and P24 profiles are from this study. SO81-4 (red line) used in this study is a MCS line coincident with our wide-angle profile 15.

Rica (R/V Sonne Cruise SO81 in 1992) (Hinz *et al.* 1996). On profile SO81 Line 4 (Fig. 2), a strong plate-boundary reflection bifurcates 25 km landward of the trench at about 5 s two-way traveltime (TWTT). This bifurcation extends laterally for about 15 km, the enclosed unit has been termed a 'megalens' by Flueh *et al.* (1999) and later also by Ranero & von Huene (2000) (Fig. 3). From seismic images of SO81 Line 4 two mechanisms of basal erosion were identified: One is erosion by seamount tunnelling and another is removal of large rock masses of a distending upper plate (Ranero & von Huene 2000). Sage *et al.* (2006) proposed fluid-rich trench sediment rapidly being underthrust along the Ecuadorian margin. The thin subduction channel here locally forms thickened lenses of sedimentary material resulting in interplate coupling variations (Tsuru *et al.* 2002; Sage *et al.* 2006). Ranero *et al.* (2008) proposed that tectonic erosion is closely linked to the presence of overpressured fluids migrating through the upper plate.

In this study, we use refraction seismic data acquired during cruise SO163 of the German R/V Sonne in 2002 (Weinrebe & Flueh 2002) to derive a detailed velocity-depth model along the continental slope of central Costa Rica. The newly acquired data resolve the velocity structure of the 'megalens'. Our results imply a mixture composition of the 'megalens' consisting of subducted sediment and dismembered upper plate material in a fluid-rich environment.

## 2 GEODYNAMIC SETTING

The Farallon plate broke up into the Cocos plate and the Nazca plate along a pre-existing fracture zone about 25 Ma (Fig. 1). The Cocos Ridge and the Carnegie Ridge are interpreted as hotspot tracks formed at the Galapagos hotspot (Hey 1977). The Cocos

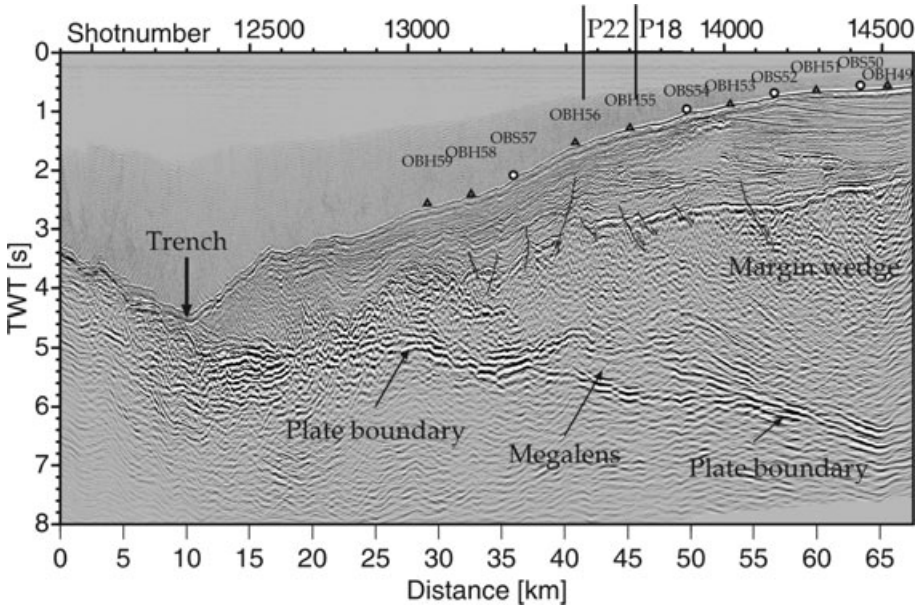


**Figure 3.** Time migrated section of SO81 Line 4. The 'megalens' is bounded by strong-amplitude reflections, which bifurcate from the plate boundary. OBH(S) stations along profile SO163-P15 are superimposed on Line 4. Black triangles mark OBH stations and circles mark OBS stations.

plate is bordered by the East Pacific Rise, the Galapagos rift zone, the north-trending Panama fracture zone near 82° W, and the Middle America arc. The Middle America trench (MAT) is a convergent plate boundary that marks the subduction of the Cocos plate beneath Central America and Mexico with varying convergence rates (Fig. 1). An estimate for the Cocos-Caribbean convergence rate is $84 \pm 5$ mm yr$^{-1}$, accompanied by a dextral, trench-parallel slip rate of $14 \pm 2$ mm yr$^{-1}$ at 88–85.5°W (DeMets 2001; DeMets *et al.* 1990; 1994). The variable morphology of the Cocos plate off Costa Rica has been recognized from high resolution multibeam swath mapping (Fig. 2). Three morphotectonic domains were defined by von Huene *et al.* (1995, 2000). Fisher Ridge marks the boundary between the smooth segment off Nicoya Peninsula and the seamount segment to the south (Fig. 2). The Cocos Ridge segment off Osa Peninsula is a broad shallow domain to the south. The segmentation is implied to have an influence on the forearc structure and the seismogenesis of the subduction zone. The Quepos plateau is dated 14 Myr and the oldest part of Cocos Ridge near the MAT is 13–15 Myr. (Werner *et al.* 1999; Barckhausen *et al.* 2001). The isodepth contours of the Wadati–Benioff zone between the Nicoya Peninsula and Osa Peninsula is about 40 km and the dip angle of the Wadati–Benioff zone decreases from 84° under Nicaragua to 60° under central Costa Rica (Protti *et al.* 1995). Bending-related earthquakes along the MAT occur in the northwest of Costa Rica and no bend-faulting occurs in the vicinity of the thick-crust Cocos Ridge (Ranero *et al.* 2005).

## 3 WIDE-ANGLE EXPERIMENT

### 3.1 Data acquisition and processing

During cruise SO163 in 2002 four profiles were collected, located approximately 25 km northeast of the Quepos plateau (SO163 P15, 18, 22, and 24, in Fig. 2). Wide angle profile 15 was shot coincident with the previous multichannel reflection seismic profile SO81 Line 4 (Hinz *et al.* 1996) (Fig. 2). In addition, a parallel wide-angle dip line and two perpendicular wide-angle strike lines were shot. Along the four profiles a total of 42 IFM-GEOMAR ocean bottom hydrophones (OBH) (Flueh & Bialas 1996) and 22 ocean bottom seismometers (OBS) (Bialas & Flueh 1999) were deployed. The average instrument spacing is about 2.5 km. The detailed station positions are displayed in Fig. 4. The sample rate for the instruments was 4 ms or 5 ms. Along each line, shots with two G-Gun clusters with a total volume of 1700 cinch were triggered at 30 s interval at an average speed of 3.5 knots, resulting in an average shotpoint distance of 54 m. Data quality for the majority of instruments is excellent. Wide-angle data processing included relocation of the instrument positions by analysis of the water wave arrivals. Frequency analysis of the data reveals that the signal is focused in a narrow frequency band. The main frequencies of arrivals recorded by OBH stations are between 9 and 16 Hz. A time- and offset-dependent frequency filter was applied to adjust for the time- and offset-dependent variations. Subsequently, a predictive deconvolution was applied to the data to improve the temporal resolution. Only selected record sections are shown here.

### 3.2 Modelling

#### *3.2.1 Forward modelling*

To image the structure of the margin and to obtain the *P*-wave velocity field, especially in the vicinity of the 'megalens', a 2-D forward modelling technique (Luetgert 1992) using a top–bottom approach was performed for all profiles. First and secondary arrivals were picked for all stations. Phase nomenclature is given in Table 1. The MCS data were used to constrain the upper units of the dip line P15, including the top of margin wedge, the periphery of the 'megalens', and the top of the downgoing slab (Fig. 3). The two strike-lines P18 and P22 were later tied to the dip-lines and thus further constrained the velocity-depth model along the continental slope off central Costa Rica (Fig. 5). The vertical velocity gradient within the different layers is constrained by the wide-angle data. However, the velocity gradient within the 'megalens' cannot directly be retrieved from the refraction data due to the velocity inversion. Therefore

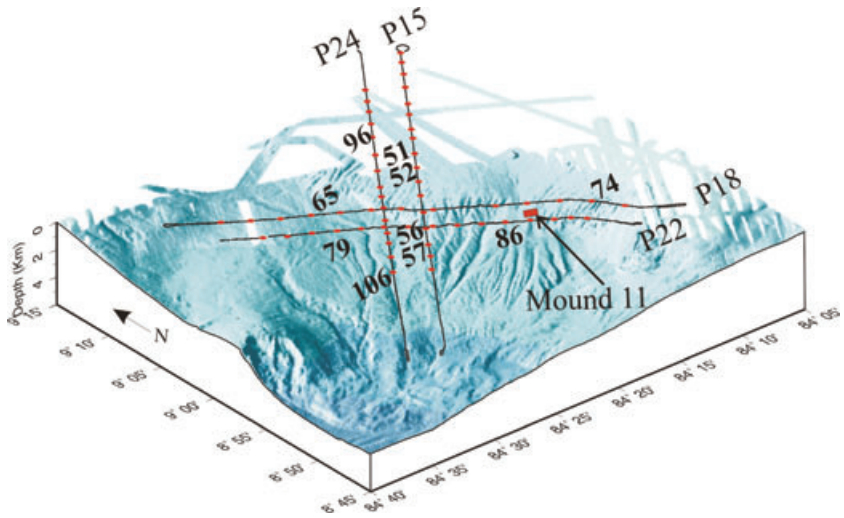


**Figure 4.** Detailed location map of wide-angle profiles in this study. 64 OBH(S) stations were deployed. Record sections from numbered OBH(S) stations are displayed in Figs 6–10 and Figs 12–15. The location of Mound 11 is from Soeding *et al.* (2003).

**Table 1.** Phase nomenclature for wide-angle arrivals

| Phase | Description |
|---|---|
| Ps | Sedimentary phases |
| Pumw | Refraction through the upper margin wedge |
| Plmw | Refraction through the lower margin wedge |
| PtP | Reflection from the top of the 'megalens' |
| PbP | Reflection from the bottom of the 'megalens' |
| PtlmP | Reflection from the top of the lower margin wedge |
| Puoc | Refraction through upper oceanic crust |
| PiP | Reflection from the top of lower oceanic crust |
| Ploc | Refraction through lower oceanic crust |
| PmP | Reflection from crust–mantle boundary |
| Pn | Refraction through the upper mantle |

different velocity gradients were tested during the forward modelling until an optimal fit of phases from the 'megalens' and the upper oceanic crust was achieved.

### *3.2.2 Amplitude modelling*

The forward ray tracing modelling technique is limited to the use of traveltimes and does not utilize the seismic amplitude information. Some high amplitude events identified in the data were modelled by calculating synthetic seismograms, especially wide-angle reflection phases when their traveltimes were not sensitive enough to sharply define the velocity gradients or the nature of interfaces. The amplitude modelling was performed using the 1D reflectivity code of Sandmeier & Wenzel (1986). The 1-D velocity-depth model was provided by strike-lines P18 and P22. The modelling procedure is a trial-and-error process in which we propose a model consisting of many plane homogeneous layers, each showing a distinct *P*-wave velocity ($V_p$), *S*-wave velocity ($V_s$), density, and P and S attenuation quality factors $Q_p$ and $Q_s$. Calculated synthetic seismograms were compared with the observed seismograms, until an optimal fit is realized. For our amplitude modelling, we used a constant Poisson ratio of 0.28 and set $Q_p = 2Q_s$ (as used by Spudich & Orcutt 1980; Christeson *et al.* 2000). $Q_p$ was varied during modelling. A $Q_p$ value of 300–500 for the forearc region is in agreement with earlier observations (Bowman 1988). Densities were set to 1.5 g cm$^{-3}$ for the slope sediments and 1.8 g cm$^{-3}$ within the margin wedge (Kimura *et al.* 1997; Christeson *et al.* 2000). Densities for oceanic crust were calculated using the relationship $\rho = 1.85 + 0.165$Vp (Christensen & Shaw 1970; Christeson *et al.* 2000).

## 4 INTERPRETATION

The crustal models of the Central Costa Rica margin along two parallel dip-lines and two parallel strike-lines are presented in Fig. 5. In the following, models are described individually from top to bottom, and related record sections are shown to demonstrate the fit between observed and modelled arrival times.

### 4.1 Dip-lines SO163-P15 and SO163-P24

#### *4.1.1 Sediment*

The sediment phase Ps is clearly observed on all record profiles and is modelled as a refraction through the sedimentary layer, which has a variable thickness of 500–1800 m, with *P*-wave velocities of 1.6–2.4 km s$^{-1}$. This thickness is constrained by the MCS data (Fig. 3) and refraction phase Pumw from the upper margin wedge. The thickness of the sediment near the trench increases to 1.5 km (Fig. 5) at profile km 10 and displays velocities of 1.8–2.3 km s$^{-1}$. The thickness of the sedimentary cover on the mid-shelf increases to 1.8 km beneath station OBH51 and the velocities reach 2.4 km s$^{-1}$. Towards the coast, sediment thickness decreases to 500 m and the velocities reach a value of 2.1 km s$^{-1}$.

#### *4.1.2 Upper and lower margin wedge*

The margin wedge is divided into two layers with different velocity gradients. Clear first arrivals observed on all OBH(S) stations are used to constrain the margin wedge (see refraction phases Pumw and Plmw through the margin wedge, Figs 6–10). The *P*-wave velocity of the upper margin wedge varies from 4.0 to 4.3 km s$^{-1}$ near the trench to 4.0–5.1 km s$^{-1}$ close to coastline (dip-line P24, Fig. 5). On the parallel dip-line P15 the velocity of the upper margin wedge varies from 4.1 to 4.5 km s$^{-1}$ near the trench to 4.2–5.3 km s$^{-1}$ near

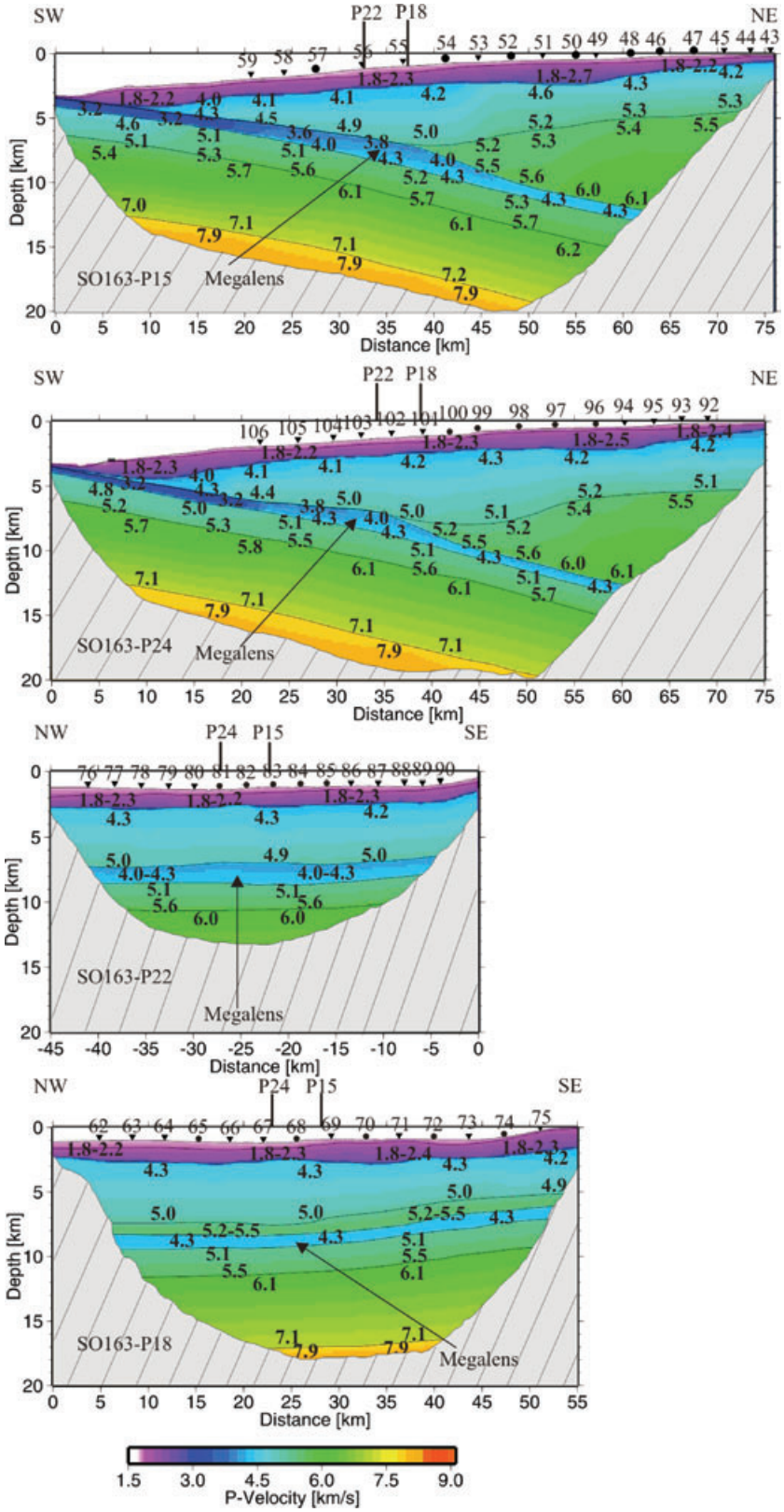


**Figure 5.** Four velocity-depth models along the Pacific margin of central Costa Rica. The subducted slab and the 'megalens' (located updip of the profile intersection) are recorded along the two dip-lines SO163 profile P15, P24 and two strike-lines P18 and P22. The detailed positions of OBH(S) and the *P*-wave velocities are marked on the profiles.

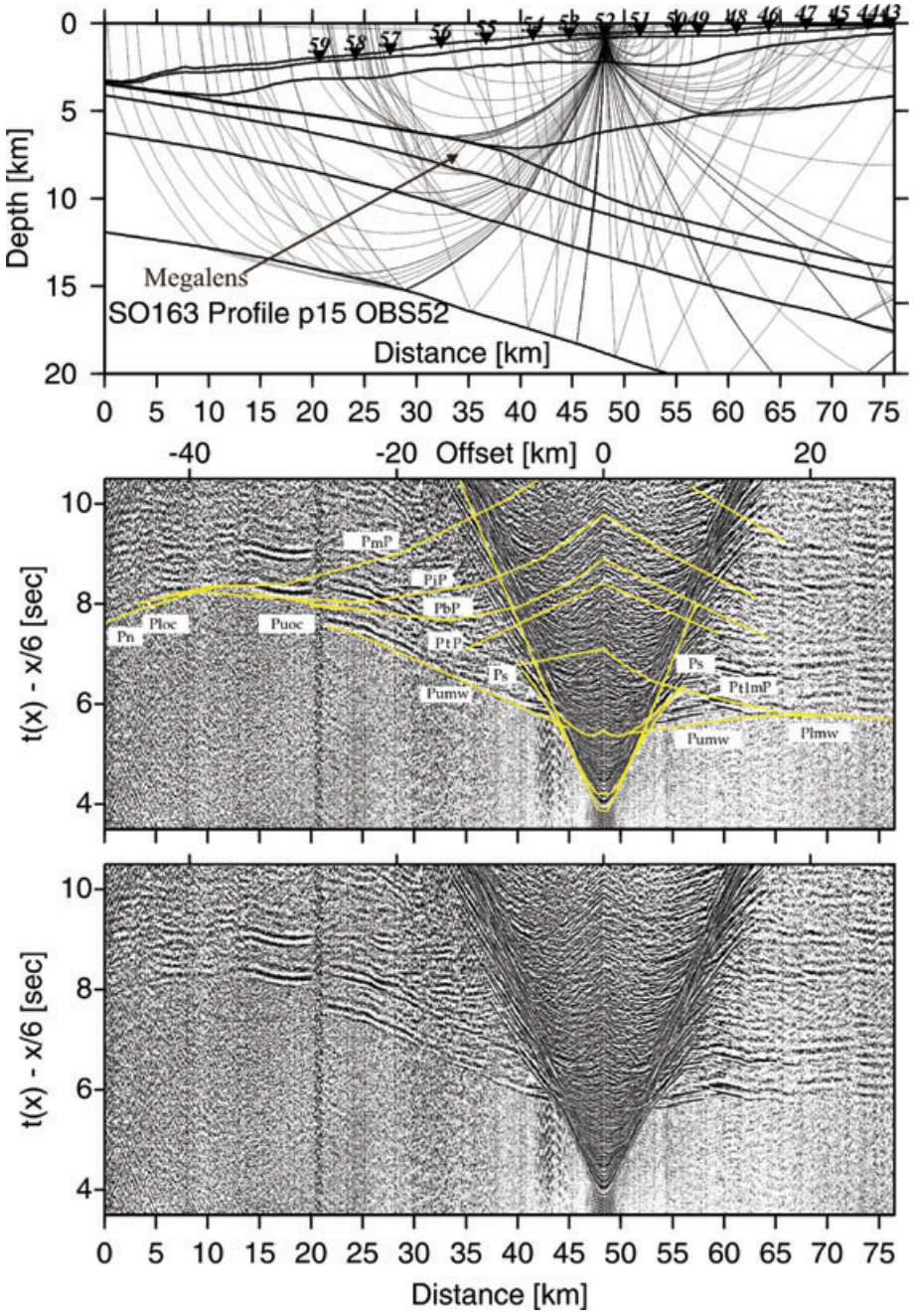


**Figure 6.** Record section from station OBS52 deployed along the dip-line SO163-P15. The uppermost image displays the ray paths through the model subsurface. The data are shown with modelled traveltimes overlain in the upper images and the raw data displayed in the lower section. See Table 1 for nomenclature. Refracted phases Puoc and Ploc and associated near vertical reflections PbP and PiP track the top of the upper oceanic crust and the top of the lower oceanic crust, respectively.

the coastline. Lateral velocity and thickness variations are observed along the two dip-lines (Fig. 5). Vertical velocity gradients are well constrained within the margin wedge by modelling of traveltime data because the reflection phase (PtlmP) from the top of the lower margin wedge and the refraction phase (Plmw) through this layer are clearly observed (Figs 6–9). Between stations OBH 105 to OBH 92 the interface between the upper and lower margin wedge is constrained with high confidence from the refraction phase Plmw (Fig. 11). The ray coverage through this layer is shown in Fig. 11 along the dip-line P24. The top and bottom velocity of the lower margin wedge increases with depth from 5.2 to 5.5 km $s^{-1}$ and 5.5 to 6.1 km $s^{-1}$, respectively. Near the landward edge of the 'megalens', the depth of this interface reaches to about 8 km and a lower margin wedge is not existent further seaward (beneath station OBH102, Fig. 11).

### *4.1.3 'Megalens' and low-velocity zone*

The 'megalens' is clearly observed in the MCS data (Fig. 3). In our starting model the interface and thickness of the 'megalens' are preliminarily estimated from the reflection data. We observe

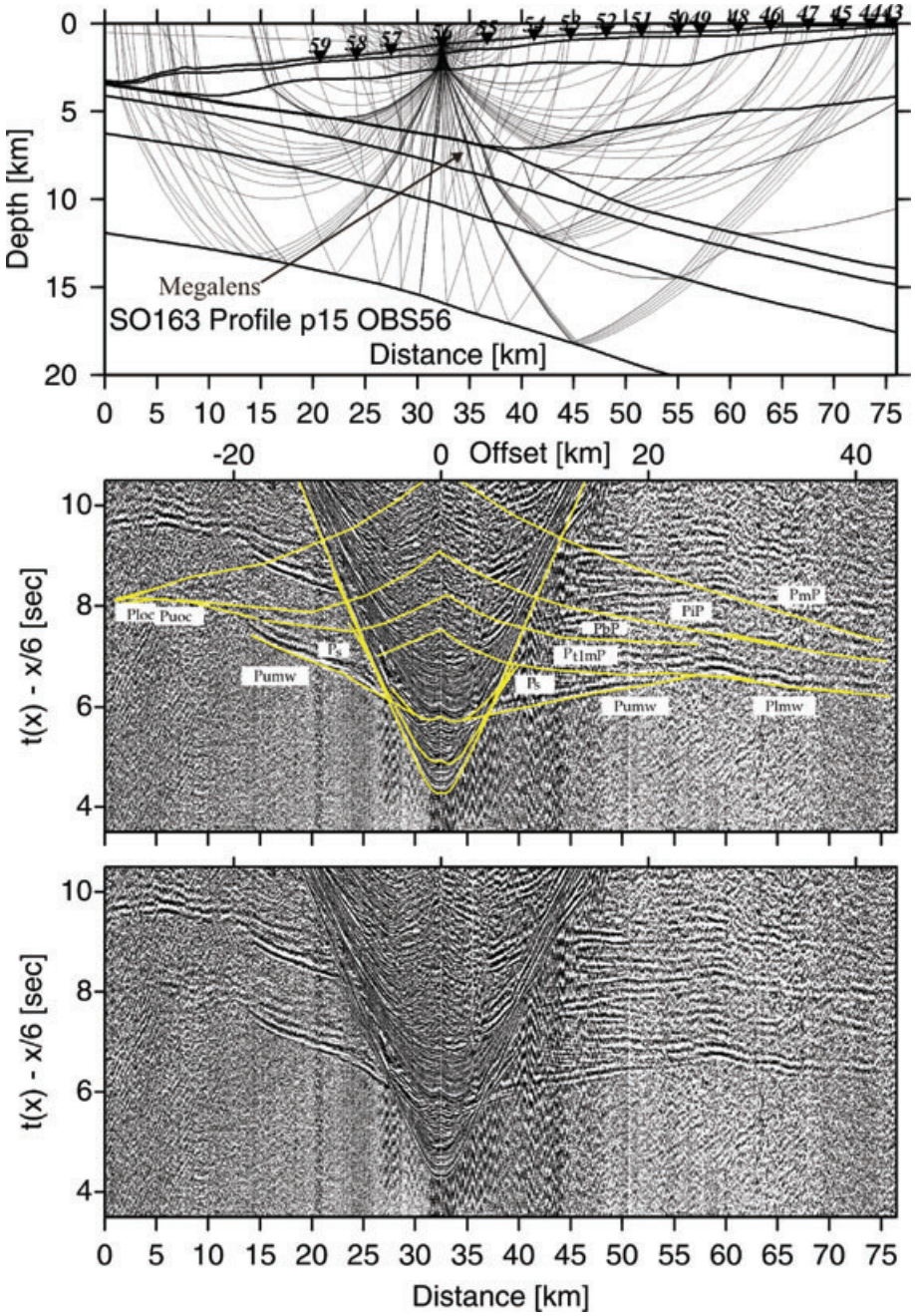


**Figure 7.** Record section and ray diagram for station OBH56 deployed along the dip-line SO163-P15. Please refer to Fig. 6 for display information. Phases PtlmP and Plmw track the lower margin wedge. Refraction phase Puoc tracks the upper oceanic crust. The oceanic crust–mantle boundary is tracked by PmP and Pn phase.

the reflection phase PbP at the bottom of the 'megalens' and the refracted phase Puoc from the top of the oceanic crust, which are used to indicate the thickness/velocity ambiguity of the 'megalens' (Fig. 6, profile distance 15–20 km; Fig. 7, Fig. 10, profile distance 3–10 km). The uncertainty analysis will further show this ambiguity (see Section 4.4). A 1–1.5 km thick lens-shaped feature with velocities of 3.8–4.3 km $s^{-1}$ best satisfies reflection arrivals as well as refraction arrivals through the upper oceanic crust.

A low-velocity zone overlaying the subducted plate is universally observed along the Costa Rica convergent margin. It was presented in previous wide-angle velocity models varying in thickness and velocity (Ye *et al.* 1996; Stavenhagen *et al.* 1998; Christeson *et al.* 1999). In our data, we observe a time delay of the slab refraction phase, which leads us to incorporate a low-velocity zone (LVZ) above the oceanic crust to improve the fit of calculated to observed traveltimes in our model (see phase Puoc, Figs 6, 7 and 10). Near the trench the thickness of the LVZ is about 400 m and we assume a constant velocity of 3.2 km $s^{-1}$ for this layer, which is interpreted as subducted sediment. Beneath the margin wedge the strong plate boundary reflection is shown in the MCS data as well as on some wide-angle records (see phase PbP from these station records, Figs 6 and 8). Negative polarity reflections indicate the presence of the

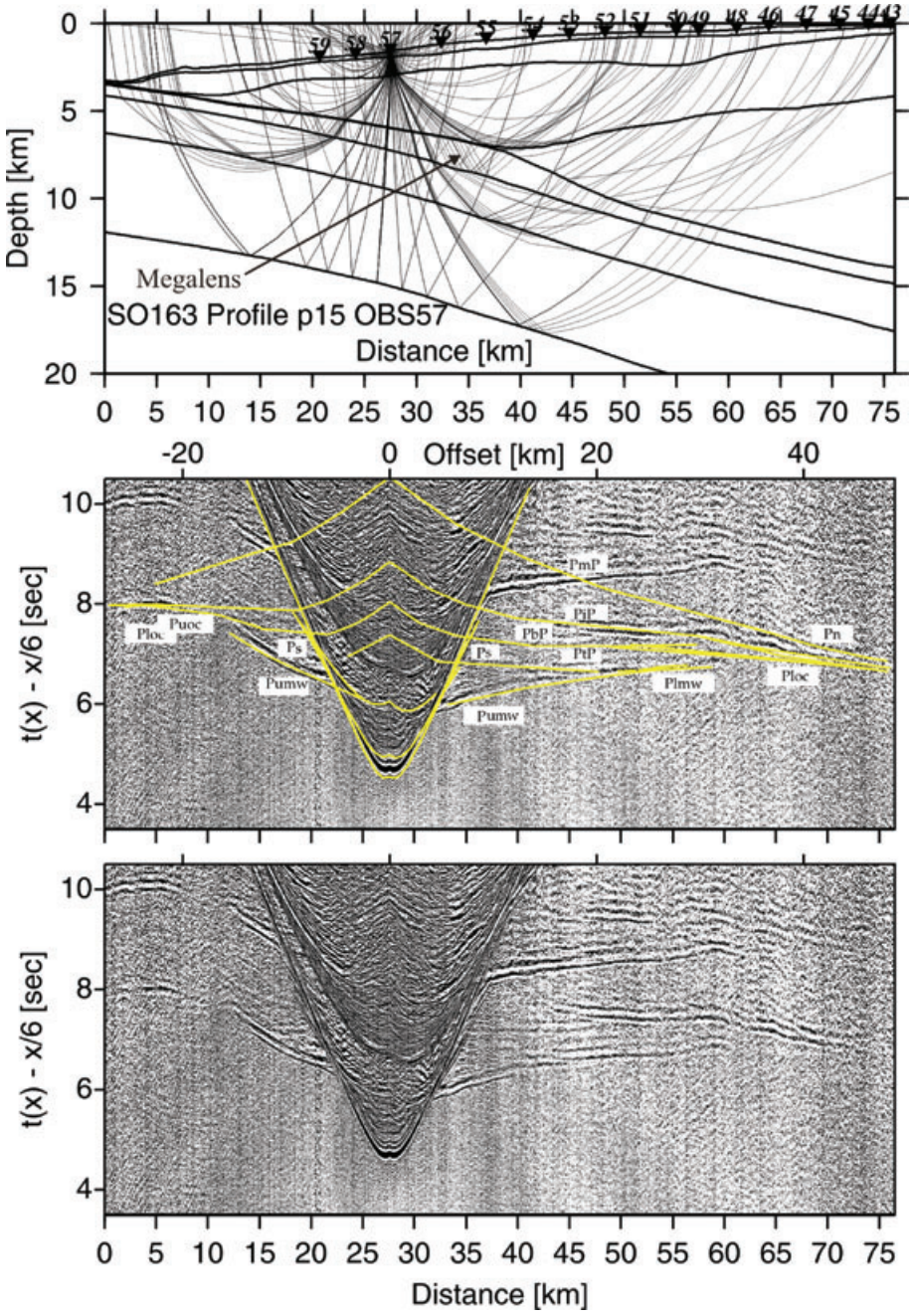


**Figure 8.** Record section and ray diagram for station OBS57 deployed along the dip-line SO163-P15. Please refer to Fig. 6 for display information. The oceanic crust–mantle boundary is recorded by phase Pn. Strong phases PiP and Ploc track the lower oceanic crust. The plate boundary is recorded as a pre-critical reflection PbP. Phase Plmw tracks the lower margin wedge and the top of the lower margin wedge is recorded as wide-angle reflection PtlmP.

fluids at the plate boundary in Costa Rica (Ranero *et al.* 2008) and are related to the LVZ.

#### *4.1.4 Upper and lower oceanic crust*

The subducting oceanic crust is divided into two layers: upper oceanic crust and lower oceanic crust. Due to the complex geometry of the dipping slab and the seafloor morphology, refracted arrivals through the oceanic crust display some traveltime variability along the dip-lines. All arrivals through the upper and lower oceanic crust were observed and modelled. In Fig. 6 (OBS52) a distinct high amplitude event is observed at profile km 12–20. It is interpreted as a refraction phase Puoc through the upper oceanic crust, which has a high-velocity gradient and therefore focuses the energy into a short offset interval. A refraction phase Ploc through the lower oceanic crust was observed on some records (Fig. 6, profile distance km 0–10; Fig. 8, profile distance km 0–8 and 60–73; Fig. 9 and Fig. 10). A clear reflection phase PiP is visible at a distance of 41–60 km (Fig. 8), which is interpreted as a reflection from the interface between upper and lower oceanic crust. A short refraction phase Pn through the upper mantle is visible in the record of OBS57 at a distance of 66–73 km (Fig. 8) and in the record section of OBS106 (Fig. 10) at a distance of 61–68 km. These refracted and

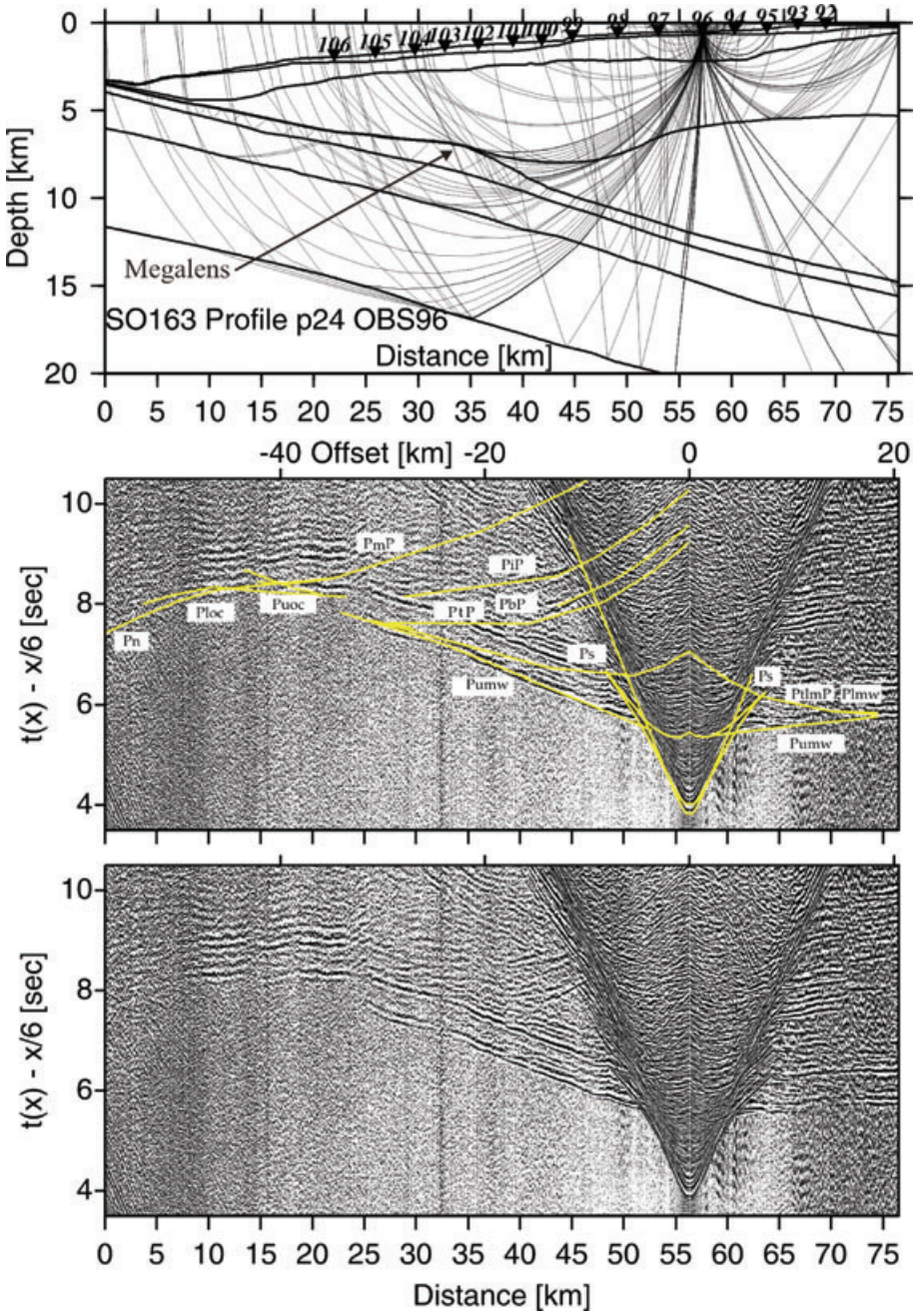


**Figure 9.** Record section and ray diagram for station OBS96 deployed along the dip-line SO163-P24. Please refer to Fig. 6 for display information. Phases Puoc and PbP track the downgoing slab. Phase Plmw travels through the lower margin wedge.

reflected phases constrain a 2–2.5 km thick upper oceanic crust with velocities of 5.0–5.5 km $s^{-1}$ and a 5.5–6 km thick lower oceanic crust with velocities of 5.8–7.1 km $s^{-1}$ (Fig. 5).

### 4.2 Strike-lines SO163-P18 and SO163-P22

Strike-lines P18 and P22 were deployed perpendicular to the two dip lines. Along line P18 a high velocity lower margin wedge is observed and modelled (Figs 12 and 13). Beneath the lower margin wedge a thin LVZ is assumed based on the model result of dip-line P24. A clear refraction phase Pumv through the upper margin wedge with velocities ranging from 4.3 to 5.0 km $s^{-1}$ was recorded on all stations (Fig. 5). The thickness of the upper margin wedge is 5.1 km in northwestern part and decreases to 3.1 km in southeastern part (Profile 18, Fig. 5). It is also found at a more shallow depth when approaching Osa Peninsula. The top of the lower margin wedge is constrained by a clear reflection phase PtlmP and refraction phase Plmw at profile distance km 40–45 (Fig. 12). A distinct plate boundary reflection phase PbP is seen on most record sections (Figs 14 and 15). In Fig. 14, the refraction phase Ploc with velocities of 6.0–7.1 km $s^{-1}$ through the lower oceanic crust is observed at profile distance km 40–45. In Fig. 15, a refraction phase Puoc through the upper oceanic crust with velocities of 5.1–5.6 km $s^{-1}$ is observed and it can be used to constrain the bottom interface of the 'megalens'/plate boundary. On line P22, the deep phases Pn and PmP were not observed on any station records and the Moho

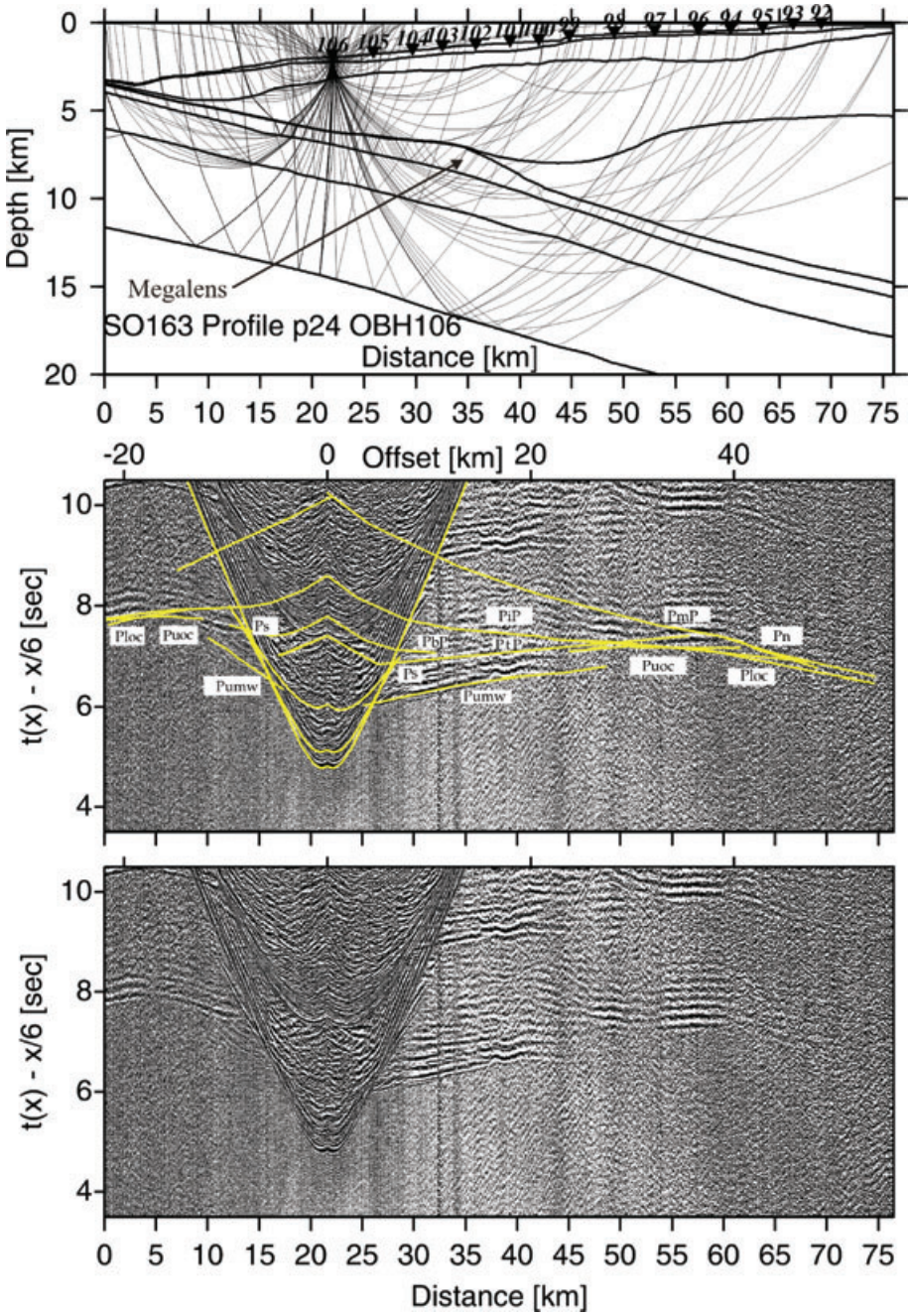


**Figure 10.** Record section and ray diagram for station OBS106 deployed along the dip-line SO163-P24. Please refer to Fig. 6 for display information. Phases Puoc and PbP track the downgoing slab. The oceanic crust–mantle boundary is tracked by PmP and Pn phase.

cannot be constrained on this line. If the result from the dip line is projected along the profile, it should appear at offsets of 23 km at about 16 km depth (Fig. 5).

### 4.3 Amplitude modelling of wide-angle data

Along the two strike-lines there are only minor lateral velocity variations. Thus we can use the reflectivity method (Fuchs & Mueller 1971; Mueller 1985; Sandmeier & Wenzel 1986) for 1-D amplitude modelling. See Section 3.2.2 for details on parameters and calculations. A comparison of the data to synthetic seismograms is displayed for OBH 88 in Fig. 16. OBH 88 records the subducting plate beneath the bottom of the 'megalens' at about 8 km depth. Using the 1-D velocity-depth function gained from the forward modelling as a reference model, we adjust the vertical velocity gradient within the margin wedge to match the amplitude-versus-offset variations. A vertical velocity gradient of approximately 0.22 $s^{-1}$ and constant Qp values of 50 within the margin wedge will reproduce the refracted phase through the upper margin (Pumw) within 30 km offset (Figs 16a–c). A decrease of the vertical velocity gradient by 0.03 $s^{-1}$ will enhance the appearance of the Pumw arrivals at offsets larger than 30 km (Fig. 16e). The refraction through the upper margin wedge (Pumw) as well as the reflection from the plate boundary (i.e. bottom of the 'megalens') and the top of the LVZ are well reproduced (Fig. 16b). Reflection amplitudes from the bottom of the 'megalens' increase from 11 km offset, whereas significant

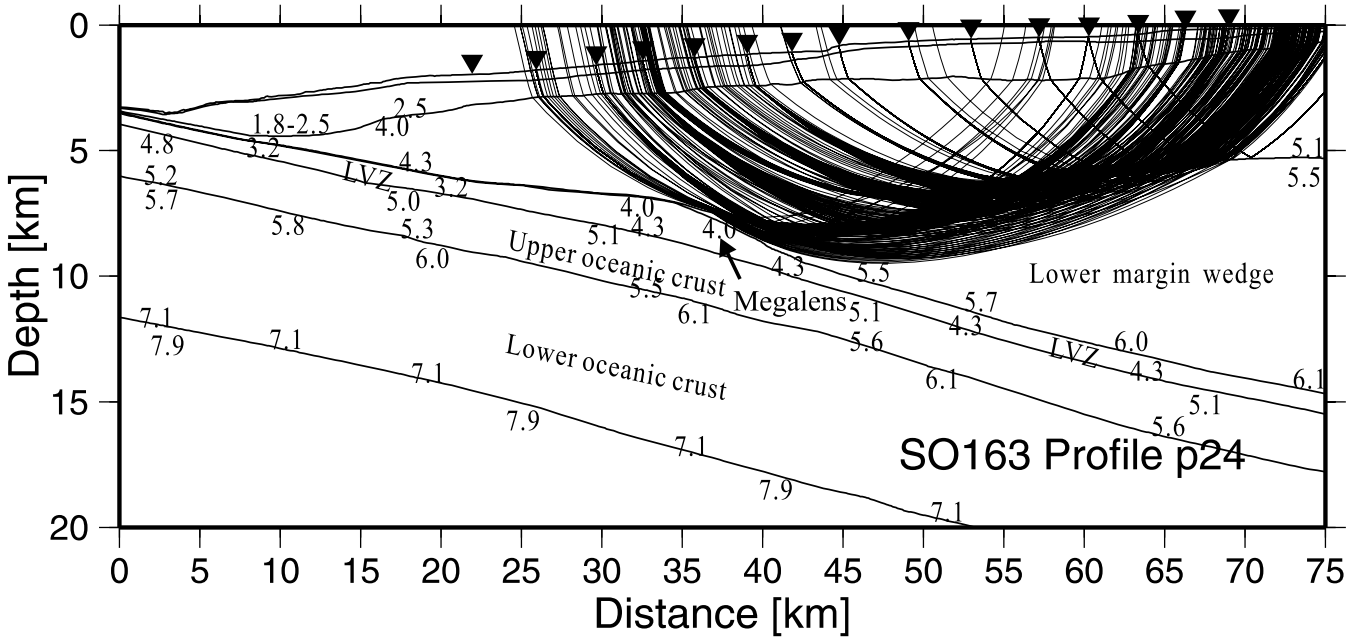


**Figure 11.** Ray coverage of the lower margin wedge displayed for dip-line P24. The top of the lower margin wedge is well constrained by the closely spaced OBH(S) stations in our velocity model.

amplitudes from the reflection PbP appear at offsets of about 11–19 km (Fig. 16a). The velocity-depth profile used for the amplitude modelling is shown in Figs 16c and e. A 200–250 m thick layer of decreased velocities above and below the 'megalens' can best reproduce the reflection similar to the original data. Although the appearance of the reflection phases from two extreme low-velocity layers is obscure due to noise and the interference with the multiple, they still may be discerned in the data (marked by arrows in Fig. 16a) and in the synthetic seismogram. The appearance of all other record sections is rather similar. The plate boundary is clearly indicated by a bright reflection in the MCS data and the amplitude of this reflection was explained by the presence of sediment and elevated pore pressure (Flueh *et al.* 1999). The amplitude modelling suggests that the 'megalens' is bounded by a low-velocity zone. Minor discrepancies in the traveltimes of real and synthetic data must be expected due to ray focusing and defocusing effects (Kopp *et al.* 2001).

### 4.4 Model sensitivity and uncertainty tests

Sensitivity analysis of the velocity and the geometry of the 'megalens' were done by changing the interlayer seismic velocities and the depths of the top interface of the 'megalens' using the forward modelling tool 'MacRay' (Luetgert 1992). Fig. 17 shows the match between the observed and predicted traveltimes for different seismic velocities and fixed top and bottom interfaces of the 'megalens'. Assuming a constant seismic velocity of 3.2 km $s^{-1}$ or 4.5 km $s^{-1}$ within the 'megalens' does not fit well the predicted traveltime (phase PbP) within the assigned 50 ms picking uncertainties [root mean square (rms) misfits >80 ms] (Fig. 17b). The best match of the calculated traveltime curve to the observed data is achieved if we assume seismic velocities that increase linearly from 3.8 to 4.3 km $s^{-1}$. Fig. 17b shows that the traveltime curve is also strongly sensitive to depth changes (±200 m) of the top interface of the 'megalens'.

To assess the uncertainties of the velocity field and the depth of the reflector, we used the tomographic inversion method of Korenaga *et al.* (2000) to apply a nonlinear Monte Carlo method (Tarantola & Valette 1982; Tarantola 1987; Korenaga *et al.* 2000). We constructed 100 Monte Carlo ensembles by inverting data with random errors with random initial velocity models. The 100 2-D initial velocity models were built by adding velocity values (randomly chosen between certain predefined limits) on a reference model beneath the basement. In addition, 100 noisy traveltime data sets were constructed by adding random phase errors (±50 ms) and common-receiver errors (±50 ms) on the original data set (Zhang & Toksöz 1998; Korenaga *et al.* 2000). Finally, we inverted each velocity model and corresponding reflector together with a noisy data set to estimate the influence of the starting model and the effect of realistic traveltime errors. We applied a top–bottom strategy to run the inversion step for each reflector, respectively. We applied the random velocities on our 2-D forward model of P15 including two floating reflectors (top and bottom of the 'megalens', random variations within ±1 km) in the upper plate and one reflector (Moho, random variations within ±2 km) in the lower plate. After 10 iterations of the inversion process, 100 inversion velocity models for the first reflector updated as 100 initial models for the second reflector. Traveltime rms misfits reduced dramatically from the beginning several hundred millisecond to about 70–90 ms and allowed us to assess the uncertainty of the velocity field.

The average and uncertainty of model parameters obtained by averaging all Monte Carlo solutions and computing the corresponding standard deviation is shown in Figs 18 (a), (c) and (e). Velocity uncertainties of the upper plate are usually lower than 0.15 km $s^{-1}$ within the margin wedge and are lowest (<0.05 km $s^{-1}$) in the upper margin wedge. Uncertainties are slightly higher within the lower margin wedge (0.06–0.16 km $s^{-1}$) because of sparse ray coverage (Fig 18b). The largest velocity uncertainties occur within the LVZ ('megalens') and reach up to 0.15 km $s^{-1}$ (Fig 18c). The depth uncertainties of the first and the second reflector are small and reach up to about 500 m within the range of ray coverage. The

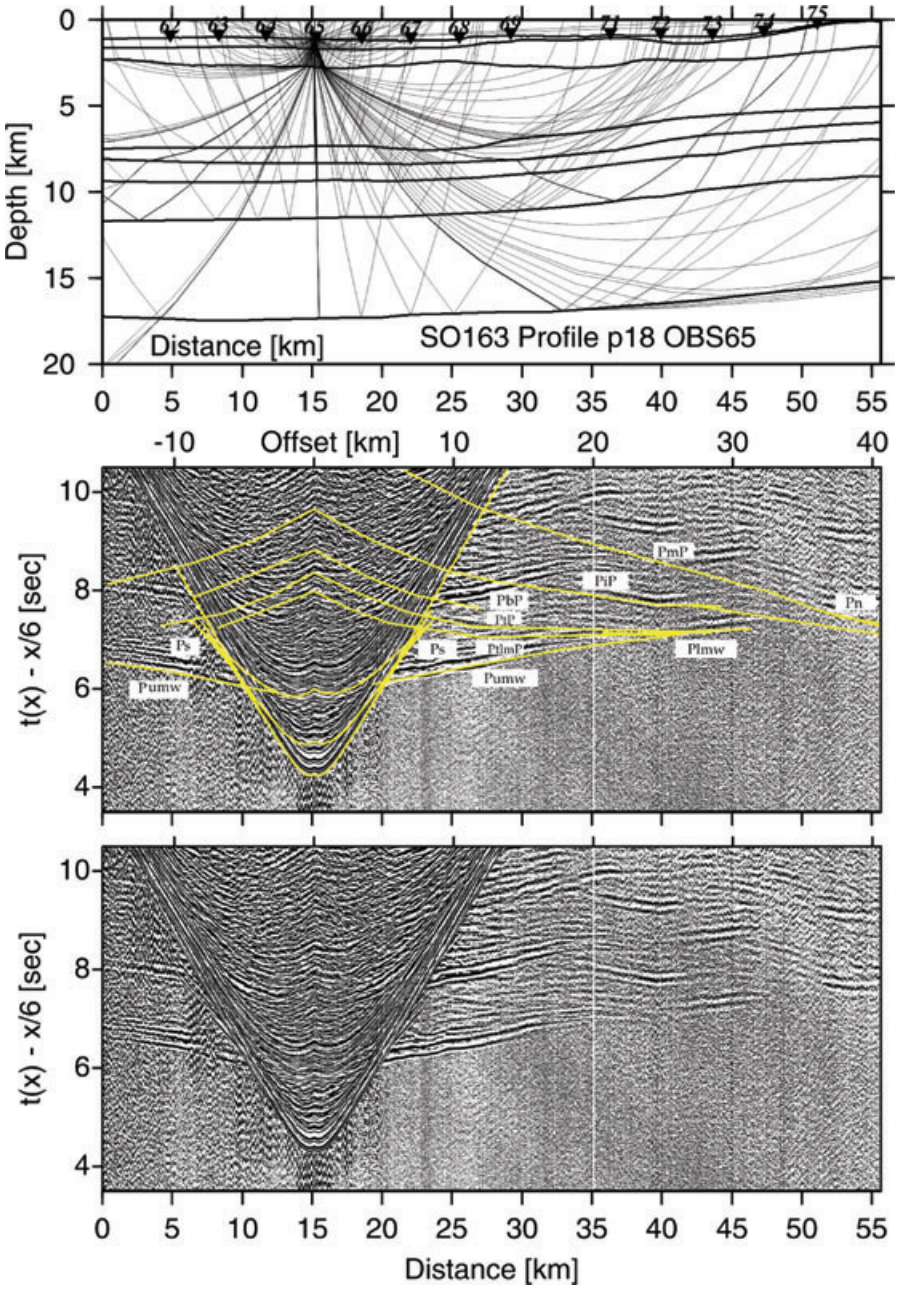


**Figure 12.** Record section and ray diagram for station OBH65 deployed along the strike-line SO163-P18. Please refer to Fig. 6 for display information. Strong phases PtlmP and Plmw track the lower margin wedge. The reflection phase PiP tracks the top of the lower oceanic crust. The oceanic crust–mantle boundary is recorded as reflection PmP.

velocity uncertainties within the subducting oceanic crust are larger (0.06–0.15 km $s^{-1}$) because of the limited amount of available data (Figs 18e and f). The Moho depth uncertainties show values around $\pm$1.5 km. In general, the uncertainties for upper plate are lower than in the lower plate and the velocity structure and geometry of the 'megalens' is a robust feature of the tomographic solutions.

## 5 DISCUSSION

### 5.1 Margin wedge

Below the cover of slope sediment, the margin wedge is defined by high velocities (4.3–6.1 km $s^{-1}$). Based on the *P*-wave velocity variations we divide the margin wedge into the upper margin wedge with velocities ranging from 4.3 to 5.0 km $s^{-1}$ and the lower margin wedge with velocities from 5.2 to 6.1 km $s^{-1}$. The top of the upper margin wedge is clearly imaged in the MCS data set and also reliably modelled based on the wide-angle data. Its top is cut by numerous normal faults and indicates the extensional forearc stress environment (Fig. 3). The interface separating the upper and lower margin wedge is defined by a sharp velocity increase from 5.1 to 5.5 km $s^{-1}$ and is well constrained by our data (see Fig. 11). The relative high velocities of the lower margin wedge result in a velocity inversion at the transition to the subducted plate landward of OBS101 (P24) and OBS54 (P15). The lower margin wedge terminates underneath the middle slope beneath OBH(S) station 102 and 55. On strike-line P22 it is not observed.

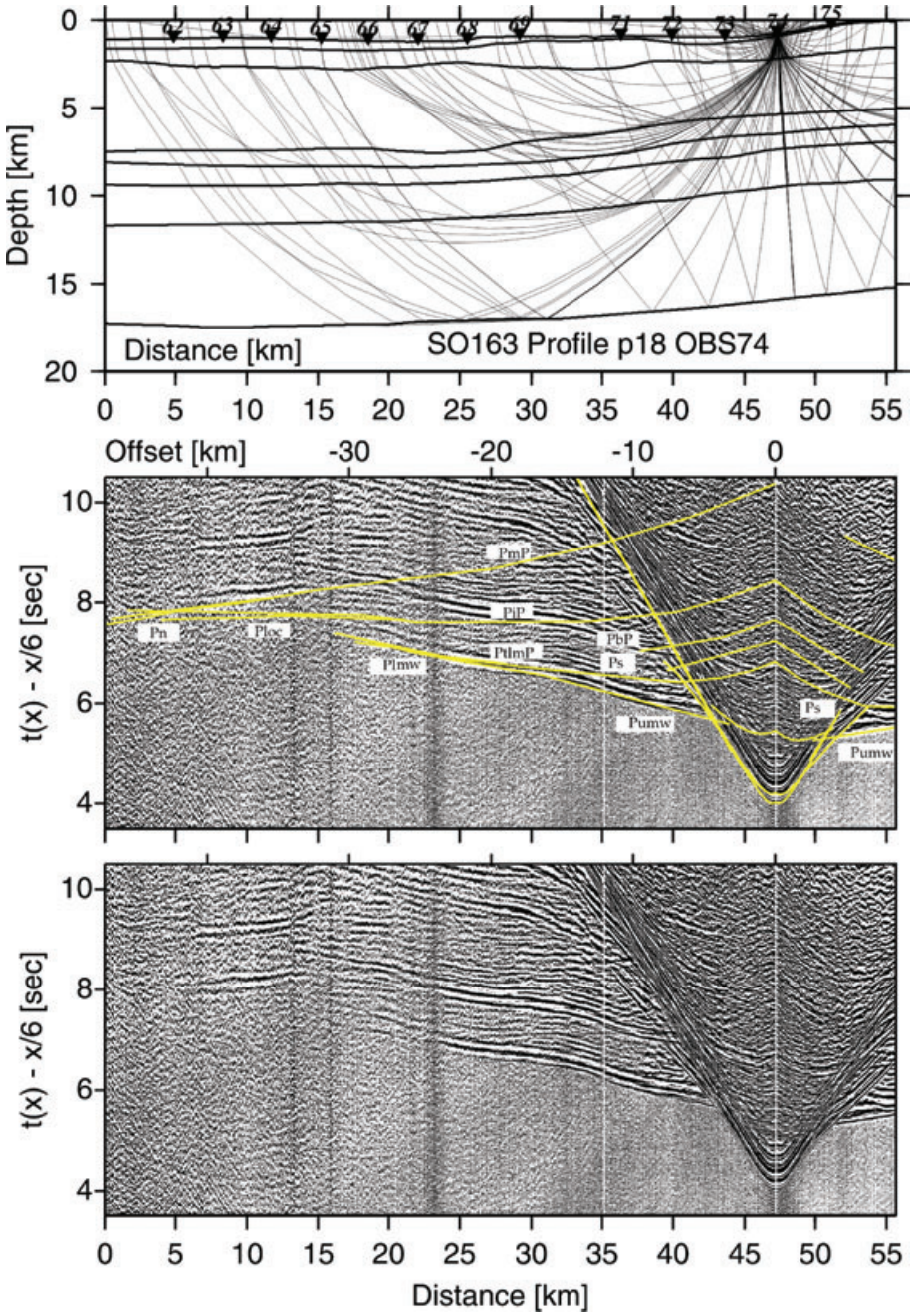


**Figure 13.** Record section and ray diagram for station OBH74 deployed along the strike-line SO163-P18. Please refer to Fig. 6 for display information. Phase Plmw travels through the lower margin wedge. The oceanic crust–mantle boundary is tracked by phases PmP and Pn.

The origin and composition of the margin wedge is defined by geophysical observations and by comparison to neighboring stratigraphic sections onshore. The margin wedge off Nicoya and Central Costa Rica was interpreted as an offshore extension of the Nicoya Complex ophiolitic rocks (Ye *et al.* 1996; Stavenhagen *et al.* 1998; Christeson *et al.* 1999; Sallarès *et al.* 2001). The uppermost unit of the Nicoya Complex onshore was constrained by land shots and shows velocities varying from 4.2 to 4.9 km $s^{-1}$. The middle unit of the Nicoya Complex displays velocities landward of the coastline varying from 4.6 to 5.5 km $s^{-1}$ and velocities at the top of wedge varying from 3.6 to 4.7 km $s^{-1}$ (Christeson *et al.* 1999). Our results for central Costa Rica show that the upper margin wedge is characterized by velocities varying from 4.0 to 5.2 km $s^{-1}$. An across-strike increase of velocities from 4.0 km $s^{-1}$ at approximately 12 km landward of the trench to 4.4 km $s^{-1}$ off the coastline (Fig. 5) is observed. The lower Nicoya complex (Christeson *et al.* 1999) corresponds to our lower margin wedge in terms of velocities. It indicates a low-velocity gradient, but the velocity also decreases trenchward from 5.5 to 5.0 km $s^{-1}$. This velocity information suggests that the upper and lower margin wedge can be interpreted as an offshore extension of the upper and the lower Nicoya complex.

The extent of the lower margin wedge within the forearc was not identified from previous wide-angle seismic studies. Previous seismic profiles could not resolve the transition between the

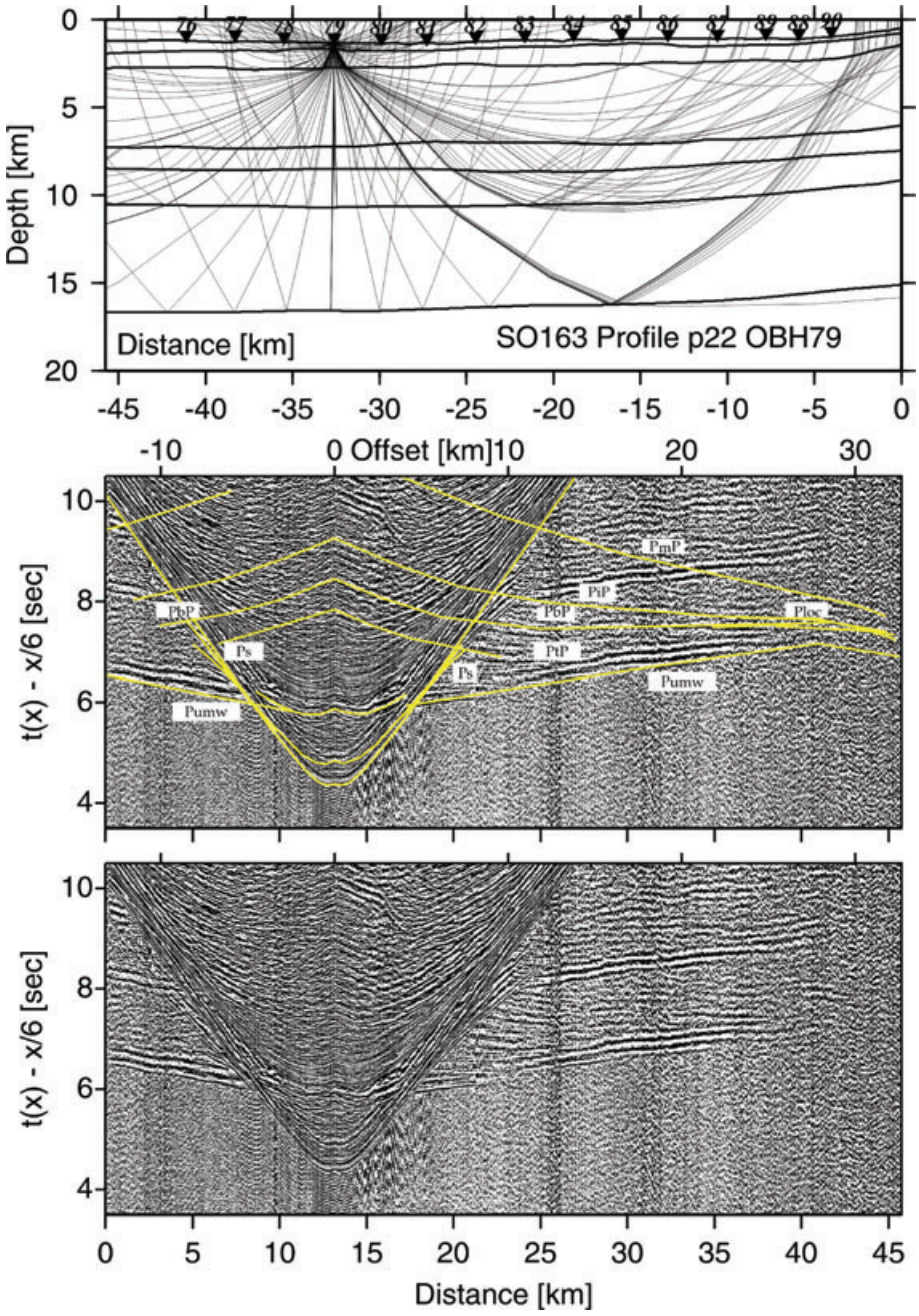


**Figure 14.** Record section and ray diagram for station OBS79 deployed along the strike-line SO163-P22. Please refer to Fig. 6 for display information. The pre-critical reflection phase PtP tracks the top of the 'megalens'. The plate boundary reflection PbP tracks the downgoing slab. The reflection phase PiP records the top of the lower oceanic crust and the refraction phase Ploc travels through the lower oceanic crust.

upper margin wedge and the lower margin wedge (Ye *et al.* 1996; Stavenhagen *et al.* 1998; Christeson *et al.* 1999; Sallarès *et al.* 1999, 2001), whereas our data constrain the extent and termination of this layer. The corresponding dense ray coverage is shown in Fig. 11.

Based on the approach of Clift & Vannucchi (2004) we calculate the average slope angle over a distance of 50 km to eliminate small-scale anomalous trends. A large slope angle ($>8^\circ$) occurs close the trench over a distance of 5 km. The mean forearc slope angles are 3.2° for dip-line P15 and 3.8° for dip-line P24. The average dip angles of the oceanic plate are 9.0° for P15 and 9.1° for P24. These parameters then yield forearc tapers of 12.2° for P15 and 12.9° for P24, which are larger than observed to the northwest at 86°W (taper angle of 7.6°) and smaller than for Mexico (99°W), Guatemala (91°W) and Nicaragua erosive margins documented by Clift & Vannucchi (2004), but fall well within the range of erosive margins.

### 5.2 'Megalens' and LVZ

Subducted sediment overlying the oceanic igneous crust is observed all along the convergent Pacific margin offshore Costa Rica and is manifested in a LVZ (Ye *et al.* 1996; Stavenhagen *et al.* 1998; Christeson *et al.* 1999). Along our dip lines, the LVZ shows a constant velocity of 3.2 km $s^{-1}$ from the trench to approximately

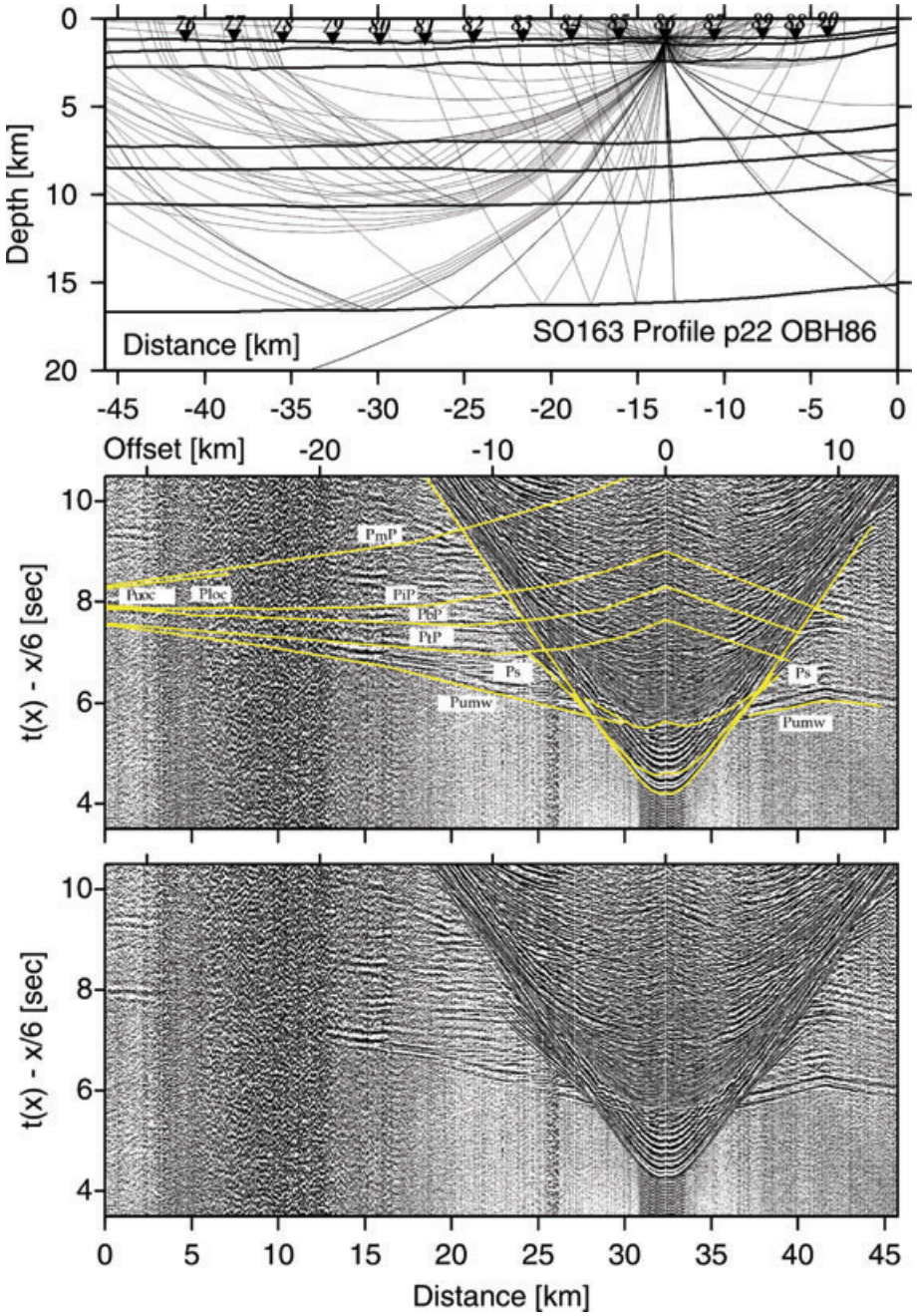


**Figure 15.** Record section and ray diagram for station OBH86 deployed along the strike-line SO163-P22. Please refer to Fig. 6 for display information. The pre-critical reflection phase PtP tracks the top of the 'megalens'. Phases Puoc and PbP track the downgoing slab.

20 km landward of the deformation front. The LVZ extends beneath the margin wedge with velocities increasing to 4.3 km $s^{-1}$ at depths exceeding 10 km (Fig. 5). The 'megalens' is concealed between the margin wedge and the subducted slab, and was first identified on MCS profile SO81 Line 4 (Hinz *et al.* 1996). We iteratively converted our velocity-depth model of P15 in two-way time to match the MCS data. In our model refracted phases from the upper oceanic crust and reflection phases from the bottom of the 'megalens' are observed and modelled on several OBH(S) stations, therefore we can be confident to constrain the bottom velocity of the 'megalens' with 4.3 km $s^{-1}$. The amplitude modelling reveals a LVZ bounding the 'megalens', which coincides with the high amplitudes observed in the MCS data.

Gravity surveys in our study area show a broad negative free-air anomaly (–50 to –30 mGal) (Barckhausen *et al.* 1998), whereas seamounts and the Quepos plateau generate a positive gravity anomaly. A gravity model by Barckhausen *et al.* (1998) distinguishes between a model with and without a seamount. Their calculated positive gravity anomaly indicates a buried seamount beneath the margin, however, along our profiles, the gravity pattern cannot be correlated to a possible subducted seamount model. Subducted seamounts have however been detected at different margins worldwide: a 13 km thick $\times$50 km wide seamount at a depth of 10 km was imaged in the Nankai subducted zone (Kodaira *et al.* 2000), with *P*-wave velocities of 5 km $s^{-1}$ increasing to 7.2 km $s^{-1}$. By comparison, the size of the 'megalens' is much smaller (1.5 km

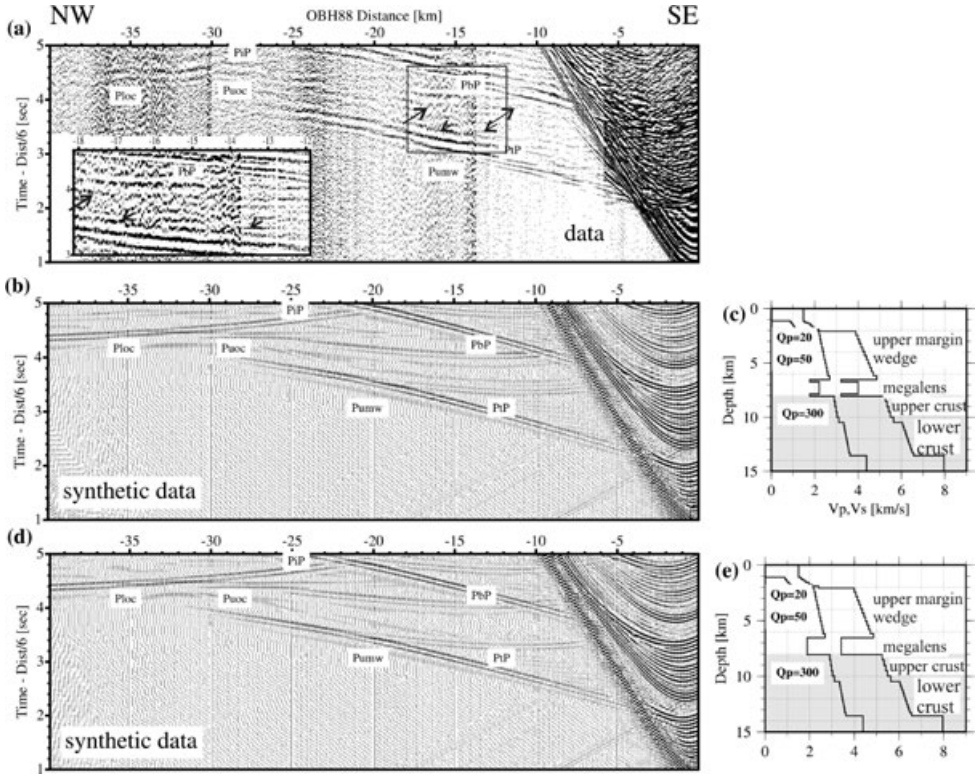


**Figure 16.** 1-D reflectivity modelling for OBH 88 deployed along the strike-line P22. (a) The different seismic phases are identified from the data of OBH 88. Phase PtP shows the reflection from the top of the first LVZ and PbP shows the reflection from the bottom of the second LVZ. The arrows show the reflections from the bottom and top of the two extreme low-velocity thin layers. Lower inset shows an enlarged part indicated by a box in the data. (b) shows the preferred synthetic seismogram matching the data and (c) displays the corresponding velocity-depth profile. (d) The low velocity gradient within the margin wedge and only one LVZ in the velocity-depth profile are shown for comparison. Reflections from a single LVZ cannot adequately match the data. Source signal input is a 12.5 Hz Fuchs–Mueller signal. In the *P*- and *S*-wave velocity-depth profiles, the depth range of the subducted slab is grey shaded.

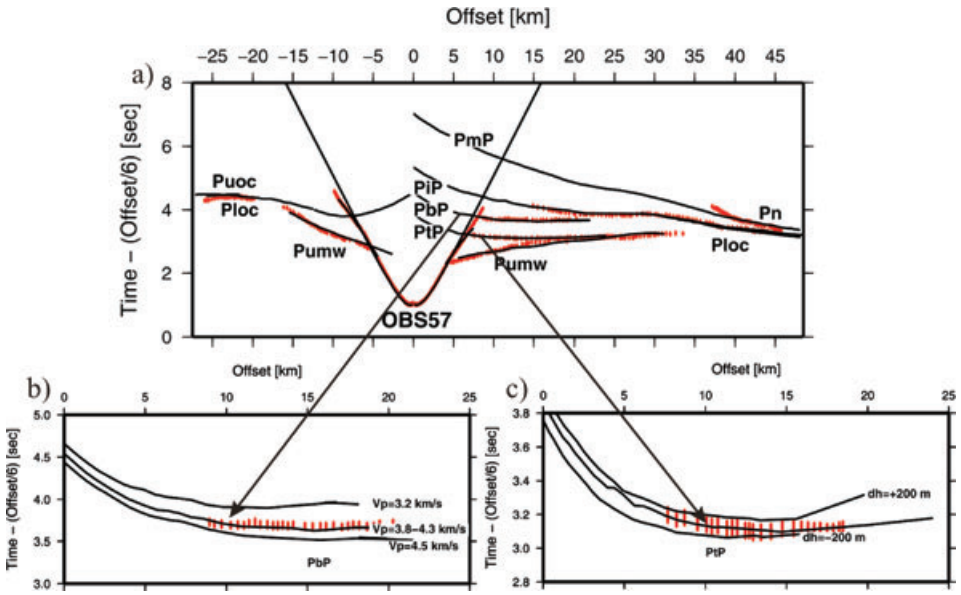


**Figure 17.** Sensitivity tests of the velocity and the geometry of the top and the bottom of the megalens demonstrated for OBS57. *P*-wave velocities of 3.2 , 3.8–4.3, and 4.5 km $s^{-1}$ within the layer of the megalens were calculated and compared to the observed traveltimes (b). Two different depths (±200 m) of the top interface of the megalens were chosen to show the fitting of the traveltime curve. Observed traveltime picks with 50 ms error are shown in red.

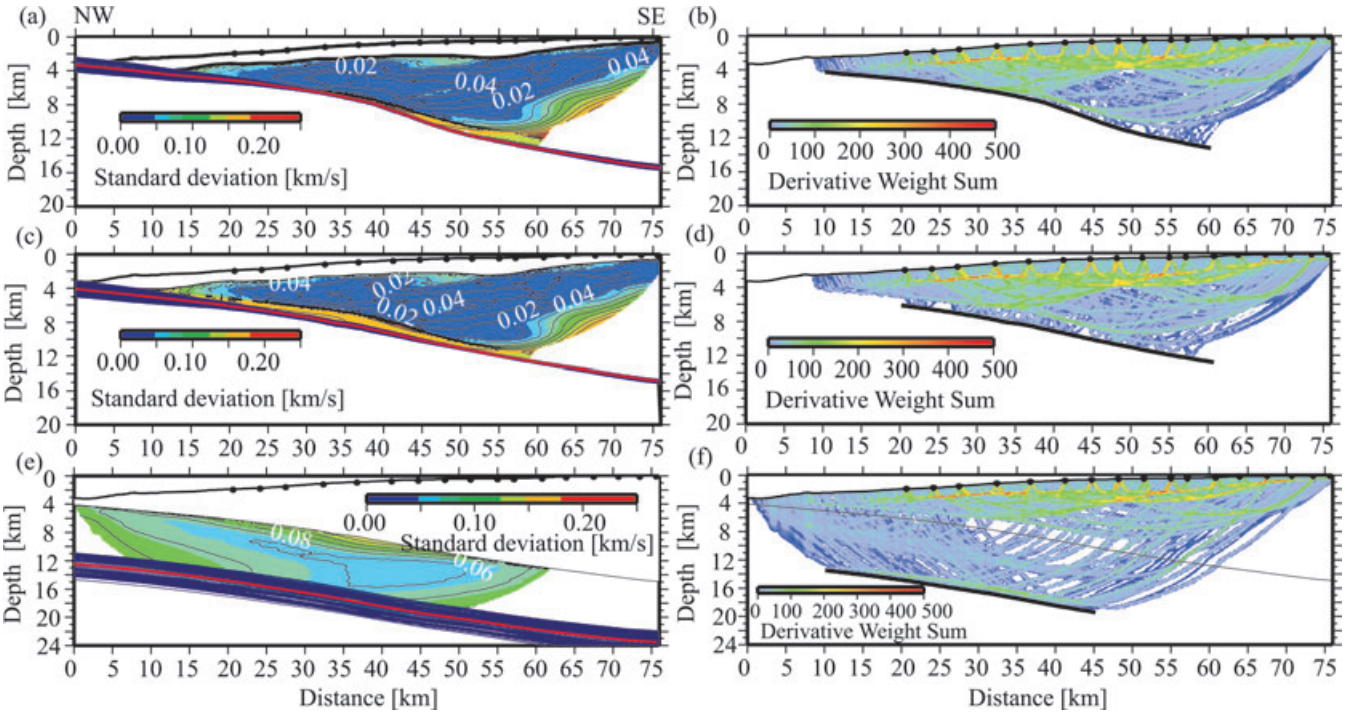


**Figure 18.** Standard deviations for velocity and reflector depth nodes derived by 100 Monte Carlo ensembles (a, c, e) and corresponding derivative weight sum from the average 100 realizations (b, d, f). Red lines show the average depth of reflectors and contours are drawn at 0.02 km s$^{-1}$ interval (a, c, e).

thick × 15 km wide) and its seismic velocities are lower (3.8–4.3 km s$^{-1}$). This is also true in comparison to the Moresby seamount in the Woodlark Basin ($V_p$ > 6 km s$^{-1}$) (Zelt *et al.* 2001). At the central Ecuador margin, an 8 km long × 0.7 km high sediment lens at approximately 4 km depth was identified from seismic images (Sage *et al.* 2006). This sediment lens is much smaller than the Costa Rica 'megalens' (Fig. 19a) and is interpreted as material accumulated in the wake of a subducting seamount. Based on our observations, the 'megalens' cannot be explained by a seamount tunnelling mechanism.

### 5.3 Subducted oceanic crust

The igneous oceanic crust is divided into an upper and a lower crustal layer with varying velocity gradients. On the two dip-lines, the refracted and reflected phases constrain the interface within the oceanic crust (Figs 6–10). The strong reflections from the plate boundary are all clearly observed (Figs 6, 8–9). Deeper PmP and Pn phases are observed on a number of stations (OBS57, Fig 8; OBH106, Fig. 10; OBS74, Fig. 13), and provide some constraint on the deep part of the model. On the strike-line P18, due to the higher velocities of the lower margin wedge (5.2–5.5 km s$^{-1}$) with respect to the upper oceanic crust, no refracted waves from the upper oceanic crust can be observed, but the strong wide-angle reflection PiP and pre-critical reflection PbP can be used to constrain the interfaces within the oceanic crust (Fig. 12). At Quepos plateau, a 3-km-thick basalt layer was interpreted as upper crust Layer-2A (Walther 2003). Along our profile, the oceanic crust shows an increased thickness of 7.5–8 km corresponding to crustal thickening towards Cocos Ridge. Line SO81-200 to the north (line d in Fig. 2) displays a crustal thickness of 7.0 km (Ye *et al.* 1996), whereas the oceanic crust to the south increases to a thickness of 14 km along the neighboring refraction profile (line f in Fig. 2) (Stavenhagen *et al.* 1998), which is located on the flank of the Cocos Ridge.

### 5.4 The nature of the 'megalens'

Understanding the nature and origin of the 'megalens' may be important to the concept of basal erosion in convergent margins. The nature of the 'megalens' was not unambiguously resolved since its first imaging in 1992 due to a lack of detailed seismic velocity information. This study clearly precludes a seamount origin.

Along the plate boundary fluids play an important role to facilitate basal erosion of the upper plate (Le Pichon *et al.* 1993; von Huene & Ranero 2003; Sallarès & Ranero 2005; Ranero *et al.* 2008). Initial sediment dewatering processes involve pore water squeezed from the subducted sediment at temperature domains of <60°C (Fig. 19a). At greater depth and increased temperatures of 50–160°C, mineral dehydration reactions pose the dominant process generating fluids at the plate boundary (e.g. Moore & Vrolijk 1992; Hensen *et al.* 2004). Along the upper boundary of the 'megalens' the expected temperatures fall between 100 and 120 °C (compare Fig. 19). As suggested by Ranero *et al.* 2008, plate boundary fluids will migrate upward through the fractured upper plate where they are detected at seeps. In the vicinity of our seismic line, expulsion of fluids generated at deep structural levels occurs at Mound 11 mud volcano (Hensen *et al.* 2004) (Figs 4 and 19a). Geochemical evidence from Cl-depleted fluid samples of Mound 11 (see Fig. 4 for location) and other seeps along the Costa Rica margin (Hensen *et al.* 2004) as well as the inverse amplitude polarity of the plate boundary reflections (Ranero *et al.* 2008) suggests a deep origin of the fluids. Compaction, increased porosity, loss of sediment and the smectite–illite transition can raise the seismic velocity of sediment to ∼4 km s$^{-1}$ at about 8 km depth (Sage *et al.* 2006), thus increasing the

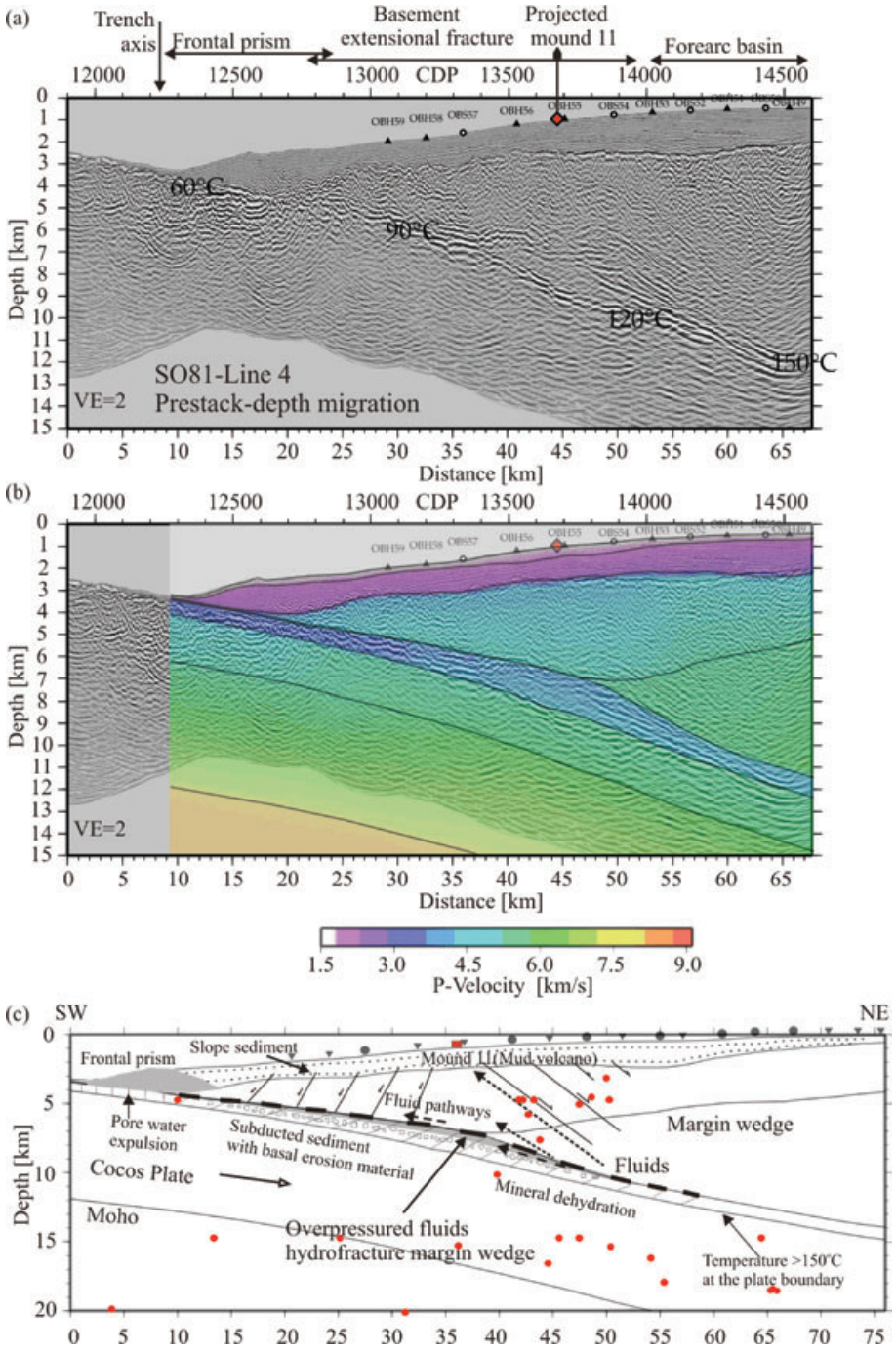


**Figure 19.** Seismic image and the interpretative velocity structure of the central Costa Rica subduction zone. (a) Prestack depth-migrated SO81-Line 4 (Ranero & von Huene 2000). Basement extensional fractures are indicated by normal faults. The OBH(S) stations are marked on the seafloor. The location of Mound 11 (mud volcano) is projected onto the Line 4 (see Fig. 4 for a detailed location). Plate-boundary temperatures are from Ranero *et al.* (2008). (b) Superimposed image of MCS Line 4 and the seismic velocity field of Profile 15. (c) The interpretative model of the basal erosion structure. Fluids are generated by mineral dehydration and transported upward to the mound site (Hensen *et al.* 2004; Ranero *et al.* 2008). Red dots indicate local seismicity (Dinc *et al.* 2007).

velocity to values comparable to the 'megalens' seismic velocities. The observed velocities of 3.8–4.3 km $s^{-1}$ in the 'megalens' may best be explained by a hybrid composition, consisting of subducted sediment, fractured upper plate material and fluids. The lens-shaped feature is part of a LVZ (Fig. 19b), however, the modelled velocities are higher than the seismic velocities of 2.2–2.8 km $s^{-1}$ determined for sediment lenses at the Ecuador margin (Sage *et al.* 2006). An exclusive composition of subducted trench sediment is less likely due to the higher velocities as well as much larger dimensions of the Costa Rica 'megalens' compared to the Ecuadorian sediment lenses.

The fate of the 'megalens' remains enigmatic: its current position aligns with the lower margin wedge and the onset of local seismicity beneath the middle slope. The microseismicity events from a local network (Dinc *et al.* 2007) are projected onto the velocity model in Fig. 19b and indicate the distribution of the intraplate seismicity

and oceanic crustal seismicity. The lack of the microseismicity over the 'megalens' suggests slow displacement there.

## 6 CONCLUSIONS

The modelling and interpretation of the seismic wide-angle data, combined with coincident seismic reflection data and amplitude modelling, have enabled us to construct a detailed velocity-depth model covering the Pacific margin of central Costa Rica. The data clearly define two layers within the margin wedge, the high velocity gradient upper margin wedge with velocities of 4.3–5.0 km $s^{-1}$ and the reduced velocity gradient lower margin wedge with velocities ranging from 5.2 to 6.1 km $s^{-1}$. The leading edge of the lower margin wedge terminates above the 'megalens' about 32 km landward of the trench. The two strike-lines confirm the seaward termination of the lower margin wedge. The 'megalens' is 15–20 km wide and has a thickness of 1–1.5 km. Its seismic velocities fall between 3.8 and 4.3 km $s^{-1}$ and are clearly much lower than the velocities of subducted seamounts or plateaus. The 'megalens' is a low velocity body with respect to the margin wedge above and is bounded by thin layers of lower velocities above and below. Our preferred interpretation is that the 'megalens' is a mixture product, which consists of a buried sedimentary mélange including rocks sheared from the lower plate and highly fractured material derived from the upper plate by basal erosion. The LVZ above the 'megalens' shows a discontinuous amplitude distribution in the seismic image (Fig. 19a) and is caused by fluids and associated localized pore pressure anomalies.

## ACKNOWLEDGMENTS

We are grateful to all colleagues and participants of Cruise SO163 for their help with data acquisition and processing, particularly to the skillful crew of the RV Sonne. Data acquisition was supported by the BMBF (grant 03G0163A). Reviews by F. Klingelhoefer and J.-Y. Collot and one anonymous reviewer, and comments by the Editor greatly improved our manuscript. We are grateful to R. von Huene and C. Ranero for their constructive comments and suggestions to improve the manuscript. We used the GMT software (Wessel & Smith 1991) to plot several figures. JZ gratefully acknowledges a scholarship granted by the German Academic Exchange Service (DAAD). This publication is contribution no. 156 of the Sonderforschungsbereich 574 'Volatiles and Fluids in Subduction Zones' at Kiel University.

## REFERENCES

Azéma, J., Bourgois, J., Baumgartner, P.O., Tournon, J., Desmet, A. & Aubouin, J., 1985. A tectonic cross-section of the Costa Rican Pacific littoral as a key to the structure of the landward slope of the Middle America trench off Guatemala, in *Init. Rep. DSDP84*, pp. 831–850, eds von Huene, R., Aubouin, J., *et al*., U.S. Gov. Print. Off., Washington, D.C.

Barckhausen, U., Roeser, H. & von Huene, R., 1998. Magnetic signature of upper plate structures and subducting seamounts at the convergent margin off Costa Rica, *J. geophys. Res.,* **103,** 7079–7093.

Barckhausen, U., Ranero, C.R., von Huene, R., Cande, S.C. & Roeser, H., 2001. Revised tectonic boundaries in the Cocos Plate off Costa Rica: implication for the segmentation of the convergent margin and for plate tectonic models, *J. geophys. Res.,* **106,** 19 207–19 220.

Behrmann, J.H., 1991. Conditions for hydrofracture and the fluid permeability of accretionary wedges, *Earth planet. Sci. Lett.,* **107,** 550–558.

Bialas, J. & Flueh, E.R., 1999. Ocean bottom seismometers, *Sea Technol.,* **40**(4), 41–46.

Bowman, J.R., 1988. Body wave attenuation in the Tonga subduction zone, *J. geophys. Res.,* **93**(B3), 2125–2139.

Christensen, N.I. & Shaw, G.H., 1970. Elasticity of mafic rocks from the Mid-Atlantic Ridge, *Geophys. J . R. astr. Soc.,* **20,** 271–284.

Christeson, G.L., McIntosh, K.D., Shipley, T.H., Flueh, E.R. & Goedde, H., 1999. Structure of the Costa Rica convergent margin, offshore Nicoya Peninsula, *J. geophys. Res.,* **104,** 25 443–25 468.

Christeson, G.L., McIntosh, K.D. & Shipley, T.H., 2000. Seismic attenuation in the Costa Rica margin wedge: amplitude modeling of ocean bottom hydrophone data, *Earth planet. Sci. Lett.,* **179,** 391–405.

Clift, P. & Vannucchi, P., 2004. Controls on tectonic accretion versus erosion in subduction zones: implications for the origin and recycling of the continental crust, *Rev. Geophys.,* **42,** RG2001, doi:10.1029/2003RG000127.

DeMets, C., Gordon, R.G., Argus, D.F. & Stein, S., 1990. Current plate motions, *Geophys. J. Int.,* **101,** 425–478.

DeMets, C., Gordon, R.G., Argus, D.F. & Stein, S., 1994. Effect of recent revisions to the geomagnetic reversal timescale on estimates of current plate motions, *Geophys. Res. Lett.,* **21**(20), 2191–2194.

DeMets, C., 2001. A new estimate for present-day Cocos-Caribbean plate motion: implications for slip along the central American volcanic arc. *Geophys. Res. Lett.,* **28**(21), 4043–4046.

Dinc, A.N., Koulakov, I., Thorwart, M., Rabbel, W., Flueh, E.R., Arroyo, I., Taylor, W. & Alvarado, G., 2008. Local earthquake tomography of Central Costa Rica: transition from seamount to ridge subduction, *Geophys. J. Int.,* submitted.

Flueh, E.R. & Bialas, J., 1996. A digital, high data capacity ocean bottom recorder for seismic investigations, *Int. Underwater Syst. Design,* **18**(3), 18–20.

Flueh, E.R., Ranero, C.R. & von Huene, R., 1999. The Costa Rica Pacific margin: from accretion to erosion. *Zbl. Geol. Paläont.,* **7–8,** 669–678.

Fuchs, K. & Mueller, G., 1971. Computation of synthetic seismograms with the reflectivity method and comparison with observation, *Geophys. J. R. astr. Soc.,* **23,** 417–433.

Hey, R., 1977. Tectonic evolution of the Cocos-Nazca spreading center, *Geol. Soc. Am. Bull.,* **88,** 1404–1420.

Hensen, C., Wallmann, K., Schmidt, M., Ranero, C.R. & Suess, E., 2004. Fluid expulsion related to mud extrusion off Costa Rica—a window to the subducting slab, *Geology,* **32,** 201–204.

Hinz, K., von Huene, R., Ranero, C.R. & PACOMAR Group, 1996. Tectonic structure of the convergent Pacific margin offshore Costa Rica from multichannel seismic reflection data, *Tectonics,* **15**(1), 54–66.

Kimura, G., Sliver, E., Blum, P., *et al*., 1997. Proceedings of the Ocean Drilling Program, *Init. Rep.,* Vol. 170, 458 p., Ocean Drilling Program, College Station, Texas.

Kodaira, S., Takahashi, N., Nakanishi, A., Miura, S. & Kaneda, Y., 2000. Subducted seamount imaged in the rupture zone of the 1946 Nankaido earthquake, *Science,* **289,** 104–106.

Kopp, H., Flueh, E.R., Klaeschen, D., Bialas, J. & Reichert, C., 2001. Crustal structure of the central Sunda margin at the onset of oblique subduction, *Geophys. J. Int,* **147,** 449–474.

Kopp, H., Flueh, E.R., Petersen, C.J., Weinrebe, W. & Wittwer, A., Meramex Scientists, 2006. The Java margin revisited: evidence for subduction erosion off Java, *Earth planet. Sci. Lett.,* **242,** 130–142.

Korenaga, J., Holbrook, W.S., Kent, G.M., Kelemen, P.B., Detrick, R.S., Larsen, H.-C., Hopper, J.R. & Dahl-Jensen, T., 2000. Crustal structure of the southeast Greenland margin from joint refraction and reflection seismic tomography, *J. geophys. Res.,* **105,** 21 591–21 614.

Le Pichon, X., Henry, P., Lallemant, S., 1993. Accretion and erosion in subduction zones: the role of fluids. *Annu. Rev. Earth planet. Sci.* **21,** 307–331.

Luetgert, J.H., 1992. MacRay-interactive two-dimensional seismic ray tracing for the Macintosh, *U.S. Geol. Surv. Open File Report* 92–356.

Meschede, M., Zweigel, P., Frisch, W., Voelker, D., 1999a. Melange formation by subduction erosion: the case of the Osa melange in southern Costa Rica, *Terra Nova,* **11,** 141–148.

Meschede, M., Zweigel, P. & Kiefer, E., 1999b. Subsidence and extension at a convergent plate margin: evidence for subduction erosion off Costa Rica, *Terra Nova,* **11,** 112–117.

Miura, R., Nakamura, Y., Koda, K., Tokuyama, H. & Coffin, M.F., 2004. "Rootless" serpentinite seamount on the southern Izu-Bonin forearc: implications for basal erosion at convergent plate margins, *Geology,* **32,** 541–544.

Moore, J.C. & Vrolijk, P., 1992. Fluids in accretionary prisms, *Rev. Geophys.,* **30,** 113–135.

Mueller, G., 1985. The reflectivity method: a tutorial, *J. Geophys.,* **58,** 153–174.

Protti, M., Guendel, F. & McNally, K., 1995. Correlation between the age of the subducting Cocos plate and the geometry of the Wadati–Benioff zone under Nicaragua and Costa Rica, in *Geologic and Tectonic Development of the Caribbean Plate Boundary in Southern Central America,* ed Mann, P., *Geol. Soc. Am. Spec.Pap.,* **295,** 309–326.

Ranero, C.R. & von Huene, R., 2000. Subduction erosion along the Middle America convergent margin, *Nature,* **404,** 748–752.

Ranero, C.R., Villasenor, A., Morgan, J.P. & Weinrebe, W., 2005. Relationship between bend-faulting at trenches and intermediate-depth seismicity, *Geochem. Geophys. Geosyst.,* **6,** Q12002, doi:10.1029/2005GC000997.

Ranero, C.R., Grevemeyer, I., Sahling, H., Barckhausen, U., Hesen, C., Wallmann, K., Weinrebe, W., Vannucchi, P., von Huene, R. & McIntosh, K., 2008. Hydrogeological system of erosional convergent margins and its influence on tectonics and interplate seismogenesis, *Geochem. Geophys. Geosyst.,* **9,** Q03S04, doi:10.1029/2007GC001679.

Sage, F., Collot, J.-Y. & Ranero, C.R., 2006. Interplate patchiness and subduction-erosion mechanisms: evidence from depth-migrated seismic images at the central Ecuador convergent margin, *Geology,* **34,** 997–1000.

Sallarès, V., Dañobeitia, J.J., Flueh, E.R. & Leandro, G., 1999. Seismic velocity structure across the middle American landbridge in northern Costa Rica, *J. Geody.,* **27,** 327–334.

Sallarès, V., Dañobeitia, J.J. & Flueh, E.R., 2001. Lithospheric structure of the Costa Rican Isthmus: effects of subduction zone magmatism on an oceanic plateau. *J. geophys. Res.,* **106,** 621–643.

Sallarès, V. & Ranero, C.R., 2005. Structure and tectonics of the erosional convergent margin off Antofagasta, north Chile (23°30′S), *J. geophys. Res.,* **110,** B06101, doi:10.1029/2004JB003418.

Sandmeier, K.J. & Wenzel, F., 1986. Synthetic seismograms for a complex crustal model, *Geophys. Res. Lett.,* **13**(1), 22–25.

Soeding, E., Wallmann, K., Suess, E. & Flueh, E., 2003. FS Meteor, cruise report M 54/2–3: Caldera-Curacao, *GEOMAR Report 111,* 366 p.

Spudich, P. & Orcutt, J., 1980. Petrology and porosity of an oceanic crustal site: results from wave form modeling of seismic refraction data, *J. geophys. Res.,* **B3,** 1409–1433.

Stavenhagen, A.U., Flueh, E.R., Ranero, C.R., McIntosh, K.D., Shipley, T., Leandro, G., Schulze, A. & Dañobeitia, J.J., 1998. Seismic wide-angle investigations in Costa Rica—a crustal velocity model from the Pacific to the caribbean coast, *Zbl. Geol. Paläont., Teil ι,* **3–6,** 393–408.

Tarantola, A., 1987. *Inverse Problem Theory: Methods for Data Fitting and Model Parameter Estimation,* 613 pp., Elsevier, New York.

Tarantola, A. & Valette, B, 1982. Inverse problems = quest for information, *J. Geophys.,* **50,** 159–170.

Tsuru, T., Park, J.-O., Miura, S., Kodaira, S., Kido, Y. & Hayashi, T., 2002. Along-arc structural variation of the plate boundary at the Japan Trench margin: implication of interplate coupling, *J. geophys. Res.,* **107**(B12), 2357, doi:10.1029/2001JB001664.

Vannucchi, P., Scholl, D.W., Meschede, M. & McDougall-Reid, K., 2001. Tectonic erosion and consequent collapse of the Pacific margin of Costa Rica: combined implications from ODP Leg 170, seismic offshore data, and regional geology of the Nicoya Peninsula, *Tectonics,* **20,** 649–668.

Vannucchi, P., Ranero, C.R., Galeotti, S., Straub, S.M., Scholl, D.W. & McDougall-Reid, K., 2003. Fast rates of subduction along the Costa Rica Pacific margin: implications for nonsteady rates of crustal recycling at subduction zones, *J. geophys. Res.,* **108**(B11), 2511, doi:10.1029/2002JB002207.

von Huene, R., 1986. To accrete or not accrete, that is the question, *Geol. Rndsch.,* **75,** 1–15.

von Huene, R. & Scholl, D.W., 1991. Observations at convergent margins concerning sediment subduction, subduction erosion, and the growth of continental crust, *Rev. Geophys.,* **29,** 279–316.

von Huene, R. & Flueh, E.R., 1994. A review of marine geophysical studies along the Middle American trench off Costa Rica and the problematic seaward terminus of continental crust, *Profil 7,* pp. 143–159, University of Stuttgart, Stuttgart, Germany.

von Huene, R. *et al*., 1995. Morphotectonics of the Pacific convergent margin of Costa Rica, in *Geologic and tectonic development of the Caribbean Plate Boundary in Southern Central America,* ed Mann, P., *Geol. Soc. Am. Spec. Pap.,* **295,** 291–308.

von Huene, R., Ranero, C.R. & Weinrebe, W., 2000. Quaternary convergent margin tectonics of Costa Rica, segmentation of the Cocos Plate, and Central American volcanism, *Tectonics,* **19,** 314–334.

von Huene, R. & Ranero, C.R., 2003. Subduction erosion and basal friction along the sediment-starved convergent margin off Antofagasta, Chile, *J. geophys. Res.,* **108**(B2), 2079, doi:10.1029/2001JB001569.

von Huene, R., Ranero, C.R. & Vannucchi, P., 2004. Generic model of subduction erosion, *Geology,* **32,** 913–916.

Walther, C.H.E., 2003. The crustal structure of the Cocos ridge off Costa Rica, *J. geophys. Res.,* **108**(B3), 2136, doi:10.1029/2001JB000888.

Weinrebe, W. & Flueh, E.R., 2002. SUBDUCTION 1, FS SONNE Cruise Report SO163 1&2, Multi-system analysis of fluid recycling and geodynamics at the continental margin off Costa Rica, *GEOMAR Report 106,* 534 p.

Wang, K & Hu, Y., 2006. Accretionary prisms in subduction earthquake cycles: the theory of dynamic Coulomb wedge, *J. geophys. Res.,* **111,** B06410, doi:10.1029/2005JB004094.

Werner, R., Hoernle, K., Van Den Bogaard, P., Ranero, C.R. & von Huene, R., 1999. Drowned 14-m.y.-old Galapagos archipelago off the coast of Costa Rica: implications for tectonic and evolutionary models, *Geology,* **27,** 499–502.

Wessel, P. & Smith, W.H.F., 1991. Free software helps map and display data, *EOS, Trans. Am. geophys. Un.,* **72,** 445–446.

Ye, S., Bialas, J., Flueh, E.R., Stavenhagen, A., von Huene, R., Leandro, G. & Hinz, K., 1996. Crustal structure of the Middle American trench off Costa Rica from wide-angle seismic data, *Tectonics,* **15,** 1006–1021.

Zelt, B.C., Taylor, B. & Goodliffe, A.M., 2001. 3-D Crustal velocity structure at the rift tip in the western Woodlark basin, *Geophys. Res. Lett.,* **28**(15), 3015–3018.

Zhang, J. & Toksöz, M.N., 1998. Nonlinear refraction traveltime tomography, *Geophysics,* **63,** 1726–1773.

*9*

Koulakov, I., Stupina, T., Kopp, H., 2010.

**Creating realistic models based on combined forward modeling and tomographic inversion of seismic profiling data.**

Geophysics, 75, doi:10.1190/1.3427637.

GEOPHYSICS, VOL. 75, NO. 3 (MAY-JUNE 2010); P. B115–B136, 25 FIGS., 2 TABLES.
10.1190/1.3427637

## Case History

# Creating realistic models based on combined forward modeling and tomographic inversion of seismic profiling data

Ivan Koulakov[1], Tatiana Stupina[1], and Heidrun Kopp[2]

## ABSTRACT

Amplitudes and shapes of seismic patterns derived from tomographic images often are strongly biased with respect to real structures in the earth. In particular, tomography usually provides continuous velocity distributions, whereas major velocity changes in the earth often occur on first-order interfaces. We propose an approach that constructs a realistic structure of the earth that combines forward modeling and tomographic inversion (FM&TI). Using available a priori information, we first construct a synthetic model with realistic patterns. Then we compute synthetic times and invert them using the same tomographic code and the same parameters as in the case of observed data processing. We compare the reconstruction result with the tomographic image of observed data inversion. If a discrepancy is observed, we correct the synthetic model and repeat the FM&TI process. After several trials, we obtain similar results of synthetic and observed data inversion. In this case, the derived synthetic model adequately represents the real structure of the earth. In a working scheme of this approach, we three authors used two different synthetic models with a realistic setup. One of us created models, but the other two performed the reconstruction with no knowledge of the models. We discovered that the synthetic models derived by FM&TI were closer to the true model than the tomographic inversion result. Our reconstruction results from modeling marine data acquired in the Musicians Seamount Province in the Pacific Ocean indicate the capacity and limitations of FM&TI.

## INTRODUCTION

The increased data density along seismic profiles progressively requires automating processing and interpretation tools. The interpretation results then provide rich information about the structure of the earth's interior for the depths, depending on the scale of the experiment — from a few meters' depth in engineering and exploration tasks (e.g., Martí et al., 2008; Yordkayhun et al., 2009) to crustal and upper mantle structures in deep seismic sounding studies (e.g., Nielsen and Thybo, 2009; Palomeras et al., 2009, among recent successful examples). Kinematic modeling schemes based on traveltime information provided by refracted seismic rays represent the dominant approach to wide-angle data modeling. In some studies, the traveltimes of reflected rays are used to constrain the a priori model and to perform joint inversion of refracted and reflected traveltimes (e.g., Korenaga et al., 2000; Sallarès et al., 2003).

There are two basic schemes for modeling refraction data: forward kinematic modeling and tomographic inversion, which usually are performed independently and in some cases complement each other (e.g., Nielsen and Thybo, 2009). Forward kinematic modeling consists of computing traveltimes in different velocity models. The aim of this approach is to find a velocity model that provides the best fit to the observed traveltimes (e.g., Luetgert, 1992; Zelt and Smith, 1992). The velocity distribution is usually adjusted manually and strongly depends on the scientist's experience. In many cases, a comparison of calculated traveltimes with the observed times provides an ambiguous, nonunique solution. It is fairly difficult to formalize this process and render it automatically. Therefore, the alternative tomographic inversion approach is more popular because it seems to be less dependent on the subjective input of the user.

During the last few decades, several different tomographic approaches have been developed for noncommercial active source profiling (e.g., Hole, 1992; Zelt and Barton, 1998; Korenaga et al., 2000; Hobro et al., 2003). Most of the codes used in practice (e.g., FAST code; Zelt and Barton, 1998) are based on first-arrival data. However, some codes use later phases (e.g., Tomo2D, Korenaga et al., 2000) and inhomogeneous starting models based on existing a priori information. We should also mention the FMTOMO code (Rawlinson and Urvoy, 2006), which includes a wide range of possibilities such as passive and active schemes, teleseismic data, direct and multiple reflecting phases, inversion for 3D velocity distribution, interface geometry, and source coordinates.

Manuscript received by the Editor 20 June 2009; revised manuscript received 17 November 2009; published online 26 May 2010.
[1]Institute of Petroleum Geology and Geophysics, Novosibirsk, Russia. E-mail: koulakoviy@ipgg.nsc.ru; E-mail: stupinata@ipgg.nsc.ru.
[2]Leibniz Institute of Marine Sciences, IFM-GEOMAR, Kiel, Germany. hkopp@ifm-geomar.de.

However, the tomographic approach has some obvious limitations, which makes the interpretation of the results quite intricate. First, in most cases, the tomography results provide a continuous velocity-depth distribution without first-order velocity contrasts. Given a starting model with predefined velocity interfaces, these cannot be shifted by the relative velocity anomalies obtained during first-arrival tomography. In most applied studies, the output of the tomographic inversion is a continuous velocity model, presented by contour lines. At the same time, however, it is common to base the geologic-tectonic interpretation on the distribution of the main petrophysical interfaces (e.g., basement, Moho), which seem to follow some contour lines (e.g., 6.0 and 7.8 km/s). This is an obvious contradiction that must be considered the main shortcoming of the tomographic approach in refraction seismic techniques.

In many cases, it is useful to predefine the starting model based on a priori information of the local study area. However, the final solution would be controlled mostly by this preconditioning of the starting model. As a consequence, it is difficult to judge if any similarities between the input model and the final output model adequately represent the natural setting. Just analyzing the rms values of traveltime residuals after inversion is not sufficient. For some parts of the study area, the solution may be well founded, resulting in small average rms values, whereas other parts of the model (especially areas with a sparse ray coverage) may not be authentic. In addition, in case of insufficient ray coverage, the solution can contain artifacts that are not easily separated from relevant patterns.

Furthermore, the damped tomographic inversion usually biases the shapes and amplitudes of the retrieved patterns with respect to real structures in the earth. It should be admitted that the velocity distribution reported in tomograms is not a direct image of real structures but just a blurred picture. Retrieving the real velocity distribution in the earth is only possible through careful investigating of properties of the tomographic operator.

We propose a new approach, called forward modeling and tomographic inversion (FM&TI), to solve some of these issues. FM&TI consists of six stages:

1) Processing the real data using tomographic inversion
2) Constructing a synthetic model with realistic velocity distribution
3) Computing synthetic traveltimes in this model
4) Processing the synthetic data using the same steps of tomographic inversion and free parameters as in stage 1
5) Comparing the tomograms derived after stages 1 and 4
6) Updating the synthetic model and iteratively performing stages 2–6

The FM&TI approach is based on a newly developed code (Koulakov, 2009b) called PROFIT (profile forward and inverse tomographic modeling), which can be applied for modeling marine and land active seismic profiling data. The code creates user-friendly complex seismic models as input for subsequent forward modeling and inversion. The same strategy can be realized using some other codes.

The approach of finding a probabilistic model based on combined forward modeling and tomographic inversion has been used in 3D passive-source tomographic imaging in central Java (Koulakov et al., 2007), in the Toba caldera (Koulakov et al., 2009b), and for some regional (Koulakov and Sobolev, 2006) and teleseismic (Koulakov et al., 2006) studies. For active-source profiling tomography, FM&TI is novel.

This paper presents the FM&TI approach for 2D refraction active-source data. To show the working ability of this approach, we use synthetic and real data sets that correspond to various geologic settings of different scales and complexity. The first data set is based on a complicated synthetic *Mount* model that may exist, for example, in tunnel exploration (Figure 1a). The second data set, the *Salt* model (Figure 2a), is based on an experiment in the Pre-Caspian area. The presented model is purely synthetic but uses realistic distributions of source-receiver pairs. We simulate two high-velocity salt domes and try to reproduce them using existing synthetic traveltimes. The third data set, *Sea*, consists of a marine profile acquired in the Musicians Seamount Province located north of the Hawaiian Chain in the Pacific Ocean (Freedman and Parsons, 1986; Sager and Pringle, 1987). Data processing is described in detail in Kopp et al. (2003) and in Appendix A.

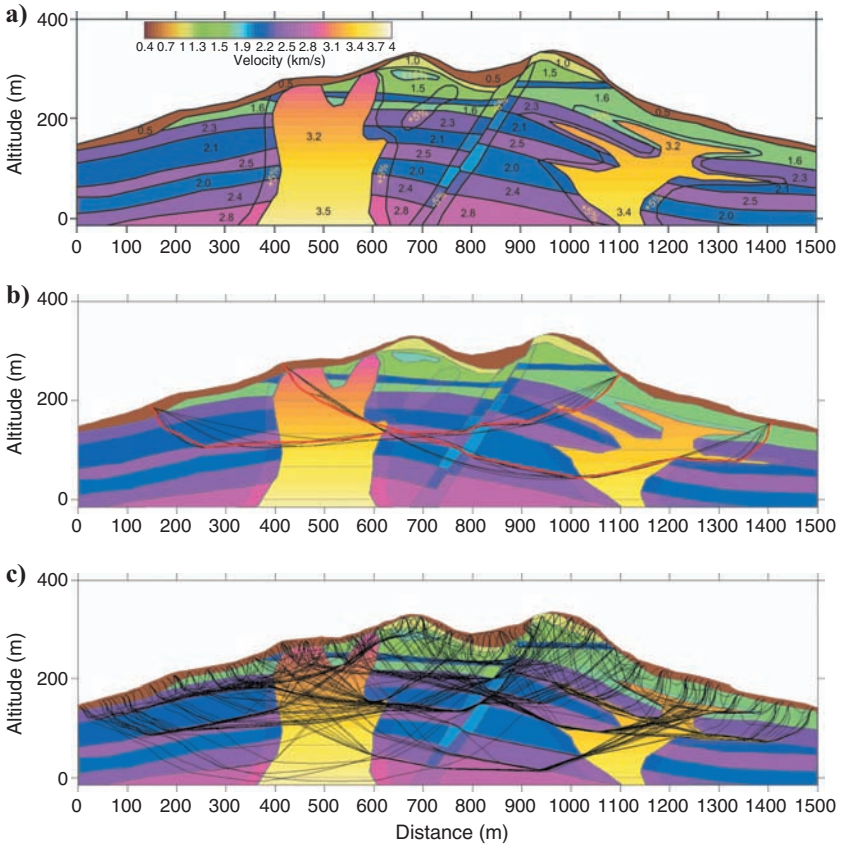


Figure 1. Synthetic Mount model. (a) Velocity definition in the model. Black numbers indicate values of velocities; white numbers are velocity variations in percent. (b) Two examples of ray construction using iterative bending. Black lines depict the evolution of the raypath in iterations; red is the final path. (c) Raypaths for sources and receivers located on the surface; one-tenth of the total ray amount in the synthetic data set is shown.

Results of tomographic modeling of this data set are presented.

The FM&TI approach, which unites the concepts of ray-tracing modeling and tomographic inversion, may provide more reliable and realistic images of the subsurface structure than applying these methods individually.

## PROFIT ALGORITHM

### General notes

To construct complex synthetic models, to compute traveltimes in 2D velocity distributions, and to perform the tomographic inversion, we have developed the PROFIT code (Koulakov, 2009b). The code consists of two major components. The first comprises the tomographic inversion; it can be used as an independent and separate tomographic code for processing seismic refraction data. The second part of PROFIT is aimed at FM&TI.

The tomographic inversion of observed data using PROFIT is performed by iteratively executing the following steps:

1) Ray trace in the 2D velocity model (starting model in first iteration or updated velocity model after previous iterations).
2) Construct the parameterization grid (first iteration only).
3) Calculate the matrix and inversion.
4) Update the velocity model and return to step 1.

In the following, we describe the most important features of each of these steps.

### Ray tracing

The ray tracing used in PROFIT is based on the Fermat principle and consists of finding a path that provides the minimum traveltime between source and receiver. This idea is the basis of the bending method of ray tracing (e.g., Um and Thurber, 1987), which has been widely applied for decades and has evolved as a standard in different practical codes of local earthquake tomography (e.g., Thurber, 1993) and seismic modeling (e.g., Korenaga et al., 2000). Some modifications of the bending method allow for ray tracing in weakly anisotropic models (e.g., Grechka and McMechan, 1996).

We have created an alternative version of the bending algorithm, shown schematically in Figure 3. Finding the path of minimum traveltime consists of consecutively executing several bending regimes. In the initial step (Figure 3a), the intersection point of the ray with the sea bottom ($b$, the bounce point) is located just beneath the source $s$. We start from the straight line between $b$ and $r$ and deform it to obtain the minimum traveltime. In the first approximation, the deviation $A$ with respect to the initial straight path is computed according to

$$A(d) = B\cos\left(\pi\frac{d-\frac{D_{\text{tot}}}{2}}{D_{\text{tot}}}\right), \tag{1}$$

where $B$ is the value of bending, $d$ is the distance along the initial path, and $D_{\text{tot}}$ is the total length of the initial path between $b$ and $r$. The value of $B$ is adjusted to obtain the curve $\gamma(B)$, which provides the minimum value of the integral:

$$t = \int_{\gamma(B)} \frac{d\gamma}{V(d)}, \tag{2}$$

where $V(d)$ is the velocity distribution along the ray.

In the second step (Figure 3b), we laterally move $b$ to obtain the minimum value of integral 2. For land observations, this step is omitted because the locations of $s$ and $b$ are identical.

At the next stages (Figure 3c and d), further deviations of the path between $b$ and $r$ are performed iteratively using a formula for bending values:

$$A(d) = \frac{B}{2}\cos\left(2\pi\frac{\frac{d-(D_2-D_1)}{2}}{(D_2-D_1)}\right)+\frac{1}{2}, \tag{3}$$

where $D_1$ and $D_2$ correspond to the length along the path in the beginning and at the end of the current segment.

During the first iteration, the bending is performed for the entire segment $b-r$ in a similar way as demonstrated in Figure 3a but using formula 3. In the second iteration (Figure 3c), the path is divided into two segments of equal lengths ($b-m_1$ and $m_1-r$), and each is bent according to formula 3. After determining the minimum time curve, the entire path is divided into three parts (Figure 3d), and the same approach of bending is performed for segments $b-m_1$, $m_1-m_2$, and $m_2-r$. This procedure is repeated for the path divided into four, five, and more parts. The bending terminates when the length of the sections becomes smaller than a predefined value.

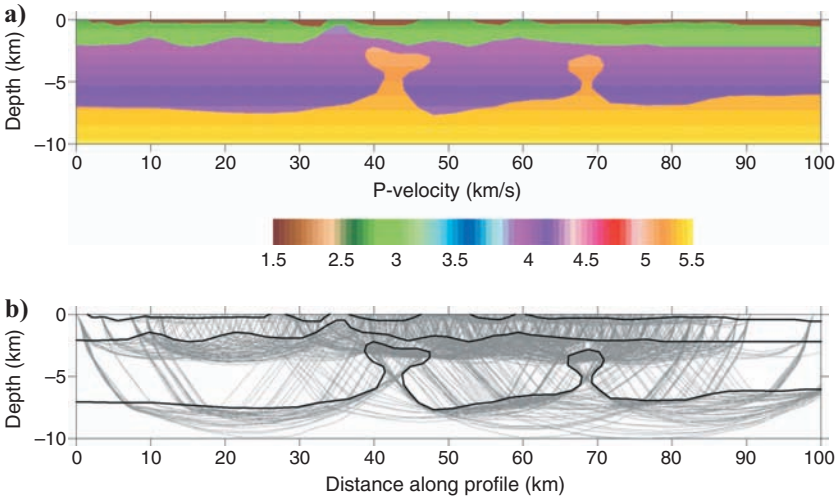


Figure 2. General setup of the Salt model. (a) Velocity distribution in the true model. (b) Raypaths used in the modeling. In this plot, only one-tenth of the total number of rays are shown.

The feasibility of the algorithm is illustrated based on the synthetic Mount model in Figure 1. Figure 1b presents examples of two rays constructed using this algorithm. Thin black lines show the paths in 20 iterations used to construct the final ray (red lines). A simple cosine-shaped line is gradually transformed into a complex shaped path that tends to pass through high-velocity patterns and avoids slow areas. The rays between sources and receivers located on the surface that were used in the experiment are shown in Figure 1c. The rays mostly travel inside high-velocity layers, and in some cases they are similar to the head waves. The low-velocity areas are generally poorly covered by the rays. Raypaths for the Salt model are presented in Figure 2b.

The bending method provides these ray solutions for a fixed calculation time that remains stable for any source-receiver pair. In a complex model such as Mount, an alternative shooting method would not be able to ensure a stable solution. It is important that our bending algorithm works for any parameterization of the velocity model (e.g., with regular or irregular grids, polygons, gradient layers). It has no limitations to the velocity values and shapes of features in the model.

In addition to the algorithm used in the PROFIT code, several other modifications of bending codes were designed for different models, e.g., 3D tracing (Koulakov, 2009a), anisotropic 2D and 3D models (e.g., Koulakov et al., 2009a), and 2D models with sharp interfaces of complex shape. The latter is described briefly in Appendix B and compared with the shooting code. We show that the bending code always provides the solution corresponding to the first arrival (global minimum), but the shooting solution may correspond to other branches of caustics (local minima that correspond to larger times than provided by bending). The misidentification of phases in shooting can result in significant errors and artifacts in further processing.

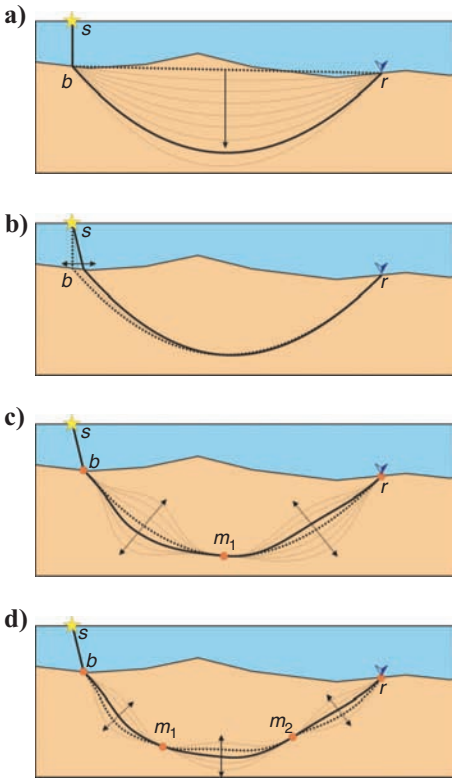


Figure 3. Sketch for explaining the principle of our version of the bending algorithm. Refer to the text for explanation of the views.

An alternative method of kinematic forward modeling is solving the eikonal equation. When the observation has few sources and many receivers (land profiles) or many sources and few receivers (marine profiles), such an approach may appear quite effective. However, for modeling first-order interfaces and strong heterogeneities, the eikonal equation requires a rather fine mesh, increasing computing time. In addition, to perform the tomographic inversion, we need the rays; the eikonal approach requires an additional step of transforming wavefronts to rays, which may create unexpected problems.

## Parameterization

We define the 2D velocity distribution using node parameterization, developed for 3D passive tomographic inversion using the LOTOS code (Koulakov et al., 2007; Koulakov, 2009a). The values of velocity anomalies are interpolated bilinearly between the nodes. The nodes are defined in a set of vertical lines with a fixed, predefined spacing. Along each line, we compute the values of the ray density (normalized total length of rays in a unit volume). The nodes are then distributed according to the ray density. To avoid excessive node fluctuations, we define the minimal spacing between the nodes in the vertical direction. In areas with lower ray density, the distance between nodes is larger. No nodes are defined in areas where the ray density is less than a predefined value (e.g., 0.1 of ray density with respect to the average value). The grid nodes are installed only in the first iteration according to the ray distribution traced in the starting model. During later iterations, velocity variations are updated based on the same nodes.

Figure 4 presents examples of grid construction for the Mount, Salt, and Sea models. The Salt and Sea cases correspond to wide-angle observations for which the node spacing in the horizontal and vertical directions is not equivalent (e.g., 2 and 0.3 km in Sea) because we expect a different vertical and horizontal resolution.

By linking the node distribution to ray density, the grid may be adapted specifically to any data set, accounting for the distinct variation in ray density. Ray distribution and density are unique features in every refraction study, depending on the instrument layout and on the composition and geometry of the subsurface. This requires a nonuniform grid with variable grid sizes dependent on the ray distribution and density. Installing a nonuniform grid as a function of ray coverage represents a novel approach that is not implemented in existing noncommercial algorithms.

In the PROFIT code, the grid sizes are smaller than the minimal resolved size of anomalies, which can be estimated from synthetic modeling (e.g., checkerboard). In this case, the resolution of the model is controlled by the damping value and the model is grid independent. Changing the grid configuration does not significantly affect the resulting model. Appendix C provides an example of inversions using two significantly different grids for the Sea data set; the images are practically identical.

## Matrix calculation and inversion

The first derivative matrix is calculated using the raypaths computed based on the ray tracing in the 2D model. Each element of the matrix $A_{ij} = \partial t_i / \partial V_j$ is equal to the time deviation along the $i$th ray resulting from a unit velocity perturbation in the $j$th node. The elements of the matrix are computed numerically.

The inversion of the overdetermined **A** matrix with a data vector perturbed by noise is unstable a priori. Therefore, this inversion should be regularized (e.g., Nolet, 1987) by adding two matrix blocks:

$$\begin{pmatrix} \mathbf{A} & \\ AM & \mathbf{I} \\ SM & \mathbf{C} \end{pmatrix} dV = \begin{pmatrix} dT \\ 0 \\ 0 \end{pmatrix},$$

where **A** is the main matrix of first derivatives, $dT$ is the data vector, **I** is the diagonal identity matrix (with only one element in each line) that controls the amplitude of the solution, and **C** is the matrix block that controls smoothing of the solution. Each line of this block contains two nonzero elements 1 and $-1$ that correspond to all combinations of neighboring nodes. Changing the values of amplitude damping $AM$ and smoothing damping $SM$ controls the amplitudes and smoothness of the derived anomalies. Inverting the entire sparse **A** matrix is performed using an iterative LSQR algorithm (Paige and Saunders, 1982; Van der Sluis and van der Vorst, 1987).

The optimum values of $AM$ and $SM$ depend on several factors.

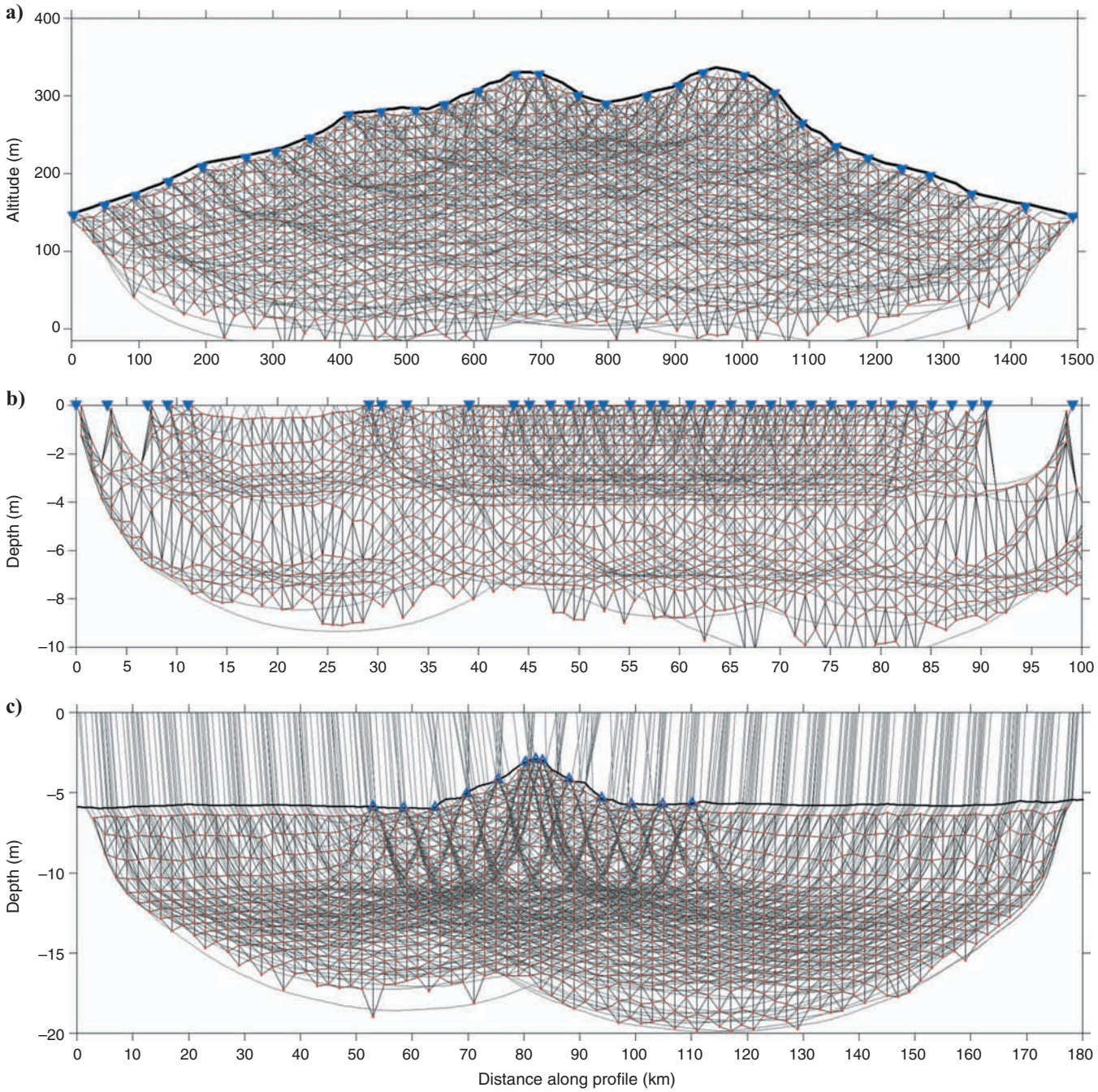


Figure 4. Raypaths in starting models (gray lines) and parameterization grids for the Mount, Salt, and Sea data sets. Nodes are indicated by red dots; thin black lines are links between the nodes used for smoothing. (a, b) The blue inverted triangles are the sources; in (c), the blue triangles are the stations on the sea bottom.

For example, when increasing the data amount, the damping parameters should be increased; in the case of increasing the numbers of nodes from smaller spacing, the damping should be decreased. In the case of larger noise levels in the data, damping should be stronger to stabilize the solution. The process of finding the damping coefficients is not formalized yet. Some authors use so-called L-curves or trade-off curves (TOCs), which show the amplitude of the solution versus rms of residuals for different damping values (e.g., Eberhart-Phillips, 1986). They propose that the value in the corner point of the L-shaped curve corresponds to the optimal damping. However, Koulakov (2009a) provides several arguments why TOCs are inappropriate for estimating damping in an iterative inversion. The most obvious argument is that in most studies (if not all), the TOC is computed in the first iteration and it does not know how many iterations will be performed. However, the same amplitude of the solution can be obtained for an underdamped inversion in one iteration and an overdamped inversion in several iterations. Furthermore, Koulakov (2009a) shows in synthetic examples that damping estimated with TOC is inadequate and does not provide the best reconstruction quality. Therefore, we strongly believe that TOC analysis should not be used in tomography.

An alternative method for determining the optimal values of damping parameters is synthetic modeling. Using realistic configurations of rays, it is possible to tune the smoothing and amplitude damping parameters to achieve optimal similarity between the synthetic and resolved patterns. These parameters can then be used to invert the observed data with the corresponding ray configuration.

The velocity anomalies obtained after inversion are recomputed in a regular grid and added to the velocity model obtained during the previous iteration. Regular representation of the velocity field is more convenient for performing the ray tracing in the next iteration.

## SYNTHETIC DATA PROCESSING (MOUNT AND SALT DATA SETS)

### Creating the synthetic data

The PROFIT code provides several different options for defining velocity models. In all cases, the velocity is a superposition of a basic velocity distribution and velocity anomalies. The basic velocity can be defined in different ways: 1D models, velocity values in a regular grid, linear velocity distributions between interfaces. For velocity anomalies, several options exist (e.g., checkerboard or anomalies inside polygons). Based on this algorithm, we have created two synthetic models that represent different realistic situations to illustrate the working ability of FM&TI.

The Mount model (Figure 1a) simulates a 1500-m-long profile that passes through a hill with an approximate relative elevation of 170 m. In this case, we model different geologic features such as magmatic batholith and sill-shaped intrusions, layered rocks with strongly varying properties, faults, and sediments. In the fault area, we produce a low-velocity anomaly that represents the fractured zone. Around the intrusions, we define a metamorphic zone with higher velocities. The basic velocity is defined inside several areas separated by polygon curves. Inside some of these polygons (high-velocity intrusions), the velocity distribution with a vertical gradient is fixed; in other polygons (sedimentary layers), velocity is constant. Additional velocity variations (such as the high-velocity zone around intrusions of lower velocities in the fault zone) are defined as velocity anomalies inside polygon areas. This model is presumably too complicated to be resolved by a detailed tomographic approach. It is designed to check the capacity and realistic limitations of the algorithms.

We consider a realistic distribution of the observation schemes that includes 30 sources and 120 receivers installed on the surface of the hill. The rays with distances of more than 1000 m between sources and receivers are not considered. In this case, 3222 rays are used. Synthetic times are calculated using the bending algorithm of ray tracing. This is the same ray tracer used for the inversion, except with a much finer integration step along the raypaths, which is required to model small-scale and sharp velocity features adequately. Some rays for this data set are shown in Figure 1c. Note that these raypaths differ considerably from those derived in the starting model (Figure 4a). Even after an iterative inversion, the paths remain rather far from the true ones. This causes a systematic error, resulting from the nonlinearity of the inversion. The traveltimes and the model are available online (Koulakov, 2009b) and can be used for testing forward-modeling and inversion codes.

The Salt model is shown in Figure 2a. In this model, we simulate two high-velocity salt domes (yellow-orange bodies) and a sedimentary layer of variable thickness (green and brown). The velocity distributions with fixed vertical velocity gradients are defined in four areas separated by three curves. The data set for this model is generated based on a distribution of sources and receivers in an experiment in the Pre-Caspian area (Kazakhstan). The main purpose of this experiment was to detect and locate salt domes, which represent a critical aspect in planned oil exploration in this area. The synthetic model was created using existing source-receiver pairs. The raypaths in the synthetic model are presented in Figure 2b. In total, 11,758 rays corresponding to 42 shots generate the Salt data set. As with the Mount data set, one person created the model and computed the synthetic data set; another person performed reconstruction with no knowledge about the model.

### Reconstructing the Mount synthetic model

The Mount synthetic model (Figure 1a) was created by one person, and the reconstruction was performed blindly by another person in the same scheme used to process measured data in real experiments.

When inverting the observed data (computed in the true model), we performed a series of trials using different starting models and different sets of damping parameters ($SM$ and $AM$). The intermediate results of this search are presented in Appendix C. The best starting velocity model, which provides the minimal rms of residuals, is shown in Figure 5a. Note that parameterization of the starting model differed from that used for defining the synthetic model. In this model, constant velocity values are defined in three polygon lines (the first coincides with the profile relief, the second is an intermediate boundary, and the lowest is the horizontal line at $z = -20$ m). For fixed $x$ along the vertical direction, we define a constant velocity gradient between these lines. Inversion results with $SM = 40$ and $AM = 30$ are presented in Figure 5b.

Now we can compare the inversion results in Figure 5b with the true model in Figure 1a. The brown sedimentary layer is resolved robustly. Velocity values and layer thickness are reconstructed correctly. The high-velocity intrusion bodies are reconstructed generally in the appropriate locations. The upper part of the left intrusion is resolved correctly in shape and amplitude. However, the lower part of this intrusion is strongly smeared horizontally, and the velocities in

this part are much lower than in the true model. As for the right intrusion, the inversion does not provide robust information about the shape of this pattern. The reconstructed body is much larger than the true intrusion. The horizontal high-velocity sills alternating with lower-velocity sedimentary layers are not resolved.

The inversion does not provide full information about the layered structure of sediments outside the magmatic bodies. However, some of the relevant patterns can be resolved. On the left side, between 150 and 350 m along the profile just below the green sedimentary layer, we observe a higher-velocity violet layer that overlies a lower-velocity blue layer. Between 800 and 1000 m, we correctly detect two inclined high-velocity layers. A thin high-velocity layer just below the right summit of the mount at about 1000 m of the profile is also visible. The other layers are not clearly detected in the inversion results.

Working blindly, we have tried to reconstruct a probabilistic synthetic model to reproduce the tomogram of the true data set inversion. To construct a probabilistic model, we cannot provide a formal algorithm that unambiguously leads to the best solution. In each concrete situation, finding a model might have some particular features. However, we have a general recipe. First, we digitize the shapes of the main patterns retrieved from the observed data inversion and create the synthetic model based on these shapes and retrieved velocities. After performing the first reconstruction using synthetic data, we can see that the velocities in some areas are too low or too high compared to the results of the observed data inversion. In this case, we correct the synthetic model in the corresponding parts and repeat the synthetic reconstruction.

Numerous different synthetic models were checked (see Appendix C). The final synthetic model that provides the best reconstruction is shown in Figure 6. However, an ideal fit of reconstructed observed and synthetic models (Figures 5b and 6b) was not achieved because of strong nonlinear effects. For example, to model a low velocity centered at $x = 850$ m and $y = 100$ m, we tried to decrease the velocity in this part. However, the reconstructed model did not implement these changes, probably because the synthetic rays avoided this low-velocity anomaly.

## Reconstructing the Salt synthetic model

Reconstruction of the Salt model started from finding the best 1D velocity model, which was estimated after several trials. The best model, which provides the minimal rms, is presented in Figure 7a. We also tested several different values of amplitude damping and smoothing. Various examples of reconstructions with different reference models and damping values are presented in Appendix C. The most robust model is derived for $SM = 0.5$ and $AM = 0.5$ (Figure 7b). This model resolves the main patterns of the original model. All variations of the uppermost sedimentary layer (brown) are reconstructed correctly. The dark blue layer in the reconstructed model repeats the shape of the basement (interface between violet and green layers). In particular, the clear thinning of the sedimentary cover at 35 km of the profile is resolved. The salt domes are mapped in correct locations; however, their sizes and amplitudes do not fully correspond to the original model.

As in the Mount case, a probabilistic model was constructed to estimate the shape of the salt domes without a priori knowledge about the true velocity distribution. The synthetic model (Figure 8a) was constructed after six trials using FM&TI (see Appendix C). The cor-

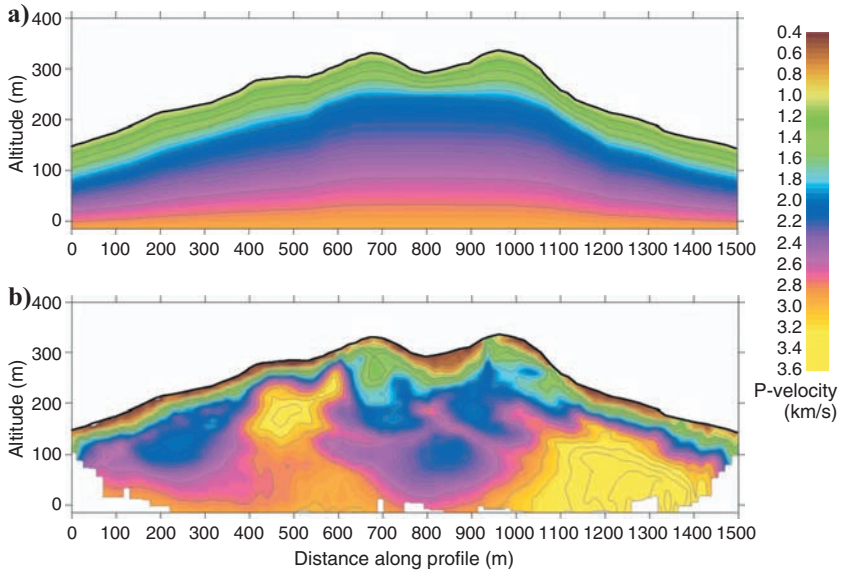


Figure 5. Result of inverting the Mount data set. (a) Starting velocity model. (b) Resulting model after 10 iterations of tomographic inversion. This result can be compared with the true model in Figure 1.

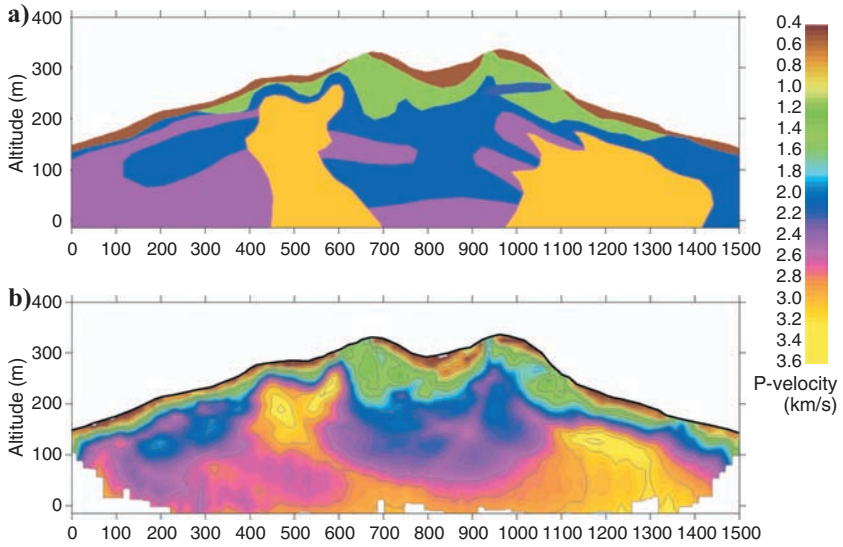


Figure 6. Blind synthetic modeling for finding a probabilistic model for the Mount data set. (a) The best synthetic model derived after several trials. (b) Result of inverting data computed by ray tracing in the model presented in (a).

responding inversion of synthetic traveltimes yields the tomogram in Figure 8b, which is strikingly similar to the observed data inversion in Figure 7b. A comparison of the retrieved synthetic model (Figure 8a) with the original model (Figure 2a) exemplifies the good fit of velocity values and shapes of the main patterns. FM&TI thus provides a structural model (Figure 8a) of geologic-tectonic features whose detailed extent would be difficult to define unambiguously based solely on the inversion result of the observed data (Figure 7b).

## Processing real experiment data (Sea data set)

In this section, we consider a marine data set acquired in 1999 in the Musicians Seamount Province in the Pacific Ocean. Details of the experiment are presented in Appendix C. The seismic structure along this profile has been investigated by Kopp et al. (2003). They could clearly resolve the extrusive style of volcanism of the Musicians Seamounts, which is manifested in the crustal thickening. The coherent and uniform phase distribution and rather clear geologic structure along the profile are favorable for testing a new approach, and these are the main reasons why this data set was selected to demonstrate the working ability of FM&TI.

The observed traveltimes of the first arrivals of the Sea data set are shown by black dots in Figure 9. The data and picking accuracy are conservatively estimated as 0.03 s at near offsets and 0.12 s at the far-offset traces. There are more than 20,000 picks for this profile. We did not consider rays of less than 5 km offset between the bounce point and the receiver because they travel in water and do not penetrate the ground; thus, this offset range does not contain information about the earth's interior. After rejecting these rays, the number of rays reduced to 18,716.

Because of the high data density of the study, it is possible to use only a subset of the data to optimize the calculation speed without loss of the resulting resolution. In Appendix C, we present the inversion result based on three data sets consisting of (a) the entire data amount, (b) one-third of the original data, and (c) one-tenth of the original data. The results show almost identical reconstruction quality. Formally, this is because frequently distributed rays with similar paths correspond to almost identical matrix lines. Two close-to-linear dependent equations do not contain more relevant information for the inversion results than one equation. On the other hand, increasing the density of ocean-bottom stations will lead to a superior ray configuration, thus improving the resolution. For the main tomographic results presented in Figure 10, we used one-third of the entire data (6237 picks); when searching the optimal parameters and most realistic synthetic model, we used the one-tenth data set to perform several trials.

The starting model was parameterized as a 1D velocity model. We defined seismic velocities at distinct depth levels and presumed constant-velocity gradients between these levels. In most trials, we defined four levels; only two of them are within the depth range of the study area. The 1D model is adjusted manually by performing only the first iteration and comparing the rms of the residuals. For some of the 1D models, we performed a full inversion consisting of nine iterations. The optimum reference model obtained in this way for the Sea data set is presented in Table 1. In addition, we performed several inversions using various values for *SM* and *AM*, which are analyzed in Appendix C.

The main results of the observed and synthetic data inversion for the Sea data set are presented in Figure 10. All results are given in absolute velocities (left column) and relative anomalies (right column) with respect to the best 1D starting model presented in Table 1. Figure 10a and b presents results of observed data inversion. A positive velocity anomaly is recognized inside the seamount edifice, indicative of an extrusive magmatic origin atop preexisting oceanic crust (Kopp et al., 2003). At a depth of 11 km, we observe a low-velocity anomaly, which shifts the contour line of

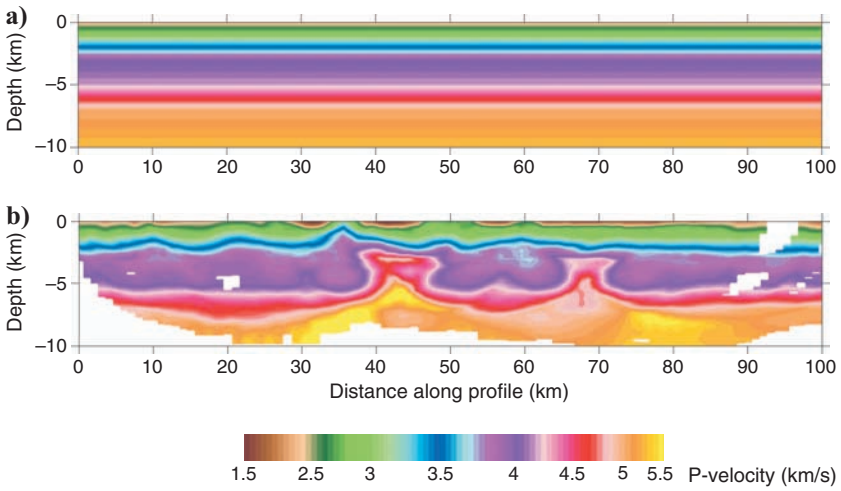


Figure 7. Result of inverting the Salt data set. (a) Starting velocity model. (b) Resulting model after 10 iterations of tomographic inversion. Compare this result with the true model in Figure 2a.

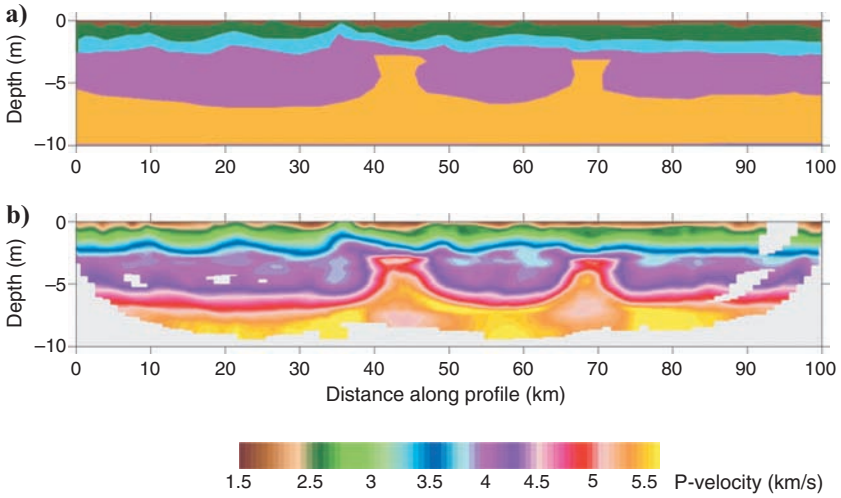


Figure 8. Result of synthetic modeling of the Salt data set. (a) Synthetic velocity model derived after several trials. Compare this result with the true model in Figure 2a. (b) Reconstruction results based on traveltimes computed in the synthetic model shown in (a). Compare this result with the observed data inversion in Figure 7b.

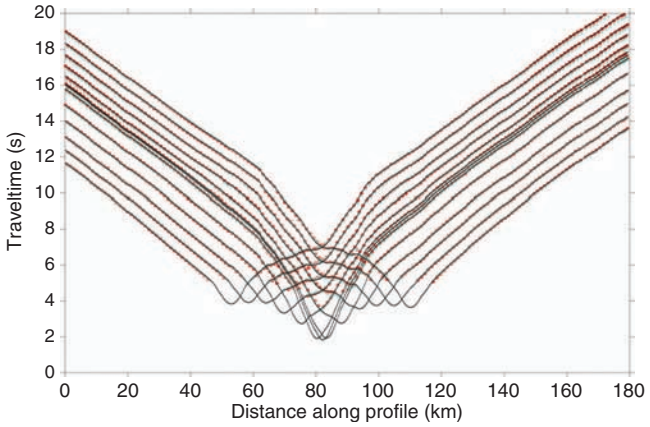


Figure 9. Traveltimes for the Sea data set. Black dots present the observed traveltimes. Blue dots are the traveltimes in the synthetic model (middle row, Figure 10). Red dots are the traveltimes in the resulting model after inverting the observed data (top row, Figure 11).

7.4 km/s from 10 km to approximately 12 km. This variation might be related to crustal thickening and a downbending of the Moho depth. Traveltimes of the derived velocity model after inversion are shown in Figure 9 with red dots.

An important test aimed at assessing the spatial resolution is the checkerboard test (see Appendix B). The reconstruction results show that most patterns discussed can be resolved robustly using the existing data.

A synthetic model, which was constrained after several trials, is presented in Figure 10c and d. The velocity distribution is defined in areas separated by layer boundaries. Furthermore, inside each velocity zone, we designate velocity anomalies with respect to the basic velocity distribution. The shapes of the anomalies are defined by polygons. The synthetic traveltimes are computed using the bending ray-tracing code. The reconstruction results based on these synthetic times are presented in Figure 10e and f. The reference model and all free parameters for tracing and inversion are identical with the observed data inversion.

Finding the best synthetic model is executed by trial and error. In Appendix C, we present examples of evolving synthetic models

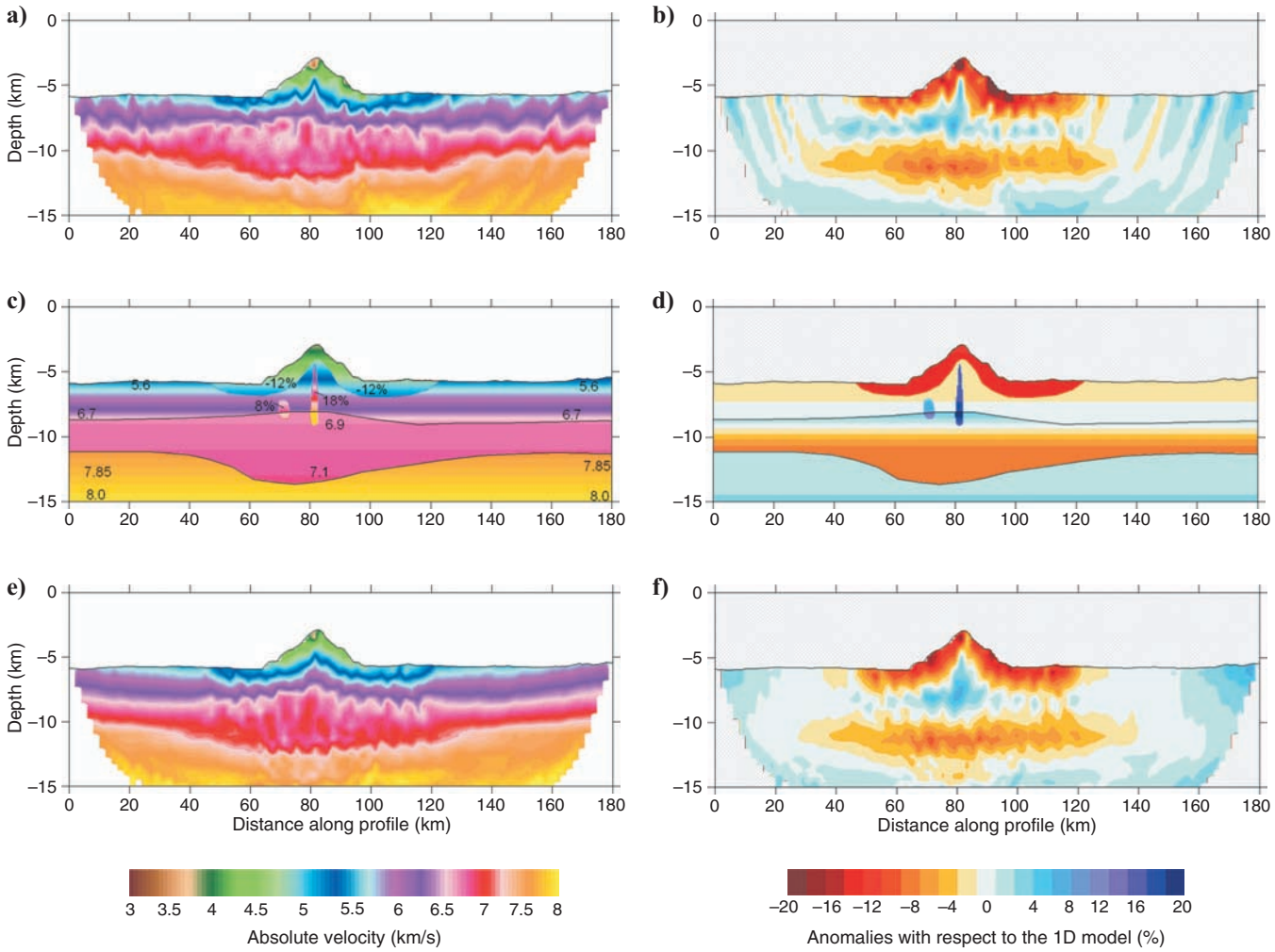


Figure 10. Results of observed data inversion and synthetic reconstruction HULA data set. (a, b) Results of tomographic inversion of observed data. (c, d) Synthetic model, constructed after several trials. (e, f) Result of the synthetic model reconstruction. In the left column, the models are presented in absolute velocity values. The right column presents relative perturbations with respect to the 1D starting model, which is identical for all three cases.

used to obtain the final synthetic model shown in Figure 10. These examples document how variations in Moho depth and of the channel contours inside the seamount affect velocities in the crust and other model parameters of the reconstruction results. Although tuning the model is rather time consuming, it is more stable and unique than in the case of classical forward modeling. Indeed, increasing the velocity or lowering the interface in one part of the synthetic model causes a velocity low in the resulting tomographic reconstruction of the same portion of the model.

We select the best model based on different criteria. The first criterion is the misfit between the observed and computed traveltimes during forward modeling in the synthetic model. The rms values of observed and synthetic traveltime differences $\|T_{obs} - T_{syn}\|$ of 12 different models are presented in Table 2. The second criterion is based on the difference between the velocity models obtained after the final inversion iteration for the observed data and the synthetic data, respectively. This value, indicated in Table 2 as $\|V_{real} - V_{syn}\|$, is computed on a regular grid for nodes where the solution exists. For the final synthetic model, we obtained good correlation between the inversion results of the observed and synthetic data. The traveltimes corresponding to the synthetic models are shown in Figure 9 with blue dots.

**Table 1. Starting 1D velocity models used for the SEA data set. Depth $z$ is given with respect to the seafloor.**

| $z$ (km) | $V$ (km/s) |
|---|---|
| 2 | 3.8 |
| 6 | 5.7 |
| 11 | 7.5 |
| 20 | 7.9 |

**Table 2. Values of time and model misfit in different synthetic models; $\|T_{obs} - T_{syn}\|$ indicates the rms between the observed and computed traveltimes in the synthetic model, and $\|V_{real} - V_{syn}\|$ is the difference between the resulting velocities after nine iterations of real and synthetic data inversions. Resulting images for the preferred models are presented in Figure 11.**

| Synthetic model | $\|T_{obs} - T_{syn}\|$ | $\|V_{real} - V_{syn}\|$ |
|---|---|---|
| 1 | 0.0278 | 0.1841 |
| 2 | 0.0284 | 0.1600 |
| 3 | 0.0283 | 0.1488 |
| 4 | 0.0281 | 0.1288 |
| 5 | 0.0172 | 0.1108 |
| 6 | 0.0184 | 0.1119 |
| 7 | 0.0180 | 0.1170 |
| 8 | 0.0277 | 0.1187 |
| 9 | 0.206 | 0.1027 |
| 10 | 0.0181 | 0.0986 |
| 11 | 0.0148 | 0.0877 |
| 12 | 0.0283 | 0.1072 |

Figure 11 presents the variance-reduction curves for different synthetic models. For the preferred model, the curve of variance reduction (orange) is close to the values obtained by the observed data inversion (blue). The similarity of the variance-reduction curves in the observed and synthetic cases is another argument for the reliability of the proposed synthetic model.

## DISCUSSION

Tomographic inversion usually biases the shapes and intensity of the real objects in the earth. Therefore, just reporting velocity values derived from tomographic inversion as a true representation of the earth's structure is not always adequate. FM&TI attempts to investigate the properties of the tomographic operator and derive estimates for the quantitative values of true structures. We propose that if two tomograms derived from inverting observed and synthetic data are identical, the known synthetic structure should be similar to the unknown structure in the real earth. At the same time, we admit that the inversion problem is fundamentally nonunique, and several different synthetic models may provide similar images on tomograms. Such nonuniqueness is shown, for example, for the Mount data set, which corresponds to a very complex velocity model. However, for simpler velocity distributions, especially when a priori information is available, the uncertainty caused by nonuniqueness of the inversion solution is strongly limited. This is illustrated by the Salt data set, for which we obtained a rather good fit.

The main motivation of using FM&TI is that grid-based inversions generally seek a smooth solution to fit observed traveltimes, failing to resolve sharp velocity contrasts. As stated, continuous velocity fields derived from tomographic inversion only represent a crude approximation to the natural velocity distribution, which originates from petrophysical material changes and distinct layer boundaries. In nature, the dominant velocity changes are related to first-order velocity changes at petrophysical interfaces. FM&TI, based on consecutively performing forward modeling and tomographic inversion, enables us to determine the most probable and realistic ve-

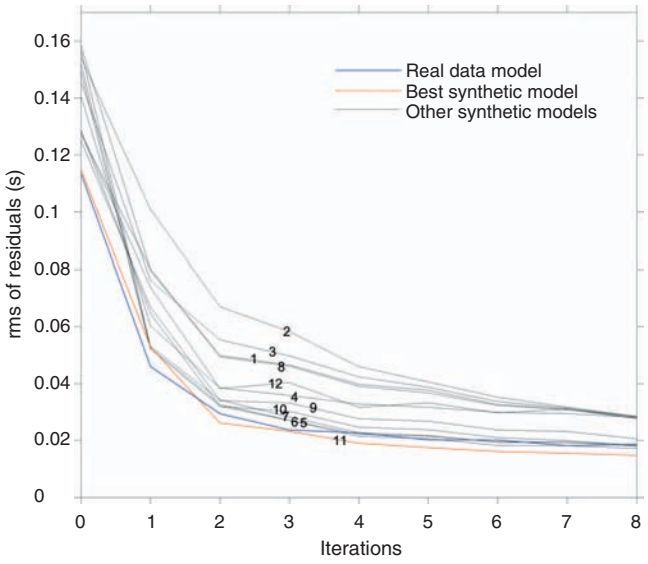


Figure 11. Variance reduction curves for different synthetic models and comparison with the real data model (blue line). The best synthetic model is represented by an orange line. The synthetic model numbers indicated in Table 2 are shown above the respective curves.

locity model. The difference of this approach compared to classical forward modeling is that in this case we compare the tomograms, not the traveltimes, which appear to be more robust and unambiguous.

At the same time, we can see with the Mount data set that a model which includes distinct vertical and lateral velocity changes linked to fine shapes of tectonic structures represents a very difficult object for reconstruction purposes. Nonlinear effects may bias the solution considerably, as seen in Figures 5 and 6. Between the intrusions, we could not achieve sufficient resemblance of the models because the velocity distribution in this area is probably controlled by smearing of the high-velocity intrusion bodies. Thus, changing velocity values in the model inside this area (e.g., adding a low-velocity body) did not improve the similarity of the images.

Despite these problems, FM&TI generally provides correct velocity values in the model. Comparing the models in Figures 1a and 6a, we can see that the main patterns in the upper part of the section (above 150-m altitude) are resolved correctly. Special caution, however, is required when interpreting deeper layers because the robustness of the reconstruction is much lower. The most important result is that even for such a complex model, the probabilistic synthetic model shown in Figure 6a is closer to the true model (Figure 1a) and contains more relevant information for geologic interpretation than the smooth result of tomographic inversion of measured data (Figure 5b).

Much more clearly, the positive effect of FM&TI is seen in the example with the Salt data set. The probabilistic synthetic model in Figure 8a correctly represents all patterns in the true model. Despite some differences in the shape of the salt domes and velocity values, this model represents the reality much better than a smooth result of tomographic inversion in Figure 7b.

For the Sea data set, we obtained some important geodynamic results. The tomographic inversion (Figure 10) supports the importance of extrusive volcanism in the Musicians Seamount Province, causing thickening. In addition, from the structural forward modeling, we were able to identify secondary intrusive processes, which added to the evolution of the volcanic elongated ridges (VERs). Whereas the velocity-depth distribution derived from the tomographic inversion provides a substantiated image of the general structure, the detailed anatomy of the volcanic ridges could be resolved only by the combined approach of tomographic forward and inverse modeling. Our new procedure obtained a realistic structural model, satisfying the observed traveltimes.

Performing the FM&TI technique provides the qualitative parameters of the velocity model. The synthetic model in Figure 10c and d consists of three layers separated by a midcrustal interface and the Moho. In the upper crust, we define a strong velocity gradient of 5.6–6.9 km/s for the depth interval of 6–9 km. In the lower crust, a decreased velocity gradient of 6.9–7.0 km/s for the depth interval of 9–13 km is applied. Beneath the Moho, we fix the velocity variation of 7.85–8 km/s for the depth interval of 12–15 km. Along the central portion of the profile beneath the seamount, the Moho depth increases from 11 km to approximately 13.5 km. Inside the seamount edifice, we define a 2–3-km-thick channel displaying a +18% velocity increase. We tested different values for the channel thickness and amplitudes and found that this configuration provides the most similar reconstruction model. To the north of the channel, we specify another positive anomaly of 8% deviation. On the flanks of the seamount, we introduce a low-velocity anomaly of −12% amplitude.

The velocity distribution gained from the tomographic inversion reveals the macrostructure of the VERs and supports earlier investigations using tomographic inversion (Kopp et al., 2003). Crustal thickening is interpreted as an indication for the extrusive character of the volcanism forming the seamounts and ridges. Top loading of the volcanoes results in a flexural structure of the oceanic crust, causing a downbending of the Moho underneath the central volcano. The fine-scale structure, however, is only disclosed from combining tomographic forward and inverse modeling, e.g., the discernible high-velocity channel that extends from the lower crust into the seamount edifice (Figure 10c and d). This feature might be caused by secondary intrusive processes, which, though suggested by Kopp et al. (2003), could not be resolved from tomographic inversion alone.

Finally, the role of nonuniqueness for the case of the Sea data set needs to be addressed. The same reconstructed anomalies can result from velocity anomalies or interface variations. For example, the low-velocity anomaly at 11 km derived in the observed data result is reproduced by a Moho decrease from 11 km down to 13.5 km in the synthetic model. The same low-velocity anomaly in the reconstruction model could be obtained by applying a smaller Moho deviation (e.g., down to 12 km) and a coeval greater-velocity step at the Moho. However, we cannot significantly change the velocity beneath the Moho because long rays are very sensitive to this value and its variation would cause increasing residuals for such rays. Thus, the contrast may be increased by a velocity decrease at the base of the crust. Nevertheless, we cannot change the velocity at the base of the crust because the value of 6.8 km/s at 8 km is fixed to model the traveltimes of shallow rays. Decreasing the velocity value in the crust at 13 km would cause a negative velocity gradient, which is unlikely. Although the theoretical problem of nonuniqueness exists in forward/inverse modeling, in practice we have little freedom in creating geologically reasonable models based on existing a priori information that satisfy the data. To reduce the ambiguity related to nonuniqueness, it is helpful to incorporate a priori information if available.

The practical value of any study is validated when many specialists in a given field further test data and compare results. We encourage colleagues to test other forward-modeling and inversion-based code results on our data sets. The synthetic velocities for the Mount and Salt models, the computed traveltimes, and detailed descriptions are available online of the Web site of the PROFIT code (Koulakov, 2009b).

## CONCLUSIONS

Using three different data sets, we have demonstrated the capability of FM&TI to provide probabilistic velocity structures that may include smooth velocity variations as well as first-order interfaces. A new code minimizes computing time by applying a new algorithm of the bending method of ray tracing. In contrast to the graph methods of pseudobending commonly used, our bending method does not require a grid; it allows any velocity parameterization (with cells or nodes, with polygons or layers, with some analytical laws). As a result, it provides more accurate solutions in significantly shorter calculation time.

The FM&TI approach is novel for active source tomography. We have presented results of its application for two synthetic and one measured data set corresponding to velocity models of different complexity and scales. The probabilistic synthetic models in all cases are closer to the true velocity distributions than continuous velocity models derived from tomographic inversion of observed data. At

the same time, the solution based on FM&TI seems to be advantageous compared to classical forward modeling based on ray tracing of refracted rays. It allows updating velocity based on analysis of tomograms, not traveltimes, as in the case of forward modeling. This provides more stable and unambiguous solutions for velocity distributions.

FM&TI allows one to construct a geologically reasonable synthetic model of the study area. This procedure is beneficial to the geologic-tectonic interpretation because it provides a structural model in addition to the continuous velocity field created by the tomography.

All of these features of FM&TI allow applying this approach in real experiments with different observation schemes and on various scales. We have shown an example of the Mount data set, which may be used as a template for engineering tasks such as planning tunnels or monitoring dams. The example with the Salt data set demonstrates that the approach can be of great use for exploring the shapes of highly contrasted bodies such as salt domes and intrusions. This could be very important when exploring for oil or ore. Future work will address successful examples of using this approach in other situations, from small-scale crosswell cases to deep seismic sounding profiles in subduction zones.

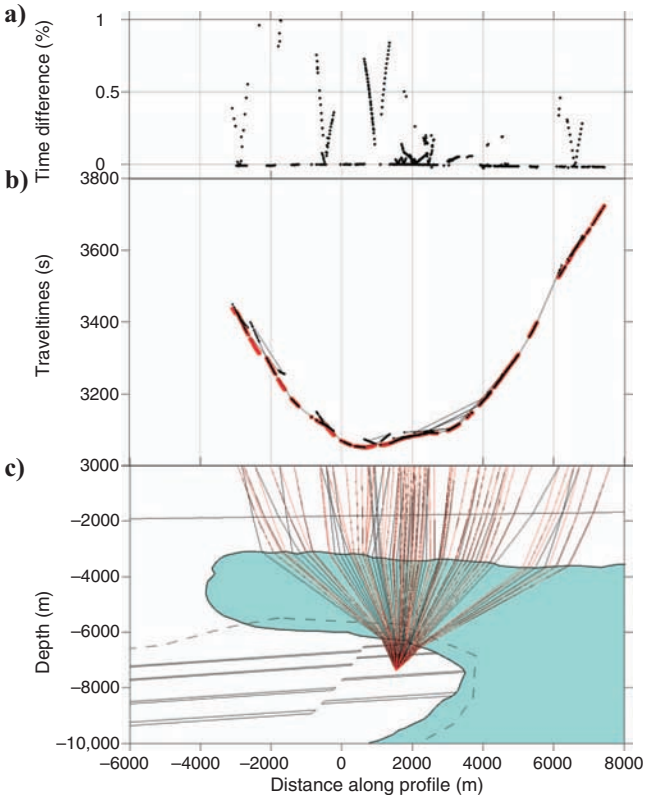


Figure A-1. Comparison of the results of tracing computed with shooting and bending algorithms. (a) Normalized difference between traveltimes computed by shooting and bending, $100\%*(T_{shooting} - T_{bending})/T_{bending}$. (b) Traveltimes computed by shooting (black dots) and bending (red dots). The data correspond to the step of ray shooting equal to 0.1°. (c) Raypaths computed by shooting (black) and bending (red). These rays correspond to the step of ray shooting equal to 1°.

## ACKNOWLEDGMENTS

The refraction data were acquired by the *RV Sonne* in the 1998 Sea experiment (supported by the German Ministry of Finance and Education BMBF). I. Koulakov and T. Stupina were supported by the Russian Foundation for Basic Research (RFBR) (grant 08-05-00276) and the Helmholtz Society/RFBR Joint Research Project (09-05-91321-SIG). We thank A. Shulgin for fruitful discussions on seismic tomography. We are grateful to Associate Editor Sergio Chávez-Pérez, Børge Arntsen, and four anonymous reviewers for their rigorous and constructive criticism, which helped us to improve the paper.

## APPENDIX A

## VERSION OF THE BENDING RAY-TRACING CODE FOR MODELS WITH SHARP INTERFACES AND COMPARISON WITH THE SHOOTING METHOD OF RAY TRACING

The bending ray-tracing code used in PROFIT is rather stable and fast. However, we have designed other versions of the bending algorithms that are oriented to specific conditions of modeling and are used in other codes. One is created for modeling rays in complex 2D media with sharp interfaces of complex shape (e.g., salt domes). In this case, we start from a straight line and find the intersection points, with all interfaces having velocity contrasts larger than a predefined value. Then we move these points along the interfaces to achieve the minimum of traveltime. After finding a curve consisting of straight segments with nodes on the main interfaces, we continue iteratively bending the entire ray using the cosine approximation.

This algorithm has been tested using a realistic salt dome model (Figure A-1c). For this case, we made the comparison with the results obtained from the shooting algorithm. We used our version of a 2D one-point shooting code (ray traced from a fixed point with fixed starting direction) based on solving the ray differential equations. If rays met first-order interfaces, we used Snell's Law. For discontinuous and rough features in the velocity model, the shooting algorithm does not provide a stable solution of the two-point problem (ray tracing between two fixed points).

To compare the bending and shooting algorithms, we performed a series of shots with fixed steps of the starting angle (from −20° to 40° with a step of 0.1°). Then we put the receivers in points of intersection of shooting rays with the upper surface and traced another ray for this source-receiver pair using the bending algorithm. The raypaths that resulted from the shooting and bending algorithms are shown in Figure A-1c. The traveltimes computed by shooting and bending methods are shown in Figure A-1b, and the normalized differences between shooting and bending times, $100\%\ (T_{shooting} - T_{bending})/T_{bending}$, are shown in Figure A-1a.

In most cases, the bending and shooting rays coincide with each other and the traveltimes are almost identical (difference is <0.01%). However, in some cases, the raypaths and traveltimes computed by shooting and bending methods do not fit each other. In these cases, traveltimes of shooting rays are always larger than provided by bending. The reason for such discrepancies is that in a highly heterogeneous model, the traveltimes are usually perturbed by caustics when several rays with different traveltimes correspond to one offset. The bending method enables the first-arrival solution, but

the shooting may provide the ray corresponding to any caustics branches. Actually, when performing shooting, we cannot know whether the modeled ray corresponds to the primary of secondary branches. If the observed traveltimes are picked as the first arrivals and computed times correspond to secondary phases, this can result in considerable error of time residual computing when the shooting method is used. On the other hand, the incapacity of the bending tracing to model secondary phases might be a shortcoming of this method.

## APPENDIX B

## CHECKERBOARD RESOLUTION TEST

Besides reconstructing realistic shapes of anomalies, it is important to perform other synthetic tests to assess the resolution capacity of the resolved models. Here, we present the results of a traditional checkerboard test with different parameters of the periodic patterns.

The initial models for the tests (left column, Figure B-1) are represented by alternating positive and negative anomalies of $\pm 3\%$

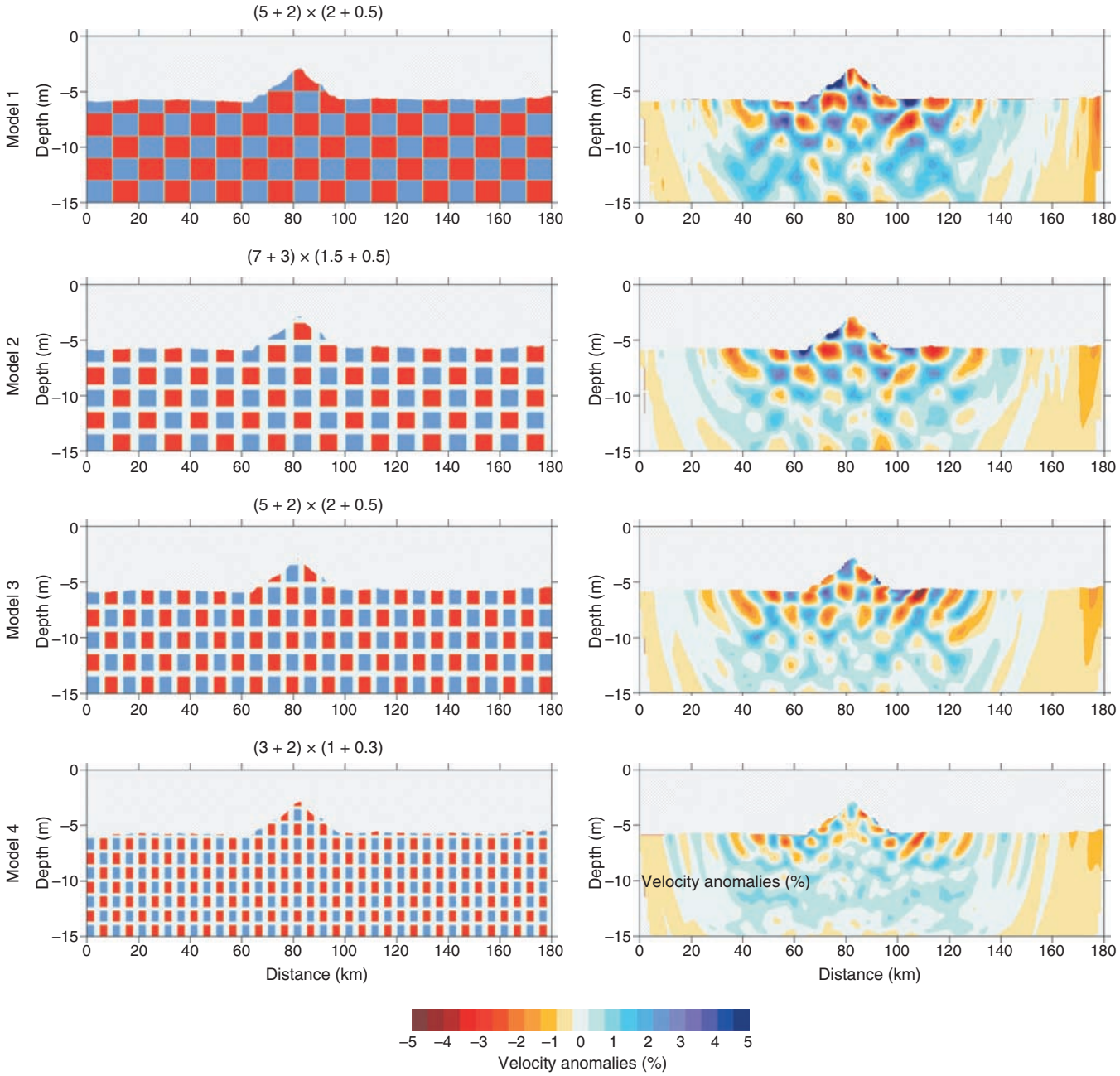


Figure B-1. Results of different checkerboard tests with different sizes of patterns (relative anomalies in percent). Left column presents the synthetic models. Numbers above each plot indicate pattern size. For model 3, $(5 + 2) \times (2 + 0.5)$ means that in the horizontal direction, the width of the anomaly is 5 km and tapering is 2 km; in the vertical direction, the height of the anomaly is 2 km and tapering is 0.5 km. In all models, the amplitude of synthetic anomalies is $\pm 3\%$. The right column shows reconstruction results after nine iterations.

amplitude. Horizontal and vertical sizes of each block are indicated above each plot. A variety of tests with different sizes of anomalies allows us to evaluate the resolving capacity of the algorithm based on the observed configuration of rays. Even the 3-km-wide and 1-km-deep patterns can be resolved in the center of the profile in the uppermost part. The larger anomalies are resolved in larger areas.

The traveltimes were computed using a 2D bending ray tracer. Rays computed in this way tend to travel through high-velocity anomalies. Therefore, the reconstruction in the first iteration is strongly biased to the positive value. After several iterations, the solution becomes more balanced regarding the amplitudes of positive and negative anomalies. Iteration 9 (right column, Figure B-1) shows a fairly stable reconstruction of most patterns in the area beneath the stations.

This test documents the importance of using a nonlinear iterative approach in tomographic inversions because the raypaths in the first and final iterations differ significantly.

## APPENDIX C

## EFFECT OF GRID CONFIGURATION ON TOMOGRAPHIC INVERSION RESULTS

In the text, we present the algorithm of grid construction for parameterizing a velocity model. We use fine grids with node spacing smaller than the size of minimal resolved patterns. Further decreasing the node spacing does not lead to any change in the resulting model. This is illustrated by an example with the sea data set (Figure C-1). The left column presents the results based on 2 km of horizon-

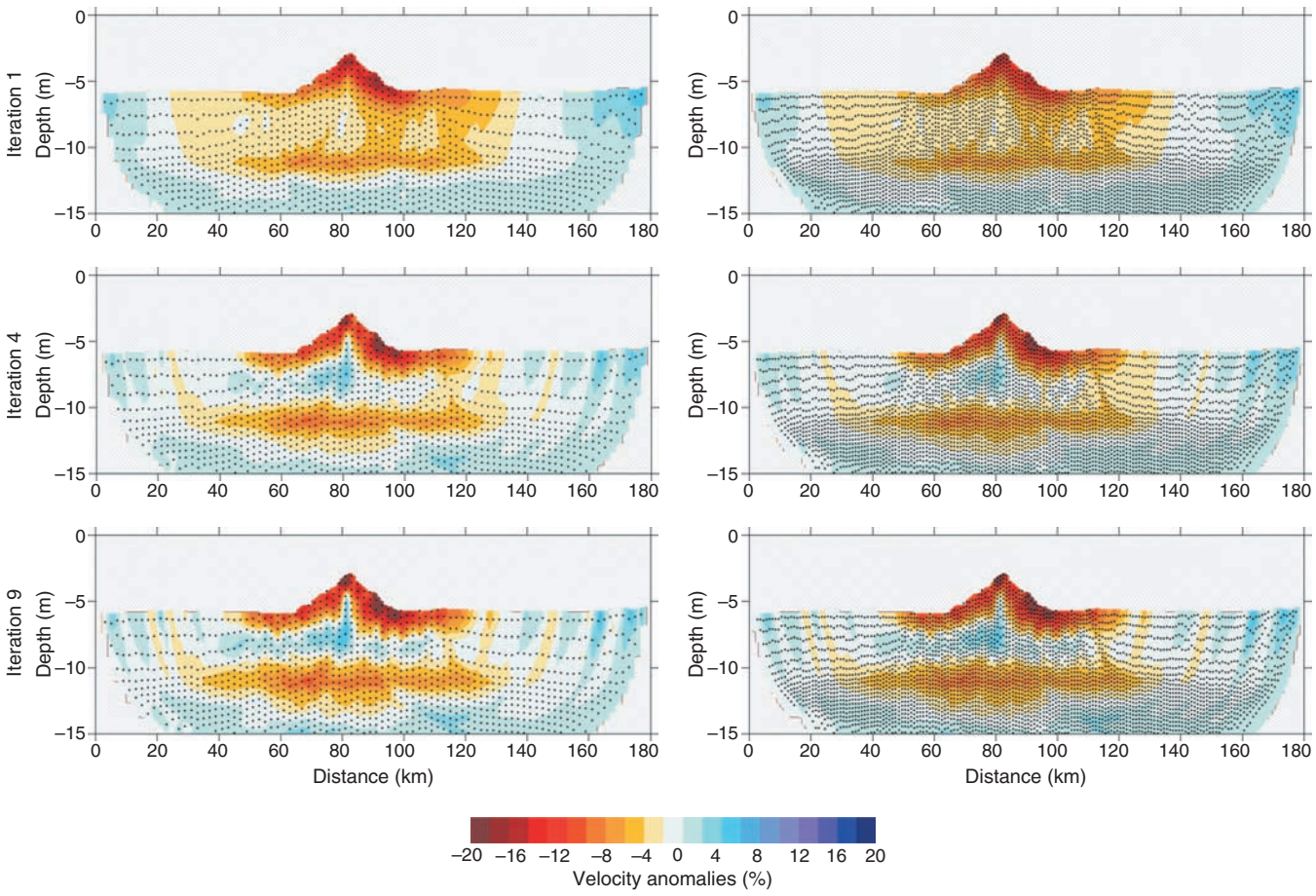


Figure C-1. Inversion results for the Sea data set based on two grids with different spacing. Velocity anomalies with respect to the starting model after iterations 1, 4, and 9 are presented for both cases. Left column: spacing $dx = 2$, $dy = 0.5$ km. Right column: spacing $dx = 0.5$, $dy = 0.1$ km.

tal spacing and 0.5 km of minimal vertical spacing (parameters used for the main results). In the right column, the corresponding parameters are 0.5 and 0.1 km. In all iterations, the solutions are very similar; if the grid spacing is less than the size of an expected anomaly, further decreasing the spacing will not affect the model.

## Tuning starting model and free parameters

When processing any data set, we tested several different parameters to find the most appropriate ones. The most important parameters, which determine the solution, are starting-velocity distribution and damping (smoothing and amplitude regularization). Here, we present examples that show how these parameters affect the solution.

In the main text, we present the reconstruction results for the Mount data set. To obtain the results, we tested dozens of different starting and free parameters to find the most optimal ones. Figure C-2 illustrates two cases of using different starting models for the Mount data set. These are the inversion results after 10 iterations with the same free parameters used to compute the main model (Figure 6). Despite considerably different starting values, the final solutions are quite similar, especially in the upper part of the section. Figure C-3 presents the inversion results for different *SM* and *AM* values. The starting model is the same as for Figure 6. Finding the best-

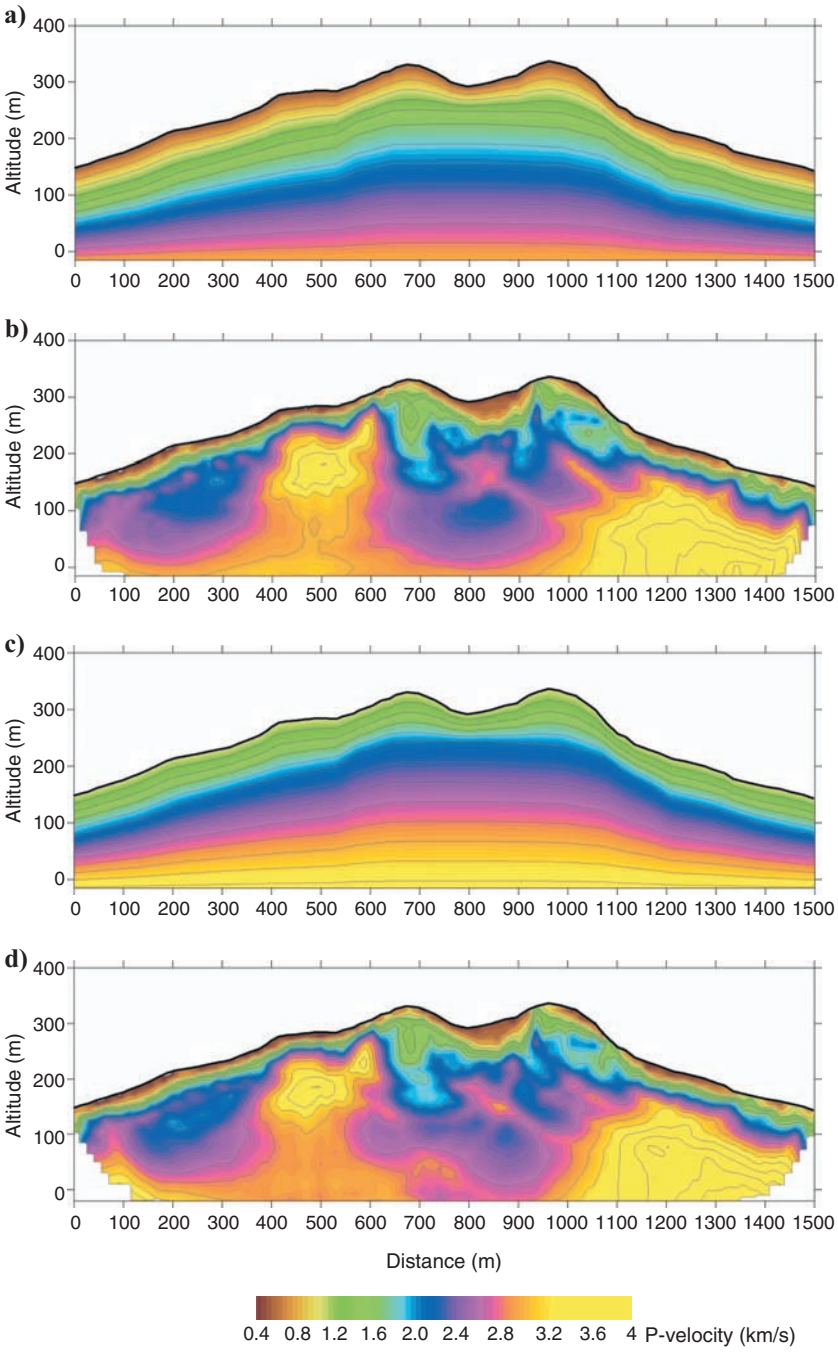


Figure C-2. Inversion results for the Mount data set based on two different starting models. (a) Model 1 starting-velocity distribution. (b) Inversion result for model 1. (c) Model 2 starting-velocity distributions. (d) Inversion result for model 2.

model is based on analyzing the rms of residuals. In Figure C-4, we graph variance reduction in 10 iterations for different starting models and $SM/AM$ values.

For the Salt data set, Figure C-5 presents several examples of inversions with different $SM$ and $AM$ parameters. The best solution provides the minimal rms of residuals: $SM = 0.5$ and $AM = 0.5$.

For the sea data set, we only present the curves of variance reduction for different reference models and values of $SM$ and $AM$ (Figure C-6). For the models with weak damping, the solutions become unstable. For the overdamped solutions, the rms is also larger than in the optimal case.

## The real marine experiment (sea data set)

The Sea real data set corresponds to a marine profile in the central Pacific near Musicians Ridge. The inactive Musicians Seamounts form coherent volcanic elongated ridges (VERs), which originated from hot-spot/ridge interaction. Their evolution is related to off-axis volcanism overlying partially melting asthenospheric flow channels linking the Euterpe hot spot and the Pacific-Farallon spreading center. The previously conducted tomographic inversion could clearly resolve the extrusive style of volcanism of the Musicians Seamounts, which is manifested in crustal thickening. This data set was

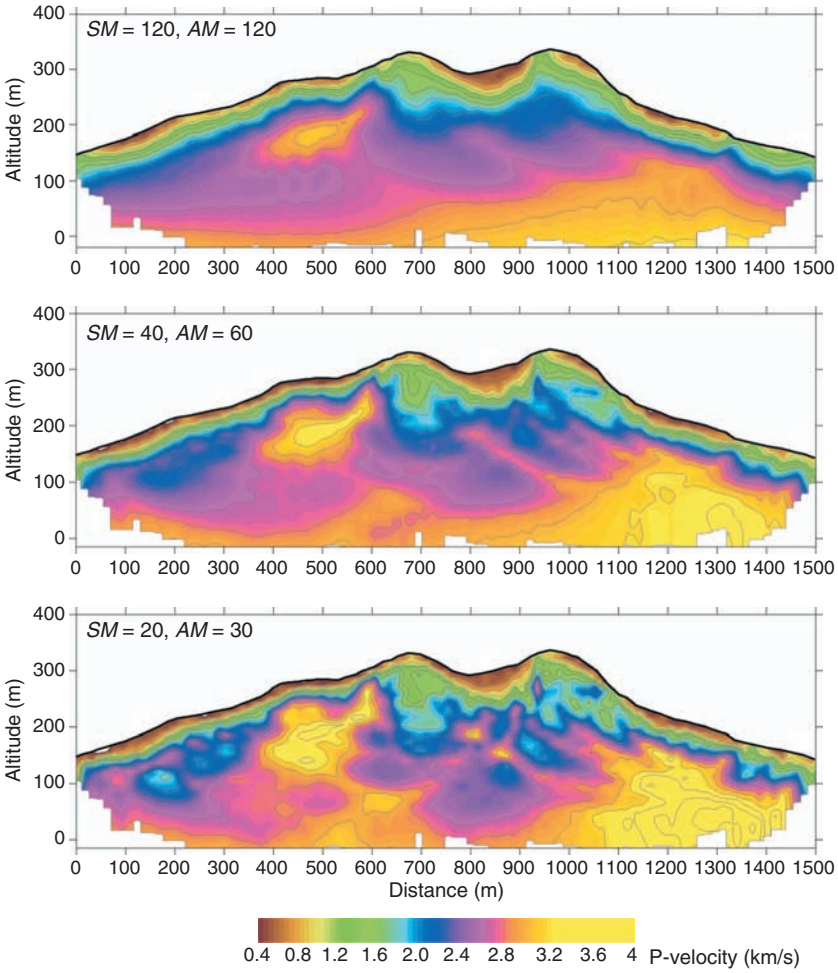


Figure C-3. Inversion results for the Mount data set, based on different values of smoothing ($SM$) and amplitude damping ($AM$).

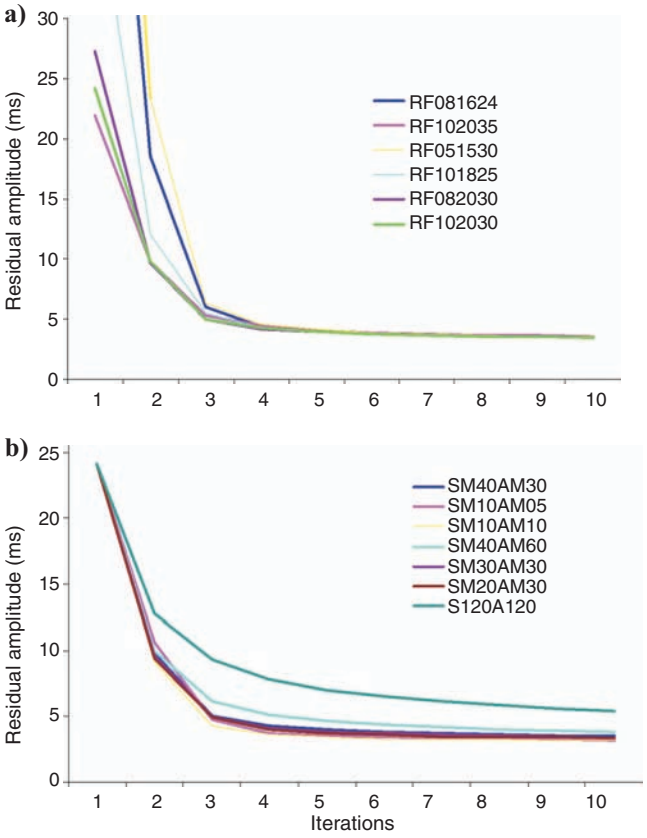


Figure C-4. Variance-reduction curves during iterative inversions based on (a) different starting models and (b) different *SM* and *AM* parameters.

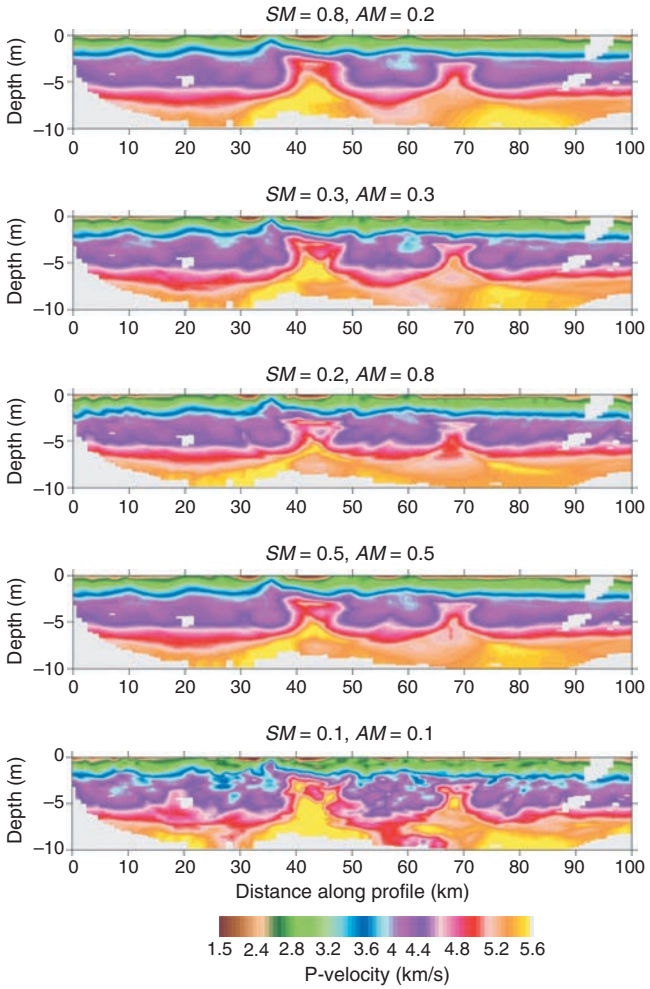


Figure C-5. Results of inversion for the Salt data set based on different values of smoothing (*SM*) and amplitude damping (*AM*).

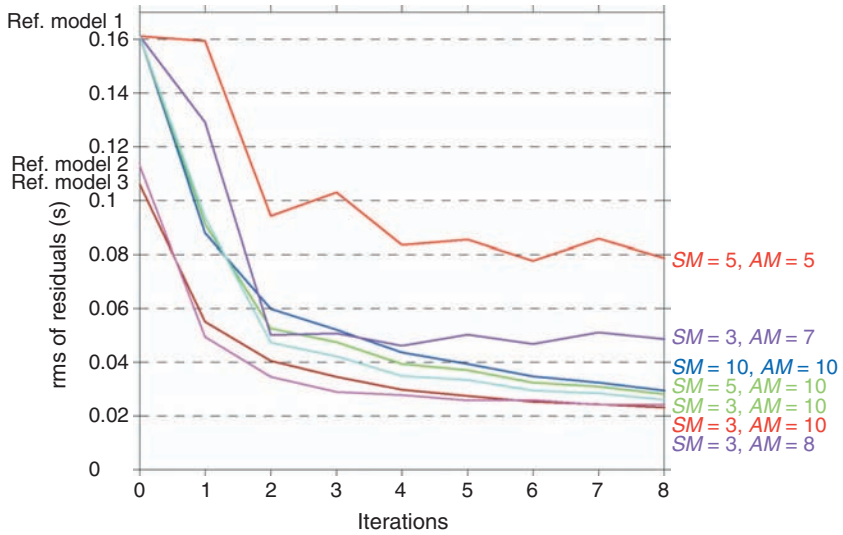


Figure C-6. Values of residual amplitudes after eight iterations for the Sea data set. The curves correspond to different values of *AM* and *SM*. Here, we consider three different reference models.

chosen because the coherent and uniform phase distribution in the seismic sections is favorable for testing a new code.

The tomographic inversion is applied to one of several active seismic refraction lines acquired in 1999 in the Musicians Seamount Province (Figure C-7). Thirteen IFM-GEOMAR ocean-bottom hydrophones (OBHs) (Flueh and Bialas, 1996) were deployed along the 180-km-long SO142 line 02, which crosses the Italian Ridge, expressed by an approximately 30-km-wide and 3-km-high bathymetric elevation. The 220-km-long SO 142 line 04 is covered with 12 OBHs. It crosses the Bach Ridge and covers several smaller and larger seamounts. The mean instrument spacing along both profiles is approximately 4 km. Two Bolt air guns with a total volume of 64 l served as the seismic source, with a shot interval of 60 s and an approximate shot spacing of 120 m at a speed of 4 knots.

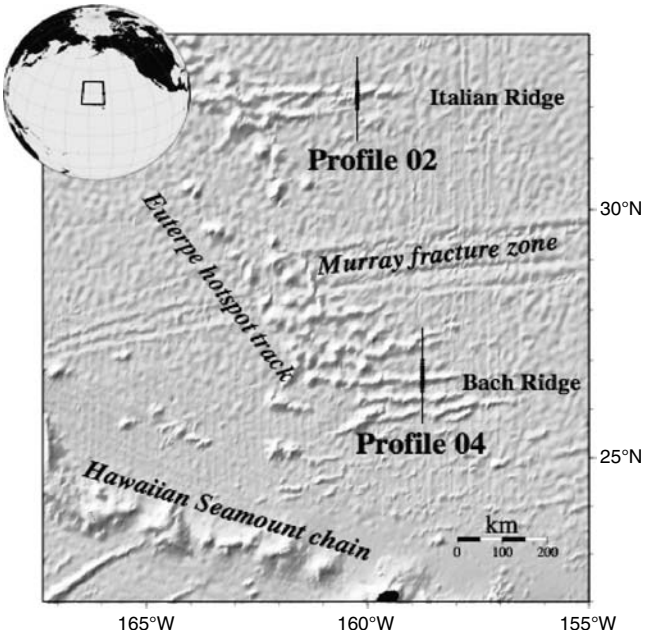


Figure C-7. Tectonic setting of the study area in the central Pacific. The Sea data set corresponds to profile 02. Volcanic features include hot-spot tracks, isolated seamounts, and VERs. The Musicians Seamount Province is bordered on the west by the Euterpe hot-spot track, to the north and south by the Italian and Bach Ridges, respectively; it terminates in the east at the former location of the Pacific-Farallon spreading center.

As is common for oceanic crustal structure investigations, the uniform tectonic structure of the study area yields excellent data quality, with phases recorded to offsets commonly exceeding 120 km and a high signal-to-noise ratio (S/N) (Figure 5). Only in the central part of line 4 do some stations display a lower S/N attenuating-phase coherency beyond 50–70 km offset. The oceanic crustal and upper mantle structure of the study area is fairly uniform, especially away from the volcanic edifices. The bathymetric elevations caused by the seamounts produce pronounced variations in apparent velocities. The generally smooth interval velocity distribution along the profiles, however, results in clearly differentiated upper and lower crustal refractions (Puc and Plc) as well as mantle refraction phases (Pn), which cover the entire shot-receiver offset range on most stations. The upper crustal refraction extends to offsets of about 25 km on most record sections, where it merges into the lower crustal arrival of gradually increasing velocities (Figure C-8). The mantle refraction appears between 50- and 60-km offset on both profiles, reaching maximum offsets of 140 km.

In the text, we discuss the problem of using data subsets instead of the entire data amount. Sources located close to each other can lead to almost linearly dependent equations in the inversion, which does not improve the solution. In Figure C-9, we consider three data subsets for the sea model that provide almost identical solutions, despite considerably different data amounts.

The best Mount model (Figure 9a) was constructed after performing six trials. Figure C-10 presents four of them. The model is too complicated, and the inversion appears to be very nonlinear. Changing velocities in the model does not necessarily cause a corresponding velocity change in the retrieved models. Some trials for a probabilistic model for the Salt data set are shown in Figure C-11. Analysis of the shapes of the retrieved anomalies in the trial-and-search process allows constructing realistic shapes of the salt domes in the synthetic model. Ten models used to construct a probabilistic model for the observed sea data set are presented in Figure C-12.

Figure C-8. Seismic wide-angle sections for OBH 11 of profile 02. Clear phases from the upper crust (Puc), lower crust (Plc), and mantle (Pn) are recognized to offsets of more than 100 km on several stations. Seafloor topography causes strong apparent velocities.

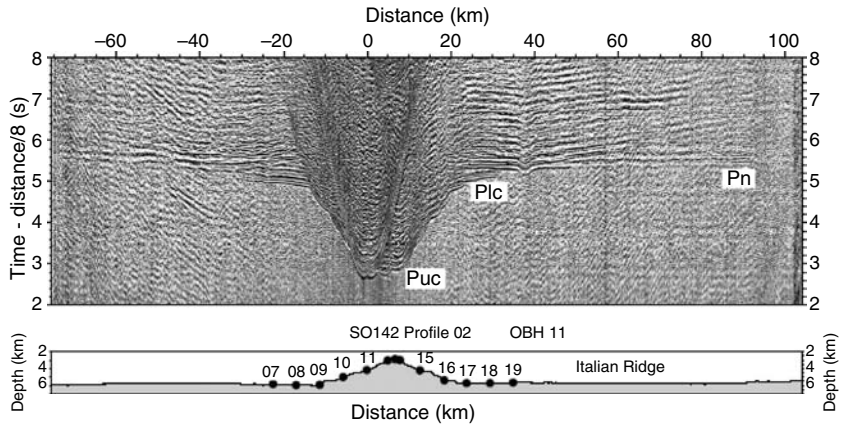

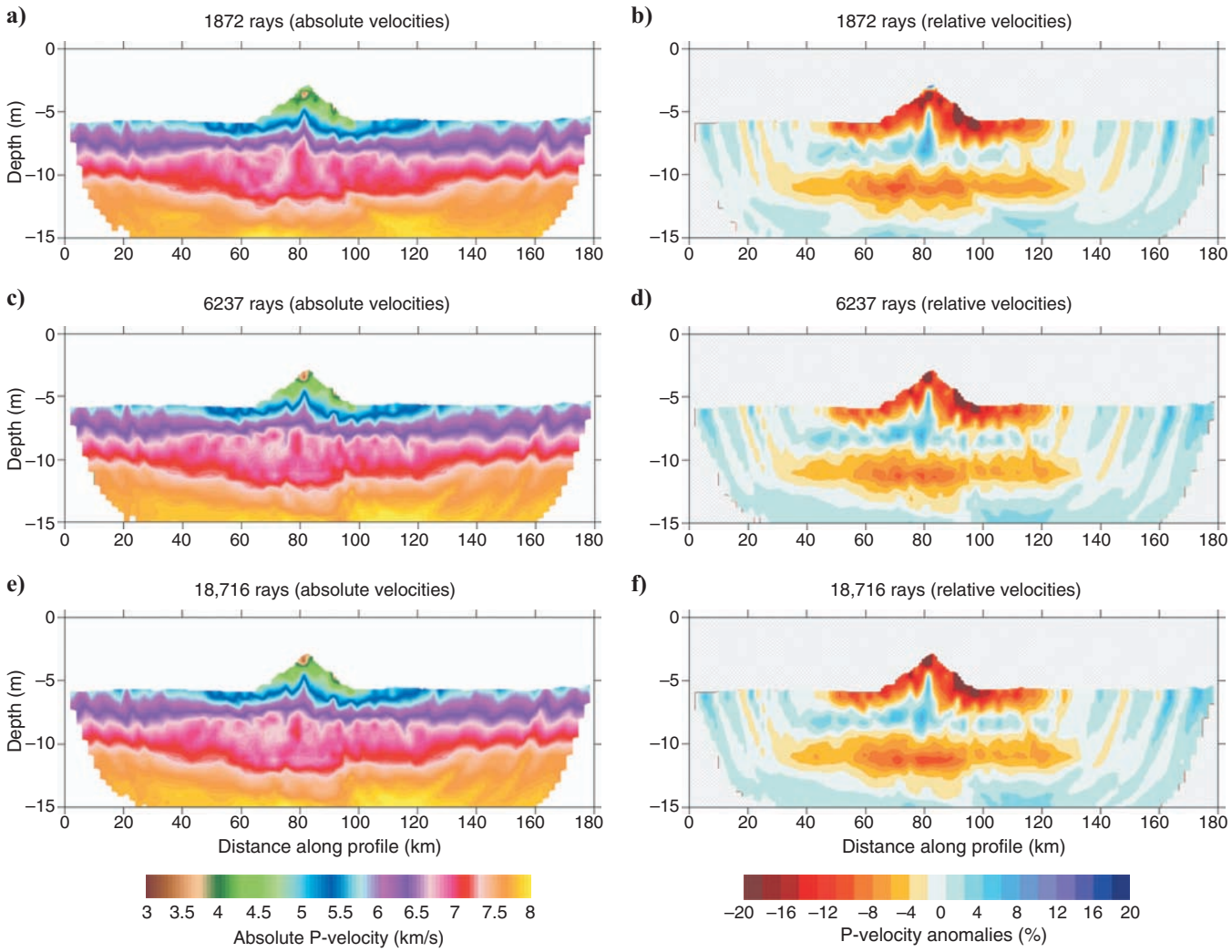


Figure C-9. Inversion results based on (a, b) one-tenth and (c, d) one-third data subsets and on (e, f) the entire data set. Numbers of rays for each case are indicated. Left column: absolute-velocity values. Right column: relative perturbations with respect to the 1D starting model, which is identical for all three cases.

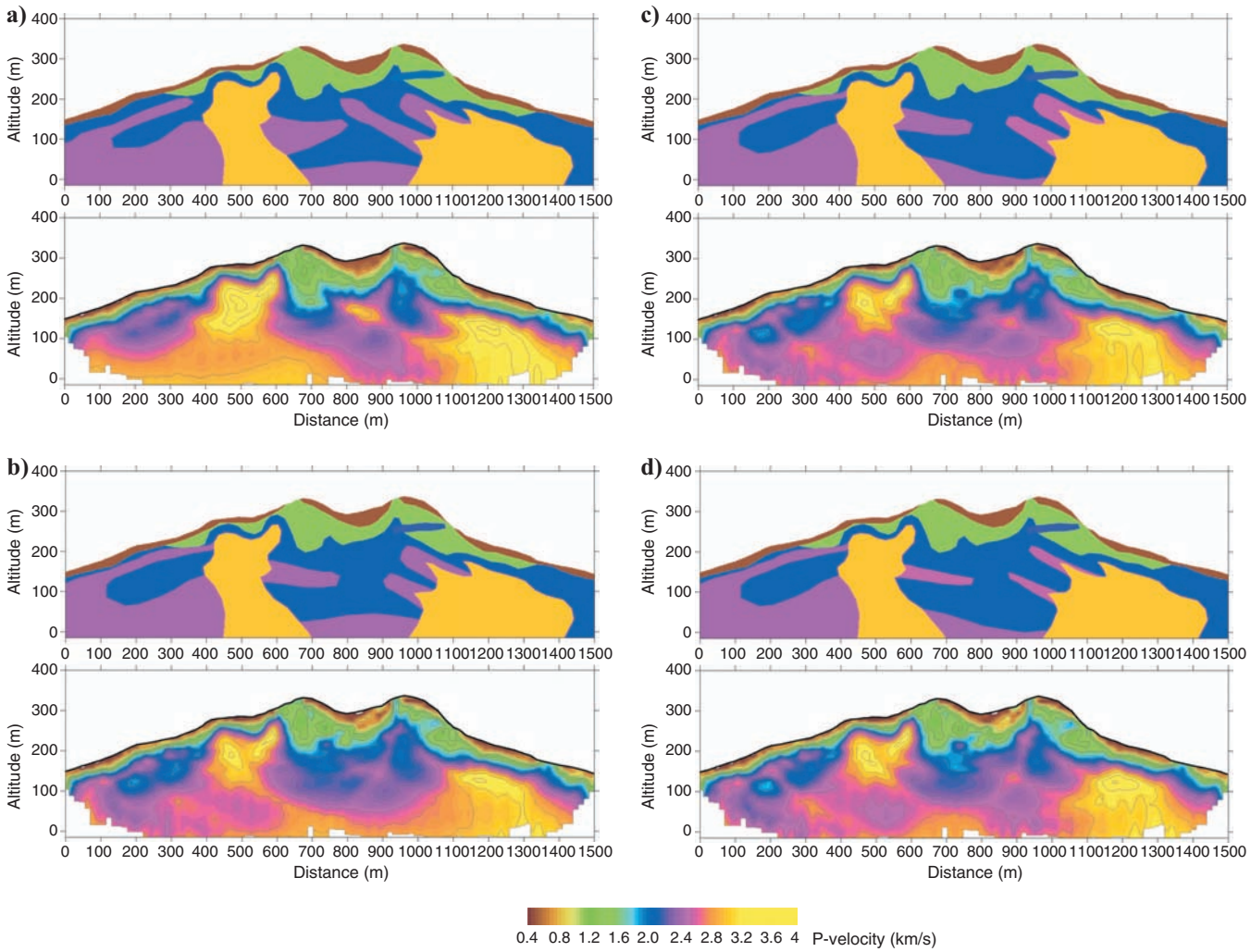


Figure C-10. Synthetic models (a) 1, (b) 2, (c) 3, and (d) 4, used to reproduce the results of observed data inversion for the Mount data set. In each pair, the upper plot is the synthetic model and the lower plot is the reconstruction result (after forward modeling and tomographic inversion).

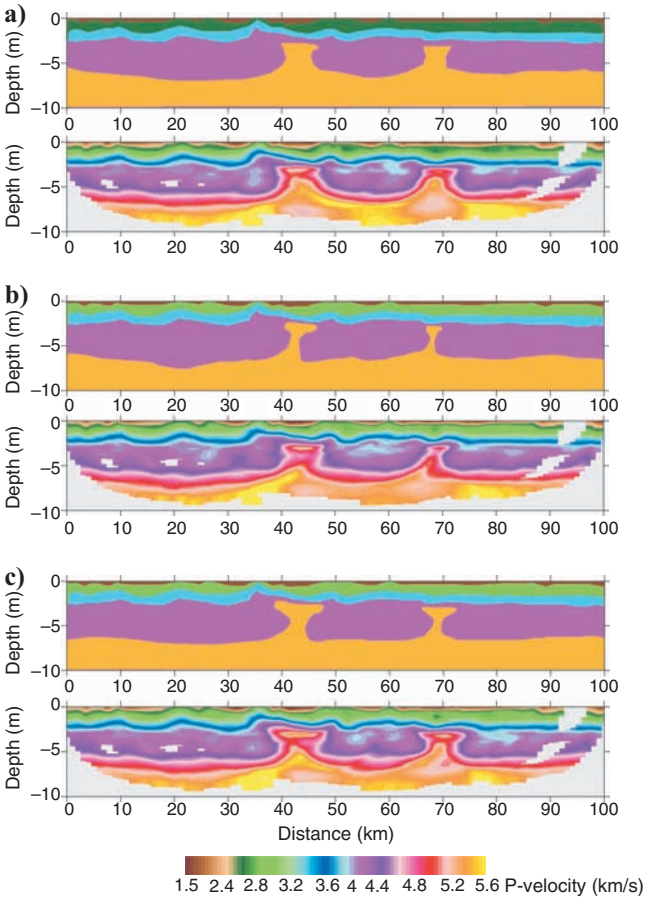


Figure C-11. Synthetic models (a) 1, (b) 2, and (c) 3, used to reproduce the results of observed data inversion for the Salt data set. In each pair, the upper plot is the synthetic model and the lower plot is the reconstruction result (after forward modeling and tomographic inversion).

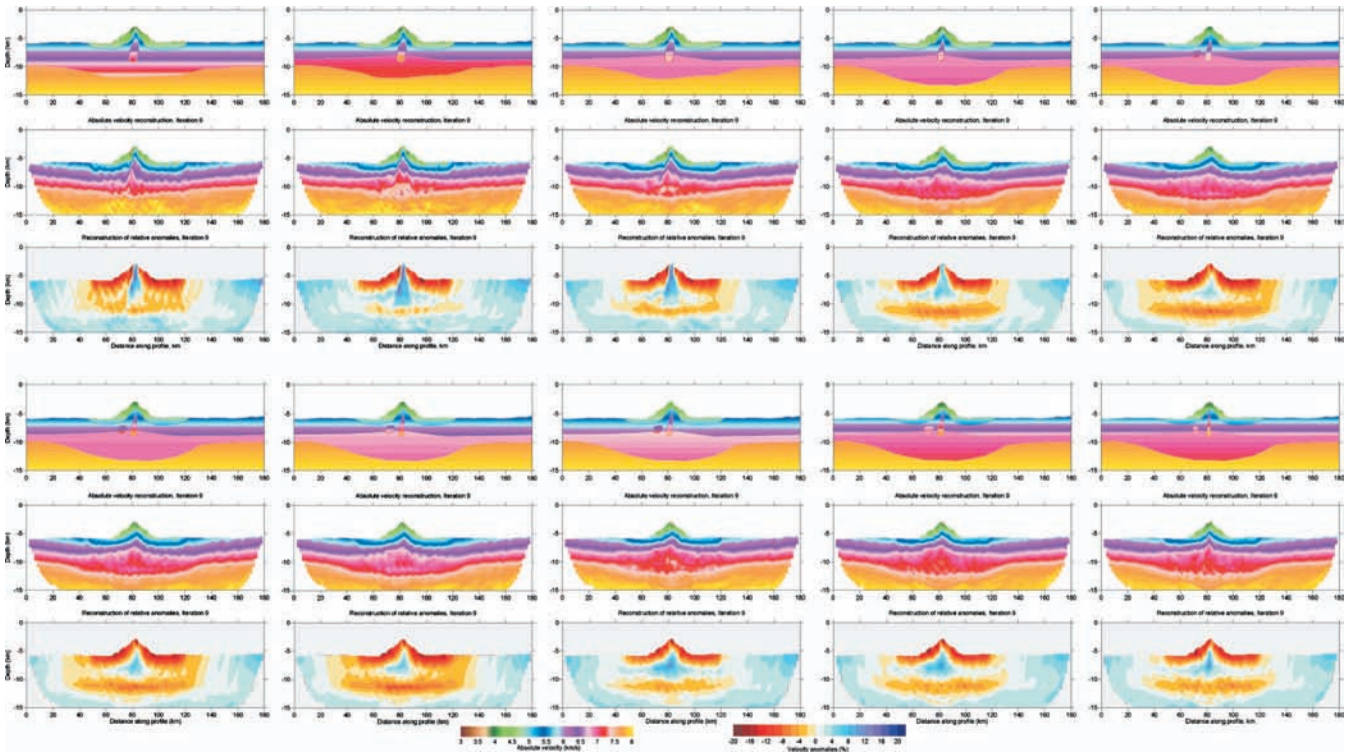

Figure C-12. Ten synthetic models for the Sea data set, used to reproduce the realistic model. Synthetic models are presented in rows 1 and 4. Results in absolute velocities are shown in rows 2 and 5. Resulting velocity anomalies with respect to the same 1D model are shown in rows 3 and 6.

## REFERENCES


Eberhart-Phillips, D., 1986, Three-dimensional velocity structure in northern California Coast Ranges from inversion of local earthquake arrival times: Bulletin of the Seismological Society of America, **76**, 1025–1052.

Flueh, E. R., and J. Bialas, 1996, A digital, high data capacity ocean bottom recorder for seismic investigations: International Underwater Systems Design, **18**, no. 3, 18–20.

Freedman, A. P., and B. Parsons, 1986, SEASAT-derived gravity over the Musicians seamounts: Journal of Geophysical Research, **91**, 8325–8340.

Grechka, V., and G. A. McMechan, 1996, 3-D two-point ray tracing for heterogeneous, weakly transversely isotropic media: Geophysics, **61**, 1883–1894.

Hobro, J. W. D., S. C. Singh, and T. A. Minshull, 2003, Three-dimensional tomographic inversion of combined reflection and refraction seismic traveltime data: Geophysical Journal International, **152**, no. 1, 79–93.

Hole, J. A., 1992, Nonlinear high-resolution three-dimensional seismic travel time tomography: Journal of Geophysical Research, **97**, no. B5, 6553–6562.

Kopp, H., C. Kopp, J. Phipps Morgan, E. R. Flueh, W. Weinrebe, and W. J. Morgan, 2003, Fossil hot spot-ridge interaction in the Musicians seamount province: Geophysical investigations of hot spot volcanism at volcanic elongated ridges: Journal of Geophysical Research, **108**, doi: 10.1029/2002JB002015.

Korenaga, J., W. S. Holbrook, G. M. Kent, P. B. Kelemen, R. S. Detrick, H.-C. Larsen, J. R. Hopper, and T. Dahl-Jensen, 2000, Crustal structure of the southeast Greenland margin from joint refraction and reflection seismic tomography: Journal of Geophysical Research, **105**, no. B9, 21591–21614.

Koulakov, I., 2009a, LOTOS code for local earthquake tomographic inversion: Benchmarks for testing tomographic algorithms: Bulletin of the Seismological Society of America, **99**, 194–214.

———, 2009b, PROFIT code, http://www.ivan-art.com/science/PROFIT, accessed 8 April 2010.

Koulakov, I., M. Bohm, G. Asch, B.-G. Lühr, A. Manzanares, K. S. Brotopuspito, Pak Fauzi, M. A. Purbawinata, N. T. Puspito, A. Ratdomopurbo, H. Kopp, W. Rabbel, and E. Shevkunova, 2007, P and S velocity structure of the crust and the upper mantle beneath central Java from local tomography inversion: Journal of Geophysical Research, **112**, B08310.

Koulakov, I., A. Jakovlev, and B. G. Luehr, 2009a, Anisotropic structure beneath central Java from local earthquake tomography: Geochemistry Geophysics Geosystems, **10**, Q02011.

Koulakov, I., and S. V. Sobolev, 2006, A tomographic image of Indian lithosphere break-off beneath the Pamir Hindukush region: Geophysical Journal International, **164**, 425–440.

Koulakov, I., S. V. Sobolev, M. Weber, S. Oreshin, K. Wylegalla, and R. Hofstetter, 2006, Teleseismic tomography reveals no signature of the Dead Sea Transform in the upper mantle structure: Earth and Planetary Science Letters, **252**, no. 1–2, 189–200.

Koulakov, I., T. Yudistira, B.-G. Luehr, and Wandono, 2009b, *P*, *S* velocity and *VP*/*VS* ratio beneath the Toba caldera complex (northern Sumatra) from local earthquake tomography: Geophysical Journal International, **177**, 1121–1139.

Luetgert, J. H., 1992, MacRay — Interactive two-dimensional seismic raytracing for the Macintosh: U.S. Geological Survey Open-File Report, 92–356.

Martí, D., R. Carbonell, I. Flecha, I. Palomeras, J. Font-Capó, E. Vásquez-Suñé, and A. Pérez-Estaún, 2008, High-resolution seismic characterization in an urban area: Subway tunnel construction in Barcelona, Spain: Geophysics, **73**, no. 2, B41–B50.

Nielsen, C., and H. Thybo, 2009, No Moho uplift below the Baikal rift zone: Evidence from a seismic refraction profile across southern Lake Baikal: Journal of Geophysical Research, **114**, B08306.

Paige, C. C., and M. A. Saunders, 1982, LSQR: An algorithm for sparse linear equations and sparse least squares: Association for Computing Machinery (ACM) Transactions on Mathematical Software, **8**, 43–71.

Palomeras, I., R. Carbonell, I. Flecha, F. Simancas, P. Ayarza, J. Matas, D. Martinez Poyatos, A. Azor, F. Gonzalez Lodeiro, and A. Perez-Estaun, 2009, Nature of the lithosphere across the Variscan orogen of SW Iberia: Dense wide-angle seismic reflection data: Journal of Geophysical Research, **114**, B02302.

Rawlinson, N., and M. Urvoy, 2006, Simultaneous inversion of active and passive source datasets for 3-D seismic structure with application to Tasmania: Geophysical Research Letters, **33**, L24313.

Sager, W. W., and M. S. Pringle, 1987, Paleomagnetic constraints on the origin and evolution of the Musicians and south Hawaiian Seamounts, central Pacific Ocean, *in* B. H. Keating, P. Fryer, R. Batiza, and G. Boehlert, eds., Seamounts, islands, and atolls: American Geophysical Union, 133–162.

Sallarès, V., P. Charvis, E. R. Flueh, and J. Bialas, 2003, Seismic structure of Cocos and Malpelo volcanic ridges and implications for hot spot-ridge interaction: Journal of Geophysical Research, **108**, doi: 10.1029/2003JB002431.

Thurber, C., 1993, Local earthquake tomography: Velocities and Vp/Vs — Theory, *in* H. Iyer, and K. Hirahara, eds., Seismic tomography — Theory and practice: CRC Press, 563–583.

Um, J., and C. Thurber, 1987, A fast algorithm for two-point seismic ray tracing: Bulletin of the Seismological Society of America, **77**, 972–986.

Van der Sluis, A., and H. A. van der Vorst, 1987, Numerical solution of large, sparse linear algebraic systems arising from tomographic problems, *in* G. Nolet, ed., Seismic tomography: D. Reidel, 49–83.

Yordkayhun, S., A. Tryggvason, B. Norden, C. Juhlin, and B. Bergman, 2009, 3D seismic traveltime tomography imaging of the shallow subsurface at the $CO_2$SINK project site, Ketzin, Germany: Geophysics, **74**, no. 1, G1–G15.

Zelt, C. A., and P. J. Barton, 1998, Three-dimensional seismic refraction tomography: A comparison of two methods applied to data from the Faeroe basin: Journal of Geophysical Research, **103**, 7189–7210.

Zelt, C. A., and R. B. Smith, 1992, Seismic traveltime inversion for 2-D crustal velocity structure: Geophysical Journal International, **108**, 16–34.

# 10

Weinzierl, W. & Kopp, H., 2010.

**Statistical separation strategy to analyze velocity structure obtained by seismic tomography.**

Geophysics, 75, doi:10.1190/1.3432406.

GEOPHYSICS, VOL. 75, NO. 4 (JULY-AUGUST 2010); P. R75–R82, 13 FIGS.
10.1190/1.3432406

# Statistical separation strategy to analyze velocity structure obtained by seismic tomography

Wolfgang Weinzierl[1] and Heidrun Kopp[1]

## ABSTRACT

General solutions of inverse problems often can be obtained by introducing probability distributions to sample the model space. We have developed a simple approach to define an a priori space in a tomographic study and retrieve the velocity/depth posterior distribution by a Monte Carlo method. Utilizing a fitting routine designed for very low statistics to set up and analyze the obtained tomography results, we can statistically separate the velocity/depth model space derived from inverting seismic refraction data. A profile acquired in the Lesser Antilles subduction zone reveals the effectiveness of this approach. Resolution analysis of the structural heterogeneity includes a divergence analysis that can dissect long, wide-angle profiles for deep crust and upper mantle studies. The complete information of any parameterized physical system is contained in the a posteriori distribution. Methods for analyzing and displaying key properties of the a posteriori distributions of highly nonlinear inverse problems are therefore essential in the scope of any interpretation. It is possible to map velocity variations in their extent and structure by measuring the total as well as relative divergence of the velocity structure in the a posteriori space. We have applied the divergence analysis to a part of the transect where a backstop structure has been identified, and the method resolves shallow features and returns information concerning the confidence level of results. Assuming a relationship between forearc and backstop, we can obtain a structural image in accordance with previous interpretations.

## INTRODUCTION

Numerous studies dealing with inverse problems have been approached in as many ways as there are questions to be answered by them (Parker, 1994). The theory of seeking parameters by indirect measurements has been applied successfully by Parker and Dziewonski (1995) in a more phenomenological fashion than the one Hjelt (1992) chooses by inference in a more qualitative way or the rigorous mathematical approach of Kirsch (1996). The reformulation of the theory in a nonparametric fashion has enabled a statistical approach and error analysis to quantitatively evaluate and investigate the solutions to any inverse problem.

In the Bayesian formulation, the most general solution of any inverse problem is a probability distribution of the model space. Analytic techniques solving this problem only apply in the simplest case, i.e., only one global minimum and no local minima exist. Because this ideal case is almost never met, the model space must be explored extensively. There are numerous examples of solutions to inverse problems by means of Monte Carlo methods (e.g., Press, 1968, 1971; Mosegaard and Tarantola, 1995; Jacobsen et al., 1996; Mosegaard and Sambridge, 2002; Sambridge and Mosegaard, 2002).

A major concern in the Bayesian approach is knowing the a priori distribution for setting up the starting models that sample the model space (Hansen et al., 2006). One way of simplifying and reducing such a search to a limited band of models for inversion is to introduce envelopes for parameter estimates. A difficulty with this approach is inconclusive knowledge of sampling the complete model space because we are introducing boundary conditions on the P-wave velocities at depth (Sato and Kennett, 2000). By expanding or broadening the envelopes, we can expand the a priori distributions and decrease the effects of the boundary conditions.

We present a statistical separation strategy to explore the velocity/depth model space derived from inverting seismic refraction data. After an initial tomography with a simple 1D velocity setup hanging below the seafloor, we separate the transect according to its assumed tectonic units, i.e., their velocity/depth distribution. Fitting the velocity/depth distributions $V(z)$ in predefined regions on the grid provides us the essential probability density distributions for setting up a Monte Carlo ensemble for a subsequent inversion. To test our approach, we use a data set from the Lesser Antilles margin south of Guadeloupe. The 280-km-long profile traverses the island arc from the active arc region up to the accretionary prism. We invert more than 22,500 first-arrival traveltimes in over 50 starting models to enhance the statistical resolution of the final average model.

Manuscript received by the Editor 21 July 2009; revised manuscript received 12 January 2010; published online 2 August 2010.
[1]IFM-GEOMAR Geodynamics, Kiel, Germany. E-mail: wweinzierl@ifm-geomar.de; hkopp@ifm-geomar.de.

The advantages of the Monte Carlo method become even more apparent in the subsequent resolution analysis. We use the total as well as relative divergence of the velocity structure of the a posteriori information to map velocity variations in their extent and structure.

## DATA ACQUISITION AND TOMOGRAPHIC MODELING

We inverted first-arrival data from a marine transect acquired with the RV *Maria S. Merian*, cruise 4, leg 2 (MSM04/2), in 2007 in the Lesser Antilles subduction zone (Figure 1). The profile was shot with a five-element seismic source array, a volume of 112 L, and a trigger interval of 60 s at a ship speed of 3.7 kn on average, resulting in a shot spacing of approximately 100 m. Forty-four ocean-bottom seismometer (OBS) receivers were positioned at 5-km spacing along the profile. The 280-km-long profile traversed the island arc and ended 70 km southeast of the trench on the accretionary prism. Standard processing of the OBS data included clock-drift correction, relocalization, deconvolution, and filtering. Signal-to-noise ratios varied considerably, and clear arrivals on some stations could be traced to 100–130-km offsets. The transmitted energy decreased rapidly, entering the accretionary complex where first arrivals could be identified for up to 20-km offsets on average.

An initial 2D velocity/depth model along the transect was obtained using the tomographic inversion method of Korenaga et al. (2000). The velocity field $V_{ik} = V(x_i,z_k)$ was parameterized by a homogeneous grid of nodes with $1 \le i \le n_x$ and $1 \le k \le n_z$ below the seafloor. The matrix equation

$$\mathbf{d}_{\mathrm{th}} = \mathbf{G}\,\delta\mathbf{m}, \tag{1}$$

with $\mathbf{d}_{\mathrm{th}}$ the theoretical traveltime residual vector, $\mathbf{G}$ the Frechet derivative matrix, and $\delta\mathbf{m}$ an unknown model perturbation, formed the basis of this traveltime tomography. This linearized inversion procedure was adopted from Toomey et al. (1994) and applied iteratively until the model converged. The models were parameterized with a lateral nodal spacing of 0.5 km and variable vertical spacing of 0.05 km within the upper 2 km, increasing to 0.5 km at $z_{\max} =$ 25 km. To stabilize the inversion, we used depth-dependent smoothing constraints and correlation lengths. Correlation lengths of 1–5 km horizontally and 0.1–1 km vertically provided reliable results while using computationally less expensive, larger smoothing constraints.

The starting model for the first tomographic inversion was a simple layered 1D velocity model. The result of this inversion gave us an

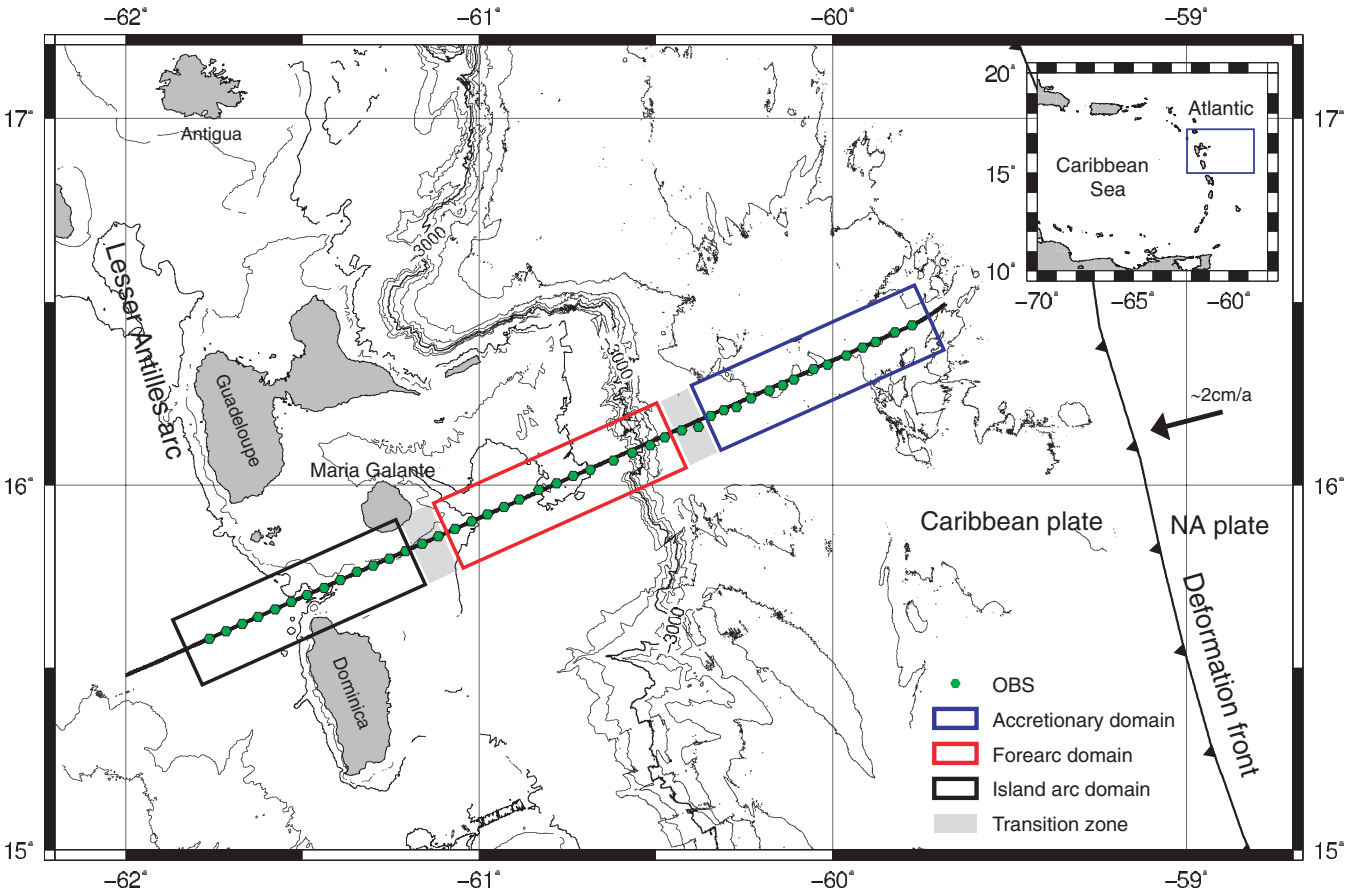


Figure 1. Map of the survey site, showing the deformation front between the North American (NA) and Caribbean plates. Profile P02 of cruise MSM04/2 of the German vessel RV *Maria S. Merian* was shot at 100-m spacing and a station separation of 5 km. Circles denote relocated positions of the seismic instruments. The color coding of the transect boxes refers to the subsequent data analysis and approximately defines the arc (black), forearc (red), and accretionary (blue) regions. The inset is a regional map of the Lesser Antilles. Bathymetry comes from data sets acquired during cruises EW 9803, MSM 04-2, and Sismantilles I. Convergence rate is from Feuillet (2000).

estimate of the velocity structure along the transect and provided the basis for defining three distinct geologic parts of the margin: (1) the island arc, (2) the forearc high, and (3) the accretionary complex. The velocity distribution and segment definition agreed with earlier seismic refraction tomography results conducted in the study area (Christeson et al., 2003).

The major drawback of the inversion problem was its nonuniqueness; a family of models could fit the arrivals within the error range. With a total number of $N_{tt}$ traveltimes with the residuals $\mathbf{d_{th}}$ as well as the observed residuals $\mathbf{d_{obs}}$, a satisfactory model resulted in

$$\chi^2 = \frac{\sum_{i=1}^{N_{tt}} \left( \frac{d_{\text{obs}}(i)}{d_{\text{th}}(i)} \right)^2}{N_{\text{tt}}} \qquad (2)$$

of nearly one, with an rms misfit close to the assumed picking error. We let $\mathbf{m}$ denote the solution vector of realizations and $E(\mathbf{m})$ be the a posteriori expectation of $\mathbf{m}$ (Tarantola, 1987; Matarese, 1993). With $\sigma_m(\mathbf{m})$ being the a posteriori marginal density function, we wrote the a posteriori model covariance matrix $\mathbf{C}$ as

$$\mathbf{C} = \int [\mathbf{m} - E(\mathbf{m})] \cdot [\mathbf{m} - E(\mathbf{m})]^T \sigma_m(\mathbf{m}) d\mathbf{m}. \qquad (3)$$

where $T$ denotes transposition. This form of the covariance matrix can be approximated, assuming all realizations $N$ are equally probable. as

$$\mathbf{C} \approx \frac{1}{N} \sum_{i=1}^{N} [\mathbf{m}_i - E(\mathbf{m})] \cdot [\mathbf{m}_i - E(\mathbf{m})]^T, \qquad (4)$$

with $\mathbf{m}_i$ the $i$th realization of the solution vector $\mathbf{m}$.

At this stage, we chose a Bayesian approach to identify the resolution of the outcome and to analyze the a posteriori probability density in the model space. This was expressed in form of a product (Tarantola, 1987):

$$\sigma_M(\mathbf{m}) = k \rho_M(\mathbf{m}) L(\mathbf{m}), \qquad (5)$$

with $k$ an appropriate normalization constant, $\rho_M$ the a priori information on the model parameters, and the likelihood function $L(\mathbf{m})$ as a measure of the quality of the model $\mathbf{m}$ in fitting the data (Mosegaard and Tarantola, 1995).

To account for this nonuniqueness, we fitted the velocities of the three distinct regions over a range of 40 km with Gaussian curves (Figure 2). The regions were expressed in terms of $x_i$:

$$x_1 - 20 \le x_i \le x_1 + 20 \rightarrow \overline{V_{1k}},$$

$$x_2 - 20 \le x_i \le x_2 + 20 \rightarrow \overline{V_{2k}},$$

$$x_3 - 20 \le x_i \le x_3 + 20 \rightarrow \overline{V_{3k}},$$

with the corresponding profile $x_1 = 80$ km, $x_2 = 145$ km, and $x_3 = 260$ km. With equally weighted bins and an (improved) log-likelihood method resulting from the very low statistics (40 km ≅ 80 $x$-nodes) (James and Roos, 1975; Brun and Rademakers, 1997), we were able to use the fitting parameters, mean and deviation, to set up a priori probability densities (see Figure 3). Ultimately, they were used to define a model space $M$. Under the assumption of laterally variable transition zones in between the three tectonic regimes, we created more than 50 2D starting models $m(V_1, V_2, V_3, z) \in M$ for the inversion. A schematic overview of this setup is shown in Figure 4.

The retrieval of the posterior distributions of the input ensemble was achieved in two main steps. Step 1 was prior input. The starting model was defined using velocity distributions $V_1(z)$, $V_2(z)$, and $V_3(z)$, with their corresponding confidence intervals given by the standard deviation. By interpolating linearly in between the two transition zones with variable width, we constructed a 2D initial model for the inversion, which was completely randomized in its corresponding tectonic regions according to its confidence level.

Step 2 was model retrieval. Rather than a forward calculation to retrieve the posterior distibution through a Markov-chain Monte

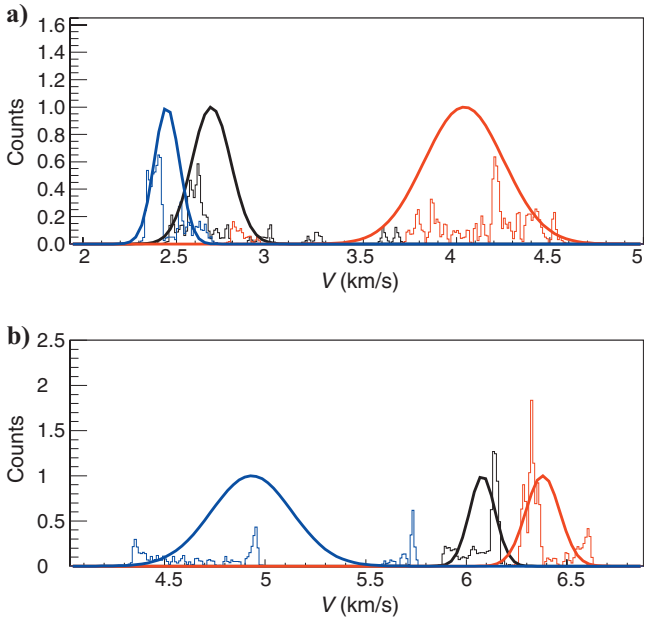


Figure 2. Representative fits of the velocities in the predefined regions used for the Monte Carlo estimation of 2D initial starting models. Fit at (a) $z = 1$ km and (b) $z = 7$ km below the seafloor (SF). Black curve is the island arc, red curve is the forearc high, and blue curve is the accretionary prism.

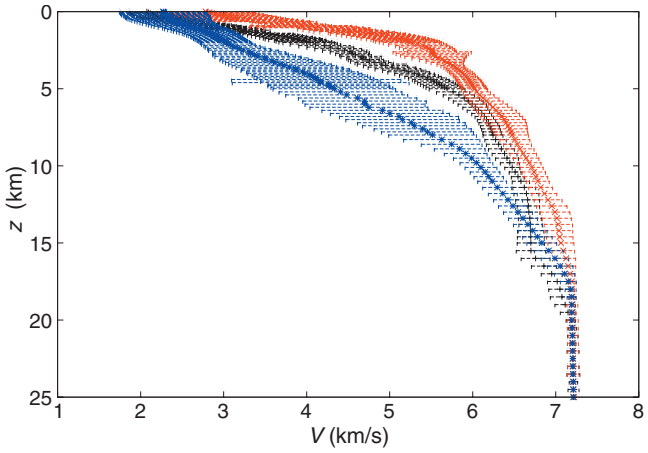


Figure 3. A priori velocity probability density functions used for creating 2D starting models. Mean values and confidence levels, recovered by the fitting procedure (Figure 2), define the a priori information for parameter estimation. Black markings are the island arc, red are the forearc high, and blue are the accretionary prism.

Carlo method, we solved the inverse problem (Tarantola, 1987) at hand with the tomographic procedure from Korenaga et al. (2000). To minimize the artifacts introduced by large model updates, we chose a top-to-bottom approach, increasing the number of arrivals according to the offset ranges 0–20 km, 0–50 km, and 0–130 km, with spatially varying smoothing and correlation parameters.

## RESULTS OF MONTE CARLO ESTIMATION

The solution of any inverse problem is never one result or image but a probability distribution of samples of the a posteriori probability density $\sigma(m)$ (Tarantola, 1987). The practice of calculating the mean of an ensemble of Monte Carlo realizations yields an oversimplified (smoothed) solution to the inverse problem. If a collection of solutions is available, it is possible to give a more quantitative measure for features under investigation rather than merely constraining the interpretation on a smoothed mean.

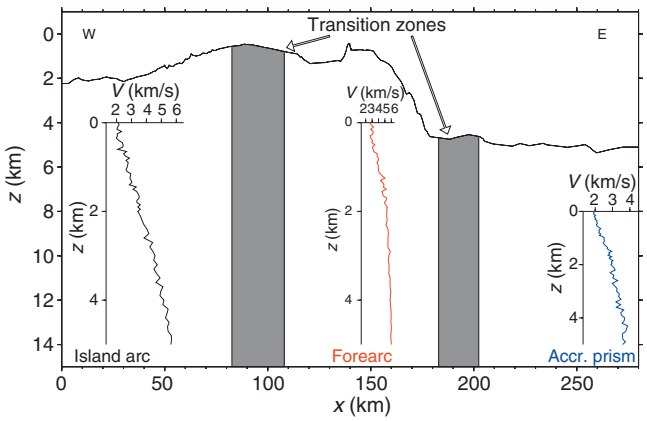


Figure 4. Schematic of model setup along the profile. Representative velocity functions used for the setup of the starting model are depicted; transition zones are dark gray planes in between. Seafloor bathymetry is shown by the slightly thicker black line, based on swath data.

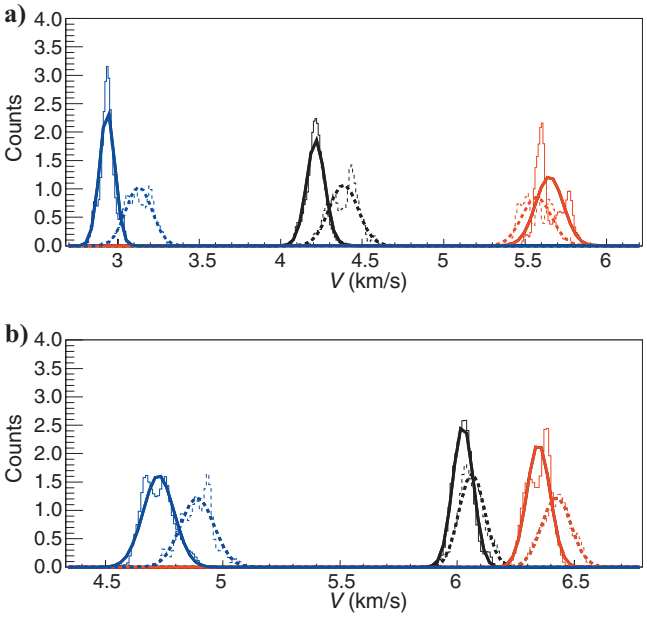


Figure 5. Comparison of a priori probability density (dashed) and a posteriori probability density (solid) at (a) 3.0 km and (b) 7.2 km below the seafloor. The histograms were fitted with Gaussian curves to visualize the decrease of the variance, directly visible in the peaks and widths of the distributions, because the amount of statistics is identical. The lateral shift comes from the smoothing of the initial model before the fitting procedure to set up the 2D models. Black curves are the island arc, red curves are the forearc high, and blue curves are the accretionary prism.

At this point, we can compare the a priori with the a posteriori probability distributions (Figure 5). The evidence that the P-wave velocities are converging into a minimum can be deduced from the distribution of velocities from the final Monte Carlo ensemble in comparison with the starting models. The variance of the final models is reduced; therefore, velocities converge into a minimum. This test is strongly dependent on ray coverage, as can be seen in the deeper parts of the model. Only where ray coverage is sufficient can we increase the resolution.

The actual power of the statistical approach becomes even more evident if we start analyzing the velocity structure on the basis of our initialization. Calculating the rms values $\Delta V$ at each horizontal grid point $x$ for each model, we are able to analyze the deviations along the profile according to the mean velocity function $(\overline{V_1},\overline{V_2},\overline{V_3})$ used in the setup:

$$\Delta V_i(x) = \sqrt{\frac{\sum_{k=0}^{nz}(\overline{V_i}(x,z_k) - V(x,z_k))^2}{nz-1}}, \quad i = 1,2,3. \tag{6}$$

Gaussian fitting of each distribution gives an estimate of the correlation between the mean velocity/depth distributions of the distinct regions and the velocity functions along the profile. The results of this fitting procedure are shown in Figure 6. As expected, the divergence from the mean velocity functions mimics the structural composition of the predefined tectonic regions. The divergence is smallest in the areas of highest resemblance. The transitions between these regions can be quantified by the overlap of distributions moving along the transect (Figure 7). Again, the rms for each region is shown. The superposition of the fits and therefore total distribution is

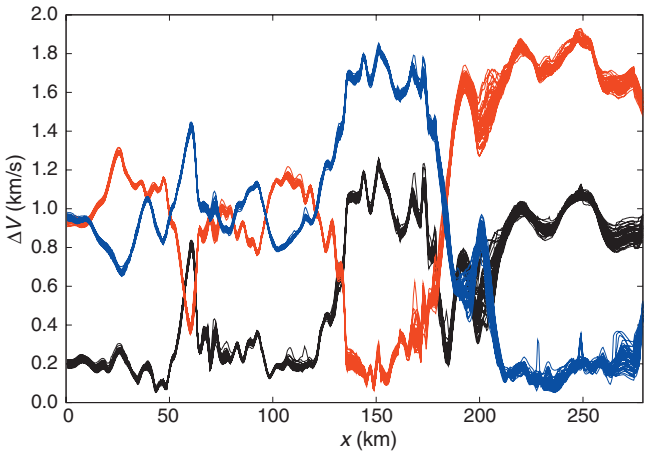


Figure 6. Divergence $\Delta V_i$ with $i = 1$ (black), $i = 2$ (red), and $i = 3$ (blue) along the profile. The divergence of each of the models of the resulting Monte Carlo ensemble was calculated according to equation 6. Black curves are the island arc, red curves are the forearc high, and blue curves are the accretionary prism.

given by

$$f_{\text{tot}}(x) = \sum_{i=1}^{3} \text{const}_i \, e^{-0.5((\overline{dV_i})/\sigma_i(dV))^2}, \quad (7)$$

with $\text{const}_i$, $\overline{dV_i}$, and $\sigma_i(dV)$ the normalization constant, mean, and standard deviation of the misfit to the reference distributions $\overline{V_i}$, respectively, and shown by the dashed green line in Figure 7.

The value of equation 6 is in measuring the resemblance or divergence, whereas the value of equation 7 is in measuring the mixing ratio between the given distributions. The validity of dissecting the profile according to significant velocity/depth distributions and comparing the expected distributions with the deduced velocity field can be seen around profile 60 km (Figure 6). The resemblance to the forearc high function is much higher because we see an increase in seismic velocities close to the seabed.

Between 120 and 140 km, we see a fairly abrupt change in the match to $\Delta V_1$ and $\Delta V_2$ (Figure 6). This coincides with the transition zone between the forearc high and island arc region. Moving along the transect, the divergence to the forearc high distribution $\Delta V_2$ starts increasing from 165 km until it enters the accretionary complex, where it reaches the highest value of divergence. The distance between 170 and 210 km is not clearly identifiable as a result of mixing the island arc and accretionary complex distributions $\Delta V_1$ and $\Delta V_3$ (Figure 6). Between 165 and 190 km, the distributions interchange their divergent behavior.

Besides the small-scale structures mimicked by the match to the mean curves, we can clearly define regions of accretionary, forearc, and island arc character (Figure 6). Moving along the profile, we enter the forearc high at 130 km and leave it at 180 km, where we enter a sedimentary basin from 180 to 190 km. Strong mixing and a sudden increase in the uncertainty of the fit result indicate a structural change between an island arc and a velocity-field characteristic of a sedimentary accretionary prism. At 202 km, the divergence seems to be large in relation to each fit (Figure 7). One reason for this might be a velocity increase related to a geologic-tectonic backstop feature identified in previous studies (Bangs et al., 2003; Christeson et al., 2003). The parameterization of the model space allows a direct comparison between the velocity structure of a tomographic solution and an assumed velocity distribution for a defined tectonic setting. Furthermore, we can test different tectonic settings given a mean velocity distribution for each of them.

The statistics obtained by variable starting models in a Monte Carlo ensemble help define tolerance intervals for the deviation. We chose two schemes to compare the velocity structure along the profile. The first method allows an overall estimate of conformity ($\chi^2$/rms) between the velocity structure at a given position $x$ up to a certain depth in a tomographic solution and the velocity structure we would expect for a predefined tectonic setting. This provides an overall estimate of the divergence along the profile for a tectonic setting ($x$-estimate). A different approach is a singular comparison of velocity values resulting in a deviation between expected (reference) and calculated (model) values. This yields an estimate of structural change moving deeper in the model and allows a comparison at particular depths ($xz$-estimate):

$$\Delta V_{1k_{\max}}(x) = \sqrt{\frac{\sum_{k=0}^{k_{\max}} (\overline{V_i}(x,z_k) - V(x,z_k))^2}{k_{\max} - 1}}, \quad 1 \le k_{\max} \le nz, \quad (8)$$

$$dV_{1k}(x,z_k) = \sqrt{(\overline{V_i}(x,z_k) - V(x,z_k))^2}. \quad (9)$$

With these two methods it is possible to analyze the structural changes along the profile. We chose to compare the three tectonic regions used for the Monte Carlo ensemble setup to achieve a higher estimate of equivalence and divergence.

## ANALYZING THE BACKSTOP

The divergence in the transition zone between the forearc and accretionary regions can be better understood by comparing $\Delta V$ of equation 6 — not over the complete range of z ($k = 1,\ldots,n_z$), but sequentially moving deeper into the model ($k = 1,\ldots,k_{\max}$; equation 8). We would expect a higher resemblance to the accretionary distribution for the shallower terms, i.e., summation up to $k_{\max} \ll n_z$, whereas the resemblance to the island arc velocity distribution would become predominant in the deeper part from an increase in velocities. This is visualized in Figure 8 with increasing depth range. Figure 9 shows the distributions at 4.9 km below the seafloor. If we analyze the mean distributions, adding more values as we move deeper, we see the structural change associated with the three tectonic regimes. This gives a qualitative measure of the velocity structure at a certain $x$-position along the profile and consequently provides a regional approximation of the velocity field.

As a second approach, we chose a direct comparison of velocities at all $z$-node positions along the profile (equation 9; Figure 10). This is a one-bin-thick $z$-filter returning the deviation between the model and expectation values of the mean distributions. We move parallel to the seafloor and calculate the deviation at each position ($x$,$z$). The approach allows a direct match between the reference and calculated

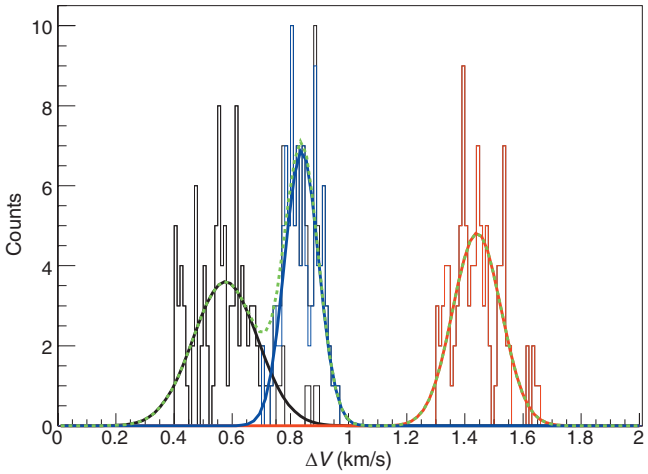


Figure 7. Example of the overlap of the cumulative divergence $\Delta V$ in the transition zone from the forearc high into the accretionary complex. The distributions are projected in the $\Delta V$ plane and subsequently fitted with Gaussian functions. The green curve corresponds to equation 7. Black curve is the island arc, red curve is the forearc high, and blue curve is the accretionary prism. In this figure, $x$ = 201–202 km.

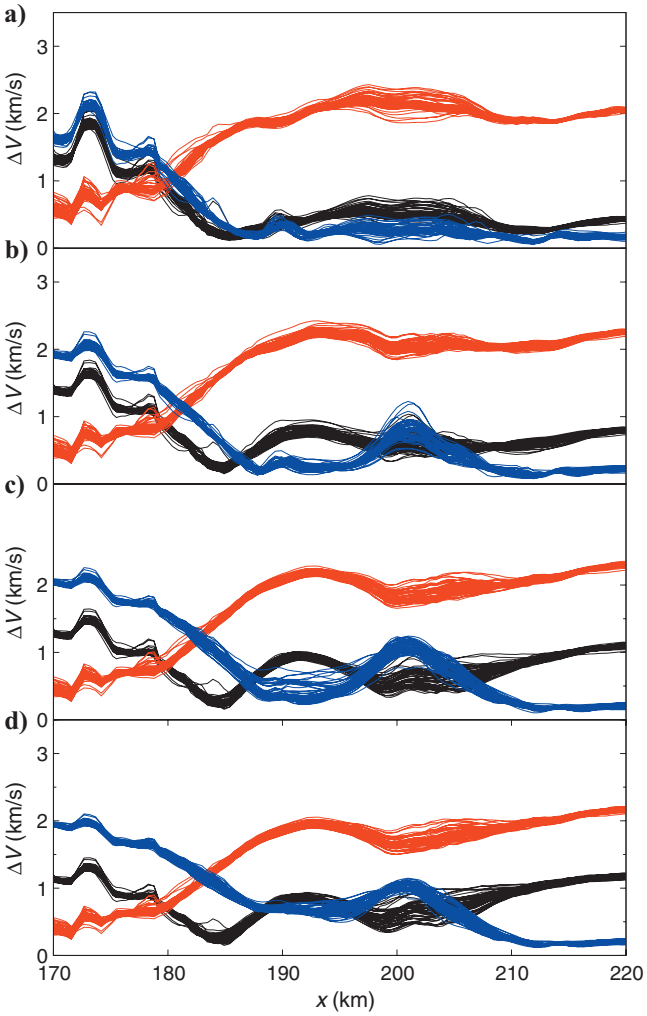


Figure 8. Cumulative divergence of actual $V(x_i,z_k)$ to the mean velocity up to depths of $z_k$ equals (a) 1.95 km, (b) 3.4 km, (c) 4.9 km, and (d) 9.2 km below the seafloor between profile $170 \leq x_i \leq 220$. Black curves are the island arc, red curves are the forearc high, and blue curves are the accretionary prism.

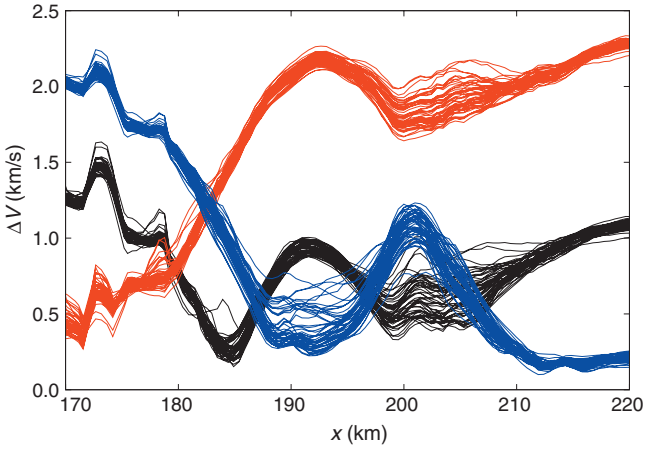


Figure 9. Distribution of $\Delta V$ functions after fit for $z = 4.9$ km ($k_{max} = 70$) below the seafloor, showing a clear distinction in the velocity structure in the vicinity of the backstop feature. Black curves are the island arc, red curves are the forearc high, and blue curves are the accretionary prism.

velocities. Because we compare with three different distributions, we have an estimate of the structural setting.

Furthermore, we can provide tolerance intervals of the match to a given distribution by a Gaussian fit at each $x$-position. At profile 195 km, where $z = 2.9$ km below the seafloor, the mean velocity of the accretionary distribution at this depth deviates, whereas the mean velocities from the forearc and island arc match. Further tracing the match at depth, the behavior can be mapped (Mosegaard and Tarantola, 1995). This is valid at each $x$-node only where the ray coverage in the model is sufficient. Figure 10 shows the distributions at increasing depths below the seafloor, ultimately yielding a qualitative measure of the velocity structure at a certain position $x$ and a certain depth $z$.

Comparing this with the previous method, we see higher horizontal as well as vertical structural changes in the velocity field and obtain a quantitative measure of divergence for each $(x,z)$ node. The maximum depths reached by the rays in this part of the profile range from 6.5 to 14.5 km below the seafloor, which makes a comparison

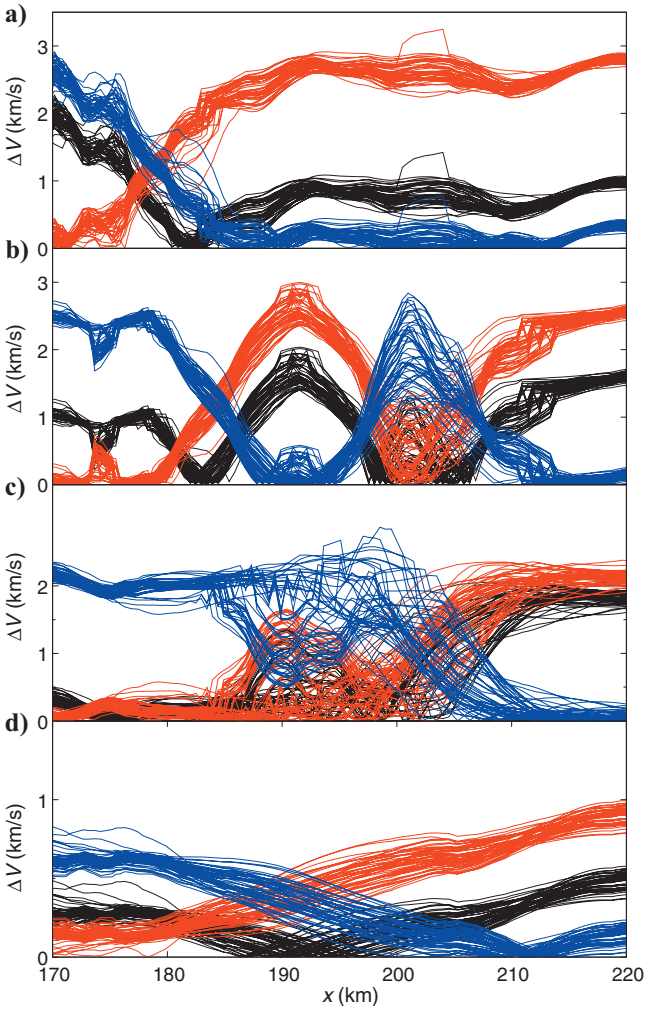


Figure 10. Singular deviation of $V(x_i,z_k)$ for $170 \leq x_i \leq 220$ to the mean velocity at depths $z_k$ equals (a) 1.95 km, (b) 3.4 km, (c) 4.9 km, and (d) 9.2 km below the seafloor. Clear structural changes are visible below the seafloor. Black curves are the island arc, red curves are the forearc high, and blue curves are the accretionary prism.

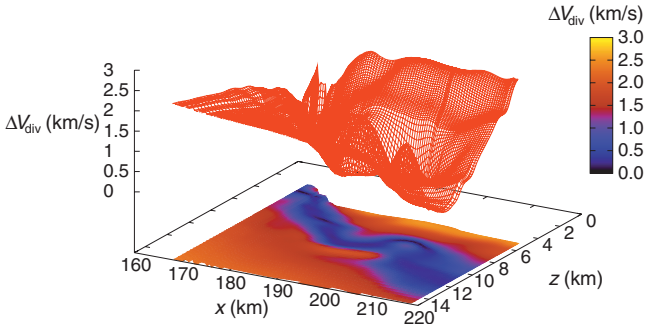


Figure 11. Example of the divergence for one output model moving deeper. The dark areas represent higher matching of the velocity structure in comparison with the mean curve $\overline{V_2}$.

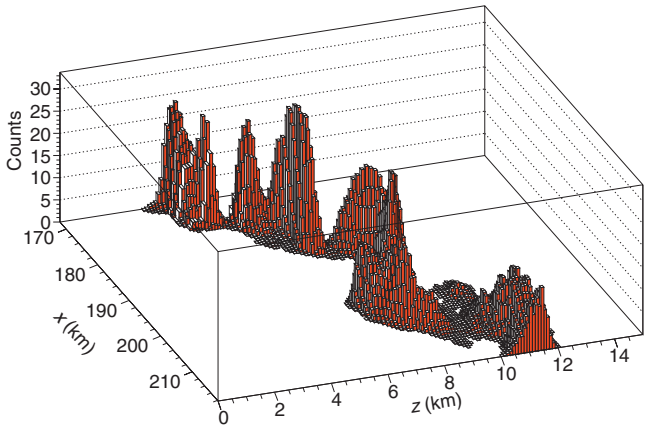


Figure 12. Perspective view of the backstop structure according to a divergence analysis with $15 \le k_{div} \le 25$. Projecting onto the $z$-axis and subsequently fitting the result gives the most probable depths for the backstop along the profile.

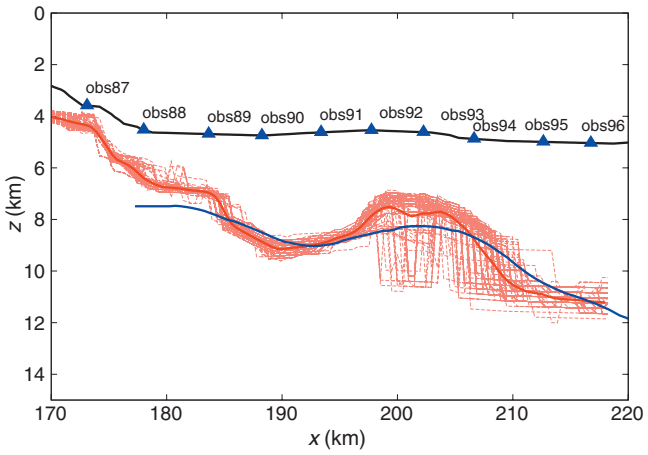


Figure 13. Backstop structure (pastel lines) according to a divergence analysis with $\overline{V_2}(i,k_{div})$ $15 \le k_{div} \le 25$. The parameterization is clearly visible, and the resolution decreases as a result of weaker penetration depths in the accretionary domain. The thick red curve denotes the minimal structure of the backstop; the blue curve denotes the interpretation according to the 4.5-km/s isocontour line of Christeson et al. (2003); and the black curve is the bathymetry.

in deeper parts of the profile impossible, as can be seen in Figure 10d, where no clear match is traceable.

The backstop (Bangs et al., 2003; Christeson et al., 2003) was interpreted by a match between tomographic and near-vertical data analysis. The comparison resulted in a best match of isocontours between 3.5 and 5.5 km/s. Assuming a geologic relationship between forearc and backstop, we should be able to trace the velocity gradients according to this interpretation. On the basis of the preceding interpretation gained by divergence analysis, we designed a 2D filter. We chose to analyze the 2D profile with the mean velocity distribution $\overline{V_2}$ between $V_{min} = 3.797 \le V_{div}$ km/$s \le V_{max} = 5.064 (15 \le k_{div} \le 25)$. Figure 11 shows the divergence of the match moving deeper along the profile for a single model. For each $x$-node, we calculate the divergence $dV$ at each $z$-node.

Doing this for all models, we retrieved a minimal matching distribution of the backstop structure. Figure 12 shows a perspective view of this distribution and visualizes the fitting routine on finding the most probable — i.e., mean — values of the depths according to a best match between forearc and backstop. Projections of the distribution are made in depth and subsequently fitted with Gaussian functions. Figure 13 shows the result of minimal matching of all models. Model binning is clearly visible. We do not reach the same depths in forward-calculating the rays in all of the models, so we can neglect certain results. This analysis is strongly dependent on the information to be gained. However, it generally applies to any facies in a purely homogeneous study if the search algorithm resembles the result.

## CONCLUSION

From this study, we infer several conclusions concerning the interpretation of the tomographic approach. By calculating a global as well as singular misfits of velocities, we are able to map tectonic regions along the profile. Comparing velocity distributions with the result of a tomographic inversion along the profile, we can mimic the subsurface structures in their extent and composition. The possibility of gaining a priori information for seismic refraction analysis by a simple solution to an inverse problem and subsequent resolution of structural heterogeneities through a divergence analysis is a new and simple way of defining a priori space and estimating the a posteriori mean and covariance in singular and general forms.

The major advantage of a Monte Carlo-based approach in our case study is the gained knowledge of velocity/depth distributions. Certainly, the decision of where to extract velocity information on the profile for setting up a Monte Carlo ensemble limits the a priori space. However, the general conclusion of analyzing the velocity field according to distinct reference distributions gives us the possibility of defining the covariance according to any tectonic environment if we have a priori information on the velocity/depth distributions.

Using the wide-angle data recorded across the Lesser Antilles, we resolved a shallow feature like the backstop by a robust and simple divergence analysis. Our new methodology effectively extracts some key features and properties from the inversion results by including information concerning the confidence level of results. This new, simple approach provides a simple solution to an inverse problem and subsequent resolution analysis of structural heterogeneity.

## ACKNOWLEDGMENTS

We are grateful to the master, officers, and crew of the *Maria S. Merian* cruise 04/2 for their cooperation. The refraction data used in this case study were acquired in the scope of the European Union-funded THALES project (grant FP6-029080-2). We thank C. Papenberg, E. Flueh, D. Klaeschen, A. Krabbenhoeft, A. Hirn, and M. Laigle for many helpful discussions. Thorough reviews by assistant editor M. Sacchi and associate editor B. Wang as well as three anonymous reviewers helped sharpen the manuscript and improved an earlier version.

## REFERENCES

Bangs, N. L., G. L. Christeson, and T. H. Shipley, 2003, Structure of the Lesser Antilles subduction zone backstop and its role in a large accretionary system: Journal of Geophysical Research (Solid Earth), **108**, 2358–2372.

Brun, R., and F. Rademakers, 1997, ROOT—An object oriented data analysis framework: Nuclear Instruments and Methods in Physics Research A, **389**, 81–86.

Christeson, G. L., N. L. Bangs, and T. H. Shipley, 2003, Deep structure of an island arc backstop, Lesser Antilles subduction zone: Journal of Geophysical Research (Solid Earth), **108**, 2327–2343.

Feuillet, N., 2000, Sismotectonique des Petites Antilles: Ph.D. dissertation, Universite Paris VII, Denis Diderot Universite.

Hansen, T. M., A. G. Journel, A. Tarantola, and K. Mosegaard, 2006, Linear inverse Gaussian theory and geostatistics: Geophysics, **71**, no. 6, R101–R111.

Hjelt, S., 1992, Pragmatic inversion of geophysical data: Springer-Verlag Berlin, Lecture notes in earth sciences 39.

Jacobsen, B. H., K. Mosegaard, and P. Sibani, 1996, Inverse methods: Springer-Verlag Berlin.

James, F., and M. Roos, 1975, Minuit—A system for function minimization and analysis of the parameter errors and correlations: Computer Physics Communications, **10**, 343–367.

Kirsch, A., 1996, An introduction to the mathematical theory of inverse problems: Springer-Verlag New York, Inc.

Korenaga, J., W. S. Holbrook, G. M. Kent, P. B. Kelemen, R. S. Detrick, H.-C. Larsen, J. R. Hopper, and T. Dahl-Jensen, 2000, Crustal structure of the southeast Greenland margin from joint refraction and reflection seismic tomography: Journal of Geophysical Research, **105**, 21591–21614.

Matarese, J., 1993, Nonlinear traveltime tomography: Ph.D. dissertation, Massachusetts Institute of Technology.

Mosegaard, K., and M. Sambridge, 2002, Topical review: Monte Carlo analysis of inverse problems: Inverse Problems, **18**, 29–54.

Mosegaard, K., and A. Tarantola, 1995, Monte Carlo sampling of solutions to inverse problems: Journal of Geophysical Research, **100**, 12431–12448.

Parker, R., 1994, Geophysical inverse theory: Princeton University Press.

Parker, R. L., and A. M. Dziewonski, 1995, Geophysical inverse theory: Physics Today, **48**, 92.

Press, F., 1968, Earth models obtained by Monte Carlo inversion: Journal of Geophysical Research, **73**, 5223.

——–, 1971, An introduction to earth structure and seismotectonics: Proceedings of the International School of Physics Enrico Fermi.

Sambridge, M., and K. Mosegaard, 2002, Monte Carlo methods in geophysical inverse problems: Reviews of Geophysics, **40**, 1009–1038.

Sato, T., and B. L. N. Kennett, 2000, Two-dimensional inversion of refraction traveltimes by progressive model development: Geophysical Journal International, **140**, 543–558.

Tarantola, A., 1987, Inverse problem theory: Methods for data fitting and model parameter estimation: Elsevier Science Publ. Co., Inc.

Toomey, D. R., S. C. Solomon, and G. M. Purdy, 1994, Tomographic imaging of the shallow crustal structure of the East Pacific rise at 9 deg 30 min N: Journal of Geophysical Research, **99**, 135–159.

# 11

Kopp, H., Weinzierl, W., Becel, A., Charvis, P., Evain, M., Flueh, E. R., Gailler, A., Galvé, A., Hirn, A., Kandilarov, A., Klaeschen, D., Laigle, M., Papenberg, C., Planert, L., Roux, E., Trail and Thales teams, 2010.

**Deep structure of the central Lesser Antilles Island Arc: relevance for the formation of continental crust.**

Earth Planet. Sci. Lett., submitted.

# Deep structure of the central Lesser Antilles Island Arc: relevance for the formation of continental crust

**H. Kopp[a], W. Weinzierl[a], A. Becel[b], P. Charvis[c], M. Evain[c], E. R. Flueh[a], A. Gailler[c], A. Galvé[c], A. Hirn[b], A. Kandilarov[d], D. Klaeschen[a], M. Laigle[b], C. Papenberg[a], L. Planert[a], E. Roux[b], and the Trail and Thales Teams**

[a] IFM-GEOMAR Leibniz-Institute of Marine Sciences, Kiel, Germany
[b] IPG Institut de Physique du Globe, Paris, France
[c] UMR Géoazur, Villefranche-sur-Mer, France
[d] Department of Earth Science, University of Bergen, Norway

submitted to: **Earth and Planetary Science Letters,** 2010**.**

**Abstract**
Oceanic island arcs are sites of high magma production and contribute to the formation of continental crust. Geophysical studies may provide information on the configuration and composition of island arc crust, however, to date only few seismic profiles exist across active island arcs, limiting our knowledge on the deep structure and processes related to the production of arc crust. We acquired active-source wide-angle seismic data crossing the central Lesser Antilles island arc north of Dominica where the oceanic Tiburon Ridge subducts obliquely beneath the forearc. A combined analysis of wide-angle seismics and pre-stack depth migrated reflection data images the complex structure of the backstop and its segmentation into two individual ridges, suggesting an intricate relation between subducted basement relief and forearc deformation. Tomographic imaging reveals three distinct layers composing the island arc crust. A three kilometer thick upper crust of volcanogenic sedimentary rocks and volcaniclastics is underlain by intermediate to felsic middle crust and plutonic lower crust. The island arc crust may comprise inherited elements of oceanic plateau material contributing to the observed crustal thickness. A high density ultramafic cumulates layer is not detected, which is an important observation for models of continental crust formation. The upper plate Moho is found at a depth of 24 kilometers below the sea floor. Upper mantle velocities are close to the global average. Our study provides important information on the composition of the island arc crust and its deep structure, ranging from intermediate to felsic and mafic conditions.

## 1. Introduction

The role of magma production along intra-oceanic arcs in the formation of continental crust in the Phanerozoic has long been recognized (e.g. Clift and Vannucchi, 2004; Davidson and Arculus, 2005; Kodaira et al., 2007a, 2007b; Tatsumi et al., 2008 and references therein), but an improved understanding of the associated tectono-magmatic processes requires an evaluation of the deep structure of these systems (e.g. Acocella and Funiciello, 2010). The Lesser Antilles island arc is characterized by a low magma production rate related the low rate of convergence (Macdonald et al., 2000). Segmentation of the margin is reflected in the variation of volcanic activity and geometry of the Benioff zone (Wadge and Shepherd, 1984; Huang et al., 2010) along the arc. The central Lesser Antilles arc around 16°N has been the site of a number of previous experiments (Westbrook et al., 1988; Bangs et al., 1990, 2003; Bangs and Westbrook, 1991; Christeson et al., 2003), which have mainly focused on the accretionary complex and backstop geometry. However, no seismic profile has been acquired traversing the central island arc itself, leaving the arc geometry and basement as well as Moho depth here undetermined. We present the results of a 280 km long regional wide-angle seismic profile conducted south of Guadeloupe between 15.5°N and 16.5°N, trending approximately perpendicular to the deformation front/parallel to convergence (Fig. 1). The profile initiates in the Grenada Basin, crosses the active island arc and extends onto the Barbados Ridge accretionary complex, where it terminates approximately 80 km west of the deformation front. A total of 44 ocean bottom seismic stations were deployed along the profile, which in addition was covered by multichannel seismic data along its northeastern extent (Fig. 1). The joint analysis of seismic refraction, wide-angle reflection and multichannel seismic data reveals a detailed image of the central Lesser Antilles margin. The study provides constraints on the previously unresolved deep crustal structure and upper mantle of the active Lesser Antilles island arc.

## 2. Regional Tectonic Setting And Previous Investigations

The Lesser Antilles are an active island arc formed by the subduction of old Atlantic crust (Lower Campanian-Maestrichtian) under the Caribbean plate. The strongly curved, ~850 km long Lesser Antilles subduction zone constitutes the eastern margin of the Caribbean plate (Westbrook, 1975) and absorbs the ENE motion between the North American and the

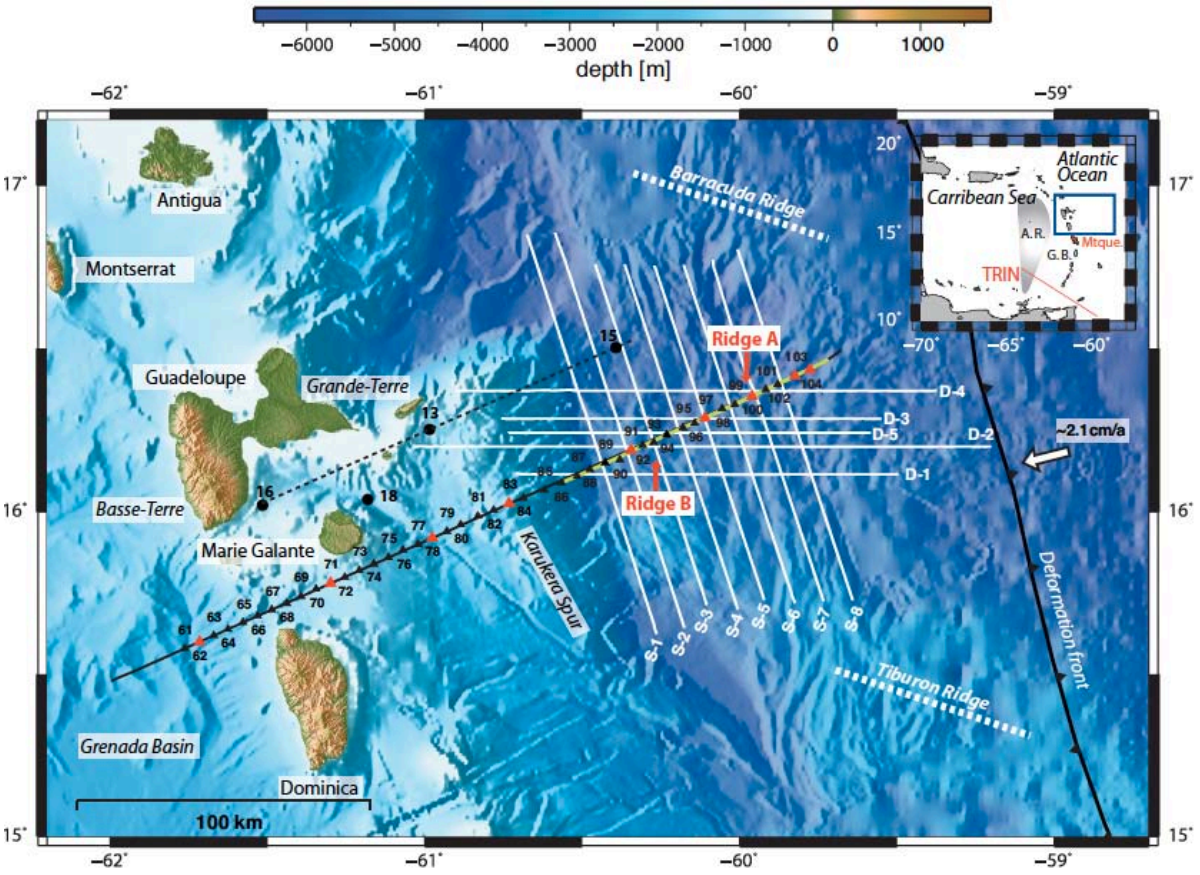


***Figure 1:*** *Location map of wide-angle seismic profile with ocean bottom stations indicated by triangles. The northeastern portion of the profile marked in yellow was additionally covered by multichannel reflection data. The Tiburon and Barracuda ridges subduct obliquely underneath the forearc. White lines (D1-D5; S1-S8) indicate seismic grid by Bangs et al. (2003) and Christeson et al. (2003). Dotted line indicates location of refraction profile with four ocean bottom stations (black dots) discussed by Roux (2007). Inset shows regional tectonic framework and location of the TRIN profile across the southern Antilles (Christeson et al., 2008). Study area indicated by black square in the inset. A.R.: Aves Ridge, G. B.: Grenada Basin, Mtque: Martinique.*

Caribbean plates that converge at a rate of 2.1 cm/a (DeMets et al., 2000) (Fig. 1). Crustal thickness of the Caribbean plate is intermediate between typical continental and oceanic values. This is compatible with thickened oceanic crust of Pacific origin modified and thickened during passage over the Galapagos hotspot prior to emplacement between the Americas (Mauffret and Leroy, 1997). The Caribbean igneous province is characterized by a number of volcanic plateaus and closely resembles large igneous provinces such as Kerguelen or Ontong-Java. Deep basins of thinner crust with underplated volcanic material separate the plateaus (Mauffret and Leroy, 1997). Additional crustal thickening may be associated with Eocene-Oligocene magmatic activity of the Antilles volcanic arc. To the west of the Lesser Antilles Arc lies the Grenada Basin, which is bordered on its western side by a remnant arc, the Aves Ridge (Fig. 1 inset) (Boynton et al., 1979). The origin of the Grenada Basin remains enigmatic. The velocity structure determined in the southern Grenada Basin around 12°N is consistent with oceanic crust formed by backarc spreading or alternatively sourced from the forearc region (Christeson et al., 2008 and references therein). Near our study area north of 15°N, water depth in the marine backarc domain is significantly less than that of the incoming Atlantic oceanic lithosphere. Shallow water may be considered as indicative of a lower density lithosphere. In the oceanic domain, this is commonly regarded to be easiest achieved by thickened crust, e.g. by magmatic underplating. The complex history of the Caribbean

region and the presence of a number of oceanic plateaus imply that the original primitive crust has been altered by intrusion and extrusion of volcanic material and possible thickening by deep magmatic processes, which have modified the crustal velocity structure (Mauffret and Leroy, 1997).

Our experiment was conducted along the central Lesser Antilles margin between the islands of Dominica and Guadeloupe (Fig. 1). Here, the active island arc is situated approximately 280 km west of the deformation front. The complex, episodic magmatic history of the margin resulted in two main volcanic fronts (Bouysse, 1988) from Martinique (Fig. 1 inset) northwards, where the recent arc, which is

active since the early Miocene, is progressively offset to the west. As a result, the island of Guadeloupe is partitioned into two parts of different volcanic origin in the east (Grande Terre) and west (Basse Terre) (Fig. 1). The separation of the recent, active arc and the older Eocene to mid-Oligocene arc is proposed to be the result of kinematic changes in the subduction processes in the late Oligocene (Bouysse and Westercamp, 1990). Pleistocene to recent (<2 Ma) magmatic activity is focused in a narrow band (<10 km wide) along the western volcanic front (Macdonald et al., 2000). Early gravity modeling combined with limited seismic information estimated a crustal thickness of 30-35 km for the central and northern Lesser Antilles Arc (Westbrook, 1975; Boynton et al., 1979; Maury et al., 1990). A receiver function study imaged a crust thickness of ~30 km on average for the Montserrat region (Fig. 1) with values ranging from 26 km to 34 km (Sevilla et al., 2010) and thus slightly thinner than the earlier estimates. Near the southern termination of the Lesser Antilles island arc, a crustal thickness of ~24 km was determined from refraction seismic data (Profile TRIN in Fig. 1; Christeson et al., 2008).

The Lesser Antilles forearc is dominated by a significant accretionary prism termed the Barbados Ridge accretionary complex, which forms by subduction accretion initiated in the Eocene. In our study area, approximately 1/3 of the sediment input along the portion of the margin coinciding with our study area is frontally accreted, while the remaining ~500-700 m of sediment are underthrust beneath the accretionary prism adjacent to the deformation front (Westbrook et al., 1988). The prism has a width of ~125 km here, decreasing northwards. To the south, the accretionary wedge reaches a width of more than 300 km and 20 km in thickness where it approaches the sediment source associated with the South American river systems (Westbrook, 1975; Westbrook et al., 1982).

An abrupt westward retreat (~100 km) of the deformation front occurs east of the island of Martinique and is related to the oblique subduction of the Tiburon Ridge, which blocks sediment transport to the north (Fig. 1). The portion of the Tiburon Ridge expressed in the topography of the Atlantic seafloor is 150 km long and 30-40 km wide and rises 1850 m above the surrounding oceanic basin, trending in a WNW direction (Bangs et al., 2003). To the north, east of the deformation front offshore Guadeloupe, a second aseismic ridge, the Barracuda Ridge, extends for more than 390 km onto the abyssal plain in a WNW direction, parallel to the Tiburon Ridge (Fig. 1). The Barracuda Ridge displays an irregular width, ranging from less than 25 km to ~60 km along its eastern termination. Both ridges profoundly modulate the margin architecture and geometry, causing local uplift of the forearc.

Our seismic line crosses the location of the coincident seismic reflection/refraction grid of Bangs et al. (1990; 2003) and Christeson et al. (2003) (Fig. 1) along the forearc basin and outer forearc high, which revealed the igneous forearc crust, forearc basin and accretionary wedge structure near 16°N. In particular, the island arc crust that serves as backstop to the accretionary prism was imaged in great detail. The deeply buried island arc crust is characterized by considerable relief as documented by two ridges (Ridge A and Ridge B) rising 1-6 km above the adjacent basement (Christenson et al., 2003) and possibly incorporates fragments of an accreted aseismic ridge at its toe (Bangs et al., 2003). The forearc basin sediments above the backstop are only mildly deformed in contrast to the accretionary prism fronting the island arc crust. The accretionary wedge shows little lateral variation across its 125 km width and only minimal backthrusting over the island arc crust (Bangs et al., 2003).

In a reconnaissance experiment (SISMANTILLES I) multichannel seismic reflection data (MCS) were acquired offshore Guadeloupe and Martinique in 2001 (Laigle et al., 2005; Roux, 2007) and shots were recorded by a limited number of ocean bottom seismometer (OBS) receivers as wide-angle refraction profiles (Fig. 1). For logistical reasons shotlines could not penetrate to less than 1000 m water depth, that is onto and west of the Karukera Spur (~ 80 km east of the volcanic arc) (Fig. 1). East of it only shooting was extended and with a half-power source, and only the easternmost OBS was in a position to record at a long range, but as an unreversed profile. Hence sampling of deep structure was restricted to under the accretionary wedge and the outer forearc. There, the deepest refractor evidenced at 10-15 km depth with a velocity >7 km/s appeared consistent with the interpretation as forearc Moho (Roux, 2007) as found at such depths in the case of intra-oceanic or Island arc type subduction zones, such as Alaska-Aleutian (e. g. Holbrook et al., 1999; Lizarralde et al., 2002), Mariana (e.g. Takahashi et al., 2007), Izu Bonin (e.g. Suyehiro et al., 1996), and Java (Kopp et al., 2002).

## 3. Data Acquisition and Processing

In January-February 2007 the 'Thales was Right' project investigated the central Lesser Antilles arc system between 14.5°N and 17.5°N with the German R/V Maria S. Merian (TRAIL cruise MSM04/2) and the French N/O L'Atalante (SISMANTILLES II cruise). During the TRAIL cruise, a refraction seismic line was acquired north of the Republic of Dominica, extending in a SW to NE direction and partially coincides with a reflection profile acquired during the SISMANTILLES II and ANR SUBSISMANTI cruises of N/O L'Atalante of IFREMER (Fig. 1). The seismic refraction profile was shot with a 5-element seismic source array with a trigger interval of 60 s at a ship speed of 3.7 kn on average, resulting in a shot spacing of approximately 100 m. Standard processing

of the OBS data included clock drift correction and relocalization using the water wave arrival and exact shot geometry. Subsequently, a time-gated deconvolution removed predictable bubble reverberations to produce a clean signal without disturbing interference of multiple and primary phases. In a second step, a time and offset-variant Butterworth filter was designed to account for frequency changes caused by signal attenuation. The filter's passband continuously shifts towards lower frequencies as offset and record time increase. Clear first arrivals are observed to an average offset of 60-70 km on the Caribbean Plate. Signal-to-noise ratios vary considerably and clear arrivals on some stations could be traced to 100-130 km offsets.

Following the OBS experiment, MCS data coincident on the deeper eastern part of the transect were recorded with the N/O L'Atalante using a 4.5 km long, 360 channel digital streamer and a 8865 cu.in Bolt air gun. The reflection data were gathered to reveal the sedimentary structures as well as fault deformation patterns to gain *a priori* information on the upper layers as input to the refraction seismic modeling. MCS processing included pre-stack processing and pre-stack depth migration. A time-space-variant frequency filter was applied prior to a predictive deconvolution (prediction window from 80 ms to 480 ms) and spherical divergence correction. Normal moveout correction and velocity analysis was followed by multiple suppression conducted in the tau-p-domain and common depth point stacking. For the pre-stack depth migration, we chose an iterative scheme using focusing analyses and common reflection point gathers (Mackay and Abma, 1993) to determine seismic interval velocities. The wide-angle velocity model served as input to the first macro-model for the pre-stack depth migration and was subsequently updated during several iterations.

## 4. Tomographic Inversion

A two-dimensional velocity-depth model (Fig. 2a) was obtained using the joint refraction and reflection tomographic inversion method of Korenaga et al. (2000). This tomography scheme allows a combined inversion of refracted as well as reflected phases. It employs a hybrid ray-tracing scheme combining the graph method with further refinements utilizing ray bending with the conjugate gradients method. The velocity field vik is parameterized by a homogeneous grid of nodes (xi, zk) with $1 \le i \le nx$ and $1 \le k \le nz$ hanging below the seafloor. We chose a lateral nodal spacing of 0.5 km and an increasing vertical nodal spacing ranging from 0.05-1.0 km. To account for a geometrical effect evolving from a local basement high structure we re-sampled the lateral spacing in a 8 km wide region from 136-142 profile km (Fig. 2b). Depth dependant smoothing constraints and correlation lengths ranging from 1-5 km horizontally and 0.1-1 km vertically were used to stabilize the inversion. A simple layered 1-D velocity model served as the starting model for the initial tomographic inversion. The result of this inversion provided an estimate of the velocity structure along the transect and supplied the basis for defining three distinct tectonic units of the margin, namely the active island arc (1), forearc domain (2) and accretionary domain (3) (Weinzierl and Kopp, 2010) (Fig. 2a). The velocity distribution and segment definition are in accordance with earlier seismic refraction tomography results (Christeson et al., 2003). We chose a conservative picking strategy and manually picked the first arrival travel times only where arrivals could be picked within an error range of 30-100 ms, resulting in a total of more than 22500 picks (Fig. 2c); no picks were placed where the signal-to-noise ratio inhibited exact picking. RMS travel time misfits for the final velocity model are in the order of 50 ms (Fig. 2d).

The spatial and amplitude resolution of the tomographic inversion, which depends on the ray geometry and seismic velocity field, was analysed using a checkerboard test. The final inversion is perturbed by a checkerboard pattern of 2 x 10 km (vertical x horizontal checker size) using values of ±6% between the seafloor and 10 km depth (Fig. 3). Subsequently, synthetic traveltimes are computed through the perturbed medium, using the same source-receiver geometry as for the tomographic inversion. The tomography is then re-calculated based on the synthetic traveltimes in order to recover the initial perturbation pattern. Adequate resolution is achieved to a depth of approximately 8 km, which corresponds to basement depth underneath the active island arc (Fig. 3). As the resolution depends on the ray coverage, recovery breaks down along the profile's periphery.

### 4.1 Combining the near-vertical and wide-angle data

After performing the first-arrival tomography we used the retrieved velocity field as input for a pre-stack depth migration of the MCS data. Figure 4 displays the tomography velocity distribution used in the input macro-model of the pre-stack depth migration (Fig. 4a) and the velocity field of the last migration iteration (Fig. 4b), respectively. The joint analysis of the wide-angle and reflection seismic data is based on coincident acquisition geometries. The two resulting velocity models retrieve similar velocity trends, however, due to slightly diverging acquisition geometries, some details differ. The linedrawing is based on the pre-stack depth imaging (Fig. 4c-d). The décollement zone (Fig. 4d) is traced in the MCS image to a depth of 16 km, where it becomes difficult to distinguish from the framework rock (Fig. 4c). The décollement and the top of the oceanic basement (yellow and purple stippled lines in Fig. 4c) are also observed on stations deployed in the accretionary domain. A steeply seaward dipping fault is observed between km 235 -245 (turquoise line in Fig. 4c) and is identified on stations 100 and 103 (Fig. 5). Seismic *(a)*

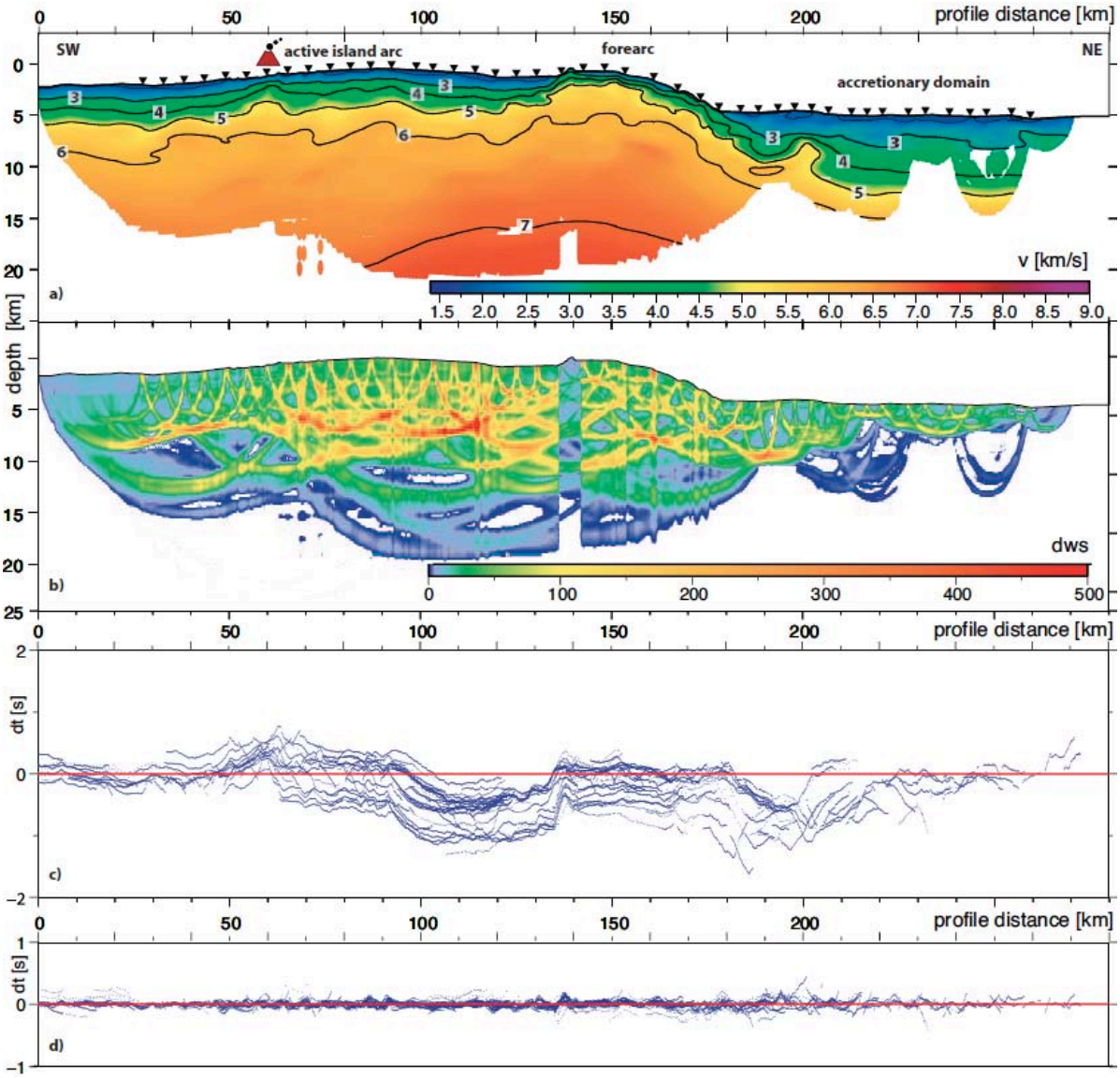


***Figure 2:*** *(a) Joint refraction and reflection tomographic inversion across the Central Lesser Antilles island arc. Numerals indicate vp velocities in km/s. Triangles indicate ocean bottom seismic stations and red volcano shows location of the active volcanic front. Only resolved areas are displayed. Three distinct tectonic regions are resolved: the accretionary domain, the forearc and the active island arc. (b) Derivative weight sum (DWS) of rays traveling through the model provides an estimate for the potential model resolution. (c) Initial and (d) final root-mean-square (RMS) misfits. The resulting residuals are in the order of 50 ms.*

reflectivity changes across this boundary, which marks the seaward extent of the forearc basin and backstop and serves as a structural backbone to incoming sediments. The basement underneath the forearc basin (blue line in Fig. 4c) shows a highly variable topography and may be traced to the backstop fault and in the refraction data (Fig. 5).

## 5. Forward Modeling

Owing to the complexity of the margin geometry and to account for secondary arrivals we used the tomography result to construct a forward model. This approach is advantageous because detailed *a priori* information on the velocity-depth distribution and the geologic structure along our profile's northeastern extent exists from previous studies (Bangs et al., 2003; Christeson et al., 2003) and may thus be incorporated into a layered forward model, which allows first order velocity discontinuities (Fig. 6). We used the hybrid forward/inverse travel time code provided by Zelt and Smith (1992), which employs a damped, least-squares approach to minimize travel time residuals. Inversion for interface depth with an upper structure determined by first arrival tomography can exploit the complementary nature of the subjective forward and tomographic approach (Zelt et al., 2003). The final model of the first arrival travel time inversion (Fig. 2a) was used as a starting model converted into 6 layers by extracting iso-velocity contours along the transect where the travel time fit did not exceed our desired error estimate of 0.05 s. The upper portions of the model, which were well constrained by the tomography and pre-stack depth migration results, were kept fixed. In addition to the first arrivals already

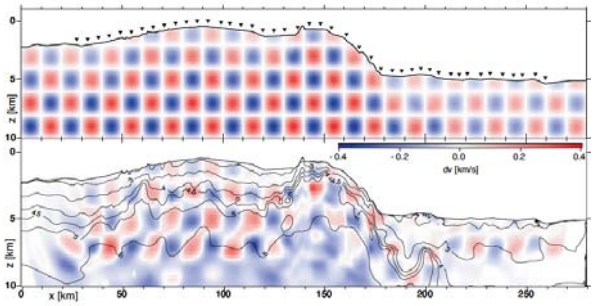


***Figure 3:*** *Checkerboard test to analyse the spatial and amplitude resolution along the profile. A checkerboard pattern of 2x10 km (vertical x horizontal) is adequately resolved to a depth of 10 km. Amplitude variation is ±6%.*

used in the tomographic inversion, we picked an additional 3611 secondary arrivals for the forward modeling.

The décollement and the top of the downthrusting oceanic crust underneath the accretionary wedge are traced by clear near-vertical reflections PdecP and PtocP (see Table 1 and e.g. OBS 103 in Fig. 5). Moving towards the island arc, the oceanic Moho is constrained by PmPoc reflections from underneath the backstop (OBS 97 in Fig. 7). Stations 97 and 91 document the lateral increase in seismic velocities from the forearc high to the island arc crust (backstop) (Pg phases in Fig. 7). A weak PmPoc phase (oceanic Moho reflection) is visible on station OBS 83 (Fig. 8) at 60-80 km offset, tracing the Atlantic crust-mantle boundary to around 40 km depth. Secondary arrivals identified on stations located on the island arc crust reveal an intracrustal impedance contrast (PicP) in addition to the crust-mantle boundary (PmP) (Fig. 9). These arrivals are accounted for by incorporating an intracrustal boundary in the island arc crust during modeling (Weinzierl, 2010). Based on PmP reflections (e.g. OBS 71 in Fig. 8), the upper plate Moho is placed at 28 km depth with upper mantle velocities of 8.0 km/s.

**6. Results**

On the incoming plate, the wide-angle results reveal an 8 km thick oceanic crust below the accretionary prism and forearc high (Fig. 6). Underneath the island arc crust around profile km 200, the slab dips at an angle of ~14.5°, steadily increasing underneath the island arc. Velocities of the incoming oceanic crust rise from 5.5 km/s at the oceanic basement to 7.3 km/s above the crust-mantle boundary. A distinction between oceanic layers 2 and 3 is not resolved (Fig. 6). Due to the lack of refracted mantle phases, upper mantle velocities of the subducting slab also remain unresolved. A décollement zone is imaged on the reflection profile (Fig. 4c) as well as on selected wide-angle record sections (e.g. OBS 103 in Fig. 5) and is characterized by low seismic velocities (~3.6 km/s) and a thickness of 1.3 –1.8 km. Previous investigations of the lower slope and accretionary wedge approximately 70-80 km to the east of our profile imaged 0.5-0.75 km of sediment underthrust beneath the prism within the décollement zone (Westbrook et al., 1988; Bangs and Westbrook, 1991; Bangs et al., 1990; 2003). At the northeastern termination of our profile, the accretionary wedge is defined by seismic velocities ranging from 2.0 km/s near the surface to over 4.0 km/s at the décollement; the wedge gradually thickens to 40-45 km towards the island arc with little lateral variation in seismic velocities (Fig. 6). The approximate 30 km of MCS data covering the accretionary wedge between profile km 245 - 275 resolve the thickening of the wedge by imbricate thrusting (Fig. 4). Apart from the thrusts, few coherent reflections are imaged, other than strata trapped in a small basin (profile km 260). A discontinuous bottom-simulating reflector at a depth of 1 km bsf mimics the seafloor (Fig. 4c) and indicates the presence of gas hydrates, as is common for many accretionary wedges worldwide (Waite et al., 2010), however, was previously not observed for the Lesser Antilles.

Previous seismic investigations on a grid of profiles imaged the backstop geometry and resolved two ridges (Ridge A and Ridge B, Fig. 1) (Bangs et al., 2003; Christeson et al., 2003). Ridge A is bounded by the seaward-dipping fault (turquoise stippled line in Fig. 4c) and marks the transition from the seaward forearc high to the forearc basin and is associated with laterally increasing velocities retrieved in the pre-stack depth migration (Fig. 4b). This velocity increase causes a moderate upward bending of velocity isolines in the tomographic inversion (Fig. 2) and forward model (Fig. 6) around profile km 230. Moving towards the island arc, Ridge B is resolved by our inversion results (profile km 190-210; Fig. 6) with seismic velocities exceeding 5.0 km/s, which corresponds to the results of Christeson et al., 2008. Ridge B is also imaged in the MCS data (Fig. 4) and correlates to a moderate uplift of the seafloor by several hundred meters. The variation in seafloor topography in this 2-D cross section, however, is of lower magnitude than the corresponding trend of the basement reflector. A steeply seaward vergent fault indicates a structural boundary below 10 km depth (profile km 240, Fig. 4c).

The steep slope in the seafloor topography ~20 km southwest of Ridge B marks the transition to the active island arc. Here, the seafloor rises by 3900 m and seismic velocities abruptly increase from the forearc basin sediments to the island arc crust (from 2.5 km/s to over 4.5 km/s) (Fig. 4c-d). As inferred from low seismic velocities of < 3.0 km/s, the island arc is covered by a sediment layer increasing in thickness from a few hundred meters near the forearc basin transition to 1100 m at the transition to the Grenada Basin (Fig. 6). Approximately 1900 m of sediment are trapped in the Grenada Basin, however, the basin's eastern margin is only covered by four seismic

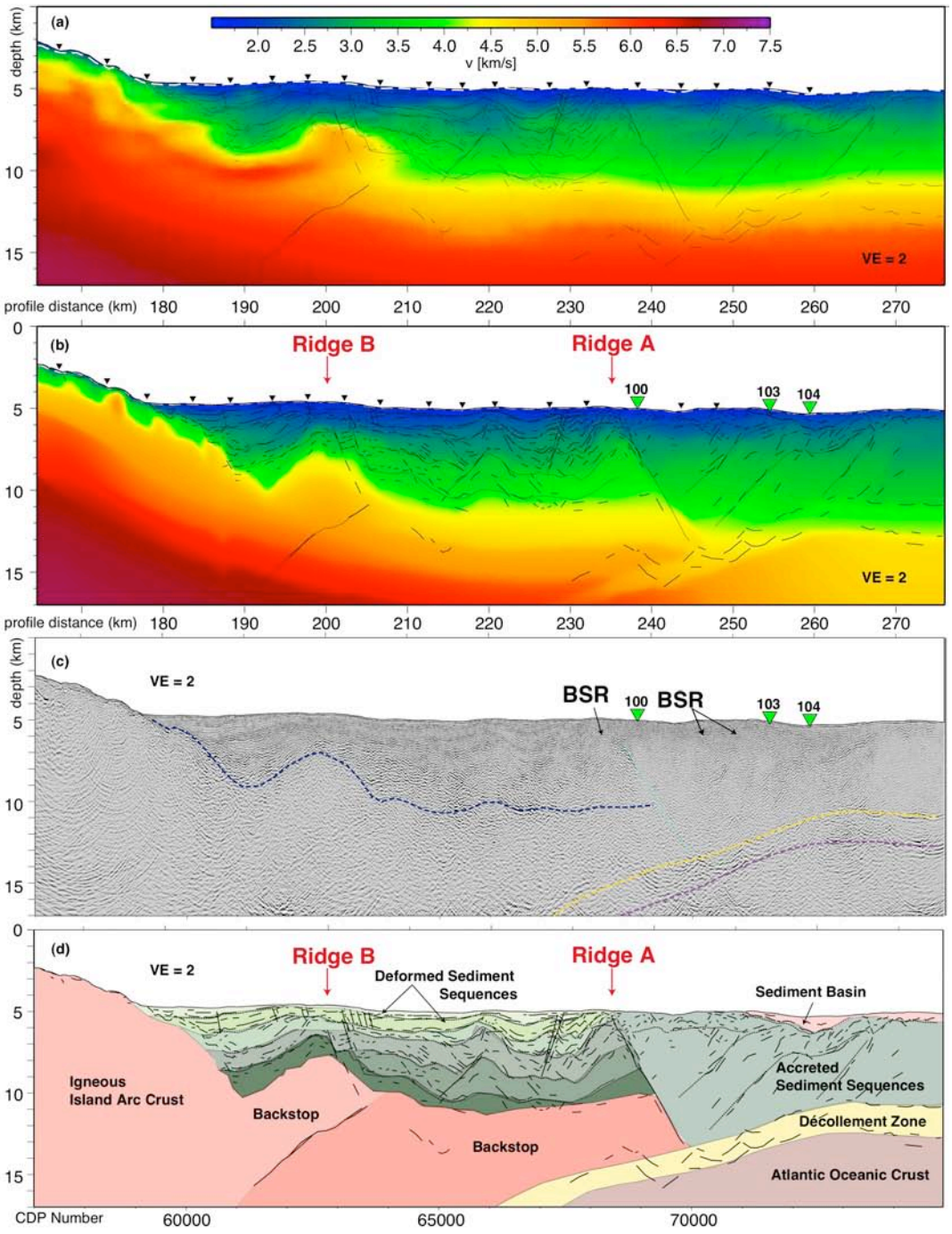


***Figure 4:*** *Combined analysis of wide-angle and reflection data. (a) final tomographic velocity model for the accretionary domain. This velocity distribution was used as input for the initial macro-model of the pre-stack depth migration of the multichannel reflection data. Linedrawing based on the reflection image presented in (c). Triangles indicate locations of ocean bottom stations. (b) final velocity model retrieved by depth focusing analysis during pre-stack depth migration of the multichannel data. Linedrawing is identical to (a). Ridge A and B are based on the interpretations by Bangs et al. (2003) and Christeson et al. (2003). (c) pre-stack depth migrated section across the accretionary domain and forearc basin. Discontinuous bottom simulating reflections (BSR) are indicative of gas hydrates. Stippled lines indicate the décollement (yellow), oceanic basement (purple), backstop thrust (turquoise) and forearc basement (blue) modeled by stations 100, 103-104 as presented in Figure 5. (d) interpretive section based on the velocity model presented in (b) and the pre-stack imaging shown in (c). The décollement zone dips gently underneath the thrust packages of the accretionary prism (240-275 km offset). A steeply seaward dipping fault marks a change in reflectivity and the transition to the forearc basin and backstop at depth. This fault forms the eastern flank of Ridge A. To the west, Ridge B deforms the overlying sediment layers trapped in the forearc basin. A landward dipping fault at 10-15 km depth around 190-200 km offset demonstrates that the two ridges form individual blocks as proposed by Bangs et al. (2003).*

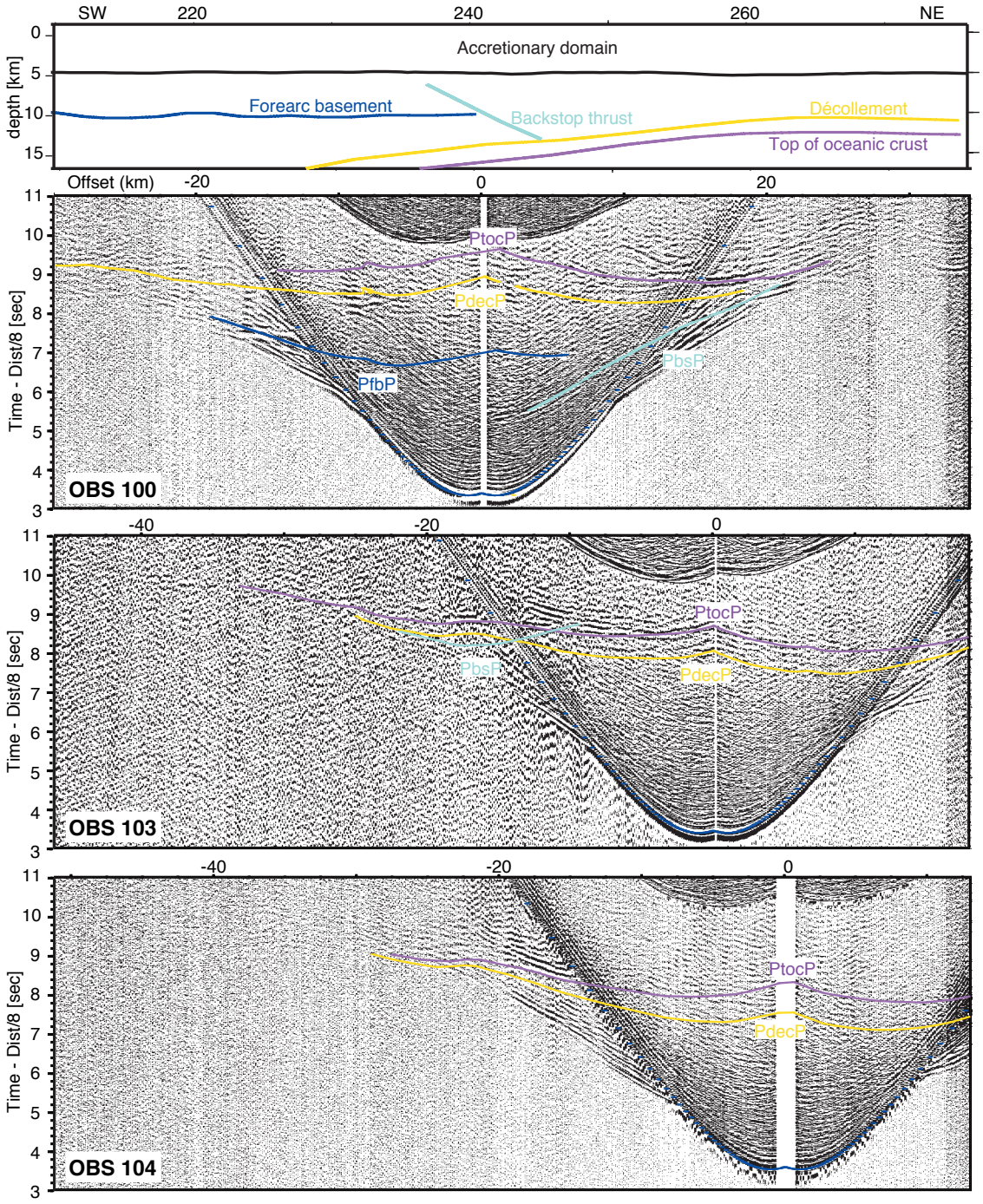


***Figure 5:*** *Selected record sections of stations located on the accretionary prism (exact location shown in Figure 4c). These stations show clear arrivals from the structural interfaces displayed in the upper panel: the décollement (yellow), oceanic basement (purple), backstop thrust (turquoise) and forearc basement (blue). Modeling was conducted in the final velocity model used in the migration of the MCS data and displayed in Figure 4b. Boundaries shown in upper panel are identical to structures displayed in Figure 4c. Phase nomenclature given in Table 1.*

stations (OBS 61-64) and resolution beyond the instrument layout is limited due to lower ray coverage (Figs. 2 and 6). Sediments are mainly sourced from the island arc, where a well-developed canyon system provides transport paths to the basin (Fig. 1).

Two distinct island arc crustal layers below the upper volcanogenic sedimentary rock unit are resolved: a middle crust with a velocity gradient of 0.28 $s^{-1}$ and a lower crustal layer with a gradient of 0.038 $s^{-1}$. The crust-mantle boundary is found at an average depth of 28 km (Fig. 6). Upper mantle velocities of 8 km/s are well constrained by reverse shots along the central portion of the island arc beneath the volcanic front (Fig. 9). Whereas the crust underneath the Grenada Basin shows a uniform structure at a constant

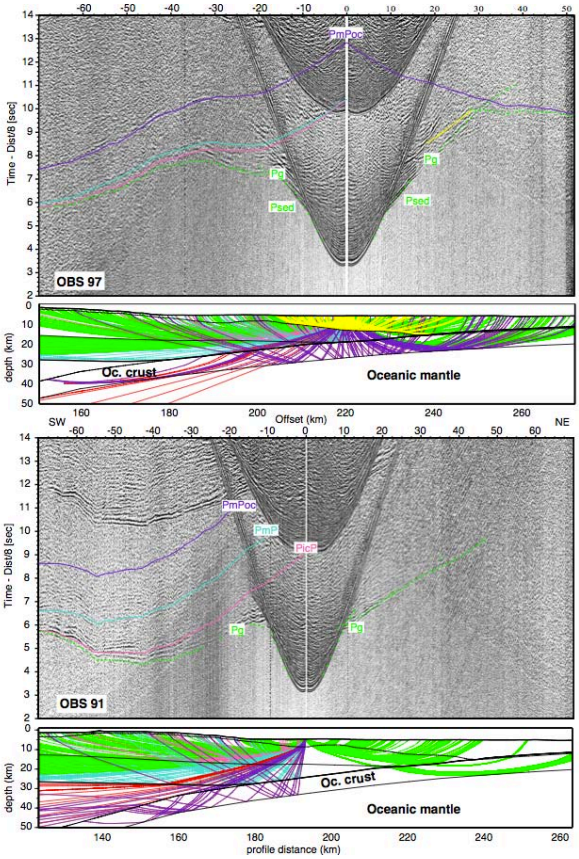


***Figure 7:*** *Seismic wide-angle sections for OBS 97 and 91 and corresponding ray penetration through the model. See Figure 6 for instrument location. Calculated travel times through the forward model displayed in Figure 6 are shown as color-coded lines. Reduction velocity is 8 km/s. See Table 1 for phase information. Pg refractions are shown in green; intracrustal as well as PmP reflections of the Caribbean plate are shown in pink and turquoise, respectively. Oceanic basement and PmP reflections are displayed in purple and orange. The yellow arrival traces the forearc basement reflection.*

thickness of 23 km; the crustal geometry underneath the island arc is characterized by locally thickened segments. The PicP reflector at the base of the middle crust smoothly bends upwards underneath stations 71 to 82 (Fig. 6). As the basement does not follow this trend, the thickening of the lower crust here corresponds to a locally thinned middle crust. The eastern portion of the island arc is characterized by a basement high extending from profile km 130 to 170. Only a thin sediment cover of a few hundred meters and less is resolved over the basement high; sediment thickens towards the volcanic front. The mid-crustal reflection PicP can be traced northeastwards underneath Ridge B.

## 7. Discussion and conclusions

### 7.1 Oceanic domain

Due to the thick accumulation of sediment on top of the incoming North American oceanic crust, seismic energy penetration along our profile is not sufficient to resolve the velocity structure of the oceanic mantle. Low upper mantle velocities (~7.5 – 7.8 km/s) have been documented for a number of subduction zones globally and have been attributed to highly fractured crust facilitating mantle hydration processes (e.g. Faccenda et al., 2009; Planert et al., 2010). The oceanic basement is well resolved along a ~50 km segment by our forward model (220-270 km offset), where there is little indication for considerable basement relief related to deeply penetrating normal faults (Fig. 4). Convergent margins displaying a thick sedimentary blanket are less prone to hydration processes than margins where permeable basement rock is widely exposed on the seafloor. Here, water may enter the igneous crust along outcropping basement highs or tectonic faults breaching the seafloor (Faccenda et al., 2009). The thick sedimentary cover characteristic for the Lesser Antilles margin likely inhibits ocean-basement interaction and hinders penetration of seawater into the crust and mantle. The structure and seismic velocities of the incoming oceanic crust show typical values for mature, unaltered oceanic crust (Carlson, 1998). We speculate that upper mantle velocities follow this trend and are in the range of 7.9-8.3 km/s associated with an anhydrous condition of peridotite in the upper mantle (Peacock, 1990).

| Phase | Description |
|---|---|
| Psed | Sedimentary phases |
| Pg | Refraction through the crust |
| PfbP | Reflection from the forearc basement |
| PbsP | Reflection from the backstop thrust zone |
| PdecP | Reflection from the décollement |
| PtocP | Reflection from the oceanic basement |
| PmPoc | Reflection from the crust-mantle boundary of the oceanic plate |
| PicP | Reflection from middle / lower crust interface |
| PmP | Reflection from the crust-mantle boundary of the Caribbean Plate |
| Pn | Refraction through the upper mantle |

***Table 1:*** *Phase nomenclature for wideangle seismic data.*

### 7.2 Forearc-island arc transition and backstop topography

The seismic refraction and reflection grid of Bangs et al. (2003) and Christeson et al. (2003) reveals a laterally undulating topography of Ridge A, which is also imaged in our reflection profile (Fig. 4) and could be an indication that the relief originates from crustal fragments that would be easier to accrete than a continuously developed aseismic ridge. Ridge B is also well recovered along our profile (Figs. 2, 4, and 6); its top is traced between offsets of 190-215 km. The line crosses a local peak of Ridge B (Fig. 3 of Bangs et al., 2003), where it reaches a depth of 8 km. The seaward dipping geometry of the backstop resembles the backstop structure found offshore southern Sumatra and western Java. Frontal accretion dominates along this central segment of the Sunda margin (Kopp et al., 2009) and a dual backstop structure controls material transfer processes and the evolution of the accretionary prism here (Kopp et al., 2001; 2002). However, compared to the central Lesser Antilles, the backstop along the central Sunda margin

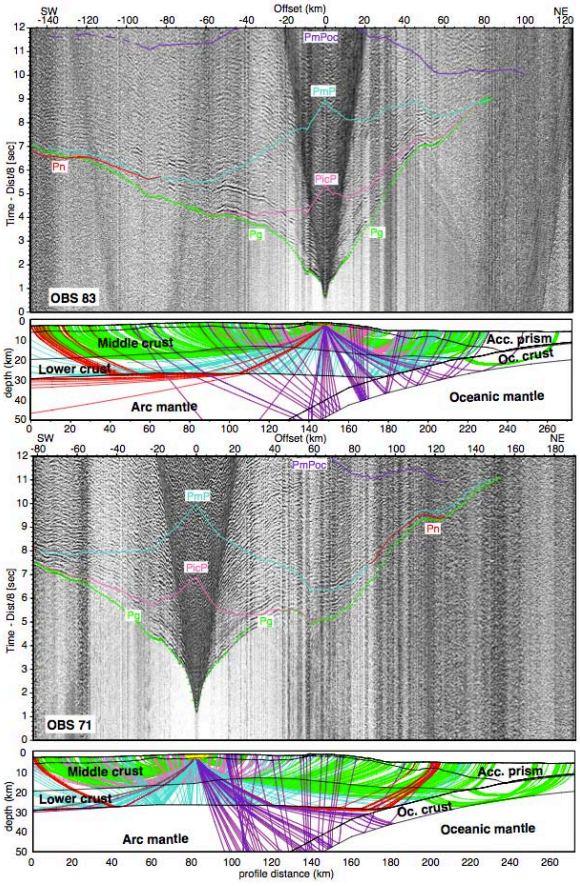


***Figure 8:*** *Seismic wide-angle sections for OBS 83 and 71 and corresponding ray penetration through the model. See Figure 7 caption for display information.*

is characterized by a much more subdued, uniform geometry without distinct ridges and troughs as imaged offshore Guadeloupe. This may be an artifact resulting from the 2D seismic coverage along Sunda (Kopp and Kukowski, 2003) compared to the three-dimensional imaging of the Lesser Antilles (Christeson et al., 2003). Another explanation would be the composite character of the Lesser Antilles backstop as proposed by Bangs et al. (2003), with incorporation of accreted fragments of oceanic crust or aseismic ridges.

A similar basement topography pattern has been documented offshore eastern Java (Shulgin et al., 2010) and has been attributed to accretion of fragments of a buoyant aseismic oceanic plateau. A composition sourced from different units is supported by the segmentation of the arc basement underneath the Ridges A and B (Fig. 4), where a steeply landward dipping fault separates two basement blocks. The original backstop fronting the volcanic arc was uplifted to form Ridge B when a second unit arrived (Bangs et al., 2003), which was subsequently deformed as Ridge A evolved. Deformation of a backstop has been documented for the Nankai margin, where a landward indentation of the crustal block of old accreted sediments, which serves as backstop, has been attributed to the subduction of oceanic basement relief (Nakanishi et al., 2002). Intense deformation of the forearc crust is also observed on the Ryukyu margin (Font and Lallemand, 2009). Strong trench-perpendicular compression of the forearc basement concurs with the uplift of a broken piece of Ryukyu arc basement caused by the subduction of oceanic relief. This complex interplay of oceanic basement block subduction and deformation of the upper plate basement thus mirrors the situation along the central Antilles margin.

A broad swell is observed between 130-170 km offset east of the active arc and is associated with a positive gravity anomaly. Sediment thickness here is greatly decreased compared to the western part of the island arc (Fig. 6). This region corresponds to an elongated high observed in the bathymetry data (Fig. 1), the Karukera Spur. It extends for approximately 80 km in a NW-SE (160°) direction (Fig. 1) and lies in the projected prolongation of the Tiburon Ridge. However, our seismic data do not reveal the subducted ridge, which would be expected at depths exceeding 25 km between OBS 83 and 88 at offsets around ~170 km. We can thus only speculate on a possible relation between ridge subduction and forearc uplift. Recent numerical modeling has shown that a stable effect of ridge subduction is an increase in local topography. The net uplift may exceed the height of the subducted seafloor relief due to additional shortening of the overriding plate (Gerya et al., 2009).

### 7.3 Island arc structure

The island arc crust is divided into three layers, with a total average thickness of 23-24 km. These values are compatible with crustal investigations along the southern extent of the Lesser Antilles island arc (TRIN transect; Christeson et al., 2008), which resolved a ~24 km thick crust underneath the island arc. The TRIN tomographic inversion of the crust was based on first arrivals and thus did not resolve an intracrustal reflector (Christeson et al., 2008). The seismic velocities retrieved for the island arc in our study are in the range of velocities found along the southern TRIN transect (Christeson et al., 2008). For the Montserrat region (Fig. 1), Sevilla et al. (2010) estimate a crustal thickness ranging from 26-34 km based on receiver function analysis. Their velocity-depth distribution identifies similar seismic velocities and provides corroboration for our interpretation of crustal velocities across the island arc. Previous investigations crossing the island arc were mainly based on gravity modeling with only sparse seismic information and slightly overestimated crustal thickness (Westbrook, 1975; Boynton et al., 1979; Maury et al., 1990).

The upper island arc crust along our transect shows little variation in thickness except where the sediment cover characterized by seismic velocities lower than 3.0 km/s is changing (e.g. increasing sediment thickness in the Grenada Basin and decreasing sediment cover across the Karukera Spur) (Fig. 6).

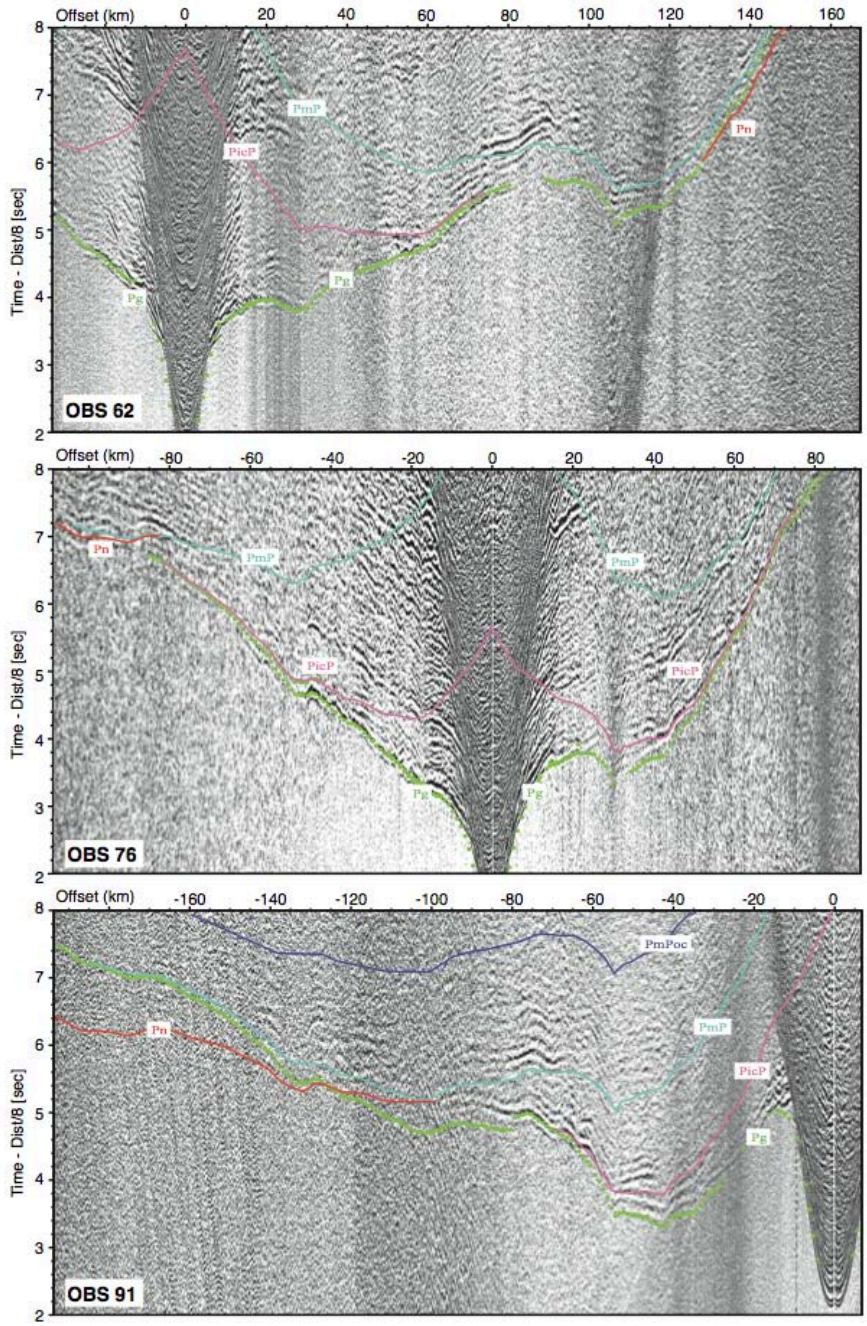


***Figure 9:*** *Record sections of stations deployed on the Caribbean plate to analyze the intracrustal boundary between the middle and lower crust as well as the upper plate Moho as displayed in Figure 6. Reverse shooting resolves two individual arrivals PicP and Pmp and supports the interpretation of an intracrustal impedance contrast in addition to the crust-mantle boundary. Instrument location is shown in Figure 6. See Figure 7 caption for further display information.*

The 160 km distance from the active volcanic front to the updip contact of the upper plate crust with the subduction lower plate as identified here by reflection-refraction data is on the order of that reported for other arcs (although the additional distance to the deformation front may vary depending on the extensions of a possible accretionary wedge) (Suyehiro et al., 1996; Holbrook et al., 1999; Lizarralde et al., 2002). The upper crust below the sediment blanket is interpreted to consist mainly of volcaniclastics and intrusive and extrusive igneous rocks with seismic velocities between sedimentary values and 5.5 – 6.0 km/s. This wide range in upper crustal velocities may be attributed to varying degrees in fluid content, fracturing and porosity and alteration.

The velocity distribution of the forearc middle crust (Figs. 2 and 6) is in the range of typical continental crust velocities, which show an average velocity of 6.4 ± 0.2 km/s (Christensen and Mooney, 1995; Rudnick and Fountain, 1995). The bulk composition of the middle crust ($v_p$< 6.8 km/s) is interpreted to be felsic to intermediate. This layer is on the order of 10 km thick with velocities increasing from 5.5-6.0 km/s to 6.8 km/s. The survey does not resolve an internal stratigraphy beyond defining a gradient with depth. This results from traveltime modeling of waves traversing it. Because of the variation in bathymetry and heterogeneous shallow cover, there is certainly a difficulty to identify short travel time branches if they existed, that could indicate the internal layering. The bulk volume and thickness of the middle crust is comparable to tomographic images of the Izu arc (Kodaira et al., 2007b) or Mariana arc (Takahashi et al., 2007) and significantly larger than for the Bonin segment (Kodaira et al., 2007a). The active volcanic front is located around stations 67-68 (Fig. 6) and is characterized by increased seismic velocities beneath the volcanic centers around 60 km offset. The sediment cover is absent on top of this active zone and the upward bending of the velocity isolines is focused along a narrow zone, corresponding to the finite area of active volcanism (Macdonald et al., 2000). A three-dimensional seismic refraction/reflection tomography around Montserrat island (Fig. 1) resolved the

andesitic cores of the volcanic centers, which are built of andesite lava domes and intrusions with seismic velocities of 3.5 km/s to 5.5 km/s (Shalev et al., 2010; Paulatto et al., 2010).

The plutonic lower crust shows velocities increasing from 7.1 km/s to 7.3 km/s. It is extending throughout the section, over at least 150 km and forms the present lower crustal layer extending from the forearc to the backarc domain. This layer has an average thickness of 12 km with notably only a long-wavelength moderate variation by 20%. A corresponding (though significantly thinner) crustal unit along the Izu-Bonin arc (Kodaira et al., 2007a) is interpreted there as gabbroic plutons. This interpretation could be shared for the Lesser Antilles, however, exposures of these rocks have not been reported for the Lesser Antilles, for which we infer an intermediate composition sourced from differentiation of deeper mafic material. It should be noted, though, that inferring composition from seismic velocity distribution depends on the thermal gradient structure (Shillington et al., 2004). There is no indication of a high density ultramafic cumulates layer as found e.g. along the Izu-Bonin arc (Kodaira et al., 2007a) and central Aleutian arc (Shilligton et al., 2004) and upper mantle velocities across the Lesser Antilles island arc are in the range of 8 km/s, with little indication for serpentinization. This observation is relevant with regards to the generation of continental crust: the andesitic bulk composition of continental crust requires differentiation of basaltic melts to form continental crust (McClennan et al., 2005). 'Foundering' or delamination of a lower ultramafic crustal layer has been proposed to occur during the growth of continental crust (e.g. Kay and Kay, 1988, 1993; Kelemen et al., 2003). This process requires the crustal section to become convectively unstable and thus be denser than the underlying mantle peridotite, which would concur with P wave velocities exceeding 7.4 km/s (Behn and Kemelen, 2006). The range of lower crust $v_p$ values (6.8-7.3 km/s) observed across the central Lesser Antilles arc along our profile corresponds to seismic observations of the Central Aleutians (Holbrook et al., 1999; Lizarralde et al., 2002), though along strike values there are higher (Fliedner and Klemperer, 1999, 2000; Shillington et al., 2004) as is the case for Izu-Bonin (Suyehiro et al., 1996; Kodaira et al., 2007a). This layer likely represents mafic rocks and intermediate plutons added to the primitive crust on which the Lesser Antilles evolved. Behn and Kelemen (2006) note that seismic P wave velocity alone is an inadequate indicator of major element chemistry and $SiO_2$ content and compositions ranging from basaltic to dacitic match the corresponding velocities (Behn and Kelemen, 2003). Against this backdrop, the average composition of the central Lesser Antilles arc crust may serve as one component for building continental crust. Delamination or transformation of major crustal units (Kay and Kay, 1993), as proposed for the central Aleutians or Izu-Bonin is not required for the Lesser Antilles where a primitive, high density cumulates section (either in the lower crust or upper mantle) is absent.

Numerical modeling suggests that the volume of new-formed crust in island arcs correlates with the age of the subducted slab. In addition, the rate of crust accumulation in the island arc depends on the velocity of plate retreat (Nikolaeva et al., 2008). Thus the dynamics of subduction will influence crustal growth and consequently shape the volume of the island arc. As mentioned earlier, the dimension from forearc to backarc is comparable to other arcs and subduction zones. However, the remarkably uniform crustal thickness spanning the entire section of ~200 km across strike is in contrast to other arc settings. Lateral heterogeneity across the central Lesser Antilles island arc, however, is insignificant compared to the tomographic images of e.g. the Izu-Bonin (Ogasawara)-Mariana arc system. Indeed, the best-studied intra-oceanic subduction systems (e.g. Alaska-Aleutian trench, Izu-Bonin (Ogasawara)-Mariana trench system) display a distinct variability along the cross-sections regarding crustal thickness and velocity distribution. Upper plate crustal thickness varies from typical oceanic crust beneath the forearc and backarc through thickened crust underneath the volcanic front (e.g. Suyehiro et al., 1996; Holbrook et al., 1999; Takahashi et al., 2007). This is commonly interpreted as the signature of the focused material advection resulting from arc volcanism. In comparison to these typical examples, there is a reduced importance of volcanic edifices and eruptive production along the Lesser Antilles arc (Macdonald et al., 2000) and hence an expected subdued importance of magmatic advection such as intrusions or roots of cumulates and thickening of the original oceanic crust or its underplating. In summary, the considerable volume of the present lower crustal unit (if beneath what could have been originally an oceanic crust) is much larger than in sections of intra-oceanic subductions. In addition, it is not focused underneath the volcanic centers but is imaged from the forearc to the backarc regions. This layer may comprise segments of oceanic plateau material of thickened crust (Diebold, 2009). In this view, the Lesser Antilles arc may rest upon a portion of the Caribbean plateau (Mauffret and Leroy, 1997) with original oceanic crust thickened by deep magmatic processes and underplating prior to the evolution of the Lesser Antilles arc (Diebold, 2009). The present island arc structure as imaged in this survey with a crustal thickness of 25 km may exhibit an inherited structure resulting from the complex history of the original Caribbean crust.

**Acknowledgements:** We thank Master von Staa and the crew and science party of the R/V Maria S. Merian MSM 04/2 Trail cruise for their assistance in data acquisition. The TRAIL cruise MSM04-02 was financed by the German National Science Foundation DFG. The marine operations were coordinated and partly funded in the frame of the "Thales was Right" project under the European Union DG XII INSIGHT programme.

**References:**

Acocella, V., Funiciello, F., 2010. Kinematic setting and structural control of arc volcanism. Earth Planet. Sci. Lett., 289, doi:10.1016/j.epsl.2009.10.027

Bangs, N. L., Westbrook, G., Ladd, J. W., Buhl, P., 1990. Seismic velocities from the Barbados Ridge Complex: Indicators of high pore fluid pressures in an accretionary complex. J. Geophys. Res., 95, B6, 8767-8782.

Bangs, N. L., Westbrook, G., 1991. Seismic modeling of the décollement zone at the base of the Barbados Ridge accretionary complex. J. Geophys. Res., 96, 3853-3866.

Bangs, N. L., Christeson, G. L., Shipley, T. H., 2003. Structure of the Lesser Antilles subduction zone backstop and its role in a large accretionary system. J. Geophys. Res., 108, 2358, doi:10.1029/2002JB002040.

Behn, M. D., Kelemen, P. B., 2003. Relationship between seismic P-wave velocity and the composition of anhydrous igneous and metaigneous rocks, Geochem. Geophys. Geosyst., 4(5), 1041, doi:10.1029/2002GC000393.

Behn, M. D., Kelemen, P. B., 2006. Stability of arc lower crust: Insights from the Talkeetna arc section, south central Alaska, and the seismic structure of modern arcs. J. Geophys. Res., 111, doi:10.1029/2006JB004327.

Bouysse, P., 1988. Opening of the Grenada back-arc basin and evolution of the Caribbean Plate during the Mesozoic and early Paleogene, Tectonophysics, 149, 121-143, doi:10.1016/0040-1951(88)90122-9.

Bouysse, P., Westercamp, D., 1990. Subduction of Atlantic aseismic ridges and Late Cenozoic evolution of the Lesser Antilles island arc, Tectonophysics, 175, 349-380.

Boynton, C. H., Westbrook, G., Bott, M., Long, R. E., 1979. A seismic refraction investigation o fcrustal structure beneath the Lesser Antilles island arc. Geophys. J. R. Astron. Soc., 58, 371-393.

Carlson, R. L., 1998. Seismic velocities in the uppermost oceanic crust: Age dependence and the fate of layer 2A. J. Geophys. Res., 103(B4), 7069–7078.

Christensen, N. I., Mooney, W. D., 1995. Seismic velocity structure and composition of the continental crust: A global view, J. Geophys. Res., 100, 9761–9788.

Christeson, G. L., Bangs, N. L., Shipley, T. H., 2003. Deep structure of an island arc backstop, Lesser Antilles subduction zone. J. Geophys. Res., 108, 2327, doi:10.1029/2002JB002243.

Christeson, G. L., Mann, P., Escalona, A., Aitken, T. J., 2008. Crustal structure of the Caribbean-northeastern South America arc-continent collision zone. J. Geophys. Res., 113, B08104, doi:10.1029/2007JB005373.

Clift, P.D., Vannucchi, P., 2004. Controls on tectonic accretion versus erosion in subduction zones: Implications for the origin and recycling of the continental crust. Rev. Geophys. 42. doi:10.1029/2003RG000127.

Davidson, J. P., Arculus, R. J., 2005. The significance of Phanerozoic arc magmatism in generating continental crust, in Evolution and Differentiation of the Continental Crust, edts. M. Brown and T. Rushmer, Cambridge Univ. Press, Cambridge, 135-172.

Diebold, J., 2009. Submarine volcanic stratigraphy and the Caribbean LIP's formational environment. Geological Society London, Spec. Pub. 328, 799-808.

DeMets, C., Jansma, P. E., Mattioli, G. S., Dixon, T. H., Farina, F., Bilham, R., Calais, E., Mann, P., 2000. GPS geodetic constraints on Caribbean-North America plate motion, Geophys. Res. Lett., 27, 437-440.

Faccenda, M., T. V. Taras, and L. Burlini (2009), Deep slab hydration induced by bending-related variations in tectonic pressure, Nature Geoscience, 2, 790-793, doi: 10.1038/ngeo656.

Fliedner, M. M., Klemperer, S. L., 1999. Structure of an island arc: wide-angle seismic studies in the eastern Aleutian Islands, Alaska, J. Geophys. Res., 104 (B5), 10667-10694.

Fliedner, M. M., Klemperer, S. L., 2000. Crustal structure transition from oceanic arc to continental arc, eastern Aleutian Islands and Alaska Peninsula, Earth Planet. Sci. Lett., 179, 567-579.

Font, Y. and Lallemand, S., Subducting oceanic high causes compressional faulting in southernmost Ryukyu forearc as revealed by hypocentral determinations of earthquakes and reflection/refraction seismic data, Tectonophysics, 466, doi:10.1016/j.tecto.2007.11.018, 2009.

Gerya, T. V., Fossati, D., Cantieni, C., Seward, D., 2009. Dynamic effects of aseismic ridge subduction: numerical modeling. Eur. J. Mineral., 21, doi:10.1127/0935-1221/2009/0021-1931.

Holbrook, W. S., Lizarralde, D., McGeary, S., Bangs, N. L., Diebold, J., 1999. Structure and composition of the Aleutian island arc and implications for continental crustal growth, Geology, 27, 31-34.

Huang, J., Vanacore, E., Niu, F., Levander, A., 2010. Mantle transition zone beneath the Caribbean-South American plate boundary and its tectonic implications. Earth Planet. Sci. Lett., 289, doi:10.1016/j.epsl.2009.10.033.

Kay, R.W., Kay, S.M., 1988. Crustal recycling and the Aleutian Arc, Geochim. Cos. Acta, 52, 1351-1359.

Kay, R.W., Kay, S.M., 1993. Delamination and delamination magmatism: Tectonophysics, v. 219, p. 177–189, doi: 10.1016/0040-1951(93)90295-U.

Kelemen, P. B., Hanghoj, K., Greene, A. R., 2003. One view of the geochemistry of subduction –related magmatic arcs, with an emphasis on primitive andesite and lower crust, in The Crust, edt. R. L. Rudnick, Elsevier, New York, 593-659.

Kodaira, S., Sato, T., Takahashi, N., Miura, S., Tamura, Y., Tatsumi, Y., Kaneda, Y., 2007a. New seismological constraints on growth of continental crust in the Izu-Bonin intra-oceanic arc. Geology, 35, doi: 10.1130/G23901A.1.

Kodaira, S., Sato, T., Takahashi, N., Ito, A., Tamura, Y., Tatsumi, Y., Kaneda, Y., 2007b. Seismological evidence for variable growth of crust along the Izu intraoceanic arc. J. Geophys. Res., 112, doi:10.1029/2006JB004593.

Kopp, H., Flueh, E. R., Klaeschen, D., Bialas, J., Reichert, C., 2001. Crustal structure of the central Sunda margin at the onset of oblique subduction. Geophys. J. Int. 147, 449-474.

Kopp, H., Klaeschen, D., Flueh, E. R., Bialas, J., Reichert, C., 2002. Crustal structure of the Java margin from seismic wide-angle and multichannel reflection data. J. Geophys. Res. 107. doi:10.1029/2000JB000095.

Kopp, H., Kukowski, N., 2003. Backstop geometry and accretionary mechanics of the Sunda margin. Tectonics 6. doi:10.1029/2002TC001420.

Kopp, H., Hindle, D., Klaeschen, D., Oncken, O., Scholl, D., 2009. Anatomy of the western Java plate interface from depth-migrated seismic images. Earth Planet. Sci. Lett., doi:10.1016/j.epsl.2009.09.043.

Korenaga, J., Holbrook, S., Kent, G., Kelemen, P, Detrick, R. S., Larsen, H.-C., Hopper, J. R., Dahl-Jensen, T., (2000). Crustal structure of the southeast Greenland margin from joint refraction and reflection seismic tomography, J. Geophys. Res., 105, doi:10.1029/2000JB900188.

Laigle, M. et al., 2005. Elements of the Seismic Structure and Activity of the Lesser Antilles Subduction Zone (Guadeloupe and Martinique Islands) from the SISMANTILLES Seismic Survey, Eos Trans. AGU, 86(52), Fall Meet. Suppl., Abstract T33C-0580.

Lizarralde, D., Holbrook, W. S., McGeary, S., Bangs, N. L., Diebold, J. B., 2002. Crustal construction of a volcanic arc, wide-angle seismic results from the western Alaska Peninsula, J. Geophys. Res. 107, 2164, doi:10.1029/2001JB000230.

Macdonald, R., Hawkesworth, C. J., Heath, E., 2000. The Lesser Antilles volcanic chain: A study in arc magmatism. Earth Sci. Rev., 49, doi:10.1016/S0012-8252(99)00069-0.

Mackay, S., Abma, R., 1993. Depth focusing analysis using wavefront-curvature criterion. Geophysics 58, 1148 – 1156.

Mauffret, A., Leroy, S., 1997. Seismic stratigraphy and structure of the Caribbean igneous province. Tectonophysics, 283, 61-104.

Maury, R. C., Westbrook, G., Baker, P. E., Bouysse, P., Westercamp, D., 1990. Geology of the Lesser-Antilles, in: The Caribbean Region, vol. H, edited by G. Dengo and J. E. Case, pp. 141–166, Geol. Soc. of Am., Boulder, Colo.

McClennan, S. M., Taylor, S. R., Hemming, S. R., 2005. Composition, differentiation, and evolution of the continental crust: Constraints from sedimentary rocks and heat flow, in Evolution and Differentiation of the Continental Crust, edts. M. Brown and T. Rushmer, Cambridge Univ. Press, Cambridge, 92-134.

Nakanishi, A., Kodaira, S., Park, J.-O., Kaneda, Y., Deformable backstop as seaward end of coseismic slip in the Nankai Trough seismogenic zone, Earth Planet. Sci Lett., 203, 255-263, 2002.

Nikolaeva, K., Gerya, T. V., Connolly, J., Numerical modeling of crustal growth in intraoceanic volcanic arcs, Phys. Earth Planet. Int., 171, doi:10.1016/j.pepi.2008.06.026, 2008.

Paulatto, M., Minshull, T. A., Baptie, B., Dean, S., Hammond, J. O. S., Henstock, T., Kenedi, C. L., Kiddle, E. J., Malin, P., Peirce, C., Ryan, G., Shalev, E., Sparks, R. S. J., Voight, B., 2010. Upper crustal structure of an active volcano from refraction/refraction tomography, Montserrat, Lesser Antilles. Geophys. J. Int., 180, 685-696.

Peacock, S., 1990. Fluid processes in subduction zones. Science, 248, 329–337.

Planert, L., Kopp, H., Lueschen, E., Mueller, C., Flueh, E. R., Shulgin, A., Djajadihardja, Krabbenhoeft, A., 2010. Lower plate structure and upper plate deformational segmentation at the Sunda-Banda arc transition, Indonesia. J. Geophys. Res., in press.

Roux, E., 2007. Reconnaissance de la structure sismique de la zone de subduction des Petites Antilles (Guadeloupe et Martinique). PhD Thesis, Univ. Paris VII-Denis Diderot Univ.

Rudnick, R., Fountain, D.M., 1995. Nature and composition of the continental crust: A lower crustal perspective. Rev. Geophys., 33, doi: 10.1029/95RG01302.

Sevilla, W. I., Ammon, C. J., Voight, B., De Angelis, S., 2010. Crustual structure beneath the Montserrat region of the Lesser Antilles island arc, Geochem. Geophys. Geosyst., 11, doi:10.1029/2010GC003048.

Shalev, E., Kenedi, C. L., Malin, P., Voight, B., Miller, V., Hidayat, D., Sparks, R. S. J., Minshull, T., Paulatto, M., Brown, L., Mattioli, G., 2010. Three-dimensional seismic velocity tomography of Montserrat from the SEA-CALIPSO offshore/onshore experiment. Geophys. Res. Lett., 37, doi:10.1029/2010GL042498.

Shillington, D. J., Van Avendonk, H. J. A., Holbrook, W. S., Kelemen, P. B., Hornbach, M. J., 2004. Composition and structure of the central Aleutian island arc from arc-parallel wide-angle seismic data, Geochem. Geophys. Geosyst., 5, doi:10.1029/2004GC000715.

Shulgin, A., Kopp, H., Mueller, C., Planert, L., Lueschen, E., Flueh, E. R., Djajadihardja, Y., 2010. Structural architecture of oceanic plateau subduction offshore Eastern Java and the potential implications for geohazards, Geophys. J. Int., in revision.

Suyehiro, K., Takahashi, N., Ariie, Y., Yokoi, Y., Hino, R., Shinohara, M., Kanazawa, T., Hirata, N., Tokuyama, H., Taira, A., 1996. Continental Crust, Crustal Underplating, and Low-Q Upper Mantle Beneath an Oceanic Island Arc, Science, 272, 5260, doi:10.1126/science.272.5260.390

Takahashi, N., Kodaira, S., Klemperer, S. L., Tatsumi, Y., Kaneda, Y., Suyehiro, K., 2007. Crustal structure and evolution of the Mariana intra-oceanic island arc, Geology, 35, doi: 10.1130/G23212A.1.

Tatsumi, Y., Shukuno, H., Tani, K., Takahashi, N., Kodaira, S., Kogiso, T., 2008. Structure and growth of the Izu-Bonin-Mariana arc crust: 2. Role of crust-mantle transformation and the transparent Moho in arc crust evolution. J. Geophys. Res., 113, doi:10.1029/2007JB005121.

Wadge, G., Shepherd, J.B., 1984. Segmentation of the Lesser Antilles subduction zone. Earth Planet. Sci. Lett. 71, 297–304.

Waite, W. F.; Santamarina, J. C.; Cortes, D. D.; Dugan, B.; Espinoza, D. N.; Germaine, J.; Jang, J.; Jung, J. W.; Kneafsey, T. J.; Shin, H.; Soga, K.; Winters, W. J.; Yun, T.-S., 2010. Physical properties of hydrate-bearing sediments. Rev. Geophys., Vol. 47, No. 4, RG4003, doi:10.1029/2008RG000279.

Weinzierl., W., 2010. Crustal structure of the Central Lesser Antilles Island Arc: Seismic near-vertical and wide-angle profiling. PhD Thesis, University of Kiel.

Weinzierl, W., Kopp, H., 2010. Statistical Separation Strategy to Analyze Velocity Structure Obtained by Seismic Tomography, Geophysics, in press.

Westbrook, G., 1975. The structure of the crust and upper mantle in the region of Barbados and the Lesser Antilles. Royal Astronomical Soc. Geophys. J., v. 43, p 201-242.

Westbrook, G., Smith, M., Peacock, J., Poulter, M., 1982. Extensive underthrusting of undeformed sediment beneath the accretionary complex of the Lesser Antilles subduction zone. Nature 300, 625-628.

Westbrook, G., Ladd, J. W., Buhl, P., Bangs, N., Tiley, G. J., 1988. Cross section of an accretionary wedge: Barbados Ridge complex. Geology 16, 631-635.

Zelt, C. A., Smith, R. B., 1992. Seismic traveltime inversion for 2-D crustal velocity structure. Geophys. J. Int., 108, doi: 10.1111/j.1365-246X.1992.tb00836.x.

Zelt, C. A., Sain, K., Naumenko, J. V., Sawyer, D. S., 2003. Assessment of crustal velocity models using seismic refraction and reflection tomography. Geophys. J. Int., 153, doi: 10.1046/j.1365-246X.2003.01919.x.

# 12

Scherwath, M., Kopp, H., Flueh, E. R., Henrys, S., Sutherland, R., Stagpoole, V. M., Barker, D.H.N., Reyners, M.E., Basset, D.G., Planert, L., Dannowski, A., 2010.

**Fore-arc deformation and underplating at the northern Hikurangi margin, New Zealand.**

J. Geophys. Res., 115, doi:10.1029/2009JB006645.

JOURNAL OF GEOPHYSICAL RESEARCH, VOL. 115, B06408, doi:10.1029/2009JB006645, 2010



# Fore-arc deformation and underplating at the northern Hikurangi margin, New Zealand

M. Scherwath,[1,2] H. Kopp,[1] E. R. Flueh,[1] S. A. Henrys,[3] R. Sutherland,[3] V. M. Stagpoole,[3] D. H. N. Barker,[3] M. E. Reyners,[3] D. G. Bassett,[4] L. Planert,[1] and A. Dannowski[1]

Received 25 May 2009; revised 9 December 2009; accepted 27 January 2010; published 25 June 2010.

[1] Geophysical investigations of the northern Hikurangi subduction zone northeast of New Zealand, image fore-arc and surrounding upper lithospheric structures. A seismic velocity (Vp) field is determined from seismic wide-angle data, and our structural interpretation is supported by multichannel seismic reflection stratigraphy and gravity and magnetic modeling. We found that the subducting Hikurangi Plateau carries about 2 km of sediments above a 2 km mixed layer of volcaniclastics, limestone, and chert. The upper plateau crust is characterized by Vp = 4.9–6.7 km/s overlying the lower crust with Vp > 7.1 km/s. Gravity modeling yields a plateau thickness around 10 km. The reactivated Raukumara fore-arc basin is >10 km deep, deposited on 5–10 km thick Australian crust. The fore-arc mantle of Vp > 8 km/s appears unaffected by subduction hydration processes. The East Cape Ridge fore-arc high is underlain by a 3.5 km deep strongly magnetic (3.3 A/m) high-velocity zone, interpreted as part of the onshore Matakaoa volcanic allochthon and/or uplifted Raukumara Basin basement of probable oceanic crustal origin. Beneath the trench slope, we interpret low-seismic-velocity, high-attenuation, low-density fore-arc material as accreted and recycled, suggesting that underplating and uplift destabilizes East Cape Ridge, triggering two-sided mass wasting. Mass balance calculations indicate that the proposed accreted and recycled material represents 25–100% of all incoming sediment, and any remainder could be accounted for through erosion of older accreted material into surrounding basins. We suggest that continental mass flux into the mantle at subduction zones may be significantly overestimated because crustal underplating beneath fore-arc highs have not properly been accounted for.

**Citation:** Scherwath, M., et al. (2010), Fore-arc deformation and underplating at the northern Hikurangi margin, New Zealand, *J. Geophys. Res.*, *115*, B06408, doi:10.1029/2009JB006645.

## 1. Introduction

[2] Understanding and quantifying how mass transfer processes vary in space and time at subduction zones is essential to address questions surrounding the long-term growth of continents [e.g., *Rudnick and Fountain*, 1995]. The balance of sediment accretion, subduction erosion, and addition of mantle-derived material in the magmatic arc determines if a convergent margin is a site of net crustal growth or destruction. The structure of accretionary wedges and erosional margins is now well imaged in classic reflection seismic lines [e.g., *Davey et al.*, 1986; *Ye et al.*, 1997; *Park et al.*, 2002; *Kopp and Kukowski*, 2003; *von Huene et al.*, 2004], and many analogue and numerical simulations dedicated to convergent margin processes have focused on both the growth and erosion of convergent margins [e.g., *Davis et al.*, 1983; *Gutscher et al.*, 1998; *Upton et al.*, 2003; *Litchfield et al.*, 2007]. Based on such data and models, the global fluxes of subducted sediment and continental material have been estimated [*von Huene and Scholl*, 1991; *Clift and Vannucchi*, 2004], but large uncertainties remain. In this paper, we present new geophysical data from the northern Hikurangi margin, New Zealand, and challenge some of the assumptions that underpin estimates of global crustal fluxes in subduction zones.

[3] The processes of fore-arc crustal accretion or erosion are causally related to the behavior of the subduction thrust and faults within both the footwall and hanging wall, so our results have significance for understanding seismic hazard. Subduction zones typically show significant along-strike variability and it is clear that deep fore-arc basins point to significant regional tectonic controls on processes occurring at the plate interface, with implications for the nucleation and propagation of large-magnitude subduction earthquakes

[1]Leibniz Institute of Marine Sciences, IFM-GEOMAR, Kiel, Germany.
[2]Now at School of Earth and Ocean Sciences, University of Victoria, Victoria, British Columbia, Canada.
[3]GNS Science, Lower Hutt, New Zealand.
[4]School of Geography, Environment and Earth Sciences, Victoria University of Wellington, Wellington, New Zealand.


0148-0227/10/2009JB006645

[*Song and Simons*, 2003; *Wells et al.*, 2003]. For most subduction zones, the details of the spatial and temporal relationships between subduction accretion, erosion processes, fore-arc basin subsidence, and regional uplift patterns remain largely unresolved. However, it has been suggested that there is a correlation between the locations of large earthquakes, fore-arc basins, and gravity lows; and permanent interseismic subsidence is inferred to have been caused by plate coupling and long-term subduction erosion in those regions [*Song and Simons*, 2003; *Wells et al.*, 2003].

[4] The northern Hikurangi margin and Raukumara Peninsula of New Zealand (Figure 1) provide an ideal setting to examine these along-strike processes, because a broad range of complementary data types are available and marked differences in morphology and geological structure along and across the margin point to significant changes in subduction mechanics. The Hikurangi Plateau, a Cretaceous Large Igneous Province of the Pacific Plate [*Davy and Wood*, 1994; *Mortimer and Parkinson*, 1996], is subducting westward at approximately 60 mm/yr relative to the fore arc, causing active uplift of Raukumara Peninsula [*Litchfield et al.*, 2007; *Wilson et al.*, 2007], but farther to the east the outer trench slope is steep and subject to basal tectonic erosion [*Collot et al.* 1996; *Davey et al.*, 1997; *Barker et al.*, 2009]. Along strike towards the north, Raukumara Peninsula is replaced by a deep (>12 km) sedimentary basin coincident with a prominent –140 mgal gravity low, and is bounded to the east by a protuberant outer fore-arc high and a steep frontal margin wedge.

[5] Recently, *Sutherland et al.* [2009] presented an overview of new seismic reflection (RAU07) and refraction data acquired in 2007. These data provide a clear image of Raukumara Basin, the underlying Australian crust and subducting slab. The RAU07 data allow the stratigraphy of Raukumara Basin and some of the large-scale structure to be mapped out. *Sutherland et al.* [2009] divided the reflection strata defining Raukumara Basin into three sedimentary megasequences which they correlated with the onshore geology. The oldest sequence is interpreted as late Cretaceous and Paleogene passive margin sediments overlain by a sequence of Early Miocene allochthonous material and Neogene marine sedimentary rocks. In addition, they present a new kinematic model of the fore arc that involved frontal subduction erosion and basal accretion of the eroded material into the lower crust of the hanging wall.

[6] In this paper, we present a detailed analysis of seismic wide-angle reflection and refraction data collected along a dip profile through Raukumara Basin and across the subduction zone to the footwall. Our seismic velocity image is combined with the stratigraphy from multichannel seismic reflection profiles and ship-borne gravity and magnetic data to yield structural constraints that allow us to place constraints on the structure of Raukumara Basin and thickness of basin fill. The new velocity image also more precisely helps identify and quantify subduction processes within the upper 20 km, which in this case of relatively thin hanging wall crust includes the Moho, crust, and the accreted fore-arc material.

## 2. Tectonic Setting

[7] The region immediately northeast of the North Island of New Zealand (Figure 1), marks a transition from the Tonga-Kermadec to the Hikurangi subduction zone. The region includes a north-to-south transition on the downgoing Pacific plate from typical oceanic crust to anomalously thick oceanic crust of the Hikurangi Plateau (Rapuhia scarp, Figure 1) [*Davy and Collot*, 2000], and on the overriding plate from thin crust of possibly oceanic type to continental crust of 30–40 km thickness [*Reyners et al.*, 1999, 2006; *Sutherland et al.*, 2009]. The Cretaceous Hikurangi Plateau [*Mortimer and Parkinson*, 1996] has a crustal thickness of about 10–15 km to the east of Raukumara Peninsula [*Davy and Wood*, 1994]. The anomalous nature of this subducting plateau is implicated in models for uplift of the East Coast of the North Island and exposure of the fore arc [*Litchfield et al.*, 2007]. Geodetic measurements and active faulting indicate that the eastern part of the peninsula is currently extending normal to the plate margin [*Thornley*, 1996] and has experienced up to 6 km of extension since the Pliocene [*Nicol et al.*, 2007].

[8] In the region of the northern Hikurangi margin, the Pacific and Australian plates are converging obliquely at about 45 mm/yr [*DeMets et al.*, 1994] (Figure 1), but back-arc spreading in the Havre Trough and central North Island result in almost orthogonal convergence across the subduction thrust at approximately 60 mm/yr [*Wallace et al.*, 2004]. The general shape of the subducted plate has been revealed by compilations of seismicity from the IRIS Data Management Center, the New Zealand national seismograph network, and through a series of temporary deployments of dense networks of portable seismographs [*Reyners et al.*, 1999, 2006]. The continental crust is ~20 km thick beneath the northern Raukumara Peninsula and thickens to greater than 35 km to the south, as inferred from crustal seismic P wave velocity (Vp) estimates of 5.5–6.5 km/s [*Reyners et al.*, 1999, 2006; *Sutherland et al.*, 2009]. Earthquake hypocenters cluster within the upper part of the subducting plate at 15 km depth, and in the crust between the east coast of Raukumara Peninsula and the subduction front. The uppermost approximately 10 km of the mantle of the subducted slab consistently has Vp > 8.5 km/s, and reduces to more normal mantle velocities of approximately Vp = 8.2 km/s beneath [*Reyners et al.*, 1999]. Earthquake focal mechanisms indicate downdip tensional strain within

**Figure 1.** Regional base map, southwest Pacific, northeast of North Island, New Zealand (see small, gray scale inset for a global overview). The data profile corresponds to the seismic wide-angle data transect MANGO-1, seismic reflection line RAU07-05 and available ship-borne gravity and magnetic profiles. Yellow triangles mark locations of mapped volcanoes, and orange circles represent earthquakes larger magnitude 4.0 since 1990, scaled according to size. Plate motion of the Pacific relative to the Australian plate [after *DeMets et al.*, 1994]. Onshore Raukumara Peninsula simplified geology [after *Mazengarb and Speden*, 2000] and uplift [after *Litchfield et al.*, 2007], and offshore locations of the ocean bottom seismic receivers with those stations annotated whose data are shown in Figure 2.

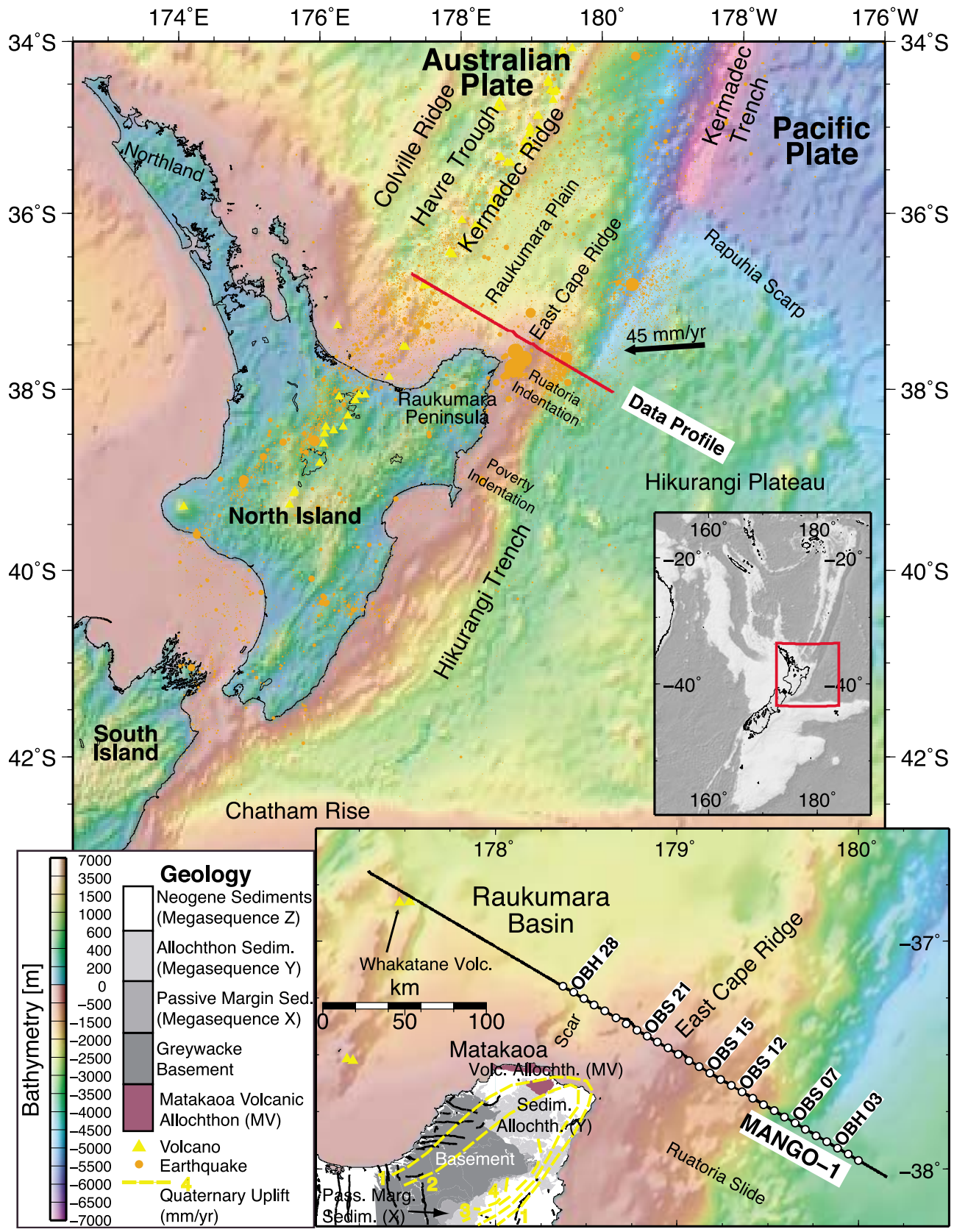
174°E
176°E
178°E
180°
178°W
176°W
34°S
36°S
38°S
40°S
42°S
Australian Plate
Pacific Plate
Colville Ridge
Havre Trough
Kermadec Ridge
Kermadec Trench
Raukumara Plain
East Cape Ridge
Rapuhia Scarp
45 mm/yr
Ruatoria Indentation
Data Profile
Raukumara Peninsula
Poverty Indentation
Hikurangi Plateau
Hikurangi Trench
Northland
North Island
South Island
Chatham Rise
160°
180°
−20°
−40°
Bathymetry [m]
7000
3500
1500
1000
600
400
200
0
−500
−1500
−2000
−2500
−3000
−3500
−4000
−4500
−5000
−5500
−6000
−6500
−7000
Geology
Neogene Sediments (Megasequence Z)
Allochthon Sedim. (Megasequence Y)
Passive Margin Sed. (Megasequence X)
Greywacke Basement
Matakaoa Volcanic Allochthon (MV)
Volcano
Earthquake
Quaternary Uplift (mm/yr)
178°
179°
180°
Raukumara Basin
Whakatane Volc.
km
0
50
100
OBH 28
OBS 21
East Cape Ridge
OBS 15
OBS 12
OBS 07
OBH 03
MANGO−1
Scar
Matakaoa Volc. Allochth. (MV)
Sedim. Allochth. (Y)
Basement
Pass. Marg. Sedim. (X)
Ruatoria Slide
−37°
−38°

**Figure 1**

the subducting plate, and NNW–SSE extensional strain within the shallow part of the upper plate [*Reyners and McGinty*, 1999], consistent with geological and geodetic observations [*Árnadóttir et al.*, 1999]. The seismogenic zone has well-constrained changes in plate coupling, where the coupling zone is shallower at the northern Hikurangi margin but deeper to the south where the risk of large megathrust earthquakes is also higher, though the interplay of the coupling parameters such as plate structure and fluid pressure is rather complex [*Wallace et al.*, 2009].

[9] Onshore, Raukumara Peninsula can be divided into distinct geological units [*Mazengarb and Harris*, 1994; *Field et al.*, 1997; *Mazengarb and Speden*, 2000] (Figure 1) that can also be recognized offshore as seismic reflection megasequences [*Sutherland et al.*, 2009]: (1) a western unit of Early Cretaceous greywacke basement in the Raukumara Range; (2) Late Cretaceous and Paleogene marine passive margin sediments (megasequence X); (3) the East Coast allochthon (megasequence Y), a belt of Late Cretaceous and Early Tertiary rocks that were thrust towards the southwest over units 1 and 2 during the earliest Miocene, and the East Coast allochthon, together with the enigmatic Matakaoa volcanic rocks, are considered concomitant with the emplacement of the Northland ophiolite terrane of northern New Zealand [*Whattam et al.*, 2004] and emplacement at about 25–22 Ma was immediately followed by the onset of arc volcanism in Northland [*Rait et al.*, 1991; *Herzer*, 1995]; (4) an eastern unit consisting of Neogene marine sedimentary rocks (megasequence Z) that overlie the allochthon in the east and is faulted against it in the west. Along the Raukumara Range broad Quaternary antiformal uplift up to 4 mm/yr [*Litchfield et al.*, 2007; *Wilson et al.*, 2007] (Figure 1) has been interpreted as a manifestation of sediment subduction and underplating at the base of the crust of the Australian plate [*Walcott*, 1987; *Reyners et al.*, 1999].

[10] It is clear from the geometry of the toe of the frontal wedge today that the subducting margin is undergoing tectonic erosion and subduction of material from the front of the wedge. Multibeam bathymetry, side scan sonar and seismic reflection studies [*Collot et al.*, 1996] indicate that the toe of the margin is indented by 10–25 km to the east of Raukumara Peninsula, relative to regions to the northeast and southwest. This is inferred to be the result of repeated impacts of the large seamounts that are abundant on the northern Hikurangi Plateau. The two most recent impacts have left the major Ruatoria and Poverty indentations [*Lewis et al.*, 1998; *Collot et al.*, 2001] in the margin east of Raukumara Peninsula (Figure 1). Also, immediately to the north of Raukumara Peninsula additional northward traveling debris avalanches have been mapped (Matakaoa Submarine Instability Complex, off Matakaoa Scarp, as part of the Raukumara Plain in Figure 1) where ~3200 $km^3$ of sediment has accumulated in the last 5 Ma [*Lamarche et al.*, 2008]. These mass transport deposits are likely to be the result of slope oversteepening associated with peninsula uplift and Raukumara Basin subsidence.

## 3. Seismic Wide-Angle Data Analysis

### 3.1. Data and Modeling

[11] In March 2007, seismic wide-angle data were acquired onboard R/V *Sonne* as part of the MANGO (Marine Geoscientific Investigations on the Input and Output of the Kermadec subduction zone) project [*Flueh and Kopp*, 2007]. A total of 29 Ocean Bottom Seismometers and Hydrophones(hereafter OBS/H) [*Bialas and Flueh*, 1999] were deployed from about 40 km east of the subduction front on the Hikurangi Plateau, across the deformation front and East Cape Ridge, and covering the eastern part of the Raukumara fore-arc basin (MANGO-1 in Figure 1). Airgun shots from a 64 liter G gun cluster, spaced nominally at 150 m, covered the line of OBS/H stations and extended across the entire Raukumara Basin and ending on the Kermadec Ridge near Whakatane volcano. Adverse weather conditions led to the occasional interruption of the shooting when the ship had to leave track to sail into the wind. The data quality generally is moderate, with signals recorded at offsets up to 30–50 km, and to 70 km in Raukumara Basin.

[12] The seismic wide-angle data were used to generate a two-dimensional (2-D) P wave velocity model of the crust and uppermost mantle using the ray tracing and travel time inversion method of *Zelt and Smith* [1992]. This method calculates arrival times through forward ray tracing in a model that consists of nodes for layer depth and velocities at the top and bottom of each layer. The calculated arrival times are compared to the observed ones and the misfit is reduced either by automatic least squares inversion or by manually adjusting the model. A resolution matrix is calculated to assess the model uncertainty [*Zelt and Smith*, 1992].

[13] Bathymetry data and structure and interval velocities from the coincident seismic reflection profile RAU07-05 (see below) provide prior information and were used to determine the shallow structure for a suitable starting model. The final model was determined from the top down, adding seismic phases with longer offsets from deeper structures. This strategy prevents smearing effects of possibly inaccurate shallow structures into deeper parts of the model. As our preferred final model should only consist of structures derived from the data plus the prior information, the final model is a "minimum parameter/prior structure" model as defined by *Zelt* [1999]. Our modeling involved both automatic inversion and manual model adjustments at complex model regions or limited data coverage where automatic inversion proved difficult.

[14] Examples of the wide-angle data are shown in Figures 2a–2f. Our interpreted P wave phases comprise first and secondary arrival refractions as well as reflections wherever they could be identified. First, we only picked signals of relatively high signal-to-noise ratios, and after a first estimate of the seismic structures, we also picked weaker signals when also observed on coincident multichannel seismic reflection data. The slope of the refracted phases provides an apparent velocity which we used to distinguish between sedimentary, crustal and mantle phases, and the reflections where matched correspondingly. The following seismic phases were picked: (1) refracted arrivals from the sediments (Psed) (e.g., Figure 2a), upper and lower crust (Pg) (e.g., Figure 2b), and uppermost Australian mantle (Pn) (Figures 2e and f); and (2) later arrivals corresponding to reflected waves from intermittent boundaries such as from the presumed decollement (PdP) (Figure 2c), midsedimentary reflection from Raukumara Basin (PsedP) (Figure 2f), and finally deeper reflections from Australian

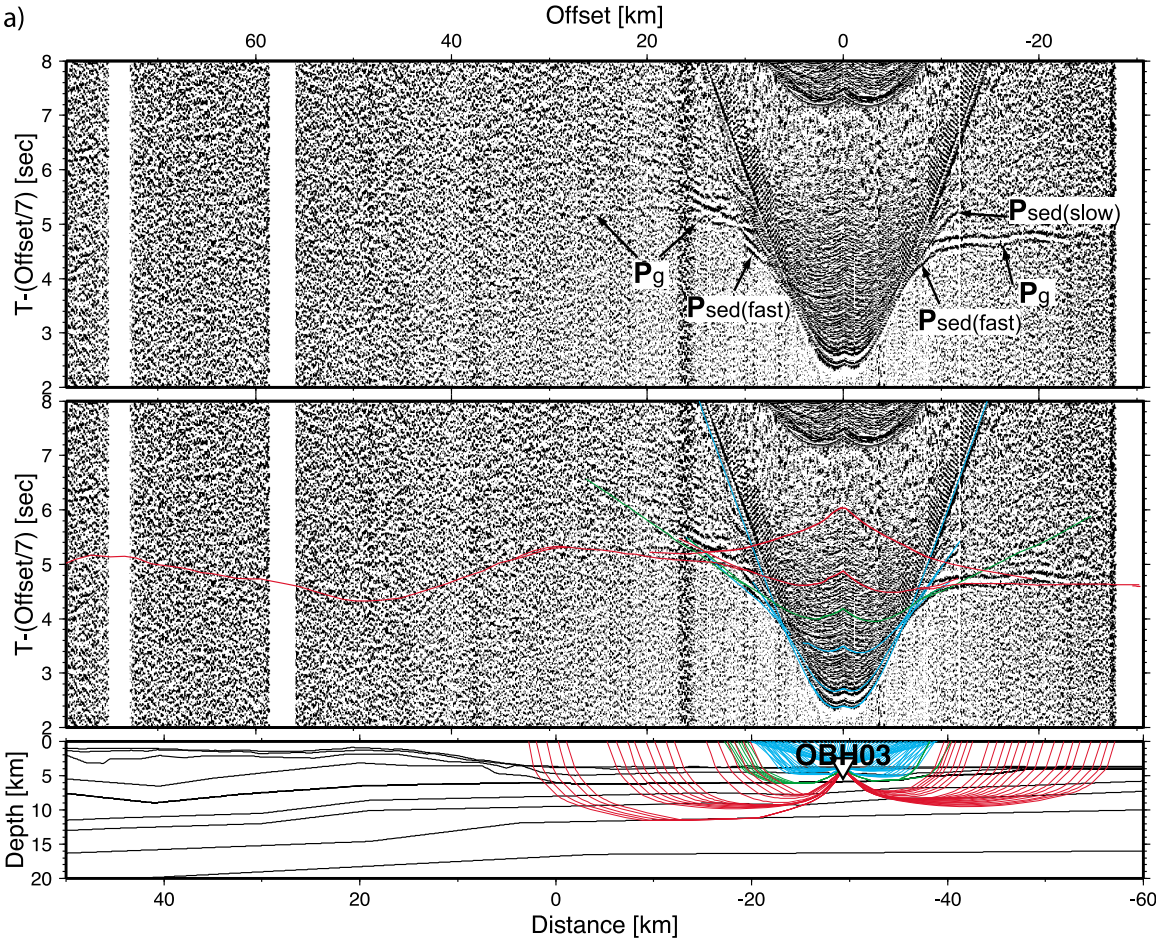


**Figure 2.** Data examples and predicted arrivals of every fifth OBS/H: (a) OBH03, (b) OBS07, (c) OBS12, (d) OBS15, (e) OBS21, and (f) OBH28. Locations of these example stations are marked in Figure 1. (top) Data with annotated seismic phases. (middle) All predicted P wave arrivals drawn on top of the seismic data, and (bottom) rays for picked arrivals only. Note the contrast in data quality and offset range between western stations on Raukumara Basin (model distance >100 km) and the eastern station on the East Cape Ridge and the Hikurangi Plateau. Annotated seismic phases are as follows: Psed(fast/slow), refraction through (fast/slow) sediments; Pg(u/l), refraction through (upper/lower) crust; Pn, refraction through mantle; Pmv, refraction through shallow high-velocity anomaly (interpreted as Matakaoa volcanics); PdP, reflection from decollement; PsP, reflection from sediments; PcP, reflection from midcrust; PmP, reflection from Moho.

crust (PcP) and Moho (PmP) (Figure 2f) identified in the coincident multichannel seismic reflection profile RAU07-05 (below). We were unable to detect deeper phases from the incoming Pacific plate, and neither could we pick reflections off the downgoing slab beneath Raukumara Basin as these arrivals were masked by the water column multiple (Figure 2f). In total 4400 arrivals were picked and modeled.

### 3.2. Seismic Velocity Model

[15] Figure 3 shows our preferred final model together with the seismicity of the northern Hikurangi margin. The shallow part below the water layer consists of three continuous sedimentary layers with seismic velocities between 1.6 and 3.6 km/s, covering both the Pacific and the Australian part. The thickness of these layers varies from around 2 km on the incoming plate to about 5 km at 25 km east of East Cape Ridge and also at 50 km west of East Cape Ridge, near the thickest part of Raukumara Basin. In the east and below the three sedimentary layers, the incoming Hikurangi Plateau also includes a 2 km thick layer with seismic velocities of 3.8–4.0 km/s which thickens under East Cape Ridge to form a 10 km thick and 20 km wide high velocity zone. As discussed below, this layer is not likely to represent a single geologic unit but allowed a simpler velocity model. The Hikurangi Plateau crust consists of three crustal layers of which the uppermost layer only marks a change in the velocity gradient of the shallow crust. The upper crust is about 4 km thick with seismic velocities from 4.9 to 6.7 km/s, and the uppermost lower crust has a velocity of about 7.1 km/s. Note that the Moho shown below the 10 km thick Hikurangi Plateau is based on the gravity modeling (below) and is not resolved by the seismic data.

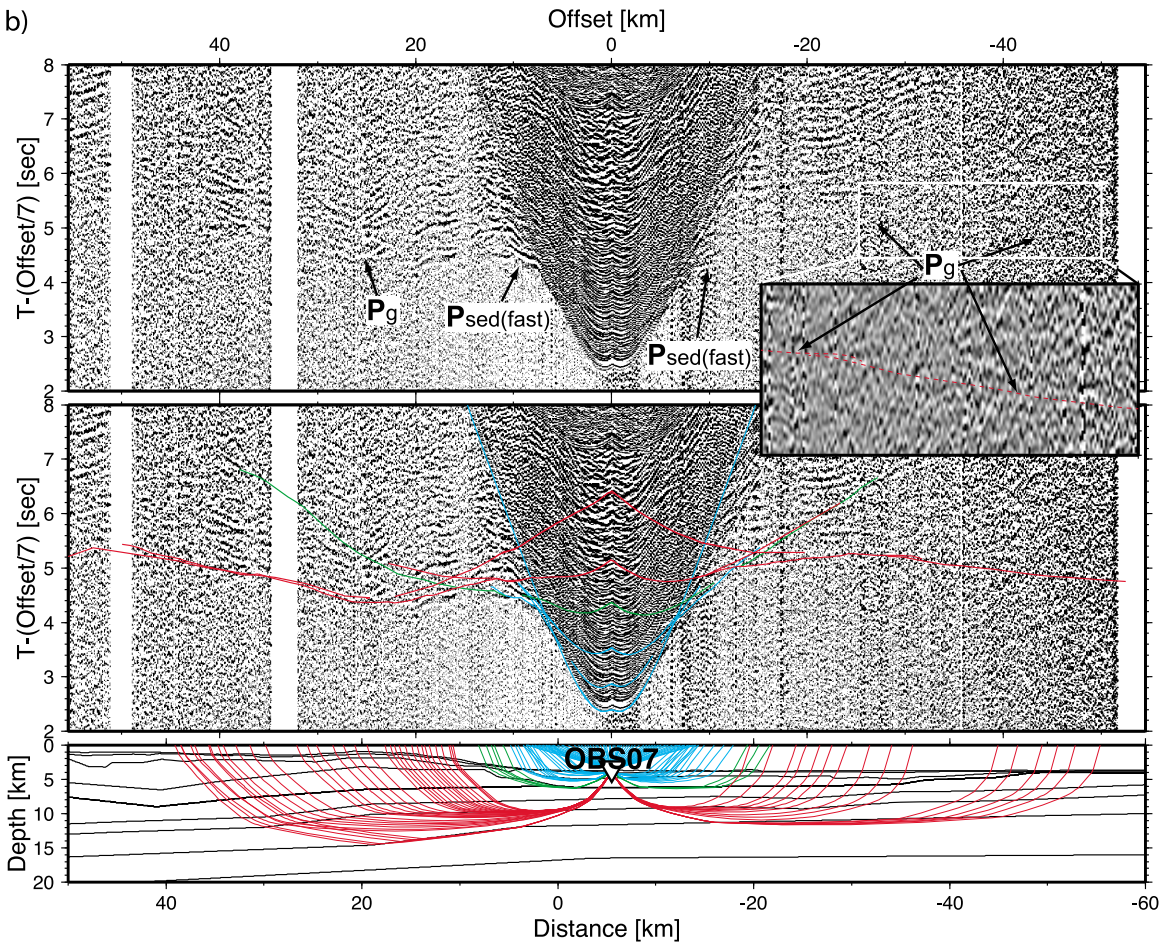


**Figure 2.** (continued)

[16] West of the trench, the fore arc has an additional sedimentary layer below the three shallow ones, with a maximum thickness of up to 5 km but thinning considerably below East Cape Ridge and also towards Kermadec Ridge to the west, with seismic velocities between 3.7 and 3.9 km/s. The Raukumara basin structures were modeled as five layers. The deepest layer has relatively fast seismic velocities of 4.6–4.9 km/s, is on average about 3 km thick, and manifests a maximum depth of 12 km for Raukumara Basin. The Australian arc crust was modeled as two crustal layers, with seismic velocities of 5.4–5.8 km/s and 6.5–6.8 km/s, respectively, forming an about 5 km thick crust below and east of the thickest part of Raukumara Basin, and thickening to approximately 10 km to the west. Finally, the uppermost Australian arc mantle has a seismic velocity of 8.0–8.1 km/s. Details of the model features are discussed below.

[17] The data examples in Figures 2a–2f also show predicted arrival times from our preferred final model. Figures 2a–2f (middle) show all predicted P waves plotted on top of the recorded data, whereas Figures 2a–2f (bottom) only shows rays that correspond only to the picked arrivals to indicate model coverage. The average RMS misfit of the predicted arrivals is 70 ms which, taking into account the relatively large data uncertainty from the reduced data quality, corresponds to a normalized chi-square value of just below 1.

[18] Model resolution and coverage are shown in Figure 4, using only the seismic wide-angle reflection and refraction data without taking into account available multichannel seismic (MCS) data (see below). Resolution values between 0.0 (small symbols) and 1.0 (large symbols) indicate how well each model parameter is resolved with respect to the relative number of rays. *Zelt and Smith* [1992] found that a node with a resolution value greater 0.5 is considered well resolved. Evaluating model resolution together with the ray paths, Figure 4 shows that the shallow structures of the Hikurangi Plateau are well resolved. In the central part, below East Cape Ridge, only few rays could be traced and used for determining the deeper structure, yet the shallow structures again appear well resolved. Raukumara Basin in the west is well resolved in its central part down to the arc mantle at 19 km depth, although its western part is increasingly less resolved by the wide-angle data. Note that the two layers defining the Australian crust have, for simplicity reasons, each a single upper velocity node at the western edge of the model. Therefore, the velocity resolution values of these two nodes, though outside the ray coverage, are relatively large due to the ray coverage from

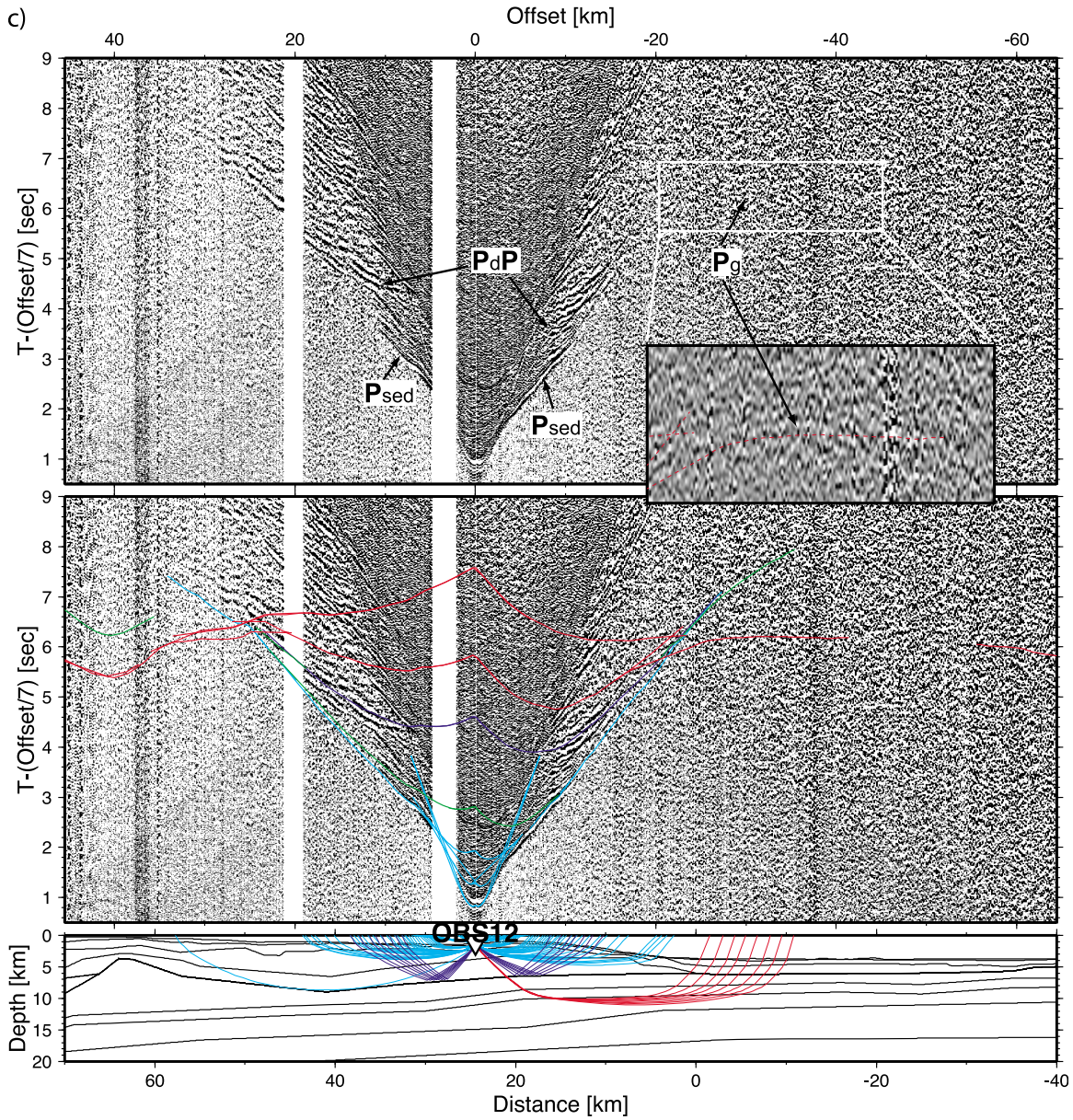


**Figure 2.** (continued)

the center of Raukumara Basin. The structures of the western Raukumara Basin are entirely based on the MCS data as shown below, and no modeling emphasis has been placed to this region outside the OBS/H station distribution. The MCS data are also the basis for modeling the shallow sedimentary structures and therefore the resolution of the high number of model nodes is not shown here. Similarly, the subducting slab is manifest as a bright reflector in the MCS data and was used to determine the slab dip below Raukumara Basin but is not visible in the wide-angle data.

[19] In order to estimate model uncertainties, we performed predominantly a trial and error sensitivity study of model parameters and examined the resulting RMS misfit. The best fit average RMS value of 70 ms, corresponding to a chi-square value of about 1, increased to levels of 100–150 ms (chi-square around 2–4) which were deemed too large, thus providing a range of suitable model parameters that still fit the data. In addition, we took into account the results provided by the RAU07 MCS data (below) and stacking velocity data determined by normal moveout velocity analysis (Figure S1).[1] Since the streamer length used in acquiring the MCS data was 7.3 km, these data provide independent constraint on the upper crustal velocity structure. The variability between travel time and depth, relative to the seabed, is shown in Figure S1, where the mean velocity depth curve (red) is compared to the velocity structure at model distance 150 km (superimposed in blue). Using these data the location of the westernmost OBH station (model km 126), the base of the upper two sedimentary

[1] Auxiliary materials are available in the HTML. doi:10.1029/2009JB006645.

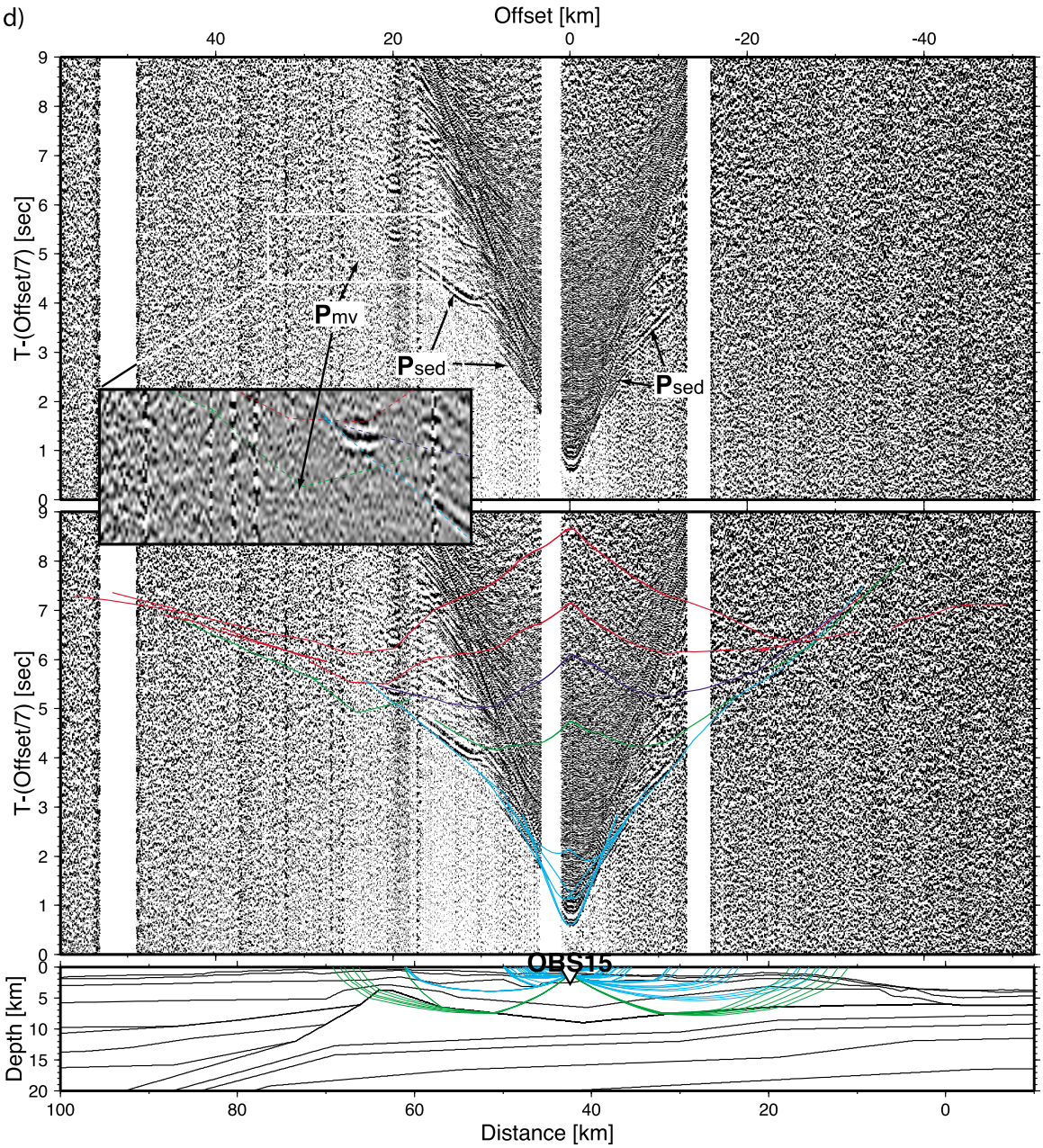


**Figure 2.** (continued)

layers (megasequence Z after *Sutherland et al.* [2009]) at 4.6 s two-way travel time (TWT) converts to 4.25 km depth, using stacking velocities, compared to 4.21 km depth in Figure 3. The interval velocity immediately above the reflector is 3.17 km/s and 3.04–3.20 km/s in the MCS and wide-angle results, respectively. Similarly, at the same location, the base of the sediments (megasequence Z, *Sutherland et al.* [2009]) at 8.4 sec TWT converts to 11.40 km (interval velocity above: 4.6 km/s) in the MCS data, compared to 11.80 km depth (velocity above: 4.6–4.9 km/s) in Figure 3. Another comparison comes from earthquake tomography immediately to the south of our working area [*Reyners et al.*, 1999], where mid- and lower crustal velocities between 5.0 and 7.5 km/s compare reasonably well with our estimates of 5.4 to 7.2 km/s. Note, however, that some parts of the model remain relatively poorly resolved, for example beneath East Cape Ridge the data penetration was reduced by scattering and attenuation. In areas without OBS/H coverage (model edges) or where ray coverage is limited the velocity model is not constrained. Given the above discussion, and considering model ray coverage and node resolution the following model uncertainties are estimated (larger estimates in brackets are for deeper or less resolved structures): Depth to sediments: ±80 (300) m; depth to crust: ±100 (500) m, depth to mantle:

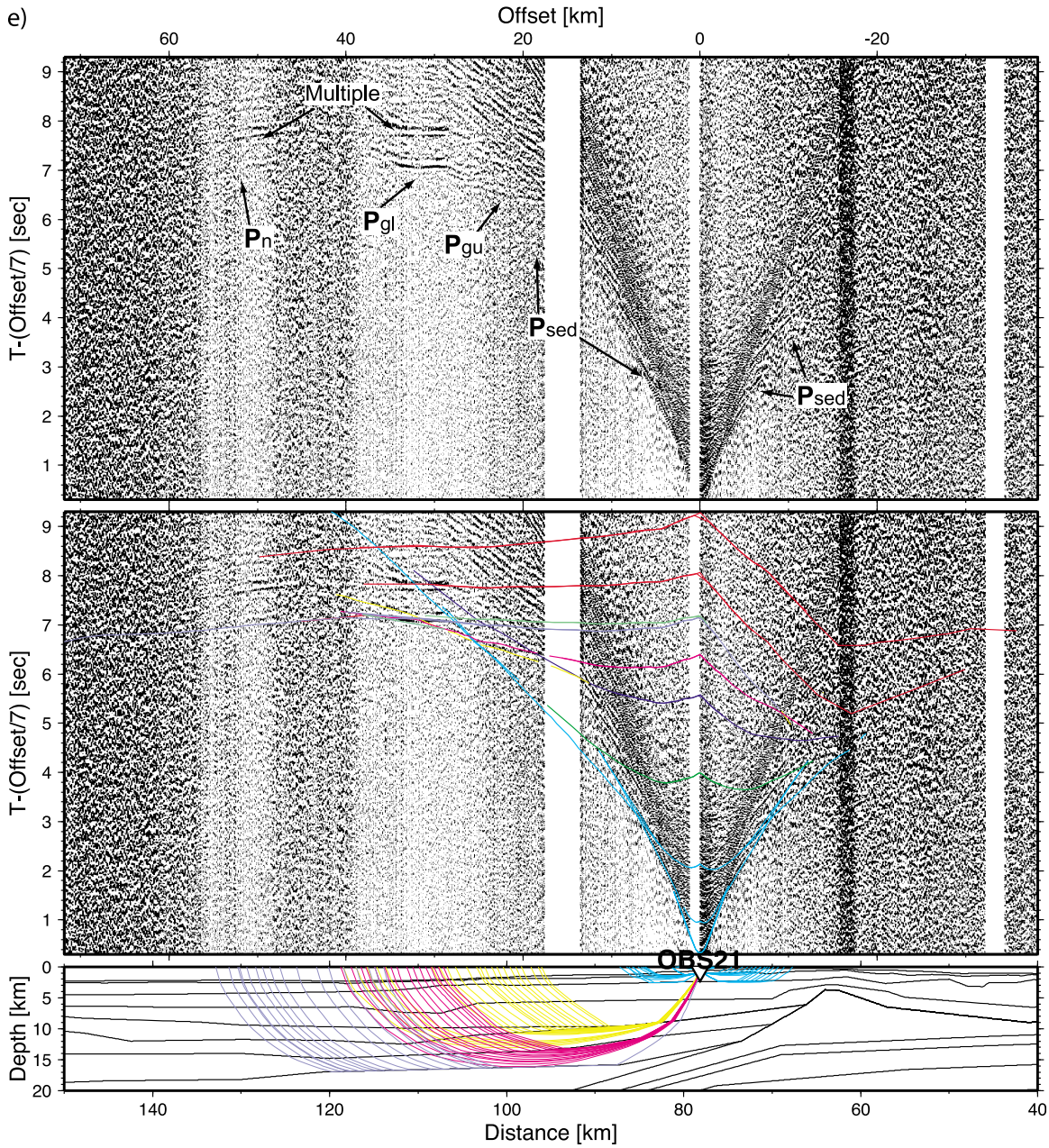


**Figure 2.** (continued)

±500 (1000) m; velocity of sediments: ±100 (300) m/s; velocity of crust 80 (400) m/s; velocity of mantle: ±150 m/s.

## 4. Coincident Seismic Reflection Profile

[20] The wide-angle reflection and refraction line MANGO-1 was colocated with the MCS line RAU07-05, which was recorded also in 2007 several months after the MANGO-1 deployment [*Sutherland et al.*, 2009]. Data for RAU07-05 were acquired using a 86.5 l (5280 cu in) source and 7.3 km streamer, with 50 m shotpoint spacing and 15.3 s record length. The data were processed in a conventional manner (including several filters and deconvolution) with an emphasis on multiple attenuation up to a prestack time migrated section (Fugro Seismic Imaging, Raukumara Basin 2-D seismic survey (RAU07), New Zealand, unpublished report, pp. 1–37, Ministry of Economic Development, Wellington, 2007, see also Table S1).

[21] Figure 5 shows an uninterpreted as well as an interpreted version of line RAU07-05. The interpreted version also shows the wide-angle model drawn as reflections in two-way travel time (TWT) on top. Following the interpretation of *Sutherland et al.* [2009], the reflection strata can be divided into three sedimentary megasequences, X, Y, and Z, (Figure 5) which were put into context by correlating them with the surrounding geology including what has been mapped onshore. Starting from the top, megasequence Z is the upper band of continuous or semicontinuous reflections

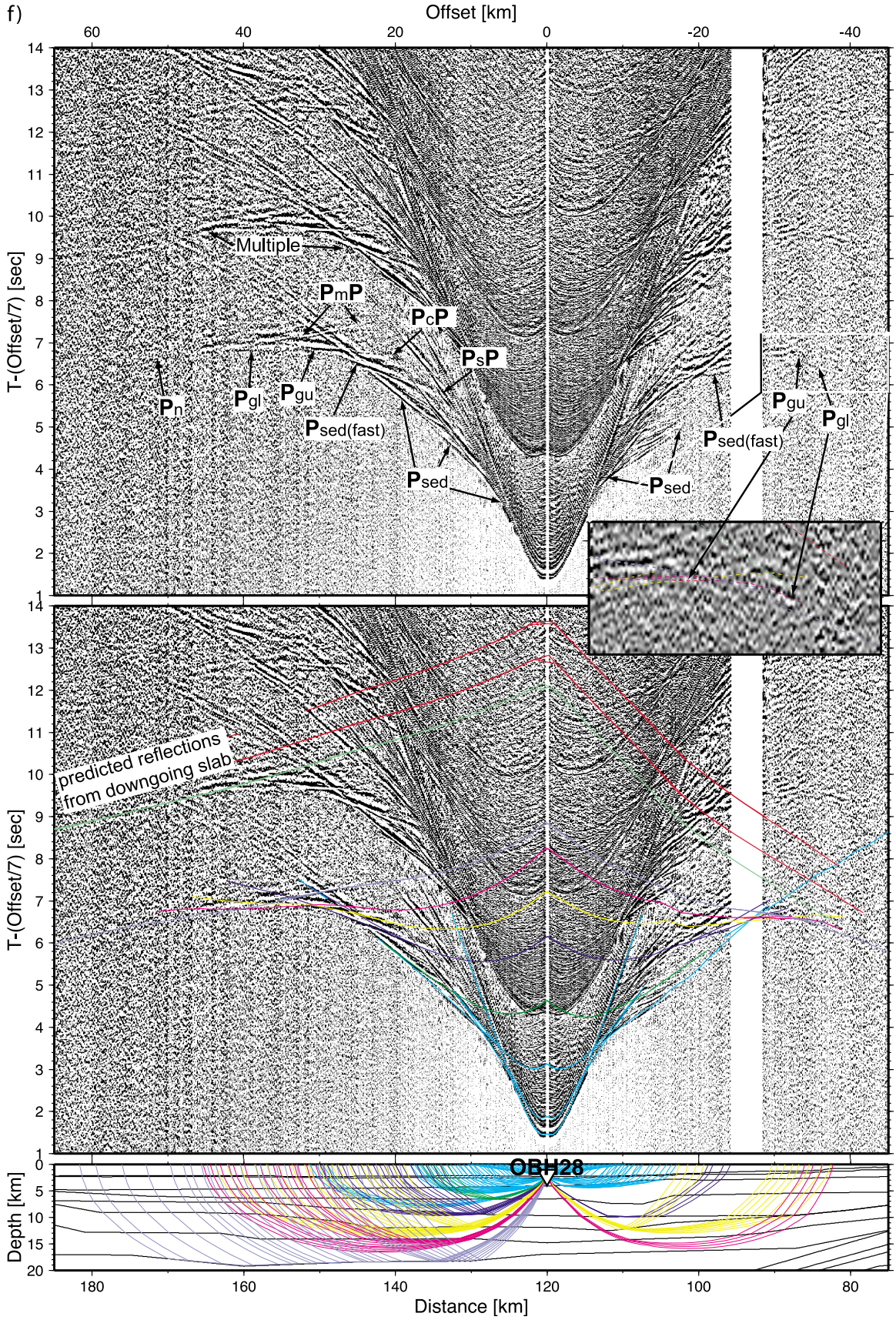


**Figure 2.** (continued)

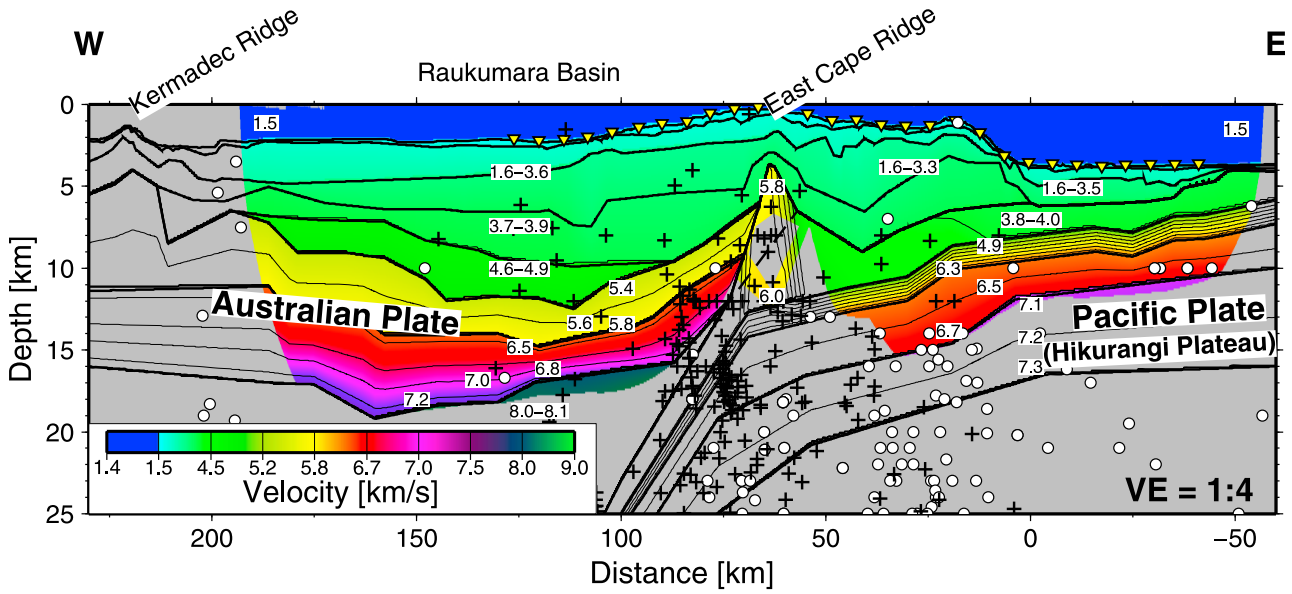


**Figure 3.** Final proposed velocity model derived from ray tracing of the seismic wide-angle data. Masked areas represent parts of the model without ray coverage, though seismic reflection data from line RAU07-05 as well as gravity data were used to place some constraints on this model as explained in the text. Also shown are earthquakes from the global database with magnitudes larger than 4 from within 50 km of either side of the model (circles) and from the Raukumara Peninsula network from *Reyners et al.* [1999] from up to 100 km to the south of our profile (crosses). Note the increased concentration of hypocenters around the location where the incoming plate bends most below the fore arc.

comprising recent slumps and slides including the Matakaoa Submarine Instability Complex across the Raukumara Plain [*Lamarche et al.*, 2008] as well as the downslope collapse structures east of East Cape Ridge [*Sutherland et al.*, 2009]. The bottom of megasequence Z is marked in our model as the bottom of the second sedimentary layer, reaching down to 4.5 km depth (2.5 km below seafloor) around model km 185, the depocenter of the more recent arc volcanic input. The base consists of mostly continuous reflectors [*Sutherland et al.*, 2009].

[22] Megasequence Y is a thin unit (0–1.6 km thick) of chaotic and variably dipping reflections extending between East Cape Ridge and the center of Raukumara Basin where it pinches out [*Sutherland et al.*, 2009]. Due to its small size, however, we did not include a small additional layer in our model (Figure 3) but combined this unit with our sedimentary layer 3. Megasequence Y is interpreted to represent a single large Cenozoic allochthonous slope failure originating from East Cape Ridge [*Sutherland et al.*, 2009].

[23] The underlying megasequence X is another band of continuous or semicontinuous reflections below megasequence Y and is up to 8 km thick in the deepest part of Raukumara Basin [*Sutherland et al.*, 2009]. The sedimentary strata are interpreted to correlate with Cretaceous onshore deposits and appear to be remarkably little deformed considering its age and the tectonic history of the region [*Sutherland et al.*, 2009].

[24] Below the sedimentary megasequences there appear clear reflections from the top of the Australian crust and the Moho, indicating the thinning of the crust around model km 110. The high amplitude sub-Moho reflection at 15 s TWT around model km 130 is interpreted and modeled as the top of the downgoing slab (Figure 5).

[25] In contrast to the relatively deep reflectivity within and beneath the Raukumara fore-arc basin, the MCS profile reveals a relatively unreflective outer fore-arc high (East Cape Ridge), indicating intensive fore-arc deformation potentially destroying coherent reflectivity here. The interpreted decollement reflection that appears on the seismic wide-angle data (PdP on Figure 2c) would be predicted on the MCS data around model km 25 at about 5.5 s TWT but does not appear as a high amplitude reflection here. Furthermore, the incoming Hikurangi Plateau appears also relatively unreflective, probably due to its rough, seismically scattering crust or its weakly reflective internal composition. Further discussion is given below.

## 5. Gravity and Magnetic Data and Modeling

[26] Potential field data from ship measurements along our profile were used to verify and improve the seismically derived structural model as well as to constrain seismically unresolved sections of the model. In particular, gravity data helped to estimate the thickness of the incoming Hikurangi Plateau, where no deep mantle phases could be identified in the seismic data. The magnetic anomalies yielded information on the occurrence of volcanic rock type and origin.

[27] For an overview, Figure 6 shows a 3-D view of gravity and magnetic anomalies draped over the bathymetry. The 3-D gravity anomalies stem from satellite data [*Sandwell and Smith*, 1997]. The magnetic grid is a compilation of aeromagnetic data [*Malahoff et al.*, 1982] and all available

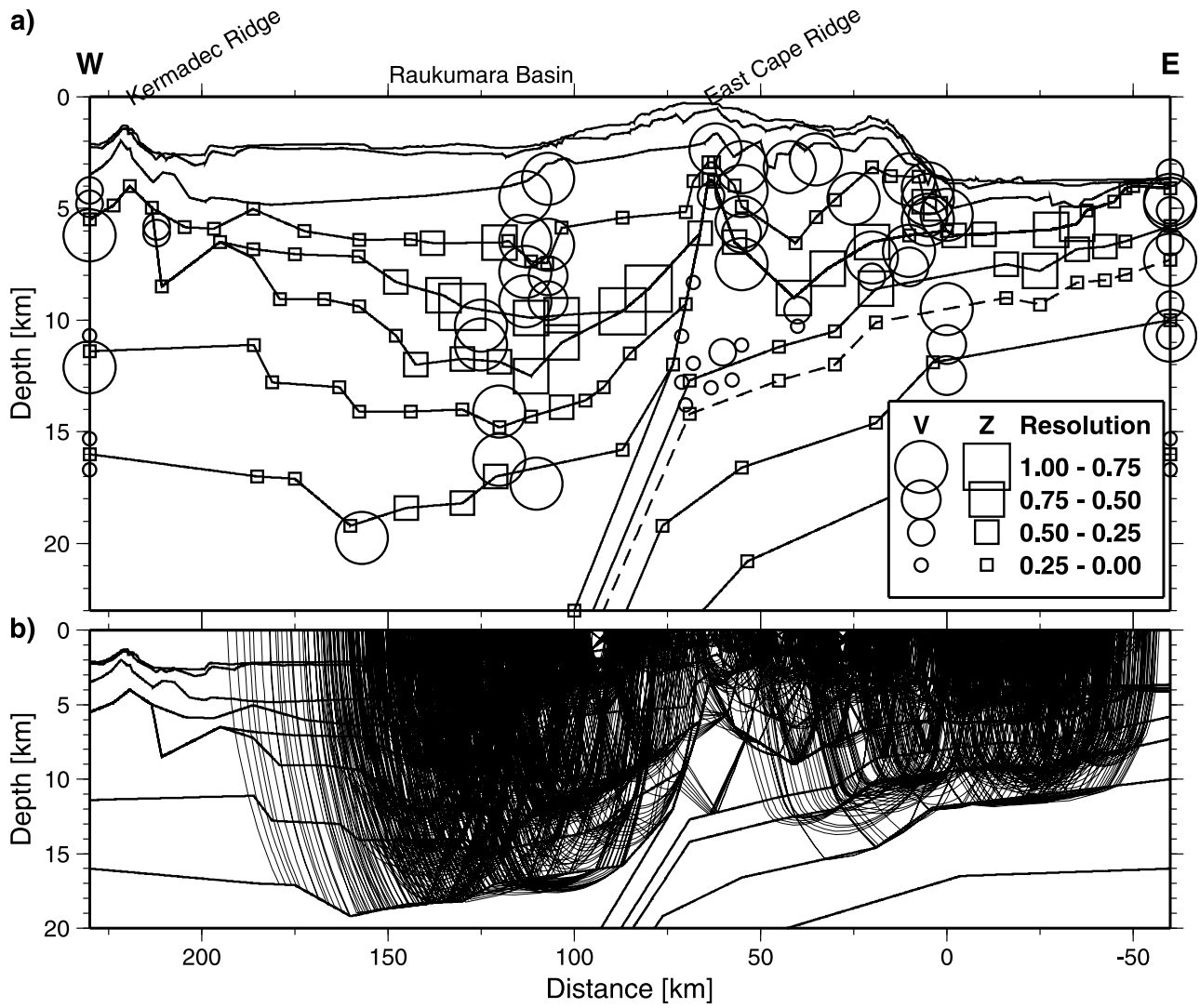


**Figure 4.** (a) Model resolution, with depth nodes (squares) and velocity nodes (circles) drawn to scale indicating node resolution; values larger than 0.5 are considered well resolved. (b) Model coverage, demonstrating the shallow coverage of the incoming Hikurangi Plateau and comparably good coverage of the Raukumara Basin structures. The gap in the center is due to relatively weak seismic signals recorded to relatively narrow offsets, probably caused by high seismic attenuation within the margin wedge of the fore arc.

ship data from the region, including newly collected data from the seismic cruises in 2007, leveled to a common surface.

[28] The most notable feature in the gravity data is the −140 mgal gravity low at the southern part of Raukumara Basin. This gravity low is associated with both the deep basin as well as the southward thickening of the Australian Plate during its transition from island arc to continental character.

[29] The magnetic field exhibits distinct positive (>150 nT) anomalies extending from the Matakaoa volcanic anomaly onshore northeastward along East Cape Ridge (Figure 6). This corroborates the suggestion by *Davey et al.* [1997] that the magnetic anomalies along East Cape Ridge are associated with the same allochthonous material as observed onshore.

[30] Gravity and magnetic data were also acquired along with the seismic reflection data of line RAU07-05. Along MANGO-1 the observed potential field data (Figure 7) were modeled using Encom's ModelVision™ software and a 2.5D geometry for each layer. The lateral extent in and out of the model plane of the deeper parts of Raukumara Basin was limited to ±50 km in accordance with the seismic reflection data [*Sutherland et al.*, 2009]. In constructing our gravity and magnetic models we used the velocity structure from wide-angle seismic data (Figure 3), all available data from samples of equivalent rocks exposed onshore, and previous interpretations of potential field data along the Hikurangi margin [*Gillies*, 1984; *Davy and Wood*, 1994; *Davey et al.*, 1997; *Davy et al.*, 2008; *Sutherland et al.*, 2009]. Oceanic crust of the Hikurangi Plateau is assumed to consist of a basaltic upper crust (2.85 g/cm$^3$, magnetic

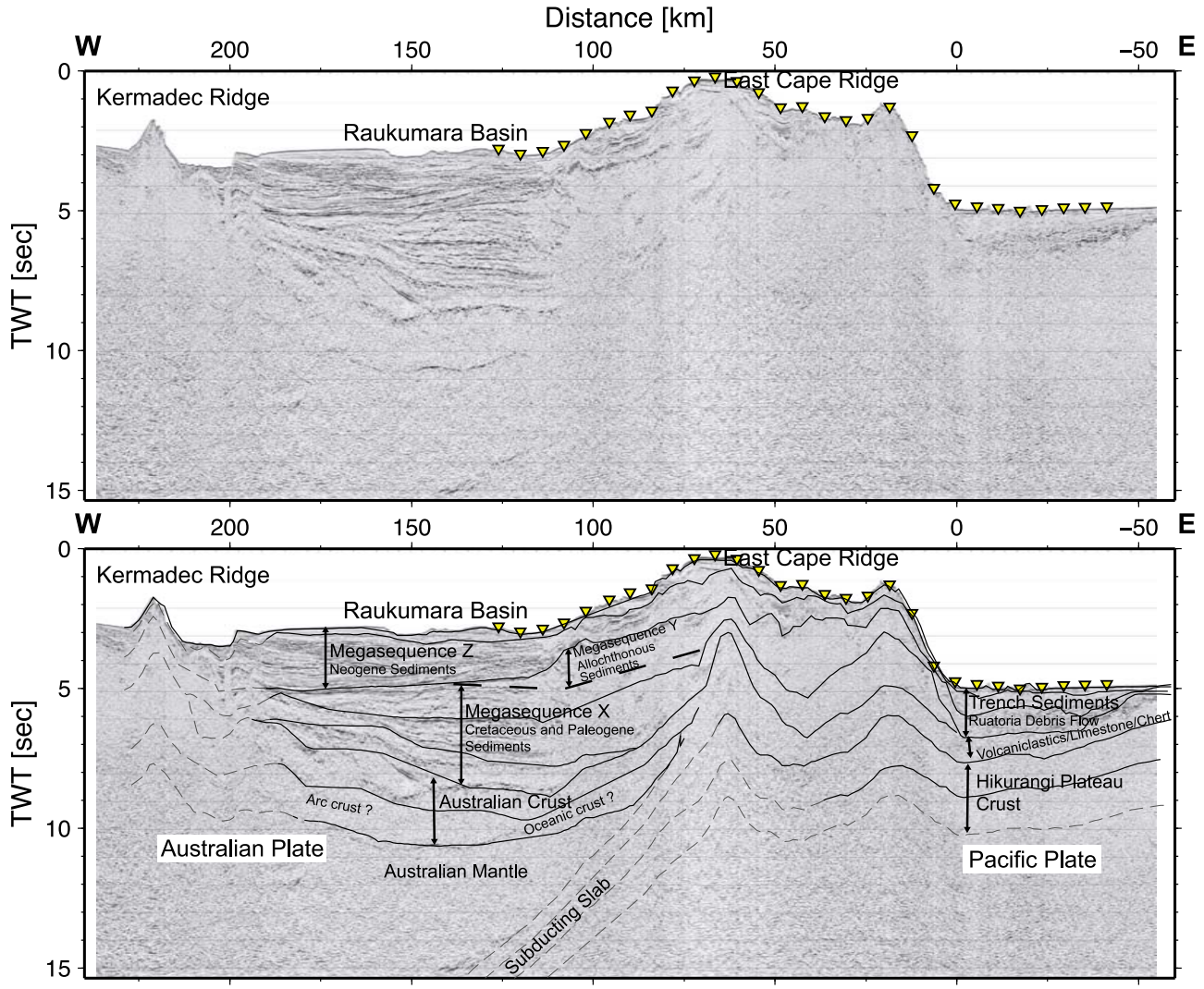


**Figure 5.** Seismic reflection data from line RAU07-05 in migrated form. (top) Without and (bottom) with velocity model structures (converted to two-way travel time (TWT)) and also the interpretation by *Sutherland et al.* [2009] overlain. Dashed reflectors are not resolved by the seismic wide-angle data. Triangles on seafloor mark OBS/H stations. West of the stations, the velocity model does not predict the reflections well, as no modeling emphasis was placed outside the region of wide-angle data coverage (Figure 4).

susceptibility 0.02) underlain by denser gabbro and metagabbro (3.15 g/cm$^3$, magnetic susceptibility 0.05) and a mantle density of 3.4 g/cm$^3$. Below the base of the reference lithosphere (at 70 km depth) a density anomaly was inserted to model the subducting plate lithosphere sinking into the asthenosphere. The lower crust of the North Island is assumed to be comprised of metamorphosed greywacke rocks (2.75 g/cm$^3$) overlying denser amphibolite and granulite (3.05 g/cm$^3$, magnetic susceptibility 0.05). The oldest sediments in the Raukumara Basin are assumed to have a density of 2.6 g/cm$^3$ and the younger basin fill has densities of between 2.2 and 2.3 g/cm$^3$. Compared with *Sutherland et al.* [2009] the model density values in Figure 7 are about 5–10% denser in the lower parts (except for the mantle) but up to 5% lighter in the shallower parts of the model. The latter discrepancy can readily be explained by the simplicity of *Sutherland et al.*'s [2009] density model which aimed at providing a consistency between the general structural interpretation and the observed densities without taking into account the accuracy of our new seismically derived crustal velocity model. While, the velocity model provides some constraints on the gravity model, alternative thicknesses of the upper and lower crust and Hikurangi Plateau are possible. For example, allowing up to 10% variations in crustal densities results in a total crustal thickness uncertainty of ±5 km. The uncertainty in the thickness of the Hikurangi Plateau from gravity models is estimated to be ±4 km [*Davy and Wood*, 1994].

[31] The magnetic anomalies proved more difficult to be modeled in 2-D and we expect much of the existing misfit to be due to 3-D effects. Our main aim here was to determine the cause of the two major positive anomalies; one at the western edge of the model, coincident with the Whakatane volcano, and the second being the East Cape Ridge anomaly

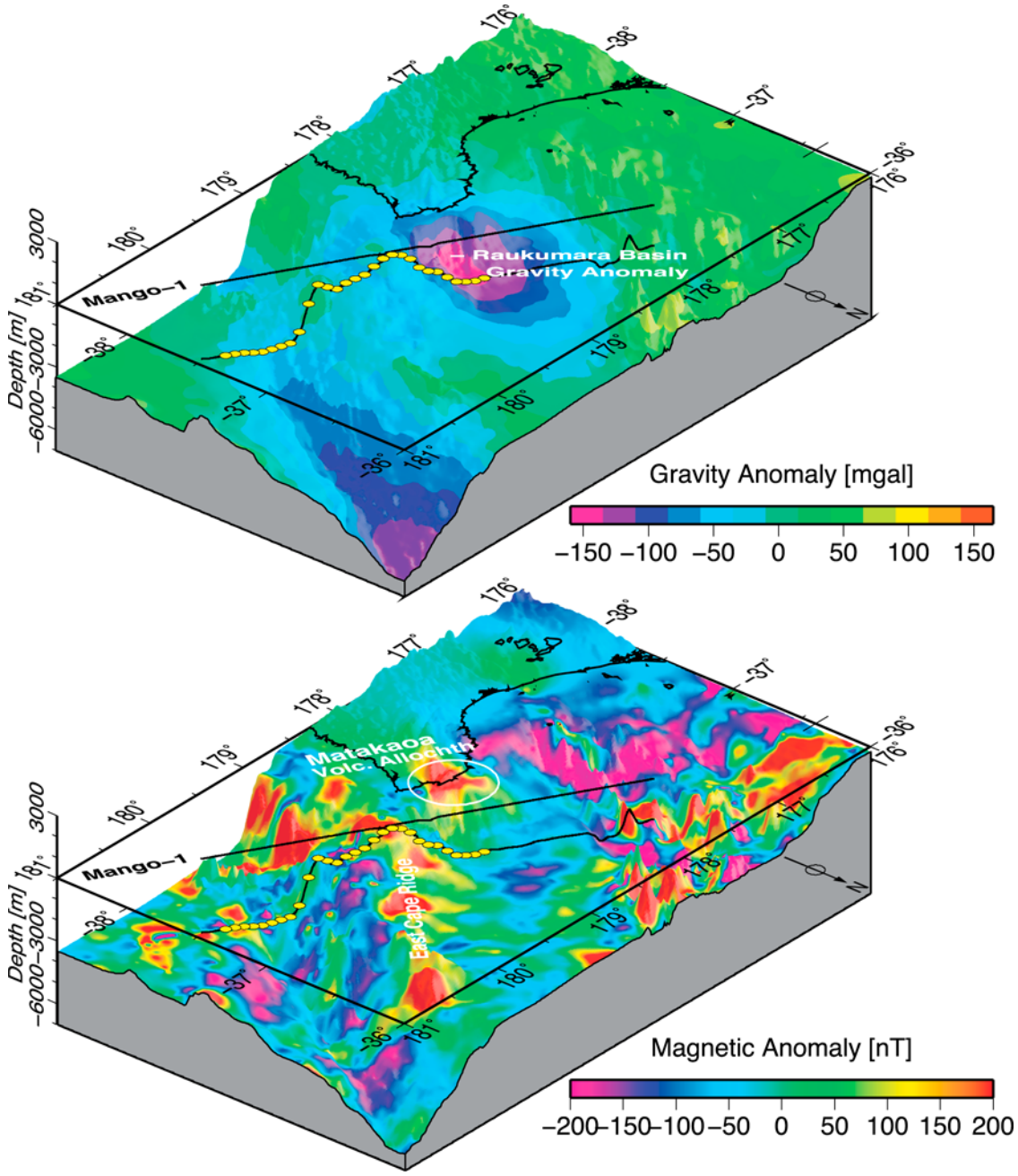


**Figure 6.** Gravity and magnetic data around the northern Hikurangi margin, viewed from northeast. (top) Gravity data reveal a prominent –140 mgal anomaly associated with Raukumara Basin. (bottom) East Cape Ridge exhibits several large magnetic positive anomalies that can be traced towards land to link up with the Matakaoa volcanics.

at model km 65. Both can be modeled by highly magnetized uppermost crust. The highest magnetic susceptibilities used were 0.085 to 0.1 and convert to magnetizations of 3.3 to 3.9 A/m. These values are larger than the largest magnetizations of up to 3.3 A/m used by *Davey et al.* [1997] but within the range of magnetizations (1.0 to 4.5 A/m) used by *Gillies* [1984], who had a more localized distribution of magnetic sources. By assigning low magnetizations to the remaining layers (magnetic susceptibility <0.05, magnetization <2.0 A/m), magnetic anomalies of similar magnitudes and wavelengths as the observed anomalies are produced. A detailed distribution of magnetic sources [*Gillies*, 1984; *Davey et al.*, 1997] to more accurately fit the observed data goes beyond the purpose of our interpretation as discussed below.

[32] A second magnetic model was produced using 2-D Euler deconvolution which uses the gradients of the magnetic anomalies to invert for source depths and location [*Durrheim and Cooper*, 1998; *Cooper*, 2002, 2004]. Figure 8 shows the most likely distribution of magnetic sources along the model. The result matches the East Cape Ridge anomaly relatively well and corresponds to the high magnetic sus-

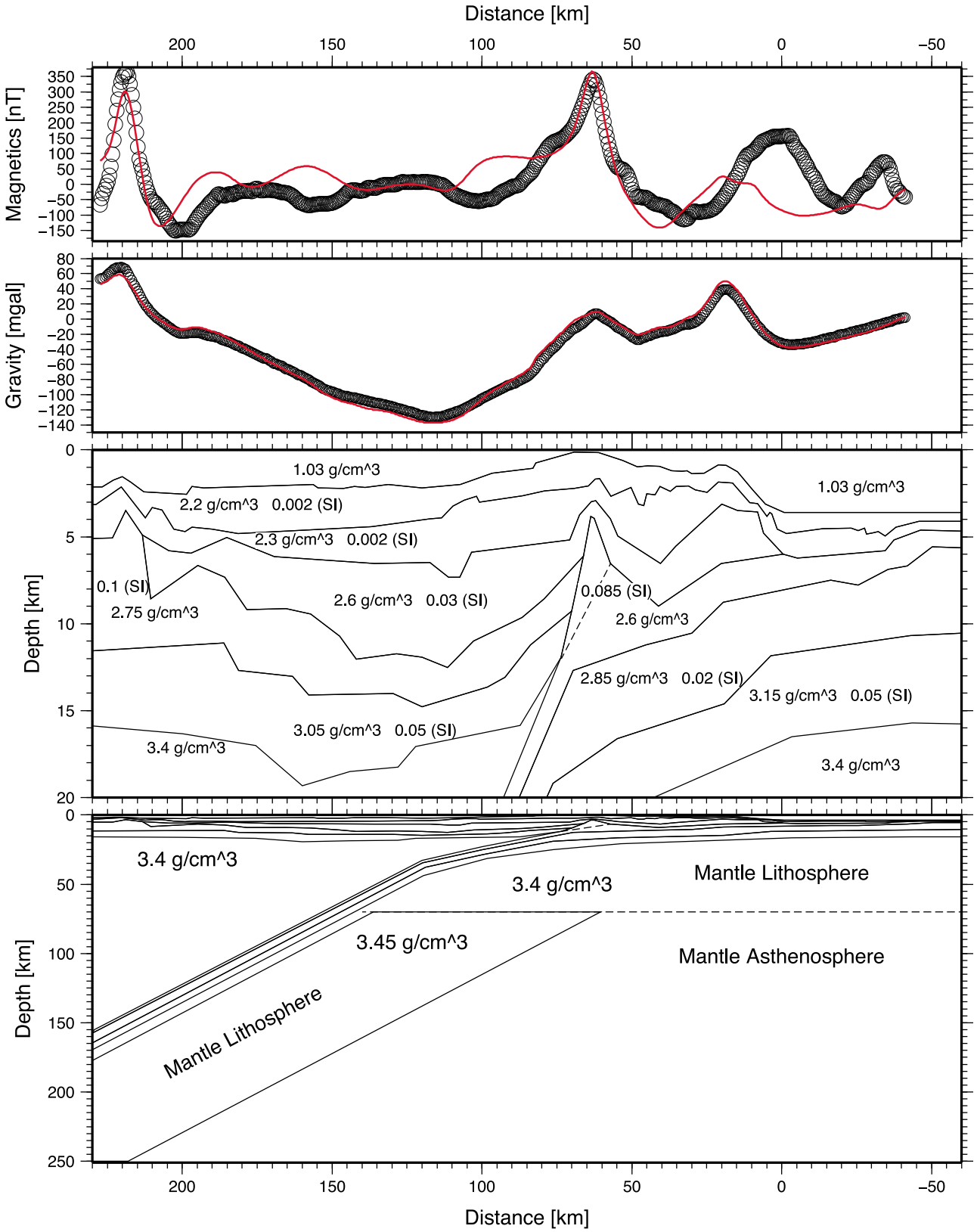


**Figure 7.** Gravity and magnetic model from 2.5-D modeling. Model layers extend practically indefinitely in all directions except the deep sedimentary layer in Raukumara Basin which was limited to 50 km in and out of the model plain. Densities are given for all layers, magnetic susceptibility (dimensionless number behind density) is given only for magnetized layers.

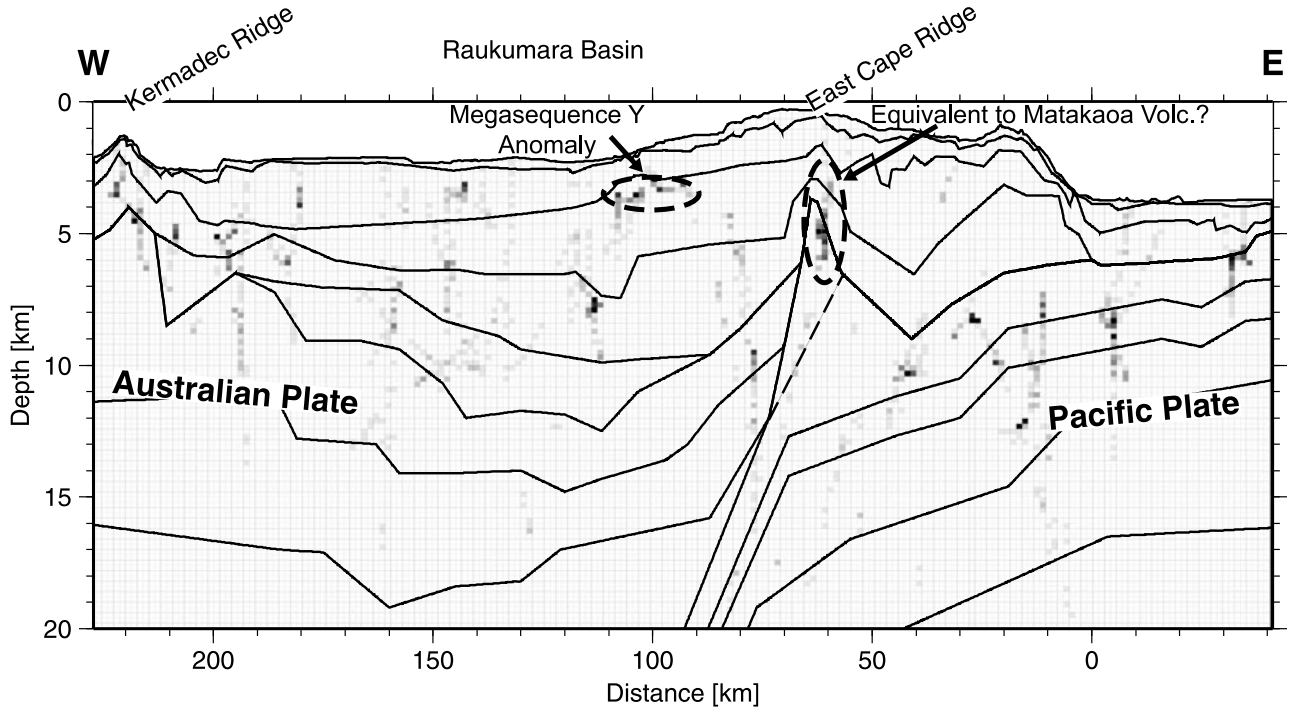


**Figure 8.** Magnetic Euler deconvolution, indicating regions for likely magnetic sources. Black marks most likely, gray marks likely, and white marks unlikely locations for magnetic sources. Note the reasonably good correlation of the East Cape Ridge anomaly of the seismic velocity structure (drawn on top). Also remarkable are the shallow anomalies at the eastern edge of Raukumara Basin, which are associated with the large slump called megasequence Y [*Sutherland et al.*, 2009], originating from the East Cape Ridge anomaly.

ceptibility body (0.085, magnetization 3.3 A/m) identified in Figure 7. But, Euler deconvolution fails to focus magnetic sources at the western model edge (Whakatane volcano) where the deconvolution window cannot capture the full wavelength of the associated magnetic anomaly. Another interesting area of magnetic sources occurs around model km 100, at about 3.5 km depth. The source coincides with the thinned frontal edge of part of the offshore allochthon (megasequence Y) as interpreted by *Sutherland et al.* [2009]. The implications are discussed below.

## 6. Discussion

### 6.1. Structure and Sediment Cover of the Subducting Hikurangi Plateau

[33] When plateaus enter subduction zones, their role in the subduction processes is manifold. Plateaus such as the Hikurangi Plateau carry a significant amount of water into the subduction zone, potentially leading to voluminous arc volcanism [*de Ronde et al.*, 2007]. Furthermore, plateau crust is usually more buoyant than normal oceanic crust and may therefore cause either subduction erosion [*von Huene and Scholl*, 1991] or enhanced uplift of the fore arc [*Collot and Davy*, 1998; *Kopp et al.*, 2006]. If its thickness is too buoyant for subduction it may halt volcanism [*McGeary et al.*, 1985] or actually stall subduction entirely [*Cloos*, 1993; *Mann and Taira*, 2004; *Davy et al.*, 2008]. Our results place some new constraints on the geometry of the subducting Hikurangi Plateau.

[34] The northern Hikurangi Plateau is modeled as a 10 (±1) km thick crust (Vp > 4.9 km/s) that is overlain by up to 4 km of seismically slow (<4.0 km/s) material (Figure 3). We interpret the topmost 2.2 (±0.1) km of sediments with seismic velocities increasing from 1.6 to 3.5 km/s to consist of predominantly coarse debris sourced by the collapsing frontal slope (e.g., Ruatoria Slide, Figure 1). Below that lies a 2 (±0.2) km thick layer with seismic velocities of 3.8–4.0 km/s which, following the recent description of the Hikurangi Plateau by *Davy et al.* [2008], is a mixed layer of volcaniclastics, limestone, and chert (Figures 5 and 9). This interpretation is based on the seismic velocities (too slow for basaltic or gabbroic crust) which are near the faster limit of volcaniclastics, dredged from adjacent to the survey area [*Hoernle et al.*, 2004], and limestone and chert as sampled by drill cores from similar oceanic plateaus in the southwest Pacific [*Davy et al.*, 2008].

[35] Where the plateau enters the fore-arc, high-amplitude reflections are observed on OBS 12 around 4.5 s (see ray diagram in Figure 2c), and these also appear on the two surrounding OBS. High amplitude reflections above the downgoing plate typically stem from the decollement with elevated pore fluid pressures in the subduction channel below [*von Huene et al.*, 2004]. Our model predicts a suitable reflection (Figure 2c) off a simple continuation of the mixed layer of volcaniclastics, limestone, and chert that produced clear first arrival refractions on the seismic record from the Hikurangi Plateau (Figures 2a and 2b). However, we cannot exclude the possibility that some of the overlying

sediments are carried within this subduction channel. In any case, if our interpretation of these high amplitude reflections is correct, we can infer that at about 20–40 km from the deformation front a subduction thrust occurs at about 7–8 km depth, below a 5–7 km thick hanging wall (Figure 9).

[36] The underlying plateau crust is divided into two layers. The upper 4–5 km thick layer displays seismic velocities of 4.9–6.7 km/s, around the typical average of 5.5 km/s for flood basalts normal for the upper plateau crust [*Coffin and Eldholm*, 1994]. The lower crust could only be detected by a few refractions of a velocity >7.1 km/s, again typical for lower plateau crust that presumably consists of gabrroic to ultramafic material [*Coffin and Eldholm*, 1994]. As no refractions could be detected from the bottom of the plateau, its thickness could only be estimated using gravity data. In our model, the depth of the Moho increases from 16 km in the east to 22 km below East Cape Ridge, yielding a plateau thickness of roughly 10 km. This value appears to be a relatively thin compared internationally to other Large Igneous Provinces (LIPs) with typical thicknesses of 20–40 km [*Coffin and Eldholm*, 1994]. Even compared to previous Hikurangi Plateau estimates of up 23 km thickness for the southern area [*Davy et al.*, 2008] it seems relatively thin, but is in good agreement with other estimates from the central and northern part of this plateau [*Henrys et al.*, 2006; *Davy and Wood*, 1994], and is sufficiently thin to subduct [*Cloos*, 1993].

[37] Subduction of the Hikurangi Plateau occurs at a relatively shallow dip angle of a few degrees up to East Cape Ridge and then appears to steepen downdip. Reflections off the slab as recorded on MCS line RAU07-05 (Figure 5) suggest that the slab dips at around 20° below Raukumara Basin, about 120 km from the deformation front, and deep seismicity indicates an angle of almost 50° further downdip toward the arc.

[38] No direct evidence has been found for the downdip extent of the Hikurangi Plateau, below which the Pacific Plate subducts as normal oceanic crust. Our gravity model (Figure 7) requires less negative density anomalies below the well-imaged Raukumara Basin; as a result we reduced the thickness of the downgoing Pacific plate in this region. This complies with previous notions from tomographic results from Raukumara Peninsula [*Reyners et al.*, 2006] or geometrical considerations regarding the possible common history of the Hikurangi and the Manihiki and Ontong-Java Plateaus [*Davy et al.*, 2008].

### 6.2. Arc and Fore-Arc Raukumara Basin

[39] The basin stratigraphy of line RAU07-05 has been described briefly above and in length by *Sutherland et al.* [2009] and is shown in Figures 5 and 9. We generally note a good correlation between what has been interpreted as Cretaceous sedimentary units and relatively fast (3.7–4.9 km/s) seismic velocities at depths between 6.0 km and 12.5 km. With an assigned density optimum of 2.6 g/cm$^3$ these basal sediments are considered to be highly consolidated and weakly metamorphosed. Whakatane volcano of the active Kermadec arc is resolved and detected by the seismic reflection line RAU07-05 and the potential field data (but not the seismic wide-angle data) at model km 220 (Figures 1, 3, 5, and 7–9), at the western margin of Raukumara Basin.

[40] With a sedimentary infill of more than 10 km, Raukumara Basin is one of the deepest known fore-arc basins at an active margin. A comparable fore-arc basin is found at the Middle American subduction zone, Sandino Basin offshore Nicaragua with an infill of up to 16 km [*Ranero et al.*, 2000; *McIntosh et al.*, 2007]. For Sandino Basin it has been suggested that it was created when a new subduction zone developed seaward of the previous (Jurassic/Cretaceous) subduction zone [*Walther et al.*, 2000]. This is strikingly similar to the interpretation in our study area [*Sutherland et al.*, 2009], and perhaps the only mechanism that allows for the development of such superdeep fore-arc basins.

[41] A correlation exists between the thickest and deepest part of Raukumara Basin and the thinnest part of the underlying crust. Below Raukumara Basin, the crustal thickness varies between up to 10 km in the west and as thin as 5 km toward the central and eastern part of the basin (Figure 3). Isostacy would have caused a natural depression at the thinnest part of the crust where sedimentation commenced at the Gondwana margin. With the eastern margin of the basin tilted upwards at East Cape Ridge, it is unclear what the eastern basin geometry was like before the onset of Neogene distortion.

[42] We speculate that the initiation of subduction in this location at 25–22 Ma was near the thinnest part of the crust, based upon the correlation between the thickness of the upper plate and the location of the plate edge near East Cape Ridge (Figures 3 and 9).

[43] Below the fore-arc crust, we measured an upper mantle Vp of 8.05 ± 0.15 km which is typical for normal, unaltered mantle without serperntinization induced by hydration [*Carlson and Miller*, 2003]. *Bostock et al.* [2002] speculate that all mantle wedges would be serpentinized, and this would inhibit subduction zone thrust earthquakes to rupture below the Moho interception [*Tichelaar and Ruff*, 1993]. Our measurements, however, imply a nonserpentinized mantle wedge at the Moho interception, and so the northern Hikurangi margin may have a different megathrust earthquake potential than otherwise assumed.

### 6.3. East Cape Ridge Volcanics

[44] We detected relatively high seismic velocities (about 5.8 km/s) at 3.5 km depth below the seafloor at East Cape Ridge (Figure 3). We also model a source region for the observed magnetic anomaly that approximately coincides with this seismic anomaly (Figures 7 and 8). We interpret the high-velocity magnetic material to be volcanic and consider possibilities that the source material is: a seamount that was subducted and accreted; or part of allochthonous unit Y within the basin [*Sutherland et al.*, 2009] and a correlative to the Matakaoa Volcanic unit mapped onshore [*Mazengarb and Speden*, 2000]; or that it represents basement to Raukumara Basin that has been uplifted.

[45] Fore-arc accretion of seamounts from the Hikurangi Plateau may be likely in this region [*Davey et al.*, 1997; *Henrys et al.*, 2006; *Pecher et al.*, 2005] because the subducting Hikurangi Plateau has numerous seamounts visible in the bathymetry (Figure 1) [*Wood and Davy*, 1994]. It has been speculated that in the vicinity of our study area subducted seamounts are required to explain localized uplift, erosion and basin evolution [*Collot et al.*, 2001; *Lewis et al.*, 2004]. Consideration of the model location and dimension

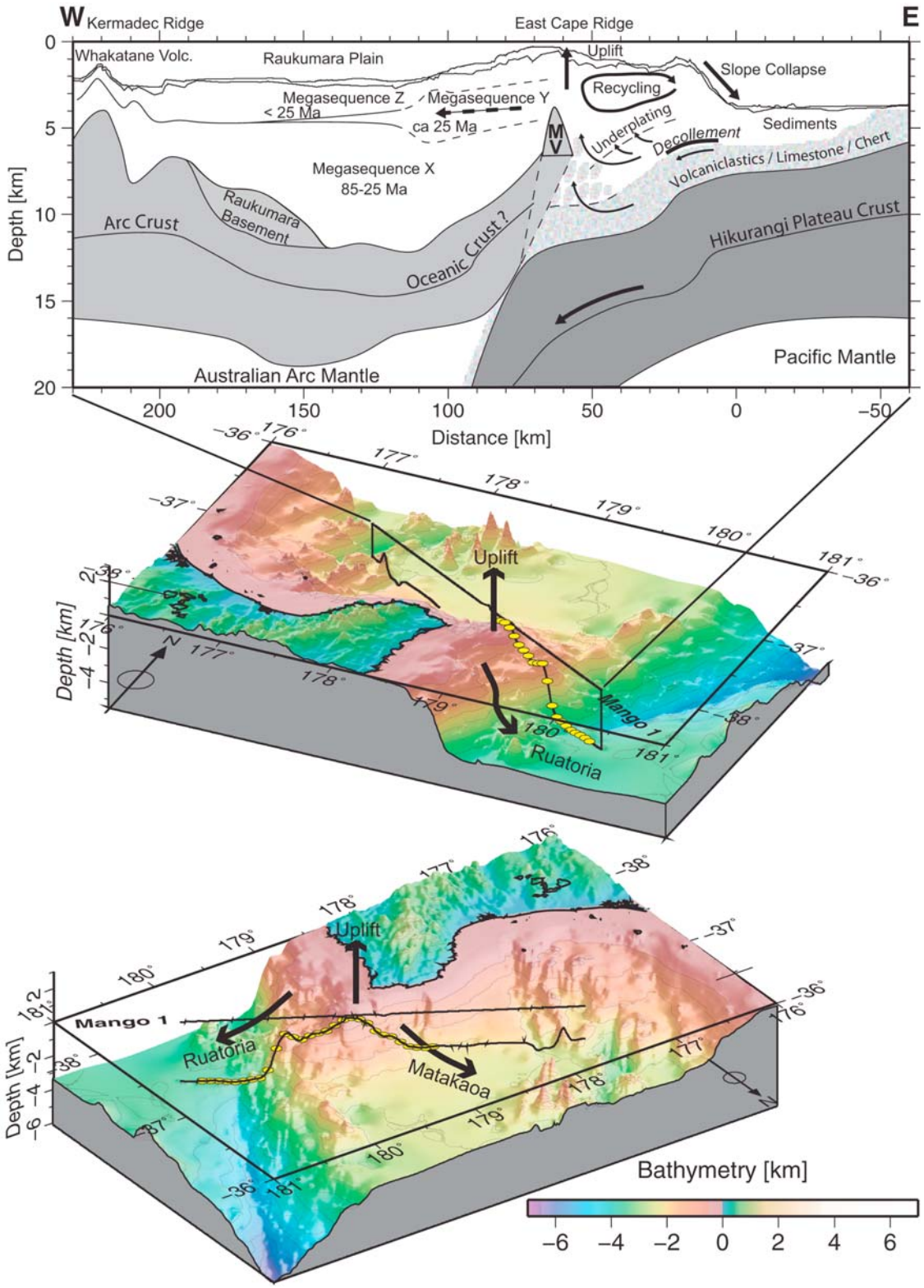


**Figure 9.** (top) Summary of structural interpretation, with concepts of material recycling within the subduction wedge (right in Figure 9 (top)) and uplift and mass wasting focused at the shallow East Cape Ridge near our data profile (see also (middle and bottom) three-dimensional views). Here, we also detected a strong shallow high velocity and strong magnetic anomalous rock (marked as "MV" in Figure 9 (top)) which is also interpreted as the source region for megasequence Y, indicated by dashed arrow (center in Figure 9 (top)).

of the specific anomaly, which lies 10 km above the subduction interface at East Cape Ridge, requires a detached and uplifted seamount. If a seamount of 1–2 km elevation, which is the average for the Hikurangi Plateau, was subducted and detached from the downgoing plate, then it has experienced an uplift of 8–9 km from the subduction interface and has attained that height against its negative buoyancy. The large rock uplift value suggests that it was accreted from the downgoing plate and has since undergone a long history of further subduction and basal accretion. Although this scenario would explain the lack of any detectable scar at the trench, we consider it unlikely that such a scenario is mechanically feasible. However, we have not made any mechanical model to simulate this process and retain it as a hypothesis.

[46] There are several magnetic anomalies associated with East Cape Ridge that have similar amplitude and wavelength and are aligned parallel to the ridge (Figure 6). The most southwestern anomaly corresponds to where the Matakaoa Volcanics unit is mapped onshore as part of an allochthonous unit emplaced at 25–22 Ma [*Mazengarb and Speden*, 2000]. Based upon our Euler deconvolution analysis (Figure 8), we note a correlation between seismic reflection megasequence Y (Figure 9), which is a correlative of the onshore allochthon [*Sutherland et al.*, 2009], and model sources of magnetization (Figure 8). As this unit is supposed to represent a slump from the southeast, now the region of East Cape Ridge, the magnetization indicates that the highly magnetic high velocity anomaly below East Cape Ridge could either be a correlative of the unit, or could be the slump source (large dashed arrow in Figure 9). Therefore, we conclude that we have very likely detected an offshore part of the Matakaoa volcanics within allochthonous megasequence Y, and our results support the conclusion by *Davey et al.* [1997] that the onshore allochthon volcanic geology extends further northeast along East Cape Ridge.

[47] The seismic velocity of the anomaly beneath East Cape Ridge (approximately 5.8 km/s) is relatively similar to that of the adjacent upper Australian crust beneath Raukumara Basin (5.4–5.8 km/s) and faster than that of the upper Hikurangi Plateau crust (4.9 km/s). Thus, the origin of the seismic and magnetic anomaly beneath East Cape Ridge could be from uplifted basement of Raukumara Basin, which in turn may be the source of allochthonous material that was emplaced into the basin during subduction initiation as the Matakaoa Volcanics and seismic reflection megasequence Y. *Cassidy* [1993] reports magnetizations of up to 5.5 A/m from similar allochthonous units in Northland that were also emplaced at 25–22 Ma, so our estimate of 3.3–3.9 A/m seems reasonable and may imply a common origin of the material.

### 6.4. Tectonic Erosion and Accretion Between East Cape Ridge and the Trench

[48] We interpret the frontal 100 km of the fore arc, from East Cape Ridge to the Hikurangi Trench, to be highly dynamic and actively deforming. Our structural model (Figures 3 and 5) exhibits relatively slow seismic velocities and high seismic attenuation in this region. It is bound to the east by the high-velocity anomaly that lies beneath East Cape Ridge. Figure 9 shows our structural interpretation. In the following, we use structural and geometrical arguments to characterize the fore-arc deformation mechanism in this region.

[49] The slope of the seafloor near the deformation front is relatively steep (~11° over a distance of 13 km in water depths of 3600 to 1100 m). High-resolution bathymetry and seismic data reveal a highly-faulted slope of acoustically reflective indurated material, apparently indicative of collapse and subduction erosion [*Collot and Davy*, 1998]. Oversteepening of trench slopes by subduction erosion can lead to dramatic, possibly tsunamogenic avalanches [*von Huene et al.*, 1989].

[50] Margin slopes can be used to distinguish between erosive and accretive margin types; however, wavelengths above 50 km need to be examined [*Clift and Vannucchi*, 2004]. The frontal fore-arc slope of our profile is around 3° over the distance from East Cape Ridge to the trench. This is steeper than observed globally at accretive margins and could, therefore, be considered as evidence for an erosive subduction margin [*Clift and Vannucchi*, 2004]. However, allowing for the shallow subduction angle of the plateau crust (~4° within 70 km of the deformation front), the taper angle is relatively shallow (7°). In global comparison, this low taper angle is not clearly erosive [*Clift and Vannucchi*, 2004], and taking into account the trench sediment supply of about 2 km and the orthogonal plate convergence rate of 60 km/Myr, the northern Hikurangi margin exhibits characteristics more consistent with an accretive margin setting [*Clift and Vannucchi*, 2004].

[51] Another argument against net subduction erosion at the margin is given by *Sutherland et al.* [2009]. They argue that tectonic erosion of the fore arc would lead to trench retreat over geologic time. Hence the Hikurangi volcanic arc would have moved westward with time, relative to Raukumara Basin, to preserve the distance between the deformation front and the arc volcanoes [*Lallemand*, 1995]. However, *Sutherland et al.* [2009] present evidence that extinct arc volcanoes are not present within the basin and hence suggest little or no net tectonic erosion of the fore arc since 22 Ma.

[52] An alternative mechanism to consider is that of lower-crustal underplating and hence fore-arc uplift caused by continuity of volume, i.e., without an increase in the total volume of the fore arc. Rather than being accreted at the toe of the fore-arc wedge, incoming sedimentary material enters a subduction channel and then, because it is too buoyant and weak to penetrate beneath the overriding mantle wedge, it is transferred upward across the subduction thrust and is underplated to the fore-arc crust to form the root of the outer fore-arc high. This mechanism was first suggested for Raukumara Peninsula by *Walcott* [1987], and was developed by *Sutherland et al.* [2009] to include both subducted sediment and material derived from frontal subduction erosion to explain the geometry and uplift of East Cape Ridge.

[53] With our new geometrical constraints we are able to test and quantify the fore-arc kinematic model of *Sutherland et al.* [2009]. The region between the trench and East Cape Ridge consists of material of relatively low seismic velocities (3.3 km/s at 6 km below the seafloor) and low sedimentary densities (<2.3 g/cm$^3$), as indicated by the depression of the sedimentary bodies at model km 40 in Figures 3 and 7. In

addition, we infer high seismic attenuation east of model km 100 based upon weak refracted signals and the incoherent seismic reflection character of MCS data (Figures 2b–2e and 5), as corroborated by seismological results for the Raukumara region to the south [*Eberhart-Phillips and Chadwick*, 2002]. We attribute these seismic and density characteristics to the considerable internal deformation of the accreted and recycled fore arc. Similar observations were made at the fore-arc high of the Sunda-Banda arc transition [*Shulgin et al.*, 2009], where the source of the material is attributed to basal accretion based on numerical modeling [*Selzer et al.*, 2008].

[54] Our identification of the material that is being recycled or actively accreted to the fore arc allows us to perform simplified calculations of mass fluxes at the subduction zone since the Neogene at 22 Ma, by taking into account the plate convergence, back-arc opening, and assuming an average thickness for the incoming sediments. The total convergence at the subduction zone at this location since 22 Ma is assumed to be the sum of the plate motion of 880 km, as computed from the rotations of *Cande and Stock* [2004], and the back-arc opening in the Havre Trough of approximately 120 km. The input of the subduction zone that is available for accretion is the sediment thickness on the downgoing plate, and any volcanics (e.g., seamounts) that could detach, integrated over the 22 Myr history of convergence. We identify 4 km of material currently entering the subduction system on our cross section: 2.2 km of sediments inferred to have collapsed off the adjacent trench slope, plus almost 2 km of some basal volcaniclastics which may be classified as part of the oceanic crust. The proximity of our profile to the Ruatoria Debris Avalanche [*Collot et al.*, 2001] results in an overestimation of how much material is added on average from outside the system; about 1 km less trench fill is observed today on seismic lines north and south of the Ruatoria Debris Avalanche. In general, the sediment thickness found on the Hikurangi Plateau away from the active trench is <1 km [*Davy et al.*, 2008], and so we estimate the total input to be $1000 \pm 500$ km$^2$. The total volume of accreted and recycled fore-arc material beneath the trench slope is estimated from our cross section to be $500 \pm 50$ km$^2$, so our best estimate is that half of the incoming material has been accreted to the margin, though the possible range is 25–100%. Crustal material may leave the fore arc through erosion into sedimentary basins to the east or west, or may be subducted into the mantle. The volumes of Neogene basins surrounding East Cape Ridge are large, but the sedimentary fill is mostly composed of clasts transported from onshore New Zealand and minor volcaniclastic input. Therefore, we cannot determine the proportion that is eroded from East Cape Ridge, but we can identify a large enough reservoir to potentially account for all of the remaining deficit in mass flux.

[55] A similar suggestion of close to zero net balance of subduction zone material transfer is made for the eastern Sunda Arc region (E. Lueschen et al., Structure, evolution and tectonic activity of the eastern Sunda forearc, Indonesia, from marine seismic investigations, submitted to Tectonophysics, 2009) that may extend as far as east of Sumba Island in the east [*Shulgin et al.*, 2009; *Planert et al.*, 2010] and Java Island in the west [*Kopp et al.*, 2006]. Another recycling system is described for the paleoaccretionary wedge in south-central Chile [*Glodny et al.*, 2005] though only an uplift and erosion balance is estimated without considering the total mass budget. And another area of pronounced uplift of the outer fore-arc high but subsidence and collapse of the trench slope is reported at the Tonga trench [*Clift et al.*, 1998], where we propose that underplating of the fore-arc crust may have been partly overlooked due to a lack of data. The steep slopes in these regions indicate a relatively high basal friction and may have higher input than output to form a pronounced outer fore-arc high [*Gutscher et al.*, 1998].

[56] Of particular interest for global models of crustal growth is the flux of material with a continental chemistry that is transported back into the mantle at subduction zones, because it is widely believed that this must be in approximate balance with the rate of production of new continental crust at volcanic arcs [e.g., *von Huene and Scholl*, 1991; *Clift and Vannucchi*, 2004; *Hawkesworth and Kemp*, 2006]. It has been widely assumed that margins with evidence for subsidence and collapse of the trench slope are regions of trench retreat and long-term recycling of fore-arc crust into the mantle [e.g., *Clift and Vannucchi*, 2004], but we challenge the underlying assumption used to estimate these rates. According to the model suggested by *Sutherland et al.* [2009] and our determination of the volume of accreted material at East Cape Ridge, past estimates of the rate of crustal recycling into the mantle could be greater than the true value because the significance of underplating at the base of the crust may not have been fully recognized. Our observations may go a long way towards explaining the discrepancy between independent estimates of crustal growth at arcs [*Reymer and Schubert*, 1984] and crustal destruction at subduction zones [*Clift and Vannucchi*, 2004].

## 7. Conclusions

[57] Seismic wide-angle and vertical reflection data together with gravity and magnetic anomalies have been used to determine lithospheric structures of the northern Hikurangi margin, where the Hikurangi Plateau subducts beneath the Raukumara fore-arc basin. A combination of seismic ray-tracing modeling, seismic stratigraphy, gravity and magnetic modeling reveal the structure and deformation of the subduction zone as well as the origin and possible age of certain rock units.

[58] The shallow structure of the Hikurangi Plateau as determined by seismic wide-angle data consists at the Hikurangi trench of up to 2 km sediments with seismic velocities up to 3.5 km/s above a unit of about 2 km of seismically faster (>3.8 km/s) volcaniclastic, limestone, and chert material. The underlying crust is composed of an upper, 4 km thick layer with velocities of 4.9–6.7 km/s above the lower crust which is characterized by velocities >7.1 km/s. The Moho depth was estimated by gravity modeling and could not be verified by the seismic data. The thickness of the plateau is approximately 10 km.

[59] The Raukumara fore-arc basin represents one of the deepest known (>10 km thick) fore-arc basins, and formed initially during the Mesozoic Gondwana subduction episode, but was reactivated during the Neogene Hikurangi subduction [*Sutherland et al.*, 2009]. This reactivation process may be the only mechanism that creates such superdeep

fore-arc basins. Raukumara Basin developed on a 5–10 km thick crust. Up to 6 km of Cretaceous and Paleogene sediment was deposited over the thinnest part of the crust, which was then overlain by an allochthon that was emplaced at 25–22 Ma. We infer sourced Matakaoa volcanic material from uplifted basement exposed on a precursor to East Cape Ridge, where a high velocity, highly magnetized anomaly point to Matakaoa volcanics exposed onshore. Neogene sediments up to 3 km thick were then deposited on top of this allochthon [*Sutherland et al.*, 2009]. Refractions from the fore-arc mantle indicate seismic velocities above 8 km/s, implying that outside the region of arc volcanism the mantle material appears unaltered. Below Raukumara Basin, seismic reflections off the subducting slab indicate that the inclination of the initially low-angled slab dip steepens to over 10°, and, according to seismicity, steepens further to almost 50° below the arc.

[60] The East Cape Ridge to the trench is a 100 km wide region that is experiencing uplift due to underplating of relatively low-seismic-velocity and low-density crust from a subduction channel. The limited depth penetration of seismic data indicates high seismic attenuation attributed to significant internal deformation related to material recycling within the hanging wall wedge. Uplift of the fore arc causes oversteepening of the frontal taper, and material collapses and enters into the subduction channel from which it can become underplated and uplifted again.

[61] A mass balance calculation indicates that the low-seismic-velocity, high-attenuation, low-density fore-arc crust that we image beneath the trench slope and interpret to be accreted and recycled material represents 25–100% of the incoming sediment from the downgoing plate, and that the remainder could be accounted for through erosion of older accreted material into surrounding sedimentary basins. We suggest that previous estimates of continental mass flux into the mantle at subduction zones may be overestimated because they have not properly accounted for crustal underplating beneath fore-arc highs.

[62] **Acknowledgments.** We thank Captain Mallon and the crew of R/V *Sonne* for a smooth and efficient acquisition of the seismic wide-angle data, the New Zealand National Institute of Water and Atmospheric Research (NIWA) for providing high-resolution bathymetry of the research area, the Editor and two anonymous reviewers for their helpful and highly constructive reviews, and finally the German Ministry for Education and Research (BMBF), the German Research foundation (DFG), the New Zealand Foundation for Research Science and Technology (FRST), the New Zealand Ministry for Economic Development (MED) for funding various aspects of this research. Most figures were made with GMT [*Wessel and Smith*, 1998].

## References

Árnadóttir, T., S. Thornley, F. F. Pollitz, and D. J. Darby (1999), Spatial and temporal strain rate variations at the northern Hikurangi margin, New Zealand, *J. Geophys. Res.*, *104*(B3), 4931–4944, doi:10.1029/1998JB900109.

Barker, D. H. N., R. Sutherland, S. Henrys, and S. Bannister (2009), Geometry of the Hikurangi subduction thrust and upper plate, North Island, New Zealand, *Geochem. Geophys. Geosyst.*, *10*, Q02007, doi:10.1029/2008GC002153.

Bialas, J., and E. R. Flueh (1999), Ocean bottom seismometers, *Sea Technol.*, *40*(4), 41–46.

Bostock, M. G., R. D. Hyndman, S. Rondenay, and S. M. Peacock (2002), An inverted continental Moho and serpentinization of the forearc mantle, *Nature*, *417*, 536–538, doi:10.1038/417536a.

Cande, S. C., and J. M. Stock (2004), Pacific-Antarctic-Australia motion and the formation of the Macquarie Plate, *Geophys. J. Int.*, *157*, 399–414, doi:10.1111/j.1365-246X.2004.02224.x.

Carlson, R. L., and D. J. Miller (2003), Mantle wedge water contents estimated from seismic velocities in partially serpentinized peridotites, *Geophys. Res. Lett.*, *30*(5), 1250, doi:10.1029/2002GL016600.

Cassidy, J. (1993), Tectonic implications of paleomagnetic data from the Northland Ophiolite, *New Zealand, Tectonophysics*, *223*(3–4), 199–211, doi:10.1016/0040-1951(93)90138-A.

Clift, P. D., and P. Vannucchi (2004), Controls on tectonic accretion versus erosion in subduction zones: Implications for the origin and recycling of the continental crust, *Rev. Geophys.*, *42*, RG2001, doi:10.1029/2003RG000127.

Clift, P. D., C. J. MacLeod, D. R. Tappin, D. J. Wright, and S. H. Bloomer (1998), Tectonic controls on sedimentation and diagenesis in the Tonga Trench and forearc, southwest Pacific, *Geol. Soc. Am. Bull.*, *110*(4), 483–496, doi:10.1130/0016-7606(1998)110<0483:TCOSAD>2.3.CO;2.

Cloos, M. (1993), Lithospheric buoyancy and collisional orogenesis: subduction of oceanic plateaus, continental margins, island arcs, spreading ridges, and seamounts, *Geol. Soc. Am. Bull.*, *105*, 715–737, doi:10.1130/0016-7606(1993)105<0715:LBACOS>2.3.CO;2.

Coffin, M. F., and O. Eldholm (1994), Large igneous provinces: Crustal structure, dimensions, and external consequences, *Rev. Geophys.*, *32*(1), 1–36, doi:10.1029/93RG02508.

Collot, J.-Y., and B. Davy (1998), Forearc structures and tectonic regimes at the oblique subduction zone between the Hikurangi Plateau and the southern Kermadec margin, *J. Geophys. Res.*, *103*(B1), 623–650, doi:10.1029/97JB02474.

Collot, J.-Y., et al. (1996), From subduction to intra-continental transpression: Structures of the southern Kermadec-Hikurangi margin from multibeam bathymetry, side-scan sonar, and seismic reflection, *Mar. Geophys. Res.*, *18*, 357–381, doi:10.1007/BF00286085.

Collot, J.-Y., K. B. Lewis, G. Lamarche, and S. Lallemand (2001), The giant Ruatoria debris avalanche on the northern Hikurangi margin, New Zealand: Result of oblique seamount subduction, *J. Geophys. Res.*, *106*(B9), 19,271–19,297, doi:10.1029/2001JB900004.

Cooper, G. R. J. (2002), An improved algorithm for the Euler deconvolution of potential field data, *Leading Edge*, *21*(12), 1197–1198, doi:10.1190/1.1536132.

Cooper, G. R. J. (2004), A semi-automatic procedure for the interpretation of geophysical data, *Explor. Geophys.*, *35*, 182–187, doi:10.1071/EG04182.

Davey, F. J., M. Hampton, J. Childs, M. A. Fisher, K. Lewis, and J. R. Pettinga (1986), Structure of a growing accretionary prism, Hikurangi margin, New Zealand, *Geology*, *14*, 663–666, doi:10.1130/0091-7613(1986)14<663:SOAGAP>2.0.CO;2.

Davey, F. J., S. Henrys, and E. Lodolo (1997), A seismic crustal section across the East Cape convergent margin, New Zealand, *Tectonophysics*, *269*, 199–215, doi:10.1016/S0040-1951(96)00165-5.

Davis, D. M., J. Suppe, and F. A. Dahlen (1983), Mechanics of fold-and-thrust belts and accretionary wedges, *J. Geophys. Res.*, *88*, 1153–1172, doi:10.1029/JB088iB02p01153.

Davy, B., and J.-Y. Collot (2000), The Rapuhia Scarp (northern Hikurangi Plateau): Its nature and subduction effects on the Kermadec Trench, *Tectonophysics*, *328*, 269–295, doi:10.1016/S0040-1951(00)00211-0.

Davy, B., and R. Wood (1994), Gravity and magnetic modeling of the Hikurangi Plateau, *Mar. Geol.*, *118*(1–2), 139–151, doi:10.1016/0025-3227(94)90117-1.

Davy, B., K. Hoernle, and R. Werner (2008), Hikurangi Plateau: Crustal structure, rifted formation, and Gondwana subduction history, *Geochem. Geophys. Geosyst.*, *9*, Q07004, doi:10.1029/2007GC001855.

de Ronde, C., et al. (2007), Submarine hydrothermal activity along the mid-Kermadec Arc, New Zealand: Large scale effects on venting, *Geochem. Geophys. Geosyst.*, *8*, Q07007, doi:10.1029/2006GC001495.

DeMets, C., R. G. Gordon, D. F. Argus, and S. Stein (1994), Effect of recent revisions to the geomagnetic time scale on estimates of current plate motions, *Geophys. Res. Lett.*, *21*, 2191–2194, doi:10.1029/94GL02118.

Durrheim, R. J., and G. R. J. Cooper (1998), Euldep: A program for the Euler deconvolution of magnetic and gravity data, *Comput. Geosci.*, *24*, 545–550, doi:10.1016/S0098-3004(98)00022-3.

Eberhart-Phillips, D., and M. Chadwick (2002), Three-dimensional attenuation model of the shallow Hikurangi subduction zone in the Raukumara Peninsula, New Zealand, *J. Geophys. Res.*, *107*(B2), 2033, doi:10.1029/2000JB000046.

Field, B. D., et al. (1997), *Cretaceous-Cenozoic Geology and Petroleum Systems of the East Coast Region, New Zealand*, *Geol. Monogr. Ser.*, vol. 19, 301 pp., GNS Sci., Lower Hutt, New Zealand.

Flueh, E. R., and H. Kopp (2007), FS Sonne Fahrtbericht/cruise report SO192 MANGO: Marine geoscientific investigations on the input and output of the Kermadec subduction zone, Rep. 11, 127 pp., IFM-GEOMAR, Kiel, Germany.

Gillies, P. N. (1984), A marine geophysical study of the junction of the Kermadec and Hikurangi subduction systems, Ph.D. thesis, Univ. of Auckland, Aukland, New Zealand.

Glodny, J., J. Lohrmann, H. Echtler, K. Gräfe, W. Seifert, S. Collao, and O. Figueroa (2005), Internal dynamics of a paleoaccretionary wedge: Insights from combined isotope tectonochronology and sandbox modelling of the South-Central Chilean forearc, *Earth Planet. Sci. Lett.*, *231* (1–2), 23–39, doi:10.1016/j.epsl.2004.12.014.

Gutscher, M.-A., N. Kukowski, J. Malavieille, and S. Lallemand (1998), Material transfer in accretionary wedges from analysis of a systematic series of analog experiments, *J. Struct. Geol.*, *20*(4), 407–416, doi:10.1016/S0191-8141(97)00096-5.

Hawkesworth, C. J., and A. I. S. Kemp (2006), Evolution of the continental crust, *Nature*, *443*, 811–817, doi:10.1038/nature05191.

Henrys, S. A., M. Reyners, I. Pecher, S. Bannister, Y. Nishimura, and G. Maslen (2006), Kinking of the subducting slab by escalator normal faulting beneath the North Island of New Zealand, *Geology*, *34*(9), 777–780, doi:10.1130/G22594.22591.

Herzer, R. H. (1995), Seismic stratigraphy of a buried volcanic arc, Northland, New Zealand and implications for Neogene subduction, *Mar. Pet. Geol.*, *12*(5), 511–531, doi:10.1016/0264-8172(95)91506-K.

Hoernle, K., F. Hauff, R. Werner, and N. Mortimer (2004), New insights into the origin and evolution of the Hikurangi oceanic plateau, *Eos Trans. AGU*, *85*(41), 401–416, doi:10.1029/2004EO410001.

Kopp, H., and N. Kukowski (2003), Backstop geometry and accretionary mechanics of the Sunda margin, *Tectonics*, *22*(6), 1072, doi:10.1029/2002TC001420.

Kopp, H., et al. (2006), The Java margin revisited: Evidence for subduction erosion off Java, *Earth Planet. Sci. Lett.*, *242*(1–2), 130–142, doi:10.1016/j.epsl.2005.11.036.

Lallemand, S. (1995), High-rates of arc consumption by subduction processes: Some consequences, *Geology*, *23*(6), 551–554, doi:10.1130/0091-7613(1995)023<0551:HROACB>2.3.CO;2.

Lamarche, G., C. Joanne, and J.-Y. Collot (2008), Successive, large mass-transport deposits in the south Kermadec fore-arc basin, New Zealand: The Matakaoa Submarine Instability Complex, *Geochem. Geophys. Geosyst.*, *9*, Q04001, doi:10.1029/2007GC001843.

Lewis, K. B., J.-Y. Collot, and S. E. Lallemand (1998), The dammed Hikurangi Trough: A channel-fed trench blocked by subducting seamounts and their wake avalanches (New Zealand-France GeodyNZ Project), *Basin Res.*, *10*, 441–468, doi:10.1046/j.1365-2117.1998.00080.x.

Lewis, K. B., S. Lallemand, and L. Carter (2004), Collapse in a Quaternary shelf basin off East Cape, New Zealand: Evidence for passage of a subducted seamount inboard of the Ruatoria giant avalanche, *N. Z. J. Geol. Geophys.*, *47*(3), 415–429.

Litchfield, N., S. Ellis, K. Berryman, and A. Nicol (2007), Insights into subduction-related uplift along the Hikurangi margin, New Zealand, using numerical modeling, *J. Geophys. Res.*, *112*, F02021, doi:10.1029/2006JF000535.

Malahoff, A., R. H. Feden, and H. S. Fleming (1982), Magnetic anomalies and tectonic fabric of marginal basins north of New Zealand, *J. Geophys. Res.*, *87*(B5), 4109–4125, doi:10.1029/JB087iB05p04109.

Mann, P., and A. Taira (2004), Global tectonic significance of the Solomon Islands and Ontong Java Plateau convergent zone, *Tectonphysics*, *389*(3–4), 137–190, doi:10.1016/j.tecto.2003.10.024.

Mazengarb, C., and D. H. M. Harris (1994), Cretaceous stratigraphic and structural relationships of Raukumara Peninsula, New Zealand; stratigraphic patterns associated with the migration of a thrust system, *Ann. Tecton.*, *8*(2), 100–118.

Mazengarb, C., and I. G. Speden (2000), Geology of the Raukumara area, geological map, 60 pp., scale 1:250,000, GNS Sci., Lower Hutt, New Zealand.

McGeary, S., A. Nur, and Z. Ben-Avraham (1985), Spatial gaps in arc volcanism: The effect of collision or subduction of oceanic plateaus, *Tectonophysics*, *119*, 195–221, doi:10.1016/0040-1951(85)90039-3.

McIntosh, K. D., E. A. Silver, I. Ahmed, A. Berhorst, C. R. Ranero, R. K. Kelly, and E. R. Flueh (2007), The Nicaragua convergent margin: Seismic reflection imaging of the source of a tsunami earthquake, in *The Seismogenic Zone of Subduction Subduction Thrust Faults*, edited by T. Dixon and J. C. Moore, pp. 257–287, Columbia Univ. Press, New York.

Mortimer, N., and D. Parkinson (1996), Hikurangi Plateau: A Cretaceous large igneous province in the southwest Pacific Ocean, *J. Geophys. Res.*, *101*, 687–696, doi:10.1029/95JB03037.

Nicol, A., C. Mazengarb, F. Chanier, G. Rait, C. Uruski, and L. Wallace (2007), Tectonic evolution of the active Hikurangi subduction margin, New Zealand, since the Oligocene, *Tectonics*, *26*, TC4002, doi:10.1029/2006TC002090.

Park, J.-O., T. Tsuru, S. Kodaira, P. R. Cummins, and Y. Kaneda (2002), Splay fault branching along the Nankai subduction zone, *Science*, *297*, 1157–1160, doi:10.1126/science.1074111.

Pecher, I. A., S. A. Henrys, S. Ellis, S. M. Chiswell, and N. Kukowski (2005), Erosion of the seafloor at the top of the gas hydrate stability zone on the Hikurangi margin, New Zealand, *Geophys. Res. Lett.*, *32*, L24603, doi:10.1029/2005GL024687.

Planert, L., H. Kopp, E. Lueschen, C. Mueller, E. R. Flueh, A. Shulgin, Y. Djajadihardja, and A. Krabbenhoeft (2010), Lower plate structure and upper plate deformational segmentation at the Sunda-Banda arc transition, Indonesia, *J. Geophys. Res.*, doi:10.1029/2009JB006713, in press.

Rait, G., F. Chanier, and D. W. Waters (1991), Landward- and seaward-directed thrusting accompanying the onset of subduction beneath New Zealand, *Geology*, *19*(3), 230–233, doi:10.1130/0091-7613(1991)019<0230:LASDTA>2.3.CO;2.

Ranero, C. R., R. von Huene, E. R. Flueh, M. Duarte, D. Baca, and K. McIntosh (2000), A cross section of the convergent Pacific margin of Nicaragua, *Tectonics*, *19*(2), 335–357.

Reymer, A., and G. Schubert (1984), Phanerozoic addition rates to the continental crust and crustal growth, *Tectonics*, *3*(1), 63–77, doi:10.1029/TC003i001p00063.

Reyners, M., and P. McGinty (1999), Shallow subduction tectonics in the Raukumara Peninsula, New Zealand, as illuminated by earthquake focal mechanisms, *J. Geophys. Res.*, *104*, 3025–3034, doi:10.1029/1998JB900081.

Reyners, M., D. Eberhart-Phillips, and G. Stuart (1999), A three-dimensional image of shallow subduction: crustal structure of the Raukumara Peninsula, New Zealand, *Geophys. J. Int.*, *137*(3), 873–890, doi:10.1046/j.1365-246x.1999.00842.x.

Reyners, M., D. Eberhart-Phillips, G. Stuart, and Y. Nishimura (2006), Imaging subduction from the trench to 300 km depth beneath the central North Island, New Zealand, with Vp and Vp/Vs, *Geophys. J. Int.*, *165*, 565–583, doi:10.1111/j.1365-246X.2006.02897.x.

Rudnick, R. L., and D. M. Fountain (1995), Nature and composition of the continental crust: A lower crustal perspective, *Rev. Geophys.*, *33*(3), 267–309, doi:10.1029/95RG01302.

Sandwell, D. T., and W. H. F. Smith (1997), Marine gravity from Geosat and ERS-1 altimetry, *J. Geophys. Res.*, *102*, 10,039–10,054, doi:10.1029/96JB03223.

Selzer, C., S. J. H. Buiter, and O. A. Pfiffner (2008), Numerical modeling of frontal and basal accretion at collisional margins, *Tectonics*, *27*, TC3001, doi:10.1029/2007TC002169.

Shulgin, A., H. Kopp, C. Mueller, E. Lueschen, L. Planert, M. Engels, E. R. Flueh, A. Krabbenhoeft, and Y. Djajadihardja (2009), Sunda-Banda arc transition: Incipient continent-island arc collision (northwest Australia), *Geophys. Res. Lett.*, *36*, L10304, doi:10.1029/2009GL037533.

Song, T. R. A., and M. Simons (2003), Large trenchparallel gravity variations predict seismogenic behavior in subduction zones, *Science*, *301*, 630–633, doi:10.1126/science.1085557.

Sutherland, R., et al. (2009), Reactivation of tectonics, crustal underplating, and uplift after 60 Myr of passive subsidence, Raukumara Basin, Hikurangi-Kermadec fore arc, New Zealand: Implications for global growth and recycling of continents, *Tectonics*, *28*, TC5017, doi:10.1029/2008TC002356.

Thornley, S. (1996), Neogene tectonics of Raukumara Peninsula, northern Hikurangi margin, New Zealand, Ph.D. thesis, Victoria Univ. of Wellington, Wellington.

Tichelaar, B. W., and L. J. Ruff (1993), Depth of seismic coupling along subduction zones, *J. Geophys. Res.*, *98*(B2), 2017–2037, doi:10.1029/92JB02045.

Upton, P., P. O. Koons, and D. Eberhart-Phillips (2003), Extension and partitioning in an oblique subduction zone, New Zealand: Constraints from three-dimensional numerical modeling, *Tectonics*, *22*(6), 1068, doi:10.1029/2002TC001431.

von Huene, R., and D. W. Scholl (1991), Observations at convergent margins concerning sediment subduction, subduction erosion, and the growth of continental crust, *Rev. Geophys.*, *29*, 279–316, doi:10.1029/91RG00969.

von Huene, R., J. Bourgois, J. Miller, and G. Pautot (1989), A large tsunamogenic landslide and debris flow along the Peru trench, *J. Geophys. Res.*, *94*(B2), 1703–1714, doi:10.1029/JB094iB02p01703.

von Huene, R., C. R. Ranero, and P. Vannucchi (2004), Generic model of subduction erosion, *Geology*, *32*(10), 913–916, doi:10.1130/G20563.1.

Walcott, R. I. (1987), Geodetic strain and the deformational history of the North Island of New Zealand during the late Cainozoic, *Philos. Trans. R. Soc. London A*, *321*, 163–181, doi:10.1098/rsta.1987.0009.

Wallace, L. M., J. Beavan, R. McCaffrey, and D. Darby (2004), Subduction zone coupling and tectonic block rotations in the North Island, New Zealand, *J. Geophys. Res.*, *109*, B12406, doi:10.1029/2004JB003241.

Wallace, L. M., et al. (2009), Characterizing the seismogenic zone of a major plate boundary subduction thrust: Hikurangi margin, New Zealand, Geochem. *Geochem. Geophys. Geosyst.*, *10*, Q10006, doi:10.1029/2009GC002610.

Walther, C. H. E., E. R. Flueh, C. R. Ranero, R. von Huene, and W. Strauch (2000), Crustal structure across the Pacific margin of Nicaragua: Evidence for ophiolitic basement and a shallow mantle sliver, *Geophys. J. Int.*, *141*, 759–777, doi:10.1046/j.1365-246x.2000.00134.x.

Wells, R. E., R. J. Blakely, Y. Sugiyama, D. W. Scholl, and P. A. Dinterman (2003), Basin-centered asperities in great subduction zone earthquakes: A link between slip, subsidence, and subduction erosion?, *J. Geophys. Res.*, *108*(B10), 2507, doi:10.1029/2002JB002072.

Wessel, P., and W. H. S. Smith (1998), New version of generic mapping tools released, *Eos Trans. AGU*, *79*, 579, doi:10.1029/98EO00426.

Whattam, S. A., J. G. Malpas, J. R. Ali, I. E. M. Smith, and C. H. Lo (2004), Origin of the Northland Ophiolite, northern New Zealand: Discussion of new data and reassessment of the model, *N. Z. J. Geol. Geophys.*, *47*(3), 383–389.

Wilson, K., K. Berryman, U. Cochran, and T. Little (2007), Holocene coastal evolution and uplift mechanisms of the northeastern Raukumara Peninsula, North Island, New Zealand, *Quat. Sci. Rev.*, *26*(7–8), 1106–1128, doi:10.1016/j.quascirev.2007.01.005.

Wood, R., and B. Davy (1994), The Hikurangi Plateau, *Mar. Geol.*, *118*(1–2), 153–173, doi:10.1016/0025-3227(94)90118-X.

Ye, S., E. R. Flueh, D. Klaeschen, and R. von Huene (1997), Crustal structure along the EDGE transect beneath the Kodiak shelf off Alaska derived from OBH seismic refraction data, *Geophys. J. Int.*, *130*(2), 283–302, doi:10.1111/j.1365-246X.1997.tb05648.x.

Zelt, C. A. (1999), Modelling strategies and model assessment for wide-angle seismic traveltime data, *Geophys. J. Int.*, *139*, 183–204, doi:10.1046/j.1365-246X.1999.00934.x.

Zelt, C. A., and R. B. Smith (1992), Seismic traveltime inversion for 2-D crustal velocity structure, *Geophys. J. Int.*, *108*, 16–34, doi:10.1111/j.1365-246X.1992.tb00836.x.

D. H. N. Barker, S. A. Henrys, M. E. Reyners, V. M. Stagpoole, and R. Sutherland, GNS Science, P.O. Box 30-368, Lower Hutt 5040, New Zealand.

D. G. Bassett, School of Geography, Environment and Earth Sciences, Victoria University of Wellington, P.O. Box 600, Wellington 6140, New Zealand.

A. Dannowski, E. R. Flueh, H. Kopp, and L. Planert, Leibniz Institute of Marine Sciences, IFM-GEOMAR, Wischhofstr. 1-3, D-24148 Kiel, Germany.

M. Scherwath, School of Earth and Ocean Sciences, University of Victoria, P.O. Box 3065, STN CSC, Victoria, BC V8W 3V6, Canada. (mscherwa@uvic.ca)

# 13

Shulgin, A., Kopp, H., Mueller, C., Planert, L., Lueschen, E., Flueh, E.R., Djajadihardja, Y., 2010.

**Structural architecture of oceanic plateau subduction offshore Eastern Java and the potential implications for geohazards.**

Geophys. J. Int., doi:10.1111/j.1365-246X.2010.04834.x.

Geophysical Journal International

*Geophys. J. Int.* (2010) doi: 10.1111/j.1365-246X.2010.04834.x

# Structural architecture of oceanic plateau subduction offshore Eastern Java and the potential implications for geohazards

A. Shulgin,[1] H. Kopp,[1] C. Mueller,[2] L. Planert,[1] E. Lueschen,[2] E. R. Flueh[1] and Y. Djajadihardja[3]

[1] *IFM-GEOMAR, Leibniz Institute of Marine Sciences, Wischhofstr.* 1-3, 24148 *Kiel, Germany. E-mail: ashulgin@ifm-geomar.de*
[2] *Federal Institute for Geosciences and Natural Resources (BGR), Stilleweg* 2, 30655 *Hannover, Germany*
[3] *Agency for the Assessment and Application of Technology (BPPT), Jl.M.H. Thamrin No.* 8, *Jakarta* 10340, *Indonesia*

Accepted 2010 September 29. Received 2010 September 27; in original form 2010 April 26



## SUMMARY

The region offshore Eastern Java represents one of the few places where the early stage of oceanic plateau subduction is occurring. We study the little investigated Roo Rise oceanic plateau on the Indian plate, subducting beneath Eurasia. The presence of the abnormal bathymetric features entering the trench has a strong effect on the evolution of the subduction system, and causes additional challenges on the assessment of geohazard risks. We present integrated results of a refraction/wide-angle reflection tomography, gravity modelling, and multichannel reflection seismic imaging using data acquired in 2006 south of Java near 113°E. The composite structural model reveals the previously unresolved deep geometry of the oceanic plateau and the subduction zone. The oceanic plateau crust is on average 15 km thick and covers an area of about 100 000 km$^2$. Within our profile the Roo Rise crustal thickness ranges between 18 and 12 km. The upper oceanic crust shows high degree of fracturing, suggesting heavy faulting. The forearc crust has an average thickness of 14 km, with a sharp increase to 33 km towards Java, as revealed by gravity modelling. The complex geometry of the backstop suggests two possible models for the structural formation within this segment of the margin: either accumulation of the Roo Rise crustal fragments above the backstop or alternatively uplift of the backstop caused by basal accumulation of crustal fragments. The subducting plateau is affecting the stress field within the accretionary complex and the backstop edge, which favours the initiation of large, potentially tsunamogenic earthquakes such as the 1994 $M_w = 7.8$ tsunamogenic event.

**Keywords:** Tomography; Subduction zone processes; Oceanic plateaus and microcontinents; Crustal structure; Asia.

## 1 INTRODUCTION

The converging margins around the world are major areas for generating the most devastating earthquakes and tsunamis. Any variations in the subduction systems are of extreme importance due to the changes in the geohazards situation. In this work we investigate the subduction of a previously little investigated oceanic plateau—the Roo Rise, its structure and its interaction with the Java margin at around 113°E. We focus on the recovery of the structural architecture in the region and its tectonic interpretation. We provide insights on the following questions for this particular region: (1) what are the effects of an oceanic plateau subduction, (2) what consequences does the subducting plateau have on the forearc deformation, (3) what is the structure of the forearc in such settings and (4) what are the effects that the subducting plateau have on the earthquake and tsunami generation?

The Sunda arc forms a part of more than 5000-km-long continuous subduction system, spanning from Flores and Sumba islands in the east to Burma in the northwest. The transition from the Sunda arc to the Banda arc is located at around 121°E, where the Australian continental shelf is approaching the trench (Shulgin *et al.* 2009). Both arcs are active since the Eocene collision of India and the Sundaland (the continental core of the southeast Asia (Hamilton 1988; Hall 2002; Hall & Smyth 2008) and are formed by the subduction of the Indo-Australian Plate underneath Eurasia (Hamilton 1979). The basement underneath Eastern Java is formed by arc and ophiolithic rocks accreted during the Mesozoic (Hall & Smyth 2008). Based on zircon dating, Smyth *et al.* (2007) propose an Archean continental fragment of Australian origin to be trapped between the forearc and the present volcanic arc in Eastern Java. The current convergence rate offshore Western Java is estimated to be $6.7 \pm 0.7$ cm yr$^{-1}$ in the direction 11°N that is almost perpendicular to the trench (DeMets

*et al.* 1994; Tregoning *et al.* 1994). A northward shift of the volcanic arc is recognized in Eastern Java with the present-day arc located *ca*. 50 km to the north of an older currently inactive volcanic arc (Hall & Smyth 2008); the shift is associated with changes in the subduction setting and interaction with the proposed Gondwana revenue (Smyth *et al.* 2007).

The Roo Rise oceanic plateau is located offshore Eastern Java. Oceanic plateaus are defined as a large, relatively flat submarine region that rises well above the level of the ambient seabed [*Encyclopedia Britannica*]. Oceanic plateaus can be formed from the remnants of continental crust or be a part of marine large igneous provinces. Currently there are no definitions based on the crustal structure. Their presence at the subduction zones is crucial in the evolution and dynamics of convergent margins. The subduction of the oceanic plateau triggers qualitatively different processes in the subduction system as compared to the subduction of 'normal' oceanic crust (White *et al.* 1992). The major differences caused by the approach of elevated rough bathymetric features (sea plateau, seamounts) to the trench include active frontal erosion of the margin, uneven uplift and deformation of the forearc, and a principally different regime of seismicity (Yamazaki and Okamura, 1989; Scholz & Small 1997). The migration of the trench is also in a good agreement with the numerical modelling of oceanic plateau subduction, comparable to the subduction of the Roo Rise (Gerya *et al.* 2009; Mason *et al.* 2010).

A 135-Ma-old Indian oceanic crust is currently subducting offshore Central–Eastern Java (Moore *et al.* 1980; Masson 1991) in the vicinity of the Roo Rise oceanic plateau. The Roo Rise is a broad smooth bathymetric feature with a number of isolated summits with an average elevation of about 2000 m above the adjacent oceanic floor (Fig. 1). It forms the eastern extension of the Christmas Island Seamount Province (Fig. 1). Planert *et al.* (2010) determine a crustal thickness of 10 km and show that earlier estimates by Curray *et al.* (1977) may be regarded as a lower limit. Rock samples taken across the entire Christmas Island Seamount Province do not show any clear formation time trend across the region (Werner *et al.* 2009). Based on dredged samples (dredging location closest to the study area is shown in Fig. 1), the Roo Rise is composed of strongly altered olivine phyric lava fragments with Mn-crusts and sediment. The formation of the plateau is associated with a series of large magmatic events as no formation time trend is observed. The increased crustal thickness should be accommodated by thickening of the gabbroic or basaltic layer (van Hunen *et al.* 2002). In order to explain the absence of a correlated gravity anomaly, the presence of a low density compensating crustal root was suggested (Newcomb & McCann 1987). Currently, the northern flank of the Roo Rise enters the trench (Fig. 1). Based on the bathymetry the edge of the plateau, which already subducted could be located as far as 70 km north from the trench, implying that it started to subduct 1.1–1.3 Ma. However, there is no direct evidence.

Offshore Central–Eastern Java, where the northern portion of the Roo Rise has already started to subduct, a northward displacement of the trench by 40 km on average is observed; the subduction of the individual seamounts causes an additional landward retreat of the deformation front by up to 10 km (Kopp *et al.* 2006). The bathymetric data collected in the trench area around 113°E (Fig. 1) show the trench is mostly devoid of sediments, except for local ponded accumulations associated with original seafloor fabric (Planert *et al.* 2010). Similar observations have been reported for the trench segment in between 108°E and 114°E (Curray *et al.* 1977; Masson *et al.* 1990). This study is a part of a large scale effort where data along the margin from Java to Lombok have been collected and analysed, for details on the adjacent profiles please see Planert *et al.* (2010), Shulgin *et al.* (2009) and Lueschen *et al.* (2010). These profiles augment earlier work on the Sumatra and Sunda Strait and Western Java (Kopp *et al.* 2002), so that we are able to describe the entire Sunda Arc subduction zone.

The forearc high, characterized in this area by a number of isolated well-defined peaks, shows an average elevation of *ca*. 800–1200 m, contrasting with the deeper forearc high ridges to the west (Kopp *et al.* 2001, 2002) and to the east offshore Lombok (Planert *et al.* 2010) (Fig. 1). The location of the forearc high peaks correlates with the proposed locations of completely subducted seamounts; however, the estimated subducted volume is smaller than the observed uplift of the forearc (Masson *et al.* 1990).

A number of tsunamogenic earthquakes have been recorded in the areas of seamount subduction offshore Java, which brings these locations into special focus in terms of geohazards. In 1994 and 2006, magnitude 7.8 earthquakes stroke offshore Java causing more than 1000 deaths due to the triggered tsunamis. Abercrombie *et al.* (2001) showed that the highest slip was collocated with the proposed location of a subducted seamount. More recently, Bilek & Engdahl (2007) and Kopp *et al.* (2009a) enhanced the idea of the correlation of structural forearc highs and associated subducted structures with the maximum slip of tsunami-generating earthquakes. The distribution of shallow earthquakes shows a pronounced spatial clustering, associated with the rough oceanic seafloor (Fig. 1).

## 2 DATA ACQUISITION AND MODELLING

We present *Vp* seismic tomography models of the Java forearc (Fig. 2, discussed below) (located offshore Eastern Java at 113°E), which are further constrained by gravity modelling. The SINDBAD marine seismic experiment onboard R/V 'Sonne' in 2006 (Fig. 1) included multichannel seismic reflection profiling (MCS) accompanied by gravity measurements, seismic refraction profiling with ocean-bottom seismometers (OBS) and hydrophones (OBH) (Mueller *et al.* 2008) and high-resolution multibeam bathymetry.

### 2.1 Acquisition

The corridor near 113°E consists of three wide-angle seismic refraction/reflection profiles with collocated MCS data and gravity measurements. Two profiles (P-42 and P-43) run north–south and are joint to one continuous transect, trending approximately perpendicular to the trench (Fig. 1). A total of 46 ocean bottom stations (Bialas & Flueh 1999) were deployed along these profiles. The profiles P-42/P-43 have an overlap of about 75 km, and we will refer to this joint profile as P4–23. P-41 is a shorter, east–west trending, trench parallel line located on the top of the forearc high (Fig. 1). During OBS recording, four G-gun clusters with a total volume of 64 l shot at 210 bar were used as seismic source. The average spacing between the shots is around 150 m; the average instrument spacing is 7 km. For the MCS reflection profiling, shots of ten G-gun clusters fired at 135 bar with the total volume of 56 l at a shot spacing of 50 m were recorded on a 3000 m long 240-channel streamer (Lueschen *et al.* 2010).

### 2.2 Processing

The processing of the ocean bottom data included the localization of the ocean bottom instruments using the arrival time of the direct

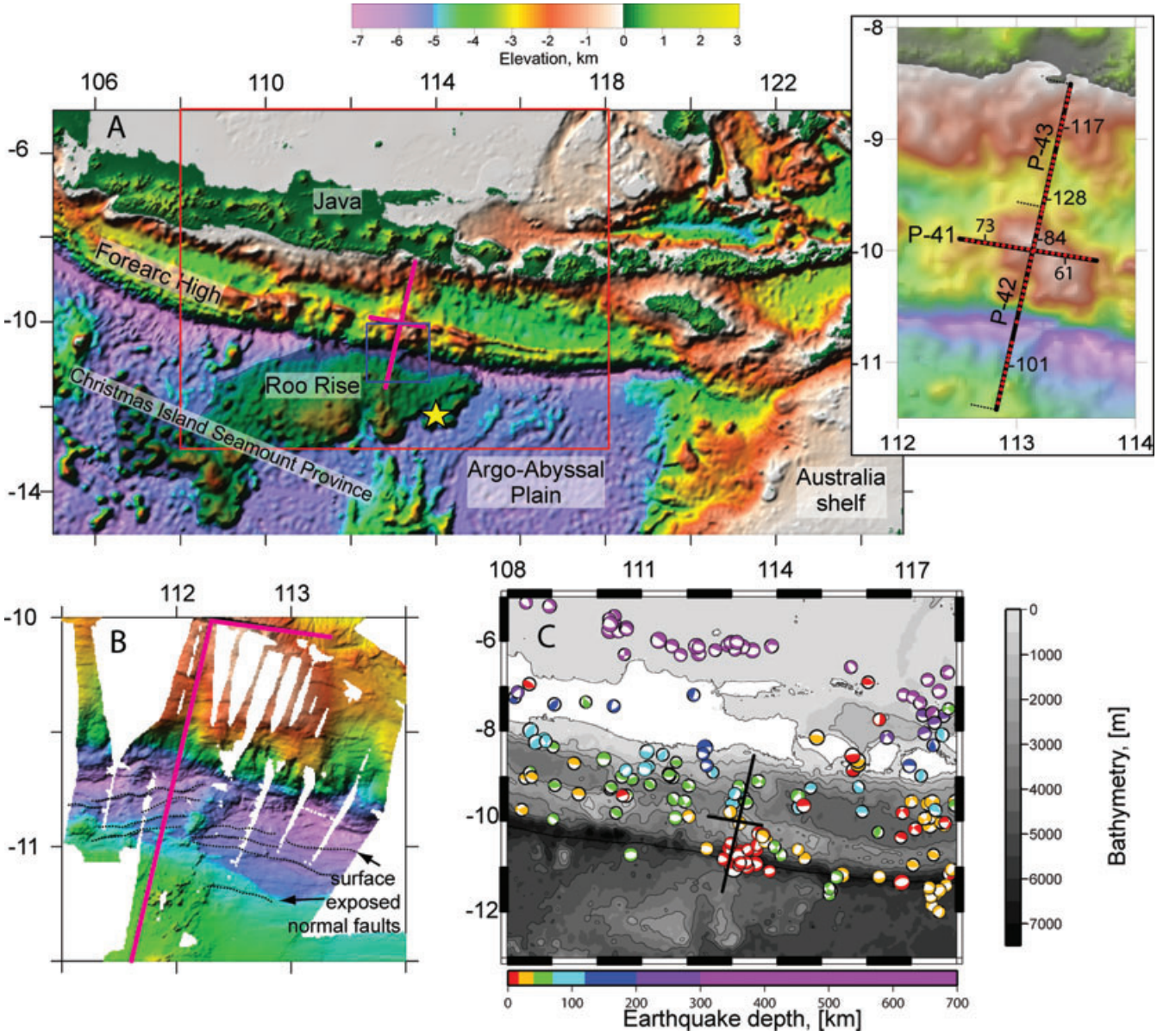


**Figure 1.** Topographic map of the study area. Seismic profiles examined in this study are shown by magenta lines in panel A and B and with black lines on C plot. Panel (a) shows the global bathymetry/elevation for the area around the Java trench. The insert map at the right shows the detailed geometry of the profiles and the location of ocean bottom stations shown in Figs 3 and 4, overlain on the bathymetry map. The spatial extent of the Roo Rise oceanic plateau is shown with dark shading. Yellow star marks the dredging samples location on Roo Rise (Werner *et al.* 2009). Panel (b) is a close up of the area marked by blue box in A. The multibeam bathymetry data collected during the cruise (the colourscale is identical to A) reveals seamounts and normal faults. Panel (c) shows the earthquake spatial and depth distribution and the focal mechanisms for the area marked by the red box in A (data are taken from the *Harvard Centroid Moment Tensor* catalogue).

water wave and the exact shot point geometry. A time-gated deconvolution was applied to remove predictable bubble reverberations to produce a signal free of the disturbing interference of multiple and primary phases (Wiener 1949). Finally, a time and offset-variant Butterworth filter, in which the pass-band moves towards lower frequencies as record time and offset increase, was applied to consider frequency changes caused by signal attenuation. The processing of the MCS data is described in detail by Lueschen *et al.* (2010).

Data examples are shown in Figs 3 and 4 for profiles P4–23 and P-41, respectively. For line P4–23, the stations located on the oceanic plate south of the trench (instruments 97–107) show clear records of the refracted phases together with clear oceanic Moho reflections (PmP) (Fig. 3a). These stations recorded Pn oceanic mantle phases reaching offsets up to 180 km (Figs 3a and b). The stations placed on top of the accretionary prism and forearc high (instruments 83–96) recorded refracted arrivals within shorter offsets compared to stations deployed on the oceanic crust. Reflections from the top of the oceanic crust (PtocP) were recorded as well as the oceanic Moho reflections (PmP) (Fig. 3b). Clear records of the forearc Moho reflections (PmfP) and the forearc Pnf phases with offsets up to 150 km are seen on the stations deployed along the northern part of the profile (instruments 108–128) (Figs 3c and d). For the trench-parallel profile P-41, the first arrival phases are clearly identified within 50 km offset, together with the reflections from the top of the

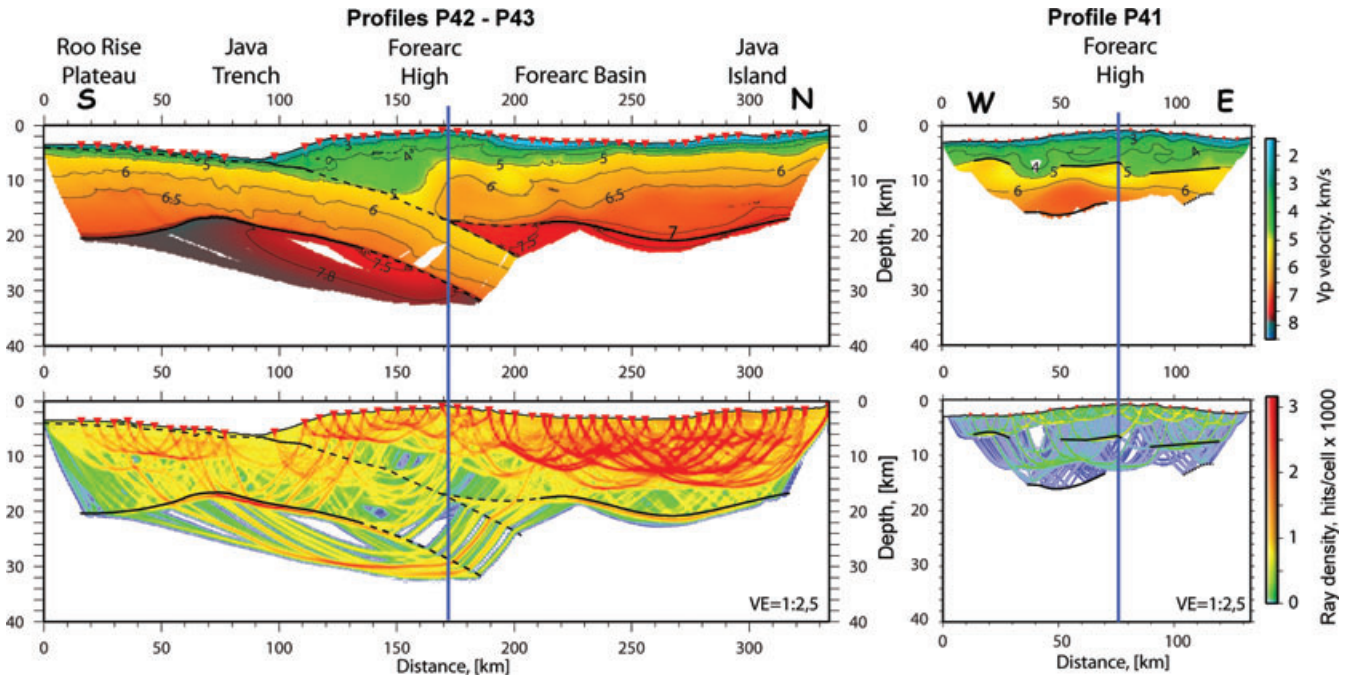


**Figure 2.** The results of the joint tomographic inversion for the profiles P4–23 and P-41. Top plots show the modelled *Vp* velocity distribution together with the recovered deep reflector geometry. Bottom plots show the seismic ray path density distributions. Both of the profiles are plotted with the identical scales and colourcodes. The solid black lines are the actually recovered positions of the reflectors and the dashed lines are the extrapolated positions based on the velocity distribution, MCS, and gravity models. Vertical blue line shows the cross points of the profiles.

basement (PtfP) (Fig. 4). Several stations (instruments 58–59, 61 and 72–74) on this profile have recorded plate interface reflections (PpintP) (Fig. 4).

### 2.3 Tomographic inversion

The seismic velocity distribution was modelled by joint refraction/reflection 2-D tomographic inversion (Korenaga *et al.* 2000). We applied a 'top to bottom' approach with a simple layered starting model. The grid spacing was defined by 250 m in the horizontal direction and with vertical spacing increasing with depth from 50 m at the top to 330 m at 40 km depth. The correlation length parameters were chosen to be 1 km × 0.2 km (horizontal × vertical) at the top and linearly increasing with depth to 8 km × 4 km at 40 km depth. Initially, the model was constrained only for the near offsets; then the depth extent of the ray coverage was increased to include the entire model space, with a simultaneous inversion for the reflector positions based on the available reflection phases. 46 stations were available for profile P4–23 with a length of 334 km, resulting in ∼36 500 first arrival traveltime picks and ∼7000 reflected picks. The shorter (135 km long) profile P-41 was covered by 21 stations, summing up to ∼9300 first arrival traveltimes and ∼1200 reflected picks. Data examples are shown in Figs 3 and 4. All available picked traveltimes and the fit of the corresponding computed traveltimes are shown on Fig. S1. The structure of the sediment and the basement topography were adopted from the MCS data (Lueschen *et al.* 2010), thus constraining the upper section of the profiles in great detail. Additionally, the top of the oceanic crust as identified in the depth-migrated MCS data was incorporated into the tomography model. The generalized routing during the inversion was as follows: constraining the interface geometry based on the corresponding MCS depth sections where available; inverting the near offset refracted phases to verify the consistency between data sets; fixing the upper section of the model with a weight of 1000 compared to the deeper sections. Then, we ran the simultaneous inversion for the velocity and reflector geometry for the next depth layer. Subsequently, we fixed the obtained layer structure and repeated the previous step for the following deeper layer. Finally, we kept the entire crustal structure fixed and inverted for the velocity in the upper mantle. The final models for all of the profiles are shown in Fig. 2.

### 2.4 Resolution tests

Several tests were performed to check the resolution of the obtained models. Initially, we used a forward ray shooting method to compute the synthetic traveltimes for the first arrival and reflected phases through our final models. The comparison of the seismic sections and the synthetic calculated traveltimes for several stations on both of the profiles is shown in Figs 3 and 4. The calculated traveltimes, as predicted by the tomographic *Vp* velocity models, are in a good agreement with the recorded seismic sections. All the refracted phases, including Pg and Pn, are fitted to the observed arrivals. The reflection phases (PmP, PmfP and PtocP) also match the recorded data; however, pre-critical reflections are not clearly identified in the seismic record sections.

Checkerboard resolution tests have been computed for both of the profiles to gain information on the spatial and amplitude resolution, which is dependent on the given ray geometry and the velocity distribution. The final *Vp* velocity model is perturbed by a small (compared to the real) value using a checkerboard pattern (for P4–23 additionally an isolated Gaussian anomaly pattern was used). Synthetic traveltimes are computed through the perturbed medium for the same source–receiver geometry as in the tomographic inversion. Subsequently, the tomography is computed based on the synthetic traveltimes in order to recover the initial perturbation pattern. The results of a test for P4–23 are shown in Figs 5(a)–(c). Three different anomaly sizes were used in the tests: 5 × 2.5 km,

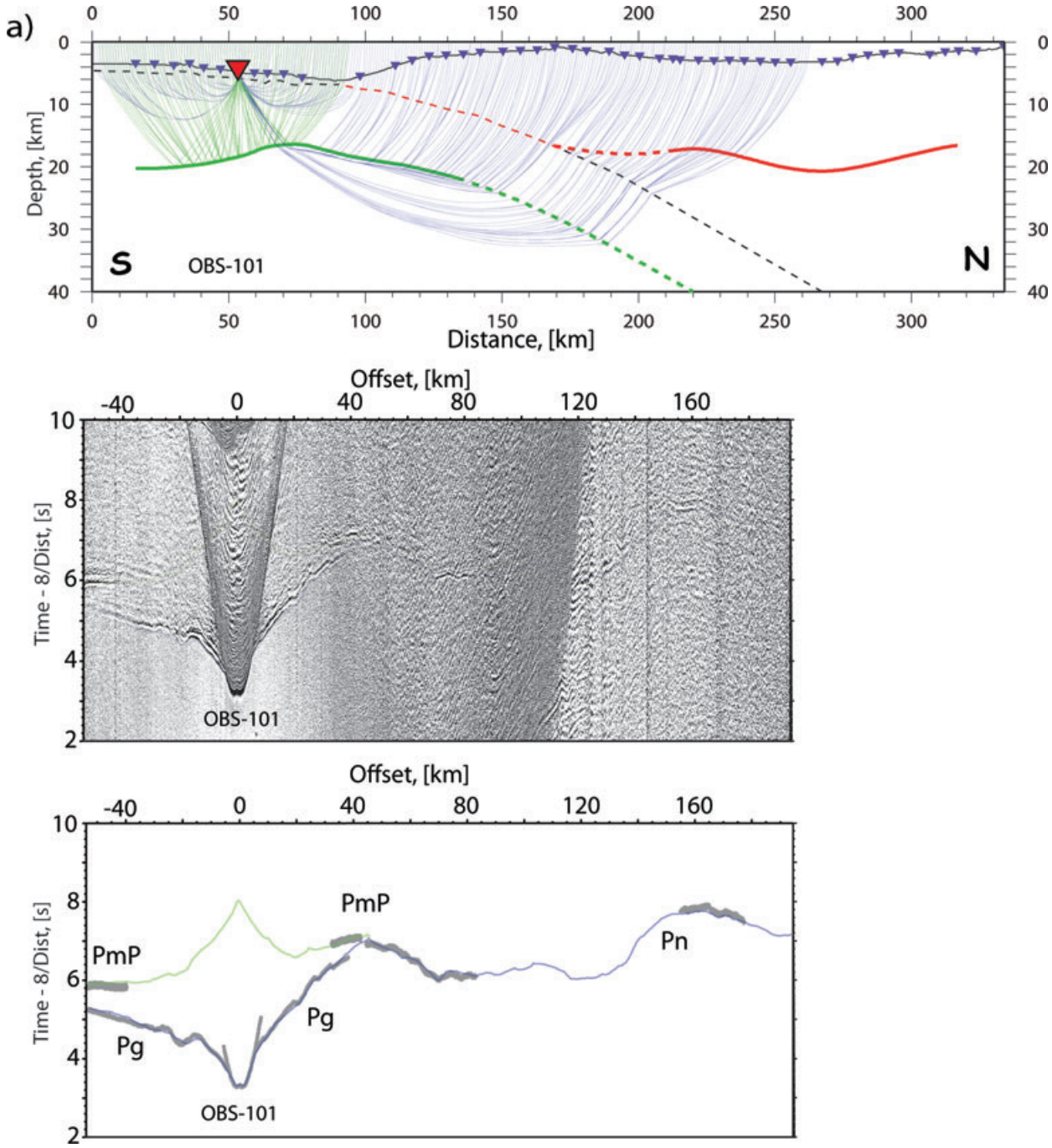


**Figure 3.** A forward ray shooting test for the selected stations on profile P4–23. For each station the first arriving and reflected traveltimes through the final model were computed and plotted on top of the actual seismic records. Bottom plots show with grey lines the picked phases, with width of the line representing the picking uncertainty. The computed traveltimes through the final model show good fit to the picked phases. Blue line – first arriving phases, green – reflections from the oceanic crust Moho, red – reflections from the forearc crust Moho. Top sections in each of the subplots show the schematic model of the profile. Solid lines correspond to well-defined reflectors constrained by wide-angle seismic data; dashed lines – structural interfaces constrained from MCS and/or gravity data, but purely resolved by the OBS data set. The corresponding ray paths, colourcoded as described above, are shown above each station in the model window.

10 × 5 km and 20 × 10 km (horizontal × vertical size). For all of them the starting model was perturbed using ±5 per cent values. For the small scale perturbation, the model is recovered down to a depth of 12 km, which roughly corresponds to the top of the forearc basement that we define to be around 5 km $s^{-1}$ isocontour (Fig. 5a). The 20 × 10 km size perturbation was adequately recovered down to a 20 km depth, which correlates with the location of the horizontal segments of the oceanic and forearc crust (Fig. 5c). The middle size pattern showed, as expected, an intermediate resolution down to a 16 km depth (Fig. 5b). Portions of the model deeper than ∼20 km failed to be recovered even with the biggest size pattern. To check the model validity for these areas, a resolution test using a single isolated Gaussian anomaly was performed. The anomaly was centred at 130 km offset and at 25 km depth. The tests were performed

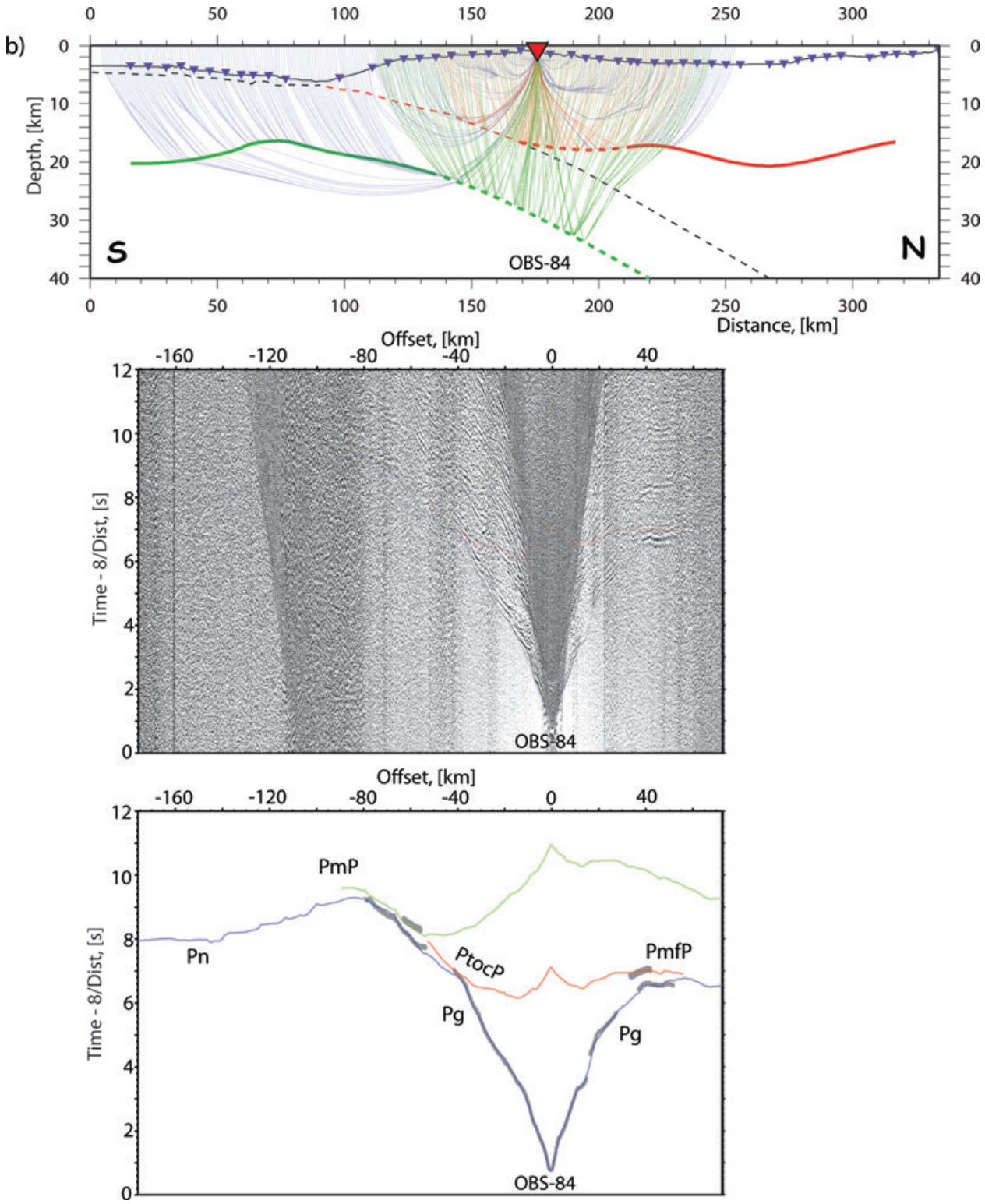


**Figure 3.** (*Continued.*)

for +10 and –10 per cent anomalies. As displayed in Figs 5(f) and (h), for the negative anomaly it was not possible to recover neither the shape nor the real amplitude of the anomaly due to the geometry of the seismic rays in this area, which are mostly non-crossing. For the positive anomaly test, the amplitudes were recovered; however, the location is smeared along the ray paths. In tomographic inversions with similar geometries (i.e. a small number of crossing rays), it is normal to observe the effect of averaging of the anomaly along the whole ray path between the crossing points. This is the case with the P4–23 profile. Additionally, the structure was checked by fitting the position of the critical distances for PmP reflections, this supports the obtained depth and velocity contrast at Moho (Fig. 6).

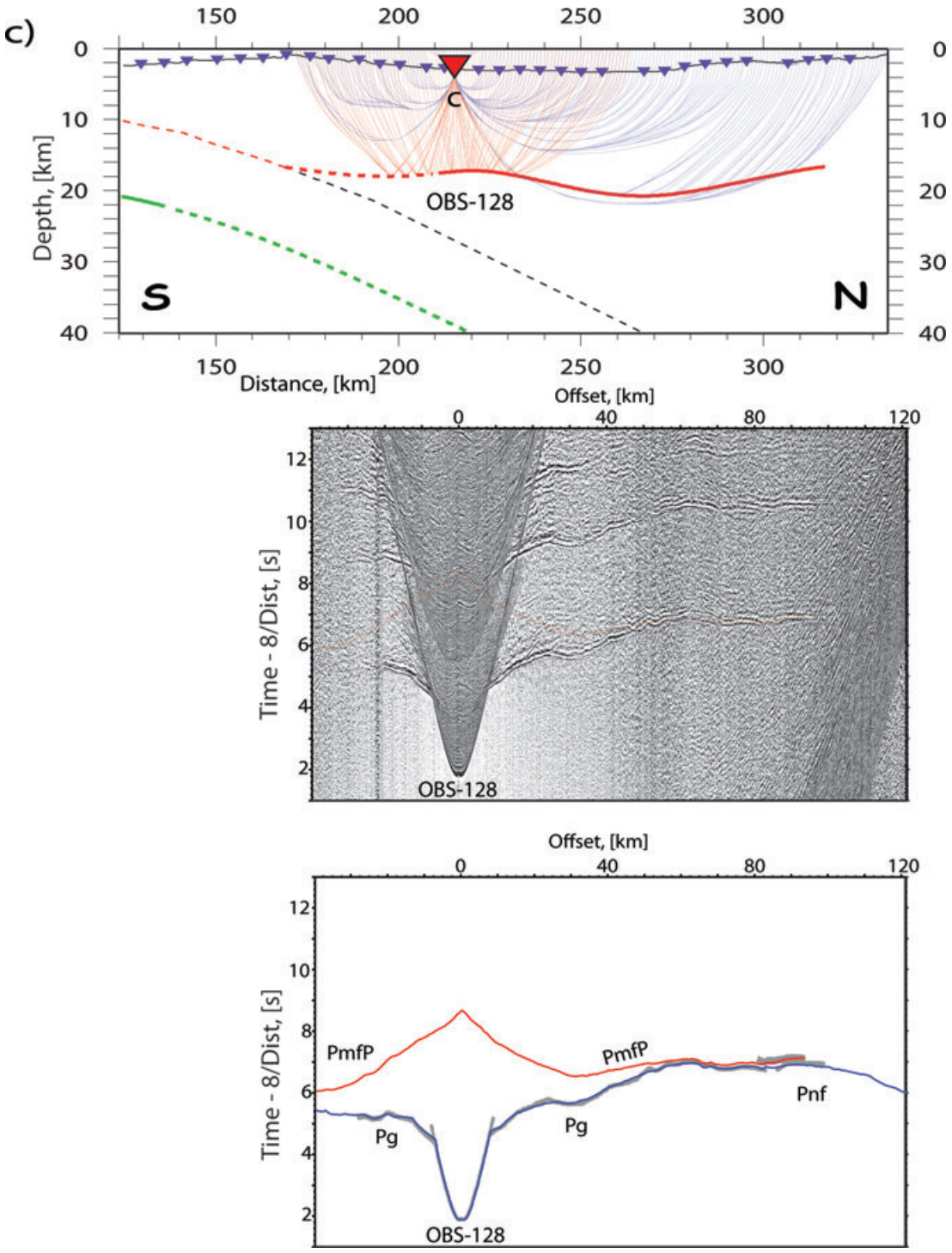


**Figure 3.** (*Continued.*)

Based on the resolution tests, it is likely that during the tomographic inversion the actual *Vp* velocity values tend to be overestimated and can be in the range of –7 to +3 per cent from the ones recovered for depths greater than 20 km.

Similar to P4–23, checkerboard tests were conducted for profile P-41. The results are shown in Figs 5(d) and (e). Two different pattern sizes were tested: 5 × 2.5 km and 10 × 5 km, both with a ±5 per cent amplitude perturbation. The smaller size anomalies are recovered down to 6 km depth, while the larger ones are recovered down to 12 km depth.

### 2.5 Gravity modelling

The resulting *Vp* velocity seismic tomography model for profile P4–23 was extended by 100 km both to the north and to the south and down to a depth of 75 km, to be used in forward gravity modelling. Seismic velocities were converted to densities using empirical and experimental relationships (Christensen & Mooney 1995; Carlson & Herrick 1990) and the subducting slab was extended down to 75 km depth, where the deep seismicity is observed. A constant density of 3.30 g cm$^{-3}$ was assumed for the forearc mantle, with

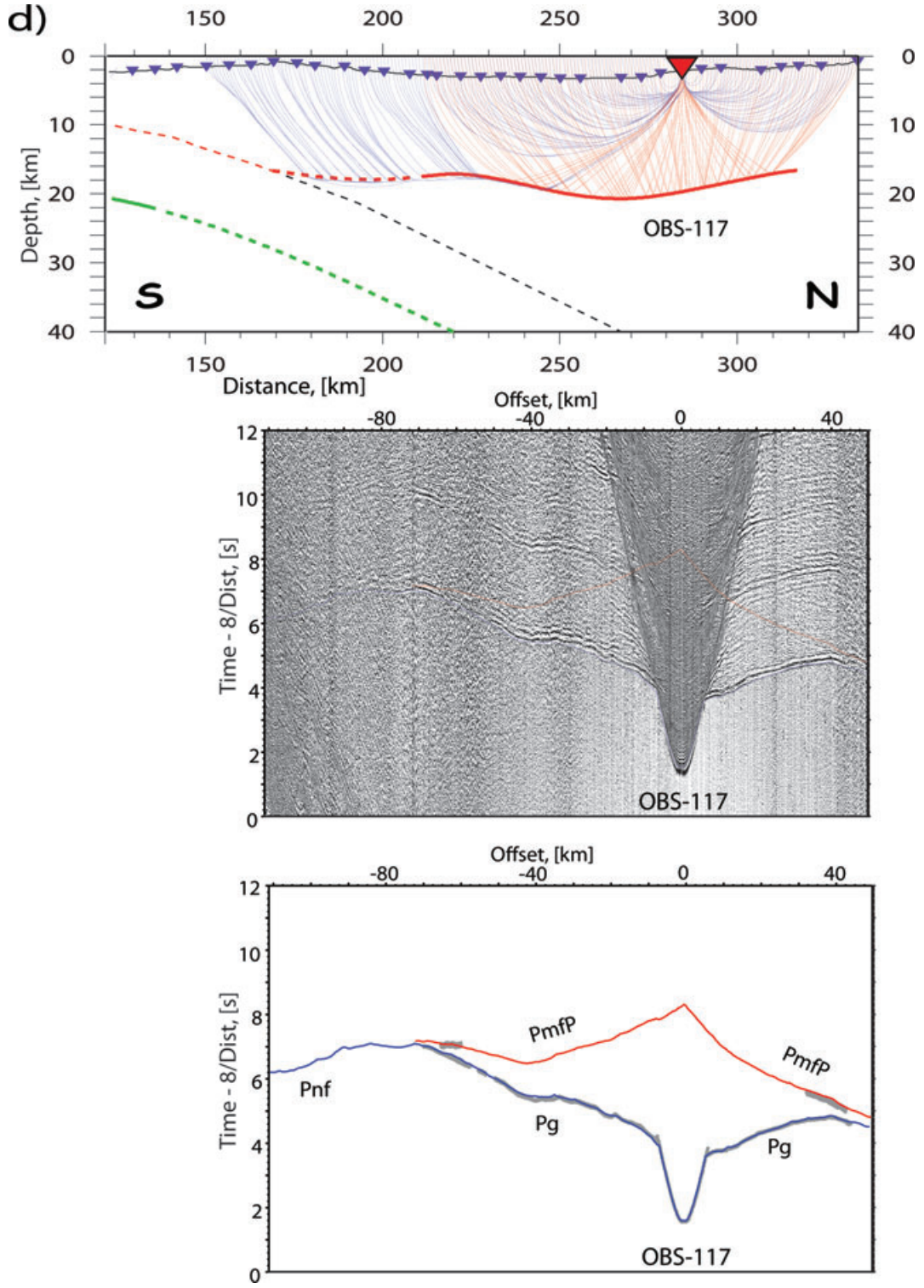


**Figure 3.** (*Continued.*)

the exception of the 30-km-long innermost mantle wedge where a density of 3.27 g cm$^{-3}$ was used (Fig. 7). The calculated gravity response of the model is in a good agreement with the observed data. The maximum misfit of 15–20 mGal is observed at the edge of the profile.

The area around the profile P4–23 shows a high degree of bathymetric changes in the east–west direction, associated with isolated forearc highs and the extended shelf zone offshore Java to the west of the northern termination of the profile. There is also a possibility for lateral variations of forearc crust offline the profile. Although these features should produce measurable 3-D effects on the gravity field along the profile, their effects were ignored in the gravity modelling. Despite the above mentioned simplifications, the gravity modelling confirms the features resolved by the tomographic

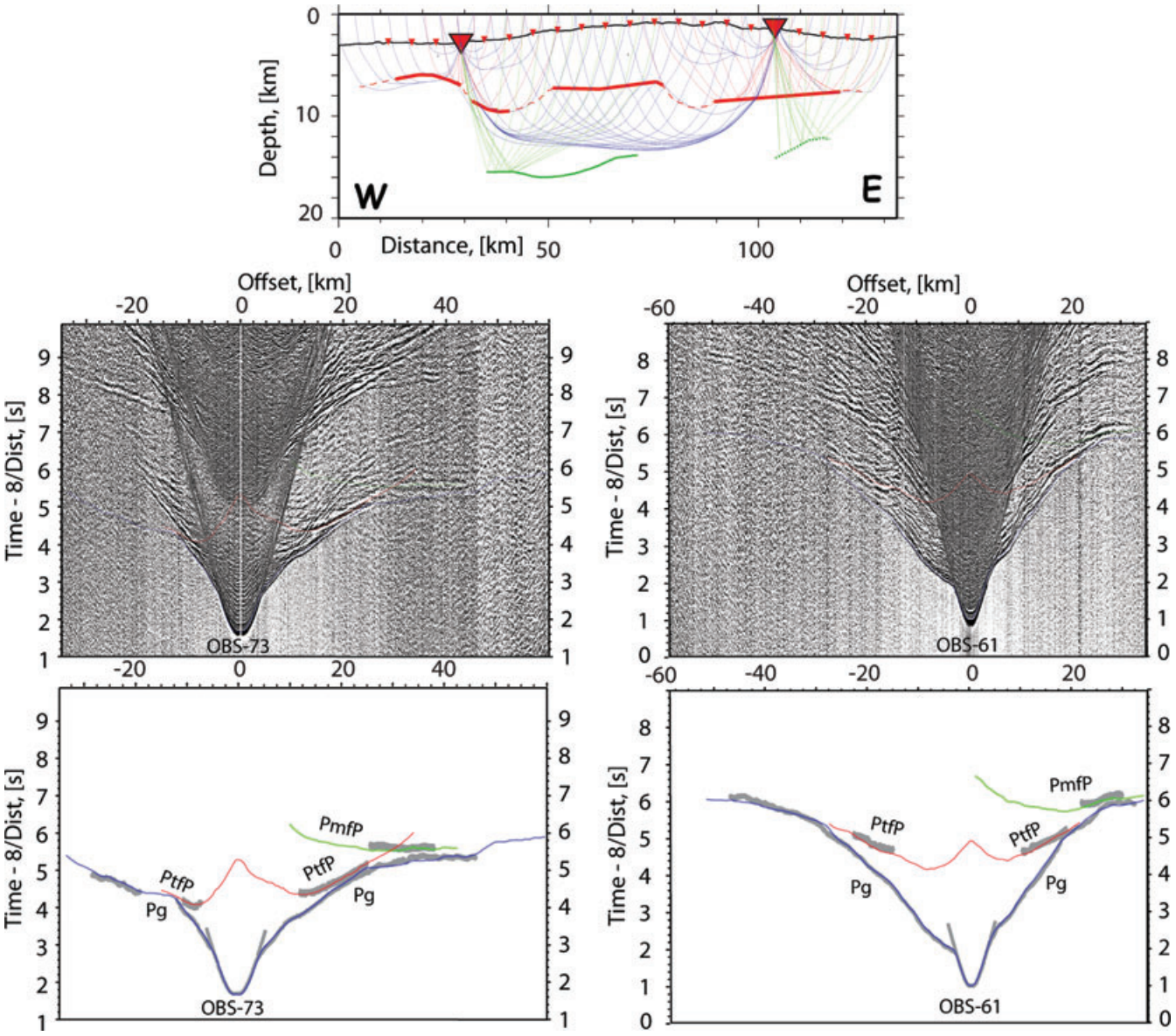


**Figure 4.** The forward ray shooting test for the selected stations on profile P-41. For each station the first arriving traveltimes (blue lines) through the final model were computed and plotted on top of the actual seismic records. Red and green lines are the synthetic reflection traveltimes from the top of the basement and plate interface, correspondingly. Bottom plots show with grey lines the picked phases, with width of the line representing the picking uncertainty. The top plot shows the locations of the corresponding stations and the ray paths for both stations, colourcoded as described above. Solid lines correspond to the well-defined portions of the reflectors. Dashed lines are reflectors that are purely resolved, or where the strong 3D propagation effects are assumed.

inversion (Fig. 7). The increased crustal thickness of the Roo Rise is required to fit the gravity field. The low mantle velocities, recovered in-between offsets of 60 and 160 km, correlate with the zone of a decreased mantle density of 3.29 g cm$^{-3}$. Such geometry of the forearc crust and the decreased density in the forearc mantle, associated with a relatively slow velocity in the forearc mantle, are required to fit the gravity data. Additionally, the possibility for the near vertical backstop, as seen offshore Lombok (Planert *et al.* 2010) has been tested (Fig. 7). The larger misfit with the observed gravity, compared to dipping backstop, further supports that the study area is transitional from Lombok domain to Java domain.

## 3 RESULTS AND DISCUSSION

The results are discussed from south to north of the region, starting from the southern segment of profile P4–23 towards Java. They are based on the joint interpretation of the wide-angle reflection/refraction tomography models, MCS data, and gravity model shown in Figs 2, 7, 8 and 9.

### 3.1 Roo Rise crustal structure

The southernmost section from 0 to 65 km offset on the north-south striking profile (P4–23) is the area where the Roo Rise oceanic

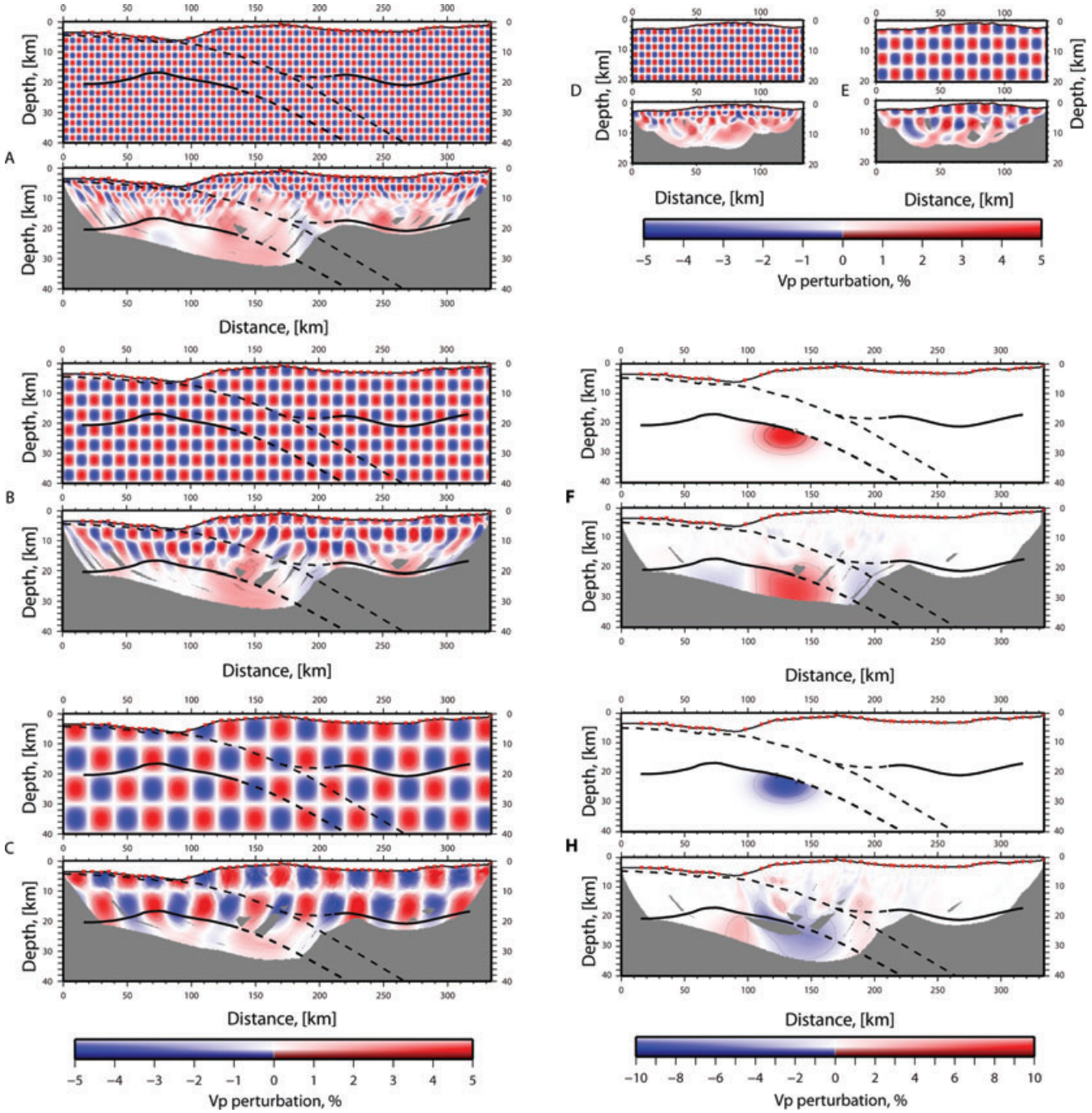


**Figure 5.** The results of the resolution tests. For each of the subplots the top figure is the synthetic resolution pattern and the bottom one is the recovery. A, B and C are the ±5 per cent *Vp* anomaly tests for profile P4–23. The sizes of the anomalies are: (A) 5 × 2.5 km; (B) 10 × 5 km; (C) 20 × 10 km (first number – horizontal extend, second – vertical). (D) and (E) are the ±5 per cent *Vp* anomaly tests for profile P41. The sizes of the anomalies are: (D): 5×2.5 km; (E) 10 × 5 km; (first number – horizontal extend, second – vertical). F and H are the resolution tests for profile P4–23 with a single isolated anomaly (F: +10 per cent; H: –10 per cent). Black solid and dashed lines are structural elements, the same as in Fig. 2.

plateau enters the trench (Fig. 2). The water depth is increasing here from 3 km at the southern end of the profile in the oceanic domain to 6 km depth at the trench. The *Vp* velocity structure of the upper portion of the oceanic plate is laterally homogeneous: velocities increase from about 2.7 to 3.0 km s$^{-1}$ below the seafloor (bsf) to 5 km ;s$^{-1}$ at about 2 km depth bsf (Fig. 8). At greater depth, the velocity gradient decreases and the velocities rise to 6.5–6.8 km s$^{-1}$ at the Moho which is located at 20–16 km depth (Fig. 2). Thus, the crustal thickness of the plateau varies from 18 km to 11 km (Fig. 2); these values are significantly greater than predicted earlier (Curray *et al.* 1977). The position of the critical distance for the PmP reflections (Fig. 6) fits the data, confirming the velocity model and the oceanic Moho topography. As is seen in the velocity model (Fig. 2), the major increase of the crustal thickness is accommodated by thickening of the lower oceanic crust. The gravity modelling of this crustal block yields a reasonable fit to the observed gravity field, which confirms the thickened (up to 20 km) crust underneath the oceanic plateau (Fig. 7). This result confirms the suggestion of

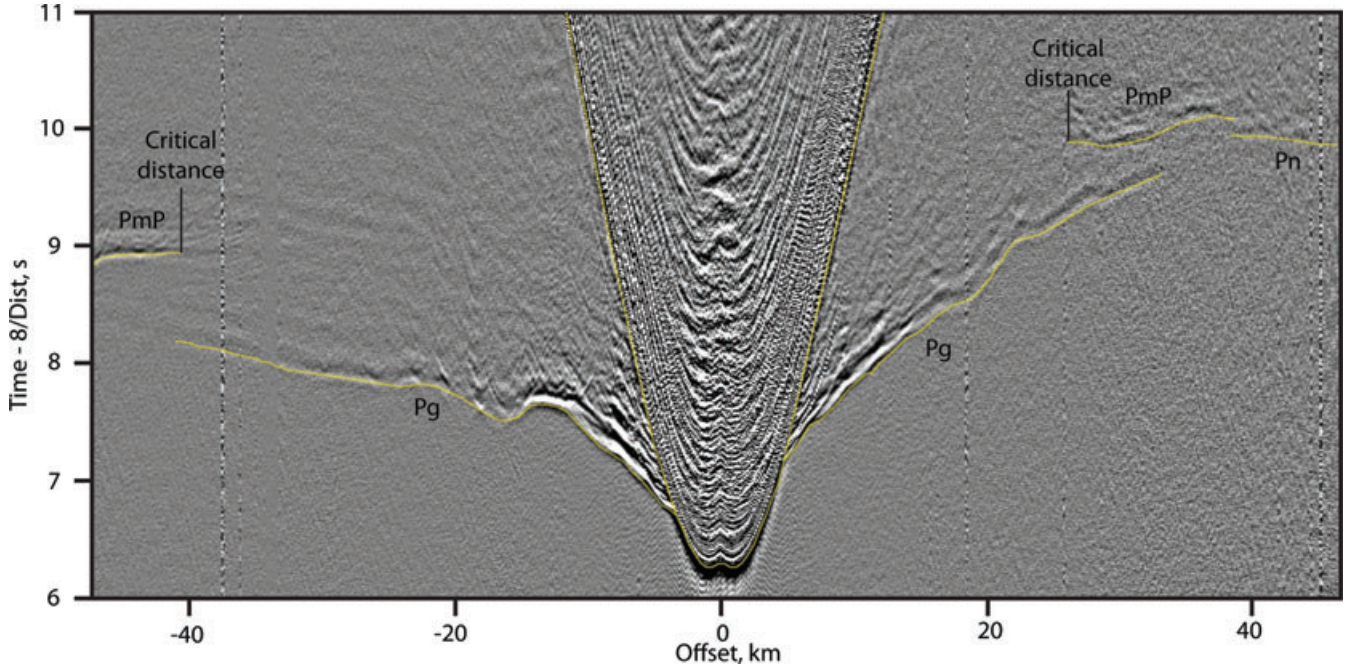


**Figure 6.** Record section of the vertical component of the OBH-101 located on the P4–23 profile around 51 km offset. Yellow lines show some selected phases. The forward ray shooting method nicely fits the observed critical points for the PmP.

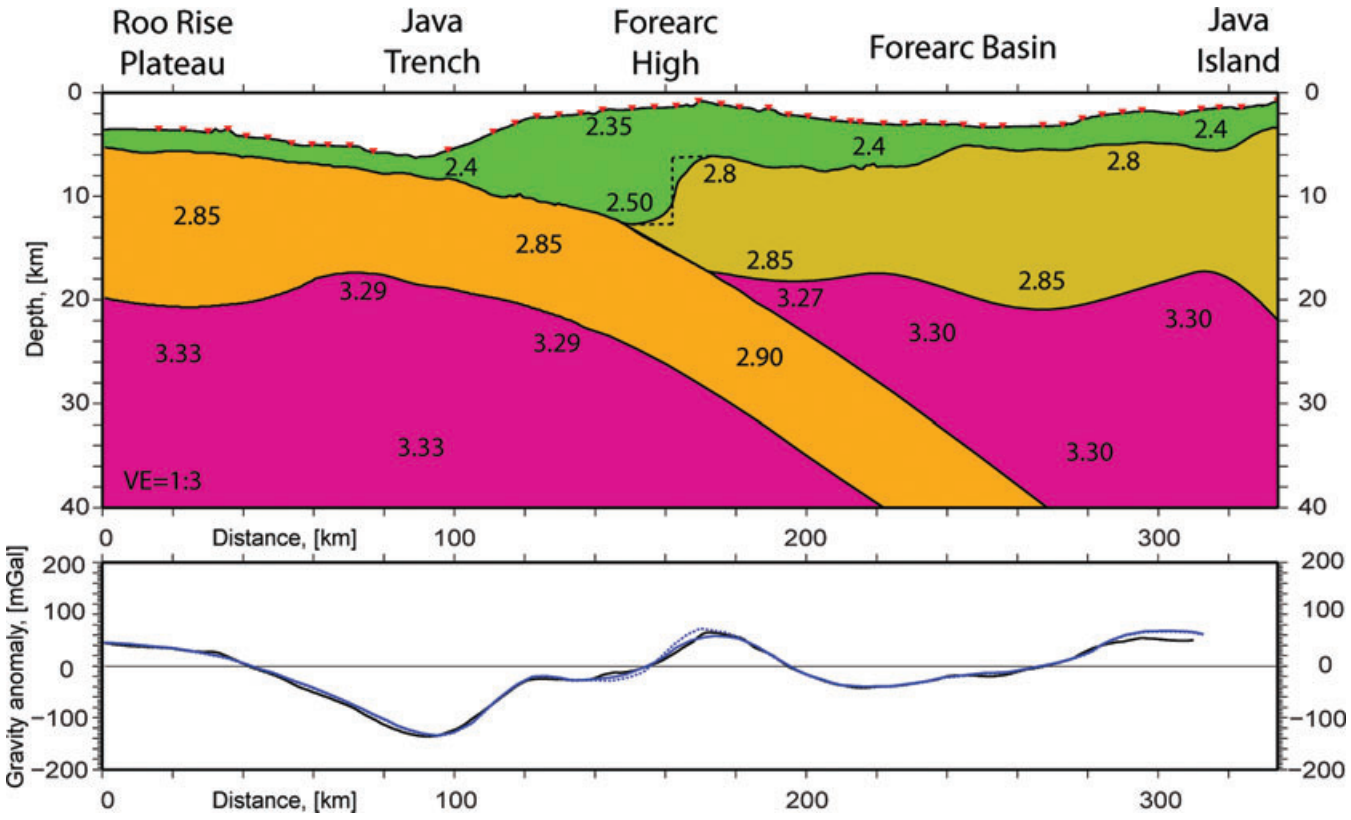


**Figure 7.** The gravity model for the profile P4–23. Top plot shows the density distribution in the model. Numbers correspond to the density values in units of g cm$^{-3}$. Densities below the shown depth are kept constant. The bottom plot shows the observed (black) and calculated (blue) free-air gravity anomalies along the profile. The dashed line on top plot corresponds to the gravity model where the backstop is assumed to be pure vertical; the computed gravity anomaly is shown on the bottom plot by dashed blue line.

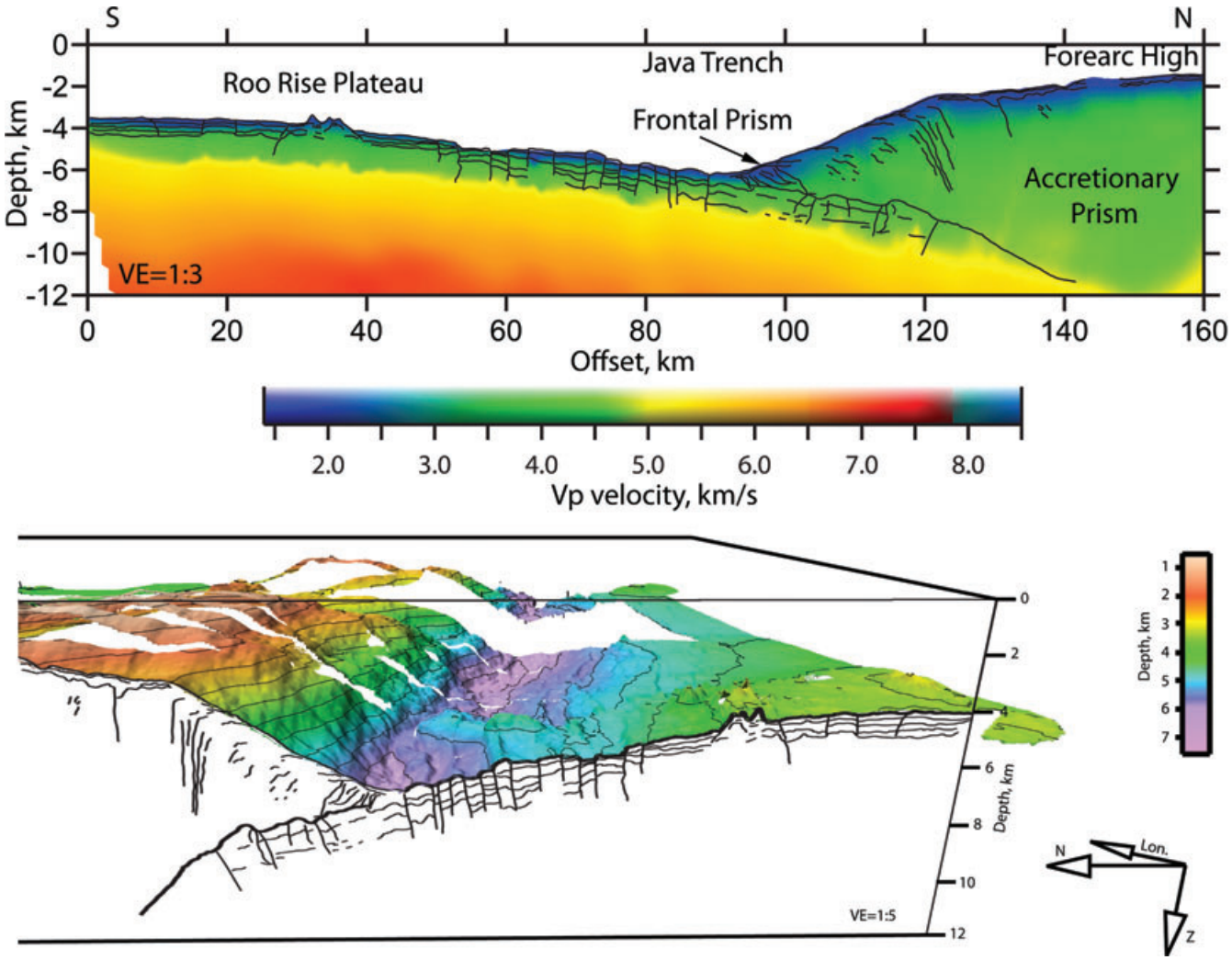


**Figure 8.** Top panel: A close look on the *Vp* distribution model around the Java trench. The black lines are the line-drawing interpretation of the collocated MCS profile. Bottom panel: 3-D view of the high-resolution bathymetry, centred at the trench location. The view is from west to east. Vertical slice is the linedrawing interpretation of the MCS line collocated with the P4–23 profile. Highly fractured upper oceanic crust is clear visible in both data sets.

Newcomb & McCann (1987) for the presence of a deep crustal root. The observed northward thinning of the Roo Rise crust (Fig. 2) may have several explanations. The most straightforward explanation is to interpret the region with the thinnest crust as the edge of the plateau and its transition to the conventional oceanic crust. Alternatively, this region may represent localized crustal thinning still within the Roo Rise that extends further north. Variations in crustal thickness of up to several kilometres are common for magmatically overprinted oceanic crust and may be associated with past, now inactive, phases of localized increased magmatic activity (Kopp *et al.* 2004). The interpretation of seismicity by Abercrombie *et al.* (2001) suggests the presence of subducted seamounts and thus implies a northward extension of the Roo Rise into the subduction complex. However, as it was shown by the numerical modelling, the presence of a buoyant oceanic plateau subducted below ∼30 km should lead to the formation of a flat subduction and ceasing of magmatism in the volcanic arc (van Hunen *et al.* 2002; Gerya *et al.* 2009; Mason *et al.* 2010). Since it is not the case in this area, we conclude that the main block of the Roo Rise is currently only approaching the trench and the anomalous crustal features present below the forearc are the isolated edge structures of the plateau (i.e. individual seamounts).

Starting from an offset of 60 km further northwards, the oceanic crust is highly fractured and is cut by a number of normal faults clearly visible in the MCS data (Lueschen *et al.* 2010) (Fig. 8) and in the multibeam bathymetry data at the surface (Fig. 1a and b). The observation of the faults and fractures is in an agreement with the results of Masson *et al.* (1990) which show that the subducted oceanic crust is fractured by normal faults due to the tension in its upper part caused by plate bending. Below the trench, the oceanic crust thins to about 10 km and maintains this thickness upon subduction (Fig. 2). The velocities at the top are about 3.5–4.0 km $s^{-1}$ increasing to 5 km $s^{-1}$ at a 2 km depth below see floor, and gradually increasing to 6.5–6.6 km $s^{-1}$ at the Moho. The modelled low velocities are presumably caused by the highly fractured, altered fluid-filled crust which causes the decrease of effective velocities. In addition, velocity smoothing implemented in the tomographic inversion is also likely to contribute to this effect. The lateral variations of the *Vp* velocity structure within the oceanic crust are small (Figs 2 and 8).

Comparison of the obtained structure of the Roo Rise with similar terrains in other regions shows similarities both in the velocity distribution and the crustal thickness. The Hikurangi plateau, offshore New Zealand, which is similar in structure but much larger, is

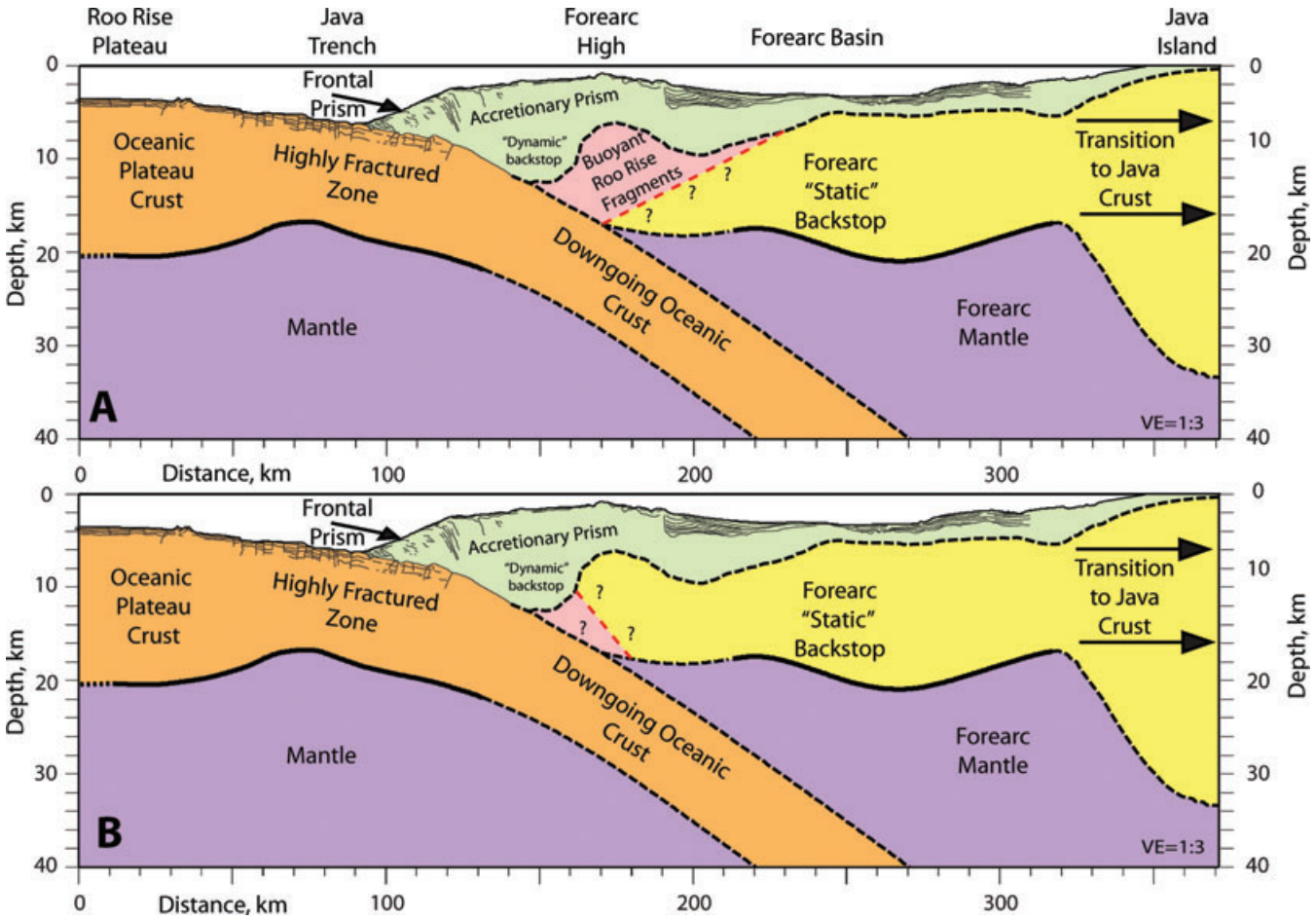


**Figure 9.** Joint interpretation models for profile P4–23 based on combined results of seismic tomography, MCS and gravity modelling. Thick solid lines are the reflectors constrained by the joint refraction/reflection inversion. Thick dashed lines are structural elements based on the results of gravity modelling. Thin lines are the line-drawing interpretation of the collocated MCS profile. Plots A and B show two variants for the structure of the backstop. (a) Interpretation based on the geometry of the forearc backstop observed to the west from our profile. (b) Interpretation based on the backstop geometry to the east of our profile and the ideas of Bangs *et al.* (2003).

reported to have 10–23-km-thick crust, and *Vp* values ranging from 4.9 to 7.2 km s$^{-1}$ (Davy *et al.* 2008; Scherwath *et al.* 2010). Similar to the Roo Rise, much of the crustal thickening is accommodated by the increase of the lower crust. However, comparing to other Large Igneous Provinces, with common thicknesses of 20–40 km (Coffin & Eldholm 1994), the Roo Rise is at the lower end of these values. This could be due to seismically resolving only the edge of the plateau, but not its centre, where the crust could be thicker. Another comparison could be done with the Nazca ridge offshore Peru, which is more comparable with the size of the Roo Rise, sampled in the study. The crustal thickness of the Nazca ridge reaches 16 km, with *Vp* values ranging from 4.5 to 6.6 km s$^{-1}$ in the upper crust and 6.7 to 7.5 km s$^{-1}$ in the lower crust (Hampel *et al.* 2004). Similar to the Roo Rise and Hikurangi plateaus most of the crustal thickening is accommodated by the lower crust. However, the velocities in the lower crust are much higher compared to the Roo Rise.

### 3.2 Accretionary prism structure

Starting from the trench (90 km offset) and further north, an active frontal prism is observed, characterized by thrust faults and fronting the accretionary prism (Fig. 8). The frontal prism extends laterally for about 12–15 km. Due to the minor sediment input into the system, the frontal slope of the accretionary prism (from 95 to 125 km offsets) is about 8°–10° with only about 2°–3° in its upper portion, so that the mean slope of ∼5.2° is at the high end of the slope angle range within the neighboring segments (Kopp *et al.* 2006). The frontal prism is characterized by low *Vp* velocity values ranging from 2 to 2.8 km s$^{-1}$. Further north, in the accretionary prism which extends from 105 to 185 km offsets, velocities increase from 2 km s$^{-1}$ below the sea floor to about 3.5 km s$^{-1}$ at a depth of 3–4 km bsf; the *Vp* velocity in the consolidated sediments in the deeper part of the accretionary prism (6 to 10 km depth) ranges from 3.5 to 5.0 km s$^{-1}$ at the top of the basement.

The accreted sediments forming the forearc high are resolved on both profiles, allowing for a 2.5-D interpretation of this area at the profiles crossing (Fig. 2). The velocity–depth distribution in the sediments is similar for both of the profiles, with *Vp* velocities starting at 2 km s$^{-1}$ and reaching 5 km s$^{-1}$ at the top of the basement at 8 km depth (for the forearc region, we assume the top of the basement to correspond to approximately 5 km s$^{-1}$ isocontour). However, the north–south striking profile suggests a semi-horizontal basement interface extending laterally for, at least, 40 km. This is in contrast to the observations along the east–west profile which reveals a rather undulating topography of the top of the basement, varying from 6 to 10 km depth. This observation can be explained in several ways. It is possible that the forearc crust is composed of several small-scale independent crustal fragments, and thus displays a blocky style of

basement. Another explanation would be to consider the subduction of the basement topographic relief located off profile P4–23, and thus unresolved on it. The presence of such features in the incoming oceanic crust would perturb and dynamically deform not only the overlaying sedimentary packages, but also affect the crustal edge of the backstop.

### 3.3 Forearc crustal structure

The forearc crust carrying a number of sedimentary basins is located further north, from ∼185 km offset and to the northern termination of the profile (Fig. 2). The depth of the basins ranges from ∼1200 to 1500 m, which is less than in the well-developed forearc basins to the east and to the west where the sediment infill reaches 3 km (Kopp *et al.* 2009a; Planert *et al.* 2010). The *Vp* velocity of the sediment in the basins ranges from 1.7 to 3.0 km $s^{-1}$ in the upper 1–1.5 km (Fig. 2). The velocities in the consolidated sediments above the basement increase from 3.5 to 5.0 km $s^{-1}$. The crystalline crust of the forearc displays *Vp* velocities ranging from 5.0 km $s^{-1}$ at the top (∼5 km depth) to 6.5–7.0 km $s^{-1}$ at the Moho. The northern segment of the profile (from ∼220 km offset) shows higher velocities in the lower crust, while in between 160 and 220 km offset the velocities in the lower crust do not exceed 6.5 km $s^{-1}$ (Fig. 2). For the same location (∼180 km offset) on the trench-parallel profile, lateral velocity variations in the lower forearc crust are even higher, reaching values up to 7.1 km $s^{-1}$ at 60 km offset of profile P-41 (unfortunately, the low signal-to-noise ratio and a complex 3-D ray propagation for most of the stations on this profile made reflection modelling debatable, especially for the plates interface). The forearc Moho shows minor undulations, as revealed by the tomography model. In the northern section, the Moho is located at a 18 km depth, deepening to ∼20 km at around 270 km offset, and then shallowing again to about 17 km at ∼320 km offset. It indicates that the thickness of the crystalline crust is in the range of 12–16 km. The results from the neighboring segments (111°E and 115°E) image the forearc Moho in a depth range of 14–18 km (Kopp *et al.* 2009b; Planert *et al.* 2010), in agreement with our results. Further to the north, the gravity modelling (Fig. 8) requires a sharp deepening of the Moho to a depth of at least 30 km underneath Java. Crustal deepening can be associated either with the transition to the island arc-like crustal block below Java, or with the presence of the Gondwana revenue as suggested by Smyth *et al.* (2007). Unfortunately, this section is not covered by the seismic data and, due to the non-uniqueness of the gravity modelling, cannot be reliably interpreted.

### 3.4 Oceanic mantle

The deep structure (below ∼20 km depth) of the profile was resolved mostly in the southern-central portion of the study area (Fig. 2). However, the model resolution is limited for the deep part (Fig. 5). The calculated *Vp* velocity values have an uncertainty of about $-7 + 3$ per cent due to the velocity averaging along the ray paths (Fig. 5). In the uppermost oceanic mantle, the velocities are estimated to be in the range from 7.5 to 7.9 km $s^{-1}$. The area of the lower seismic velocities is located between 85 and 170 km offset: it starts approximately below the trench and extends to a depth of at least 30 km where the resolution of our model diminishes. The velocities in the forearc mantle are lower as compared to the oceanic mantle; we observe the values of around 7.5–7.6 km $s^{-1}$ under the forearc Moho (Fig. 2). The calculated velocity structure of the forearc and the underlying mantle is in a good agreement with the results calculated for the adjacent segments offshore Lombok and Central Java around 110°E (Kopp *et al.* 2009b; Planert *et al.* 2010).

### 3.5 Backstop geometry and structure

The backstop edge is located at ∼160 km offset; it represents a near-vertical feature bounding the accretionary prism at depth. The forearc high pattern caused by the Roo Rise approach is unusual, as for the 'normal' oceanic subduction a continuous ridge-like forearc high structure is expected. This should be an effect caused by the oceanic plateau subduction. We speculate on possible scenarios for the structure of the forearc backstop which would explain the observed bathymetry (Fig. 1). Possible options are shown in Fig. 9.

Variant A is based on the geometry of the forearc backstop observed on the profiles to the west from this study, where the backstop gently dips towards the trench (Kopp & Kukowski 2003). The term backstop defines a region within a forearc that is characterized by an increased yield strength compared to the region trenchward of it and thus by its ability to support larger deviatoric stresses. The kinematic discontinuities which form a backstop may be 'static', as would be the case for the continental arc basement, or 'dynamic' and thus still deforming, though at a slow rate, as may be expected for compacted accreted material resulting from an earlier phase of accretion (Kopp & Kukowski 2003). In the latter case, the material located southward of the 'static' backstop would represent buoyant fragments of the oceanic plate, of the Roo Rise nature, which were detached from the plate and stacked over the static backstop (i.e. little-deforming continental arc basement, following Kopp & Kukowski (2003)). This scenario is valid under conditions that the oceanic crust, currently subducted below the accretionary complex, was as fractured as the segment currently observed at around trench, and that there were some elevated relief features that would have detached from the plate. In this case, the observed forearc high would correspond to the area of maximum stacking of such relief revenues against the static forearc backstop. This correlates with the location of the forearc highs and also explains the relatively shallow forearc basins, as they would experience uplift together with a lateral compression.

Variant B is based on the similarities of our study region to the Lesser Antilles subduction zone. The subduction of the large aseismic Tiburon ridge might be comparable by size and scale to the subduction of the Roo Rise. Following this analogy and the ideas of Bangs *et al.* (2003) and Christeson *et al.* (2003), we speculate on the other option for the backstop structure (Fig. 9b). In this case, the static forearc backstop geometry is similar to the one observed on the profile located eastwards from the study area, offshore Lombok (Planert *et al.* 2010). The observed forearc high then would be linked to the bending-related uplift of the forearc edge, caused by the presence of stacked fragments of the oceanic origin below it. The same conditions should be valid for this scenario as in option A. For this case, the location of the forearc high and its uplift are correlated with the uplift of the crystalline forearc edge.

The choice of any particular variant is governed by the geometry of the static forearc backstop at its exact location, which is not resolved in the study. However, both of the options would influence the geohazard potential for the area, including tsunami and earthquakes. The detailed assessment of the geohazards is outside of the scope of this study. Following, will provide some insight on the earthquake and tsunami potential of the region. In order to trigger a tsunami, a sufficient vertical movement of the seafloor is required. This can be achieved either by crustal movements on the

trust faults as a result of earthquake slip, or as a result of a submarine landslide, possibly triggered by an earthquake. The 2004 Sumatra earthquake and tsunami is an example of the large mega-thrust event where the major slip was accommodated on the trust faults, resulting in ∼14 m uplift (Sibuet *et al.* 2007). Similar settings are expected for the Chili and the Cascadia margins. The submarine landslides are the explanation for the tsunamis in the Atlantic region and other regions such as Papua New Guinea and Puerto Rico (ten Brink *et al.* 2009), which puts them into a special class of geohazard as the initiating earthquakes can be much smaller than in mega-thrust events. Offshore Java, where the frontal erosion causes the oversteepening of the frontal slope, any changes in the seismicity regime are of high importance. Both proposed crustal interpretations invoke local deformation of the backstop and the overlaying sediments and can lead to the formation of large laterally inhomogeneous stress gradients in the area, thus increasing the probability of rupture on the normal faults in the oceanic crust due to load as well as on thrust faults within the accretionary prism and within the seismogenic zone. It explains the observed increased level of the shallow seismicity clustered around 113°E (Fig. 1) and the dynamically caused perturbations of the basement top and associated forearc high. A similar seismicity pattern is observed in the Lesser Antilles subduction zone where the clustering of shallow seismicity is spatially correlated with the collision of the subducting aseismic ridge with the backstop (Christeson *et al.* 2003). Unfortunately, the lack of deep penetrating seismic reflection data imaging the internal structure of the observed crustal edge and the absence of local relocated seismicity leaves this question open for further research.

The northward shift of the active volcanic arc observed on Java (Fig. 1) can be correlated to the northward trench r advancing in the vicinity of the Roo Rise, approaching the trench. The presence of elevated bathymetric features associated with sea plateau subduction can cause the frontal erosion of the accretionary complex and thus the landward migration on the trench. Numerical modelling shows that it can be considered as an initial stage of the formation of a flat shallow subduction and ceasing of melt production (van Hunen *et al.* 2002; Gerya *et al.* 2009). Furthermore, a proposed Gondwana revenue (Smyth *et al.*, 2007), located in between the trench and Southern Java, can be also responsible for producing complex interaction processes within the subduction system, resulting in the northward volcanic arc propagation. The structure of this lithospheric block and the processes that it triggers are unclear and should be studied in order to understand the entire dynamics of this subduction margin.

Summarizing, we observe the complex subduction of abnormally thick oceanic crust under the rigid forearc crust. The accretionary complex is experiencing an inhomogeneous current uplift due to one of the proposed scenarios. The approach of the buoyant oceanic plateau to the trench causes active frontal erosion as well as internal deformation of the accreted sediments which, in turn, dynamically affects the tip of the forearc crust and the structure of the forearc basins. This complex deformation pattern has a strong effect on local seismicity and increases the geohazard risk for tsunamogenic seismic events.

## 4 CONCLUSION

The summary of our results is shown in Fig. 9. In the 113°E segment of the Java trench, we observe the approach of the oceanic plateau Roo Rise to the trench, and the effects it causes on the local subduction regime.

The Roo Rise is characterized by variable crustal thickness ranging from 18 to 12 km and shallowing towards Java. It extends laterally for at least 70 km within our profile (Fig. 2). Based on the bathymetric data and its link to the presence of a deep compensating crustal root, the thickened oceanic plateau crust with an average thickness of about 15 km is expected to cover an area of approximately 100 000 km$^2$ (200 km × 500 km) offshore Central-Eastern Java. The transition to normal oceanic crust is not well defined, but the plateau can extend into the subduction system up to 60 km northward from the trench.

The structure of the upper crust of the incoming oceanic plate shows a high degree of fracturing in its top section. This fracturing is clearly visible in the high-resolution bathymetry and MCS transect down to 2 km below the top of the crust (Fig. 8). It is possible that the crust is cut by faults even to a greater depth, as indicated by the low mantle velocities that require fluid percolation (Carlson & Miller 2003), and by an increased level of shallow crustal seismicity (Abercrombie *et al.* 2001; Bilek & Engdahl 2007).

Within our profiles, we do not recover any direct evidence for the presence of the bathymetric features on the oceanic plate currently present below the accretionary prism. Depth variations of the basement observed on the trench-parallel profile, may serve as evidence for bathymetric features associated to the RooRise.

Gravity modelling requires a sharp crustal thickness increase below Java. As the region is not covered with seismic data, we can only speculate on the origin of this crustal structure. The thick crust can be a part of the Gondwana revenue as suggested by Smyth *et al.* (2007).

The approach of the Roo Rise to the trench has strong effects on the local seismicity setting. The geohazard risks should be reconsidered as this segment of the margin has an increased probability for tsunamogenic earthquakes.

## ACKNOWLEDGMENTS

We would like to thank Cpt. Meyer and the crew of R/V Sonne and the SINDBAD Working group for their enormous help in collecting and processing of the data. We express great gratitude to Jun Korenaga for the discussion of seismic tomography and the Tomo2D code. We highly appreciate the reviews and comments from Saskia Goes and Gail Christeson, which improved the paper. We would like to extend special thanks to Greg Houseman and Alessandro Forte for fruitful discussions. The SINDBAD project is funded by the German Federal Ministry of Education and Research (BMBF) (grants 03G0190A and 03G0190B). Special thanks to Petersen-Stiftung foundation for their funding to complete this study.

## REFERENCES

Abercrombie, R., Antolik, M., Felzer, K. & Ekström, G., 2001. The 1994 Java tsunami earthquake: slip over a subducting seamount, *J. geophys. Res.,* **106,** 6595–6607.

Bangs, N.L., Christeson, G.L. & Shipley, T.H., 2003. Structure of the Lesser Antilles subduction zone backstop and its role in a large accretionary system, *J. geophys. Res.,* **108**(B7), doi:10.1029/2002JB002040.

Bialas, J. & Flueh, E.R., 1999. Ocean bottom seismometers, *Sea Technol.,* **40**(4), 41–46.

Bilek, S.L. & Engdahl, E.R., 2007. Rupture characterization and aftershock relocations for the 1994 and 2006 tsunami earthquakes in the Java subduction zone, *Geophys. Res. Lett.,* **34,** L20311.

Carlson, R.L. & Herrick, C.N., 1990. Densities and porosities in the oceanic crust and their variations with depth and age, *J. geophys. Res.,* **95,** 9153–9170.

Carlson, R.L. & Miller, D.J., 2003. Mantle wedge water contents estimated from seismic velocities in partially serpentinized peridotites, *Geophys. Res. Lett.,* **30**(5), 1250, doi:10.1029/2002GL016600.

Christensen, N.I. & Mooney, W.D., 1995. Seismic velocity structure and composition of the continental crust: a global view, *J. geophys. Res.,* **100,** 9761–9788.

Christeson, G.L., Bangs, N.L. & Shipley, T.H., 2003. Deep structure of an island arc backstop, Lesser Antilles subduction zone, *J. geophys. Res.,* **108**(B7), doi:10.1029/2002JB002243.

Coffin, M.F. & Eldholm, O., 1994. Large igneous provinces: crustal structure, dimensions, and external consequences, *Rev. Geophys.,* **32**(1), 1–36, doi:10.1029/93RG02508.

Curray, J.R., Shor, G.G., Rait, R.W. & Henry, W., 1977. Seismic refraction and reflection studies of crustal structure of the eastern Sunda and western Banda Arcs, *J. geophys. Res.,* **82,** 2479–2493.

Davy, B., Hoernle, K. & Werner, R., 2008. Hikurangi Plateau: crustal structure, rifted formation, and Gondwana subduction history, *Geochem. Geophys. Geosyst.,* **9,** Q07004, doi:10.1029/2007GC001855.

DeMets, C., Gordon, R.G., Argus, D.F. & Stein, S., 1994. Effect of recent revisions to the geomagnetic reversal time-scale on estimates of current plate motions, *Geophys. Res. Lett.,* **21**(20), 2191–2194.

Gerya, T.V., Fossati, D., Cantieni, C. & Seward, D., 2009. Dynamic effects of the aseismic ridge subduction: numerical modeling, *Eur. J. Mineral.,* **21**(3), 649–661.

Hall, R., 2002. Cenozoic geological and plate tectonic evolution of SE Asia and the SW Pacific: computer-based reconstructions, model and animations, *J. Asian Earth Sci.,* **20,** 353–434.

Hall, R. & Smyth, H.R., 2008. Cenozoic arc processes in Indonesia: identification of the key influences on the stratigraphic record in active volcanic arcs, *Geol. Soc. Am. Spec. Pap.,* **436,** 27–54.

Hamilton, W., 1979. Tectonics of the Indonesian region. *U. S. Geol. Surv. Prof. Pap.,* **1078,** 308–335.

Hamilton, W., 1988. Plate tectonics and island arcs, *Geol. Soc. Amer. Bull.,* **100,** 1503–1527.

Hampel, A., Kukowski, N., Bialas, J., Hebscher, C. & Heinbockel, R., 2004. Ridge subduction at an erosive margin: the collision zone of the Nazca Ridge in southern Peru, *J. geophys. Res.,* **109,** B02101, doi:10.1029/2003JB002593

Kopp, H. & Kukowski, N., 2003. Backstop geometry and accretionary mechanics of the Sunda Margin, *Tectonics,* **22**(6), 1072, doi:10.1029/2002TC001420.

Kopp, H. *et al*. 2009b. *Convergent Margin Structure and Tectonics of the Java Subduction Zone (105°E-122°E), EOS,* Vol. 90, Number 52, 29 December 2009, Fall Meet. Suppl. Abstract T33B-1916.

Kopp, H., Flueh, E.R., Klaeschen, D., Bialas, J. & Reichert, C., 2001. Crustal structure of the central Sunda margin at the onset of oblique subduction, *Geophys. J. Int.,* **147,** 449–474.

Kopp, H., Flueh, E.R., Papenberg, C. & Klaeschen, D., 2004. Seismic investigations of the O'Higgins Seamount Group and Juan Fernandez Ridge: aseismic ridge emplacement and lithosphere hydration, *Tectonics,* **23,** TC2009, doi:10.1029/2003TC001590.

Kopp, H., Flueh, E.R., Petersen, C.J., Weinrebe, W., Wittwer, A. & Meramex Scientists., 2006. The Java margin revisited: evidence for subduction erosion off Java, *Earth planet. Sci. Lett.,* **242,** 130–142.

Kopp, H., Hindle, D., Klaeschen, D., Oncken, O. & Scholl, D., 2009a. Anatomy of the western Java plate interface from depth-migrated seismic images, *Earth planet. Sci. Lett.,* doi:10.1016/j.epsl.2009.09.043.

Kopp, H., Klaeschen, D., Flueh, E.R. & Bialas, J., 2002. Crustal structure of the Java margin from seismic wide-angle and multichannel reflection data, *J. geophys. Res.,* **197**(B2), doi:10.1029/2000JB000095.

Korenaga, J., Holbrook, S., Kent, G., Kelemen, P., Detrick, R.S., Larsen, H.-C., Hopper, J.R. & Dahl-Jensen, T., 2000. Crustal structure of the southeast Greenland margin from joint refraction and reflection seismic tomography, *J. geophys. Res.,* **105,** doi:10.1029/2000JB900188.

Lueschen, E., Mueller, C., Kopp, H., Engels, M., Lutz, R., Planert, L., Shulgin, A. & Djajadihardja Y., 2010. Structure, evolution and tectonic activity at the Eastern Sunda forearc, Indonesia, from marine seismic investigations, *Tectonophysics,* in press, doi:10.1016/j.tecto.2010.06.008.

Mason, W.G., Moresi, L., Betts, P.G. & Miller, M.S., 2010. Three-dimentional numerical models of the influence of a buoyant oceanic plateau on the subduction zones, *Tectonophysics,* **483,** doi:10.1016/j.tecto.2009.08.021.

Masson, D.G., 1991. Fault patterns at outer trench walls, *Mar. geophys Res.,* **13,** 209–225.

Masson, D.G., Parson, L.M., Milsom, J., Nichols, G., Sikumbang, N., Dwiyanto, B. & Kallagher, H., 1990. Subduction of seamounts at the Java Trench: a view with long-range sidescan sonar, *Tectonophysics,* **185,** 51–65.

Moore, G.F., Curray, J.R., Moore, D.G & Karig, D.E., 1980. Variations in geologic structure along the Sunda Fore Arc, northeastern Indian Ocean, in *The Tectonic and Geologic Evolution of Southeast Asian Seas and Islands,* Vol. **23**, pp. 145–160, eds Hays, D.E., Geoph. Mon.

Mueller, C. *et al*. 2008. From subduction to collision: the Sumba-Banda Arc transition, *EOS, Trans. Am. geophys. Un.,* **89,** 49–50.

Newcomb, K.R. & McCann, W.R., 1987. Seismic history and seismotectonics of the Sunda Arc, *J. geophys. Res.,* **92**(B1), 421–439.

Planert, L., Kopp, H., Lueschen, E., Mueller, C., Flueh, E.R., Shulgin, A., Djajadiharja, Y. & Krabbenhoeft, A., 2010. Lower plate structure and upper plate deformational segmentation at the Sunda-Banda arc transition, *J. geophys. Res.,* **115,** B08107, doi:10.1029/2009JB006713.

Scherwath, M. *et al*. 2010. Fore-arc deformation und underplating at the northern Hikurangi margin, New Zealand, *J. Geol. Res.* **115,** B06408, doi:10.1029/2009JB006645.

Scholz, C.H. & Small, C., 1997. The effect of seamount subduction on seismic coupling, *Geology,* **25,** 487–490.

Shulgin, A. *et al*. 2009. Sunda-Banda arc transition: incipient continent-island arc collision (northwest Australia), *Geophys. Res. Lett.,* **36,** L10304, doi:10.1029/2009GL037533.

Sibuet, J-C. *et al*. 2007. 26th December 2004 great Sumatra-Adamant earthquake: co-seismic and post-seismic motions in northern Sumatra, *Earth planet. Sci. Lett.,* **263,** doi:10.1016/j.epsl.2007.09.005.

Smyth, H.R., Hamilton, P.J., Hall, R. & Kinny, P.D., 2007. The deep crust beneath island arcs: inherited zircons reveal a Gondwana continental fragment beneath East Java, Indonesia, *Earth planet. Sci. Lett.,* **258,** 269–282.

ten Brink, U.S., Lee, H.J., Geist, E.L. & Twichell, D., 2009. Assesment of tsunami hazard to the U.S. East Coast using relationships between submarine landslides and earthquakes, *Mar. Geol.,* **264,** doi:10.1016/j.margeo.2008.05.011.

Tregoning, P. *et al*. 1994. First geodetic measurement of convergence across the Java Trench, *Geophys. Res. Lett.,* **21**(19), 2135–2138.

van Hunen, J., van den Berg, A.P. & Vlaar, N.J., 2002. On the role of subducting oceanic plateaus in the development of shallow flat subduction, *Tectonophysics,* **352,** 317–333.

Werner, R., Hauff, F. & Hoernle, K., 2009. RV Sonne. Cruise report SO-199 CHRISP. Christmas Island Seamount Province and the Investigator Ridge: age and causes of intraplate volcanism and geodynamic evolution of the south-eastern Indian ocean, **25,** 1614–6298.

White, R.S., McKenzie, D. & O'Nions, R.K., 1992. Oceanic crustal thickness from seismic measurements and rare earth element inversions, *J. geophys. Res.,* **97,** 19 681–19 715.

Wiener, N., 1949. *Extrapolation, Interpolation, and Smoothing of Stationary Time Series,* John Wiley and Sons, New York.

Yamazaki, T. & Okamura, Y., 1989. Subducting seamounts and deformation of overriding forearc wedges around Japan, *Tectonophysics,* **160,** 207–229.

## SUPPORTING INFORMATION

Additional Supporting Information may be found in the online version of this article:

**Figure S1**. The comparison of all the picked traveltimes available for the tomographic inversion for the two profiles. The picked traveltimes are shown by black dots for the refracted phases and green dots for the reflected phases. Corresponding computed traveltimes through our final models are shown by red and blue dots, for the refracted and reflected phases, respectfully. Top plot is the fit comparison for the N–S profile, bottom—for the E–W profile. Note, the identical distance and timescale for both plots.

Please note: Wiley-Blackwell are not responsible for the content or functionality of any supporting materials supplied by the authors. Any queries (other than missing material) should be directed to the corresponding author for the article.

# 14

Kopp, H., 2010.

**The Java Convergent Margin: Structure, Deformation and Subduction Processes.**

In: Hall, R. (edt) The SE Asian gateway: history and tectonics of Australia-Asia collision. Geol. Soc. London Spec. Publ., in press.

# The Java Convergent Margin: Structure, Seismogenesis and Subduction Processes

**Heidrun Kopp**
IFM-GEOMAR Leibniz-Institute of Marine Sciences
in: **The SE Asian gateway: history and tectonics of Australia-Asia collision**
Geological Society of London Special Publication, October 2010, in press.

**Abstract**
The Java margin is characterized by a distinct variation in lower to upper plate material transfer and recurring catastrophic tsunamogenic earthquakes. Both processes are closely linked to the subduction of oceanic basement relief resulting in varying degrees of forearc deformation. Tomographic models of refraction seismic profiles and reflection seismic lines in combination with high-resolution multibeam bathymetric data reveal the variability in the deep structure and deformation of the Java forearc. Shallow subduction processes are goverened by the sediment supply in the trench as well as by the nature and fabric of the oceanic lithosphere. The deep structure of the forearc reveals a shallow upper plate crust-mantle transition, present along the entire Java margin section. The serpentinized forearc mantle wedge governs the depth extent of the seismogenic zone here, which is narrower compared to its Sumatran analog. In addition, offshore central Java, high relief oceanic basement features potentially act as asperities as well as barriers to seismic rupture, limiting the possible magnitude of subduction thrust earthquakes. However, the potential for geohazards, in particular tsunamis, is high along the entire margin. This results from tsunamogenic earthquakes, ubiquitous splay faults and potentially tsunamogenic landslides, which further increase the risk of future tsunamis.

This contribution reviews studies of the Java subduction zone (Fig. 1) with a special emphasis on the neotectonic processes and structural evolution of the forearc using tomographic images based on seismic refraction data (Fig. 2) and multibeam bathymetry (Fig. 3). Following introductory remarks on the tectonic setting, seismicity and geophysical data base, the observational and interpretative information gained from these studies will be presented area-specific for each tectonic segment along the margin. Going from west to east, these first-order segments are defined based on the dominating material transfer and nature of the lower plate, i.e. sediment accretion offshore Sunda Strait and western Java, forearc erosion offshore central-eastern Java, and continent-island arc collision offshore Sumba Island. A regional summary is presented in the conclusions.

## Tectonic setting

The Java trench forms the eastern section of the Sunda deep-sea trench and is the site where the Indo-Australian oceanic lithosphere subducts beneath the Sundaland block of Indonesia. It straddles the island of Java and the Lesser Sunda islands of Bali, Lombok and Sumbawa (Fig. 1). The Java margin is bound in the west by the transtensional regime of the southern Sunda Strait (Lelgemann et al. 2000). The Sunda Strait marks the hinge line and passage from the trench-perpendicular convergence off Java to the oblique subduction offshore Sumatra . In the east, the Java trench terminates at 121°E where it merges into the Timor trough (Audley-Charles 1975, 2004; Hall & Smyth 2008). The transition from oceanic subduction along the Java trench to continent-island arc collision along the Timor trough of the Banda arc occurs south of Sumba Island, where continental crust is colliding with the forearc (Hamilton 1979) (Fig. 1).

The Indo-Australian plate currently moves at 6.7 cm/a in a direction N11°E off western Java and thus almost normal to the trench (Tregoning et al. 1994) (Fig. 1). Convergence speed slightly increases from western Java towards the east, however, at a very subtle rate, reaching ~7 cm/a off Bali (Simons et al. 2007) and has been active since the Eocene (Hall & Smyth 2008). A local source tomography based on recordings over a period of almost six months from more than 100 seismic stations on Java images the steep dip angle of the subducting slab, reaching approximately 70° underneath the island (Koulakov et al. 2007).

The age of the incoming plate increases from Late Cretaceous offshore Sunda Strait (105°E) to Late Jurassic at 120°E. Accordingly, water depth in the trench increases from ~6 km off the Sunda Strait to more than 7 km off Lombok and Sumbawa in the east and correlates with the decrease in sediment supply from ~1500 m off western Java to the starved trench segments along the eastern Java trench.

The Java margin exhibits two prominent features on the incoming Indo-Australian plate: 1) the Christmas Island Seamount Province including the Roo Rise and 2) the Argo Abyssal Plain (Fig. 1). The Christmas Island Seamount Province forms a broad, irregular topographic swell of 135-140 Ma old oceanic lithosphere off central Java (Moore et al. 1980; Mueller et al. 1997) and is dotted with numerous seamounts. It extends in an east-west direction from 95°E to 115°E, where it terminates abruptly. The evolution of the Christmas Island Seamount Province remains enigmatic and is associated with a series of individual magmatic events. Rock sampling resolved varying formation times across the volcanic province without a clear formation time trend (Werner et al. 2009). The eastern segment of the Christmas Island Seamount Province

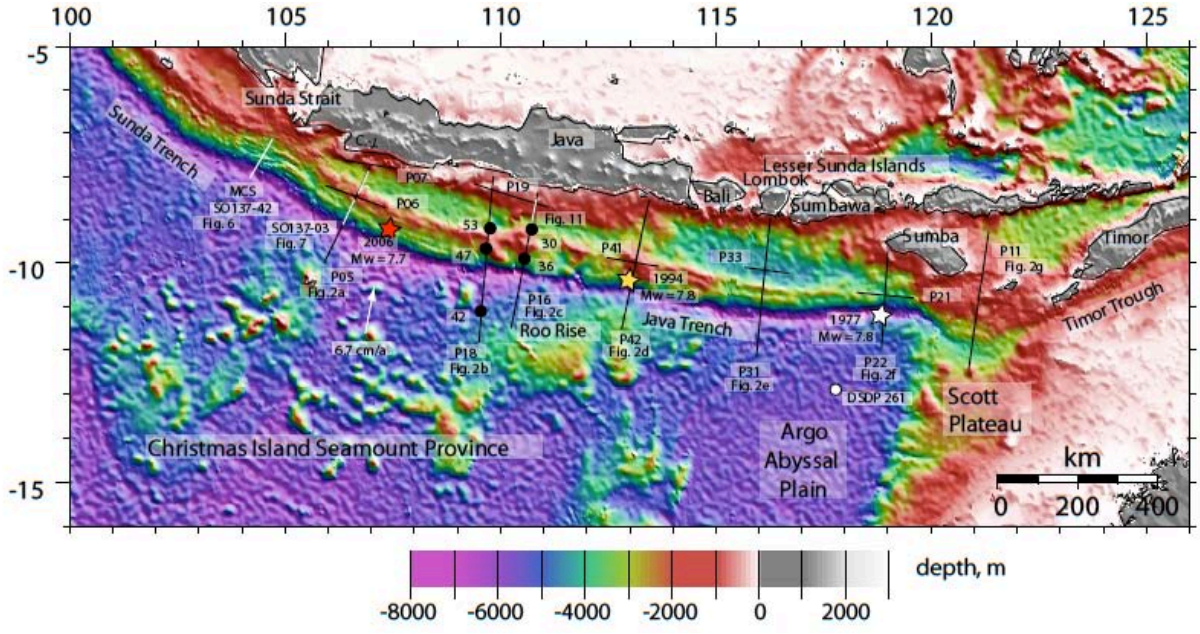


***Figure 1:*** *Morphology of the Java margin based on satellite altimetry data (Smith & Sandwell 1997). A large bivergent accretionary wedge is expressed as a continuous bathymetric ridge fronting the Java forearc basin offshore western Java. This ridge structure is broken and highly deformed offshore central Java, where the oceanic Roo Rise is colliding with the margin. The eastern Java trench offshore Bali to Sumba is characterized by the subduction of smooth oceanic crust of the Argo Abyssal Plain. The transition from oceanic subduction to continent-island arc collision occurs south of Sumba where the Scott plateau enters the trench. Black lines show wide-angle refraction profiles. Black dots show locations of ocean bottom instruments displayed in Figures 4, 5, 8, 9, 12. White lines show extent of MCS data shown in Figures 6, 7, and 11. Stars denote earthquake hypocenters of 1977 (white), 1994 (yellow) and 2006 (red). C.-J.: Ciletuh-Jampang block.*

features the oceanic Roo Rise (Fig. 1), a 400 km wide plateau rising 2-3 km above the abyssal plain. Dredged rock samples from the plateau retrieved strongly altered olivine phyric lava fragments with Mn-crusts (Werner et al. 2009). The northern flank of the Roo Rise is currently entering the trench south of eastern Java. Isolated volcanic summits on the plateau and adjacent to it represent high relief gradient features which upon subduction cause frontal erosion of the forearc south of central Java (Masson et al. 1990). A tomographic study of passive and active seismic data images the complex crustal structure of the forearc, segmented into distinct blocks (Wagner et al. 2007).

The second prominent feature in the oceanic domain is the Argo Abyssal Plain, with mean water depth around 5500 m (Fig. 1) and a crustal age of 160 Ma (Mueller et al. 1997). Though large-scale topographic features are not observed on the Argo Abyssal Plain, the seafloor nonetheless exhibits a distinct structure, comprising the original spreading fabric and a pervasive pattern of trench parallel normal faults where the plate bends into the trench (Masson 1991). The horst-and-graben structures on the outer trench wall show a maximum throw of 500 m. Individual fault segments reach lengths of more than 60 km and cut deep into the oceanic basement (Lueschen et al. 2010). 530 m of sediment on the Argo Abyssal Plain have been drilled in DSDP site 261 before reaching Late Jurassic oceanic basement (Heirtzler et al. 1974) on which Cretaceous claystones, Upper Miocene and Pliocene nannofossil oozes and Quaternary radiolarian clays have been deposited. In the east, the Argo Abyssal Plain is bordered by a continental promontory of the Australian lithosphere: the Scott Plateau (Fig. 1) governs subduction zone processes at the transition from the Sunda margin to the Banda arc.

***Recent earthquake activity***

The Java trench was the site of three major earthquakes (Mw≥7.0) in the past decades (Fig. 1). In 1977, a Mw = 8.3 normal fault earthquake ruptured the underthrusting plate (Spence 1986; Lynnes & Lay 1988) and caused a tsunami on the Lesser Sunda islands and Australia with maximum run-up heights of 8 m on Sumbawa (Kato & Tsuji 1995). The Mw=7.8 event of 1994 was a megathrust rupture, which occurred offshore eastern Java (Ammon et al. 2006; Bilek & Engdahl 2007). The triggered tsunami reached run-up amplitudes of 5-8 m along the southern coast of Java, causing more than 700 casualties. Similarly, in 2006, a Mw=7.7 megathrust earthquake offshore western Java (Fig. 1) triggered a deadly tsunami with maximum run-up heights of 20 m (Fritz et al. 2007). Both thrust events show a rupture pattern characteristic of tsunami earthquakes (Kanamori 1972; Bilek & Engdahl 2007) and both events display aftershock sequences dominated by normal faulting, suggesting relatively complete stress release on the interplate thrust (Ammon et al. 2006). The influence of the plate structure at depth, particularly regarding

subducted basement features, has been discussed for the 1994 event, for which slip over a subducted seamount was proposed to have triggered the earthquake (Abercrombie et al. 2001). This model is still debated for the 2006 event (Bilek & Engdahl 2007).

***Geophysical data***

Three major marine experiments were conducted on the Java margin since 1997 using the German RV SONNE as platform. A total of 289 ocean bottom stations (hydrophones and seismometers: OBH/S (Bialas & Flueh 1999)) were deployed along 13 transects. In 1997/1998, the GINCO cruises focused on the transition zone between frontal and oblique subduction off the Sunda Strait and acquired three coincident seismic refraction /reflection profiles offshore western Java (P05, P06, P07) (Kopp et al. 2001; Schlueter et al. 2002). It was followed by the MERAMEX cruises off central Java in 2004 during which two long refraction dip lines (P16 and P18) were shot from the oceanic lithosphere to the continental slope in addition to a coast-parallel strike-line (P19) (Fig. 1). During this onshore-offshore or amphibious project, 100 landstations were deployed onshore Java for a period of 120 days (Koulakov et al. 2007; Wagner et al. 2007). The eastern section of the margin was subsequently investigated during the SINDBAD experiment in 2006 and was covered by four coincident refraction/reflection dip lines (P42, P31, P22, and P11) and three strike lines (P41, P33, P21) located between offshore eastern Java and east of Sumba island, including the transition from oceanic subduction to continent-island arc collision.

Figure 2 displays the velocity-depth models of all acquired trench perpendicular refraction dip lines and serves as a basis for the following discussion of individual margin segments. All models were achieved by tomographic inversion of the refraction data (Shulgin et al. 2009, 2010; Planert et al. 2010; Wittwer 2010), except for the GINCO profile for which forward modeling by raytracing for the broadly spaced instruments was conducted (Kopp et al. 2001). Figure 4 shows an ocean bottom seismometer recording displaying typical phases from stations near trench locations on the upper plate: Pn is the refraction through the upper mantle, PmP is the reflection from the crust-mantle boundary, Poc is the refraction through the oceanic crust, PtocP is the reflection from the top of the oceanic crust and Psed denotes sediment phases. Pg forearc is the refraction through the forearc crust. The information contained in the seismic record sections thus returns velocity data for the different margin units from the sedimentary cover to the upper mantle.

The bathymetry data (Fig. 3) were acquired during the MERAMEX and SINDBAD experiments using RV SONNE's Simrad multibeam echosounder system, which provides accurate depth measurements and bathymetric mapping in areas at depths down to 11000 m.

**Offshore Sunda Strait and western Java: Sediment accretion**

***Observations***

Along the western margin segment (longitudes 105°E to 110°E), the incoming oceanic crust is 7.5-8.5 km thick with velocities typical of mature oceanic crust, increasing from 4.7 km/s at the basement to 7.2 km/s at the crust-mantle boundary. Upper mantle velocities are in the order of 7.8-8.0 km/s as documented by Pn mantle phases recorded by the ocean bottom seismometers (e.g. station OBS 42 on line P18 in Figure 5).

The morphology of the offshore forearc of western Java is dominated by a massive forearc high above the underthrusting plate (Fig. 2, panels a and b). The tectonic features observed here include the sediment-filled deep-sea trench, an actively accreting prism and mature forearc basin. They are morphological manifestations of the accretionary regime continuous to offshore Sumatra (Kopp et al. 2008), where the forearc high is subaerially exposed on the forearc islands. Offshore Sunda Strait, the topographic expression of the forearc high is subdued as a result of the Neogene transtensional tectonics and the increasing trench-parallel slip component towards Sumatra (Huchon & Le Pichon 1984; Malod et al. 1995). Malod & Kemal (1996) estimated about 50-70 km of extension in the Sunda Strait during the Pliocene (Diament et al. 1992).

The internal architecture of the forearc is characterized by multiple kinematic boundaries between the trench and Java continental slope. The deformation front marks the transition from the trench to the frontal prism which then transitions into the Neogene accretionary prism, that rapidly increases in thickness. In Figure 6, an approximately 0.5 km thick sheet of trench sediment is underthrust below the frontal prism. A similar décollement zone is also observed on profile P05 (Kopp et al. 2009), though discontinuous due to subducted seamounts of 1-2 km height attached to the oceanic crust (Fig. 7). This distinct lower plate relief, which is ubiquitous along the Java margin (Masson et al. 1990), potentially breaches the subduction channel and is in contact with the upper plate.

A pronounced megasplay or backstop thrust separates the Neogene prism from the Paleogene prism (Figs 6 and 7). Seismic velocities increase from the Neogene prism to the older, more consolidated material of the Paleogene prism. Station OBH 47 on profile P18 (Fig. 8) documents this increase in seismic velocities in the Pfp and Pg phases. The Paleogene prism is covered by a slope apron with seismic velocities not exceeding 2.5 km/s (Fig. 2, panels a and b). This unit displays little permanent deformation. During the GINCO cruise, Pliocene to recent sediments were sampled at various locations in the forearc basin and on the forearc high (Beiersdorf 1999). Samples retrieved hemipelagic muds with intercalated turbidites and dacitic to rhyolithic ash layers. Dredge samples from outcrops of the

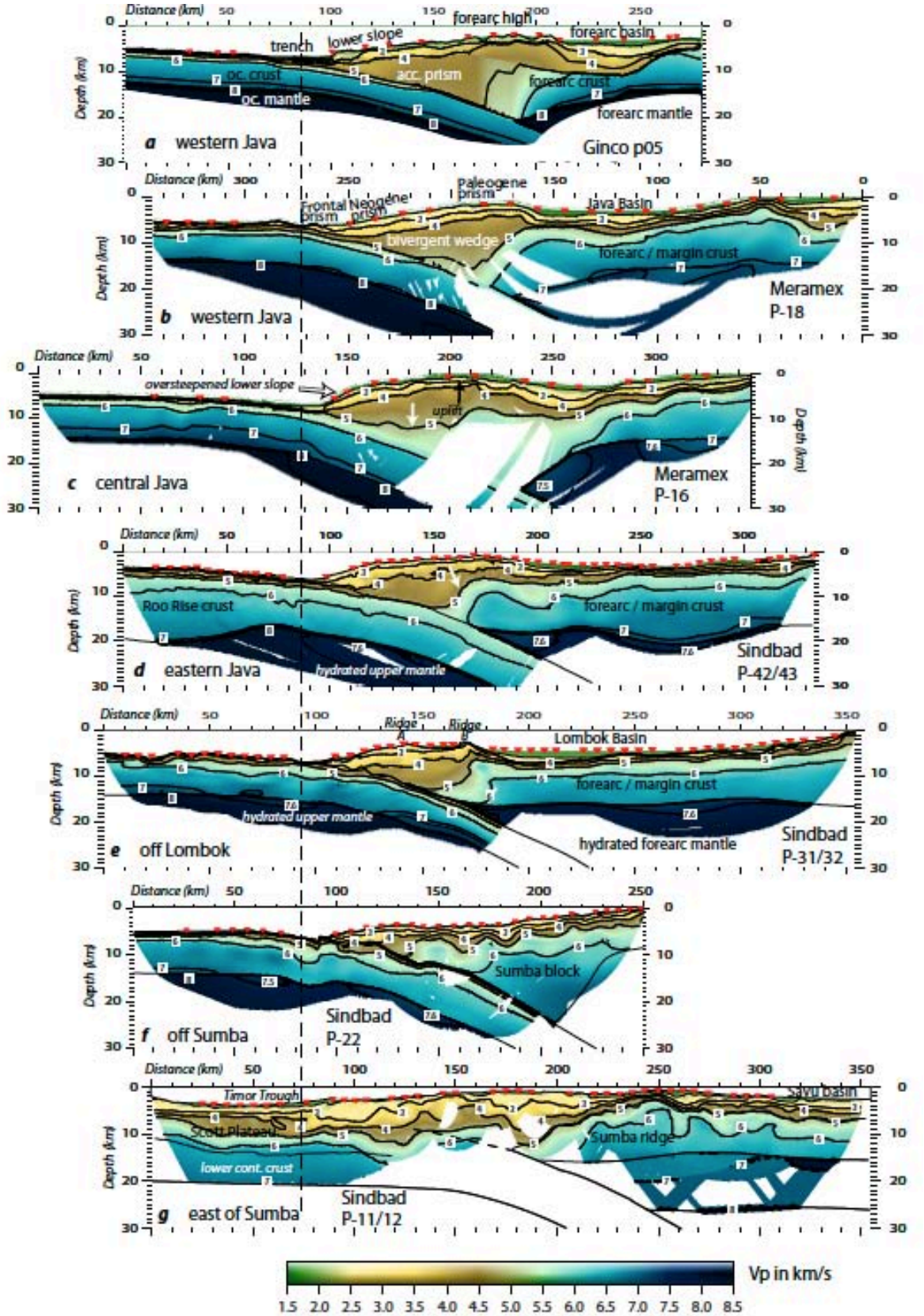


***Figure 2.*** *Tomographic images and velocity-depth distribution along seven refraction seismic dip lines crossing the forearc between western Java and east of Sumba island. The profiles document the variation from the accretionary domain (a and b) to the erosional seamount/plateau subduction regime off central to eastern Java (c and d). To the east, the transition from oceanic subduction offshore Lombok (e)) to continent-island arc collision (f and g) occurs. All profiles west of Sumba show a shallow hydrated upper plate mantle, which limits the downdip extent of the seismogenic zone. Profiles are approximately aligned along the vertical stippled line. Vertical exaggeration in all profiles is 2.5.*

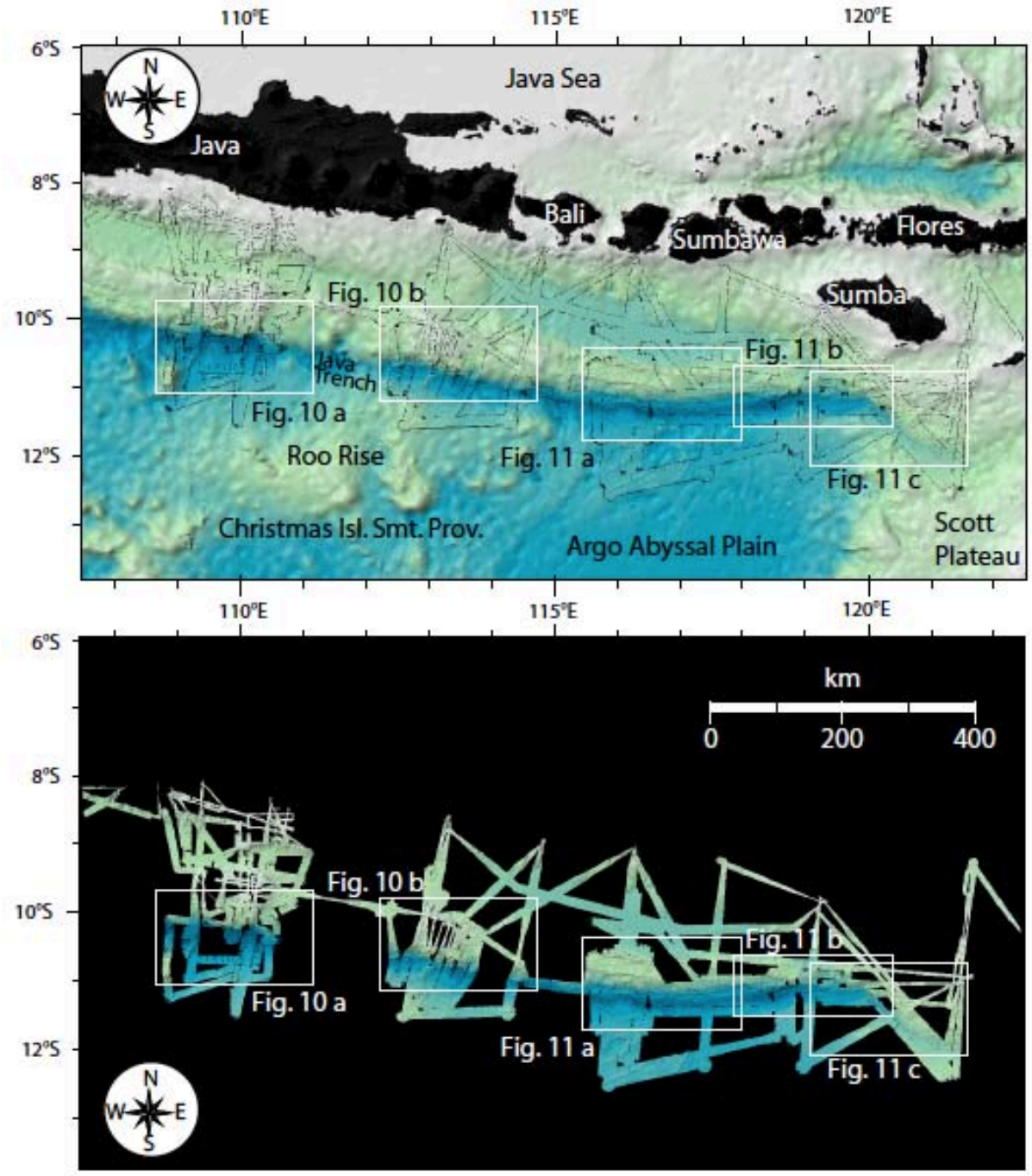


***Figure 3.*** *High-resolution seafloor bathymetric mapping along the Java margin. The upper panel shows the grid of swath data underlain by global bathymetry; the lower panel displays the high resolution data coverage. Full coverage was achieved along the deformation front and lower trench offshore Lombok, Sumbawa and Sumba. RV SONNE's EM120 multibeam echosounder system sends successive frequency-coded acoustic signals. Data acquisition is based on successive emission-reception cycles of this signal. The reception is obtained from 191 beams, with the footprint of a single beam of a dimension of 2° by 2°. Achievable swath width on a flat bottom is up to six times the water depth dependent on the character of the seafloor.*

accretionary prism revealed that they consist of silty and micaceous mud and tectonised mudstone as well as of arenitic limestone and calcareous sandstone (Beiersdorf 1999). Unfortunately, rock dredge or drill samples have not been recovered from the core of the forearc high, so that its composition must be inferred from seismic velocities.

Offshore western Java, the Paleogene prism fronts the Java forearc basin (Fig. 7). The Java basin is expressed as an elongated, 500 km long subsiding belt with an average water depth of 3500 m. Sediment thickness of the basin infill reaches 4 km (line GINCO p05, Fig. 2), decreasing towards the basin fringe (line Meramex P18, Fig. 2). The basin is underlain by a unit characterized by seismic velocities rapidly increasing from 5.5 km/s

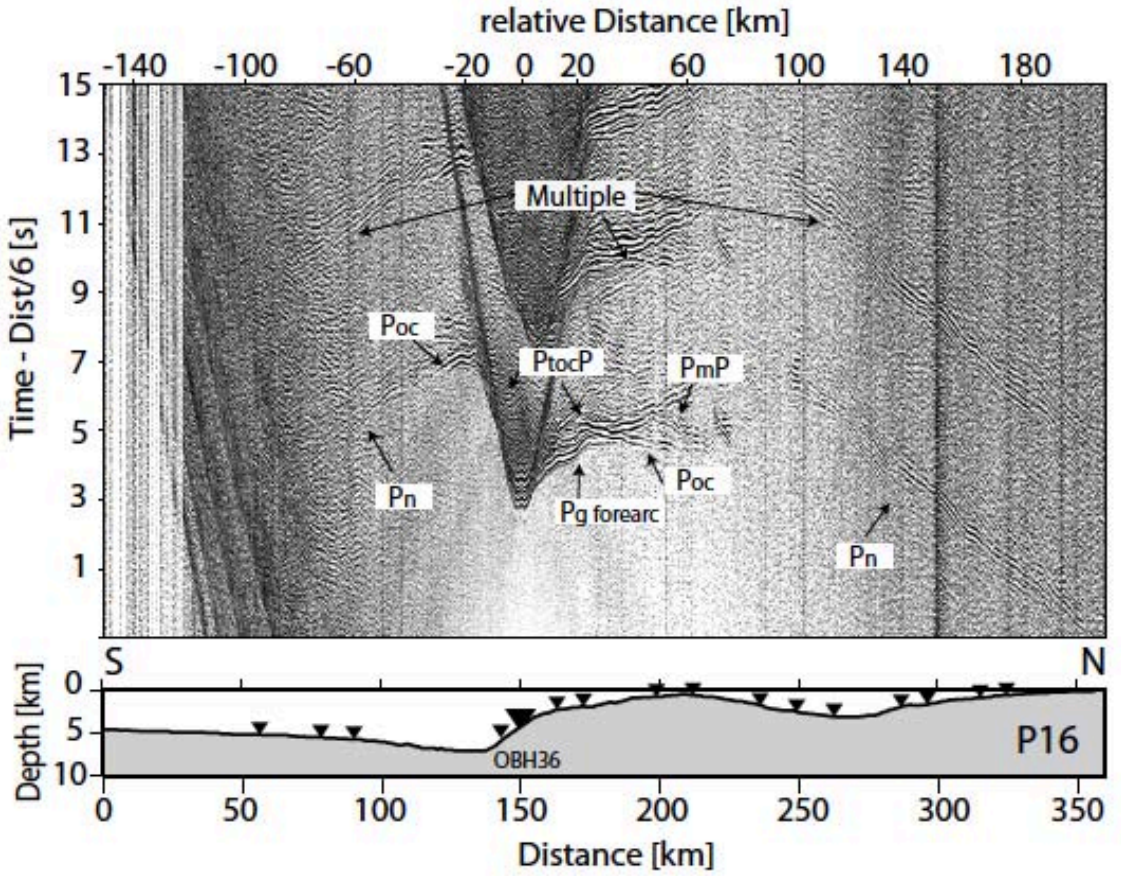


***Figure 4.*** *Data example of an ocean bottom hydrophone (OBH) located on the lower slope off central Java on profile P16. Phase nomenclature is as follows: Pg refraction through forearc crust, Poc refraction through oceanic crust, Pn refraction through upper mantle, PtocP reflection from oceanic basement, PmP Moho reflection.*

to values larger than 6 km/s (Fig. 2). OBH 53 is situated on the northern rim of the forearc high on line P18 and records phases through the Paleogene prism as well as through the forearc crust and mantle (Fig. 9). A number of stations record the forearc basement, which shows an ophiolitic character. The basement is exposed in western Java, where outcrops of peridotites, gabbros, pillow basalts and serpentinites are observed (Sukamto 1975; Schiller et al. 1991; Susilohadi et al. 2005). This Cretaceous-Paleocene complex is imaged underneath the forearc basin as a seaward dipping unit with the crust-mantle boundary located at approximately 15 km depth (Figs. 2 (panels a and b) and 7). It is bounded to the northwest by the Cimandiri fault zone, which cuts the Java forearc basin at a direction N70.8°E (Susilohadi et al. 2005) and is traced onshore along the Cimandiri river near Pelabuhan Ratu (Dardji et al. 1994).

***Interpretations***

At the deformation front, trench sediments are offscraped from the oceanic basement and transferred to the upper plate (Figs. 6 and 7). The change from tensional to compressional stress within the trench initiates thrust faulting and accretion of material to the lower slope. Discrete frontally accreted imbricate thrust slices and compressional folding are characteristic of this margin segment (Kopp et al. 2009) (Figs 6 and 7). The imbricate thrust belt and detachment folds form the frontal prism sandwiched between the trench and the Neogene accretionary prism (Kopp et al. 2001, 2002). The frontal prism forms the apex of the upper plate wedge and consists of frontally accreted, fluid-rich and thus mechanically weak material (von Huene et al. 2009). It is within the frontal prism that tectonic addition of trench sediment fill occurs by uplift displacement along the frontal thrust above the décollement (Figs. 6 and 7).

The imbricate thrust zone of the Neogene prism is primarily composed of trench sediment transferred from the frontal prism (Figs. 6 and 7). The outer Neogene prism pronouncedly contrasts in style from the inner, less compressive Paleogene prism (Kopp et al. 2001, 2002; Schlueter et al. 2002) (Fig. 7). This contrast in style has been related to the seismogenic behaviour of the subduction fault at depth (Wang & Hu 2006), predicting that the inner wedge never experiences compressive failure, thus providing a stable tectonic regime. The transition from the active Neogene prism to the tectonically more quiescent Paleogene prism occurs along a distinct zone, where a splay fault system offsets the seafloor (Kopp et al. 2009) (Figs. 6 and 7). The surface trace of this thrust fault system is observed

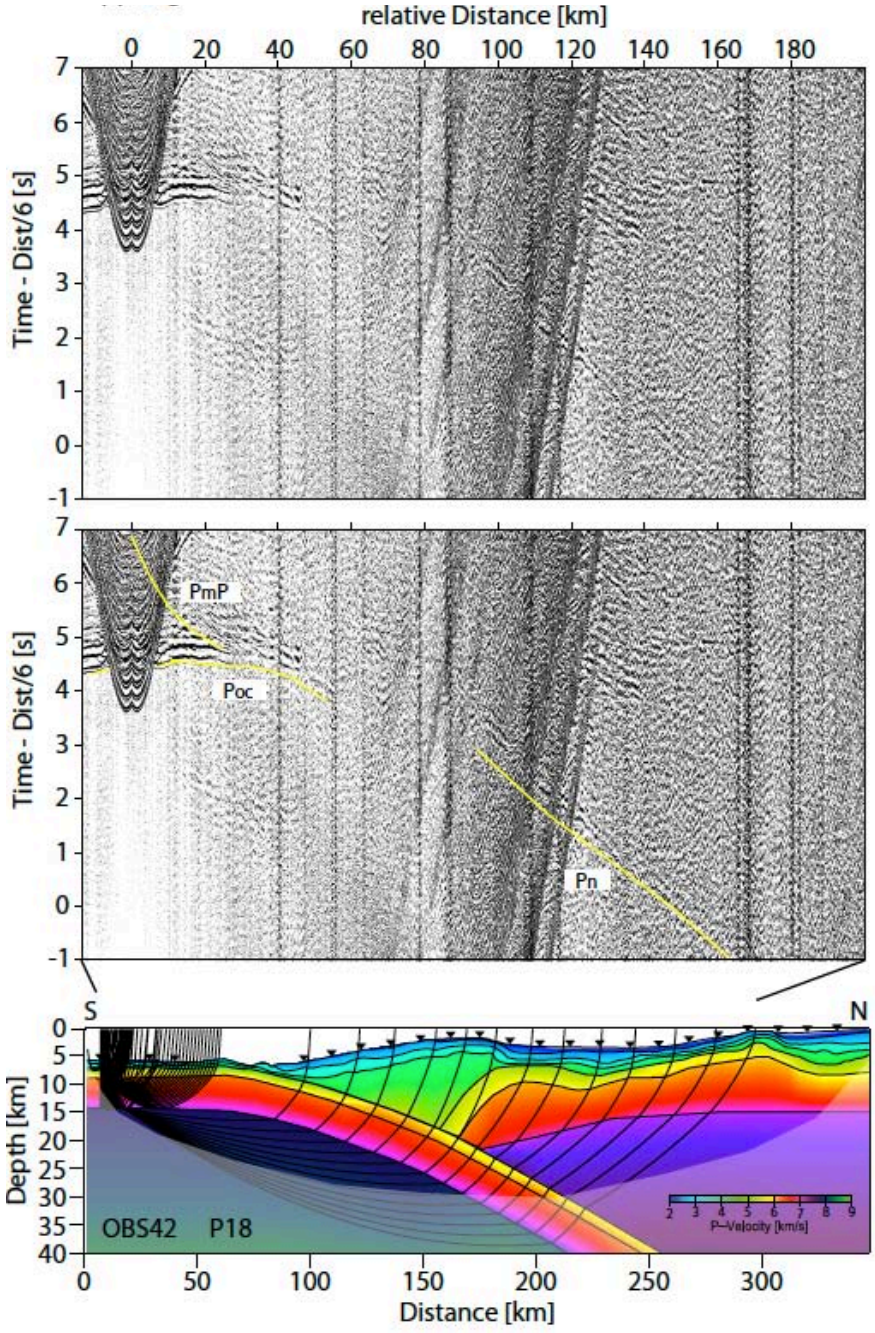


***Figure 5.*** *Seismic wide-angle section for ocean bottom seismometer OBS 42 of line P18 (upper panel), where 23 instruments were deployed (black triangles in lower panel). The gap in instrument spacing in the trench is due to the great water depth exceeding the instrument's pressure tolerance. The middle panel illustrates the calculated travel times on top of the seismic data shown in the upper panel. Rays in the lower panel are shot through a forward model with a velocity-depth distribution based on tomographic inversion. Shaded areas are not well resolved. A pronounced Pn mantle phase is recorded through the oceanic upper mantle reaching offsets of 160 km. The bending geometry of the oceanic crust underneath the trench inhibits ray coverage and results in a gap in first arrivals at 60-80 km offset. Consecutive inversion of different phases using a top-to-bottom approach recovered crustal and mantle velocities successively. See Figure 4 caption for phase information.*

over a distance of ~600 km along strike of the margin (Kopp & Kukowski 2003) and implies a continuous segmentation at an average distance of 30-35 km from the deformation front. This transition is also related to a change in surface slope, which decreases from the outer to the inner prism (Figs. 6 and 7). The Paleogene prism, which forms the forearc high, serves as backstop to the material accreted in the Neogene prism. Both prisms show active deformation, however, to a much lower degree in the Paleogene prism compared to its Neogene analog. The Paleogene prism forms the core of the large bivergent wedge, which shapes the forearc high along the central Sunda margin (Kopp & Kukowski 2003) (Fig. 2, panels a and b). The Late Paleogene rising of the Himalayan orogenic zone, which is the source for the majority of sediment in the Sumatran and western

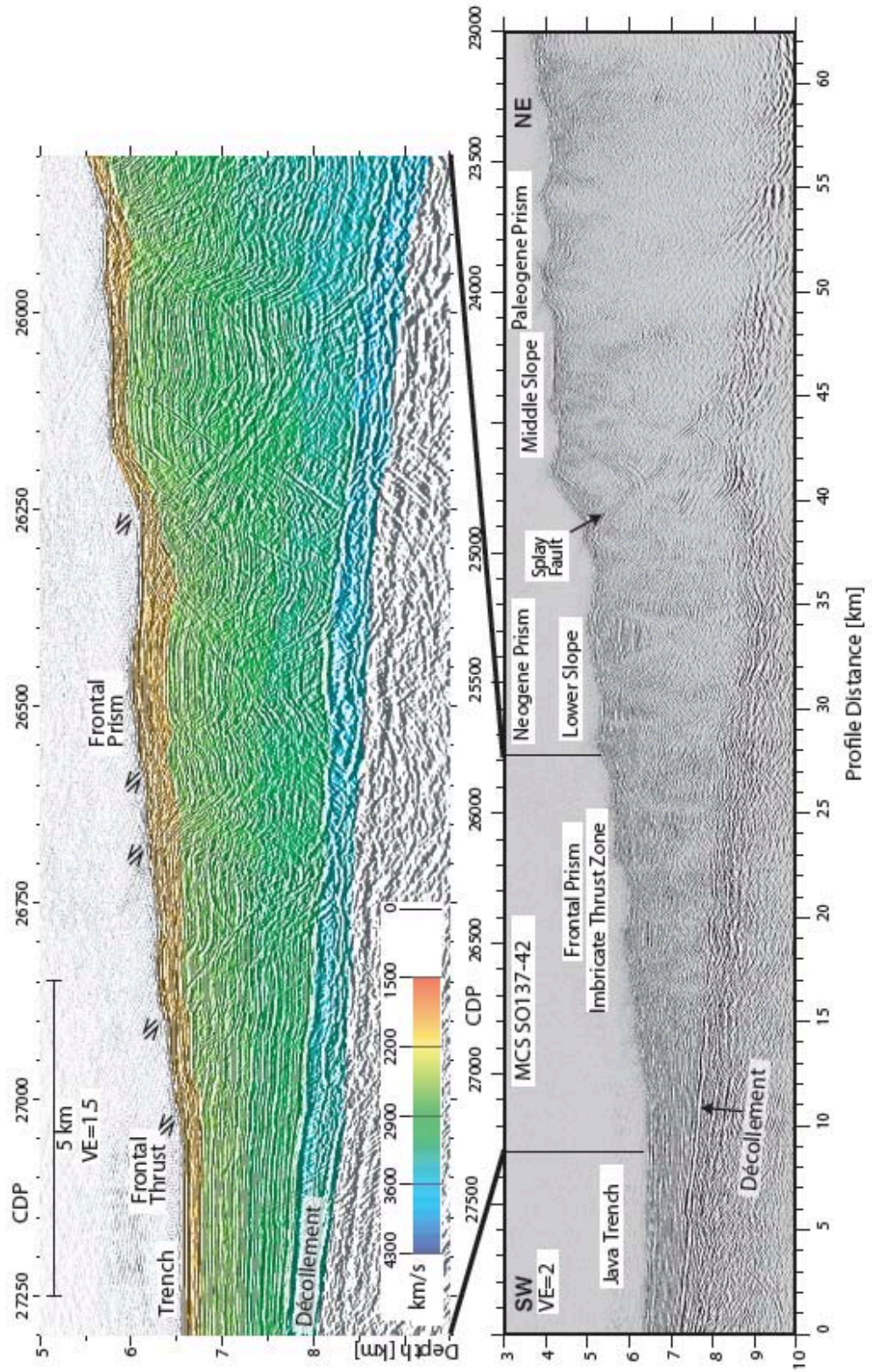


***Figure 6.*** *Pre-stack depth migrated multichannel seismic data crossing the deformation front and trench offshore Sunda Strait. Location is shown in Figure 1. The lower panel shows the underthrusting of the Indo-Australian crust underneath the lower and middle slopes of the overriding plate. In the upper panel, the fold-and-thrust belt of the frontal prism is imaged with at least four consecutive pairs of forethrusts and backthrusts. Trench sediment is uplifted along the frontal thrust and subsequently rotated as it is incorporated into the frontal prism. The lowermost 400-500 m thick unit of trench fill is underthrust beneath the frontal prism. A splay fault marks the transition from the Neogene accretionary prism to the Paleogene prism and coincides with a change in slope angle. Seismic velocities are interval velocities obtained during pre-stack depth migration. The MCS data were acquired by the BGR, Hannover, during the GINCO cruise.*

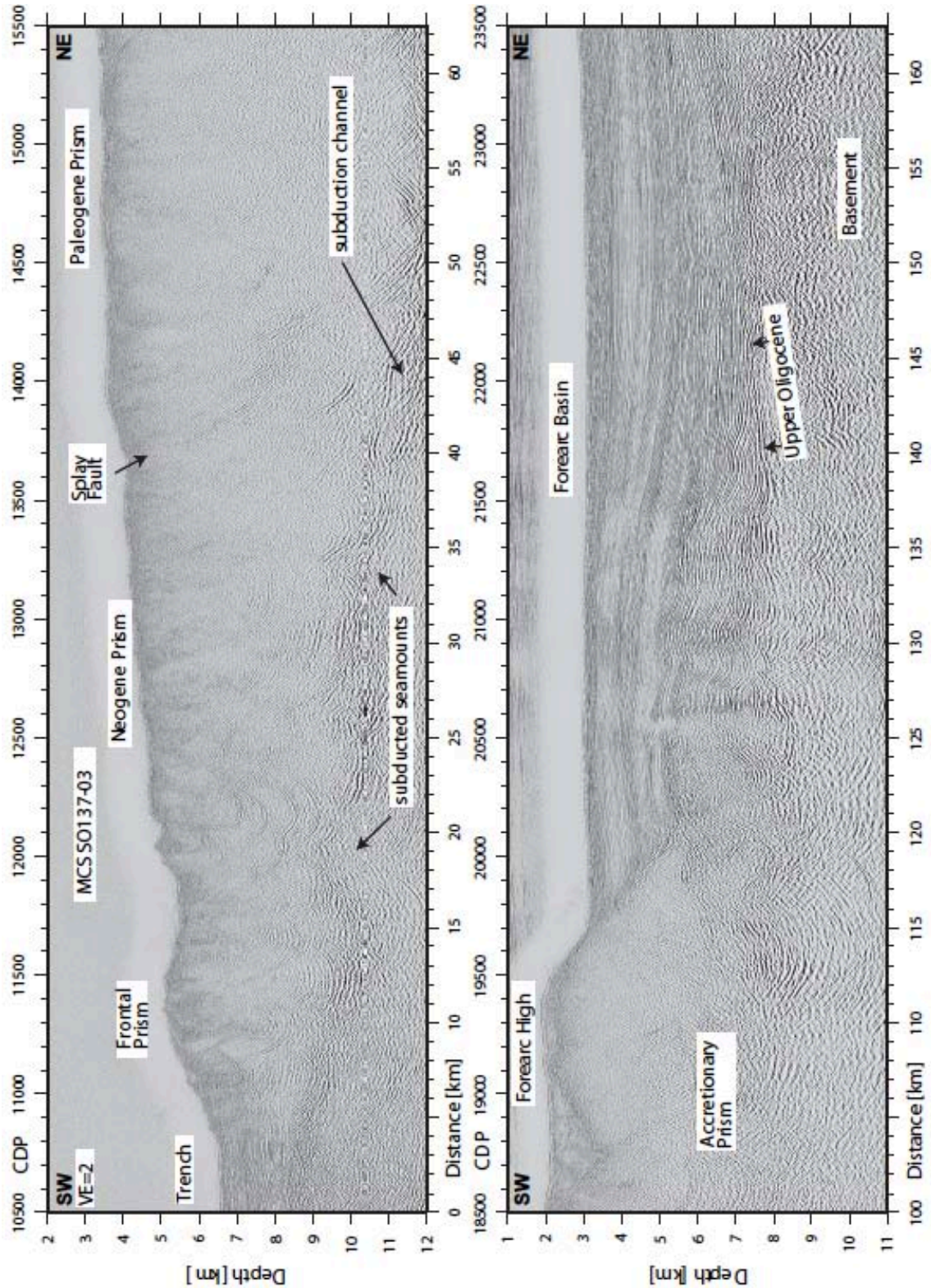


***Figure 7.*** *Pre-stack depth migrated mulichannel seismic data offshore western Java. Location is shown in Figure 1. The upper panel shows the southwestern extent of the profile from the trench to the Paleogene prism, the lower panel displays the landward part of the line from the forearc high to the forearc basin. In the frontal prism, shortening is accommodated by imbricate thrusting of the frontally accreted sediment. Approximately 1/3 of the trench material is underthrust beneath the frontal prism in a 500–900 m thick décollement zone, characterized by discontinuous high amplitudes. Two subducted oceanic basement highs of approximately 1.4 km and 0.8 km height, respectively, are imaged along the décollement zone. As off Sunda Strait (Fig. 6), a splay fault separates the Neogene and Paleogene prisms and connects to the megathrust at depth. In the lower panel, sedimentary sequences above an Upper Oligocene unconformity are deformed by thrusting at the seaward part of the basin. The MCS data were acquired by the BGR, Hannover, during the GINCO cruise. After Kopp et al. 2009.*

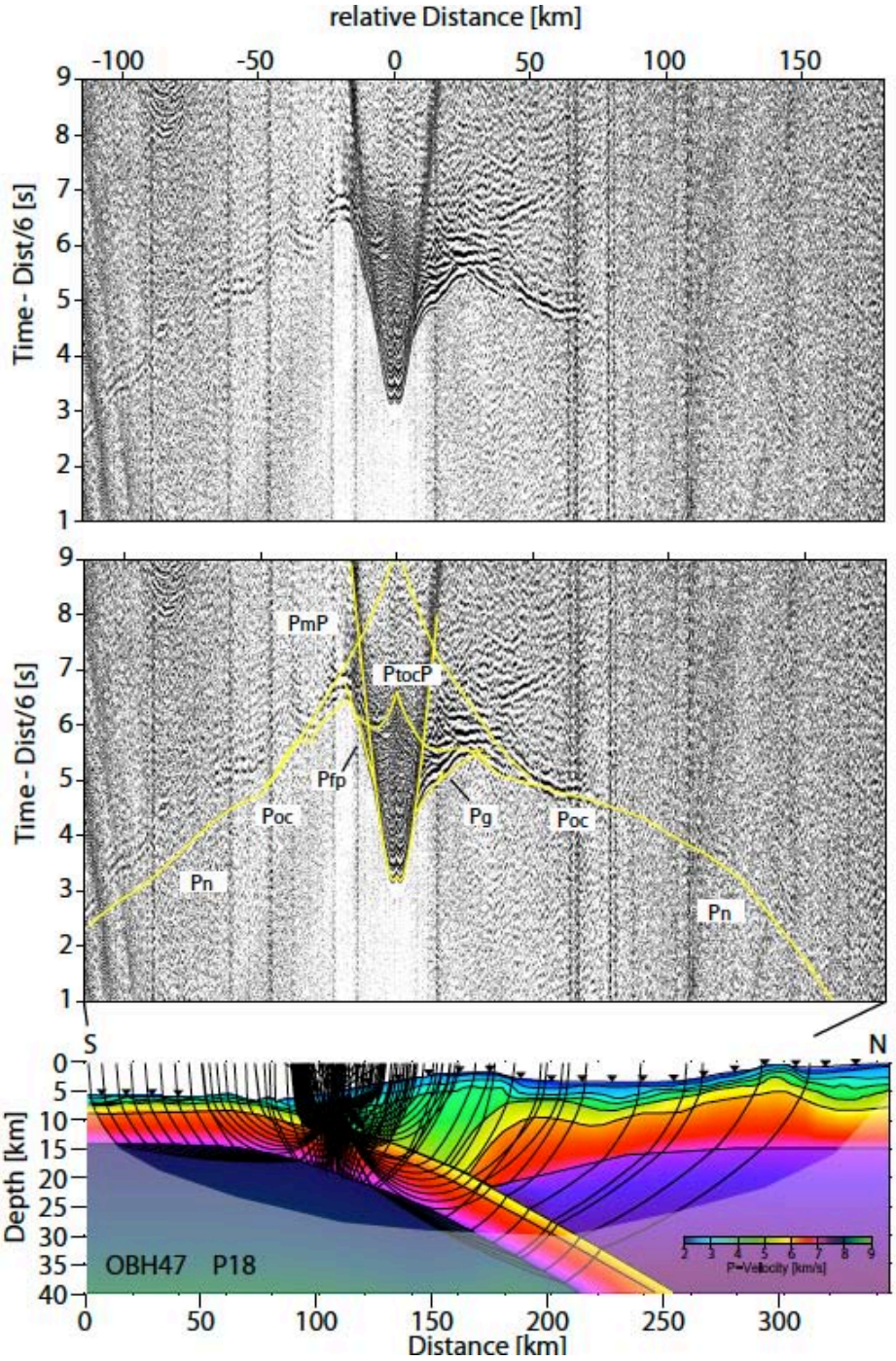


***Figure 8.*** *Seismic wide-angle section for ocean bottom hydrophone OBH 47 of line P18 (upper panel), located on the lower slope off western Java. The middle panel illustrates the calculated travel times on top of the seismic data shown in the upper panel. The landward increasing velocities of the forearc are documented by phases Pfp and Pg, which travel through the frontal prism and Neogene/Paleogene prism, respectively. See Figure 4 and 5 captions for additional phase and display information.*

Java sector of the Sunda trench (Susilohadi et al. 2005), contributed to the evolution of the accretionary forearc high, which is directly related to the sediment supply from the Himalayas.

***Remaining issues***

The internal structure of the Paleogene prism is not imaged well in reflection seismic data owing to limited energy penetration (Figs. 6 and 7). This is a common phenomenon in many accretionary margins and may possibly be associated with internal deformation related to strong shear stress along the underlying seismogenic portion of the subduction fault. In the absence of deep drilling data, information on the composition is primarily gained from wide-angle seismic surveys. Seismic velocities increase from the frontal prism to the Neogene and Paleogene prisms due to the greater rigidity of the consolidated and lithified material (Fig.

2, panels a and b). Mass balance calculations imply that the Paleogene prism formed by accretion since the Eocene-Oligocene (Kopp & Kukowski 2003). The deformational segmentation as manifested in the kinematic discontinuities imaged by the refraction data

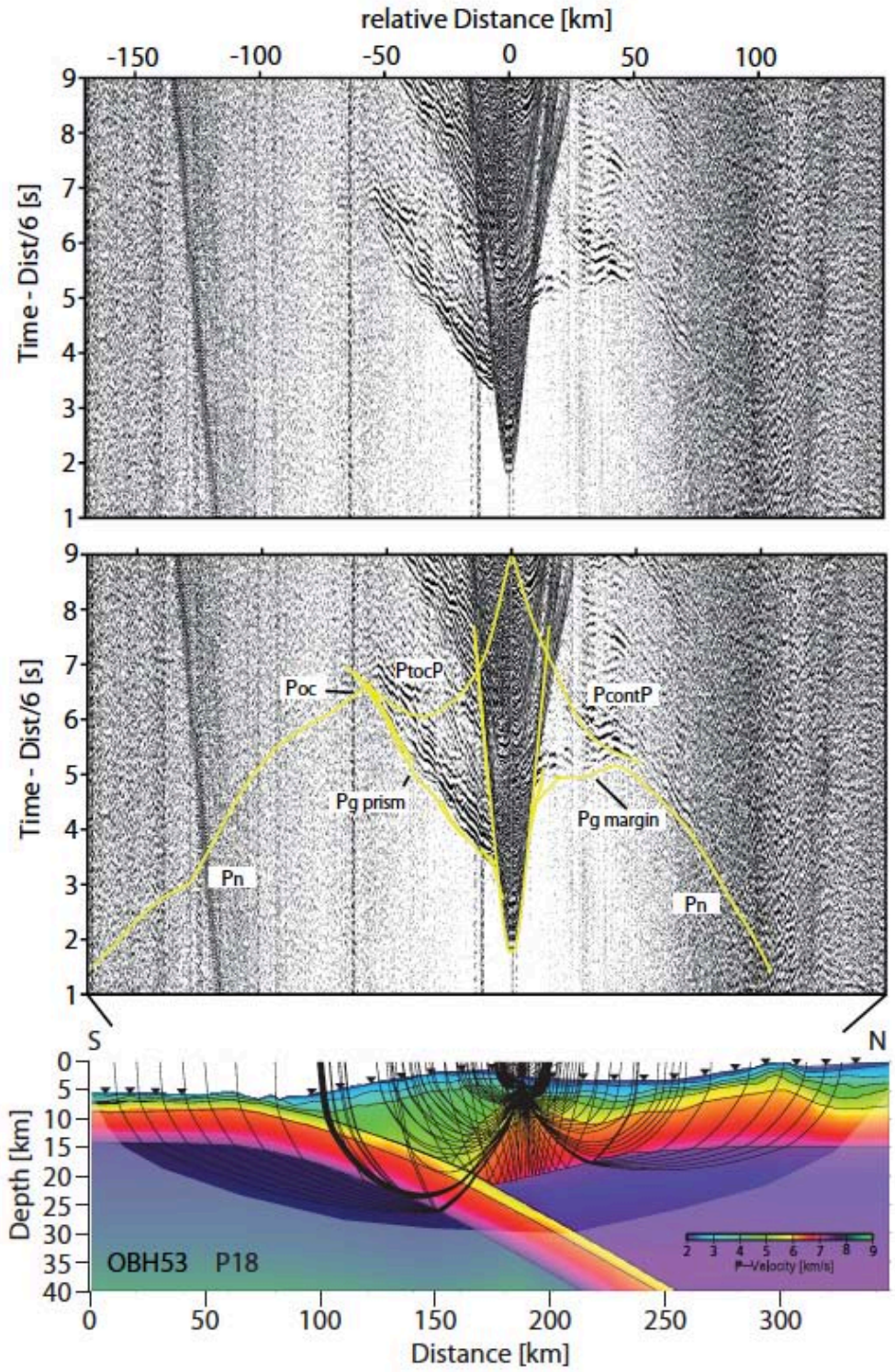


***Figure 9.*** *Seismic wide-angle section record section of OBH 53 placed on the transition from the forearc high to the forearc basin on line P18 offshore western Java. Record phases through the Paleogene prism (Pg prism) reveal slower velocities here compared to the forearc crust (Pg margin) and mantle (Pn). Strong reflections from the upper plate Moho (PcontP) specify the depth to the crust-mantle boundary below the forearc basin. See Figure 4 and 5 captions for additional phase and display information.*

suggests that accretion is non-linear. The rapid landward increase of the wedge thickness accompanied by backthrusting and uplift of the forearc high (Fig. 7) are indicative of basal accretion of the underthrust sequences (Gutscher et al. 1998), however, this process is not unambiguously imaged by seismic methods.

Backthrusting along reverse faults is observed on the northern flank of the forearc high and initiates a successive northward thrust over the southern portion of the forearc basin (Fig. 7) (Schlueter et al. 2002; Susilohadi et al. 2005). The evolution of the Java basin is governed by the accretion-driven uplift of the forearc high, which forms a barrier to the trench and abyssal plain and by tectonically induced subsidence forming a rapidly filled depression (Susilohadi et al. 2005). The mechanisms for subsidence remain unclear. In the Sunda Strait, subsidence is likely linked to graben formation related to the transtensioal regime here

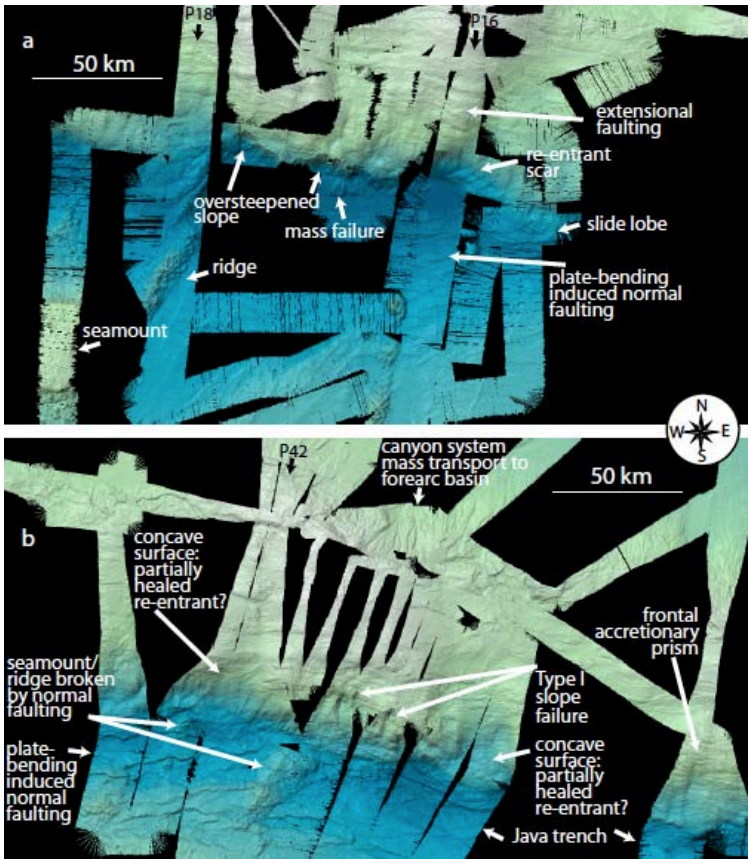


***Figure 10.*** *High-resolution bathymetric mapping offshore central-eastern Java. The swath lines represent the ship tracks, e.g. along profiles P16, P18 and P42. Black background is not covered by data. Black pings are data artifacts. Light colors represent shallow water depth, dark blue colors represent deeper water. (a) shows the trench and lower slope offshore central Java. Location is indicated in Figure 3. The lower slope is heavily sculpted by subducting seafloor relief. The oversteepened slope locally fails and mass wasting onto the trench floor occurs. A large, 20 km wide re-entrant scar along the track of profile P16 indicates subducted seafloor relief, resulting in extensional faulting related to uplift. (b) images the trench floor disrupted by plate-bending induced normal faulting, which also affects basement relief. Type I landslides are observed along the lower slope. Two locations exhibit a concave surface slope, indicative of re-entrant scars, which have partially healed. Material is effectively transported from the forearc high into the forearc basin along extensive canyon systems.*

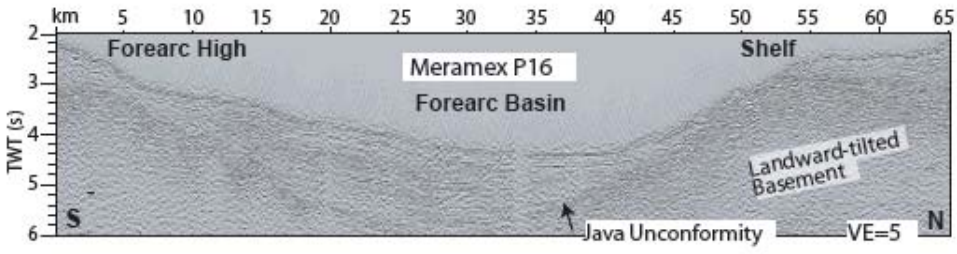


***Figure 11.*** *Four-channel streamer section across the central Java forearc basin. Location is shown in Figure 1. The forearc basin strata onlap the forearc high and are tilted landward, indicating syndepositional and postdepositional vertical movement of the seaward portion of the basin and the forearc high.*

(Lelgemann et al. 2000) and the loading effect of Krakatau volcanoclastics (Susilohadi et al. 2005). In western Java, the Ciletuh-Jampang block (Fig. 1) is tilted to the southwest. Its subsidence could reflect basal subduction erosion, however, our seismic data fail to image this process. Based on the interpretation of 20 reflection seismic profiles, Susilohadi et al. (2005) tentatively interpreted the oldest sequences in the Java basin to be of Middle Eocene to Late Oligocene age. A regional Upper Oligocene unconformity is traced as an erosional surface in the forarc basins from northern Sumatra to central Java (Fig. 7) and indicates that prior to the Neogene the shelf area was dominated by subaerial exposure or shallow water conditions

(Susilohadi et al. 2005). This is also supported by well data from the shelf and onshore outcrops (Susilohadi et al. 2005). Later, sediment supply increased during the late Middle Miocene with the rising volcanic activity of the arc (Susilohadi et al. 2005).

**Offshore central-eastern Java: Seamount subduction and forearc erosion**

***Observations***

The central-eastern Java segment is characterized by the subduction of an oceanic plateau, the Roo Rise, which is dotted with abundant basement relief (Masson et al. 1990). Relief elevation above the surrounding seafloor ranges from hundreds of meters to over 2 km. Oceanic crustal thickness is increased where the crust is altered by the emplacement of the Roo Rise. Profile P16 (Fig. 1) documents a crustal thickness of 9 km on the flank of the Roo Rise seaward of the trench (Fig. 2, panel c). Line P42, located off eastern Java and covering the Roo Rise south of the trench (Fig. 1), shows a pronounced Moho topography, with crustal thickness decreasing from 18 km in the oceanic domain to 11 km underneath the trench (Fig. 2 panel d).

The high-resolution bathymetry maps the underthrusting of basement relief underneath the upper plate, e.g. the incipient subduction of a small ridge (Fig. 10b) currently positioned in the trench. Larger topographic features on the oceanic plate are resolved by the global bathymetry (e.g. a moderate-sized seamount of 70 km diameter at a distance of 40 km from the trench (Fig. 10a)). The surface effect of seamount subduction and the corresponding deformation of the lower slope are revealed well in the absence of a thick sediment apron, as is the case for central Java (Fig. 10). Frontal erosion has sculpted the lower slope off central and eastern Java and is associated with a northward retreat of the deformation front by up to 60 km (Kopp et al. 2006). This segment of the Java margin shows extremely high surface slope values at the lower slope of the overriding plate, reaching values > 13° (Kopp et al. 2006).

Seafloor topography based on global satellite altimetry data (Smith & Sandwell 1997) reveals that the forearc high is characterized by isolated topographic summits between 109°E – 115°E trending in a NW-SE direction parallel to the trench at roughly 10°S (Kopp et al. 2006) (Fig. 1). They rise to water depth of 750 m – 1000 m and are roughly 1 km higher in elevation than the surrounding forearc high. This is documented by the two adjacent seismic profiles P16 and P18 (Fig. 2, panels b and c). The western line is located in the accretionary domain as described above and crosses the easternmost portion of the Java forearc basin. The eastern profile is positioned on the flank of the Roo Rise (Fig. 1). The difference in elevation of the forearc high on these two lines is approximately 1000 m (Fig. 2, panels b and c). Further landward, a broad swell located between profiles P18 and P42 (Fig. 1) is anomalous along the Sunda Arc's coastlines.

The tomographic inversion of profile P16 (Fig. 2, panel c) images a strongly deformed forearc and basin, which extends for 50 km in a north-south direction (compared to 80 km on line P18 (Fig. 2, panel b)). Approximately 4 km of volcanic ashes and sediment are trapped in the basin, which is carried by the landward tilted basement above the Java unconformity (Fig. 11). At a depth of ~14 km, the inversion images a subducted seamount around profile km 190 (Fig. 2, white arrow in panel c). The accretionary prism offshore Java is characterized by velocities generally not exceeding 5.0 km/s (Fig. 2). The subducted relief is inferred from the higher velocities (vp > 5.4 km/s) at the base of the accretionary prism retrieved along P16. OBH 30 (Fig. 12) covers the entire forearc and records the internal structure of the accretionary prism and subducting slab. Imaging, however, is intricate due to the severe deformation in this domain.

***Interpretations***

The transition from frontal accretion along the western Java segment to frontal erosion off central Java occurs over a short distance of some tens of kilometers and is documented by the two adjacent seismic profiles P16 and P18 (Fig. 2, panels b and c). The central Java margin segment is currently experiencing frontal erosion associated with the underthrusting of the Roo Rise. The northward migration of the Java Trench and deformation front above the leading edge of the Roo Rise has exposed an area of approximately 25,000 km2 of deeper seafloor formerly covered by the upper plate (Kopp et al. 2006). The corresponding northward shift of the axial position of the trench by about 60 km is moderate and may reflect a relatively recent onset of plateau subduction coupled with the arrival of the Roo Rise and Christmas Island Seamount Province at the trench. Based on the global satellite-derived bathymetry (Fig. 1), Shulgin et al. 2010 infer that the edge of the plateau, which already subducted, could be located as far as 70 km north of the trench, which would correspond to an onset of plateau subduction at 1.1 – 1.3 Ma ago. However, there is no direct evidence.

Topographic basement relief is abundant on the lower plate offshore Java (Masson et al. 1990) and modulates the structure and morphology of the overriding plate at various scales. The morphological perturbations of the lower slope resulting from subduction of oceanic relief depend on the size and structure of the subducted feature and on the nature of the overriding plate. Seamount subduction has been investigated at erosive margins (e.g. von Huene et al. 2000) where the seamounts leave pronounced re-entrant grooves as they plough through the small frontal prism before being subducted beneath the continental framework rock (von Huene 2008). Comparable embayments are not as distinct offshore Java (Fig. 10), where the accretionary material behaves more plastically. Topographic perturbations resulting from seamount subduction within the frontal prism are transient and the prism will heal after the relief is subducted to greater depth. Frontal erosion coincides with a steepening of the lower

slope angle in the central Java sector compared to the neighbouring segments (Kopp et al. 2006), bringing the taper into the unstable domain here. This results from subduction of basement relief, which at first causes deformation and uplift of the thin leading edge of the forearc (Taylor et al. 2005). The unstable frontal prism is marked by small-scale re-entrant scars (Fig. 10), by mass failure and extensional normal faulting (Fig. 10a). Erosive processes are enhanced by the lack of sediment in the trench and the pronounced horst-and-graben structure in the trench where the plate bends underneath the forearc (Fig. 10b).

Tectonic modification of the forearc offshore central to eastern Java is expressed in regional uplift affecting the entire marine forearc as well as in isolated zones of increased elevation (Fig. 1). The regional uplift pattern is caused by the subduction of the buoyant oceanic plateau, which results in uplift of the shelf as also described for the Hikurangi margin offshore New Zealand (Litchfield et al. 2007). Although due to the lack of independent data the onset of plateau subduction cannot be verified, it seems likely that it has been occurring since the late Pliocene when uplift and deformation of the upper plate intensified (Shulgin et al. 2010). Crustal thickening occurs mainly in the lower crust and seismic as well as gravity data confirm the presence of a crustal root here (Shulgin et al. 2010) as postulated by Newcomb & McCann (1987) to explain the absence of a correlated gravity anomaly. These results confirm numerical models, which predict crustal thickening to be concentrated in the gabbroic/basaltic layers (van Hunen et al. 2002). The observed thinning of the oceanic crust on profile P42 (Fig. 2, panel d) may either represent a local volume variation or may image the northern rim of the igneous expression. Subduction of smaller scale high relief gradient features likely accounts for the short wavelength anomalies observed along the forearc high (Masson et al. 1990; Abercrombie et al. 2001; Kopp et al. 2006). The observed uplift on profiles P18 and P42 (Fig. 2 panels c and d) is inferred to be caused by the impingement of oceanic basement relief and the associated deformation. A trench perpendicular compressive force is applied on the forearc by the relatively buoyant and thick subducting Roo Rise and its volcanic summits. This effect has also been reported for other margins, e.g. the Ryukuyu margin (Font & Lallemand 2009), Hikurangi margin (Litchfield et al. 2007), Costa Rica margin (Fisher et al. 2004) or the New Hebrides/Solomon arcs (Taylor et al. 2005). Uplift results from isostatic adjustment and is enhanced by crustal shortening of the overriding plate. The trench perpendicular compression leads to surface elevation of the forearc high, which greatly exceeds the original height of the seamount, as predicted by numerical modeling (Gerya et al. 2009). Surface uplift of 1 km is observed on P16 (Fig. 2, black arrow in panel c) and correlates with the position of the seamount at depth. Uplift is generated by crustal shortening and thickening of the overriding plate over a locked segment of the subduction thrust (Taylor et al. 2005). Backthrusting of the forearc high onto the forearc basin (Fig. 7) is observed along the entire segment and partially accommodates forearc convergence (e.g. Taylor et al. 1995).

In addition to the deformation of the overriding plate, a subducted seamount at depth experiences faulting and possible rupture. Baba et al. (2001) investigate the stress field associated with seamount subduction and conclude that shear failure and fracturing or dismemberment of subducting seamounts occur. This will in turn affect seismic velocities and limit the velocity contrast between the accretionary prism and the subducted seamount. Regarding the subducted seamount detected on line P16, gaps in the ray coverage along the profile certainly inhibit the imaging (Fig. 2 panel c). The presence of a seamount is, however, supported by a number of very distinct surface effects that document the dynamic influence of seamount subduction on the forearc morphology. These effects are associated with the subduction of moderate-sized features (Dominguez et al. 2000; Gerya et al. 2009) and include local surface uplift, topographic perturbation of the lower slope, intensification of subduction erosion, and landward trench displacement. All of these key indicators are recognized off central Java (Fig. 2 panels c and d) (Kopp et al. 2006).

***Remaining issues***

Profile P42 crosses the hypocenter location of the 1994 Java Tsunami earthquake (Abercrombie et al. 2001; Polet & Thio 2003; Bilek & Engdahl 2007) (Fig. 1). The reverse mechanism event, which is associated with slip at a previously well-coupled subducted seamount, showed normal faulting aftershocks that have been related to extension in the outer rise area (Abercrombie et al. 2001). This concept is supported by the high-resolution bathymetry of the trench area, which resolves plate-bending induced normal faulting (Fig. 10b) with vertical offsets of up to 500 m. The tomographic inversion of P42 as well as a corresponding multichannel line show indications of deeply penetrating faults (Lueschen et al. 2010; Shulgin et al. 2010) affecting the oceanic crust in the vicinity of the trench (Fig. 2 panel d). The deep structure of the forearc resolves the intricate geometry of the accretionary complex, which is characterized by heterogeneous uplift and deformation patterns. The velocity-depth distribution (Fig. 2, panel d) suggests the presence of accreted oceanic crustal fragments or detached oceanic basement relief. Remnants of accreted seamounts have been proposed to be present in the Japanese island arc (Isozaki et al. 1990), indicating shearing off and crustal underplating of oceanic basement material (Uchida et al. 2010). This scenario would also explain the forearc structure along P42. An anomalous high velocity structure is present at a depth of 13 km (Fig. 2 panel d). It is unlikely that a subducted seamount would still be intact under these conditions. Figure 10 b maps the incipient subduction of a small seamount, which currently collides with the

deformation front. This seamount as well as other bathymetric features in the trench and on the outer rise is broken by the bending-related normal faulting. The surface traces of the faults are continuous across the seafloor relief. Dismemberment of a seamount or oceanic crustal fragment will decrease seismic velocities and lower the velocity contrast to the surrounding accretionary prism. As a consequence, seismic imaging will be distorted.

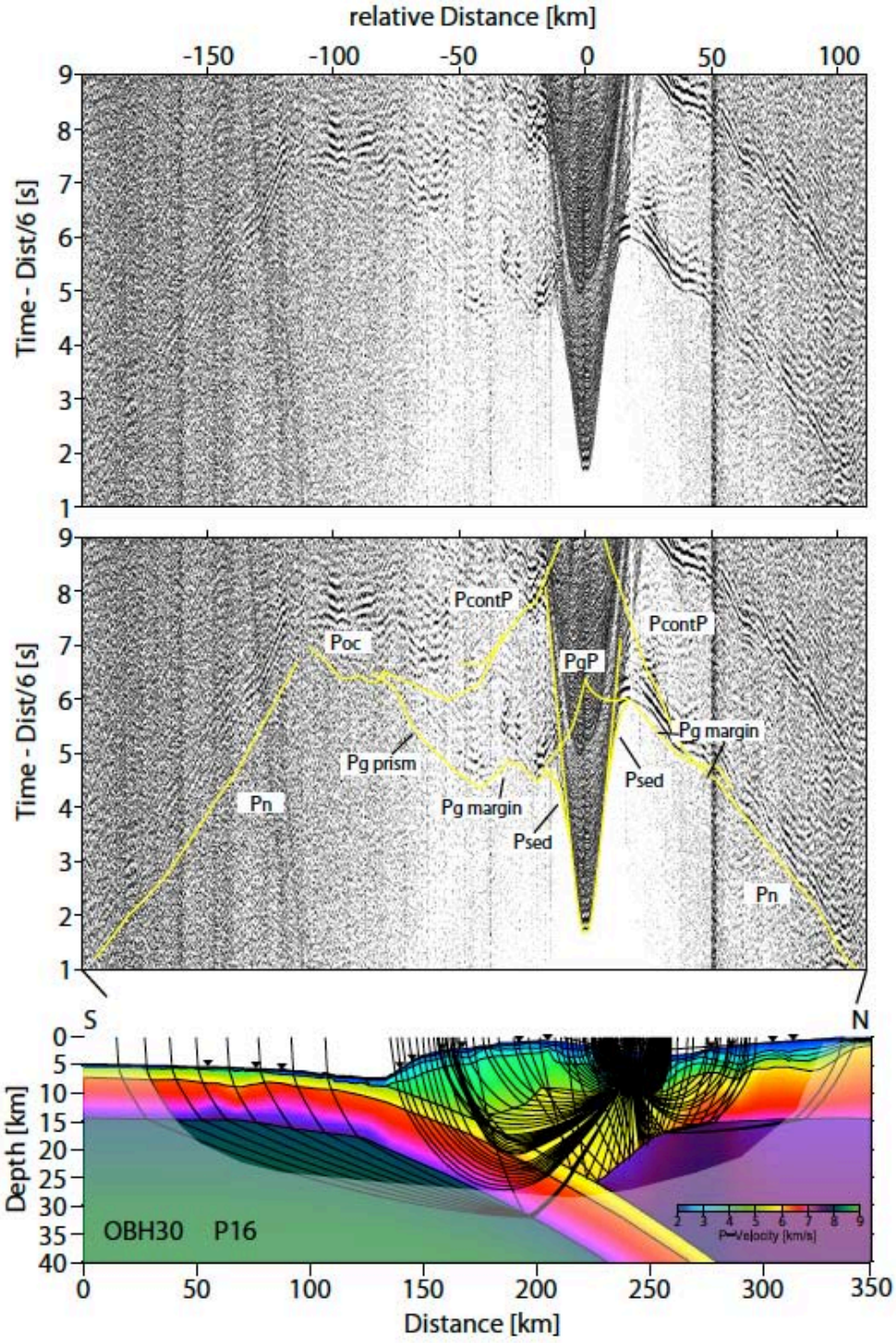


***Figure 12.*** *Seismic wide-angle section record section of OBH 30 located on the southern edge of the forearc basin offshore central Java on profile P16. This station covers the entire subduction complex and reveals the velocity structure of the accretionary prism (Pg prism) and the deep structure of the forearc (Pg margin and PcontP). PgP is the forearc crust basement reflection. The oceanic Pn phase to the south is reverse to the according phase on station OBS 42 displayed in Figure 5. See Figure 4 and 5 captions for additional phase and display information.*

**Offshore the Lesser Sunda islands: Transition from oceanic subduction to continent-island arc collision**

***Observations***

The margin segment south of the Lesser Sunda islands shows a different structure compared to its western counterpart. Here, a mature forearc basin, the Lombok basin, is observed at a water depth of 4400 m, which is limited to the west by the uplift associated with the Roo Rise subduction and to the east the by collision of the Scott Plateau with the crystalline crust of the Sumba Island (Fig. 1) (Shulgin et al. 2009; Planert et al. 2010). The forearc high and accretionary prism are much more uniformely developed than in the neighboring sector off Java, where isolated bathymetric elevations dominate the forearc high topography. Off Bali and Lombok, the forearc high is dominated by two elongated tectonic ridges (Fig. 13a) (Mueller et al. 2008; Krabbenhoeft et al. 2010) and diminishes in size and volume to the east.

The age of the oceanic lithosphere decreases from Late Jurassic at 120°E to Early Cretaceous around 110°E (Heine et al. 2004; Mueller et al. 2008). On the incoming plate, Planert et al. (2010) determine a crustal thickness of 8.6 km off Lombok, increasing to 9.0 km to the east near the transition to the Scott Plateau. The transition from the oceanic crust of the Argo Abyssal Plain to the subducting crust of the Scott Plateau occurs over short distances of less than 50 km (Fig. 13c) and concurs with an increase in crustal thickness of approximately 5 km, mainly accommodated by the upper crust (Fig. 2 panels f and g) (Planert et al. 2010).

Convergence occurs at a rate of ~70 mm/a in a direction N13°E offshore Bali (Simons et al. 2007). Figure 13 displays oceanic basement structures in the Argo Abyssal Plain trending at angles of 45-60°. Planert et al. (2010) argue that these structures trace the original seafloor spreading fabric as they trend parallel to the magnetic anomalies (Lueschen et al. 2010). Approaching the trench, plate bending induced normal faulting starts to dominate the seafloor fabric within 40 km of the trench axis (Fig. 13) (Planert et al. 2010). The resulting rough topography of the oceanic basement can be traced to several kilometers depth underneath the accretionary prism. Riffling of slope debris subparallel to the underthrust horst-and-graben relief is observed for parts of the frontal prism (Fig. 13a), similar to processes observed in northern Chile (von Huene & Ranero 2003). This region corresponds to reduced upper mantle velocities, which reach values of 7.5 km/s within a distance of 30-50 km from the trench (Fig. 2 panels e and f).

The forearc high rises steeply from the trench to water depth of less then 2500 m (Fig. 13a). Localized slope failure is observed on Figure 13 and is associated with the oversteepening of the lower slope. The seafloor morphology is dominated by two distinct, E-W trending ridge structures (Ridge A and Ridge B in Fig. 2 panel e) spaced ~25 km apart (Fig. 13a). Uplift and tilting of piggy-back basins hosted between the ridges (Fig. 13a) document active deformation and vertical displacement (Mueller et al. 2008). Seismic velocities of the forearc high do not exceed 5.5 km/s where it is in contact with the underthrusting oceanic crust at a depth of ~13 km (Fig. 2, panels d - e), indicating a sedimentary composition as inferred for other parts of the margin. This is also supported by the relatively smooth magnetic response of the forearc high (Mueller & Neben 2006). The forearc high is fronting the Lombok basin, which carries 3-4 km of sediment above a seaward dipping basement (Fig. 2, panels d - e). The ~9 km thick basement crust underneath the basin shows a high velocity gradient in its upper portion, decreasing in the lower crust. The upper plate Moho is located at a depth of ~16 km underneath the forearc basin (Fig. 2) with upper mantle velocities of 7.5-7.6 km/s.

***Interpretations***

Sediment recycling is the principal process of mass flux along the lower slope south of the Lesser Sunda islands, where mass wasting of the forearc high supplies upper plate material to the trench (Fig. 13b), which is subsequently incorporated into the frontal prism. The oceanic crust is progressively faulted and altered as it approaches the trench. The complex shape of the thrust interface as imaged in the tomographic models (Fig. 2, panels d – g) suggests a high degree of fracturing of the oceanic crust with potential dissection into singular blocks. Horst-and-graben structures with vertical offsets of up to 500 m are recognized along the outer trench wall (Fig. 13a-c). Where the lower plate relief is not as pronounced, the lower slope is not impacted by subducted seamounts and is characterized by thrust faults (Fig. 13a). Offshore Bali and Lombok, the middle slope largely remains undisturbed, however, local undulations in the topography may result from lower plate fabric subducted beyond the frontal prism. A number of landslides have been identified along this margin sector (Brune et al. 2010a) and are classified into two types (Type I and II) as proposed by Yamada et al. (2010). Type I slides are of smaller dimension, developing on the lower slope and occurring frequently. The frequency of Type II slides is much lower compared to Type I failures. They occur on the middle and upper slope and are of larger dimension compared to Type I slides. Offshore Sumbawa at 117°52'E/11°4'S, a Type II slide on the middle and lower slopes at 5300 m water depth with a width of 23 km affected a volume of approximately 15 km3 (Brune et al. 2010a) (westernmost slope failure in Fig. 13b). From the absence of a deposition lobe it may be inferred that the landslide sediment deposit has been frontally accreted and incorporated into the frontal prism seaward of the headwall scarp. A northward offset of the headwall scarp indicates segmentation of the slide and collapse in successive events. Moving to the east, at least three adjacent slope failures (Type I) are identified in Figure 13b. They are of much smaller volume and only affect the lower slope. Lateral migration of slope failures has been predicted by analogue modeling (Yamada et al. 2010). The primary single slide will lead to changes in slope topography due to sediment displacement. Adjacent areas then

become instable due to the resulting topographic undulations and another event is triggered in adjacent areas. The largest slide (Type II) with a volume of 20 km3 (Brune et al. 2010a) is encountered at 119°15'E/11°3'S where it has left a significant deposit lobe resulting from failure of the middle and lower slope (Fig. 13b-c). This is located in the transition area from oceanic subduction to continent-island arc collision at the easternmost end of the Java trench. A sequence of seaward vergent normal faults on the outer

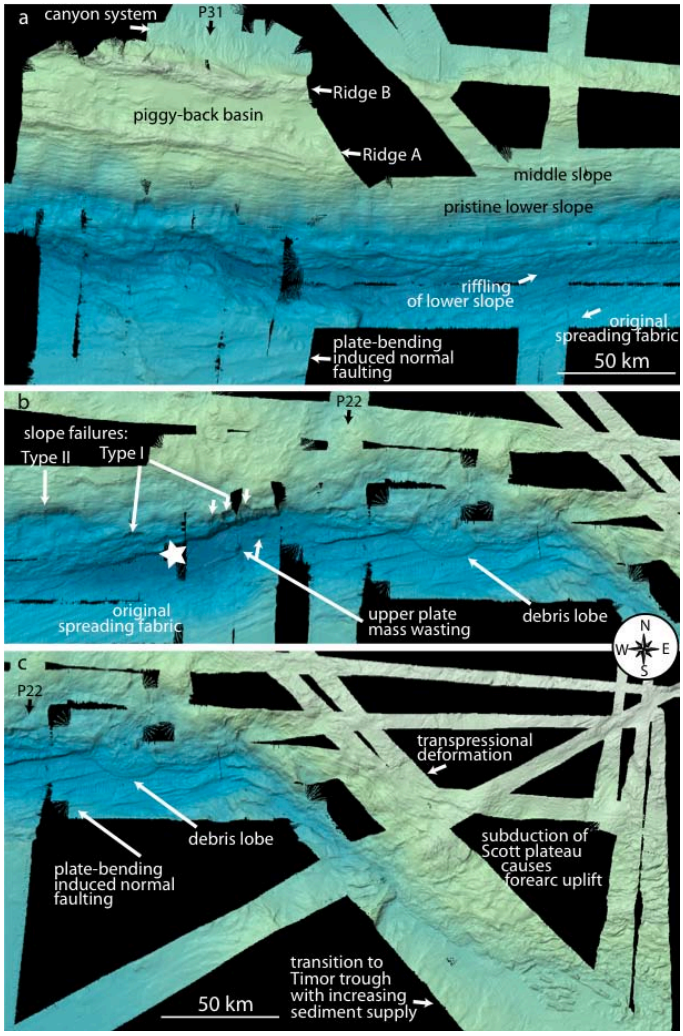


***Figure 13.*** *High-resolution bathymetric mapping offshore Lombok to Sumba. Location is indicated in Figure 3. (a) The accretionary prism is dominated by two elongated ridges which host piggy-back basins. The topography of the lower plate is dominated by plate-bending induced normal faulting locally overprinted by original seafloor spreading fabric. Oceanic crust topography causes riffling of lower slope material upon subduction underneath the frontal prism. Mass wasting occurs to the forearc basin in the north. (b) Slope failure results in landslides affecting the lower slope (Type I failure) or the middle and lower slope (Type II failure). The headwall scarp of the Type II failure is offset northwards, indicating failure in successive phases. Three adjacent Type I slides are indicated and associated upper material wasting is observed on the trench floor. White star indicates hypocenter location of 1977 Sumba earthquake. (c) Transition to the Timor trough coincides with a shallowing of the seafloor and is associated with transpressional deformation and uplift of the overriding plate. A debris lobe is observed in the trench and will eventually be re-incorporated into the frontal prism. Refer to Figure 10 caption for additional display information.*

trench wall relays the deepening of the seafloor from the Argo Abyssal Plain with a water depth of < 5000 m to the trench at 6500 m depth below the sea surface (Fig. 13b) (Planert et al. 2010). Near the deformation front, two landward vergent faults with a strike of ~65° and thus subparallel to the magnetic anomalies (Mueller et al. 2008) are sculpting the deformation front and lower slope as they are subducted (Fig. 13c). The deformation front is additionally affected by transpressional deformation related to the southward curvature of the trench as it merges into the Timor trough (Fig. 13c). The relocated epicenter of the 1977 earthquake (Engdahl & Villasenor 2002) is shown in Figure 13b. The main event and the aftershock sequence likely resulted from slip along the re-activated inherited seafloor fault fabric as it bends underneath the upper plate and ruptures the oceanic lithosphere to a depth of 30-50 km (Spence 1986; Lynnes & Lay 1988).

One of the most prominent features on the wide-angle profiles is the shallow upper plate mantle, which is found at a depth of ~16 km underneath the forearc basin. The low seismic velocities of ~7.5 km/s detected here (to ~2 km below the Moho) are attributed to hydration and serpentinization of mantle peridotite (Faccenda et al. 2009), requiring faults to penetrate the oceanic crust and reach deep into the mantle. This is supported by the hypocenter relocation of the 1977 Sumba earthquake sequence, which resolved normal faulting to affect the oceanic lithosphere to a depth of 34 km (Spence 1986) as indicated above. The shallow position of the upper plate mantle may fundamentally affect seismogenesis along the Java margin as it limits the extent of the seismogenic zone. The interface contact with weak, hydrated minerals such as serpentinite, which mechanically cannot support stick-slip behavior, would result in stable sliding downdip of the seismogenic zone (e.g. Hyndman et al. 1997; Oleskevich et al. 1999). However, exceptions to this concept may exist, e.g. offshore Sumatra, where earthquake nucleation has been proposed to occur in the mantle (Dessa et al. 2010; Klingelhöfer et al. 2010) or offshore Japan, where earthquake clusters below the depth of the forearc Moho are related to seamount

detachment (Uchida et al. 2010). Along with the depth extent of the seismogenic zone, the size of the lateral rupture zone determines the potential magnitude of subduction thrust earthquake. Local asperities that may act as barriers to rupture thus will also influence the magnitude. The eastward propagating minimum 200 km rupture of the 1977 Sumba normal faulting event was likely limited by the thick crust of the Scott plateau, acting as a barrier to further rupture propagation.

***Remaining issues***

The transition from oceanic subduction to the collisional regime along the Timor trough occurs south of Sumba Island (Fig. 13c), where the crystalline crust of the Sumba block is imaged in the tomographic model (Fig. 2, panel f). The easternmost profile is located east of Sumba Island around 121°E (Fig. 1) (Shulgin et al. 2009) and documents the early stages of continent-island arc collision along the westernmost extension of the Timor trough (Fig. 2g). The relative motion along this segment of the Timor trough has slowed to ~15 mm/a. The incoming crust of the Scott plateau reaches a thickness of 15 km as it subducts below the fold-and-thrust belt of the upper plate. The increased sediment thickness is reflected in decreasing water depth in the trough (Fig. 13c). Sediments are likely sourced from the Australian continent and contribute to the evolution of a large accretionary body with a width of ~130 km. This evolving collisional system is dominated by the Sumba Ridge, a high velocity block that acts as backstop to the accretionary prism in the south (Fig. 2, panel g). Backthrusting onto the Savu Basin in the north originates from the compressional deformation caused by the northward propagation of the Australian lithosphere (Bock et al. 2003).

## Conclusions

This study investigates contrasting modes of deformation in three segments of the Java convergent margin, defined by varying processes of mass transfer. Sediment supply to the trench acts as the principal factor governing lower to upper plate material transfer. The decreasing sediment supply to the Java trench from west to east correlates with a changing pattern of mass flux: from sediment accretion offshore western Java to tectonic erosion off central Java. Sediment accretion characterizes the Sumatra sector of the Sunda margin, where sediment input on the oceanic plate continuously increases to the north with closer proximity to the Ganges-Brahmaputra system (Moore et al. 1980). The western Java segment is characterized by a net addition of material from the lower plate to the upper plate and by an oceanic seafloor topography smoothed by a sediment apron. Offshore western Java, frontal sediment accretion dominates and approximately 2/3 of the trench sediment sequence is incorporated into an imbricate thrust belt (Schlueter et al. 2002) (Figs. 6 and 7). The thickness of material subducting beyond the frontal accretionary prism ranges from 500 m to 1000 m per trench km here. Basal accretion likely occurs below the forearc high, contributing to the evolution and uplift of a >100 km wide bivergent wedge (Fuller et al. 2006; Kopp et al. 2009).

To the east, offshore central Java, the transition from sediment accretion to tectonic erosion occurs over a distance of less than 100 km around 110°E (between profile P18 and P16 in Figure 1). Here, the trench is devoid of sediments except for isolated sediment ponds (Masson et al. 1990). A complex canyon system traverses the continental slope and supplies material to the Java and Lombok forearc basins. Sediment discharged from Java and the Lesser Sunda islands does not reach the trench, but is trapped in the forearc basins as the distance from the trench to the active volcanic arc increases from west to east. The nature of the basement of the arc framework crust underneath the Java and Lombok forearc basins remains enigmatic. Based on previous work by Curray et al. (1977) and Kopp et al. (2002), it is proposed that the forearc crust could be composed of an altered oceanic terrane, which resisted subduction due to increased positive buoyancy (Planert et al. 2010). An alternative view is based on the rock record of Sumba Island: the seaward extent of continental crust south of Java and the Lesser Sunda islands could be the lateral continuation of the Late Cretaceous arc massif (Rutherford et al. 2001).

High relief oceanic basement is subducting offshore central and eastern Java, leading to a rough seafloor and causing frontal erosion of the forearc (Fig. 10). The margin geometry is influenced by the subduction of an oceanic plateau, the Roo Rise, underneath the Java forearc. The Nusa Tenggara segment offshore the Lesser Sunda islands experiences the transition from oceanic subduction to continent island arc collision (Fig. 13), with a rapid change in upper plate structure along strike.

The eastern Sunda margin is prone to large potentially tsunamigenic landslides. Landslides are categorized in Type I and Type II slides, following the nomenclature of Yamada et al. (2010). Type I slides are of smaller dimension and occur on the lower slope, while Type II slides affect a larger area / volume and are observed on the middle and upper slopes. Both types are triggered by the oversteepening of the slope either due to the subduction of relief or near a thrust surface in the frontal imbricate thrust fan (Fig. 13). While the smaller Type I slides are ubiquitous along the Java margin, the larger Type II slides are only observed in the easternmost segment. Brune et al. (2010b) have identified 12 landslides along the Sunda margin from high-resolution multibeam bathymetry. While the volume of the Type I landslides is typically less than 5 km3, the three largest ones, which are located in the transition zone from the Java trench to the Timor trough, show large volumes of 15-20 km3 and have originated on the middle slope, which qualifies them as Type II slides (Fig. 13b). A potential contribution of the

Type II slides identified in the vicinity of the 1977 Sumba earthquake is not verified. Tsunami propagation modeling successfully predicted the observed run-up heights from the earthquake tsunami alone and does not necessarily require a further contribution from a landslide tsunami (Brune et al. 2010a).
An additional process for tsunami generation is the potential activation of splay faults during the co-seismic phase. Splay faults connect to the megathrust at depth and dip steeply to the surface, as imaged offshore western Java (Kopp et al. 2009) (Figs. 6 and 7) and off the Lesser Sunda islands (Lueschen et al. 2010). Thus the low-angle slip of the megathrust will potentially be transferred to a higher angle, which may greatly enhance seafloor displacement (Tanioka & Satake 1996). Due ot the lack of deeply penetrating multichannel seismic data, the role of potential splay faults in the generation of the 1994 and 2006 Java tsunamis remains unresolved.

Deep-seated subduction processes excert control on the structure and deformation of the upper plate as well as on the seismogenesis of the forearc. The most dramatic effects are observed in the central-eastern Java segment, where deformation of the sedimentary units in the forearc basin (Figs. 7 and 11) and backthrusting of the forearc high onto the basin (Fig. 2 panels c and d) are documented. A decrease in the subduction angle of the underthrusting plate, as detected off South America, however, is not observed here (Koulakov et al. 2007). This concurs with results from numerical modeling, which predict that a moderate-sized plateau will not significantly alter the subduction angle (Gerya et al. 2009). In addition, the modeling also predicts that a decrease in magmatic activity is unlikely. Tomographic inversion has revealed the interplay between the forearc and the volcanism on Java, where the high vp/vs ratio of a pronounced low velocity anomaly in the Javanese crust is indicative of fluid ascent from the underthrusting plate to the volcanic arc (Koulakov et al. 2007) and has been interpreted to image the related fluid ascending paths (Wagner et al. 2007). Other predictions based on numerical modeling regarding the forearc morphology are also matched: a local increase in topography is observed in the overriding plate as well as a northward displacement of the deformation front (Kopp et al. 2006), indicative of erosive processes here. Stress fluctuations govern erosion, which requires a strong subduction thrust fault and a mechanically weak overlying wedge. On short timescales, earthquakes are a common mechanism to cause variations of stress, which then occur from the interseismic phase to the co-seismic activity (Wang et al. 2010). Changes in basal fault strength may also be caused by the rough topography of an oceanic plate lacking a significant sediment cover. Deformation of the wedge caused by the impinging bathymetric features will mechanically weaken the prism, which is then overlying a strong basal detachment, providing conditions favoring subduction erosion.

Basal subduction erosion would pose a tectonic mechanism for basin subsidence; however, this would require the underthrusting plate to remain in contact with the upper plate from the trench to underneath the forearc basin. The tomographic images of Figure 2 clearly demonstrate that the underthrusting plate dips into the upper mantle beneath the outer forearc high. Further evidence for this configuration comes from earthquake hypocenters distribution (Wagner et al. 2007; Wittwer, 2010) and gravity modeling (Grevemeyer and Tiwari, 2006; Planert et al. 2010; Shulgin et al. 2010). In addition, satellite magnetic data record a significant anomaly extending seaward, resulting from a hydrated mantle wedge underneath the forearc (Blakeley et al. 2005). This then raises the question if subduction erosion of the upper plate's lithospheric mantle wedge occurs and if this accomplishes basin subsidence. This issue, however, is beyond the scope of this paper.

***Seismogenesis***

The Java margin is characterized by a notable absence of Mw>8 earthquakes compared to its Sumatran counterpart, leading to the question of what controls seismic rupture and consequently the potential size of earthquakes offshore Java. The magnitude of an earthquake is associated with the size of its rupture zone. Slip motion on a fault will depend on the tectonic environment of the source region (Bilek, 2007). Two aspects are related to slip motion: (1) the role of the décollement zone and (2) the role of seafloor relief acting as asperities or barriers to rupture.

The notion that trench sediments affect seismogenesis was brought forward by Larry Ruff (Ruff, 1989) and is here extended to the concept of the subduction channel in general. On a global scale, giant megathrust earthquakes (Mw ≥ 8.5) are observed in systems characterized by sediment-flooded trenches (e.g. Sumatra (1883, 2004, 2005), Southern Chile (1960, 2010), Alaska/Aleutians (1964, 1965, 1986)) as well as at erosional margins (Kamchatka (1952), Kuril Islands (1963), Northern Chile (1868, 1877)), which show a subduction channel of several hundred meters in thickness. The existence and geometry (thickness) of a subduction channel thus influences rupture propagation to a greater degree than the nature of the material in it (trench sediment vs. upper plate erosional debris) (Tanioka et al. 1997; Bilek & Lay, 1999). A discussion on the role of fluids in this context, however, is beyond the scope of our data.

The second aspect regards sea floor roughness and the question of whether basement relief acts as an asperity or barrier to seismic rupture (Bilek & Lay, 2002). Certainly this will not play a role where basement highs are deeply buried in the subduction channel. Here, subduction channel material smoothes sea floor relief and cushions upper plate contact. Where this is not the case, underthrusting seamounts or ridges may pose a limit to lateral rupture propagation, as do crustal faults

(Collot et al. 2004). Bathymetric relief on the underthrusting plate will lead to variations in mechanical coupling and high friction models as well as low friction models have been proposed (Cloos 1992; Mochizuki et al. 2008). Large seamounts (≥ 3 km height) may increase the normal stress between the plate and raise interplate coupling (Scholz & Small 1997). On the contrary, reduction of normal stress has been proposed to result from elevated pore pressure of entrained fluid-rich sediment during erosion (von Huene et al. 2004). Weak interplate coupling may be related to the damage caused by erosion that inhibits the accumulation of elastic strain energy (Mochizuki et al. 2008). Recurring Mw ~7 earthquakes are related to seamount subduction in the Japan trench (Mochizuki et al. 2008) where weak coupling has been linked to fluid-rich sediment and migration of fluids at the base of the seamount.

Along the Java subduction zone, different tectonic features exert a first-order control on the seismogenesis of the margin and govern the lack of Mw > 8 megathrust earthquakes:

1) Our tomographic images reveal a shallow upper plate Moho with low mantle velocities, indicative of hydrated minerals (Fig. 2). Hydration is caused by fluids, which are released from the subducting slab and entrenched sediments, leading to serpentinization of the mantle wedge (Hyndman & Peacock 2003). The limited downdip extent of the seismogenic zone is also supported by gravity data and thermal modeling (Grevemeyer & Tiwari 2006) as well as by the forearc morphology (Krabbenhoeft et al. 2010).

2) In the central Java segment, seismic rupture would additionally be limited along strike by subducted basement relief acting as barriers that will resist co-seismic slip. Erosional damage related to seamount/Roo Rise plateau subduction may hinder the accumulation of elastic strain (Mochizuki et al. 2008). Local elevation in pore pressure of sediment entrained during underthrusting of a seamount may also be expected. The uneven slip distribution recorded during the co-seismic phases of the recurring tsunami earthquakes on this margin sector (Fig. 1) (Ammon et al. 2006; Bilek & Engdahl 2007) document the highly heterogeneous plate coupling of the forearc. The structural diversity of the underthrusting plate in conjunction with fluid-related processes governs the heterogeneous plate coupling offshore Java.

A heterogeneous structure has also been documented for the onshore portion of the upper plate forearc. Two high velocity, rigid blocks sandwich a low velocity anomaly in southern Java, which is interpreted as a weakened contact zone. The predominantly strike-slip focal mechanism of the Mw=6.3 Java event in May of 2006 corresponds to the orientation of this contact zone (Wagner et al. 2007). However, our data lack the resolution to precisely determine the role of upper plate heterogeneity in seismic rupture propagation patterns.

In summary, the complex megathrust interface geometry is the main factor for the observed absence of large (> 8) magnitude earthquakes offshore Java (Newcomb & McCann 1987), while smaller magnitude earthquakes frequently occur. The interplay between the tectonic habitat of the source region and the seismogenesis of large megathrust earthquakes is only crudely understood to date. The topic invites further research in the future to better understand the seismogenic segmentation and the specific geohazard potential of convergent plate boundaries.

**Acknowledgements**

I am indebted to numerous colleagues who have been involved in the Java margin studies. The concepts presented here have evolved from the many discussions with the members of my group at IFM-GEOMAR (D. Hindle, L Planert, M. Scherwath, A. Shulgin, A. Wittwer, J. Zhu and M. Zillmer). The data acquisition would not have been possible without the enthusiastic support of J. Bialas, A. Krabbenhoeft, C. Papenberg, J. Petersen, I. Trummer, D. Wagner. Special thanks go out to E. R. Flueh for his readiness to lead the cruises. W. Weinrebe is warmly thanked for processing of the multibeam data. The studies were conducted in collaboration with Y. Djajadihardja (BPPT Jakarta), B. Luehr and O. Oncken (GFZ Potsdam), C. Mueller, C. Gaedicke, C. Reichert (BGR Hannover), and W. Rabbel (CAU Kiel). This work would not have been possible without the continuous support of the SONNE program by the German Federal Ministry for Science and Technology BMBF. We are indebted to the captains and crews of RV SONNE for the excellent support and performance at sea. Cruises SO137, SO138, SO176, SO179 and SO190 were supported by grants 03G0137A (GINCO I), 03G0138A (GINCO II), 03GO176A (MERAMEX), 03G03G0190A and 03G0190B (SINDBAD project)). Additional support was supplied by the DFG through the SUNDA project (grant KO2961/1-2) and by the GEOTECHNOLOGIEN program of BMBF and DFG for the SUNDAARC project (grant 03G0579B).

**References**

Abercrombie, R., Antolik, M., Felzer, K. & Ekström, G. 2004. The 1994 Java tsunami earthquake: Slip over a subducting seamount. *Journal of Geophysical Research*, **106**, 6595-6607.

Ammon, C. J., Kanamori, H., Lay, T. & Velasco, A. A. 2006. The 17 July 2006 Java tsunami earthquake. *Geophysical Research Letters*. **33**, L24308, doi:10.1029/2006GL028005.

Audley-Charles, M. G. 1975. The Sumba fracture: a major discontinuity between eastern and western Indonesia. *Tectonophysics*, **26**, 213-228.

Audley-Charles, M. G. 2004. Ocean trench blocked and obliterated by Banda forearc collision with Australian proximal continental slope. *Tectonophysics*, **389**, 65-79.

Baba, T., Hori, T., Hirano, S., Cummins P., Park. J.-O., Kameyama, M. & Kaneda, Y. 2001. Deformation of a seamount subducting beneath an accretionary prism: Constraints from numerical simulation. *Geophysical Research Letters*, **28**, 1827-1830.

Beiersdorf, H. 1999. *Geoscientific investigations at the active convergence zone between the eastern Eurasian and Indo-Australian plates off Indonesia*. BGR Cruise Report SO139 GINCO 3.

Bialas, J. & Flueh, E. R. 1999. Ocean Bottom Seismometers. *Sea Technology*, **40**, 4, 41-46.

Bilek, S. & Engdahl, R. 2007. Rupture characterization and aftershock relocations for the 1994 and 2006 tsunami earthquakes in the Java subduction zone. *Geophysical Research Letters*, **34**, doi:10.1029/2007GL031357.

Bilek, S. & Lay, T., 1999. Rigidity variations with depth along interplate megathrust faults in subduction zones, *Nature*, 400, 443-446.

Bilek, S. & Lay, T., 2002. Tsunami earthquakes possibly widespread manifestations of frictional conditional stability. *Geophys. Res. Lett.,* 29, 14, doi: 10.1029/2002GL015215.

Bilek, S., 2007. Influence of subducting topography on earthquake rupture. In: Dixon, T. & Moore, J.C. (eds) *The seismogenic zone of subduction thrust faults*. Columbia University Press.

Blakely, R. J., Brocher, T. M. & Wells, R. E. 2005. Subduction-zone magnetic anomalies and implications for hydrated forearc mantle, Geology, 33, 6, 445-448.

Bock, Y., Prawirodirdjo, L., Genrich, J. F., Stevens, C. W., McCaffrey, R., Subarya, C., Puntodewo, S. S. O. & Calais, E. 2003. Crustal motion in Indonesia from Global Positioning System measurements. *Journal of Geophysical Research*, **108** (B8), 2367, doi:10.1029/2001JB000324.

Brune, S., Ladage, S., Babeyko, A.Y., Müller, C., Kopp, H. & Sobolev, S.V. 2010a. Submarine landslides at the eastern Sunda margin: observations and tsunami impact assessment. *Natural Hazards*, doi:10.1007/s11069-009-9487-8.

Brune, S., Babeyko, A. Y., Ladage, S. & Soboloev, S. V. 2010b. Landslide tsunami hazard in the Indonesian Sunda Arc. *Natural Hazards and Earth System Sciences,* **10**, 589-604.

Cloos, M. 1992. Thrust-type subduction zone earthquakes and seamount asperities: A physical model for earthquake rupture. *Geology*, **20**, 601–604.

Collot, J.-Y., Marcaillou, B., Sage, F., Michaud, F., Agudelo, W., Charvis, P., Graindorge, D., Gutscher, M.-A. & Spence, G. 2004. Are rupture zone limits of great subduction earthquakes controlled by upper plate structures? Evidence from multichannel seismic reflection data acquired across the northern Ecuador-southwest Colombia margin. *Journal of Geophysical Research*, **109**, doi:10.1029/2004JB003060.

Curray, J. R., Shor, G. S., Raitt, R. W. & Henry M. 1977. Seismic Refraction and Reflection Studies of Crustal Structure of the Eastern Sunda and Western Banda Arcs. *Journal of Geophysical Research*, **82**, 2479-2489.

Dardji, N., Villemin, T. & Rampnous, J.P. 1994. Paleostress and strike-slip movement: the Cimandiri Fault Zone, west Java, Indonesia. *Journal of SE Asian Earth Sciences*, **9**, 3-11.

Dessa, J.-X., Klingelhoefer, F., Graindorge, D., André, C., Permana, H., Gutscher, M.-A., Chauhan, A., Singh, S. C. & the SUMATRA-OBS Science Team. 2009. Megathrust earthquakes can nucleate in the forearc mantle: Evidence from the 2004 Sumatra event. *Geology*, **37**, doi: 10.1130/G25653A.1.

Diament, M., Harjono, H., Karta, K., Deplus, C., Dahrin, D., Zen, M. T., Jr., Gérard, M., Lassal, O., Martin, A. & Malod, J. 1992. Mentawai fault zone off Sumatra: A new key to the geodynamics of western Indonesia. *Geology*, **20**, 3, 259-262, DOI: 10.1130/0091-7613(1992)020<0259:MFZOSA>2.3.CO;2.

Dominguez, S., Malavieille, J. & Lallemand, S. E. 2000. Deformation of accretionary wedges in response to seamount subduction: Insights from sandbox experiments. *Tectonics*, **19**, 1, DOI:10.1029/1999TC900055.

Engdahl, E.R. & Villaseñor, A. 2000. Global Seismicity: 1900–1999. In: Lee, W. H. K., Kanamori, H., Jennings, P. C. & Kisslinger, C. (eds) *International Handbook of Earthquake and Engineering Seismology, Part A* , Academic Press.

Faccenda, M., Taras, T. V. & Burlini, L. 2009. Deep slab hydration induced by bending-related variations in tectonic pressure. *Nature Geoscience*, **2**, 790-793, doi: 10.1038/ngeo656.

Fisher, D., Gardner, T., Sak, P., Sanchez, J., Murphy, K. & Vannucchi, P. 2004. Active thrusting in the inner forearc of an erosive convergent margin, Pacific coast, Costa Rica, *Tectonics*, **23**, doi:10.1029/2002TC001464.

Font, Y. & Lallemand, S. 2009. Subducting oceanic high causes compressional faulting in southernmost Ryukyu forearc as revealed by hypocentral determinations of earthquakes and reflection/refraction seismic data. *Tectonophysics*, **466**, doi:10.1016/j.tecto.2007.11.018.

Fritz, H., Kongko, W., Moore, A., McAdoo, B., Goff, J., Harbitz, C., Uslu, B., Kaligeris, N., Titov, V. & Synolakis, C. E. 2007. Extreme run-up from the 17 July 2006 Java tsunami. *Geophysical Research Letters*, **34**, doi:10.1029/2007GL029404.

Fuller, C. W., Willet, S. D., Fisher, D. & Lu, C. Y. 2006. A thermomechanical wedge model of Taiwan constrained by fission-track thermochronometry. *Tectonophysics*, **425**, doi:10.1016/j.tecto.2006.05.018.

Grevemeyer, I. & Tiwari, T.M. 2006. Overriding plate controls spatial distribution of megathrust earthquakes in the Sunda-Andaman subduction zone. *Earth and Planetary Science Letters,* **251**, 199-208.

Gutscher, M.-A., Kukowski, N., Malavieille, J. & Lallemand, S.1998. Episodic imbricate thrusting and underthrusting: Analog experiments and mechanical analysis applied to the Alaskan accretionary wedge. *Journal of Geophysical Research*, **103**, 10161-10176.

Gerya, T. V., Fossati, D., Cantieni, C. & Seward, D. 2009. Dynamic effects of aseismic ridge subduction: numerical modeling. *European Journal of Mineralogy*, **21**, doi:10.1127/0935-1221/2009/0021-1931.

Hall, R. & Smyth, H. R. 2008. Cenozoic arc processes in Indonesia: Identification of the key influences on the stratigraphic record in active volcanic arcs. *Geological Society of America Special Paper*, **436**, 27–54.

Hamilton, W. 1979. Tectonics of the Indonesian region. *U.S. Geological Survey Professional Paper,* **1078**.

Heine, C., Mueller, R. D. & C. Gaina, C. 2004. Reconstructing the lost Tethys Ocean basin: Convergence history of the SE Asian margin and marine gateways. In: Clift, P. et al. (eds) *Continent-Ocean Interactions Within East Asian Marginal Seas*. Geophysical Monograph Series, American Geophysical Union, Washington D.C., **149**, 37-54.

Heirtzler, J. R., Veevers, J. J., Bolli, H. M., Carter, A. N., Cook, P. J., Krasheninnikov, V., McKnight, B. K., Proto-Decima, F., Renz, G. W., Robinson, P. T., Rocker, K. & Thayer, P. A. 1974. Site 261. Initial Reports of DSDP, **27**, pp. 129-192.

Huchon, P. & Le Pichon, X. 1984. Sunda Strait and Central Sumatra Fault. *Geology*, **12**, 668–672.

Hyndman, R.D., Yamano M. & Oleskevich, D.A. 1997. The seismogenic zone of subduction thrust faults. *Island Arc,* **6**, 3, doi: 10.1111/j.1440-1738.1997.tb00175.x.

Hyndman, R.D. & Peacock, S.M. 2003. Serpentinization of the forearc mantle. *Earth and Planetary Science Letters*, **212**, 417-432.

Isozaki, Y., Maruyama, S. & Furuoka, F. 1990. Accreted oceanic materials in Japan. *Tectonophysics*, **181**. 171-205.

Kanamori, H., 1972. Mechanism of Tsunami earthquakes. *Physics of the Earth and Planetary Interiors*, **6**, 346-359.

Kato, K. & Tsuji, Y. 1995. Tusnami of the Sumba earthquake of August 19, 1977. *Journal of Natural Disaster Sciences*, **17**, 2, 87-100.

Klingelhoefer, F., Gutscher, M.-A., Ladage, S., Dessa, J.-X., Graindorge, D., Franke, D., André, C., Permana, H., Yudistira, T. & Chauhan, A. 2010. Limits of the seismogenic zone in the epicentral region of the 26 December 2004 great Sumatra-Andaman earthquake: Results from seismic refraction and wide-angle reflection surveys and thermal modelling. *Journal of Geophysical Research*, **115**, B01304, doi:10.1029/2009JB006569.

Kopp, H., Flueh, E.R., Klaeschen, D., Bialas, J. & Reichert, C. 2001. Crustal structure of the central Sunda margin at the onset of oblique subduction. *Geophysical Journal International*, **147**, 449-474, doi: 10.1046/j.0956-540x.2001.01547.x.

Kopp, H., Klaeschen, D., Flueh, E.R. & Bialas, J. 2002. Crustal structure of the Java margin from seismic wide-angle and multichannel reflection data. *Journal of Geophysical Research*, **197**, B2, doi:10.1029/2000JB00009.

Kopp, H. & Kukowski, N. 2003. Backstop geometry and accretionary mechanics of the Sunda margin. *Tectonics*, **22**, doi:10.1029/2002TC001420.

Kopp, H., Flueh, E.R., Petersen, C.J., Weinrebe, W., Wittwer, A. & Meramex Scientists. 2006. The Java margin revisited: Evidence for subduction erosion off Java. *Earth and Planetary Science Letters*, **242**, 130-142, doi:10.1016/j.epsl.2005.11.036.

Kopp, H., Weinrebe, W., Ladage, S., Barckhausen, U., Klaeschen, D., Flueh, E. R., Gaedicke, C., Djajadihardja, Y., Grevemeyer, I., Krabbenhoeft, A., Papenberg, C. & Zillmer, M. 2008. Lower slope morphology of the Sumatra trench system. *Basin Research*, doi: 10.1111/j.1365-2117.2008.00381.x.

Kopp, H., Hindle, D., Klaeschen, D., Oncken, O., Reichert, C. & Scholl, D. 2009. Anatomy of the western Java plate interface from depth-migrated seismic images. *Earth and Planetary Science Letters*, doi:10.1016/j.epsl.2009.09.043.

Koulakov, I., Bohm, M., Asch, G., Luehr, B.-G., Manzanares, A., Brotopuspito, K. S., Pak Fauzi, Purbawinata, M. A., Puspito, N. T., Ratdomopurbo, A., Kopp, H., Rabbel, W. & Shevknova, E. 2007. P and S velocity structure of the crust and upper mantle beneath central Java from local tomography inversion. *Journal of Geophysical Research*, **112**, doi:10.1029/2006JB004712.

Krabbenhoeft, A., Weinrebe, W., Kopp, H., Flueh, E. R., Ladage, S., Papenberg, C., Planert, L. & Djajadihardja, Y. 2010. Bathymetry of the Indonesian Sunda margin – relating morphological features of the upper plate slopes to the location and extent of the seismogenic zone. *Natural Hazards and Earth System Sciences*, **10**, 1899-1911, doi:10.5194/nhess-10-1899-2010.

Lelgemann, H., Gutscher, M.-A., Bialas, J., Flueh, E. R., Weinrebe, W. & Reichert, C. 2000. Transtensional basins in the western Sunda Strait. *Geophysical Research Letters*, **27**, 21, 3545-3548.

Litchfield, N., Ellis, S., Berryman, K. & Nicol, A. 2007. Insights into subduction-related uplift along the Hikurangi Margin, New Zealand, using numerical modelling. *Journal of Geophysical Research*, **112**, doi:10.1029/2006JF000535.

Lueschen, E., Mueller, C., Kopp, H., Engels, M., Lutz, R., Planert, L., Shulgin, A. & Djajadihardja, Y. 2010. Structure, evolution and tectonic activity at the Eastern Sunda forearc, Indonesia, from marine seismic investigations. *Tectonophysics*, doi:10.1016/j.tecto.2010.06.008.

Lynnes, C. & Lay, T. 1988. Source process of the Great Sumba Earthquake. *Journal of Geophysical Research*, **93**, 13407-13420.

Malod, J. A., Karta, K., Beslier, M. O. & Zen, M. T., Jr. 1995. From normal to oblique subduction: Tectonic rela- tionships between Java and Sumatra. *Journal of Souteast Asian Earth Sciences*, **12**, 85–93.

Malod, J. A. & Kemal, B. M. 1996. The Sumatra margin: Oblique subduction and lateral displacement of the accretionary prism. In: Hall, R. & Blundell, D. (eds) *Tectonic Evolution of South-east Asia*. Geological Society, London, Special Publications, **106**, 19–28.

Masson D.G., Parson L.M., Milsom J., Nichols G., Sikumbang N., Dwiyanto B. & Kallagher H. 1990. Subduction of seamounts at the Java Trench: a view with long-range sidescan sonar. *Tectonophysics*, 18551– 18565.

Masson D.G. 1991. Fault patterns at outer trench walls. *Marine Geophysical Research*, 13209– 13225.

Mochizuki, K., Yamada, T., Shinohara, M., Yamanaka, Y. & Kanazawa, T. 2008. Weak Interplate Coupling by Seamounts and Repeating M ~ 7 Earthquakes. *Science*, **321**, 5893, 1194-1197, doi:10.1126/science.1160250.

Moore G.F., Curray J.R., Moore, D.G. & Karig, D.E. 1980. Variations in geologic structure along the Sunda Fore Arc, northeastern Indian Ocean. In: Hays, D. E. (ed) *The Tectonic and Geologic Evolution of Southeast Asian Seas and Islands*. Geophysical Monograph, **23**, 145– 160.

Mueller, C. & Neben, S. 2006. *Seismic and geoacoustic investigations along the Sunda-Banda Arc transition*. BGR Cruise Report SO190 Leg 1.

Mueller, C., Kopp, H., Djajadihardja, Y., Barckhausen, U., Ehrhardt, A., Engels, M., Flueh, E. R., Gaedicke, C., Keppler, H., Lutz, R., Lueschen, E., Neben, S., Seeber, L. & Dzulkarnaen, D.P.S. 2008. From subduction to collision: The Sunda-Banda Arc transition. *EOS Transactions*, **89**, 6, 49-60.

Mueller, R.D., Roest, W.R., Royer, J.-Y., Gahagan, L.M. & Sclater, J.G., 1997. Digital isochrons of the world's ocean floor, *Journal of Geophysical Research*, **102**, 3211-3214.

Newcomb, K.R. & McCann, W.R. 1987. Seismic history and seismotectonics of the Sunda Arc. *Journal of Geophysical Research*, **92**, (B1), 421–439.

Oleskevich, D. A., Hyndman, R. D. & Wang, K. 1999. The updip and downdip limits to great subduction earthquakes: Thermal and structural models of Cascadia, south Alaska, SW Japan, and Chile. *Journal of Geophysical Research*, **104** (B7), 14965–14991.

Planert, L., Kopp, H., Lueschen, E., Mueller, C., Flueh, E.R., Shulgin, A., Djajadihardja, Y. & Krabbenhoeft, A. 2010. Lower plate structure and upper plate deformational segmentation at the Sunda-Banda arc transition, Indonesia. *Journal of Geophysical Research*, **115**, doi:10.1029/2009JB006713.

Polet, J. & Thio, H. K. 2003. The 1994 Java tsunami earthquake and its 'normal' aftershocks. *Geophysical Research Letters*, **30**, 9, doi:10.1029/2002GL016806.

Ruff, L., Do Trench Sediments Affect Great Earthquake Occurrence in Subduction Zones? *Pageoph*, **129**, 1-2, 262-282, 1989.

Rutherford, E., Burke, K. & Lytwyn, J. 2001. Tectonic history of Sumba Island, Indonesia, since the Late Cretaceous and its rapid escape into the forearc in the Miocene. *Journal of Asian Earth Sciences*, **19**, 453-479.

Schiller, D. M., Garrad, R. & Prasetyo, L. 1991. Eocene submarine fan sedimentation in southwest Java. Proceedings of IPA 20th Ann. Conv., 125-181.

Schlueter, H. U., Gaedicke, C. Roeser, H.A. Schreckenberger, B. Meyer, H. Reichert, C. Djajadihardja, Y. & Prexl, A. 2002. Tectonic features of the southern Sumatra-western Java forearc of Indonesia. *Tectonics*, **21**, doi:10.1029/2001TC901048.

Scholz, C. & Small, C. 1997. The effect of seamount subduction on seismic coupling. *Geology*, **25**, 487-490.

Shulgin, A., Kopp, H. Mueller, C. Lueschen, E. Planert, L. Engels, M., Flueh, E.R. Krabbenhoeft, A. & Djajadihardja, Y. 2009. Sunda-Banda arc transition: Incipient continent-island arc collision (northwest Australia). *Geophysical Research Letters*, **36**, L10304, doi:10.1029/2009GL037533.

Shulgin, A., Kopp, H. Mueller, C. Planert, L., Lueschen, E., Flueh, E.R. & Djajadihardja, Y. 2010. Structural architecture of oceanic plateau subduction offshore Eastern Java and the potential implications for geohazards. *Geophysical Journal International*, in revision.

Simons, W.J.F., Socquet, A., Vigny, C., Amrosius, B.A.C., Haji Abu, S., Promthong, C., Subarya, C., Sarsito, D.A., Matheussen, S., Morgan, P. & Spakman, W. 2007. A decade of GPS in Southeast Asia: Resolving Sundaland motion and boundaries. *Journal of Geophysical Research*, **112**, B06420, doi: 10.1029/2005JB003868.

Smith, W. H. F. & Sandwell, D. T. 1997. Global seafloor topography from satellite altimetry and ship depth soundings. *Science*, **277**, 1957-1962.

Spence, W. 1986. The 1977 Sumba earthquake series: Evidence for slab pull force acting at a subduction zone. *Journal of Geophysical Research*, **91**, 7225-7329.

Sukamto, R. 1975. Geologic map of Ujung Pandang, Indonesia. Direktorat Geologi, Bandung.

Susilohadi, S., Gaedicke, C. & Erhardt, A. 2005. Neogene structures and sedimentation history along the Sunda forearc basins off southwest Sumatra and southwest Java. *Marine Geology*, **219**, doi:10.1016/j.margeo.2005.05.001.

Tanioka, Y. & Satake, K. 1996. Tsunami generation by horizontal displacement of ocean bottom. *Geophysical Research Letters*, **23**(8), 861–864.

Tanioka, Y., Ruff, L. & Satake, K. 1997. What controls the lateral variation of large earthquake occurrence along the Japan Trench? *Island Arc*, **6**, 3, 261-266, 10.1111/j.1440-1738.1997.tb00176.x

Taylor, F. W., Bevis, M. G., Schutz, B. E., Kuang, D., Recy, J., Calmant, S., Charley, D., Regnier, M., Perin, B., Jackson, M. & Reichenfeld, C. 1995. Geodetic measurements of convergence at the New Hebrides island arc indicate arc fragmentation due to an impinging aseismic ridge. *Geology*, **23**, 1011-1014.

Taylor, F. W., Mann, P., Bevis, M. G., Edwars, R. L., Cheng, H. Cutler, K., Gray, S. C., Burr, G. S., Beck, J. W., Phillips, D. A., Cabioch, G. & Recy, J. 2005. Rapid forearc uplift and subsidence caused by impinging bathymetric features: Examples from the New Hebrides and Solomon arcs. *Tectonics*, **24**, TC6005, doi:10.1029/2004TC001650.

Tregoning P., Brunner F.K., Bock Y., Puntodewo S.S.O., McCaffrey R., Genrich J.F., Calais E., Rais J. & Subarya C. 1994. First geodetic measurement of convergence across the Java Trench. *Geophysical Research Letters*, **21**, 19, 2135– 2138.

Uchida, N., Kirby, S., Okada, T., Hino, R. & Hasegawa, A. 2010. Supraslab earthquake clusters above the subduction plate boundary offshore Sanriku, northeastern Japan: Seismogenesis in a graveyard of detached seamounts? *Journal of Geophysical Research*, **115**, doi:10.1029/2009JB006797.

van Hunen, J., van den Berg, A.P. & Vlaar, N.J. 2002. On the role of subducting oceanic plateaus in the development of shallow flat subduction. *Tectonophysics*, **352**, 317-333.

von Huene, R., Ranero, C. & Scholl, D. 2009. Convergent Margin Structure in High-Quality Geophysical Images and Current Kinematic and Dynamic Models, In: Lallemand, S. & Funiciello, F. (eds) *Subduction Zone Geodynamics,* doi:10.1007/978-3-540-87974-9.

von Huene, R. 2008. When Seamounts subduct. *Science*, 10.1126/science.1162868.

von Huene, R., Ranero, C. & Vannucchi, P. 2004. Generic model of subduction erosion. *Geology*, **32**, 913-916 doi: 10.1130/G20563.1

von Huene, R., Ranero, C.R., & Weinrebe, W. 2000. Quaternary convergent margin tectonics of Costa Rica, segmentation of the Cocos plate, and Central American volcanism. *Tectonics*, **19**, 314–334.

von Huene, R. & Ranero, C.R. 2003. Subduction erosion and basal friction along the sediment-starved convergent margin off Antofagasta, Chile. *Journal of Geophysical Research*, **108**, B2, doi:10.1029/2001JB001569.

Wagner, D., Koulakov, I., Rabbel, W., Luehr, B.-G., Wittwer, A., Kopp, H., Bohm, M., Asch, G. & the MERAMEX Scientists, 2007. Joint inversion of active and passive seismic data in Central Java. *Geophysical Journal International*, **170**, doi: 10.1111/j.1365-246X.2007.03435.x.

Wang, K. & Hu, Y. 2006. Accretionary prisms in subduction earthquake cycles: The theory of dynamic Coulomb wedge. *Journal of Geophysical Research*, **111**, B06410, doi:10.1029/2005JB004094.

Wang, K., Hu, Y., von Huene, R. & Kukowski, N. 2010. Interplate earthquakes as a driver of shallow subduction erosion. *Geology*, **38**, 5, 431-434.

Werner R., Hauff F. & Hoernle K. 2009. *SO-199 CHRISP: Christmas Island Seamount Province and the Investigator Ridge: age and causes of intraplate volcanism and geodynamic evolution of the south-eastern Indian ocean*. IFM-GEOMAR Report, 25.

Wittwer, A. 2010. *Crustal and upper mantle structure of the central Java subduction zone from marine wide-angle seismics,* PhD Thesis, University of Kiel.

Yamada, Y., Yamashita, Y. & Yamamoto, Y. 2010. Submarine landslides at subduction margins: Insights from physical models. *Tectonophysics*, **484**, doi:10.1016/j.tecto.2009.09.007.